

Nano-size Effects on Opto-Electronic,  
Structural and Vibrational Properties of Vanadium and Tungsten  
Oxides Produced by Laser and Ultrasonic Spray Pyrolysis  
Techniques

**Bonex Wakufwa Mwakikunga**

School of Physics

University of the Witwatersrand, Johannesburg

Republic of South Africa



A thesis submitted to the Faculty of Science, University of the Witwatersrand,  
Johannesburg in the Republic of South Africa, in fulfilment of the award of  
the Degree of Doctor of Philosophy

## Abstract

The thesis reviews two pyrolysis techniques - ultrasonic spray pyrolysis (USP) and laser pyrolysis (LP). The two techniques - USP at the Physics LP at the National Laser Centre, CSIR in Pretoria, South Africa - were designed and assembled by the candidate for the purpose of producing two related materials -  $\text{VO}_2$  and  $\text{WO}_3$ . The two smart materials find applications in energy regulation for air conditioning alternatives, gas sensing for pollution control purposes, recording industry and computer memory. The thesis shows the pursuit for small particles of these materials in order to see the change in their properties at nano-scale. Novel structures that were not expected were found - nanowires and nanotips of  $\text{WO}_3$  and nanobelts and nano-ribbons of  $\text{VO}_2$ . The confinement of the  $700\text{ cm}^{-1}$  and  $800\text{ cm}^{-1}$  optical phonons is reported in  $\text{WO}_3$  nanowires, enhanced thermochromism of  $\text{VO}_2$  nano-structures with a hysteresis width of  $80^\circ\text{C}$  is presented, the  $145\text{ cm}^{-1}$  phonon splitting is reported in  $\text{VO}_2$  nanoribbons and attributed to surface phonons as a greater portion of atoms become surface atoms at nanoscale. A number of theoretical models have been proposed in order to explain some inexplicable phenomena: the new solid-vapor-solid growth mechanism of the nanowires, a modified phonon confinement model to suit phonon confinement in nano-ribbons geometry, a model to relate the hysteresis width in the thermochromism of  $\text{VO}_2$  to the ribbon thickness and grain size based on martensitic type of transformations and a simple "charge-up" model to predict how hot the laser-aerosol interaction zone gets at various laser power settings. More questions have been unearthed and these are also addressed and the way forward is proposed.

## **Dedication**

To my uncle, Lackos Kasaye Mwenempiki, for bringing me up and giving me  
education to university level

To Patricia Mwakikunga, my wife,  
for her support and inspiration and having attained the stature of a perfect  
“man”.

To Lusubilo (daughter), Joel (son),  
Sarah (daughter), Baketi (son) and Hattiewright (daughter)  
for their endurance during my long absence from home.

And to my sister, Jenala-Emily my sister and  
our late parents

## Declaration

I declare that this thesis is truly my own original, unaided work. It is being submitted for the Degree of Doctor of Philosophy in the University of the Witwatersrand, Johannesburg, South Africa. This work has not been submitted for any degree or examination in any other university or academic institution

---

*(Signature of candidate)*

This

---

day of

---

in the year of our Lord

---

## Preface

In the middle of 2003, while teaching in Blantyre, Malawi, at the Polytechnic of the University of Malawi, and after failing to get a normal Malawi government scholarship, I made proposal applications to several potential sponsors including the World Bank in Washington to conduct research in a range of areas of physics – condensed matter and solid state, nuclear physics, particle physics *etc.* – toward my MSc. One of the applications was successfully granted by the Joint Japan/World Bank Graduate Scholarship Programme for me to study for my MSc at the School of Physics of the University of the Witwatersrand in Johannesburg, South Africa under the guidance of Dr. Malik Maaza. In February, 2004, I arrived in Johannesburg to commence my studies upon which I was given an immediate task to design and assemble an ultrasonic spray system for the synthesis of thin films. Within three months, I had this system up and running and I successfully deposited VO<sub>2</sub> nanoparticles for the first time. I later also had several samples of WO<sub>3</sub> made from this set up. Upon characterisation with scanning electron microscopy, it was found that the particle size for VO<sub>2</sub> was about 30 nm when my intended particle size was below 10 nm. These results, coupled with others, were enough for me to submit my MSc dissertation through Prof. E. Sideras-Haddad after the now Prof. Maaza had left.

In 2006, just before submission of my MSc, some scientists, Dr. Andrew Forbes, Dr. Sisa Pityana and Mr. Mathew Moodley, from the Council for Scientific and Industrial Research (CSIR), Pretoria, South Africa in the department called National Laser Centre visited me and Prof. E. Sideras-Haddad. Prof. Haddad had some unused funds in a project at the CSIR at that time that had to be used away or they would be returned to the sponsors. I lodged my proposal to use these funds to design and build a system called Laser Pyrolysis which would hopefully bring the particle size to lower than 10 nm- a regime where we expected the VO<sub>2</sub> optical and thermochromic properties and the WO<sub>3</sub> electrochromic and phononic properties to drastically change due to size and quantum effects.

By 2007 the laser pyrolysis project was running smoothly, thanks to Prof. Haddad for the seed funding, with the first report of the realization of  $\text{WO}_3$  nanowires for the first time. I also observed nanobelts in  $\text{VO}_2$ . These results were un-intended and un-expected although they were exciting. The objectives of the research slightly changed as a result. Since the nanowires and nanobelts from laser pyrolysis were obtained only after thermal annealing, the question was “would this procedure work for any particles or was this a special contribution of the  $\text{CO}_2$  laser beam?” To answer this question, I annealed the  $\text{WO}_3$  particles from ultrasonic spray pyrolysis. It was conclusively shown that it was the procedure of annealing rather than the laser that produced nanowires and nanobelt, for these structures were also found in ultrasonic spray pyrolysis particles after annealing them.

Although most of these procedures, results, theoretical models, calculations, interpretations and publications (journal papers and book chapter) were solely initiated and, often accomplished, by me, there were many times when I truly needed guidance from Prof. Elias Sideras-Haddad, Dr. Andrew Forbes and Dr. Christopher Arendse among others. There were times when Elias and I would be in the scanning electron microscopy lab and celebrate and mourn together owing to what we would behold. Andrew was quite instrumental in providing the optics, laser characterization facilities and optical alignment skills. And last but not least, Chris and Elias helped with critical analysis of the characterization procedures and also providing annealing facilities.

## Acknowledgements

The following sponsorships are acknowledged:

- The material, emotional and paternal support from Prof. Elias Sideras-Haddad of the School of Physics at the University of the Witwatersrand and also for supporting the ultrasonic spray pyrolysis assembly that the candidate set up. Dr. Andrew Forbes of the CSIR National Laser Centre for allowing the candidate to introduce, design and implement the laser pyrolysis technique at CSIR and Dr. Christopher J. Arendse of the CSIR NCNSM who, at the time of completion of this thesis, was at the School of Physics at the University of Western Cape for the characterization facility.
- CSIR National Centre for Nano-Structured Materials (NCNSM) in Pretoria, South Africa for the materials characterization facility and PhD post
- The National Research Foundation (NRF) of South Africa in collaboration with the CSIR National Laser Centre (NLC) and the School of Physics for allowing the candidate to set up the laser pyrolysis facility at NLC.
- The Joint Japan-World Bank Graduate Scholarship Program (JJWBGSP) in Washington D.C. for the ultrasonic spray pyrolysis project
- The Polytechnic of the University of Malawi in Blantyre, Malawi for the seed funding and allowing the candidate leave.
- Prof. Malik Maaza for introducing me to the interesting material of VO<sub>2</sub> and its intriguing optical properties.



## Table of Contents

List of Figures.....	12
List of Tables.....	23
List of acronymns.....	24
Chapter 1 Vanadium and Tungsten oxides.....	34
1.1 Introduction.....	34
1.2 The Possible Next 'Big Thing' .....	35
1.3 Nanotechnology-'The Next Big Thing?' .....	38
1.4 Vanadium and Tungsten in South Africa.....	40
1.5 Why VO <sub>2</sub> , WO <sub>3</sub> , ultrasonics spray pyrolysis and laser pyrolysis?.....	41
Chapter 2 Progress in ultrasonic spray pyrolysis and laser pyrolysis.....	47
2.1 Ultrasonic nebulisation phenomenon.....	50
2.2 Capillary wave mechanism.....	51
2.3 Cavitation mechanism.....	56
2.4 A Combination of Capillary and Cavitation hypotheses.....	58
2.5 Effects of Pressure and Temperature on Surface Tension, Density and Viscosity.....	62
2.6 Surface Tension as a Function of Temperature and Pressure.....	62
2.7 Density as a Function of Temperature and Pressure.....	69
2.8 Effect of Pressure and Temperature on Viscosity of Fluids.....	71
2.9 Final Droplet and Particle Size Formulae.....	74

2.10 Theory of Pyrolysis for Materials Processing.....	76
2.11 Ultrasonic spray pyrolysis.....	78
2.12 Laser pyrolysis.....	102
2.12.1 Bowden <i>et al.</i> (1977) low level excitation model.....	103
2.12.2 Models based on resonant ionisation.....	104
2.12.3 Kaldor <i>et al.</i> 's review.....	105
2.12.4 El- Diasty <i>et al.</i> (2003) SiH <sub>4</sub> pyrolysis theory.....	106
Chapter 3 Size Matters: Properties of materials at nano-scale.....	109
3.1 Surface and bulk .....	109
3.2 Lattice vibrations (phonons) in nano-structures.....	111
3.3 Raman spectroscopy of nano-composites.....	116
3.4 Size effects and surface phonons.....	118
3.5 Red-shifts due to size effects.....	119
3.6 Size effects on the thermo-chromism.....	120
Chapter 4 Production of VO <sub>2</sub> and WO <sub>3</sub> nano-structures by Laser Pyrolysis (LP) and Ultrasonic Spray Pyrolysis (USP) .....	124
4.1 Production of VO <sub>2</sub> by Ultrasonic Spray Pyrolysis (USP).....	128
4.2 Production of Tungsten Oxides by USP.....	130
4.3 Post-Synthesis Annealing of the USP-produced WO <sub>3</sub> .....	132
4.4 Laser Pyrolysis .....	132
4.5 Current model for estimating the temperature of the plume at the laser- aerosol interaction region.....	141
4.6 Characterization.....	143

4.6.1 Scanning electron microscopy.....	143
4.6.2 X-ray diffraction (XRD).....	143
4.6.3 Raman spectroscopy.....	144
4.6.4 Atomic force microscopy.....	144
4.6.5 Electronic properties measurement: Co-Linear Four-Point Probes on VO <sub>2</sub> Nano-Ribbons.....	145
Chapter 5 Results and Discussion.....	146
5.1 Results from USP .....	146
5.1.1 First-fruits of VO <sub>2</sub> nanoparticles by USP.....	146
5.1.2 VO <sub>2</sub> nano-ribbons by USP without post-synthesis annealing.....	148
5.1.3 Atomic force microscopy of the VO <sub>2</sub> nano-ribbons.....	154
5.1.4 Structure of the VO <sub>2</sub> ribbons and the particles from USP.....	155
5.1.5. Raman spectroscopy results from VO <sub>x</sub> ribbons .....	162
5.2.1 WO <sub>3</sub> nano-sphere produced by USP at varying furnace temperatures....	168
5.2.2 WO <sub>3</sub> spheres into W <sub>18</sub> O <sub>49</sub> nano-tips and nano-belts after thermal annealing.....	171
5.3 Results from Laser Pyrolysis.....	174
5.3.1 WO <sub>3</sub> nanowires from laser pyrolysis.....	174
5.3.2 Brief review of nanowire growth mechanism.....	182
5.3.3 Need for a new model of nanowire growth mechanism .....	185
5.3.4 The Solid-Vapour-Solid Nanowire Growth Theory .....	187
5.3.5 VO <sub>2</sub> nanobelts from laser pyrolysis.....	188

Chapter 6 Concluding remarks and other research spin-offs from the current study.....	199
6.1 Summary of objectives.....	199
6.2 From USP to LP.....	199
6.3 Discovery of the nanowires in LP.....	200
6.4 From Laser Pyrolysis Back to Ultrasonic Spray Pyrolysis - Role of annealing in the realization of one-dimensional growth.....	200
6.5 Change of Properties at the Nanoscale .....	201
6.7 Research spin-offs and new possible projects from this study.....	202

## List of Figures

Fig 1.1 Relative abundance of silicon in our galaxy [from <a href="http://en.wikipedia.org/wiki/File:SolarSystemAbundances.jpg">http://en.wikipedia.org/wiki/File:SolarSystemAbundances.jpg</a> ].....	38
Fig 1.2 Map of South Africa showing the two major region-shown expanded by arrows- where the important materials covered in this study are found- (a) Okiep district in Northern Cape province known to have $WO_3$ reserves and (b) Brits, North West Province where there are mines for Vanadium ores...40	
Fig. 2.1 An illustration of generalized chemical deposition methods.....	49
Fig. 2.2 A sketch showing idealized droplet formation from standing-wave crests showing one period of wall vibration. Note that Ref. 53 carried out a thorough stability analysis of wave formation which included the film thickness, $h$ , wall-vibration amplitude, $a$ , and viscosity, $\mu$ in addition to the parameters of forcing frequency, $f$ , surface tension, $\sigma$ , and liquid density, $\rho$ , which were in the original work of Kelvin as reported in Ref. 43. Permission from The Royal Society, A. J. Yule & Y. Al-Suleimani, Proc. R. Soc. Lond. A 456, 1069 (2000) .....	53
Fig. 2.3 Plots for correlations E and H of water droplets. The dotted line is a line that indicates the points where calculated quantity is exactly equal to the experimentally measured quantity.....	60
Fig. 2.4 A typical parity plot for a Newtonian liquid, glycerine (From Ref. 117).....	61

Fig. 2.5 Pressure and temperature dependence of the surface tension $\sigma$ in the system methane-water; all data published in Ref. 119 until 1995. $\Delta$ , Ref. 120; $\bullet$ , Ref. 121; $\oplus$ , Ref. 122 and $\circ$ , Ref. 123.....	65
Fig. 2.6 Surface tension as a function of temperature and pressure [From Park <i>et al.</i> , J. Phys. Chem. (2007)].....	67
Fig. 2.7 Sketches in Mathematica of how density varies with (a) pressure and (b) temperature from Eq. 34 (Density values are not realistic and are not specific to any materials).....	70
Fig. 2.8 Variation of viscosity with pressure and temperature (a) and temperature (b) for jet lube Mil L23699 (open circles) and a traction liquid (closed circles) [S. Bair <i>et al.</i> (2001)].....	72
Fig. 2.9 A Mathematica plot showing the variation of droplet size with liquid temperature .....	76
Fig. 2.10 Experimental observation of the dependency of droplet and hence particle size on nebuliser frequency (a) and precursor concentration (b). From S. Gurmen <i>et al.</i> , Mater. Res. Bull. (2006) Ref. 139.....	77
Fig. 2.11 A nebulised spray pyrolysis by C.N.R. Rao's group (from Ref. 241).	80
Fig. 2.12 A typical example of an ultrasonic spray pyrolysis employing a multi-zone furnace for control of product shape, particle size and other parameters. From Taniguchi's group Ref 194. ....	82
Fig. 2.13 Scheme of the asynchronous-pulse ultrasonic spray pyrolysis (APUSP) method used to obtain $\text{Bi}_2\text{S}_3$ rod-like particle thin films with (1) substrate, (2) furnace, (3) spray nozzles, (4) carrier gas, (5) solution, (6)	

membrane and (7) ultrasonicator. From S.- Y. Wang *et al.* (2002), *J. Cryst. Growth* (Ref. 242)..... **82**

Fig. 2.14 Example of a USP system where the precursor liquid flow passes through the nebuliser (a) From Lee *et al.* [274] , (b) From Patil & Patil (2000) [256,260] and (c) the substrate is cut into several plates so that several samples are made out one run. From Baykul & Balcioglu, *Microelectronic Eng.* (2000) [259] ..... **84**

Fig. 2.15 An example of a USP set-up where both the precursor solution container and the particle collector are maintained at controlled temperature (right). Zinc oxide-dispersed silver particles by spray pyrolysis of colloidal solution. From Kang and Park, *Mater. Lett.* 1999..... **85**

Fig. 2.16 Microstructure of the surface of the thin films deposited on quartz substrates. The films (a), (b) and (c) were deposited at 873, 923 and 1023 K respectively. (d) An illustration of the Infrared USP (e) Grain size as a function of temperature of the substrate. From Matsuzaki *et al.*, *TSE* (1999) [263]..... **86**

Fig. 2.17 (a) Electrostatic assisted USP (EAUSP), note that aerosol are directed onto the substrate from the top From Chen *et al.*, *Mater. Res. Bul*, 2007 [Ref. 140] (c) Electrostatic spray deposition (ESD); note that deposition is from bottom to top From Zaouk *et al.*, *Micro Eng.* 2000 [Ref. 175]..... **89**

Fig. 2.18 Flame assisted USP (FAUSP) From: Chen *et al.*, *Eur. J. Solid State & Inorg. Chem.* (1998) ..... **91**

Fig. 2.19 The figure shows the effect of calcination temperature on morphology and crystallinity of  $\text{Co}_3\text{O}_4$ ,  $\text{CuO}$  and  $\text{NiO}$ . From S. W. Oh *et al.*, *J. Power Sources* (2007) [Ref. 182]..... 92

Fig. 2.20 Effect of furnace temperature during synthesis on the morphology and crystallinity of  $\text{BZrO}_3$  nanopowders by USP (from M.M. Bucko & J. Obłakowski, *J Eur Ceram Soc.*, (2007) [Ref. 284]).....94

Fig. 2.21 (a) and (b) SEM images of hydroxyapatite (Hap) powders by the USP/SAD method showing the gaping hole in one of the spheres in (b) an indication of the possibly hollow nature of these spheres [Permission from G.-H. An *et al.*, *Mater. Sci. Eng.* (2007) Ref. 163] (c) More vivid proof of hollow  $\text{NiO-Sm}_{0.2}\text{Ce}_{0.8}\text{O}_{1.9}$  composite spheres [S. Suda *et al.*, *Solid State Ionics* (2006) Ref. 185] (d) and (e) HRTEM image of  $\text{LiFePO}_4/\text{C}$  composite prepared at  $450^\circ\text{C}$  showing a shell structure and the intersection of the shells of other spheres [From M. R. Yang, *J. Power Sources* (2006) Ref. 180] (f) A conceptual model proposed by Yang *et al.* (2006) on how the hollow  $\text{LiFePO}_4/\text{C}$  composites form with or without voids..... 95

Fig. 2.22 Examples of XRD, SEM and TEM micrographs of  $\text{LiMn}_2\text{O}_4$  particles prepared from various precursors (1) dense  $\text{LiMn}_2\text{O}_4$  with porous surface structure (2) hollow  $\text{LiMn}_2\text{O}_4$  particles with hybrid surface structure (3) hollow  $\text{LiMn}_2\text{O}_4$  particles with smooth surface structure and (4) hollow  $\text{LiMn}_2\text{O}_4$  with shrinkage surface structure. From Matsuda & Taniguchi, *Journal of Power Sources* (2004) [Ref. 217] ..... 97



Fig. 2.23 SEM images of ZnO microrods deposited by USP at (a) 550°C (b) 500°C, (c) 450°C and (d) 400°C [From U. Alver <i>et al.</i> , Mater. Chem. Phys. (2007) Ref. 147].....	<b>98</b>
Fig. 2.24 ZnO samples grown from one kind of precursor for 120 mins at (a) 300°C, (b) 400°C, (c) 500°C and another kind of precursor for same period of time at (d) 300°C, (e) 400°C and (f) 500°C [From Htay <i>et al.</i> , Jpn J Appl. Phys. (2007) Ref.248].....	<b>99</b>
Fig. 2.25 Annual frequency of publications on laser pyrolysis from 1974 to 2008.....	<b>102</b>
Fig. 3.1 The difference between surface and bulk atoms. In 2D, surface atoms are each surrounded by about 3 other atoms whereas the inner (bulk) atoms are surrounded by at least 6 atoms.....	<b>110</b>
Fig. 3.2 Real space and q-space illustration of how the three-dimensional confinement, $d^3q$ , is transformed to two-dimensional confinement $2\pi qdq$ in a nanowire.....	<b>116</b>
Fig. 3.4 Hysteresis loops for heating-up and cooling-down cycles in VO <sub>2</sub> thin films and VO <sub>2</sub> nanocrystals. Note the variations in the hysteresis width and hysteresis jump as the size of the VO <sub>2</sub> crystals tends to nano-scale.....	<b>123</b>
Fig. 4.1 Schematic set up of USP: (1) ultrasonic nebuliser transducer, (2) precursor liquid (3) carrier gas inlet (4) nebuliser power supplier (5) connecting bellow (6) quartz tube (7) tube furnace (8) substrate (9) substrate holder (10) exhaust pipe (11) temperature controller. (From the Ref. 41)....	<b>130</b>

Fig. 4.2 The outline of the laser pyrolysis set up: (1) laser beam (2) focussing lens (3) stepper-motor (4) substrate (5) three-way nozzle (6) argon gas inlet (7) carrier gas inlet (8) precursor liquid droplets and carrier gas inlet (9) power meter (From Ref. 41)..... **133**

Fig.4.3 (a) FTIR spectra of some of the precursor materials used in this study showing the absorption bands that fall close to the CO<sub>2</sub> laser frequency.... **136**

Fig. 4.3(b) A schematic of the laser beam delivery for the synthesis of tungsten trioxide by laser pyrolysis, with the six arm pyrolysis chamber shown (two arms are in and out of the page). The HeNe laser was used only for visible alignment of the infrared laser beam. The final focussing element was a 2 m curvature gold coated mirror..... **138**

Fig. 4.4 (a) when the precursor flow-rate is larger than the encapsulating carrier gas (Ar) and (b) when the precursor flow-rate is smaller than the flow-rate of Ar. The precursor is driven either by C<sub>2</sub>H<sub>2</sub> or O<sub>2</sub>. The particle deposition in (a) has profile of a hump whereas the deposition in (b) has a vacancy at the centre as indicated on the substrates..... **139**

Fig 4.5 Laser power as it affects the temperature of the C/O atoms moving transversally to the laser beam direction. The fitted curve is from the present theory and the straight line graph is from the model by Bowden *et al.* (1977)..... **142**

Fig. 5.1 First report on the production of VO<sub>2</sub> by USP (a) Undecomposed AMV precursor (b) Decomposed AMV into a mixture of V<sub>2</sub>O<sub>5</sub> and VO<sub>2</sub> (B) (c)

monoclinic VO <sub>2</sub> (d) transmittance at various temperature and (e) hysteresis plots characteristic of VO <sub>2</sub> .....	<b>147</b>
Fig. 5.2 Scanning micrographs of VO <sub>2</sub> nano-particles synthesized on Corning glass in 11 L/min of argon with a deposition time of 25 min at (a) 600°C (inset is EDS) (b) 700°C (EDS in inset) .....	<b>150</b>
Fig. 5.3 Size distribution of the particles of VO <sub>2</sub> on the samples grown by USP at 600°C .....	<b>151</b>
Fig. 5.4 SEM micrographs of VO <sub>2</sub> nano-ribbons a low resolution image showing the overall density of the nanostructures with an inset the same on a different spot of the sample.....	<b>152</b>
Fig. 5.5 SEM micrographs of VO <sub>2</sub> nano-ribbons (a) a higher resolution with (b) an EDS spectrum showing the V and O peaks. Note how the image reveals how gossamer (transparent) to electron the ribbons are. ....	<b>153</b>
Fig. 5.6 Cross-sectional SEM image of the VO <sub>2</sub> sample prepared by USP Inset (a) is a close-up of the interface between the borosilicate substrate and the VO <sub>2</sub> layer exposing the in-homogeneity of this layer (b) the arrangement of the cross-sectional SEM experiment.....	<b>154</b>
Fig. 5.7 (left) AFM images of a single VO <sub>2</sub> nano-ribbon. The profile (right) shows that the VO <sub>2</sub> ribbon is typically 10 nm thick.....	<b>155</b>
Fig. 5.8 X-ray diffraction of the VO <sub>2</sub> nano-ribbons from USP showing the diminishing presence of VO <sub>2</sub> (A) and V <sub>2</sub> O <sub>5</sub> as the furnace temperature is raised from 400°C in argon (b) to 700 °C in argon (a) and at 700°C in hydrogen (c). A broad hump from 2θ = 20 – 40° is from the SiO <sub>2</sub> substrate..	<b>157</b>

Fig. 5.9 Transmission electron microscopy, SAED pattern and local EDS on a single VO<sub>x</sub> nano-ribbon revealed bi-layered structure: V<sub>2</sub>O<sub>5</sub> and VO<sub>2</sub>. Lattice parameters for the two regions are as indicated. Inset (a) and (b) are SAED patterns for V<sub>2</sub>O<sub>5</sub> and VO<sub>2</sub> regions respectively and inset (c) and (d) are local EDS spectra of outer V<sub>2</sub>O<sub>5</sub> and core VO<sub>2</sub> layers respectively. (Detector used was Gatan 1000 camera, accelerating voltage =200 kV and for EDX, the spot size was 1μm and the take off angle of 15°)..... 158

Fig 5.10 Illustration of phonon geometry in a slab..... 162

Fig. 5.11 (a) Raman spectroscopy of VO<sub>2</sub> nanoribbons of different thickness; the new phonon confinement equation 61 has been fitted to the 10 nm thick ribbon data. The 5 nm ribbon data has been described by phonon splitting of equation 64. Compare the TO-splitting in VO<sub>2</sub> nanoribbons with the LO-splitting (c) in WO<sub>3</sub> nano-platelets (b) with details in the text..... 165

Fig. 5.12 The VO<sub>2</sub> TO phonon (145 cm<sup>-1</sup>) splitting as a function of VO<sub>2</sub> ribbon thickness suggesting that the splitting increases as ribbon thickness decreases. The inverse nature of the present results agrees with the theory and experiment on LO phonons in ZnSe quantum wires from Lerman *et al.* (see text) and the TO splitting in GaAs quantum wires as discussed by Volodin *et al.* (see text for details)..... 166

Fig. 5.13 WO<sub>3</sub> nanospheres obtained by ultrasonic spray pyrolysis (Mwakikunga et al [42]) at various temperatures ..... 168

Fig. 5.14 The decrease in diameter of $WO_3$ nanospheres as USP furnace temperature is raised (Mwakikunga et al [42]) .....	<b>169</b>
Fig. 5.15 $W_{18}O_{49}$ nanowires and nanotips after annealing the $WO_3$ nanospheres produced by USP .....	<b>170</b>
Fig. 5.16. Low resolution TEM of $W_{18}O_{49}$ nanotips (Mwakikunga et al [42]).	<b>171</b>
Fig 5.17 FEGSEM micrographs of $WO_3$ nano-rods grown under $O_2$ as a central carrier gas and $C_2H_2$ as the secondary carrier gas showing a thin film that has flaked up into orderly slabs between which are numerous nano-wires. Inset (a) shows a close look at the nano-wires in between the slabs. Inset (b) zooms in onto the nano-wire area and inset (c) display one nano-wire's end. ....	<b>174</b>
Fig 5.18. Optical phonon confinement observed by the asymmetrical broadening of the $WO_3$ 's $700\text{ cm}^{-1}$ and $800\text{ cm}^{-1}$ phonon peaks (Mwakikunga et al [42]). Eq. 3.6 fitted and shown in red .....	<b>175</b>
Fig 5.19 Scanning electron micrographs of $WO_3$ nano-rods grown under $C_2H_2$ as a central carrier gas and oxygen as the secondary carrier gas; the spherical droplets from the precursor maintain their shape until their deposition into micro-particles. Inset (a) is a micro-particle before annealing showing the genesis of the growth of a nano-wire. After annealing there are numerous nano-wires growing from and in between the spheres. Dotted box (b) shows a region where a number of nano-wires are seen sprouting from spheres...	<b>177</b>

Fig. 5.20 TEM micrograph of a single WO<sub>3</sub> nanowire in (b) reveals that the nanowire is a core with a shell of carbon, Au and Pd from pre-to-SEM coating as confirmed by EDS in (a) and (c). In (d) is the micrograph of carbon nanotube found segregated by the WO<sub>3</sub> nano-wires ..... **178**

Fig. 5.21 (a) The micro-spheres of WO<sub>3</sub> are but agglomerates of yet smaller nano-spheres. The nanospheres' size distribution in (c) showing the most probable diameter of 185 nm and nanowires seen propping up a ball of nanospheres in (b) ..... **180**

Fig. 5.22 (a) In situ TEM heating of the WO<sub>3</sub> nanospheres with the sphere images taken at different times as indicated (b) sphere diameter as a function of time due to in situ heating ..... **181**

Fig. 5.23 (a) length of nanowire versus its diameter and length versus 1/d<sup>2</sup> fitted with Eq. 5.16 and (b) aspect ratio of the nanowire versus d and 1/d<sup>3</sup> fitted with Eq. 5.16 divided by d ..... **191**

Fig. 5.24 Scanning electron micrographs of VO<sub>2</sub> nano-rods grown from VCl<sub>4</sub> + ethanol under oxygen as a central carrier gas and C<sub>2</sub>H<sub>2</sub> as the secondary carrier gas ..... **192**

Fig. 5.25 (a) Scanning electron micrographs of VO<sub>2</sub> nano-rods grown from aqueous V<sub>2</sub>O<sub>5</sub> under C<sub>2</sub>H<sub>2</sub> as a carrier gas (inset) typical dense distribution of the belts at low resolution (b) low resolution TEM image of bamboo structured carbon nanotube found amidst the VO<sub>2</sub> ribbons and (c) a higher magnification of the CNT showing disorder amidst ordered growth ..... **193**

Fig 5.26 Resistance of a VO<sub>2</sub> nanoribbon film versus temperature for heating and cooling phases showing an enhanced hysteresis ..... **194**

Fig 5.27 (a) HW against d: The numbers over each point indicate source of data: (1) Current work (unpublished), (2,3,4) Lopez *et al.* , Ref. 429, (5) Miyazaki *et al.* , Ref. 432 (6) Choi *et al.*, Ref 433, (7,9) Current work, Ref. 39, (8) Kivaisi *et al.* , Ref. 434 (b) HW against d<sup>-0.5</sup> showing the linearity limited to bulk VO<sub>2</sub>; at nanoscale, linearity is broken as illustrated with a broken line in order to guide the eye ..... **197**

## List of Tables

Table 3.1 The surface to volume ratio expression for various structures...	111
Table 3.2 Lattice parameters for the four polymorphs of VO <sub>2</sub> .....	121
Table 4.1 Experimental parameters for the production of various VO <sub>2</sub> ....	131
Table 4.2 Experimental parameters for the production of various WO <sub>3</sub> samples .....	131
Table 4.3 Experimental parameters for the annealing of WO <sub>3</sub> samples...	132
Table 4.4 Experimental variables for the production of vanadium oxides by LP.....	140
Table 4.5 Experimental variables for the production of tungsten oxides by LP.....	140
Table 5.1 Calculated Miller indices for the system VO <sub>2</sub> (B).....	155
Appendix T1 Precursors, target materials and the synthesis condition by USP.....	260
Appendix T2 List by year of materials synthesized by laser pyrolysis from 1974 .....	262



## Appendices: Publications included in this Thesis

- A1 B. W. Mwakikunga, Elias Sideras-Haddad and Malik Maaza, *First synthesis of vanadium dioxide by ultrasonic nebula-spray pyrolysis*, *Optical Mater* 29(5), 481 (2007) [doi:10.1016/j.optmat.2005.10.007](https://doi.org/10.1016/j.optmat.2005.10.007) ..... 264
- A2 B. W. Mwakikunga, E. Sideras-Haddad, M. Witcomb, C. Arendse, A. Forbes, *WO<sub>3</sub> nano-spheres into W<sub>18</sub>O<sub>49</sub> one-dimensional nano – structures through thermal annealing*, *J. Nanosci. & Nanotechnol* 9, 3286 (2008) [doi:10.1166/jnn.2008.VC12](https://doi.org/10.1166/jnn.2008.VC12) ..... 271
- A3 B. W. Mwakikunga, A. Forbes, E. Sideras-Haddad, R M Erasmus, G. Katumba, B. Masina, *Synthesis of tungsten oxide nanostructures by laser pyrolysis*, *Int. J. Nanoparticles* 1, 3 (2008) [doi:10.1504/IJNP.2008.020895](https://doi.org/10.1504/IJNP.2008.020895) ..... 280
- A4 B. W. Mwakikunga, A. Forbes, E. Sideras-Haddad, C. Arendse, *Raman spectroscopy of WO<sub>3</sub> nanowires and thermochromism study of VO<sub>2</sub> belts produced by ultrasonic spray and laser pyrolysis techniques*, *Phys. Stat. Solidi (a)* 205, 150 (2008) [doi:10.1002/pssa.200776829](https://doi.org/10.1002/pssa.200776829) ..... 298
- A5 B. W. Mwakikunga, A. Forbes, E. Sideras-Haddad, C. Arendse, *Optimization, yield studies and morphology of WO<sub>3</sub> nanowires synthesized by laser pyrolysis in C<sub>2</sub>H<sub>2</sub> and O<sub>2</sub> ambients – validation of a new growth mechanism*, *Nanoscale Res. Lett.* 3, 372 (2008) [doi: 10.1007/s11671-008-9169-6](https://doi.org/10.1007/s11671-008-9169-6) ..... 300
- A6 B. W. Mwakikunga, E. Sideras-Haddad, C. Arendse and A. Forbes, *Can universal conductance fluctuations (UCFs) be observed at temperatures above room temperature at nanoscale?*, *OAtube Nanotechnol.* 2, 109 (2009) <http://www.oatube.org/2009/01/bwmwakikunga.html> (Page...)

A7 B. W. Mwakikunga, E. Sideras-Haddad, C. Arendse, A. Forbes, P. C. Eklund, T. Malwela, T. K. Hillie, S. Sinha-Ray, VO<sub>2</sub> nano-ribbon growth by ultrasonic spray pyrolysis and the nano-scale effects on the thermo-chromism, novel electronic conductivity and phonon dynamics, Nano Lett (2009) (under internal review) **(Page...)**

A8 **Invited Chapter:** B. W. Mwakikunga, E. Sideras-Haddad, A. Forbes, S. S. Ray, C. Arendse, G. Katumba, *Thermochromism of VO<sub>2</sub> at Nanoscale* to appear in *Chromic Materials, Phenomena and Their Applications* (Ed. P. Somani), Applied Science Innovations Private Limited (ASIPL), Maharashtra, India (2009) **(Page...)**

## Publications co-authored and discussed but not included in this Thesis

- [9] E. Sideras-Haddad, T. Schenkel, D. B. Rebuli, A. Persaud, S. Shrivastava, D. H. Schneider, B. Mwakikunga, *Electron emission and defect formation in the interaction of slow, highly charged ions with diamond surfaces*, Nucl Instrum & Methods in Phys Res. 256 (1), 464-467 (2007) [doi:10.1016/j.nimb.2006.12.098](https://doi.org/10.1016/j.nimb.2006.12.098)
- [10] G. Katumba, L. Olumekor, A. Forbes, G. Makiwa, B. Mwakikunga, J. Lu, E. Wackelgard, *Optical, thermal and structural characteristics of carbon nanoparticles embedded in ZnO and NiO as selective solar absorbers*, Solar Energy Mater & Solar Cells 92, 1285 (2008) [doi:10.1016/j.solmat.2008.04.023](https://doi.org/10.1016/j.solmat.2008.04.023)
- [11] G. Katumba, B. W. Mwakikunga and T. R. Mothibinyane, *FTIR and Raman Spectroscopy of Carbon Nanoparticles in SiO<sub>2</sub>, ZnO and NiO Matrices*, Nanoscale Res Lett 3, 421 (2008) [doi: 10.1007/s11671-008-9172-y](https://doi.org/10.1007/s11671-008-9172-y)
- [12] C. J. Arendse, G. F. Malgas, T. F. G. Muller, D. Knoesen, C. J. Oliphant, D. E. Motaung, B. W. Mwakikunga, *Thermally induced nano-structural and optical changes of nc-Si:H deposited by hot-wire CVD*, Nanoscale Res Lett 4, 308 (2009) [doi:10.1007/s11671-008-9243-0](https://doi.org/10.1007/s11671-008-9243-0)

### Papers the candidate has peer-reviewed

- (1) L. Jiang, X. Wang, C. Liu, H. Xiao, J. Ran, C. Wang, G. Hu, J. Li and J. Li, *Structural and magnetic properties of Sm implanted GaN*, J. Nanosci. & Nanotechnol. (2008), (in press)
- (2) H. Bai, B. Reedy, A. Dowd, M. Cortie, *Characterization of transition in nanoparticle VO<sub>2</sub> prepared by aqueous method*, Mater. Lett. (2008) (rejected)
- (3) W. Wu, D. Dey, O. G. Memis, A. Katsnelson, H. Mohseni, "*Fabrication of large area periodic nanostructures using nanosphere photolithography*" Nanoscale Res Lett. 3, 123 (2008)
- (4) M. Watanabe, H. Takamura, H. Sugai, *Preparation of ultrafine Fe-Pt alloy and Au nanoparticle colloids by KrF excimer laser solution photolysis*, Nanoscale Res. Lett. (in review Jan, 2009)

### **Symposia co-organized by candidate**

- (1) Symposium title: Light and sound for nanosynthesis and characterization  
Virtual Conference on Nanoscale Science and Technology, University of  
Arkansas, Fayetteville, Arkansas, USA 24<sup>th</sup> – 29<sup>th</sup> July, 2008
- (2) International Organizing Committee, Villa Conference on Interaction  
Among Nanostructures (VCIAN), St. Thomas, US Virgin Islands, 6-11<sup>th</sup>  
September 2009. Organised by the Physics Department of the University of  
Arkansas, Arkansas, USA.

## List of Acronymns

APUSP	asynchronous pulse USP
CNT	carbon nanotube
CVD	chemical vapour deposition
EAUSP	electrostatically activated USP
EBIT	electron beam ion trap
FAUSP	flame assisted USP
FET	field effect transistor
HFCVD	hot filament CVD
HOPG	highly oriented pyrolytic graphite
HRTEM	high resolution TEM
HWCVD	hot wire CVD
LP	laser pyrolysis
N-V	nitrogen vacancy centre
PECVD	plasma enhanced CVD
SEM	scanning electron microscope
TEM	transmission electron microscopy
USP	ultrasonic spray pyrolysis
$a,b,c$	lattice parameters of the unit cell
$\alpha$	absorption coefficient
$\beta$	$1/k_{\text{B}}T$
$k_{\text{B}}$	Boltzmann's constant
$\hbar$	Planck's constant

$H_l$	depth of liquid from the nebulizer surface
$\phi$	rate potential in capillary waves
$\lambda$	wavelength of capillary waves
$\mu$	viscosity of precursor liquid
$\mu_c$	chemical potential of precursor liquid
$\nu$	frequency of photons
$\Pi$	parachor, a constant that depends on temperature of liquid and its vapor
$\rho$	density of precursor liquid
$\rho_v$	density of vapor
$\sigma$	surface tension of precursor liquid
$\tau$	$1-T/T_c$
$T_c, P_c, Z_c$	critical temperature, pressure and compressibility factor
$T_0, P_0$	room temperature and atmospheric pressure
$T_g$	glass transition temperature
$\mu_g$	viscosity at glass transition temperature
$m_{pr}$	mass of solute precursor material
$M_{pr}$	molar mass of precursor material
$C_{pr}$	concentration of precursor solution
$m_p$	mass of deposited particles
$M_p$	molar mass of deposited particles
$\rho_p$	density of deposited particle material
$d$	diameter of deposited particles

$t_{res}$	time of residence of droplet in the reactor
$L$	length of reactor
$d_L$	diameter of the reactor
$Q_0$	volumetric flow rate of precursor droplets
$\xi$	amplitude of capillary waves
$\zeta$	function of liquid state and vapor state densities and temperatures
$f$	frequency of capillary waves
$F$	frequency of ultrasound from nebulizer
$D_L$	Lang's droplet diameter
$k_j$	wavenumber in Jokanovic's capillary waves
$t_j$	thickness of skin in Jokanovic's capillary waves
$k_M$	proportionality constant in Mwakikunga's droplet equation
$A$	surface area acted upon by cavitation waves
$We$	Weber's number
$Oh$	Ohnesorge's number
$I_N$	intensity number
$A_m$	amplitude of cavitation waves
$v_s$	velocity of sound
$k_R$	constant in Rayleigh's cavitation droplet diameter
$k_W$	constant in Walzel's cavitation droplet diameter
$k_D$	constant in Davies's cavitation droplet diameter
$H_D$	height difference in Lynde's manometer



$r_{\text{tube}}$	radius of tube
$k_{\sigma}$	proportionality constant in Palmer's theory of fluids
$N_0$	number of molecules at surface
$n_{\text{bulk}}$	number of molecules in the bulk
$H$	energy required to increase the area of the liquid in contact with air by a unit area
$\omega$	vibrational frequency
$\omega_0$	zone centre frequency in Raman spectroscopy or resonant frequency
$\omega_R$	Rabi frequency
$\Delta$	detuning: difference between the vibrational and resonant frequencies
$\Delta v_L$	Lorentz's pressure broadening
$\Delta v_D$	Doppler pressure broadening
$\Gamma_0$	full width at half maximum of Raman peaks of bulk materials
$\Omega_R$	coherence exchange rate
$\perp$	perpendicular
$\sigma_A$	absorption cross-section
$\sigma_0$	absorption cross-section without pressure broadening
$\sigma_{\text{surf}}$	surf-to-volume ratio
$I_D$	intensity of the Raman's disorder peak in carbon allotropes
$I_G$	intensity of the Raman's graphite peak

$C(\lambda)$	Tuinstra and Koenig constant dependent on the laser wavelength in a Raman spectrometer
$L_g$	diameter of grain
$ C(0,q) ^2$	Lorentz's coefficient which may be Gaussian, sine or any peak function
$A_0$	prefactor in the Richter's phonon confinement model
$\omega_{SO}$	frequency of surface optical phonons
$\omega_{LO}$	frequency of longitudinal-optical phonons
$\omega_{TO}$	frequency of transverse-optical phonons
$\epsilon$	dielectric constant
$\epsilon_M$	dielectric constant of surrounding medium
$\epsilon_\infty$	high frequency dielectric constant of the material
$\gamma$	exponent, integer
$\eta$	damping coefficient during laser-droplet interactions

## Chapter 1

### Vanadium and Tungsten Oxides

#### 1.2 Introduction

Just as it was at the ushering-in of the “computer age”, it seems history is repeating itself in the ushering-in of what would, in the present study, be called the “quantum computer age”. At that time, there were so many proposals as to how the computer would work. From Blaise Pascal and his calculating machine [1], a bunch of cogs and wheels, to Konrad Zuse [2] with the first microprocessor more and more advances and proposals were made to improve computation. A computer at that time would occupy a large laboratory room with cooling systems to control heating as cogs would move and relay the right motion through the assemblage for one single operation. The vacuum tube, after the discovery of the electron by J. J. Thompson, was a great improvement to the electronics industry. Diodes, triodes, pentodes and transistors based on “thermionics”, as it soon came to be called, quickly came on the market for device making. The computer was one of the beneficiaries of this great achievement. The thermionic transistor, whose operation is based on an incandescent light bulb with an anode and a gate, could amplify, process and transmit information but at the expense of a lot of energy loss through heat. It was only the Nobel-winning silicon semiconductor transistor by Brattain, Shockley and Bardeen [3] in 1947 that revolutionized the electronics world by changing the size of the circuits by a great number of orders of magnitude. Indeed silicon with its 4-valent bonding, its abundance

in nature (sand) and its excellent semiconducting properties emerged as the material of choice for the electronics world and silicon still rules this industry today. This is the time when physics truly needed chemistry in addition to other disciplines to make any project in this area successful.

However, miniaturizing on a silicon wafer seems has reached its limits. Moore's law [4] predicted a doubling of components per unit area on a chip every year. This was true for so many years. It has now become clear that the rate of miniaturizing is going at a slow pace in the few recent years. It has proven difficult to go beyond the micro-electronics where technology is right now. This saturation is natural. Problems include current leakage and subsequent short circuits as components become very close to each other to a distance where tunnelling is possible. The question has been, "What shall the next 'big thing' be?"

## **1.2 The Possible Next 'Big Thing'**

On the parallel, at the beginning of the 20<sup>th</sup> century, laws of physics that were prevailing at the time, referred to as classical physics at present, were increasingly failing to explain a number of newly observed phenomena including the blackbody radiation and the so-called 'ultraviolet catastrophe', the photo-electric effect, the structure of the atom and the like. It was apparent that as objects got smaller, their behaviour and properties showed steps or "quanta"- some steps allowed and other not allowed. The birth of

quantum physics gave the world a revolutionary way of looking at the universe – that matter can exist as waves (de Broglie’s wavelength), that waves can be thought of as being packets or particles with quite a list of names for particles that mediate the four fundamental forces in nature- photons, gravitons, Z and W mesons. There are other “particles” that mediate other kinds of forces such as phonons for mechanical forces in crystal lattice vibrations.

Combining the miniaturized world of electronics and the right physics to explain what happens at that scale is seen as probably the next step to another surprise. To overcome the problem of short circuits at sub-micron scale, the electronics changes from one of manipulating memory and logic operations by moving charge to one of storing and processing information through the spin of electrons. This has been coined ‘spintronics.’ This is another junction of time when another ‘next big thing’ is possibly about to happen. Who is to bring about the first quantum computer chip? In the U.S.A., there are about 14 groups working on different projects under the sponsorship of the USA defence force in attempt to realise a computer that will be employed in quantum communication. Some of the projects on spectral hole burning [5], nitrogen vacancy complexes in diamond [6], single ion implantation in silicon [7], quantum processing on liquid helium surface [8] and so forth. Single ion implantation is accomplished by using an electron beam ion trap (EBIT) instrument [9] which is able to copiously and controllably produce one-two-three ... electron-stripped ions or ions with

practically no electrons at all around them to the choice of the scientist. These ions interact very interestingly with any material they come in contact with. They can induce what is called “Coulomb explosion” on surfaces releasing a lot of electrons [10], x-rays [11] other atoms synonymous to sputtering [12] and in the process forming nano-craters [13] nano-blisters [14] and nano- or quantum- dots [15]. On this aspect, the current project (not reported in this thesis) has delved into the successful quantification of the electron emission from diamond surfaces through the work of Sideras-Haddad *et al.* (2007) [16]. Recently, this project (not reported in this thesis) has also reported diamond-like nano-structures on the surface of highly oriented pyrolytic graphite (HOPG) after irradiation with several types of slow highly charged ions [17]. Quantum communication with nitrogen vacancy in diamond, for instance, has been demonstrated experimentally [18] by using the zero-phonon-line (ZPL) at a wavelength of 575 nm of the photoluminescence of the N-V centre in diamond as a source of photons for carrying the information about spin of one electron to the other electron a few meters (~500 m) away. Some of the problems with storing and processing information using electron spins have been the noise from spin of nuclei that hosts these electrons [19]. Also the technology is currently so exorbitant that even a smart scientist let alone one from the developing world can hardly afford to take this route.

### 1.3 Nanotechnology-‘The Next Big Thing?’

Among the above attempts, nanotechnology has been hailed as one of the most promising routes to the realization of quantum information and processing. A single electron transistor has been demonstrated [20]. Nano-science, the study of materials with one of the materials’ dimensions being less than 100 nm, is becoming one of the most pursued multi-disciplinary fields. Nano-technology is the application of it. The cost-effectiveness and the wide range of methods available for practising nano-scale science makes this route an affordable one and hence a way to making the anticipated quantum computer, if accomplished, available to the general public.

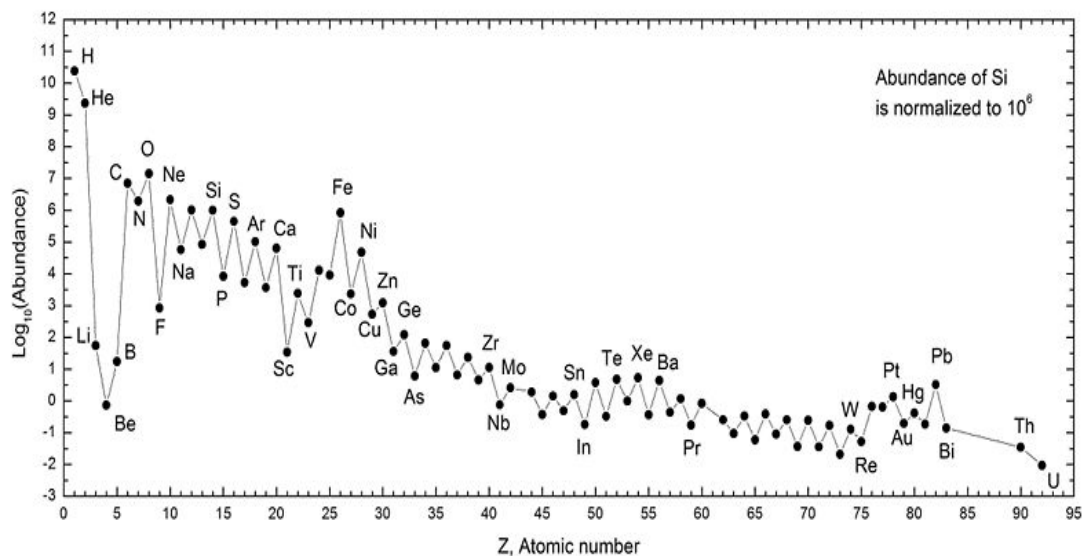


Fig 1.1 Relative abundance of silicon in our galaxy [from [http://en.wikipedia.org/wiki/File: SolarSystemAbundances.jpg](http://en.wikipedia.org/wiki/File:SolarSystemAbundances.jpg) ]

One of the materials that has been earmarked to override silicon has been carbon with the same valence as silicon and much more abundant in nature than its competitor as shown in Fig 1.1 although silicon is more

abundant than carbon in the earth crust. It has been seen that carbon is capable of forming different structures: diamond, graphite, amorphous carbon, carbon nano-tubes, and fullerenes. Carbon nano-tubes (CNT) were known to the public in 1981 by S. Iijima in Japan [21] although other scientists are known to have seen these structures in early 1970's in Russia and other countries. A lot of publications on carbon nano-tubes have appeared since then including the first FET transistor based on a CNT appearing in a Nature journal [22]. The problem with carbon replacing its "downstairs" neighbour on the periodic table has been the inability of repeatably producing CNTs of the same electronic properties. CNTs can come as metallic or semiconducting depending on whether the atomic arrangement, or what is called chirality, is armchair or zig-zag or other novel atomic arrangement such bamboo shapes. The success of a method for producing good CNTs will depend on going around this dilemma.

On the other hand, there have been other nanostructures based on metals and metal compounds. Most metal oxides especially those derived from transition metals such as Zn, W, V e.t.c. possess semiconducting properties. Metal oxides are more controllable and their synthesis and final properties are much more predictable and repeatable than CNTs. It was therefore one reason for this project's interest in inorganic nano-structures.



## 1.4 Vanadium and Tungsten in South Africa

South Africa, apart from being the world supplier of gold, is the producer and supplier of 50% of the vanadium ore on the world market [23].

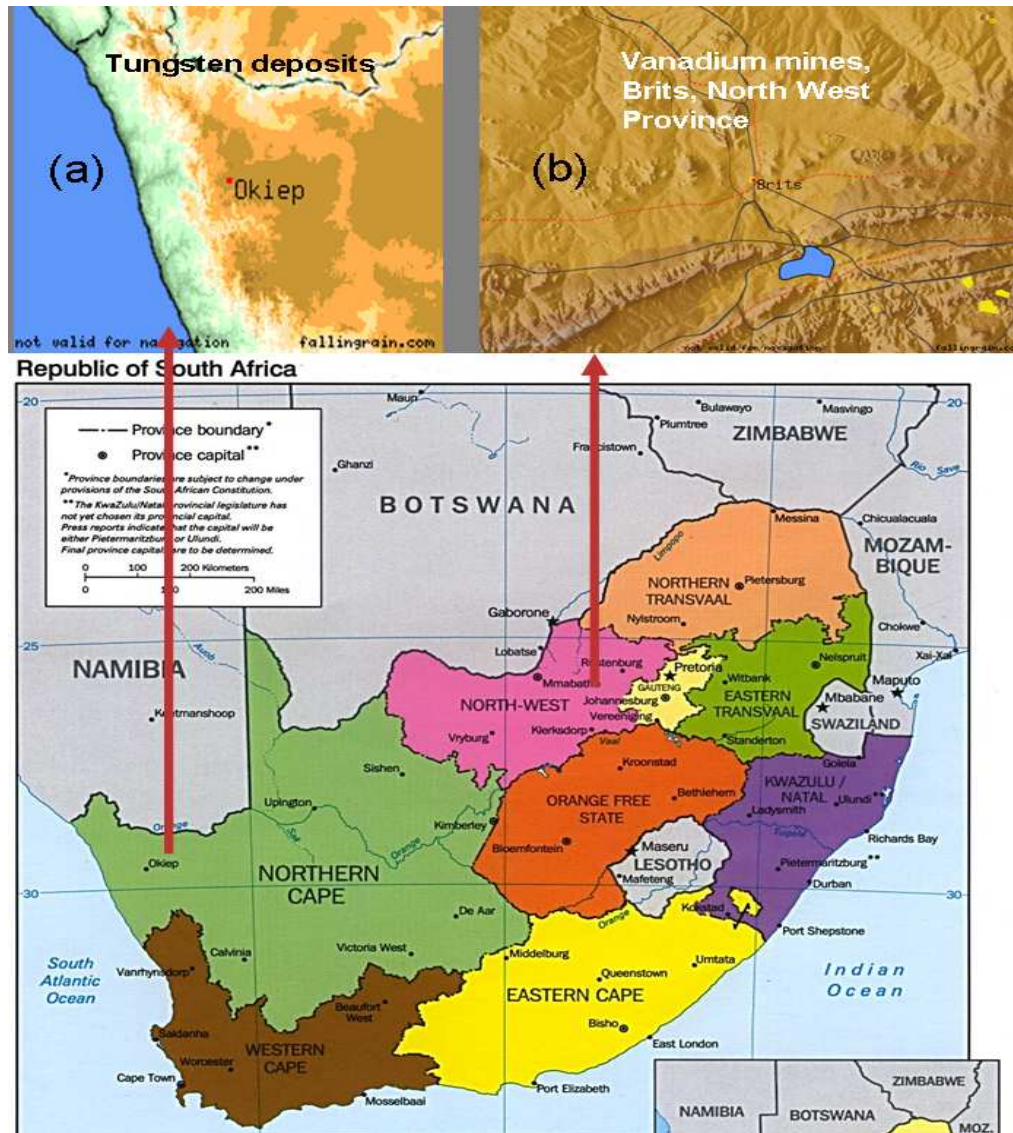


Fig 1.2 Map of South Africa showing the two major region-shown expanded by arrows- where the important materials covered in this study are found- (a) Okiep district in Northern Cape province known to have  $WO_3$  reserves and (b) Brits, North West Province where there are mines for Vanadium ores.

Mines of such a transition metal are located in Brits in Gauteng province on the west of Johannesburg and Pretoria as illustrated in Fig. 1.2. Most of this metal ends up in the steel industry where it is used during the hardening of iron into steel. Highveld Steel is a company that is currently mining about 25,000 tonnes per year of vanadium oxides from a reserve of 25,000,000 tonnes near Brits in the North Western Province of South Africa. This private mining company can make £12 million per year from this ore.

As for tungsten, China is the leading supplier. South Africa, however, is known to have substantial reserves especially in Okiep district in Namaqualand. About 1800 metric tones which contained 65.3%  $WO_3$  are known to have been sampled for further analysis and shipped to Europe from this region [24]

### **1.5 Why $VO_2$ , $WO_3$ , ultrasonics spray pyrolysis and laser pyrolysis?**

Tungsten trioxide ( $WO_3$ ) is a very important semiconducting oxide. It has a number of properties that are of technological application including electro-chromism. This is the effect of change of color of a material when electrical current flowing through it, or charge injection, is changed. Electro-chromism was discovered by Faughnan *et al.* (1975) [25].  $WO_3$  is the best of the known electro-chromic materials. Another very important property is that  $WO_3$  is also gaso-chromic, that it changes its optical and hence its electronic properties in the presence of some gases. It has been observed to be very sensitive to  $NO_x$ ,  $CO_x$ ,  $H_2S$ ,  $NH_3$ ) [26]. Photo-chromism of  $WO_3$  has been

reported by [27] where it can be used in flat panel displays, UV sensitive spectacles and an innumerable list of optical devices. A combination of photo- and electro- chromism leads to 'smart windows' for homes and offices which are able to replace expensive air conditioning systems. Writing - reading - erasing optical devices such as CDs and DVDs have been fabricated from this material [28].

VO<sub>2</sub> is thermo-chromic and due to this structural change, depending on ambient temperature, VO<sub>2</sub> has a myriad of applications: energy efficient windows [29], optical disc media and holographic storage [30], bit recording [31], write-erase stable devices [32], ultra fast switches (~100 femtoseconds) [33], defense/shield and laser protection and laser guided missiles [34].

Thermo-chromism's application to energy-efficient windows is an important application with the promise of such VO<sub>2</sub> windows complimenting and eventually replacing the current air conditioning systems. This would contribute to the global call for reduction of green-house gases, save energy, less reliance on oil for heating and cooling buildings, vehicles, aero-planes and space craft. For this cause, this project has been involved in parallel efforts in developing new materials and nano-composites for the fabrication of solar water heaters. The new composite of carbon allotropes in host of NiO has been found to be an efficient absorber of the useful portion of the sunlight for heating applications [35-37]. In this area, this project (not reported in this thesis) has been involved in the analysis of Raman spectroscopy data for nanoclusters of carbon in NiO, ZnO and SiO<sub>2</sub> especially the role of phonon

(heat) confinement as carbon particle size reduces to nano-scale. Both high resolution TEM and Raman spectroscopy showed that the carbon nano-clusters had an average diameter of 6 nm [37]

The original objectives of the study were as follows

1. To obtain  $\text{WO}_3$  and  $\text{VO}_2$  from commonly available precursor solutions using the low-cost but highly efficient ultrasonic spray pyrolysis (USP)
2. To attempt to resolve the conflict between the theory and experiment with respect to crystallites sizes by Lang and Jovanovic models and XRD/SEM experiments
3. To improve the resolution of the USP by coupling the setup with a low-cost gas analyzer
4. To reduce the noxious gas sensing optimum temperature of  $\text{WO}_3$  to close to room temperature by reducing its grain size
5. To improve the colouration efficiency of the electro-chromic  $\text{WO}_3/\text{V}_n\text{O}_{2n+1}$  system by trying  $\text{VO}_2$  rather than  $\text{V}_2\text{O}_5$  as the complimentary electro-chromic material
6. To attempt to resolve the conflict in Raman studies of  $\text{VO}_2$  lattice dynamics by rather using neutrons to obtain phonon dispersion spectra for mechanical and thermodynamic properties of  $\text{VO}_2$

These objectives have since been reviewed and modified to suit the current study. Objectives 1 and 2 have been accomplished and reported in Mwakikunga *et al.* [38, 39]. For the sake of completeness, some of the new

findings with regard to these two objectives will be reviewed in Chapter 2.

For instance, Objective 1 was transformed to the following:

7. Reduce the particles to nanoscale by switching from Ultrasonic Spray Pyrolysis (USP) to Laser Pyrolysis (LP)

Objective 3 was accomplished by the direct observation of the phases present at the period of deposition as manifested by the multi-colour deposition in the exhaust quartz tube which was reported [40,41]

8. Study thermo - chromism of  $\text{VO}_2$  of varying particle size
9. Size effects on the electro - chromism/ gas sensing properties of  $\text{WO}_3$

By switching from USP to LP in objective 7 it was hoped that the particle size of either  $\text{VO}_2$  or  $\text{WO}_3$  material would reduce to below that which could be found by USP. USP and LP are reviewed in Chapter 2.

When the LP experiments were realized, the particle size as seen by SEM increased to an average diameter of 1.5  $\mu\text{m}$ ! When these so-obtained particles were further annealed the particle size increased up to an average diameter of 2  $\mu\text{m}$ . This was seen as due to agglomeration. However, amidst the large spheres were one-dimensional nanostructures.  $\text{WO}_x$  was found to preferentially self assemble into nano-wires of diameters from 14 nm up to 72 nm with the most probable diameter of 51 nm as reported in Mwakikunga *et al.* [40]. For  $\text{VO}_x$ , it was discovered that it would preferentially form belts and ribbon-like nano - structures. The  $\text{WO}_x$  nano-wire vibrational (phononic)

properties and the VO<sub>2</sub> nano-belt thermo-chromic properties and their growth procedures by laser pyrolysis were reported in Mwakikunga *et al.* [41]. These properties were compared with the optical, vibrational and thermo-chromic properties reported in Ref. 41 and these are briefly reproduced in Chapter 3 of this thesis. The growth of particles by laser pyrolysis into nano-wires and nano-belts only happened after thermal annealing in a specific environment. This gave a clue as to the possible role of annealing in the one-dimensional growth among other unknown parameters in the laser interaction with the precursors. Then some samples that were synthesized by ultrasonic spray pyrolysis were revisited and were taken for thermal annealing using the same annealing procedure used in the LP samples. For WO<sub>x</sub> nano-spheres grown at 100, 200, 300, 400, 500, 600 and 700°C, the annealing process, which is explained in detail in Chapter 4, produced the 500°C sample as an optimum sample with a substantial population of W<sub>18</sub>O<sub>49</sub> tip-like nano-wires. Structural properties of these nano-tips were studied by TEM and the stoichiometry determination by selected area electron diffraction will be explained in Chapter 4. The results from this work were reported in Ref. 42. There was need to introduce a new growth mechanism as these wires were grown by a totally unique process other than the growth mechanisms available in literature. For the first time, the current project proposed the so-called Solid-Vapour-Solid mechanism of growth as discussed in Mwakikunga *et al.* [42]. Recently this mechanism has been followed-up by comprehensively re-looking at the WO<sub>x</sub> nano-wires grown by LP in different carrier gas

environments. In this recent work, statistical-mechanical aspects of the SVS mechanism were followed-up and, the model developed there-from, was used to fit the nanowire length-and-diameter data. This has been reported in Mwakikunga *et al.* [43] and most of this discussion is made in Chapter 6. Recently dense nano-ribbons of VO<sub>2</sub> were discovered in some samples grown by USP. Luminescence and thermo-chromic properties have been performed. Selected area electron diffraction and high magnification TEM has been conducted. Some of these ribbons have been characterized preliminarily by non-contact mode AFM and they have been found to be as thin as 10 nm on average. Raman spectroscopy is expected to produce interesting size-dependent phonon confinement properties in these ribbons. These phonon structure studies are related to gas-sensing, thermo-chromic and electro-chromic properties. It is shown here how phonons have a role in understanding gas-sensing, thermo-chromism and electro-chromism in Chapter 6. Concluding remarks, the proposed outlook and possible future student project spin-offs from this work are suggested and presented in Chapter 7.

With these properties, most of the objectives can be said to have been met to a satisfactory degree of fulfillment. To help with reading, the publications pertaining to this work have been attached in the Appendices.

## Chapter 2

### **Progress in Ultrasonic Spray Pyrolysis and Laser Pyrolysis**

This chapter shows the versatility of an old technique that is based on the phenomenon of sound and how sound interacts with matter in liquid state. It also shows how this phenomenon is employed in the synthesis of nano-sized materials in chemical vapour synthesis. The chapter shows the overwhelming progress ultrasonic spray pyrolysis has achieved and the future challenges that lie ahead.

Chemical vapour thermal deposition methods form one of the largest groups of techniques for realising a variety of materials in condensed matter science. The starting material is either a gas or liquid carefully chosen to end up into a stoichiometric material desired. The general process entails a source of chemical vapours/droplets which are carried into a heated zone for evaporation and decomposition and finally ending up either on a substrate (for thin films) or a filter (for powders) as shown in Fig. 2.1. When dealing with vapours/gases as starting materials, the method is usually referred to as chemical vapour deposition (CVD) and there are many forms of CVD; whereas the term “spray pyrolysis” (SP) is used when dealing with liquid droplets as precursor materials.

The word pyrolysis is taken from a Greek word “pyre”<sup>1</sup> which means “a pile of fuel or pile of wood” with specific reference to heating by flame

---

<sup>1</sup> A reference from the book of The Exposition of the Seven Church Ages by William Marrion Branham states “... In fact, Polycarp, the first bishop at Smyrna was martyred and people had to carry the wood that would make his



[44]. Since such heating raises the precursor material to a plasma state where radicals, electrons and ions prevail, this process can be used in in-situ spectral analysis of elemental composition of the precursors in addition to the decomposition mechanisms, reaction kinetics and formation of new condensed matter. The source of heat can be a furnace (thermal CVD), a hot wire/filament (HWCVD, HFCVD), an intense light source such as an I.R. CO<sub>2</sub> laser or a UV excimer laser (laser pyrolysis LP), plasma source (plasma enhanced PE-CVD), an I. R. lamp or, simply, a heated substrate.

A number of previous review articles have been presented on different forms of CVD: thermal CVD [45-54], plasma enhanced PE-CVD [55-63], hot-wire or hot filament (HWCVD or HFCVD) [64-71] and not many of them have been as exhaustive in their respective areas. Pyrolysis, although classified under CVD in some text, has become a wide area of research and technology covering synthesis of new products, qualitative and quantitative spectroscopic analysis of fluids and, lately, alternative route to production of debris-free x-ray sources; these aspects are elaborated further in the sections that follow. In spray pyrolysis the droplets or vapours can be generated either by pneumatic nozzles in whistle-type sprayers or ultrasonic nebuliser.

---

funeral pyre...” [page 112 paragraph 3]; also from the Hebrew Lexicon, “ a pile of fuel, pyre, a pile of wood”; as well see Isaiah 30:33. With the advent of the laser, where low-level laser power leads to atomic dissociation without necessarily having a flame, the meaning of pyrolysis has slowly changed meaning to include this new class of reactions, pyrolysis for chromatography and time of flight experiments

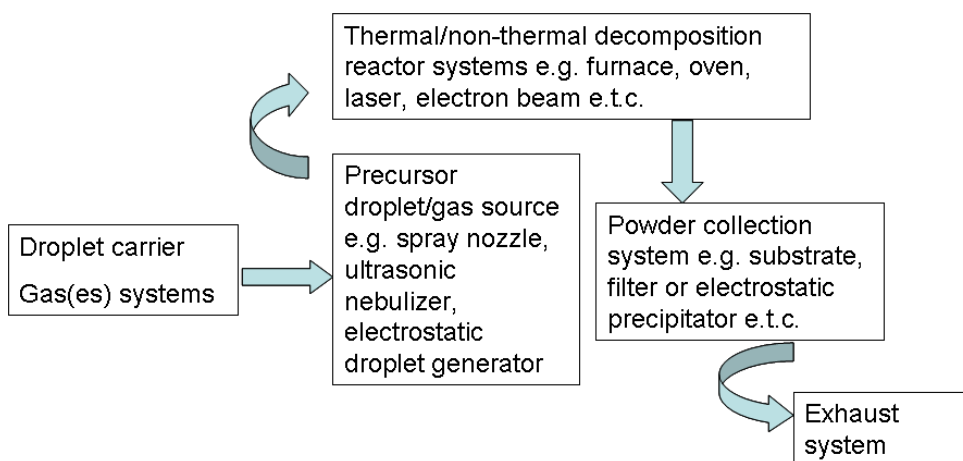


Fig. 2.1 An illustration of generalized chemical deposition methods

In the former the process is simply called spray pyrolysis (SP) and in the latter case, the process assumes the name “ultrasonic spray pyrolysis” (USP). An article on the versatility of spray pyrolysis by Pramod Patil [72] among other aspects tabulated publications up to early 1999 listing materials and spray pyrolysis parameters. Other reviews have been on specific materials employing spray pyrolysis as one of the wide range of methods used in producing such materials: superconductors [73], semi-coke [74], ceramic nano-composites [75], carbon nitride films [76], and magnetic nano-particles [77, 78]. The present review chapter will restrict its discussion to ultrasonic spray (USP) technique on a wide range of materials especially from 1999 to the present and on laser spray (LP) pyrolysis. This is a period that has seen a lot of improvements to pyrolysis techniques to the extent that structures with new shapes and novel growth dimensionality have been produced in a controlled manner. The scarcity of specific review papers in a period like this one where numerous publications pertaining to materials synthesis by

various versions of pyrolysis was the main motivation of the present compilation. First, a historical outline of the droplet generation phenomenon by ultrasonic nebulisation is given. This has not been covered in most previous reviews except by Yule *et al.* [79], Barreras *et al.* [80] and Nevolin [81]. These reviews have not covered pyrolysis but restricted themselves to the nebulisation phenomenon. The triumphs and challenges in ultrasonic spray pyrolysis are also presented. A tabulated literature survey and database from 1999 to 2008 is given and some unsolved problems in pyrolysis for materials processing with regard to droplet and particle size under different pyrolysis parameters are discussed.

## **2.1 Ultrasonic nebulisation phenomenon**

Ultrasonic atomization is a very effective method for production of ultra-small droplets and, after the droplets are pyrolyzed, the realisation of nano-sized materials. Quantum dots have been produced by spray pyrolysis [82]. Three approaches are common in the droplet production: (1) passing the liquid across a standing ultrasonic wave, (2) depositing the liquid over an ultrasonic transducer and (3) immersing a focussing ultrasonic transducer in the liquid in such a way that the liquid depth is equal to the focal length of the ultrasound lenses in the transducer.

Generation of droplets by means of ultrasonic waves was first reported in 1927 by Wood and Lomis [83]. A number of mechanisms have been proposed to explain this phenomenon. At low excitation frequencies (20 - 100kHz), we

can imagine that only surface atoms respond to form droplets; such waves are called *capillary waves*. At higher excitation frequencies (0.1- 5 MHz) and intensities, bulk atoms of the liquids come into play and this effect is called *cavitation*.

## 2.5 Capillary wave mechanism

The capillary wave proposal enjoyed intense research interest from the first known studies by Faraday [84] in 1831 to the present. It was Lord Kelvin, as elaborated in Rayleigh's book [85] in 1871, who derived the well-known equation for the wavelength of capillary waves as

$$\lambda = \left( \frac{2\pi\sigma}{\rho f^2} \right)^{1/3} \quad (2.1)$$

Here,  $\lambda$  is the wavelength,  $\sigma$  is the surface tension,  $\rho$  is the liquid density and  $f$  is the frequency of the surface waves. This equation was later modified by Rayleigh [85,86] to give

$$\lambda = \left( \frac{8\pi\sigma}{\rho F^2} \right)^{1/3} \quad (2.2)$$

Note that  $F$  which is equal to  $2f$  is not the frequency of the surface waves but rather the frequency of the forcing sound. The fact that the frequency of the surface waves is *half* the exciting frequency was empirically obtained from experimental measurements. Numerous experimental workers in the 1950's [86-92] pointed to unstable surface capillary waves as the origin of droplet formation relying on the simplified linear instability analysis. The 1962 experimental determination by Robert Lang [93] of the relationship

between the wavelength of the capillary waves and the size of the droplets so formed spurred the capillary wave mechanism to greater heights. Lang showed that the droplet size,  $D_L$ , and the capillary wave length  $\lambda$  were related by the empirical equation

$$D_L = 0.34\lambda \quad (2.3)$$

The subscript  $L$  in Eq. 3 signifies the Lang's droplet diameter in distinction from other droplet diameter symbols to follow. Extra support from Sindayihebura & Bolle [94] in 1998 brought more assurance that capillary waves were probably the main mechanism. How drop formation may occur by unstable surface capillary waves was illustrated schematically as reproduced in Fig. 2.2 and this phenomenon is usually called the Taylor instability [95]. In the Taylor instability the liquid capillary waves are composed of crests (peaks) and troughs. Atomization takes place when unstable oscillations tear off the crests of the capillary waves away from the bulk of the liquid. Thus the droplets are produced at the crests whose size is proportional to the wavelength.

A major revision to the Lang's equation was done by Peskin & Raco [96] in 1963 and later, 1996, by Jokanovic *et al.* [97] who, rather than adopting an existing empirical equation, chose to derive a general equation from first principles. The analysis especially by Jokanovic *et al.* started from applying the Bernoulli's equation to an incompressible fluid of density,  $\rho$ , surface tension,  $\sigma$ , under pressure,  $p$ , due to an ultrasonic excitation,  $f$ , from a depth,  $y$ , and thereby generating a disturbance of amplitude,  $\zeta(x,t)$  given by

$$\rho gh + \rho \frac{\partial \phi}{\partial t} + \sigma \frac{\partial^2 \xi}{\partial x^2} = 0 \quad (2.4)$$

In this equation,  $\phi$  is the rate potential. The boundary conditions employed were that when  $y = -h$ ,  $v = 0$  and  $\partial^2 \phi / \partial x^2 = 0$  then

$$\phi = \frac{1}{h} \frac{dy}{dt} c_J \cdot h \cdot [k_J (y + x)] e^{ikh} \quad (2.5)$$

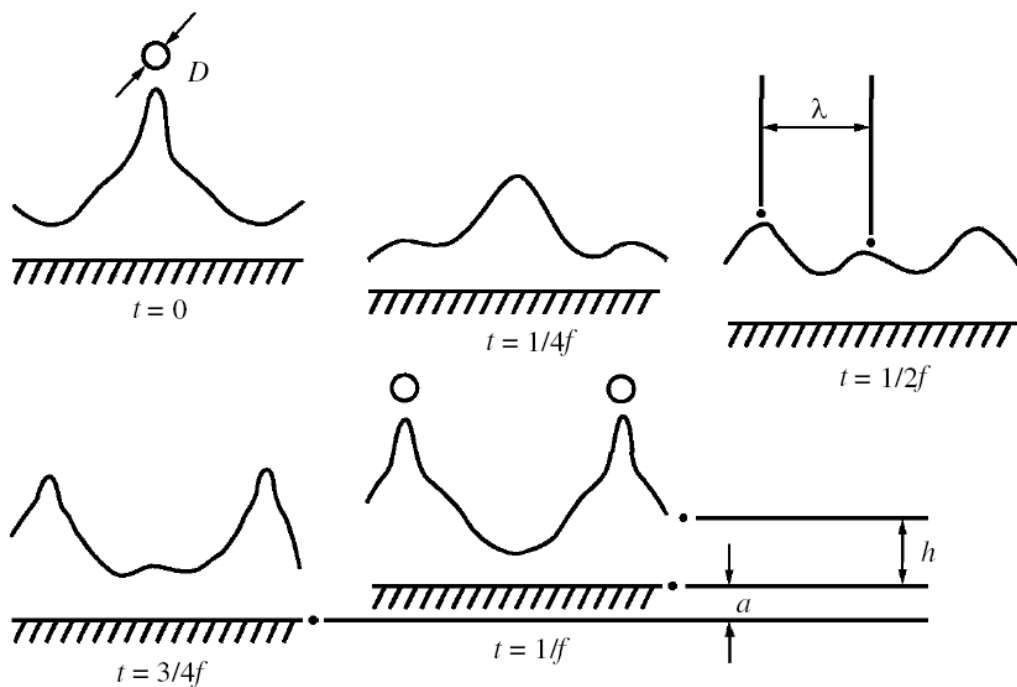


Fig. 2.2 A sketch showing idealized droplet formation from standing-wave crests showing one period of wall vibration. Note that Ref. 53 carried out a thorough stability analysis of wave formation which included the film thickness,  $h$ , wall-vibration amplitude,  $a$ , and viscosity,  $\mu$  in addition to the parameters of forcing frequency,  $f$ , surface tension,  $\sigma$ , and liquid density,  $\rho$ , which were in the original work of Kelvin as reported in Ref. 43. Permission from The Royal Society, A. J. Yule & Y. Al-Suleimani, Proc. R. Soc. Lond. A 456, 1069 (2000)

Here,  $c_j$  is a constant,  $k_j$  was taken to be the wave-number ( $2\pi/D_j$ ) where in turn  $D_j$  is the Jokanovic's aerosol droplet diameter (again to distinguish it from that of Lang above). The Mathieu's function was then adopted which was observed to explain the typical shape of the relationship between the amplitude of the oscillation of the meniscus surface and the wave-number. The Mathieu's function was given as

$$\frac{dy}{dt} + \left[ \frac{\sigma k^3}{\rho} t.h(k.h) - k.g.t.h.(k.h) \right] y = 0 \quad (2.6)$$

The solution of Eq. 2.6 for  $h \gg \xi(x,t)$ , that is, for small disturbances, found by Jokanovic was seen to be similar to that previous found by Peskin & Raco using a different analysis route (not reproduced here)

$$D_j = \left( \frac{\pi\sigma}{\rho f^2} \right)^{1/3} = \frac{1}{0.68} D_L \quad (2.7)$$

Note that the relationship between droplet diameter and the Kelvin relation for capillary wave length can also be derived from dimensional analysis as shown in by Mwakikunga *et al.* [38] given as

$$D = k_M \cdot \left( \frac{\sigma}{\rho f^2} \right)^{1/3} \quad (2.8)$$

Where  $k_M$  is a dimensionless constant which according to Lang is  $0.68\pi^{1/3}$  while, according to theoretical derivation by Peskin & Raco and Jokanovic, the constant  $k_M$  is equal to  $\pi^{1/3}$ . This means the droplet diameter as calculated by Lang's equation is smaller by the factor of 0.68 in comparison with that

determined by Jokanovic's equation. Jokanovic *et al.* were able to show experimentally that their freshly derived equation yielded better agreement between calculated and experimentally determined droplet sizes. It must also be noted that Jokanovic *et al.* have arrived at Eq. 2.7 using various forms of the equation of motion of the liquid at the surface including one given by [98]

$$\frac{\partial \varphi}{\partial t} + g\xi - \frac{\sigma}{\rho} \left[ \frac{\partial^2 \xi}{\partial x^2} + \frac{\partial^2 \xi}{\partial z^2} \right] = 0 \quad (2.9)$$

However, a number of more recent studies employing ultrasonic spray pyrolysis (an application to be discussed in the next section) and using either the Lang's empirical formula (Eq. 2.3 and/or the Jokanovic's revision Eq. 2.7) have shown that both equations have limitations. A serious conflict between theory and experiment reported by Nedeljkovic *et al.* [99] states:

“Comparison of the theoretically [ $d_j = 195$  nm,  $d_L = 132$  nm] obtained results with the experimentally determined [ $d_{exp} = 286$  nm] regardless of the equations being used for the determination of the aerosol droplets diameter undoubtedly shows that there is a substantial difference between the theory and the experiment, if the theoretical density of the particles packing was assumed...”

And also according to Saponjic *et al.* [100]

“Significant differences between the experimentally determined (285 nm) and the theoretically predicted values of the mean particle diameter (132 nm and 195 nm) were found indicating that the powder was highly porous...”



The reasons for this gross under-estimation by the theory of the experimentally determined particle size could be

- (1) the basic assumption in the Kelvin wavelength on which both the Lang's formula and that of Jokanovic *et al.* are based and
- (2) the absence of the dependence of droplet size on liquid viscosity and the volumetric flow rate which is contrary to experimental observations.

This calls for the consideration of the liquid's bulk properties in the models. These shortfalls are discussed in the unsolved problems in USP in section.

## **2.6 Cavitation mechanism**

Cavitation theory is necessary in explaining the capillary wave hypothesis. Cavitation hypothesis is generally applied to high frequency and high energy intensity systems. When a liquid is irradiated with an intense ultrasound field, cavitation bubbles are formed. During the implosive collapse of these bubbles near the surface of the liquid, high intensity hydraulic shocks are generated which in turn initiate disintegration into droplets. At such large intensities the excitation is beyond the liquid surface but extends into the liquid bulk contrary to the capillary hypotheses. Properties of the liquid bulk such as viscosity come into play as parameters affecting the nature of the final droplet. Sollner [101] was probably the first in 1936 to explain Wood & Loomis's ultrasonic atomization demonstration in terms of cavitation produced under the liquid film. While Lang and the other workers developed

the capillary hypothesis, the cavitation hypothesis was almost abandoned thanks to Eknadiosynats and co-workers [102,103] who resumed this area in the mid-60's. Several studies after these tried to combine both hypotheses [104-108]. The effect of viscosity and surface tension on the Taylor instability has been studied [109], that the rate of growth of amplitude disturbance is affected by viscosity has been observed [110], the increasing importance of viscosity as surface tension decreases has been suggested [111] and the effects of density, viscosity, interfacial tension and relative fluid velocity on drop formation have been elaborated by Clark [112,113]. Another empirical equation for the prediction of the droplet size at high liquid flow rates was proposed in 1978 by Mochida [114] as

$$D = 31.7 \left( \frac{\sigma}{\rho} \right)^{0.354} \mu^{0.303} Q^{0.139} \quad (2.10)$$

In this equation,  $\sigma$  and  $\rho$  have the usual meanings,  $\mu$  is the viscosity and  $Q$  is the volumetric flow rate of the liquid. However, this equation does not account for the excitation frequency. Clark found that the dependence of droplet size on viscosity roughly followed the proportionality

$$D \approx \mu^{0.166-0.303} \quad (2.11)$$

Tsai *et al.* [115] found in 1996 that droplet size and volumetric flow rate were correlating approximately thus

$$D \approx Q^{0.25-0.30} \quad (2.12)$$

This was quite in conflict with Mochida with his exponent being outside the range set in the Tsai *et al.* improved measurement.

## 2.7 A Combination of Capillary and Cavitation hypotheses

More careful observations have shown that apart from the traditional parameters of surface tension, viscosity, density, forcing frequency and volumetric flow rate additional parameters such as geometry of the vibrating surface, the amplitude of the oscillations, the intensity of the ultrasound power or the energy density have a lot to do with the size of the droplet so produced. To this end Rajan and Pandit [116] in 1996 developed a new correlation equation to take into account some of these extraneous parameters and was found to be

$$D = \left( \frac{\pi\sigma}{\rho \cdot f^2} \right)^{1/3} \left[ 1 + A \cdot (We)^{0.22} (Oh)^{0.166} (I_N)^{-0.0277} \right] \rightarrow E \quad (2.13)$$

The symbols  $A$ ,  $We$ ,  $Oh$ ,  $I_N$  are respectively the surface area of the droplet, the Weber's number (the number that describes atomization), the Ohnesorge's number (or the viscous number) and the intensity number (the number affected by the geometry of the vibrating surface) defined in the following expressions:

$$We = \frac{fQ\rho}{\sigma} \quad (2.14)$$

$$Oh = \frac{\mu}{f \cdot A_m^2 \rho} \quad (2.15)$$

$$I_N = \frac{f^2 A_m^4}{v_s \cdot Q} \quad (2.16)$$

Most symbols have usual meaning but  $Am$  is the amplitude,  $v_s$  is the speed of sound. Three alternate correlations to Eq. 13 (labelled here as E) were derived by Rajan and Pandit [116]:

(1) using the Rayleigh instability criterion,

(2) using the Walzel relation and

(3) using Davies approach respectively labelled, in this review, as F, G and H below.

$$D = \frac{\mu Q k}{3.74 \sigma A_m} \rightarrow F \quad (2.17)$$

$$D = \frac{1.06 k Q \frac{\mu}{\rho} \left( \frac{\rho}{\pi \sigma f} \right)^{1/3} \left( \frac{\rho f^2}{\pi \sigma} \right)^{2/3}}{f A_m \left[ 2 + 0.6 \frac{\mu}{f A_m^2 \rho} \right]^{1/3}} \rightarrow G \quad (2.18)$$

$$D = k_1 \left[ \sigma + \frac{\mu(A_m \cdot f)}{4} \right]^{0.6} \rho^{-0.6} \left[ \frac{1}{2} v_s A_m (2\pi \cdot f)^2 \right]^{-0.4} \rightarrow H \quad (2.19)$$

A parity plot is one of the most convenient graphical techniques for evaluating the theoretically calculated quantity and the experimentally observed quantity. Rajan and Pandit [117] also presented parity plots for correlations E and H and we reproduce them in Fig. 2. 3

From the parity plots one sees that most points are below the equality line signifying that the measured drop size is mostly less than the calculated drop size. This means that the Rajan-Pandit correlations are over-estimating the observed droplet size.

Avvaru *et al.* [117] have recently, in 2006, modified Eq. 2.13 to suit the so-called “Newtonian viscous liquids” given as

$$D = \left( \frac{\pi\sigma}{\rho f^2} \right)^{1/3} + 0.0013(We)^{0.008} (Oh)^{-0.14/n} (I_N)^{-0.28} \quad (2.20)$$

In order to validate their theory, one of the Newtonian liquids — glycerine — was used in their study and the parity plots done using correlations E and H were presented and are herein reproduced in Fig. 2.4. In comparison with the Rajan-Pandit parity plots, one can clearly see a remarkable improvement in the alignment of the calculated –experimental points to the equality line.

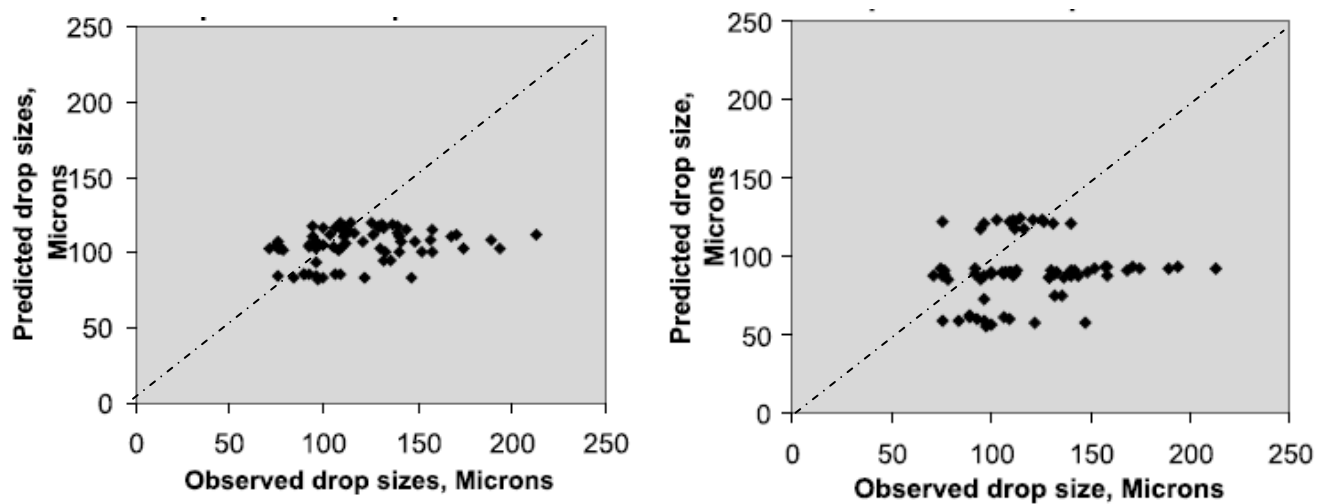


Fig. 2.3 Plots for correlations E and H of water droplets. The dotted line is a line that indicates the points where calculated quantity is exactly equal to the experimentally measured quantity.

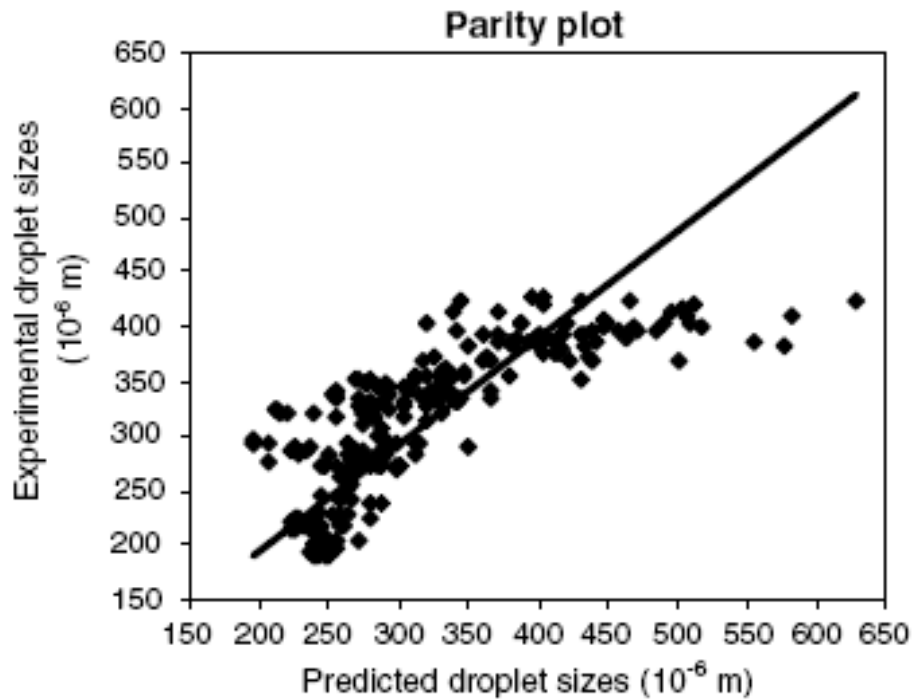


Fig. 2.4 A typical parity plot for a Newtonian liquid, glycerine (From Ref. 117).

However, one can also see departure from the ideal equality line when droplet diameters exceed 400  $\mu\text{m}$ . Therefore beyond this point the Avvaru correlation over-estimated the droplet sizes. Also even within the region where there is apparently good agreement, more points are above the equality line indicating that, in this region (200 - 350  $\mu\text{m}$ ), the Avvaru correlation under-estimated the droplet size. Overall, however, the Avvaru correlation is a big improvement over that of Rajan-Pandit. Avvaru *et al.* are also able to confirm and demonstrate the presence of cavitation in the droplet ejection by arranging an ingenious experiment. In this experiment, the ultrasonic generator is tilted horizontally and the force of droplet ejection is balanced with the environmental drag force from which the ejection velocity is

determined. Using their so-derived differential equation, they are able to show that the Newtonian liquids such as glycerine yield an ejection velocity of  $12.6 \text{ ms}^{-1}$  whereas the non-Newtonian liquids yield an ejection velocity of  $3.5 \text{ ms}^{-1}$ . In both cases the ejection velocity is higher than the cavitation-less ejection velocity of  $0.144 \text{ ms}^{-1}$  which is attributed to capillary theory.

## 2.5 Effects of Pressure and Temperature on Surface Tension, Density and Viscosity

With improvements of the theory, it is hoped that the future is bright with regard to understanding the phenomenon of ultrasonic generation of droplet from liquids. One of the many unsolved problems concerning the droplet size as a function of the liquid properties of surface tension,  $\sigma$ , viscosity,  $\gamma$ , density,  $\rho$  and so forth involves finding from thermodynamics how these properties vary when the liquid temperature and pressure change. In Mwakikunga *et al.* [Ref. 38], such a temperature-and-pressure dependent droplet size was dealt with by considering that droplet size took the expression in Eq. 8. Eq. 2.20 could also be re-written in the like manner as

$$D = \left( \frac{\pi\sigma(p, T)}{\rho(p, T)f^2} \right)^{1/3} + 0.0013(We(p, T))^{0.008} (Oh(p, T))^{-0.14/n} (I_N(p, T))^{-0.28} \quad (2.21)$$

## 2.6 Surface Tension as a Function of Temperature and Pressure

One of the earliest experimental studies on surface tension determination at varying pressure was carried out by Lynde [118] in 1906. In

this study the surface tension at the interface between two liquids was determined via the derived equation

$$\sigma \cos \theta = \frac{H_D r_{tube}}{2} (\rho_2 - \rho_1) \quad (2.22)$$

$\theta$  was the angle of contact,  $H_D$  was the difference in height between the two liquids in the manometer,  $r_{tube}$  was the radius of the capillary tube and  $\rho_2$ ,  $\rho_1$  were densities of the two respective liquids. Taking a differential of Eq. 22 with respect to pressure  $p$ , Lynde got

$$\frac{\delta \sigma}{\delta p} = \frac{r_{tube}}{2} (\rho_2 - \rho_1) \frac{\delta H_D}{\delta p} + \frac{H_D r_{tube}}{2} \left( \frac{\delta \rho_2}{\delta p} - \frac{\delta \rho_1}{\delta p} \right) \quad (2.23)$$

By dividing Eq. 23 by Eq. 22, Lynde arrived at the following expression

$$\frac{1}{\sigma} \frac{\delta \sigma}{\delta p} = \frac{1}{H_D} \frac{\delta H_D}{\delta p} + \frac{\frac{\delta \rho_2}{\delta p} - \frac{\delta \rho_1}{\delta p}}{\rho_2 - \rho_1} \quad (2.24)$$

The first term on the right hand side of Eq. 2.24 was measured experimentally by observing the change in height at varying pressure. The second term was determined from compressibility factors of the two liquids at varying pressure since  $d\rho/dp$  is compressibility factor in the first place. With these measurements, Lynde was able to establish that a plot  $\sigma^{-1}(\delta\sigma/\delta p)$  versus  $p$  was a positive linear graph for mercury-water system and for mercury-ether system. The same was a negative linear plot for water - ether system and for chloroform-water system. However, for the carbon bi-sulphide - water system a parabolic line-shape was obtained. These results showed that



the surface tension–pressure relation depends on not only on the liquid types but also on how the liquid densities vary with pressure which is discussed in the next few pages. For the case where the  $\sigma^{-1}(\delta\sigma/\delta p)$  versus  $p$  graphs are linear,

$$\frac{1}{\sigma} \frac{\delta\sigma}{\delta p} = \pm k_{\sigma} p \quad (2.25)$$

$k_{\sigma}$  is a proportionality constant in  $Pa^{-2}$ . Surface tension can then be written in terms of pressure as follows:

$$\sigma(p) = \sigma_0 \exp\left[\pm \frac{1}{2} k_{\sigma} (p^2 - p_0^2)\right] \quad (2.26)$$

$\sigma_0$  is the surface tension at atmospheric pressure  $p_0$ . Sachs *et al.* [119] in 1995 summarized all  $\sigma$ - $p$  data from methane-water system up to that time [119-123] and their charts are reproduced in Fig. 2.5

For one to see the effect of temperature on surface temperature, one can turn to the important work of S. J. Palmer [124] in 1976. Palmer's theory based on

(1) the calculation of the difference in energies of interaction between molecules in bulk and those on the surface or 'excess energy'

(2) the minimum potential energy of these molecules due to a balance between attractive and repulsive forces at a critical temperature  $T_c$ .

The derivation led to the following expression:

$$\sigma(T) \approx (n/4)(N_0\rho/M)^{2/3} k_B (T_c - T) \quad (2.27)$$

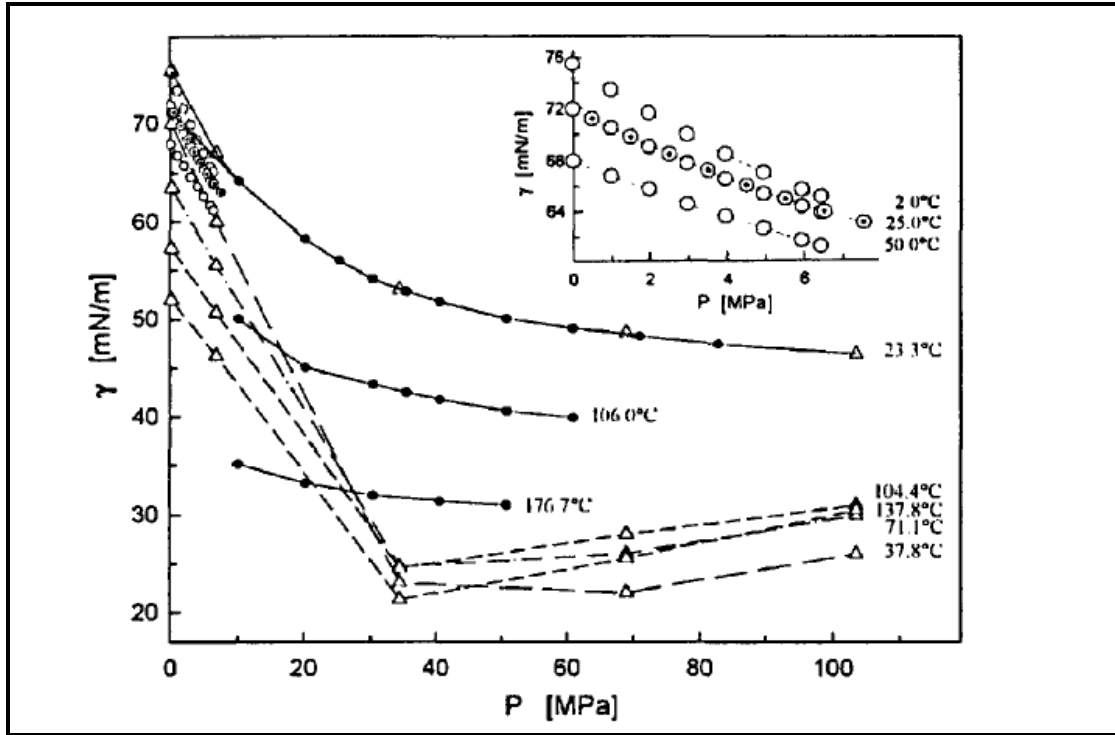


Fig. 2.5 Pressure and temperature dependence of the surface tension  $\sigma$  in the system methane-water; all data published in Ref. 119 until 1995.  $\Delta$ , Ref. 120;  $\bullet$ , Ref. 121;  $\oplus$ , Ref. 122 and  $\circ$ , Ref. 123.

Where  $n$  and  $N_0$  are the co-ordination numbers or the number of nearest neighboring molecules around one molecule in bulk and on the surface respectively,  $\rho$  is the density of the liquid,  $M$  is the molar mass of the liquid and  $k_B$  is the Boltzmann's constant.

It was shown in Mwakikunga *et al.* [Ref. 38] that based on fundamental thermodynamics, the general relationship between surface tension and temperature is given as [125-127]

$$\sigma(T) = H + \frac{d\sigma}{dT}T \quad (28)$$

where  $H$  is the energy required to increase the area of the liquid in contact with air by a unit area. It should be noted that  $H$  is always positive. Since  $\sigma$  always decreases as  $T$  increase, in accordance also with the Palmer equation in Eq. 2.27, then the derivative  $d\sigma/dT$  is always negative. It can be shown that Eq. 2.28 carries the same meaning as Eq. 2.27 with  $H = (n/4)(N_0\rho/M)^{2/3}k_B T_c$  and  $d\sigma/dT = -(n/4)(N_0\rho/M)^{2/3}k_B$ . Based on the two separate relationships of surface tension as a function of pressure according to the current generalization of Lynde's empirical study and temperature from Palmer's theory, one can write a combined relationship as follows

$$\sigma(p, T) \approx \sigma_0 (n/4)(N_0\rho/M)^{2/3} k_B (T_c - T) \exp\left[\pm \frac{1}{2} k_\sigma (p^2 - p_0^2)\right] \quad (2.29)$$

However, from Lynde's experiments, it is difficult to ascertain the  $\sigma$ - $p$  relationship since the nature of dependence is also dependent on the  $\rho$ - $p$  dependence which was not yet known but which will be shown in the sections that follow. Also in Palmer's theory, density of the liquid is assumed constant with temperature. However, so far this could be the only equation that combines the effect of pressure and temperature on surface tension.

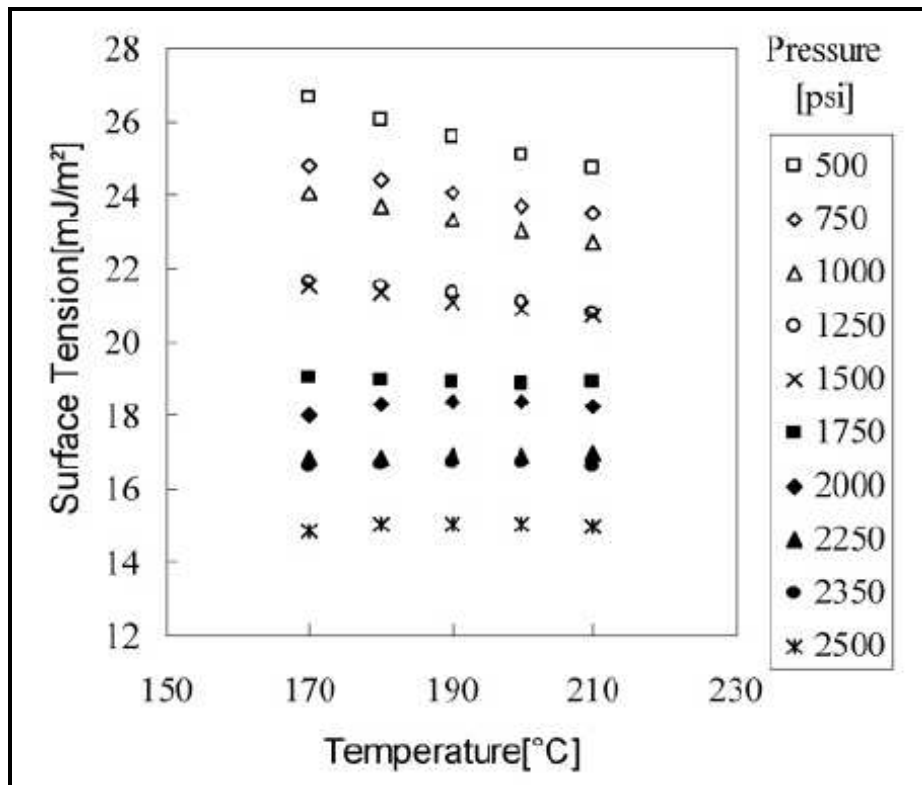


Fig. 2.6 Surface tension as a function of temperature and pressure for glycerine [From Park *et al.*, J. Phys. Chem. (2007)]

There have been other recent  $\sigma(p,T)$  equations specific to some materials such as the one by Park and co-workers [128] who showed empirically the effect of surface tension of polystyrene droplets in supercritical carbon dioxide which was found to be

$$\sigma(p,T) = 38.7032 - 0.0559T - 0.0100p + 2.596 \times 10^{-5} pT \quad (30)$$

And which was true only in the temperature range from 170°C to 210°C and from pressure of 500psi to 2500 psi. Their experimental results on  $\sigma(p,T)$  were plotted on a chart which is reproduced in Fig. 2.6

An article on surface tension given by Escobedo & Mansoori (1996) [129] based on the 1923 proposal by Macleod that surface tension of a liquid could be expressed in terms of its vapour  $\rho$  and liquid  $\rho_v$  densities thus:

$$\sigma = \Pi(\rho - \rho_v)^4 \quad (31)$$

Where  $\Pi$  is called the parachor. Although it was thought to be a constant but, lately, it has been realized that parachor is in turn temperature dependent since both surface tension and density are temperature dependent. From statistical calculations, Boudh-Hir & Mansoori (1990) [130] derived an expression for  $\Pi$  of the following nature:

$$\begin{aligned} \Pi &= \frac{kT}{4} \tau^{4-2B} \frac{z}{z_c} \zeta(\tau, \rho_l, \rho_v); \\ \tau &= 1 - \frac{T}{T_c} \\ z &= \left( \frac{2\pi m k_B T}{h^2} \right)^{1/2} \exp \left[ \frac{\mu_c}{k_B T} \right] \end{aligned} \quad (2.32)$$

where  $B$  is an exponent, the subscript  $c$  denotes the critical temperature values,  $z$  is the activity,  $\mu_c$  is the chemical potential,  $h$  is the Planck's constant and  $\zeta(\tau, \rho, \rho_v)$  is a statistical-mechanical function that shows liquid surface tension dependency on its liquid-state and vapour-state densities and temperature.

Another theoretical and empirical study of the surface tension data by Pandey [131] of ternary liquid system comprising liquid nitrogen, liquid oxygen and liquid argon revealed the relation to take the form a relation developed by Brock & Bird in 1955. This expression for non-polar liquids was derived by utilizing the power law concept applicable to temperature away from the critical point and is here given by

$$\sigma(T) = (P_c^2 T_c^2)^{1/3} \left( \frac{0.432}{Z_c} - 0.951 \right) \left( 1 - \frac{T}{T_c} \right)^{11/9} \quad (2.33)$$

$P_c$ ,  $T_c$  and  $Z_c$  are respectively critical temperature, pressure and compressibility factor.

## 2.7 Density as a Function of Temperature and Pressure

When one needs to consider the effects of pressure on density, thermodynamical equations of state (EOS) are used. Wong *et al.* (1996) [132] used the van der Waal's EOS to study the pressure and temperature effects on density of liquid lubricants. They found that density increases with increasing pressure but decrease upon a raise in temperature as confirmed by their experiments. The van der Waal's equation of state for a real gases was used to find the  $\rho(p, T)$  expression which was used to modify the droplet equation in Eq. 2.8 [38]. An improved and more appropriate EOS for liquids was

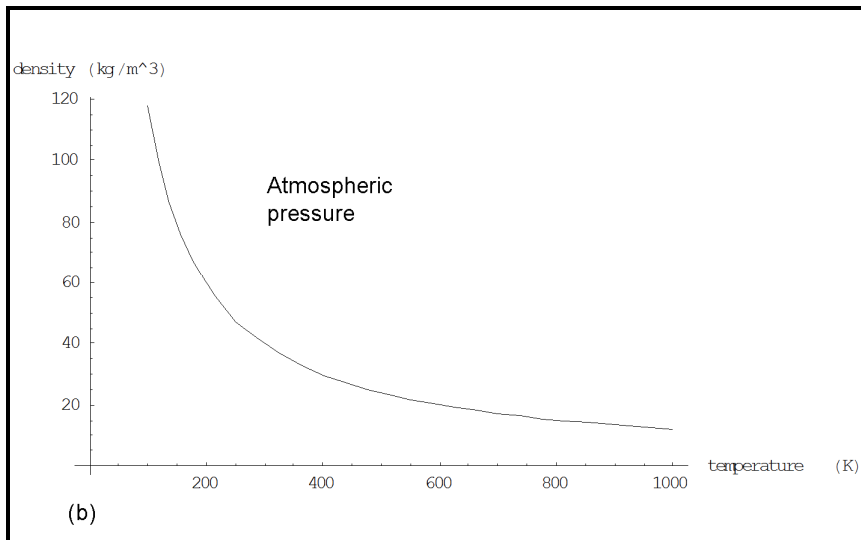
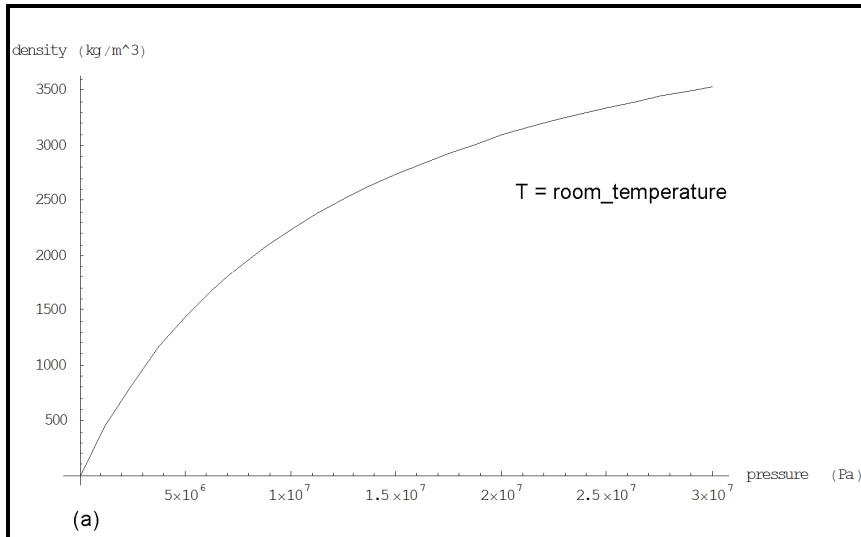


Fig. 2.7 Sketches in Mathematica of how density varies with (a) pressure and (b) temperature from Eq. 34 (Density values are not realistic and are not specific to any materials)

proposed by Redlich & Kwong in 1949 [132 (b)] that accurately predicts densities of fluids thus

$$p = \frac{\rho RT}{1 - b\rho} - \left[ \frac{a\rho^2}{T^{1/2}(1 + b\rho)} \right]; \quad b = \left( \frac{0.08664RT_c}{P_c} \right) \delta \quad (2.34)$$

$\delta$  is a parameter which further depends on temperature. By finding  $\rho$  as the subject of this equation, one can find the expression of density as a function of temperature and pressure and this variation of density is sketched in Fig. 2. 7 (a) and (b)

## 2.8 Effect of Pressure and Temperature on Viscosity of Fluids

The principal observed qualitative facts are that

(1) all gases at ordinary pressures become more viscous as the temperature is raised,

(2) most liquids become less viscous as the temperature is raised,

(3) highly compressed gases resemble liquids, they become less viscous and

(4) for a few liquids (such as liquid helium and liquid sulphur).

There is a range of temperatures over which the viscosity increases as the temperature is raised. As was the case with surface tension, the variation of viscosity with pressure is expected to be one of the inverse nature.

It is known from Wright [133] that, as early as 1886, Reynolds proposed an expression for the change of viscosity with temperature for liquids and compressed gases given as

$$\mu \propto \exp(const./T) \quad (2.35)$$



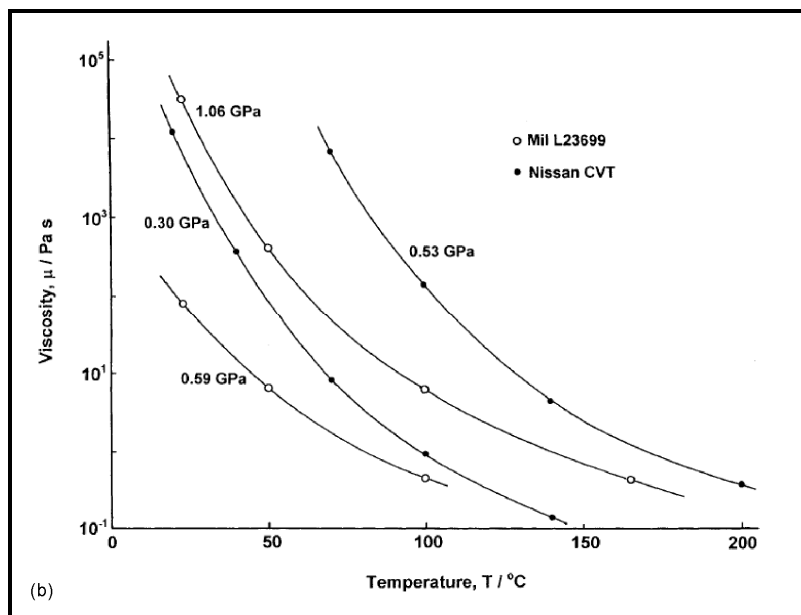
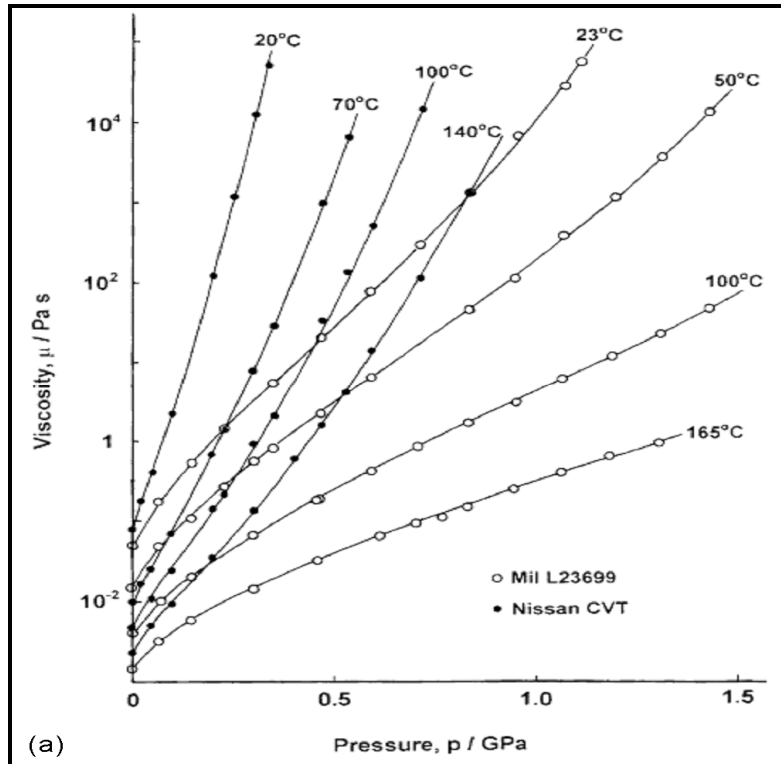


Fig. 2.8 Variation of viscosity with pressure and temperature (a) and temperature (b) for jet lube Mil L23699 (open circles) and a traction liquid (closed circles) [S. Bair *et al.* (2001)]

This was based on the observation of the similarity of viscous flow to diffusion (diffusion coefficient is given by  $D$  being  $\propto \exp(const/T)$  and also by regarding the flow of molecules past each other as analogous to a chemical reaction (the effect of temperature on the rate of chemical reaction  $R$  being also  $\propto \exp(E/RT)$  where  $E$  is the activation energy). The general form of the pressure [134] and temperature [135] dependence of viscosity has been known for at least 50 years. Viscosity is now known to vary with temperature in a greater than exponential manner and temperature -viscosity equations generally allow for an unbounded viscosity at some characteristic temperature. At high pressure, the pressure-viscosity response is likewise greater than exponential, often following a less exponential response at low pressures [135].

Fein [136] considered that the low shear viscosity,  $\mu$ , was an exponential of fluid density. Later, the so called "free volume model was developed [137]. A viscosity model that can describe the temperature and pressure response is the pressure modified equation introduced by Yasutomi *et al.* using the free volume model [138] given here as

$$\mu(p, T) = \mu_g \exp \left[ \frac{-2.3C_1 \langle T - (T_{g0} + A_1 \ln|1 + A_2 p|) \rangle \{1 - B_1 \ln(1 + B_2 p)\}}{C_2 + \langle T - (T_{g0} + A_1 \ln|1 + A_2 p|) \rangle \{1 - B_1 \ln(1 + B_2 p)\}} \right] \quad (2.36)$$

$\mu_g$  is the viscosity at a glass transition temperature  $T_g$  given by the expression in the triangular brackets. The expression in curly brackets is the relative free

volume expansivity and  $A_1, A_2, B_1, B_2, C_1, C_2$  and  $T_{g0}$  are parameters that are determined by fitting Eq. 2.36 to experimental data for a specific fluid. Eq. 2.36 suggests that increase in pressure raises viscosity whereas the raise in temperature drops viscosity as shown in Fig. 2.8

## 2.9 Final Droplet and Particle Size Formulae

Every ultrasonic transducer/nebulizer generates heat into the liquid which it is intended to produce droplets from. Since ultrasonic spray pyrolysis set-ups are closed systems, an increase in the temperature accompanies an increase in pressure. The subsequent increases in temperature and pressure affect the density, surface tension and viscosity. As such the droplet size, which is heavily dependent on these parameters, is also affected. In this section, the study on how these changes in temperature and pressure in the precursor liquid would affect the droplet size and hence the final particle sizes after pyrolysis are consolidated.

From sections 2.1 to 2.3 is seen that all the three parameters decrease as temperature is increased. However, as pressure is increased, only surface tension decreases; the other two parameter- density and viscosity- increase.

$$D = \left( \frac{\pi\sigma(p,T)}{\rho(p,T)f^2} \right)^{1/3} + 0.0013(We(p,T))^{0.008}(Oh(p,T))^{-0.14/n}(I_N(p,T))^{-0.28}$$

$$We = \frac{fQ\rho(p,T)}{\sigma(p,T)} \tag{2.37}$$

$$Oh = \frac{\mu}{f \cdot Am^2 \rho(p, T)} \quad (2.38)$$

$$I_N = \frac{f^2 Am^4}{v_s \cdot Q} \quad (2.39)$$

After substituting the pertinent parameters, the droplet size can be written in terms of the temperature and pressure dependent liquid density, viscosity and surface tension as

$$D = 1.14 \times 10^{-4} \left( \frac{\sigma}{\rho} \right)^{1/3} + 0.021 \frac{\left( \frac{\rho}{\sigma} \right)^{0.008}}{\left( \frac{\mu}{\rho} \right)^{0.14}} \quad (2.40)$$

The density-temperature function was adopted from the Redlich-Kwong equation in Eq. 2.34, surface tension was taken from the presently derived expression from Lynde and Palmer theories given in Eq. 2.29 and viscosity-temperature profile was determined from Eq. 2.36. Eq. 2.37, plotted in Fig. 2.9, shows the variation of droplet size as a function of liquid temperature. The droplet size decreases as temperature is increased.

The small changes in liquid pressure in a typical pyrolysis session lead to very small changes in surface tension, density and viscosity and hence on the droplet size. The droplet-size versus liquid pressure is therefore not shown.

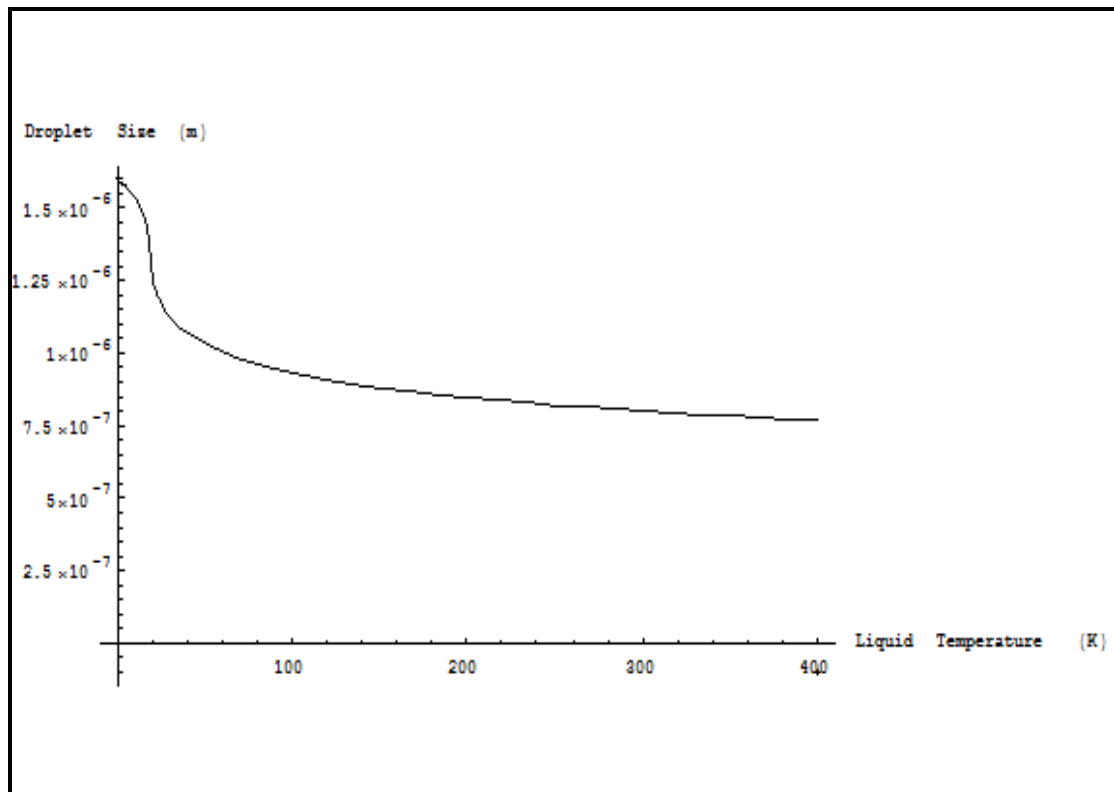


Fig. 2.9 A Mathematica plot showing the variation of droplet size with liquid temperature

## 2.10 Theory of Pyrolysis for Materials Processing

Pyrolysis is an application of the phenomenon of droplet generation from liquids by ultrasound waves. It involves materials deposition by carrying the so-produced liquid droplets into a heated zone where the droplets undergo (1) evaporation, (2) decomposition (3) reaction into new products and (4) condensation of the new product onto a filter or a substrate.

The theory of transitions of the liquid precursor droplet of initial diameter,  $D$ , in the heat field and the consequent transformation into a new

material particle of diameter  $d$  is simple. During the preparation of the precursor solution suitable for spray pyrolysis, a precursor material of mass

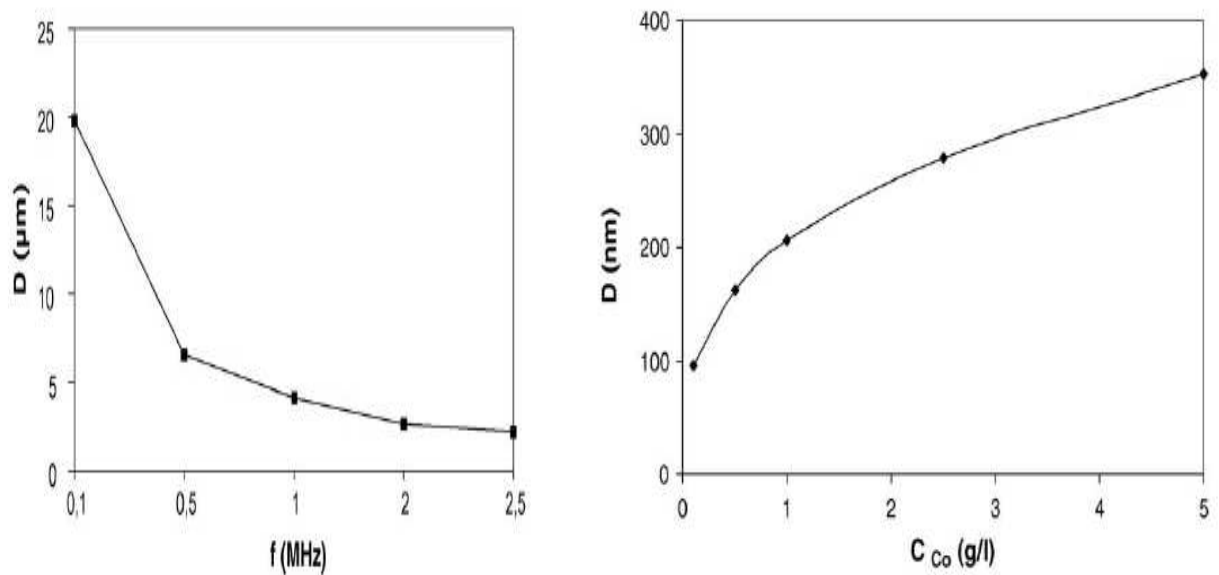


Fig. 2.10 Experimental observation of the dependency of droplet and hence particle size on nebuliser frequency (a) and precursor concentration (b). From S. Gurmen *et al.*, Mater. Res. Bull. (2006) Ref. 139

$m_{pr}$  is dissolved in a solvent so that if the concentration of this precursor in the solvent is  $c_{pr}$  then

$$m_{pr} = c_{pr} \cdot \frac{4}{3} \pi D^3 \quad (2.41)$$

$D$  is dependent on both frequency of the sound and the concentration of the precursor as shown in the previous sections and as illustrated in Fig. 2.10

After pyrolysis-dissociation and decomposition - the precursor material, a remnant of evaporation, is further reduced to the final particulate of mass of  $m_p$  plus other species that mostly are in gaseous state and hence

evaporate off without depositing. The particulate mass after assembly can be written as

$$m_p = \frac{M_p}{M_{pr}} m_{pr} \quad (2.42)$$

$M_p$  and  $M_{pr}$  are the molecular masses of the final particle and the precursor material respectively. Assuming that the initial liquid precursor droplets and the final solid particles are spherical Eq. 2.41 and Eq. 2.42 can be combined to give

$$\frac{4}{3} \pi \rho_p d^3 = \frac{M_p}{M_{pr}} c_{pr} \cdot \frac{4}{3} \pi D^3 \quad (43)$$

$d$  is the final particle diameter. This simplifies to the following equation

$$d = D \left( \frac{c_{pr} M_p}{\rho_p M_{pr}} \right)^{1/3} \quad (43)$$

Eq. 2.43 has been widely used by a number authors employing ultrasonic spray pyrolysis in production of nano-particles to predict the final particle sizes.

## 2.11 Ultrasonic spray pyrolysis

USP as an application of the ultrasonic droplet generation phenomenon has attractive features, like the traditional spray pyrolysis, of simplicity, economic viability, high deposition rate, possibility of coating over large areas and continuous operation [38]. But unlike other commonly known pneumatic atomizers, it has been described to possess the advantages of "... chemical purity and stoichiometry" and allows a narrow distribution of

particle sizes. A large proportion of the droplets is below 20  $\mu\text{m}$  and these are produced with low in-flight speed. This prevents the droplets from being removed from the gas phase by impact onto the walls of the reactor and through droplet-to-droplet collisions and consequent coalescence. The major disadvantages are potential for hollow structure or fractured particles which could be good for other applications and that the droplet production rate is typically low and highly dependent on the throughput of the nebuliser.

Since there are numerous publications, in the period from 1999 to the present [Appendix T1], on materials processing using ultrasonic pyrolysis, it was seen as convenient that these publications be tabulated for a quicker identification. The tabulation, presented in Table 2.1, is categorized in fields of

- (1) final material and applications,
- (2) suitable precursor liquid,
- (3) nebuliser frequency and flow rates.

Worth noting are a few USP set-ups that have attracted attention through the years and the novel nano-structured materials they have produced. A setup by CNR Rao's group illustrated in Fig 2.11 had an ingenious provision for constant precursor liquid level apart from the usual USP components [281,282].

One of the most important parameters for optimization of ultrasonic spray pyrolysis is flow rate of the precursor droplet. At extremely low flow rates, the throughput of the USP system is small at the benefit of obtaining



truly nano-sized, nano-structured and completely-decomposed targeted materials. At extremely high flow rates, yield is high but complete

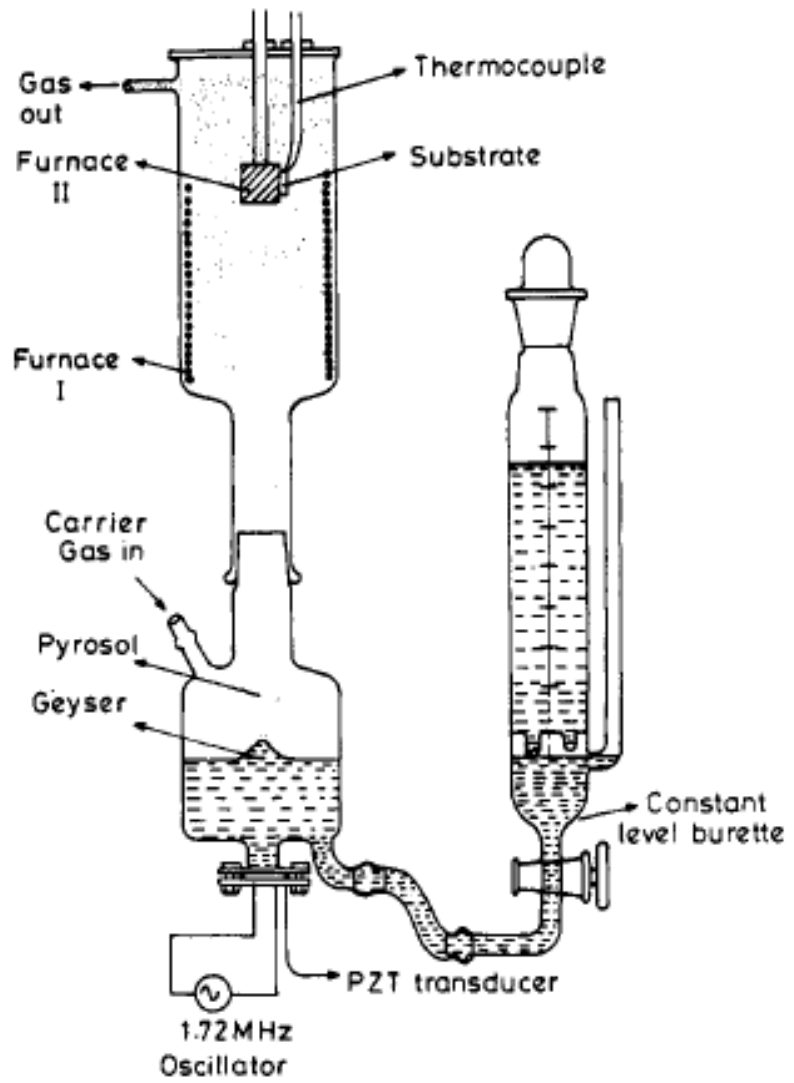


Fig. 2.11 A nebulised spray pyrolysis by C.N.R. Rao's group (from Ref. 241)

decomposition of the precursor is compromised as the residence time of the precursor in the heated zone is small. An optimum flow rate is therefore necessary to obtain both high yield and pure materials. The relationship for residence time can be easily shown to be  $d$  and  $L$  are the diameter and length of the reactor respectively and  $Q_0$  is the flow rate of the precursor assuming

that the velocity of the carrier gas is the same as the velocity of the carried precursor droplets. In the real case where the above assumption does not apply, temperature,  $T$ , and pressure,  $p$ , of the system are taken into account.

$$t_{res} = \frac{\pi d^2 L}{4Q_0} \quad (2.44)$$

In this case then the expression for residence time is given by C. Michel *et al.* (2006) [190] as

$$t_{res} = \frac{\pi d^2 L}{4Q_0} \left( \frac{P_0}{P} \right) \left( \frac{T_0}{T} \right) \quad (2.45)$$

$T_0$  is room temperature,  $P_0$  is the atmospheric pressure.

In order to maximize  $t_{res}$  one can increase  $L$  to the maximum possible length. Increasing  $L$  has the disadvantage of an uneven temperature profile over a long distance. One then needs to have several short heating zones whose temperature profiles are constant and manageable. Since the nature of products from USP depends in part on the control of the furnace temperature, Taniguchi and co-workers [194] have made an elaborate setup with a furnace having several heating zones. A typical example of such multi-zone furnaces was well illustrated by Taniguchi's group [194]. This is illustrated in Fig. 2.12

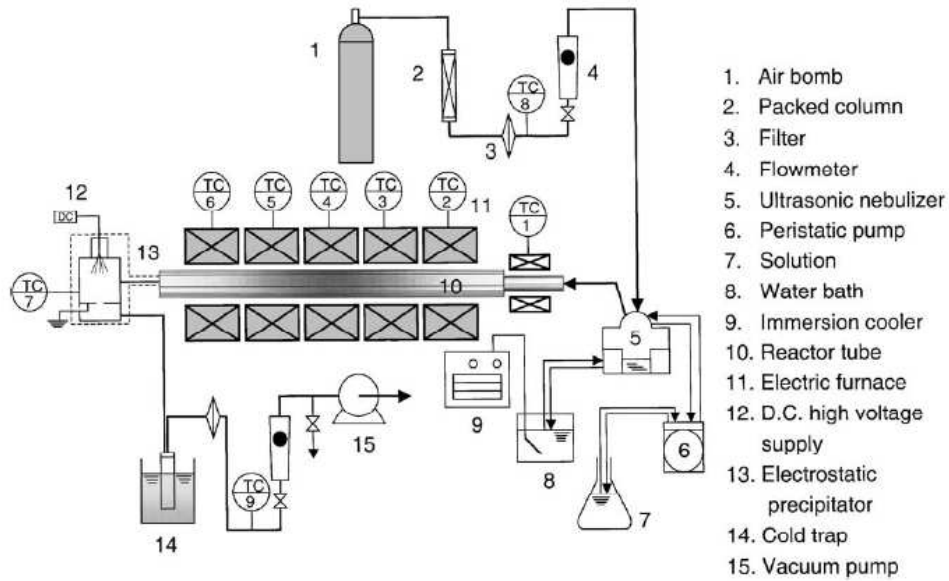


Fig. 2.12 A typical example of an ultrasonic spray pyrolysis employing a multi-zone furnace for control of product shape, particle size and other parameters. From Taniguchi's group Ref 194.

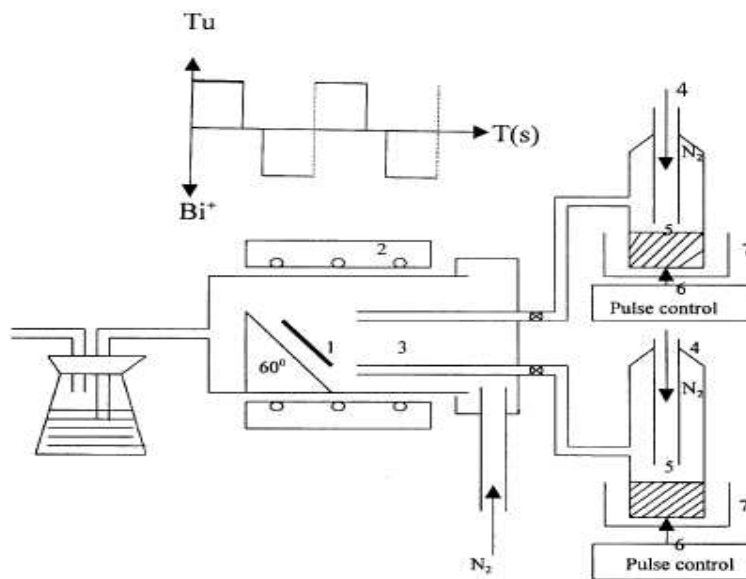


Fig. 2.13 Scheme of the asynchronous-pulse ultrasonic spray pyrolysis (APUSP) method used to obtain  $\text{Bi}_2\text{S}_3$  rod-like particle thin films with (1) substrate, (2) furnace, (3) spray nozzles, (4) carrier gas, (5) solution, (6) membrane and (7) ultrasonicator. From S.- Y. Wang *et al.* (2002), *J. Cryst. Growth* (Ref. 242)

The asynchronous-pulse ultrasonic spray pyrolysis (APUSP) is another interesting design suitable for growth of stacked films or controlled doping and development of superlattices. In APUSP, two more ultrasonicator-containing chambers are harnessed. Each chamber contains the appropriate precursor solutions that are to be deposited – the host and the dopant etc. The “sonicators” in these chambers are controlled by a pulse generator one at a time in an asynchronous manner. The period of each chamber’s pulse determines the level of doping, or the thickness of the layers in the superlattices.

In a typical APUSP (Michel Lopez and Zea 2006 Ref. 190) an inert gas is first introduced to the reaction chamber at relatively low and steady flow rate for about 30 minutes to drive the air out. The nebulised solutions – precursor and dopant are delivered to the substrates in pulses through the nozzles. Each spray lasts 5 seconds for both but after the spray of the dopant is conducted, a delay of 2-4 seconds was employed to ensure that the introduced dopant was completely decomposed before conveying a pulse spray of the host. The deposition is carried out by repeatedly performing these spray processes. It took 12-14 s for each cycle and the deposition time lasted for 15 -30 mins for the preparation of one sample. An appropriate interval between the pulse spray of dopant and host solutions play an important role in depositing high crystallinity films.

There are cases where the precursor liquid to be sonicated passes through the ultrasonicator and introduced from the top rather than from the

bottom as shown in Fig. 2.14. This design has the advantage of high yield of final desired product. However, introducing droplets from below has the advantage of selecting on the small droplets with most of the large one returning to the precursor under gravity.

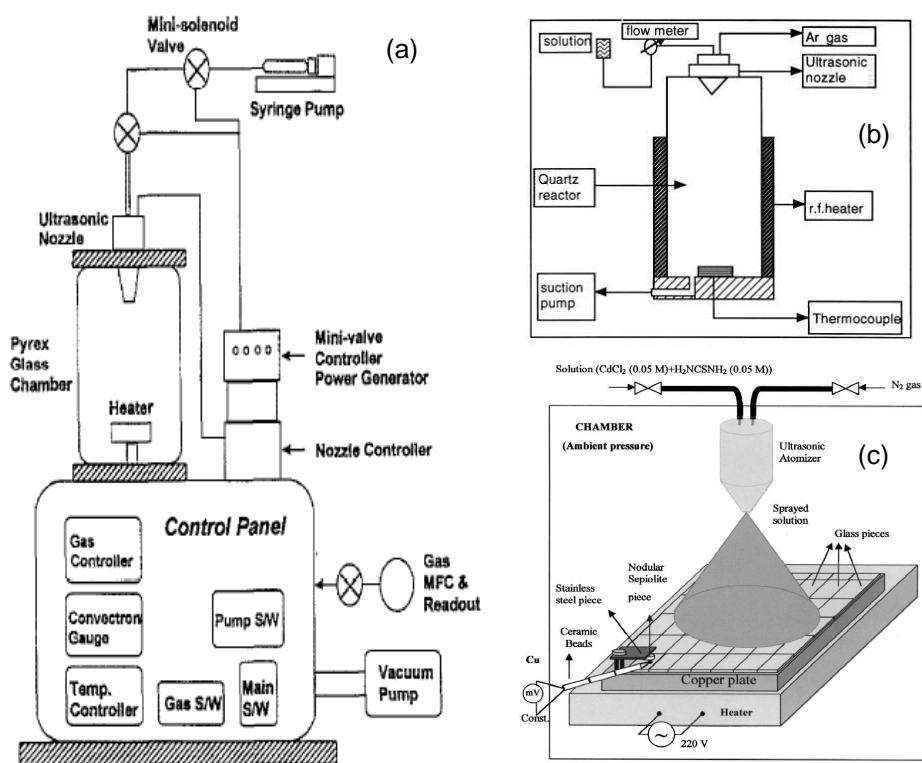


Fig. 2.14 Example of a USP system where the precursor liquid flow passes through the nebuliser (a) From Lee *et al.* [274] , (b) From Patil & Patil (2000) [256,260] and (c) the substrate is cut into several plates so that several samples are made out one run. From Baykul & Balcioglu, *Microelectronic Eng.* (2000) [259]

In both the Lee *et al.* (1998) [274] set up shown in Fig. 2.14(c) and that of Patil & Patil (2000) [256,260], the substrate has its own special heater apart from the standard furnace. Contrary to heating substrates, Kang & Park (1999) [262],

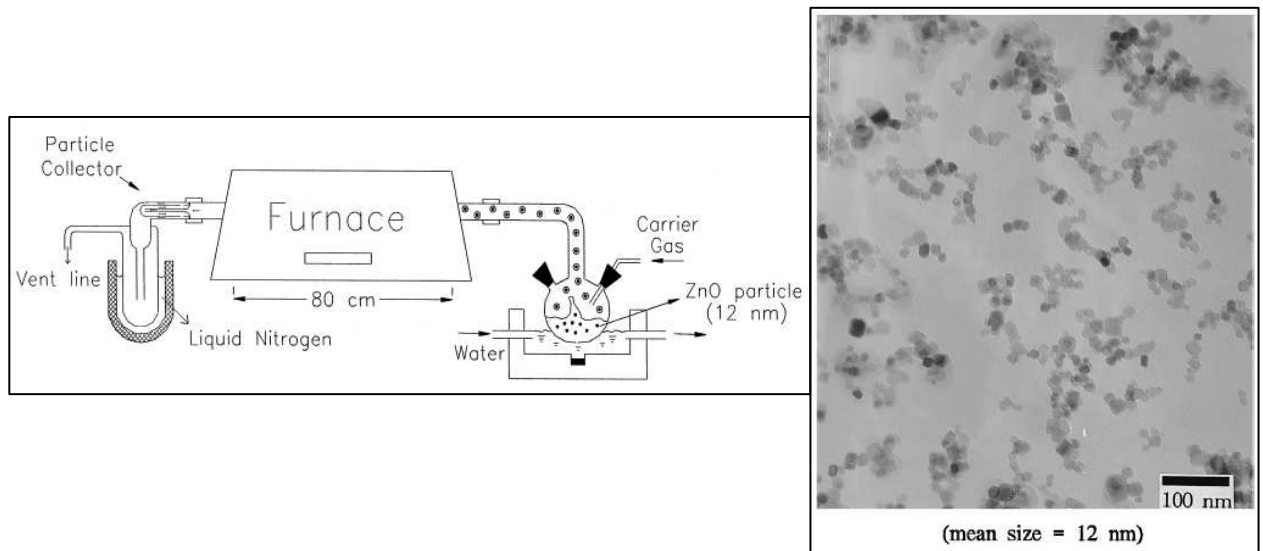


Fig. 2.15 An example of a USP set-up where both the precursor solution container and the particle collector are maintained at controlled temperature (right). Zinc oxide-dispersed silver particles by spray pyrolysis of colloidal solution. From Kang and Park, *Mater. Lett.* 1999

realised that subjecting the particle collector to coolants such liquid nitrogen helped prevent Ag nano-particle agglomeration and they become well dispersed in ZnO as illustrated in Fig. 2.15. Note that in their USP design, they included a temperature controlling water bath around the precursor container to prevent changes in temperature and pressure which in turn have an effect on droplet size as shown in the previous sections.

An interesting USP system employing a novel heating source was reported by Matsuzaki and co-workers [263] when synthesizing yttria stabilized zirconia thin films. Their substrates temperatures were controlled by heating a “susceptor” with an infrared radiation heater [Fig. 2.16 (d)].

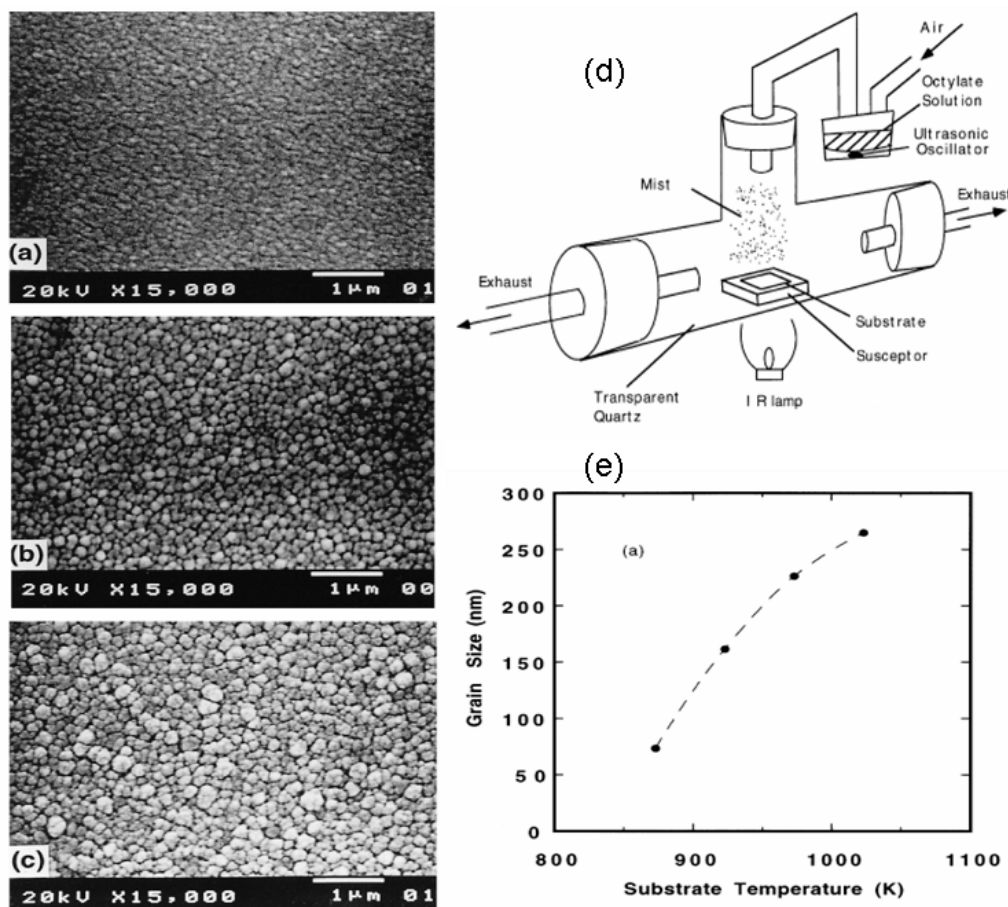


Fig. 2.16 Microstructure of the surface of the thin films deposited on quartz substrates. The films (a), (b) and (c) were deposited at 873, 923 and 1023 K respectively. (d) An illustration of the Infrared USP (e) Grain size as a function of temperature of the substrate. From Matsuzaki *et al.*, TFS (1999) [263]

The substrate temperature could be tuned from 873 K to 1023 K. Materials obtained from this setup have a type of morphology as illustrated in Fig. 2.16 (a)-(c). It is interesting to note that grain size increases with substrate temperature, the Arrhenius plot shows that the activation energy for yttria stabilized zirconia is about 68 kJ mol<sup>-1</sup> and grain size increases with increase in deposition rate. The particles obtained by this work were rather large in general. This could be due to

(1) agglomeration at higher substrate temperatures an effect known as the Oswald's ripening

(2) spraying from the top as alluded to before.

The Ostwald's ripening observed here should be distinguished from the opposite effect which was observed recently and reported in Mwakikunga *et al.* [42].

In the current study [B Mwakikunga *et al.*, JNN (2008) Ref. 42], spheres of WO<sub>3</sub> shrank in diameter as the furnace temperature was increased without heating the substrates where the perfect sphere would land. In the case of shrinkage in diameter as a function of surrounding temperature, it was found that the data was in agreement with the Tiller equation given as

$$d_c = \frac{4\sigma_e \Omega_M}{RT \ln(p/p^*)} \quad (2.46)$$

$\sigma_e$  is the interfacial energy between the nucleating materials and the surrounding environment and  $\Omega_M$  is the molar volume of the nucleating



material. A number of authors have used this equation in explaining the growth of nano-wires by chemical vapour deposition [Tan *et al.*, APL (2003) Ref. 283]

Recently, another innovation to USP has been the manner in which droplets are produced from the precursor liquid. Apart from spraying with ultrasonic nebulisers, it has been realized from the days of Lord Kelvin that by applying a high potential difference to the liquid surface makes such a

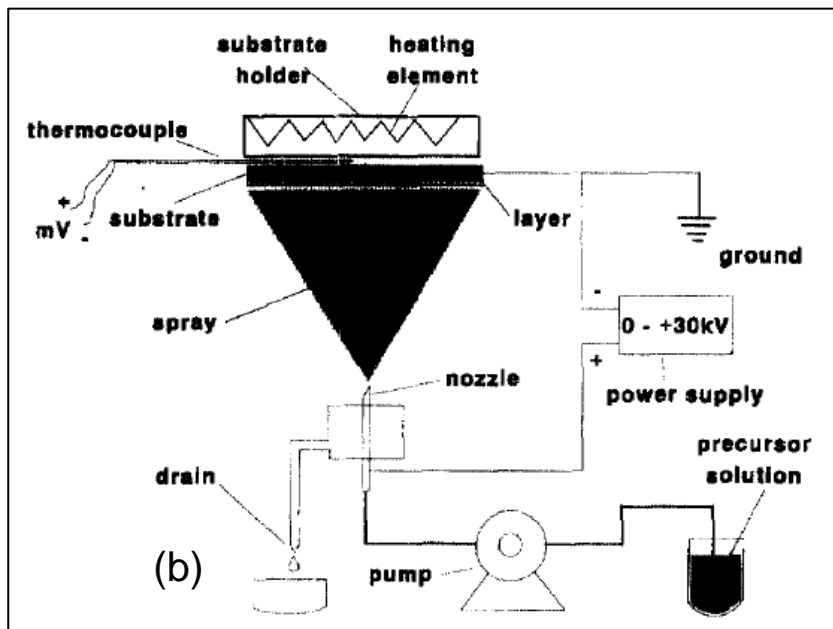
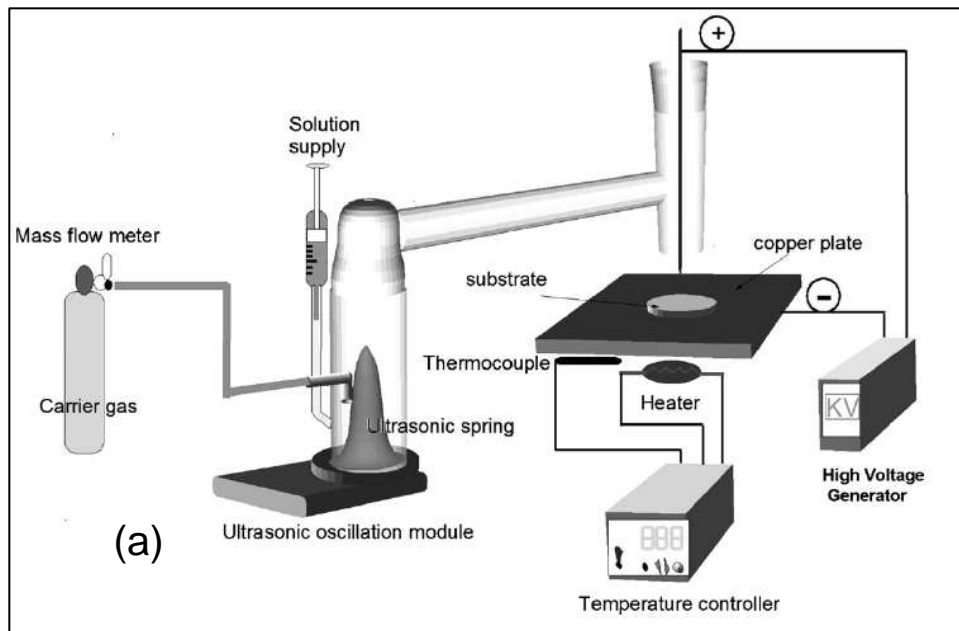


Fig. 2.17 (a) Electrostatic assisted USP (EAUSP), note that aerosol are directed onto the substrate from the top From Chen *et al.*, Mater. Res. Bul, 2007 [Ref. 140] (c) Electrostatic spray deposition (ESD); note that deposition is from bottom to top From Zaouk *et al.*, Micro Eng. 2000 [Ref. 175]

surface erupt into liquid droplets. In electrostatic assisted USP (EAUSP), a high tension is applied between the liquid and the substrate. There are cases where the precursor liquid to be sonicated passes through the ultrasonicator and introduced from the top rather than from the bottom as shown in Fig. 10. This design has the advantage of high yield of final desired product. However, introducing droplets from below has the advantage of selecting on the small droplets with most of the large one returning to the precursor under gravity. If a liquid is forced to flow through a small nozzle which is subjected to an electric field, the liquid will exit the outlet in different forms or modes as a result of different electrodynamic mechanisms. These modes include among others dripping mode, cone mode, cone-jet mode and spindle mode [Zaouk *et al.*, 2000 Ref. 175]. The kind of mode the spray displays depends on the electrical potential applied to the nozzle, the flow rate, the conductivity and the surface tension. For film deposition, the cone-jet mode is the most suitable, it is a continuous mode and the formation of a homogeneous fine spray is possible. In this mode, there exists the so-called "Taylor cone" with  $49.3^\circ$  half angle at the apex of the cone (see Taylor instability in the previous section). This cone is extended by a jet which breaks up into spray droplets to generate an aerosol of the precursor liquid. Chen *et al.* [140] final particle morphology has large particles and large flakes. This could be due to agglomeration of droplet as they descend. The best way to select only the small droplets is to have the substrate above the spray. The large ones cannot make it to the substrate and therefore are forced to return to the ultrasonic

nebuliser. As for Zaouk *et al.*, the potentials need to be optimized for self assembly

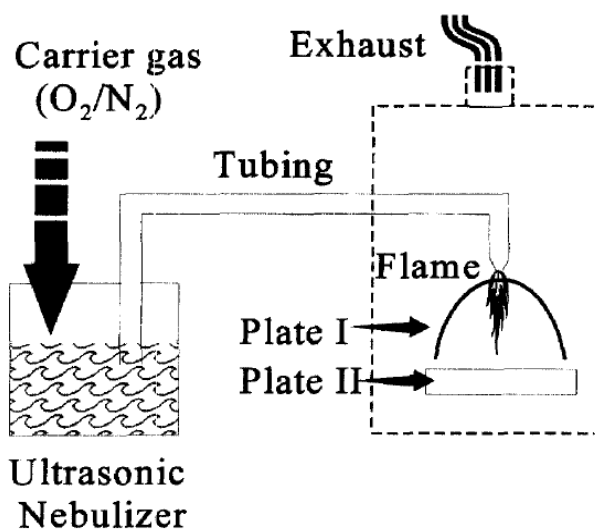


Fig. 2.18 Flame assisted USP (FAUSP) From: Chen *et al.*, Eur. J. Solid State & Inorg. Chem. (1998)

An interesting kind of pyrolysis is called flame assisted USP (FAUSP). FAUSP was developed in the 1980's. It operates by injecting the spray of a precursor solution obtained from an aerosol generator into a combustion chamber where the individual droplets are rapidly combusted. Fuel such as natural gas or hydrogen is introduced in order to generate the appropriate high temperature. In some case, instead of external fuels, flammable alcoholic solutions are used as precursors.

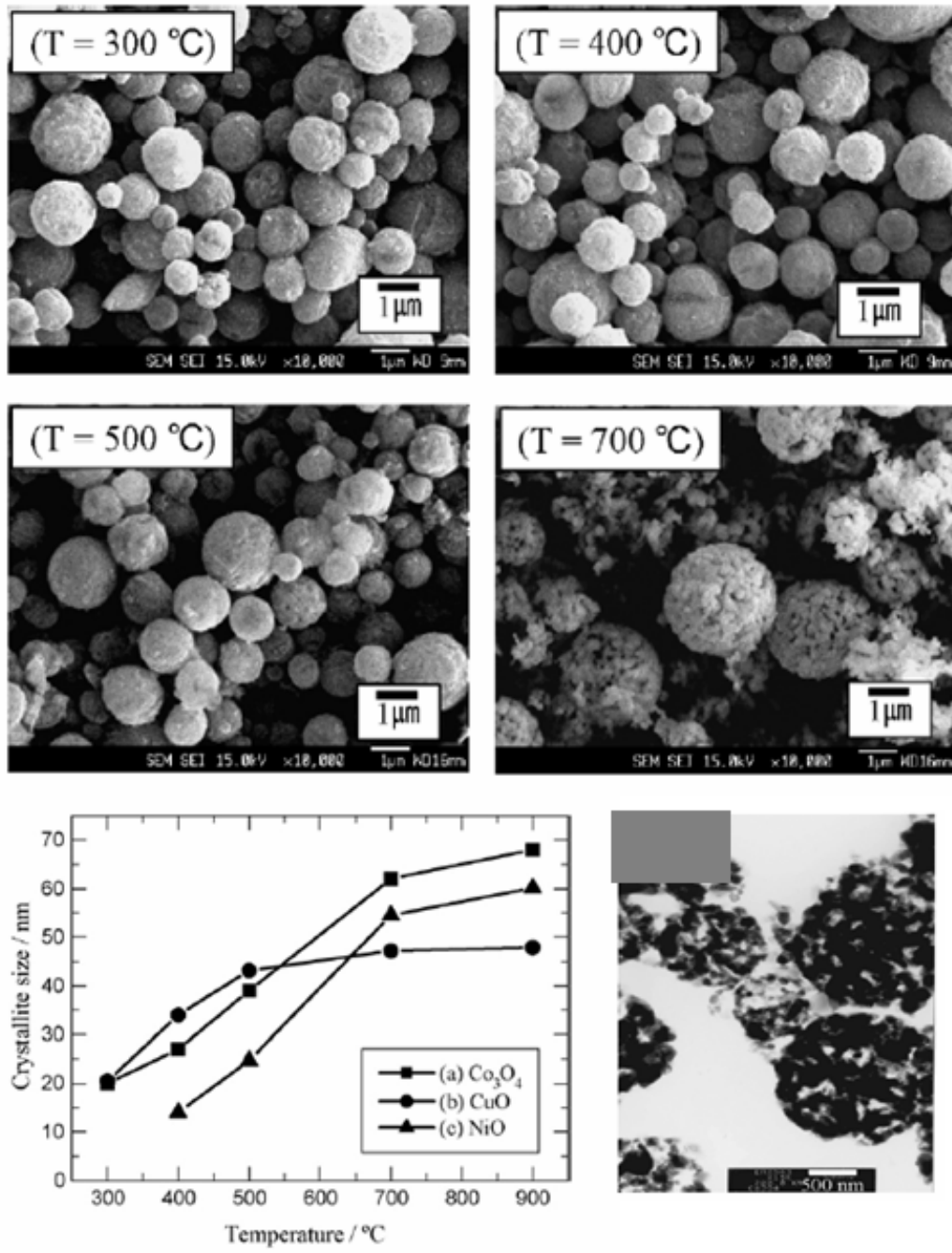


Fig. 2.19 The figure shows the effect of calcination temperature on morphology and crystallinity of  $\text{Co}_3\text{O}_4$ ,  $\text{CuO}$  and  $\text{NiO}$ . From S. W. Oh *et al.*, J. Power Sources (2007) [Ref. 182]

The spherical shape of the particles definitely comes from the spherical droplets from the precursor liquid [50]. When scanning electron microscopy is performed on these particles one can see the manifestation of spherical daughter particles from mother spherical liquid droplets. The particle size may be less than 3  $\mu\text{m}$  [see Fig. 2.19] from the four SEM micrographs (a) but at higher magnification with TEM (bottom right) the morphology changes to one showing that the spheres are composed of numerous crystallites whose size as determined by the Scherrer equation from X ray diffraction shows they are nano-crystalline. The crystallite size increases as the calcinations temperature is increased. Bucko, Ref. 284]. This is equivalent to increasing substrate temperature and thereby increasing particle and crystallites sizes as seen above. However, this is to be contrasted from the in-situ furnace temperature increase which has the reverse effect of decreasing the particle and crystallite size as shown in Fig. 2.20 [from M Yuan *et al.* (1998) [Ref. 268] also found hollow spheres when preparing zirconia and yttria-stabilized-zirconia (YSZ) fine powders by flame- assisted ultrasonic spray pyrolysis. This was attributed to the presence of nitrates in the precursor.

Prior to this study, Messing *et al.* [285, 286] had studied the spray pyrolysis of nitrate solutions and proposed a mechanism to explain the particle morphology. During the pyrolysis of spray droplets in the flame, the evaporation of the solvent and the reaction/decomposition of the solute proceed successively from the outer part to the inner part of the droplets. When a nitrate solute with a relatively low melting point is present, it melts to

fill the pores of the structure. The molten salt will inhibit the removal of the trapped solvent in the inner parts of the droplets as a result of the reduction of the gas permeation. This leads to a build-up of internal gas pressure and, finally, explosion or foaming of the particles to form hollow particles or particle fragmentation with a broad size distribution.

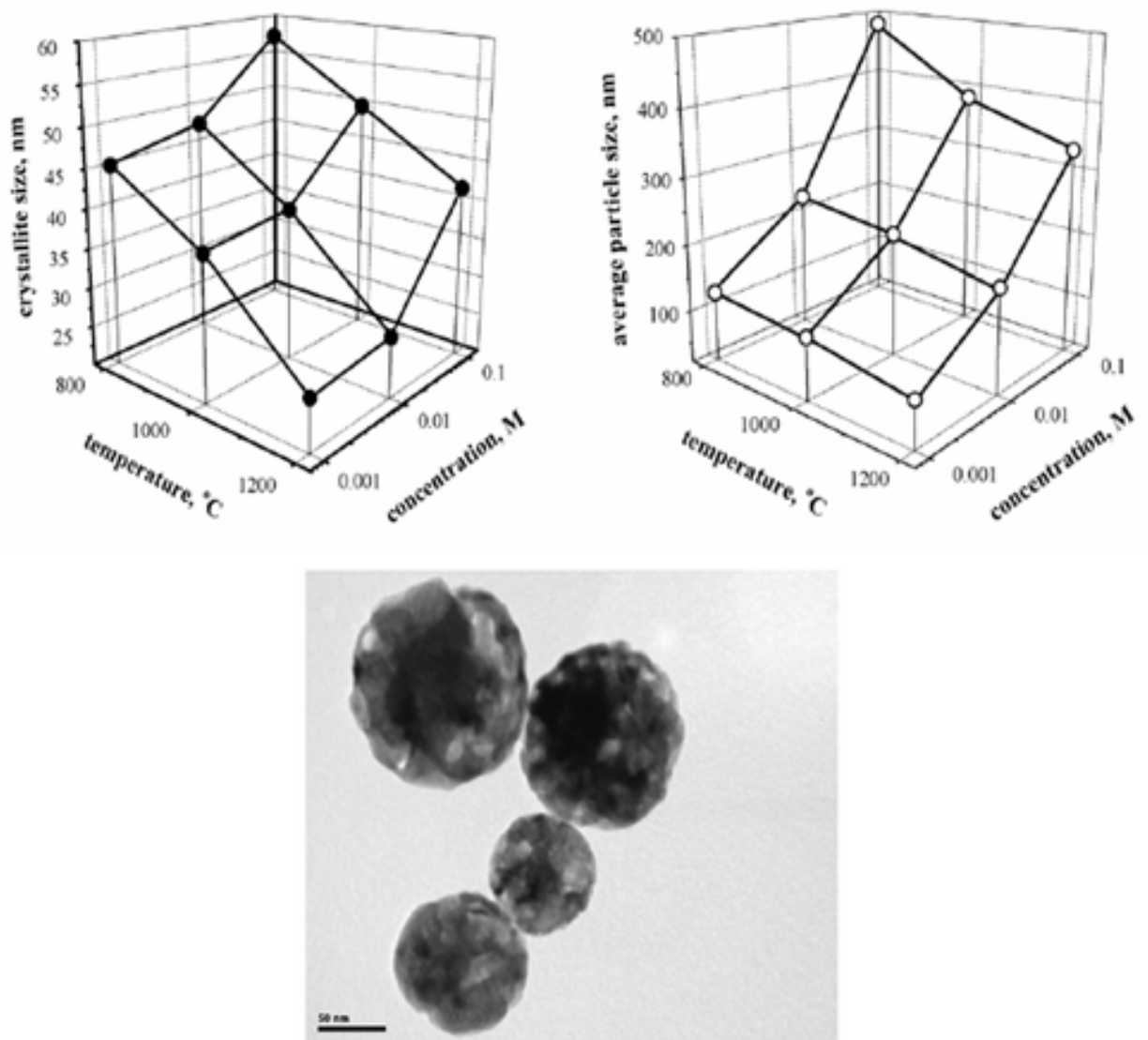


Fig. 2.20 Effect of furnace temperature during synthesis on the morphology and crystallinity of  $BZrO_3$  nanopowders by USP (from M.M. Bucko & J. Obłąkowski, *J Eur Ceram Soc.*, (2007) [Ref. 284])

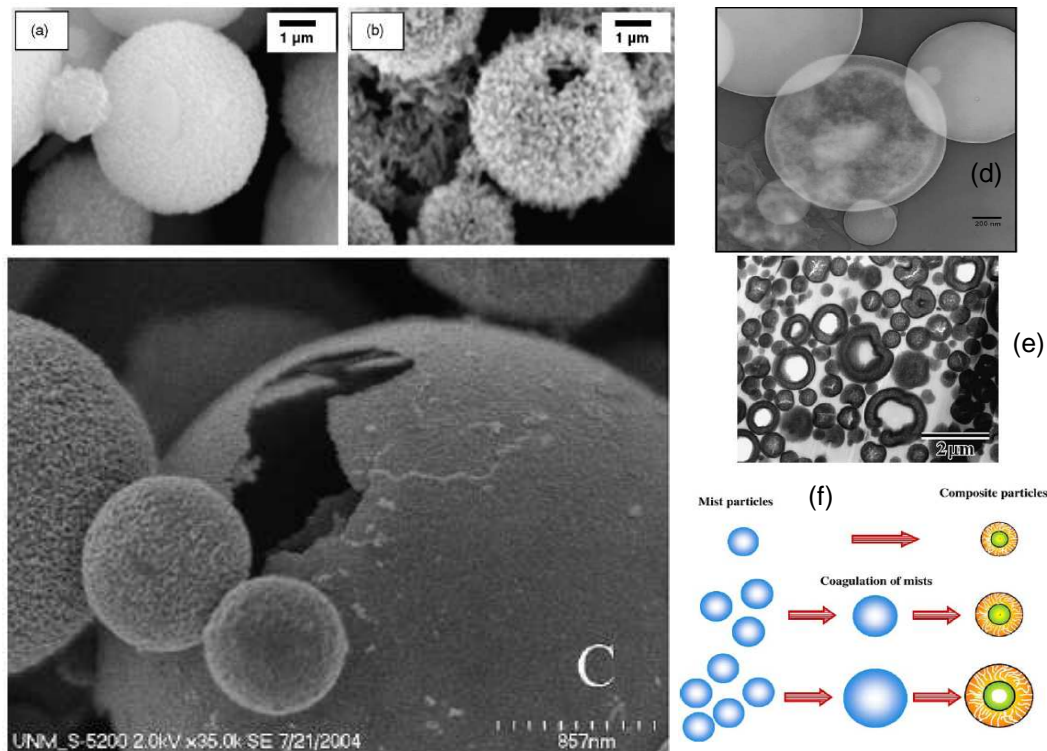


Fig. 2.21 (a) and (b) SEM images of hydroxyapatite (Hap) powders by the USP/SAD method showing the gaping hole in one of the spheres in (b) an indication of the possibly hollow nature of these spheres [From G.-H. An *et al.*, Mater. Sci. Eng. (2007) Ref. 163] (c) More vivid proof of hollow NiO-Sm<sub>0.2</sub>Ce<sub>0.8</sub>O<sub>1.9</sub> composite spheres [S. Suda *et al.*, Solid State Ionics (2006) Ref. 185] (d) and (e) HRTEM image of LiFePO<sub>4</sub>/C composite prepared at 450°C showing a shell structure and the intersection of the shells of other spheres [From M. R. Yang, J. Power Sources (2006) Ref. 180] (f) A conceptual model proposed by Yang *et al.* (2006) on how the hollow LiFePO<sub>4</sub>/C composites form with or without voids.



Of interest, apart from the production of nano-particles by ultrasonic spray pyrolysis, has been the attainment of one-dimensional structures. Many of the one-dimensional structures have been micro-sized such as the ZnO nanorods grown almost at right angles to the substrate surface [147,166,168] as shown in Fig. 2.23. This one-dimensional growth only happens at specific conditions. Note that as furnace temperature is reduced that micro-rod diameter decreases.

Another interesting case of one dimensional growth by USP was observed by Htay *et al.* [287] who reported micro-sized platelets, wires and tips of ZnO obtained at controlled conditions. Temperature of synthesis was found to dictate the morphology of the micro and submicron-structures that they obtained. In this case different furnace temperatures yield different structures- rods, wires or platelets. One-dimensional growth from spheres of  $WO_3$  which transform themselves into  $W_xO_y$  nanowires after thermal annealing at 500°C in argon for 17 hours [Mwakikunga *et al.*, JNN (2008) Ref. 42] has been observed.

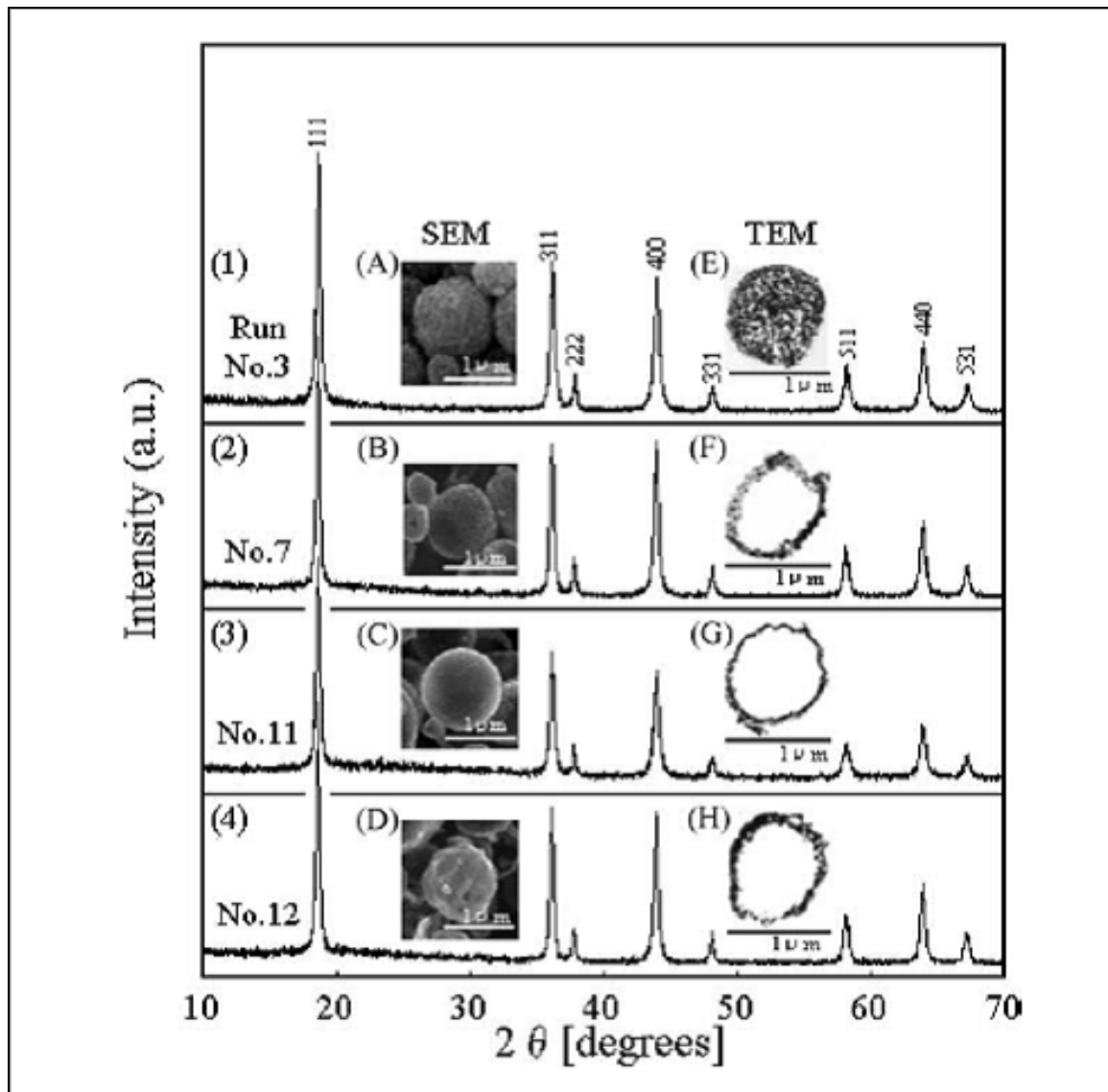


Fig. 2.22 Examples of XRD, SEM and TEM micrographs of  $\text{LiMn}_2\text{O}_4$  particles prepared from various precursors (1) dense  $\text{LiMn}_2\text{O}_4$  with porous surface structure (2) hollow  $\text{LiMn}_2\text{O}_4$  particles with hybrid surface structure (3) hollow  $\text{LiMn}_2\text{O}_4$  particles with smooth surface structure and (4) hollow  $\text{LiMn}_2\text{O}_4$  with shrinkage surface structure. From Matsuda & Taniguchi, *Journal of Power Sources* (2004) [Ref. 217]

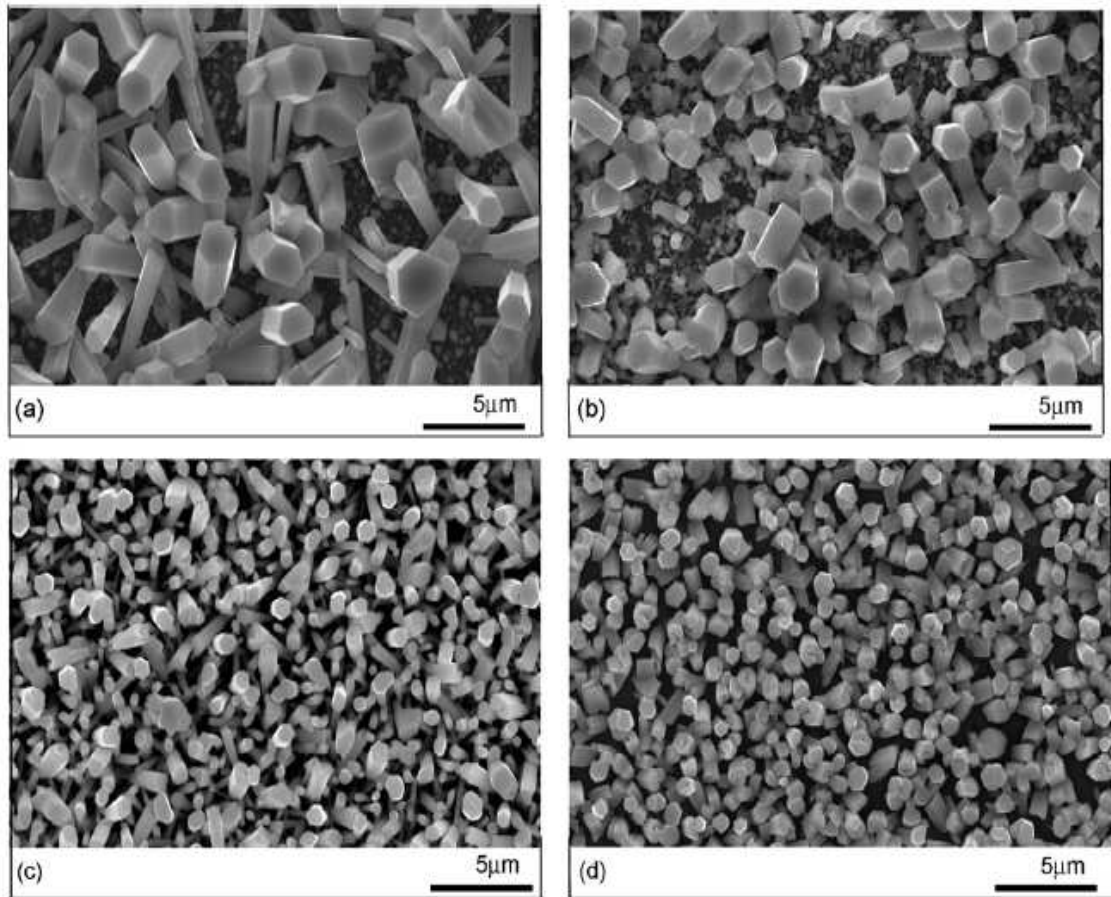


Fig. 2.23 SEM images of ZnO microrods deposited by USP at (a) 550°C (b) 500°C, (c) 450°C and (d) 400°C [From U. Alver *et al.*, Mater. Chem. Phys. (2007) Ref. 147]

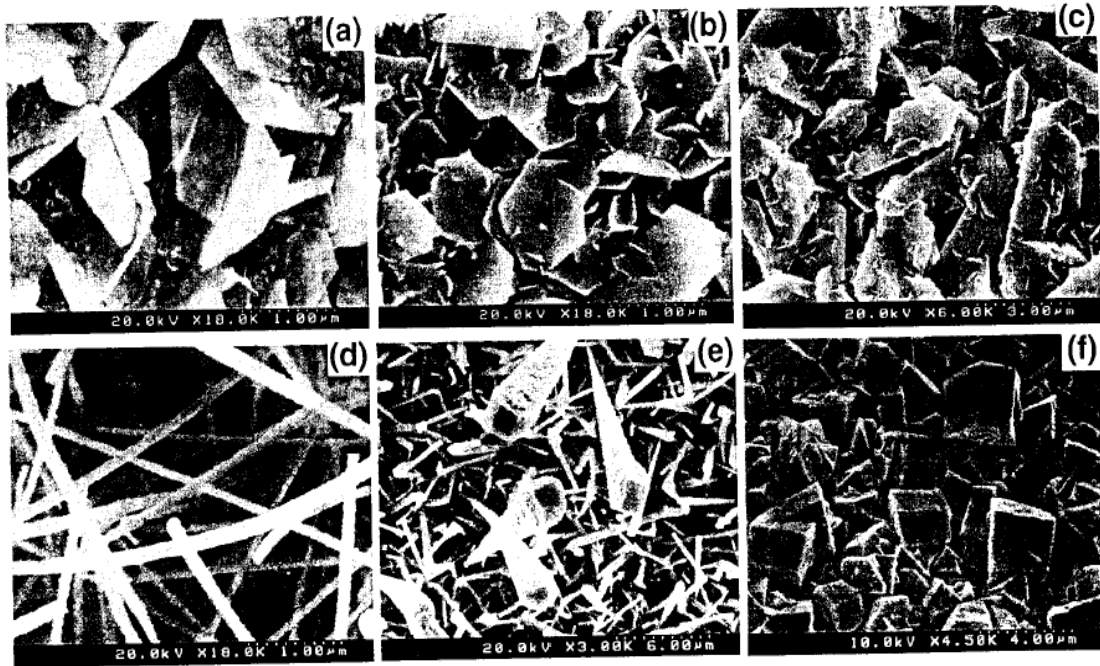


Fig. 2.24 ZnO samples grown from one kind of precursor for 120 mins at (a) 300°C, (b) 400°C, (c) 500°C and another kind of precursor for same period of time at (d) 300°C, (e) 400°C and (f) 500°C [From Htay *et al.*, Jpn J Appl. Phys. (2007) Ref.248]

Recently dense one-dimensional nano-ribbons of VO<sub>2</sub> grown by USP at 700°C in argon carrier gas without the need for thermal annealing was also observed. Their electronic transition temperature at 70°C was confirmed using a four-point probe technique. Most of the present results are discussed in Chapter 5. It was found that for the same synthesis conditions, furnace temperature, precursor flow rate etc, vanadium oxides yielded mostly nanobelts, nanoribbons and sheets where tungsten oxides showed nanowires

and nanorods. The role of the crystal structures of the final products on the surface morphology of the samples is discussed in the forthcoming chapters.

## 2.12 Laser pyrolysis

The novelty of the laser pyrolysis technique and the quantum-mechanical nature of the interaction of coherent and quasi-monochromatic radiation with matter deserved a separate section. The decision to try this approach to producing nano-structures of Vanadium and Tungsten oxides was open an addition view to the world of one-dimensional growth over and above the spherical particles and quantum dots. In this section, the use of light in general and lasers in particular in interacting with matter and materials processing applications is briefly reviewed.

As early as 1873, James Clerk Maxwell used the electromagnetic theory to calculate force on solid bodies due to absorption or reflection of light [288] and in the early 1900s quantitative measurement of the force on bodies and gases were done especially as well demonstrated by the Crooke's radiometer [289]. In 1917 Albert Einstein [290,291] using the quantum theory to calculate the influence of the electromagnetic radiation on the motion of molecules, showed the importance of the Planck's blackbody spectrum in his calculation. In later years, 1933, Otto Frisch performed the first experiment showing momentum transfer to atoms by photon absorption [292] and also in 1950 Alfred Kastler used light to cool and heat atoms [293]. In the 1970s, with the advent of more intense lasers, more pronounced effects on deflection of atom beams were observed. The first laser pyrolysis experiments (named differently then) with the CO<sub>2</sub> laser tuned at its 10P<sub>20</sub> line of wavelength 10.59  $\mu\text{m}$  are known to have been first performed by Bachmann between 1974 and

1975 [294]. The types of materials that have been reported to have been synthesized by this method in the period 1974–2008 are listed in Table 2.2 from Refs 305 to 405. In Fig. 2.25, a graph showing the progress in materials processing research by laser pyrolysis from 1974 to 2008 in terms of number of publications per year are presented.

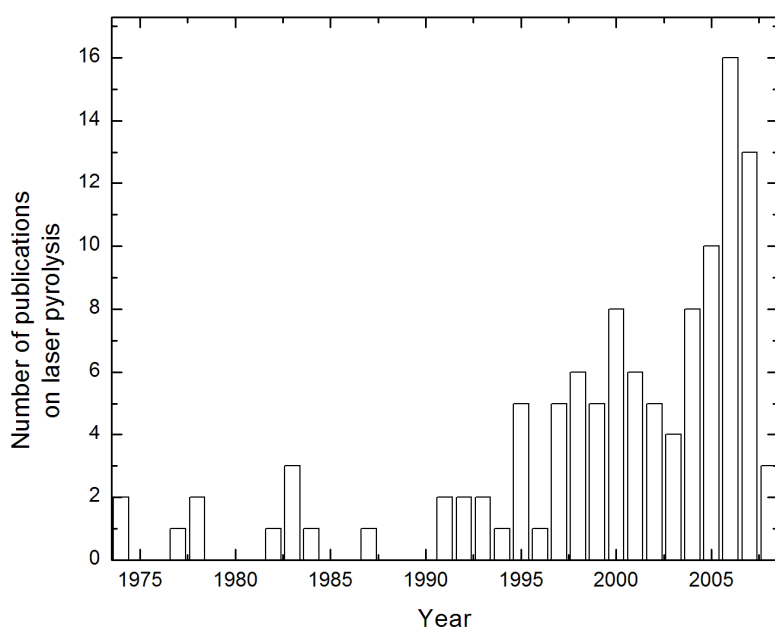


Fig. 2.25 Annual frequency of publications on laser pyrolysis from 1974 to 2008

One of the crucial subjects on laser pyrolysis is the measurement of the temperature of the aerosol at the time of its interaction with the laser beam. Measurement of this temperature cannot be accomplished with the traditional thermometer or thermocouple. Any contact with the hot aerosol changes the

temperature one is intending to measure. For this reason, non-contact methods are preferred. In this case, bolometers can be used. The most popular methods have been optical methods.

However, the understanding of the role of the laser intensity on the raising of the temperature of the aerosol has attracted a great deal of attention. In the next section various attempts to understanding the relationship between laser intensity, laser wavelength on the temperature and dissociation protocols are outlined. Since these theories have failed to explain some recent experimental data on laser intensity versus aerosol temperature, another way to get around this problem in the Chapter 5.

### 2.12.1 Bowden *et al.* (1977) low level excitation model

Bowden *et al.* [295] proposed a model for laser-induced photo-chemical reactions in which selective low-level excitation of a molecular species by the laser beam was assumed to incorporate coherent resonant energy transfer with collision damping. The resonant bonds were seen to be the heat sources and the non-resonant ones were the heat sinks. The Bowden *et al.* model was designed based on a pulsed CO<sub>2</sub> laser source. In the case where the laser pulse width is much smaller than the molecule collision times, one has a collision-free interaction and vice versa. The Hamiltonian which Bowden *et al.* developed especially for the laser interaction with gas molecules with collisions and collision damping led them to the following important equation

$$n = \frac{1}{e^{\beta h \omega} - 1} + \frac{I}{(\Delta + \Omega_R)^2 + \eta^2} \quad (2.47)$$



$n$  is the expectation value (or transition probability) that the molecule is promoted from ground state to excited state at a Rabi flopping frequency  $\omega_R$ . The Rabi frequency is related to laser intensity  $I$  by  $I = \omega_R^2$ . The laser detuning  $\Delta$  is the deviation of the resonance frequency  $\omega_0$  from the laser frequency,  $\omega$ . In this equation,  $\beta$  is equal to  $1/k_B T$ ,  $\Omega_R$  is the coherent exchange rate,  $\eta$  is the damping coefficient whose meaning will become clearer in the next sections. Aerosol temperature as a function of laser intensity and detuning can be written from Eq. 2.47 as

$$T = \frac{\hbar\omega}{k_B} \left[ \text{Ln} \left( \frac{\eta^2 + n\eta^2 + n\Delta^2 + I + 2\Delta\Omega_R + 2n\Omega_R + \Omega_R^2 + n\Omega_R^2}{\eta^2 + n\Delta^2 + I + 2n\Omega_R + n\Omega_R^2} \right) \right]^{-1} \quad (2.48)$$

When plotted in Mathematica for the usual values of  $h = 6.676 \times 10^{-34}$  J.s,  $k_B = 1.38 \times 10^{-23}$ ,  $\eta = 6.16 \times 10^7$  s<sup>-1</sup> and any values of  $\omega$ ,  $\Delta$ , and  $\Omega_R$ , this equation shows a generally direct linear relationship between aerosol temperature,  $T$  and laser intensity  $I$  [see for example Fig 4.5]. This is expected only for low level excitation as proposed by Bowden *et al.* However, the model fails at high laser power where the relationship clearly shows non-linearity.

### 2.12.2 Models based on resonant ionisation

Another important theoretical work on the interaction of laser light with atoms was presented by Hurst & Payne (1988) [296]. This work is more relevant to resonance ionization spectroscopy (RIS) rather than heating. Hurst & Payne developed a quantum mechanical treatment which could deal with coherent excitation and the related ionization. They assumed that the laser

either has a band width which is limited by Fourier analysis or has only a few cavity modes present in the spectrum. The functional form of the laser field was generally assumed and the effects of *collisions* on the laser excitation and magnetic sub-state redistribution were ignored. With regard to temperature of molecules, this model uses the blackbody radiation as empirically determined by Max Planck and theoretically derived by Albert Einstein. The laser frequency is assumed to be at exact resonance with the molecule system that is being excited by the laser. Not much has been accounted for with regard to the role of laser intensity or detuning on the temperature of the gas molecules or atoms.

### **2.12.3 Kaldor *et al.* 's review**

Kaldor *et al.* (1982) [297] reviewed some of the important underlying science aspects of photochemical and photo-thermal processes. Their discussion concentrated on those areas of laser chemistry which offered a considerable potential for commercial application and examples were selected which illustrated this point. Specific subjects treated included laser isotope separation, purification, chemical synthesis, laser pyrolysis, laser production of novel materials, laser-initiated chain reactions, laser control of electronic effects, and laser chemistry at surfaces. In this review it was important to note the three phenomena possible during the laser light interaction with matter:

(1) the molecule is initially vibrationally excited without any electronic excitation

- (2) electronically excited where chemical reactions are possible and
- (3) ionisation.

In the first case the pathways to molecular vibration are

- (a) absorption of a single IR photon
- (b) a sequence of many IR photons
- (c) coherent multi-photon excitation
- (d) excitation by an overtone and
- (e) combination band of the molecular vibration using a visible laser.

All these pathways produce molecules which are vibrationally excited in the electronic ground state. The second phenomenon, where molecules are excited electronically leading to photo-chemical reactions is accomplished using a visible or a UV laser. The third phenomenon, production of ionic species, is accomplished using all wavelengths of a laser (IR, visible, UV) with large intensity via single or multi-photon absorption or via dielectric breakdown.

#### **2.12.4 El- Diasty *et al.* (2003) SiH<sub>4</sub> pyrolysis theory**

El-Diasty *et al.* (2003) [298], in line with Kaldor *et al.* classification, outlines four mechanisms through which molecule excitation by the CO<sub>2</sub> laser possibly happens:

- (A) Linear absorption mechanism from Haggerty & Cannon [299] and Party *et al.* [300], that is, one photon per dissociation. But, from activation energy for the reaction of SiH<sub>4</sub> with

C<sub>2</sub>H<sub>4</sub> into SiC which is about 3 eV, one would need about 30 photons from the 10.6 - μm CO<sub>2</sub> laser energy of 0.1 eV. Also, for instance, the Si-H bond energy, which is about 2.8 eV, would require about 28 photons from the 10.6 μm laser to break it. These instances call for a non-linear absorption phenomenon [301]. This then calls for another mechanism B

- (B) A collision free multi-photon absorption (MPA), where laser pulses are shorter than the molecular collision times and mechanism C,
- (C) a collision induced MPA. El-Diasty *et al.* classify mechanism D, pyrolysis, separately from the mechanisms A, B and C.
- (D) In an attempt to elaborate on pyrolysis, El-Diasty *et al.* start from the Beer-Lambert's law  $I = I_0 \exp(-\alpha.p.L)$  where  $\alpha$  is the absorption coefficient, p is the pressure and L is the length along which the laser beam traverses during the transverse interaction with the molecules. The absorption cross-section  $\sigma_A$  was written in terms of Lorentz or pressure broadening  $\Delta\nu_L$  as

$$\sigma_A = \sigma_0 \frac{\Delta\nu_L}{(\Delta\nu_L)^2 + \Delta^2} \quad (2.49)$$

$\sigma_0$  is the absorption without pressure broadening and  $\Delta$  is the detuning or frequency mismatch as also seen in the Bowden *et al.* model above. The

frequency dependent absorption coefficient  $\alpha(\nu)$  corrected for the so-called “Doppler pressure broadening” is given as

$$\alpha(\nu) = \alpha_0 \exp\left[-\frac{2(\nu - \nu_0)(\ln 2)^{1/2}}{\Delta\nu_D}\right]^2 \quad (2.50)$$

$\Delta\nu_D$  is the Doppler FWHM determined previously by Lengyel [15] empirically in terms of line position  $\nu_0$  of the laser and temperature  $T$  of the surrounding which in the present case is the temperature of the molecules being excited by the laser

$$\Delta\nu_D = 7.162 \times 10^{-7} \left(\frac{T}{M}\right)^{1/2} \quad (2.51)$$

After such a quantitative analysis of the pyrolysis of silane by El-Diasty *et al.*, no direct relationship is provided between how hot the gas gets for a given laser power.

Due to the lack of a conclusive theoretical model that would be used to predict the temperature of the aerosol while in the laser beam, this discussion is continued in Chapter 5 where a current alternative model is presented and used to estimate the temperatures of the precursor plume in the chamber.

In conclusion, this chapter has shown the many forms of spray pyrolysis. The role of the temperature of the precursor liquid in changing the final particle size has been demonstrated. Also the known theories of laser pyrolysis have been reviewed with the intention of exposing some gaps in the understanding on photo-chemical and photo-thermal reaction. More proposed theories are presented in the Discussion chapter.

## Chapter 3

### **Size Matters: Properties of Materials at the Nano-scale**

This chapter considers some theoretical aspects and the physics of the properties of materials as their geometrical dimensions reduce down to nano-scale. There are numerous properties that are affected by the size but only some of them will be considered such as hysteresis width of the thermochromism of  $\text{VO}_2$ , electronic properties of  $\text{VO}_2$  ribbons and vibrational (phonon) properties of  $\text{WO}_3$ . The change in properties is chiefly due to the increase in surface to volume (bulk) ratio as the particle shrinks in size.

#### **3.1 Surface and bulk**

It has long been realised that surface atoms in materials behave completely differently from those in the bulk of the material. If one considers the illustration in Fig. 3.1 one notes that the number of neighbouring atoms around the surface atom A, for instance, is smaller by a factor of 50% than that which is surrounding atom B in the bulk. As a result of this fact, one notes further that there are some un-shared electrons on atom A whereas atom B is fully filled.

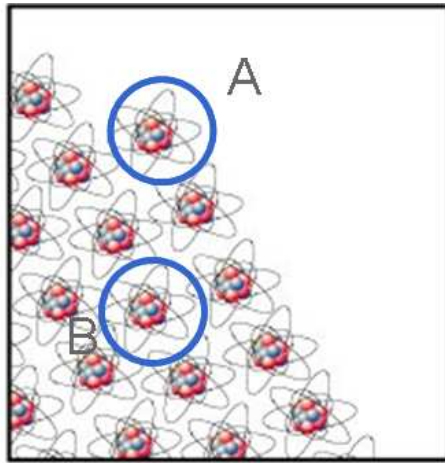
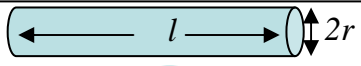

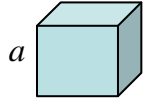
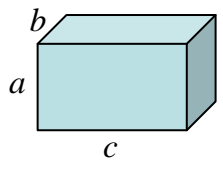
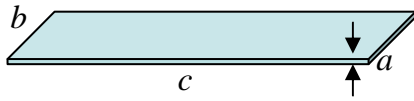
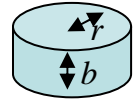
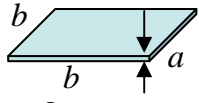
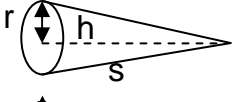
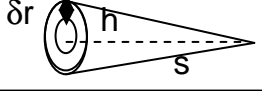


Fig. 3.1 The difference between surface and bulk atoms. In 2D, surface atoms are each surrounded by about 3 other atoms whereas the inner (bulk) atoms are surrounded by at least 6 atoms.

The un-shared electrons on the part of A are often referred to as dangling bonds. For this reason, mechanical, vibrational, electronic and, consequently, optical properties of surface atoms/molecules are different from those in the bulk.

It is also easy to see that the proportion of surface atoms to those in the bulk material  $N_{\text{surf}}/N_{\text{bulk}}$  can be represent by the ratio,  $\sigma_{\text{surf}}$ , of the surface area to the volume of the particle.

Table 3.1 The surface to volume ratio expression for various structures

	rod/ wire	$(\sigma_{surf})_{rod} = \frac{2}{l} + \frac{2}{r}$
	sphere	$(\sigma_{surf})_{sphere} = \frac{3}{r}$
	cube	$(\sigma_{surf})_{cube} = \frac{6}{a}$
	cuboid	$(\sigma_{surf})_{cuboid} = \frac{2}{a} + \frac{2}{b} + \frac{2}{c}$
	strip/ belt/ ribbon	$(\sigma_{surf})_{ribbon} = \frac{2}{a} + \frac{perimeter}{area_{bc}}$
	disc	$(\sigma_{surf})_{disc} = \frac{2}{a} + \frac{2}{r}$
	sheet/ film	$(\sigma_{surf})_{sq.disc} = \frac{2}{a} + \frac{4}{b}$
	solid cone/ tip	$(\sigma_{surf})_{tip} = 3\left(\frac{s}{rh} + \frac{1}{h}\right)$
	horn/ cone	$(\sigma_{surf})_{horn} = \frac{3}{h\delta r}(s+r)$

An isolated atom can be said to be completely a surface atom since there are no neighbouring atoms around it. As the number of atoms aggregate the number of bulk atoms increase, thereby decreasing the surface to volume ratio. The expressions for  $\sigma_{surf}$  for different shapes that materials can adopt are tabulated in Table 3.1. As the dimensions of the structure decrease, the value of  $\sigma_{surf}$  increases very rapidly.



### 3.2 Lattice vibrations (phonons) in nano-structures

The effect of size on the vibrational properties of materials appears in the early work of Tuinstra & Koenig who developed their equation in 1970 for carbon systems such as amorphous carbon, graphite, diamond, carbon nanotubes e.t.c. [406].

$$\frac{I_{D(1350\text{cm}^{-1})}}{I_{G(1580\text{cm}^{-1})}} = \frac{C(\lambda)}{L_{\text{grain}}} \quad C(\lambda = 514.5 \text{ nm}) = 44 \text{ nm} \quad (3.1)$$

This equation relates the ratio of phonon intensities  $I_D$  of the disorder (defect) peak to the perfect phonon intensity  $I_G$  of the perfect graphite peak to the carbon allotrope grain size. For grain sizes that are smaller than 44 nm, the D peak is higher than the G peak, otherwise the grain size is larger than 44 nm.

In the 80's it became apparent that Raman spectral lineshapes for micro-crystals could not follow the perfect Gaussian profile. It then was realised that there was need for deeper understanding of the origin of this asymmetry. Spatial correlation modelling, as it was called, then became one way to extract information from Raman spectroscopy data. The justification is that, for a perfect (bulk) crystal of diameter  $d$  having vibrational modes of momentum  $q$ , the Heisenberg's uncertainty principle ( $\delta l \cdot \delta q \sim h$ ) means that as  $\delta l \rightarrow \infty$  (bulk) then  $\delta q \rightarrow 0$  (the " $q = 0$ " selection rule applies). As the diameter,  $\delta l \rightarrow 0$  (nano-metric) then the vibrational momentum,  $\delta q \rightarrow \infty$ . In this case, the " $q = 0$ " selection rule breaks down; a contribution from the  $q \neq 0$  phonons

determined by the dispersion relation  $\omega(q)$  is allowed. This accounts for the asymmetric broadening of the peaks in a Raman spectrum. The Richter equation for confined phonons in spherical nano-particles [407] was modified to include Gaussian distribution of the phonon momenta and particle size by Campbell & Faucet [408]. And this equation is given here as

$$I(\omega) = A_0 \int_{-\infty}^{\infty} \left[ \frac{|C(0, q)|^2}{(\omega - \omega(q))^2 + (\Gamma_0 / 2)^2} \right] d^3 q \quad (3.2)$$

In the Eq. 3.2,  $\Gamma_0$  is the full-width-at-half-maximum (FWHM) for bulk material Raman peak (for instance  $\Gamma_0 = 6.5 \text{ cm}^{-1}$  for  $\text{WO}_3$  [41]),  $\omega(q)$  is the phonon dispersion curve relation (PDR) for the material (for instance  $A = 713 \text{ cm}^{-1}$ ,  $a = 0.76 \text{ nm}$  for the  $713 \text{ cm}^{-1}$  phonon branch whereas  $A = 808 \text{ cm}^{-1}$  and  $b = 0.38 \text{ nm}$  [41] for the  $808 \text{ cm}^{-1}$  phonon branch). The Richter *et al.* model is valid for spherical nano-crystals of mean diameter  $d$  for which the Fourier coefficient  $C(0, q)$  was assumed to be Gaussian of the form  $\exp(-q^2 d^2 / 14\pi^2)$  with a phonon amplitude at the boundary of  $1/e$ . When geometry deviates from a sphere then adjustment has to be carried out. For a nanowire shape for instance, confinement is in two dimensions of the diameter of the nanowire since the length of the rod can be as long as  $1 \mu\text{m}$ . Campbell & Faucet (1986) extended the Richter *et al.* model to (1) remove the non-physical boundary condition of  $1/e$  and tried other values (2) check the effect of other particle-size distribution functions such as (a)  $\sin(ar)/(ar)$  by analogy with the ground state of an electron in a hard sphere (b)  $\exp(-\alpha r)$  by analogy with a lossy medium and (c)  $\exp(-\alpha r^2/d^2)$ . Campbell & Faucet further extended the

Richter model to other shapes of the micro-crystals such as what they called columnar (now called rod-like or nano-wires) and also thin films. They argued that for these two additional shapes, the following Fourier coefficients should be incorporated in the Richter *et al.* equation:

$$|C(0, q)|^2 \cong \exp\left(-\frac{q_1^2 d_{rod}^2}{16\pi^2}\right) \cdot \exp\left(-\frac{q_2^2 l_{rod}^2}{16\pi^2}\right) \left|1 - \operatorname{erf}\left(\frac{iq_2 l_{rod}}{\sqrt{32\pi}}\right)\right|^2 \quad (3.3)$$

for a rod of diameter  $d_{rod}$  and length  $l_{rod}$  and

$$|C(0, q)|^2 \cong \exp\left(-\frac{q_1^2 \tau_{film}^2}{16\pi^2}\right) \left|1 - \operatorname{erf}\left(\frac{iq_1 \tau_{film}}{\sqrt{32\pi}}\right)\right|^2 \quad (3.4)$$

for a thin film of thickness,  $\tau_{film}$ .

Campbell & Faucet admittedly saw very small significance in replacing the Gaussian with other size-distribution functions especially for spherical nano-crystals. Also the Fourier coefficients for thin films and columnar shapes make the Richter *et al.* equation even more complicated in that one performs integration within another numerical integration. A simpler approach to modifying the Richter equation to include other novel nano-crystal shapes has been considered.

Consider a small slice of with  $dr$  and a distance  $r$  from the centre of the wire in real space as illustrated in Fig. 3.2. In momentum space, this slice contains phonons of momentum  $dq_{\perp}$  perpendicular to the length of the wire and a distance  $q_{\perp}$ . In this case, the cross-section surface in the 2D confined phonons in phonon-momentum space of the wire is equal to  $2\pi q dq_{\perp}$ .

Following this argument, the Richter equation has been modified to account for the geometry of nano-wires by Piskanec [409] and by Adu *et al.* [410,411] by changing the  $d^3q$  term for a sphere to  $2\pi q dq$  for rods

$$I(\omega) = A_0 \int_{-\infty}^{\infty} \left[ 2\pi q_{\perp} \frac{\exp\left(\frac{q_{\perp}^2 d_{wire}^2}{\alpha}\right)}{(\omega - \omega(q))^2 + (\Gamma_0 / 2)^2} \right] dq_{\perp} \quad (3.5)$$

Note that the constant  $16\pi^2$  has been replaced with a scaling parameter  $\alpha$  that can be evaluating during the data fitting. Battacharyya *et al.* [411] also modified the Richter equation to include size distribution of oxide-coated silicon nanowires.

Quantum dot structured are assumed to be quasi-zero dimensional and hence all the atoms are surface atoms. Therefore, the  $d^3q$  term in Richter *et al* equation can be replaced [409] by momentum volume of  $4\pi q^2 dq$ .

$$I(\omega) = A_0 \int_{-\infty}^{\infty} \left[ 4\pi q^2 \frac{\exp\left(\frac{q^2 d^2}{\alpha}\right)}{(\omega - \omega(q))^2 + (\Gamma_0 / 2)^2} \right] dq \quad (3.6)$$

Kim *et al.* [412] have also modified the Richter equation to suit their data on nano-slabs. Slab-like nano-structures such as nano-belts and nano-ribbons have phonon confinement only in one dimension like thin films as in the Campbell-Faucet model.

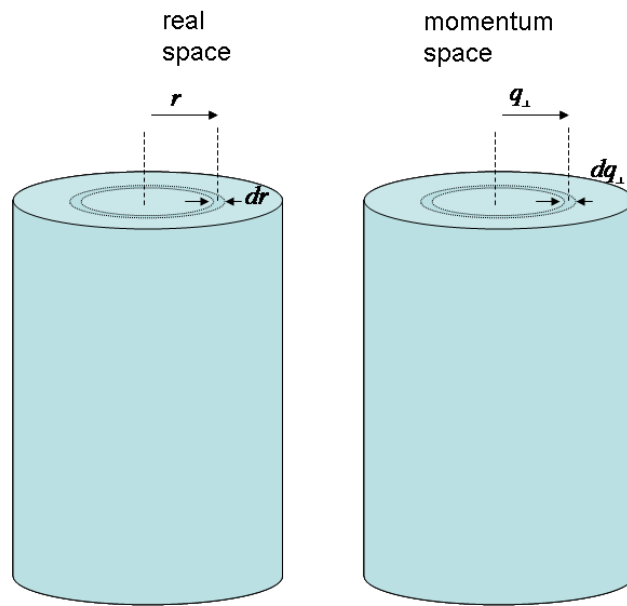


Fig. 3.2 Real space and  $q$ -space illustration of how the three-dimensional confinement,  $d^3q$ , is transformed to two-dimensional confinement  $2\pi q dq$  in a nanowire

### 3.4 Raman spectroscopy of nano-composites

Arora *et al.* [415] observed that when nanocrystals of diamond are dispersed in a surrounding medium of similar materials such as amorphous carbon, phonon confinement becomes rather weak due to phonon leakage to this medium. They developed another modification to the Richter *et al.* equation based on summation of the discrete standing waves of the phonons that define the asymmetrical Raman spectral peak for the nano-crystal. The Arora *et al.* equation is suitable in cases where any scattering nano-crystal is embedded in any matrix. The Arora equation is given as

$$I(\omega) = A \sum_{n=1}^N \frac{b_n}{1 + \left( \frac{\omega - \omega(q_n)}{\Gamma_o / 2} \right)^2} \quad (3.7)$$

A is a pre-factor to be determined after the fitting session, the summation runs over the phonon modes  $\omega(q_n)$  representing the contribution of phonons away from the zone centre and is given as  $\omega(q_n) = \omega_0 \beta \sin^2(aq/4)$ , where  $a$  is the lattice constant,  $\omega_0$  is the zone centre phonon frequency. One expects  $b_n$  to be a monotonically decreasing function of  $n$ , as the probability of exciting phonons far removed from the zone centre is expected to reduce rapidly with the magnitude of the wave vector and  $b_n$  is assumed to vary according to a power law  $b_i = b^i$  ( $b < 1$ ). Arora *et al.* [17] also gave  $q_n$  as

$$q_i = \frac{iQ_B}{N}, \quad (1 \leq i \leq N) \quad (3.8)$$

$Q_B$  is the wave-vector corresponding to the Brillouin zone boundary. Particle size is estimated to be  $d = Na$ . This model has been used to analyse nano-clusters of carbon in the hosts of ZnO, NiO and SiO<sub>2</sub> [37] and also this model has been used to calculate the size of the diamond-like nano-crystals created when slow highly charged ions interact with highly oriented pyrolytic graphite (HOPG) [17], although this calculation was not shown in this paper for the reason that the presence of nano-diamonds was not definite.

The equations can not be solved analytically and therefore numerical integration codes have to be developed. The codes for the analysis of Raman spectroscopy data for WO<sub>3</sub> nano-wires were written as reported in Mwakikunga *et al.* [41], carbon in ZnO, carbon in SiO<sub>2</sub> and carbon in NiO by

Katumba & Mwakikunga [37], diamond-like nano-carbon in HOPG by Arora *et al.* [17] and VO<sub>2</sub> ribbons in Mathematica™ (manuscript in preparation) and the results are discussed in the next chapter. The Campbell – Faucet model and the present model are tested on the same nano-ribbons data in the chapter that follows.

### 3.5 Size effects and surface phonons

For particles with less than 5 nm in diameter almost all atoms in that particle are surface atoms. The ratio of surface to bulk atom is estimated by the surface area (S) to volume ratio (V). For a spherical particle this ratio is  $S/V = 3/r$  where  $r$  is the radius of the particle as shown in Table 3.1. If  $r = 5$  nm then  $S/V$  is  $6 \times 10^8 \text{ m}^{-1}$ . Compare this with a sphere of 1 m where  $S/V$  is simply  $1 \text{ m}^{-1}$ . The peaks 1300 and 1304  $\text{cm}^{-1}$  could be due TO-LO splitting. This phenomenon has been observed in particles of less than 5 nm. This regime of particle sizes is known to be a region where phonon confinement models fail. The essential characteristic of the Raman-active SO phonon modes is that their peak position and line shape are sensitive to the real part of the dielectric function of the dielectric medium in contact with the surface [8]. As a consequence of the TO-LO splitting, a third peak called surface optical (SO) phonon peak between the TO and LO phonon peaks. For cubic systems, the peak position of the SO phonon,  $\omega_{\text{SO}}$ , is given by [416-420]

$$\omega_{SO} = \sqrt{\frac{\frac{m+1}{m} \omega_{TO}^2 + \frac{\epsilon_{\infty}}{\epsilon_M} \omega_{LO}^2}{\frac{m+1}{m} + \frac{\epsilon_{\infty}}{\epsilon_M}}} \quad (3.9)$$

In this equation  $m = 1, 2, 3, \dots$ ,  $\epsilon_{\infty}$  is the high frequency dielectric constant of the semiconductor (in the present case the diamond-like nano-carbon) and  $\epsilon_M$  is the frequency independent dielectric constant of the surrounding medium (in the present case, graphite). For the publication by Mwakikunga *et al.* in Ref. 17 it was noted that  $\epsilon_{\infty}$  for diamond varies from 5 to 10 and, for graphite,  $\epsilon_{\infty}$  varies from 10 to 15. With some calculation, it is found that the dielectric constants of 13.41 for diamond-like carbon and 15.24 for the surrounding graphite is responsible for the LO-TO splitting of the surface optical (SO) phonon positioned at  $1305 \text{ cm}^{-1}$ . Both dielectric constants are higher than their bulk counterparts. These measurements seem to be in agreement with the fact that most materials become less conductive when their particle sizes are reduced to nano-meter scale. The effect of size on the dielectric constant is enhanced on the diamond-like carbon than on the graphite that is surrounding it.

### 3.6 Red-shifts due to size effects

Redshifts in Raman spectroscopy owing to the particle size has been well observed by Zi *et al.* [422] in Si nanocrystals of spherical and columnar shape with sizes from 5 nm down to 1 nm. Redshifts up to  $30 \text{ cm}^{-1}$  have been



reported for nanocrystals of diameter of 1 nm. The Richter *et al.* phonon confinement model failed to explain the Zi *et al.* data on Si nanocrystals. Therefore they used what is known as the Bond Polarizability Model [423] to derive another confinement model [422] given by

$$\omega_{vib}(d) = \omega_0 - A \left( \frac{a}{d} \right)^\gamma \quad (3.10)$$

In this equation  $d$  is particle size,  $\omega_{vib}$  is the new peak position due to particle size,  $\omega_0$  is the original peak position,  $A$  and  $\gamma$  are constants that are attributes of the geometry of nanocrystal. For instance, according to Zi *et al.*, for spherical Si nano-crystals  $A = 44.41 \text{ cm}^{-1}$  and  $\gamma = 1.44$  whereas for columnar shapes one has  $A = 20.92 \text{ cm}^{-1}$  and  $\gamma = 1.08$ .

### 3.7 Size effects on the thermo-chromism

A number of transition-metal oxides exhibit insulator - (or semiconductor-) to-metal transition [39, 424]. The three main groups among the vanadium oxides are  $V_nO_{2n-1}$  (e.g.  $V_2O_3$ ,  $V_7O_{13}$  [424]),  $V_nO_{2n+1}$  (e.g.  $V_2O_5$ ,  $V_6O_{13}$  [425] and  $V_3O_7$  [426]),  $V_nO_n$  (e.g. VO) and  $V_nO_{2n}$ . Among these,  $VO_2$  is the most interesting because its transition temperature is close to room temperature ( $T_c \sim 340 \text{ K}$ ), and it displays a  $\sim 10^5$  decrease in resistivity as well as a large change in transparency in the infrared region.  $VO_2$  belongs to the  $V_nO_{2n}$  class and it is known to exist in four polymorphs -  $VO_2(R)$ ,  $VO_2(M)$ ,  $VO_2(A)$ ,  $VO_2(B)$  - given in Table 3.2 (a) the most stable  $VO_2$  rutile  $VO_2(R)$  (b) the

metastable VO<sub>2</sub>(M) with a slightly distorted rutile structure (c) a tetragonal VO<sub>2</sub> (A) and (d) the metastable VO<sub>2</sub>(B) with a monoclinic structure.

Table 3.2 Lattice parameters for the four polymorphs of VO<sub>2</sub>

		Lattice parameters						
		a (Å)	b (Å)	c (Å)	α	β	γ	T (K)
VO <sub>2</sub>	(M)	12.09	3.702	6.433	90	122	90	300
rutile								
(monoclinic)								
VO <sub>2</sub>	(R)	4.554	4.554	2.854	90	90	90	> 340
rutile								
tetragonal								
VO <sub>2</sub>	(A)	8.4403	8.4403	7.666	90	90	90	300
		No	transition					>340
VO <sub>2</sub>	(B)	12.03	3.693	6.42	90	106	90	300
		No	transition					>340

Thermo-chromism of VO<sub>2</sub> is attributed largely to structural change [427]. Characteristics of this change include the formation of cation - cation pairs and the displacement of vanadium from the centre of its interstice in the monoclinic phase- a feature characteristic of an anti-ferroelectric-type distortion. The actual values of the transition temperature and its sharpness and the lack thereof, have previously been related to variations in stoichiometry, misorientation between grains, and other morphological faults only in a qualitative fashion [428]. One of the important properties in the VO<sub>2</sub> transition that has been related to grain size is the hysteresis width (HW) of

the transition. Hysteresis is the change of path during the heating up cycle and during the cooling down cycle in the resistivity-temperature or transmittance-temperature or reflectivity-temperature or roughness-temperature charts. Lopez *et al.* [429] have shown that as the grain size is reduced the hysteresis width increases with an accompanied loss in what in this thesis is called the hysteresis jump (HJ). The Lopez *et al.* illustration of their experimental observation of this fact is represented in Fig. 3.4 with the present additional labels of HW, HJ for the sake of illustration.

In order to understand the dependence of the transition on the VO<sub>2</sub> particle size, Lopez proposed that the semiconductor-to-metal transition is related to the nucleation mechanism of the VO<sub>2</sub> crystals. For this they assumed that (1) the VO<sub>2</sub> particles were spherical (2) the classical nucleation theory applied in which the stress-free Gibbs free energy expression  $\Delta G = - (4\pi/3)R^3\Delta g_{ex} + 4\pi R^2\gamma$  (with R being the particle size,  $\Delta g_{ex}$  being the bulk free energy decrease per unit volume which was assumed to be proportional to  $|T-T_c|$  determined by the entropy energy difference between the parent and the product phase as 0.657 MJ/(m<sup>3</sup>K) and  $\gamma$  being the surface energy per unit area which was estimated to lie in the range 10-20 mJ/m<sup>2</sup>). From this equation, a barrier of 10<sup>-16</sup> J ( $\sim 6 \times 10^2$  eV) was estimated which translated to  $10^4 k_B T$  at the temperature where the VO<sub>2</sub> transition occurs spontaneously. Since the thermal energy was too small for homogenous nucleation, Lopez *et al.* suggested that nucleation took place at special sites like those observed in the martensitic transformations. Lopez's assumption of spherical shape of the

VO<sub>2</sub> particles is the first weakness in the whole of their attempt to attribute particle size to the SMT transition since, according to their SEM micrographs, their VO<sub>2</sub> particles are far from spherical.

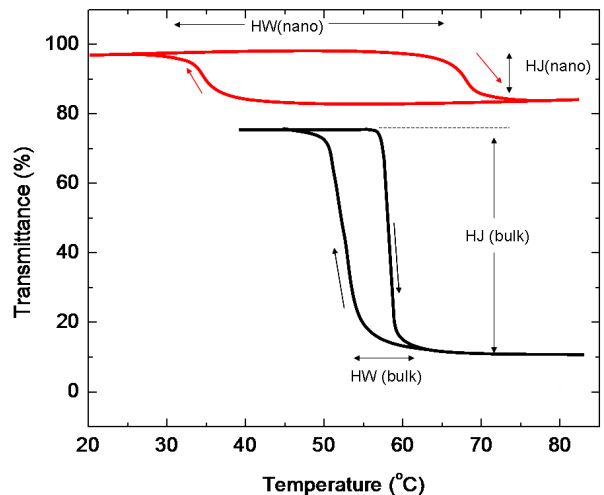


Fig. 3.4 Hysteresis loops for heating-up and cooling-down cycles in VO<sub>2</sub> thin films and VO<sub>2</sub> nanocrystals. Note the variations in the hysteresis width and hysteresis jump as the size of the VO<sub>2</sub> crystals tends to nano-scale

In fact they are belt-like as has clearly been observed in the present results. Also their nucleation theory as it is assumed to affect the SMT transition cannot be stress-free as it is well known that there is tremendous amount of stress as the VO<sub>2</sub> crystal changes from a monoclinic structure with volume of  $12.05 \sin(122) \times 3.702 \times 6.433 \text{ \AA}^3$  to the smaller volume of tetragonal symmetry of  $4.554^2 \times 2.854 \text{ \AA}^3$ . This stress cannot be negligible and has to be accounted for. Also, Lopez *et al.*'s important work shows that as annealing

time of the samples is increased that equivalent radius increases. Hysteresis loops at different annealing times (and hence particle sizes) are compared only qualitatively.

Lopez *et al.*'s important pioneering observation of the dependency of the SMT transition on particle size,  $d$  is extended. From their qualitative comparison of the SMT- $d$ , one can draw a conclusion: the smaller the particles the larger the hysteresis width (HW) and the smaller the hysteresis jump (HJ) as shown in the illustration in Fig. 3.4. The first quantity, HW, in Mwakikunga *et al.* [Ref. 41] was introduced also only qualitatively. In this work, the statistical description of the VO<sub>2</sub>'s SMT introduced by Pan and co-workers in 2004 [430] is adapted. Pan *et al.*, using Raman spectroscopy of VO<sub>2</sub> noted that some phonons that are present in the low-temperature monoclinic structure of VO<sub>2</sub> are not present in the high-temperature tetragonal structure. Since the existence of a phonon is either yes or no before and after the phase transition, Pan *et al.* gave the following delta function:

$$\theta(T - T_c) = \begin{cases} 1 & (T < T_{tr}) \\ 0 & (T > T_{tr}) \end{cases} \quad (3.11)$$

where  $\theta$  indicates the existence or not of a certain phonon mode in a crystal grain with either semiconductor or metallic phase,  $T_{tr}$  is the equilibrium phase transition temperature.

Pan *et al.* also considered the effect of the spread in the grain size on the hysteresis loop during the transition process. It was assumed that each grain had its own hysteresis loop and that each elementary loop was located

normally to the temperature axis. Pan *et al.* were able to develop expressions for the intensity of the Raman mode as a function of the temperature by using the delta function above and performing integration of all the loops of grains whose size distribution was assumed to be Gaussian distribution. However, no direct dependency of the HW and HJ on the particle size was shown. It has been observed that, while it is true that grain size has a distribution which is assumed to be Gaussian, it is the temperature which leads to a force of change. The Gaussian is expressed to take into account the independent variable T (expressed as thermal energy  $k_B T$ ) and strain energy (expressed as  $\sigma_E V$ - where  $\sigma_E$  is the strain energy per unit area at transition and V is the volume of the grain where the thermal energy is expended). So during the heating up cycle, the number  $N_+$  of grains that transform from monoclinic phase to tetragonal phase is given as

$$N_+ = \begin{cases} 0 & \infty > T > T_{tr1} \\ A_+ \exp\left[-\alpha\left(\frac{(T - T_{C1})}{\sigma_{sd}}\right)^2\right] & T_{tr1} > T > 0 \end{cases} \quad (3.12)$$

Similarly, during the cooling down cycle, the number of crystallites  $N_-$  that transform from tetragonal back to monoclinic is

$$N_- = \begin{cases} 0 & T_{tr2} > T > 0 \\ A_- \exp\left[-\alpha\left(\frac{(T - T_{tr2})}{\sigma_{sd}}\right)^2\right] & \infty > T > T_{tr2} \end{cases} \quad (3.13)$$

The dependent variable value (transmittance, intensity of the Raman phonon mode or the resistivity) can be found by using the delta function in

Eq. 3.11 and the number of crystallites that give rise to the observed property, thus:

$$I_+ \approx 1 - C_+ \int_{-\infty}^T N_+ dT \quad (3.14)$$

$$I_- \approx C_- \int_{-\infty}^T N_- dT \quad (3.15)$$

In this study it was possible to calculate the HW as a difference between  $T_{c1}$  and  $T_{c2}$  in Eqs. 3.14 and 3.15. It was found that HW increases as the particle size increases- a fact that opposes experimental observations by Mwakikunga *et al.* [455] and several others such as Lopez [429]. Also, the limits of integration are not physical. For instance, there is no such thing as negative temperature on the Kelvin scale and lowest on the Celsius is  $-273^\circ\text{C}$  and not  $-\infty$ . This discussion is continued and concluded in Chapter 5

## Chapter 4

### **Production of VO<sub>2</sub> and WO<sub>3</sub> Nano-Structures by Laser Pyrolysis (LP) and Ultrasonic Spray Pyrolysis (USP)**

In Chapter 2, a background to ultrasonic spray pyrolysis (USP) and laser pyrolysis (LP) techniques has been laid. Characteristic of USP is the low cost when compared to the purity of materials it is capable of realizing, ease of assembly, operational safety and simplicity of the operational procedures. LP on the other hand is probably fifty-times more expensive than USP on both the initial purchasing and running costs, laser safety procedures to be adhered to and the requirement for the on-the-dot alignment of the optical system. In addition, in the present system, the source of impurities has been difficult to trace since the materials that the laser excites cannot all be known at the beginning.

Although expensive, LP has advantages of being able to produce new materials that cannot be produced when using other traditional methods. This is accomplished through LP's

- (1) selective dissociation and
- (2) rapid quenching.

In the present case, going through the LP process helped us realize the possibility to produce one-dimensional materials by annealing. This is due to the requirement that arose as a result of the LP process to complete the



reaction, for instance, of  $WO_x$  to stoichiometric  $WO_3$  by post-deposition annealing.

#### 4.1 Production of $VO_2$ by Ultrasonic Spray Pyrolysis (USP)

Some considerable detail on the experimental set for USP was fully outlined in Mwakikunga *et al.* [39] where the first-ever production of stoichiometric  $VO_2$  by this technique was reported attached in the appendices. For the sake of completeness, how materials were obtained by this method will be re-described here. The USP system composes

1. A container comprising a transducer that produces ultrasound waves and the precursor liquid to be “pyrolyzed”. The ultrasonic waves of frequency 1.67 MHz were focused to the solution surface to produce a vapor of ultra-small droplets.
2. The carrier gas system for the delivery of the precursor droplets. The droplets were carried in a quartz tube by a constant flow of argon at 11  $L\ min^{-1}$  for samples  $VO_2$ -400,  $VO_2A$  and  $VO_2B$  and 18  $L\ min^{-1}$  for sample  $VO_2NB$
3. The heated zone which could be a furnace, oven or any heater. The most vital part of the USP system is the heating system which has to comprise, for instance, a furnace and temperature controlling electronics. Controlling temperature and flow rates in turn controls the shape, size and structure of the materials produced.

4. Powder collection system: The powders were deposited at the exit of the furnace on Corning glass substrates and on borosilicate glass
5. The exhaust system.

Fig. 4.1 is a schematic of the full USP system where the above systems can be identified. For the production of VO<sub>2</sub> particles, the water-soluble precursor of NH<sub>4</sub>VO<sub>3</sub> (ammonium meta-vanadate) + VCl<sub>3</sub> (vanadium tri-chloride) was used. The combination of NH<sub>4</sub>VO<sub>3</sub> and VCl<sub>3</sub> is due to the fact that V has a valence of 5+ in NH<sub>4</sub>VO<sub>3</sub> and 3+ in VCl<sub>3</sub>.

The average valence of the combination gives a valence of 4+ which is exactly the valence of V in VO<sub>2</sub>. However the production of VO<sub>2</sub> is a little more than playing with the precursor; the nature and flow rate of the carrier gas, temperature and the nature of substrate have their influences on the stoichiometry and morphology of the VO<sub>2</sub>. For instance one got spherical particle at low flow rates [39] but one obtained dense nano-ribbon at high flow rates for the same temperature without the need for post-synthesis annealing.

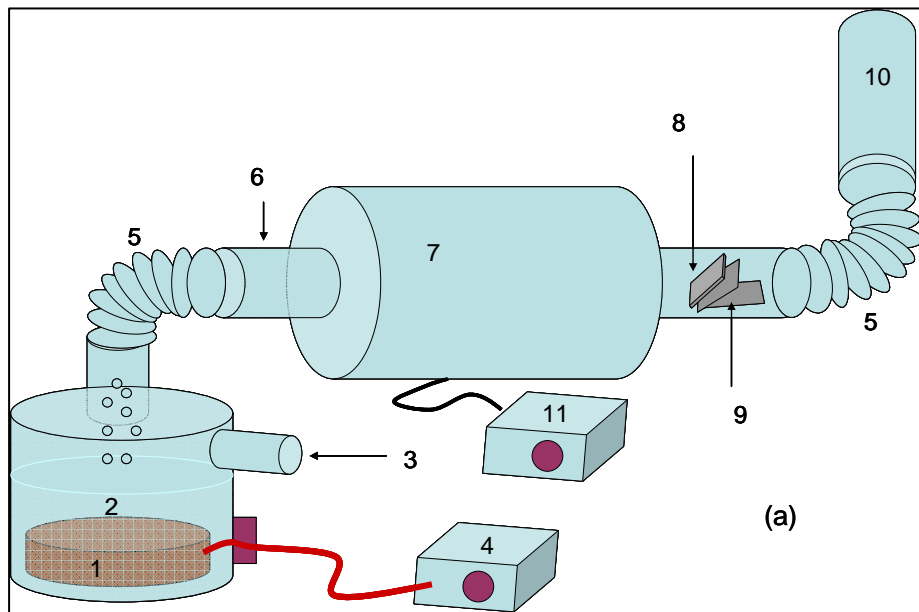
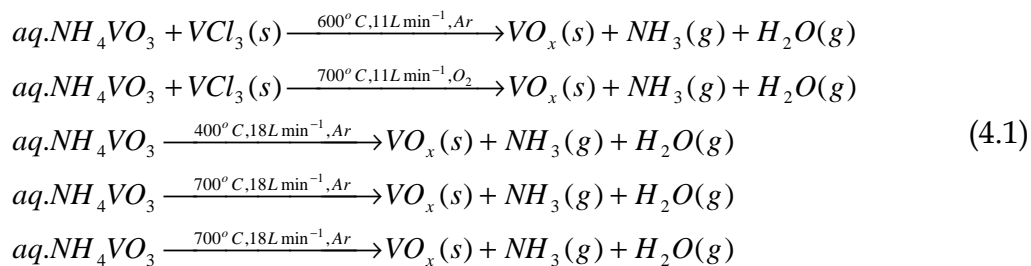


Fig. 4.1 Schematic set up of USP: (1) ultrasonic nebuliser transducer, (2) precursor liquid (3) carrier gas inlet (4) nebuliser power supplier (5) connecting bellow (6) quartz tube (7) tube furnace (8) substrate (9) substrate holder (10) exhaust pipe (11) temperature controller. (From the Ref. 41)



## 4.2 Production of Tungsten Oxides by USP

For the production of  $WO_3$ , the water-soluble  $(NH_4)_6W_7O_{24} \cdot 6H_2O$  (ammonium meta-tungstate hexahydrate) was employed. In this case, the temperature of the furnace played an important role in changing the composition of the W and O in the  $WO_x$  phases. At low temperatures- 100 to  $300^\circ C$ - the W-oxide phases are rich in oxygen with x being greater than 3.

Above 700°C the value of x is below 3 showing that the oxides are oxygen deficient [42].

Table 4.1 Experimental parameters for the production of various VO<sub>2</sub> samples

Sample ID	Flow rate L min <sup>-1</sup>	Gas type	Furnace temp	Deposition time
VO2-400	11	Ar	400	25
VO2A600	11	Ar	600	25
VO2B700	11	Ar	700	25
VO2WG700	18	Ar	700	40
VO2CNG700	11	H <sub>2</sub>	700	25

Table 4.2 Experimental parameters for the production of various WO<sub>3</sub> samples

Sample ID	Flow rate L min <sup>-1</sup>	Gas type	Furnace temp	Deposition time
W1	11	Ar	100	25
W2	11	Ar	200	25
W3	11	Ar	300	25
W4	11	Ar	400	25
W5	11	Ar	500	25
W6	11	Ar	600	25
W7	11	Ar	700	25

### 4.3 Post-Synthesis Annealing of the USP-produced WO<sub>3</sub>

More important for the production of dimensional nano-structures is post-synthesis annealing which was done for 17 hours at 500°C in argon environment.

Table 4.3 Experimental parameters for the annealing of WO<sub>3</sub> samples

Sample ID	Flow rate L min <sup>-1</sup>	Gas type	Furnace temp	Annealing time (hrs)
W1-500	2	Ar	500	17
W2-500	2	Ar	500	17
W3-500	2	Ar	500	17
W4-500	2	Ar	500	17
W5-500	2	Ar	500	17
W6-500	2	Ar	500	17
W7-500	2	Ar	500	17

### 4.4 Laser Pyrolysis

The present laser pyrolysis experimental set up as fully described in Mwakikunga *et al.* [40-43] is presented in Fig. 4.2 and Refs. 40-43 are attached in Appendices. Ref. 40 described all the technical details- the reaction chamber, the laser alignment procedures, the laser beam physics, the nozzle design, the precursor preparation and the preliminary IR spectral experiments on the precursor (see Fig 4.3 (a)). A six arm chamber was designed and built

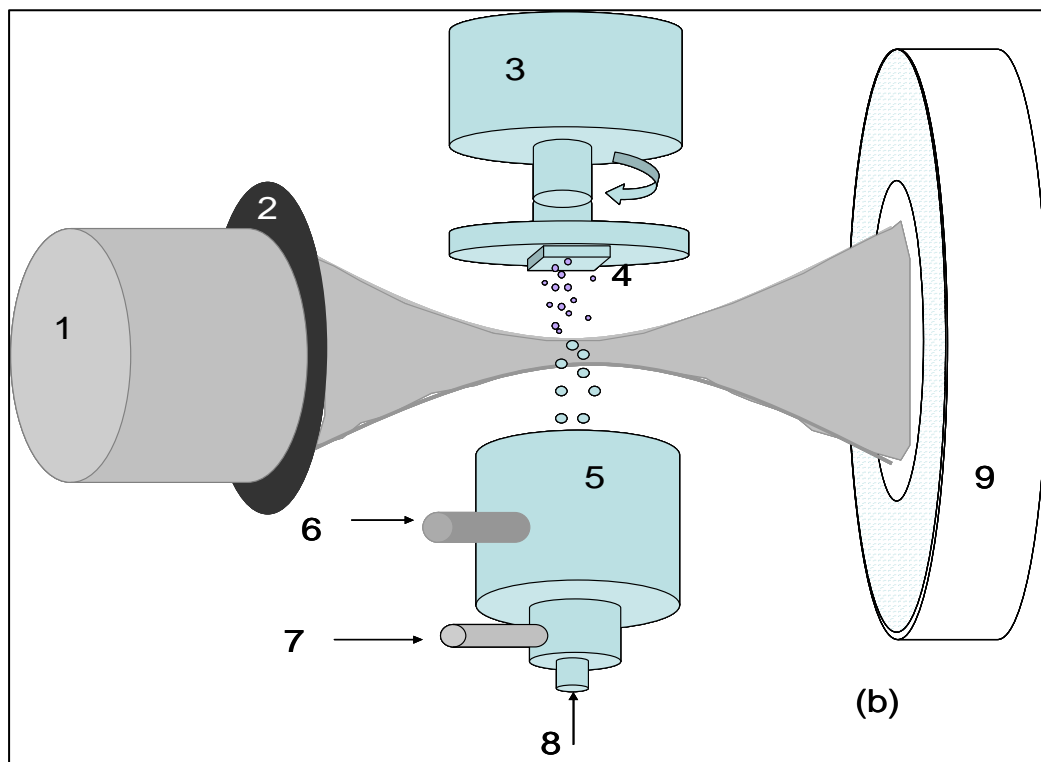


Fig. 4.2 The outline of the laser pyrolysis set up: (1) laser beam (2) focussing lens (3) stepper-motor (4) substrate (5) three-way nozzle (6) argon gas inlet (7) carrier gas inlet (8) precursor liquid droplets and carrier gas inlet (9) power meter (From Ref. 41)

with adjacent arms orthogonal to one another. Two opposite arms were mounted with 2 inch ZnSe windows tilted slightly from normal incidence to avoid back reflections into the laser cavity; these formed the input and output windows for the laser beam, which propagated in the horizontal plane, parallel to the optical table, through the two-arm length. The entrance window was 145 mm from the focussing element, and the total length from entrance to exit window was 590 mm. Orthogonal to the laser beam axis, in

the vertically upwards direction, the precursor droplets were released into the chamber and travelled into the laser beam volume. The subsequent products were collected in one of two configurations:

- (a) onto a substrate for production of thin films or,
- (b) onto a filter, connected to a pump, for the production of powders.

In the thin film configuration, the substrate was mounted on a rotating stage driven by a controllable step-motor, which in turn was powered and controlled from outside the chamber via vacuum-to-atmosphere adaptors. The last pair of arms, not used in this experiment, allows for viewing the pyrolysis process through either visual or spectroscopic means. A schematic representation of the laser pyrolysis concept is shown in Fig. 4.2.

The experimental system for delivery of the laser beam is shown in Figure 4.3. A wavelength tuneable continuous wave (cw) CO<sub>2</sub> laser was used in the experiments (Edinburgh Instruments, model PL6). Wavelength tuneability of the laser was possible with an intra-cavity mounted grating, allowing line tuneable output in the 9.2–10.8 μm range. A pop-up mirror in the optical set-up allowed the laser beam to be directed to a diagnostics table for power measurements (Coherent power meter, model 201) and for determining the lasing wavelength using a spectrum analyser (Optical Engineering Inc, model 16A). A polarisation based attenuator was used to allow power variability (this could also be achieved through adjustment of the laser discharge current). A Helium Neon laser was aligned co-linear with the CO<sub>2</sub> beam for ease of alignment through the optical system. The laser beam was focused

using a 2 m radius of curvature concave mirror (gold coated from II-VI Inc) and the profile of the laser beam was measured at various distances from the mirror with a scanning slit to determine the complete propagation characteristics inside the reactor. Careful choice of the slit width was made for each measurement in order to ensure accurate results following the approach of Chapple (1994).

The beam radius at each position was calculated by using a Gaussian fit to the data. A non-linear least squares fit was used to extract the necessary laser beam parameters, such as waist, waist position and laser beam quality.

It was necessary to study the absorption characteristics of the precursor materials before performing the laser pyrolysis in order to ascertain whether or not they would be able to absorb the 10.6- $\mu\text{m}$  emission from the laser and result in the necessary dissociation of the resonant bonds. Also this was done to find out if this was going to be a photochemical process (chemical change due to resonance with the light wavelength) or a photothermal one (chemical change due to heating of the infrared radiation). Fourier transform infrared spectroscopy was carried out on the following precursor materials:

1. Ammonium metatungstate  $[(\text{NH}_4)_6\text{W}_7\text{O}_{24}\cdot 6\text{H}_2\text{O}]$
2. Dodeca-tungstophoric acid  $[\text{H}_3\text{PW}_{12}\text{O}_{40}\cdot n\text{H}_2\text{O}]$
3. Vanadium pentoxide powder  $[\text{V}_2\text{O}_5]$
4. Ammonium metavanadate  $[\text{NH}_4\text{VO}_3]$

The FTIR of the first three are represented in Fig. 4.3 (a). The spectra show all the precursor materials have IR active local vibrational modes close to, but not



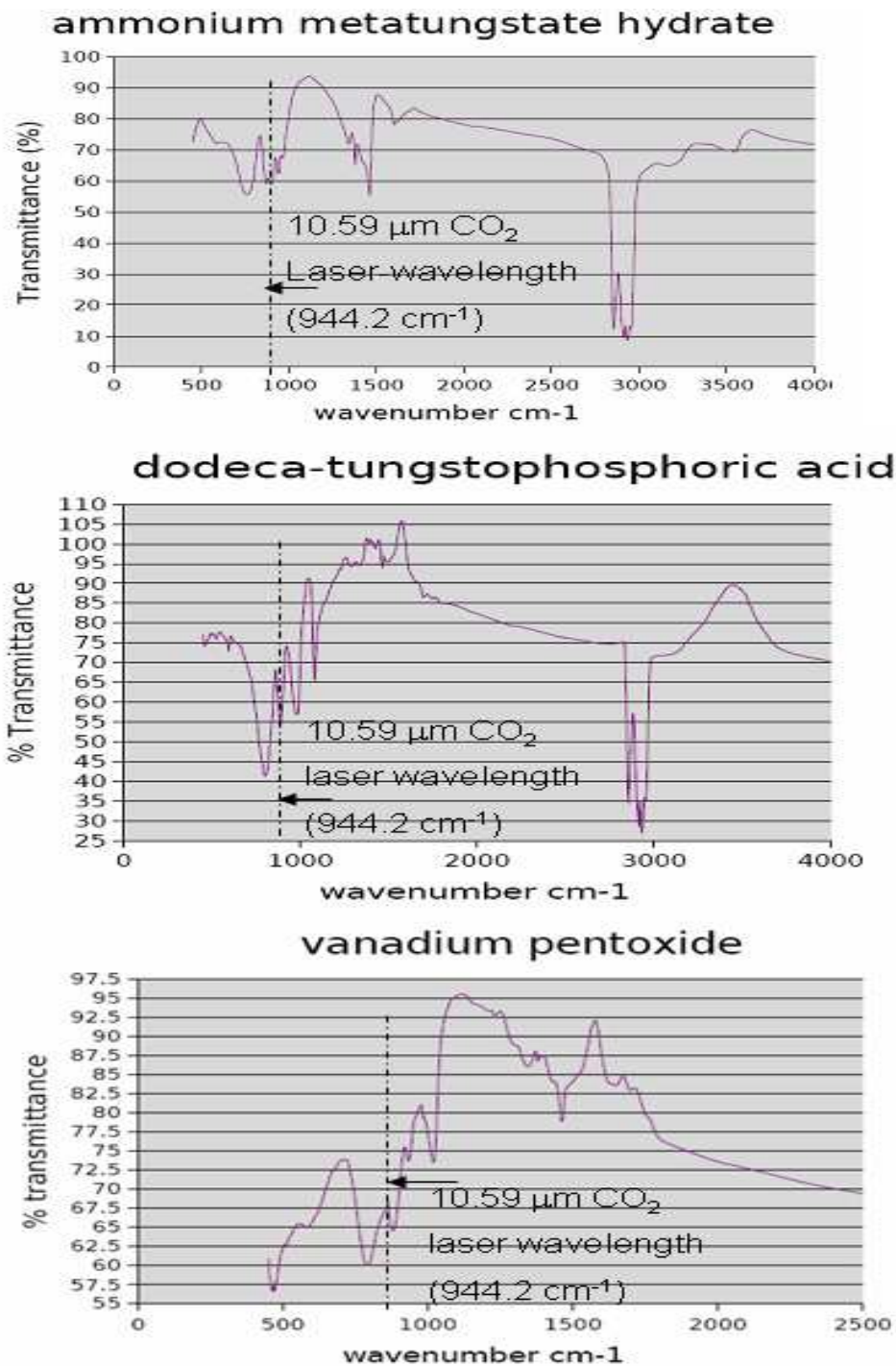


Fig.4.3 (a) FTIR spectra of some of the precursor materials used in this study showing the absorption bands that fall close to the CO<sub>2</sub> laser frequency

at, the laser emission line of 10.6 μm. The assurance was that normally, when the detuning is very small, multiphoton absorption process (as discussed in

section 2.12) would help bring the materials vibrational modes to resonance in a very short time and hence a photochemical process could be induced. Also, in the presence of sensitizer gases such  $C_2H_2$ , these reactions were seen to be feasible.

In Mwakikunga *et al.* [Ref. 42], the elaboration in greater detail on how the flow rates of the precursors and the carrier gases affected the final morphology of the samples was continued as re-shown in Fig. 4.4. The particle deposition showed a void at the centre [Fig. 4.4 (b)] when the encapsulating carrier gas flow rate was higher than the carrier gas driving the precursor droplets.

When the flow rates were reversed, the deposition showed the profile of a hump [Fig. 4.4 (a)] showing there was more deposition at the centre of the substrate than in periphery. This was found to be in agreement with Bernoulli's theorem which requires that there should be reduced pressure in fast flowing fluids.

When the central gases are larger, the pressure is lower in this region and hence the droplets and the particles (after laser pyrolysis) are trapped in this low pressure. Therefore there is high deposition at the centre of the substrate and vice versa.

Here, these experimental parameter summarized in Table 4.4 and 4.5 are listed out. Particles from this process were collected on Corning glass substrates, placed on a rotating stage, at room temperature and at

atmospheric pressure. The so-obtained samples were further annealed in argon atmosphere at 500°C for 17 hours.

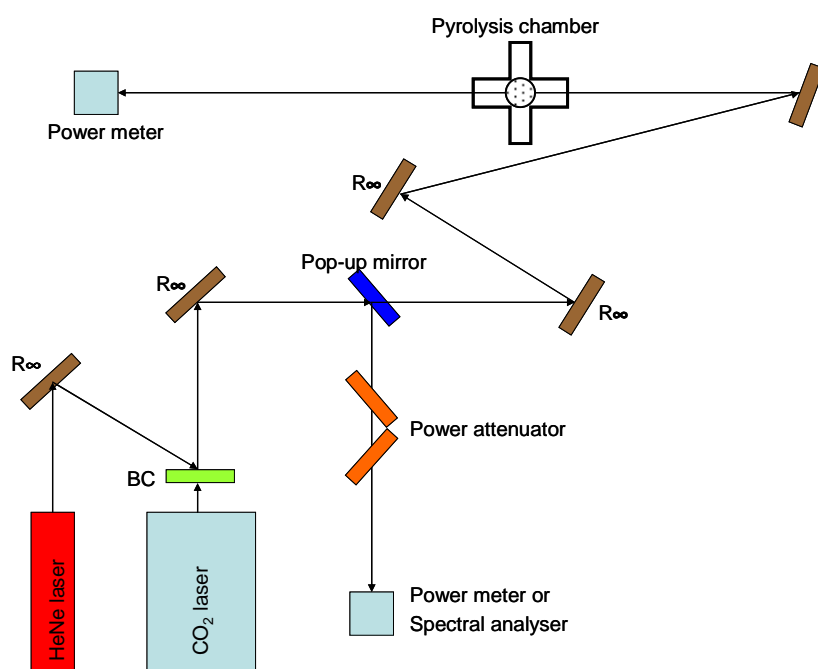


Fig. 4.3(b) A schematic of the laser beam delivery for the synthesis of tungsten trioxide by laser pyrolysis, with the six arm pyrolysis chamber shown (two arms are in and out of the page). The HeNe laser was used only for visible alignment of the infrared laser beam. The final focussing element was a 2 m curvature gold coated mirror.

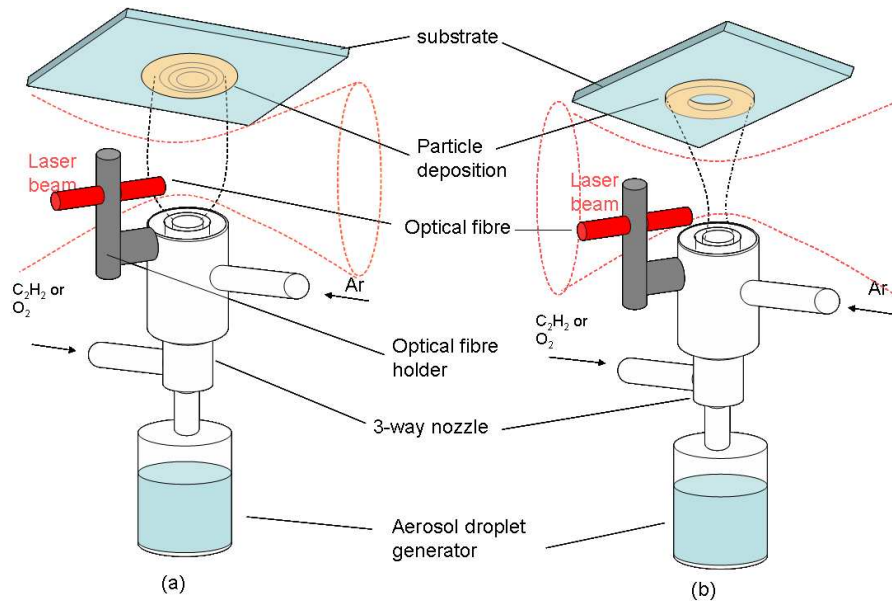


Fig. 4.4 (a) when the precursor flow-rate is larger than the encapsulating carrier gas (Ar) and (b) when the precursor flow-rate is smaller than the flow-rate of Ar. The precursor is driven either by C<sub>2</sub>H<sub>2</sub> or O<sub>2</sub>. The particle deposition in (a) has profile of a hump whereas the deposition in (b) has a vacancy at the centre as indicated on the substrates.

Table 4.4 Experimental variables for the production of vanadium oxides by LP

Sample	Precursor	Channel 1 8cm <sup>3</sup> /min	Channel 2 8cm <sup>3</sup> /min	Channel3 Variable	Nanowire or Nano- belt yield	Structure
V2O5A	aq.V <sub>2</sub> O <sub>5</sub>	O <sub>2</sub>	Ar	Ar	None	Film
V2O5B	aq.V <sub>2</sub> O <sub>5</sub>	C <sub>2</sub> H <sub>2</sub>	Ar	Ar	High	Belts+scrolls
VCL1	VCl <sub>4</sub> +ethanol	O <sub>2</sub>	Ar	Ar	None	Film
VCL2	VCl <sub>4</sub> +ethanol	C <sub>2</sub> H <sub>2</sub>	Ar	Ar	Low	Long belts

Table 4.5 Experimental variables for the production of tungsten oxides by LP

Sample	Precursor	Channel 1 8cm <sup>3</sup> /min	Channel 2 8cm <sup>3</sup> /min	Channel 3 Variable	Nanowire yield	Morphology
W1	WCl <sub>6</sub> +ethanol	O <sub>2</sub>	Ar	Ar	High	Slabs +Rods
W2	WCl <sub>6</sub> +ethanol	C <sub>2</sub> H <sub>2</sub>	Ar	Ar	Low	Sphere+Rod

#### 4.5 Current model for estimating the temperature of the plume at the laser-aerosol interaction region

The Bowden *et al.* model introduced in Chapter 2 suggests that laser intensity affects aerosol temperature in a direct linear manner. This is only valid for low laser power. One way to arrive at a more realistic model is to extend the Bowden *et al.* model to higher excitation.

By looking closely at the experimental data by Tenegal *et al.* (2001) [304], another approach was conceived. This approach consists of imagining that the aerosol system is synonymous to a thermal capacitor whose thermal capacitance at a temperature  $T_{\infty}$  serves as an upper temperature limit to which one can possibly heat the aerosol system. The laser energy  $\xi_L$ , which is equal to  $\psi_L t$  where  $\psi_L$  is laser power, defines the flow rate of photons that “charge-up” this aerosol system similar to the electrical current of electrons that charge up the capacitor in classical electricity theory. Since the aerosol temperature is  $T_{room}$  when the laser is OFF, one takes this point to be the initial boundary condition. Similar to derivation of the capacitor charging theory, it is possible to show that the aerosol temperature is affected by laser power,  $P_L$  in the following manner:

$$T = T_{room} + T_{\infty} [1 - \exp(-\alpha_L \xi_L)] \quad (4.2)$$

The coefficient  $\alpha_L$  in units of  $W^{-1}$  will vary from atomic system to another. This model was fitted to experimental data as illustrated in Fig. 4.5 and one

can estimate the values of  $T_{\infty}$  as  $1693.047 \pm 4.913$  K and  $\alpha_L$  as  $0.0078 \pm 0.0001$  W<sup>-1</sup> when  $T_{\text{room}}$  is equal to 300 K for this aerosol system.

At a laser power of 50 W which was used throughout the current experiments, this simple equation predicts a temperature of 846 K. The laser used in the current study could stabilize at 30 W. Using Eq. 4.2, the temperature of the aerosol inside the laser beam has been calculated to be 653 K. Both of the above temperatures are not detectable by the spectrometer that was employed in the current pyrolysis of WO<sub>x</sub> and VO<sub>x</sub> compounds.

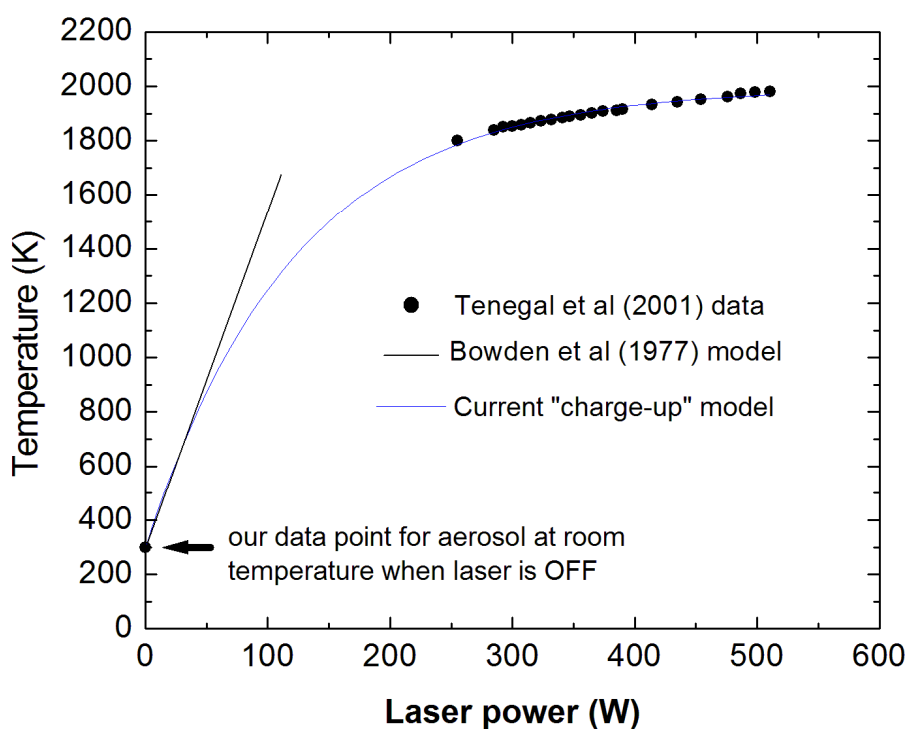


Fig 4.5 Laser power as it affects the temperature of the C/O atoms moving transversally to the laser beam direction. The fitted curve is from the present theory and the straight line graph is from the model by Bowden *et al.* (1977)

As a consequence of this low temperature and the undetectability of it, all the attempts to determine the experimentally are not complete. The calculated temperatures above were taken as enough for the current study with more sensitive temperature measurements ongoing but could not be reported in this Thesis.

## **4.6 Characterization**

### **4.6.1 Scanning electron microscopy**

Morphology studies were carried out using two types of scanning electron microscopes

(1) a Jeol JSM-5600 scanning electron microscopy (SEM) microscope

(2) a LEO 1525 field emission gun scanning electron microscope (FEG-SEM) operated at 3–20 kV. Both of these were equipped with energy dispersive x-ray spectroscopy (EDS) setup. In order to avoid charging effects during SEM analysis, the samples were made conductive by carbon coating. Infrared and Raman spectroscopy experiments on the as-obtained  $\text{WO}_3$  and  $\text{VO}_2$  materials are report elsewhere [Mwakikunga *et al.* 2007].

### **4.6.2 X-ray diffraction (XRD)**

Structural studies were done using a Philips Xpert powder diffractometer equipped with a  $\text{Cu K}\alpha$  wavelength of 0.154184 nm. The experimental procedure showed good reproducibility of results.



### 4.6.3 Raman spectroscopy

Raman spectroscopy was carried out using a Jobin-Yvon T64000 Raman spectrograph with a 514.5 nm line from an argon ion laser. The power of the laser at the sample at the post-annealed samples was small enough (0.384 mW) in order to minimise localised heating of the sample. The T64000 was operated in single spectrograph mode, with the 1800 lines/mm grating and a 20× objective on the microscope. The Richter equation given in Refs.16 & 17 and herein reproduced as Equation 3.5 was fitted to experimental data and the pertinent parameters were extracted. In the equation,  $d$  is the nano-wire diameter,  $\Gamma_0$  is the full-width-at-half-maximum (FWHM) for bulk material Raman peak ( $\Gamma_0 = 6.5 \text{ cm}^{-1}$  for  $\text{WO}_3$ ),  $\omega(q)$  is the phonon dispersion curve relation (PDR) for the material,  $A = 713 \text{ cm}^{-1}$ ,  $a = 0.76 \text{ nm}$  for the  $713 \text{ cm}^{-1}$  phonon branch whereas  $A = 808 \text{ cm}^{-1}$  and  $b = 0.38 \text{ nm}$  for the  $808 \text{ cm}^{-1}$  phonon branch. For the purposes of the fitting session, the phonon dispersion relation,  $\omega^2(q) = A^2 + AB\sin^2(aq) + B^2\sin^4(aq)$ , was derived from the simple relation of the form  $\omega(q) = A + Ba^2q^2$ . The latter assumes isotropic dispersion curves; however the former provided a much smoother fit than the latter for the present  $\text{WO}_3$  Raman spectroscopy data.  $B$  was determined after non-linear fitting of Eq. 3.5 to experimental Raman spectral data. This was carried out using Mathematica™.

#### 4.6.4 Atomic force microscopy

AFM imaging was carried out on VO<sub>2</sub> nanoribbons by suspending a few ribbons in ethanol and placing a drop of the ultrasonicated ribbons onto a clean Si surface. Imaging was done in tapping mode on VEECO atomic force microscope and varying scan rates and magnifications.

#### 4.6.5 Electronic properties measurement: Co-Linear Four-Point Probes on VO<sub>2</sub> Nano-Ribbons

A co-linear four-point probe system from Cascade Microtech, Inc., Oregon, U.S.A. was used to perform conductance measurements on the VO<sub>2</sub> nano-ribbons by following procedures from the University of Texas at Dallas. The equidistant tungsten carbide probes have a separation distance,  $a$ , of 0.127 cm and a probe radius of 0.005 cm. The Keithley 4200 Semiconductor Characterisation System (SCS), equipped with four supply-and-measure units (SMUs) and a pre-amplifier, was used to perform high precision direct-current characterisation capable of probing sensitive voltages and injecting currents ranging from 1 fA - 1 mA with a resolution of 0.1 fA. In this work, a constant 1  $\mu$ A current was injected through probe 1 through the sample of nano-ribbons to the ground at probe 4. The potential difference was measured across probes 2 and 3. For each scan, 100 measurements were taken for 5 minutes.

The sample was heated with a temperature controlled heater. Voltage-time scans were done at temperatures of 22°C-80°C during the heating-up cycle and another set from 75°C-24°C during the cooling-down cycle.

## Chapter 5

### Results and Discussion

In this chapter, important results that address the present objectives are presented. In cases where the results are published, the reader can confirm in the attached journal articles and manuscripts in press in the Appendices. Unpublished results and those that are being considered for publication will be presented in considerable detail.

#### 5.1 Results from USP

##### 5.1.1 First-fruits of VO<sub>2</sub> nanoparticles by USP

The production of VO<sub>2</sub> nano-particle for the first time by USP was reported [39] attached in the Appendices A1 but also summarized herein and illustrated in Fig. 5.1. When the precursor NH<sub>4</sub>VO<sub>3</sub> (AMV) in water was deposited on quartz at 400°C, XRD [Fig. 5.1 (a)] showed the presence of the same precursor AMV. This showed that most of the precursor is not decomposed at this temperature. However when deposited on Corning glass at 700°C in hydrogen environment XRD of the decomposed thin film showed a mixture of V<sub>2</sub>O<sub>5</sub> and VO<sub>2</sub>. Later in this chapter, it will be shown that these were in fact bilayers of VO<sub>2</sub> (B) and V<sub>2</sub>O<sub>5</sub> nanoribbons. It was only when the deposition was done on window glass at 700°C in argon atmosphere that VO<sub>2</sub> (monoclinic) was obtained [Fig. 5.1 (c)]. Transmittance of such a glass at different temperatures showed interesting switching from a transparent

material at room temperature to a less transparent one at 90°C as shown in Fig 5.1 (d). This was found to be a reversible process as transmittance was measured during the cooling down cycle as well (not shown here). However, plotting transmittance at chosen wavelengths of 2800 nm, 2500 nm, 2000 nm and 1500 nm as shown in Fig 5.1 (e) showed hysteresis type of reversible change as is the case for stoichiometric VO<sub>2</sub>.

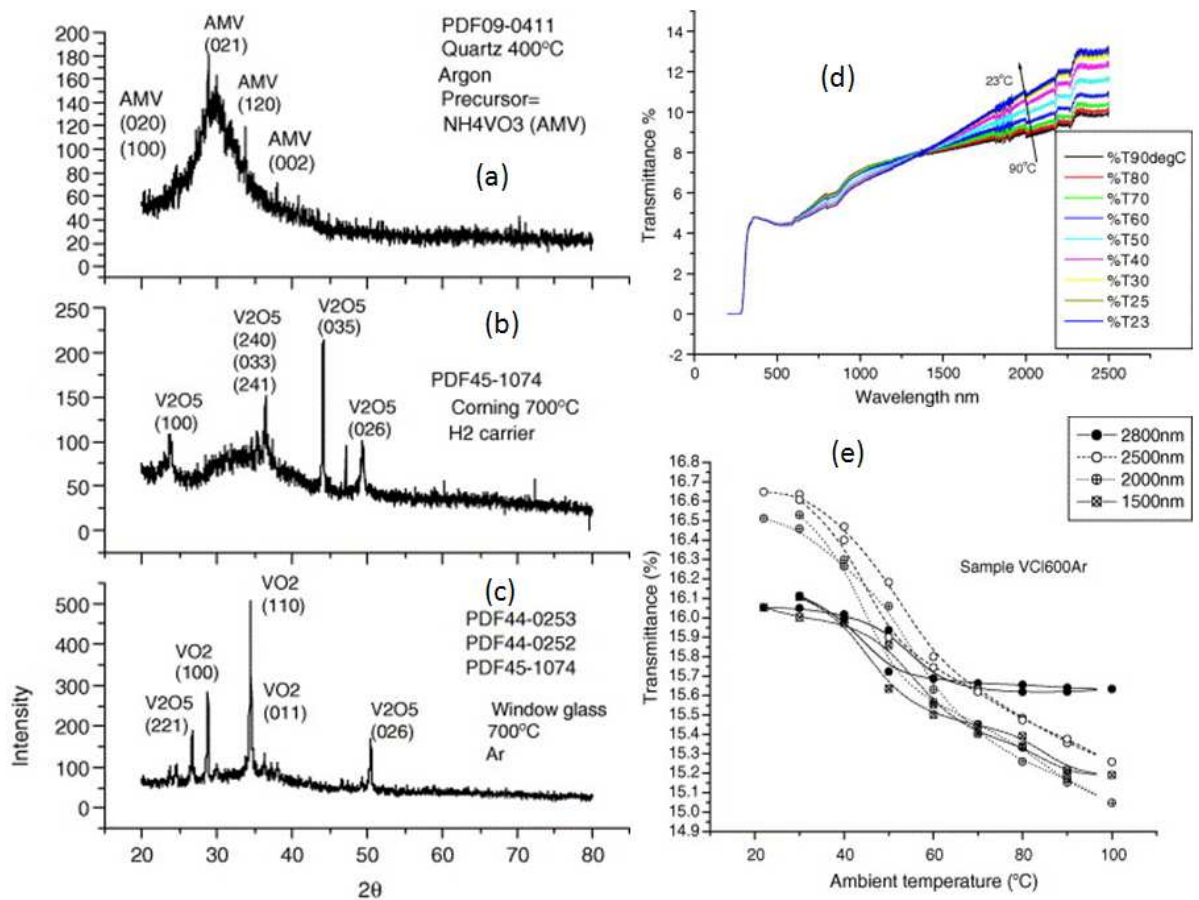


Fig. 5.1 First report on the production of VO<sub>2</sub> by USP (a) Undecomposed AMV precursor (b) Decomposed AMV into a mixture of V<sub>2</sub>O<sub>5</sub> and VO<sub>2</sub> (B) (c) monoclinic VO<sub>2</sub> (d) transmittance at various temperature and (e) hysteresis plots characteristic of VO<sub>2</sub>.

At that time, the scanning electron microscopy of the samples was carried out by a Jeol JSM-5600 microscope whose micrograph quality was only modest as can be seen in the attached Ref. 39. The spherical particles obtained were found to have an average diameter of 800 nm as seen by this kind of microscope. The imaging was since repeated in a better microscope - a LEO 1525 field emission scanning electron microscope (FESEM) - operated at 3 - 22 kV. The new images for two samples produced in a flow rate of 11 L/min at a furnace temperature of 600 and 700°C are presented in Fig. 5.2 and 5.3. In both micrographs, the EDS spectra indicate that, apart from the V and O peaks from VO<sub>2</sub>, strong peaks from Si alongside Na, K and Al are present which are due to the Corning glass substrate. The size distribution charts of the VO<sub>2</sub> at 600°C and 700°C are given in Fig. 5.3.

### **5.1.2 VO<sub>2</sub> nano-ribbons by USP without post-synthesis annealing**

Nano-ribbons of VO<sub>2</sub> illustrated in Fig. 5.4 are seen at the following synthesis parameters:

- (1) at higher flow rate of 18 cm<sup>3</sup>/min of argon of the NH<sub>4</sub>VO<sub>3</sub> precursor
- (2) the substrate of borosilicate glass
- (3) positioned at a region in the furnace where the substrate temperature was ~300°C and
- (4) the furnace temperature of 700°C in the central zone which is regarded to be the pyrolysis temperature.

No post-synthesis annealing was done on this sample. This suggests that these one-dimensional ribbons grow by a different mechanism from the nano-wires of  $\text{WO}_3$  to be discussed in the forthcoming sections of this chapter. Scanning electron microscopy was done on the LEO microscope and samples were prepared by scrapping a small portion of the powder on to a carbon tape tailored for the SEM [Fig. 5.5(a)]. Note the EDS spectra shows only V and O peaks with some C peak from the carbon tape (Fig. 5.5).

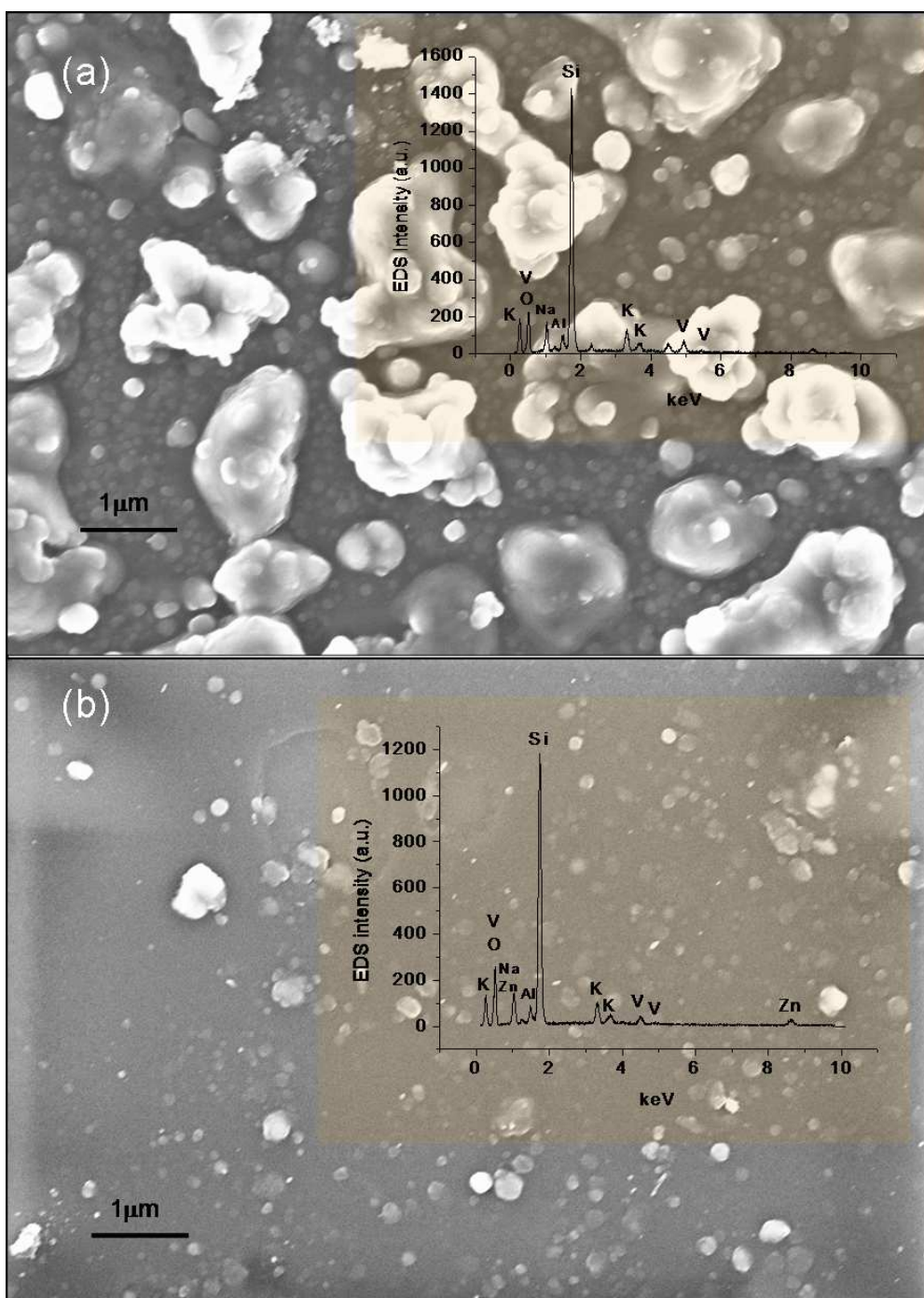


Fig. 5.2 Scanning micrographs of VO<sub>2</sub> nano-particles synthesized on Corning glass in 11 L/min of argon with a deposition time of 25 min at (a) 600°C (inset is EDS) (b) 700°C (EDS in inset)

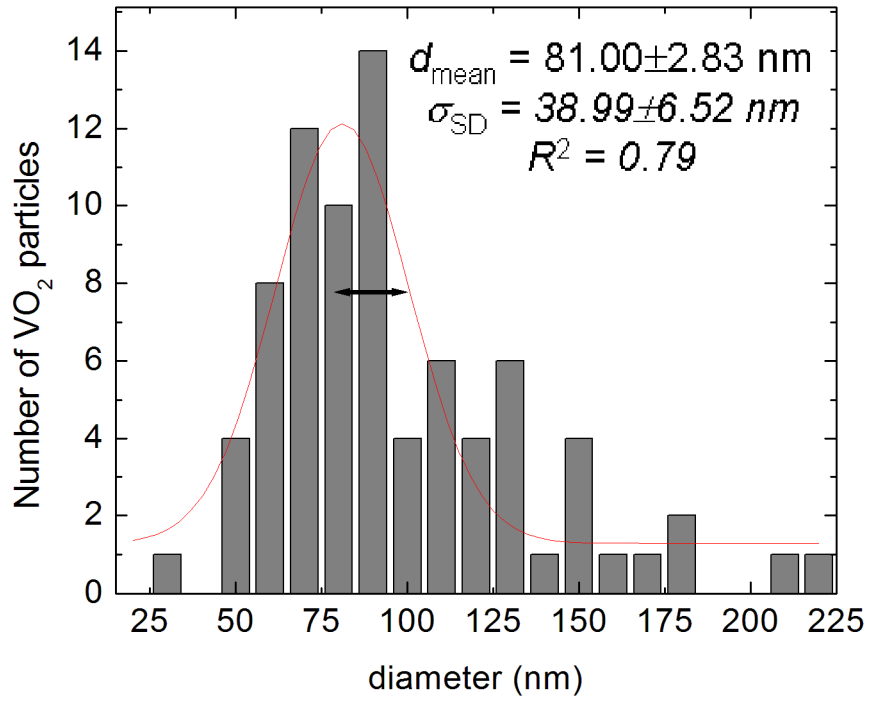


Fig. 5.3 Size distribution of the particles of VO<sub>2</sub> on the samples grown by USP at 600°C



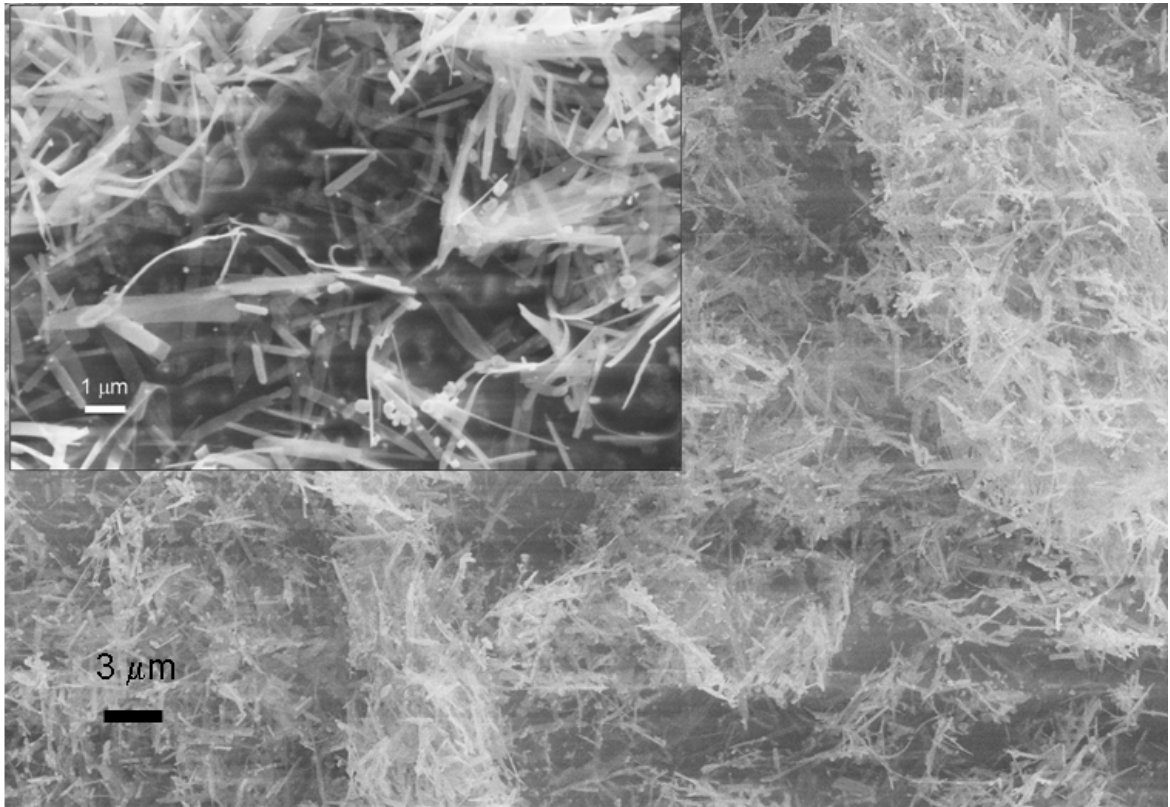


Fig. 5.4 SEM micrographs of VO<sub>2</sub> nano-ribbons a low resolution image showing the overall density of the nanostructures with an inset the same on a different spot of the sample

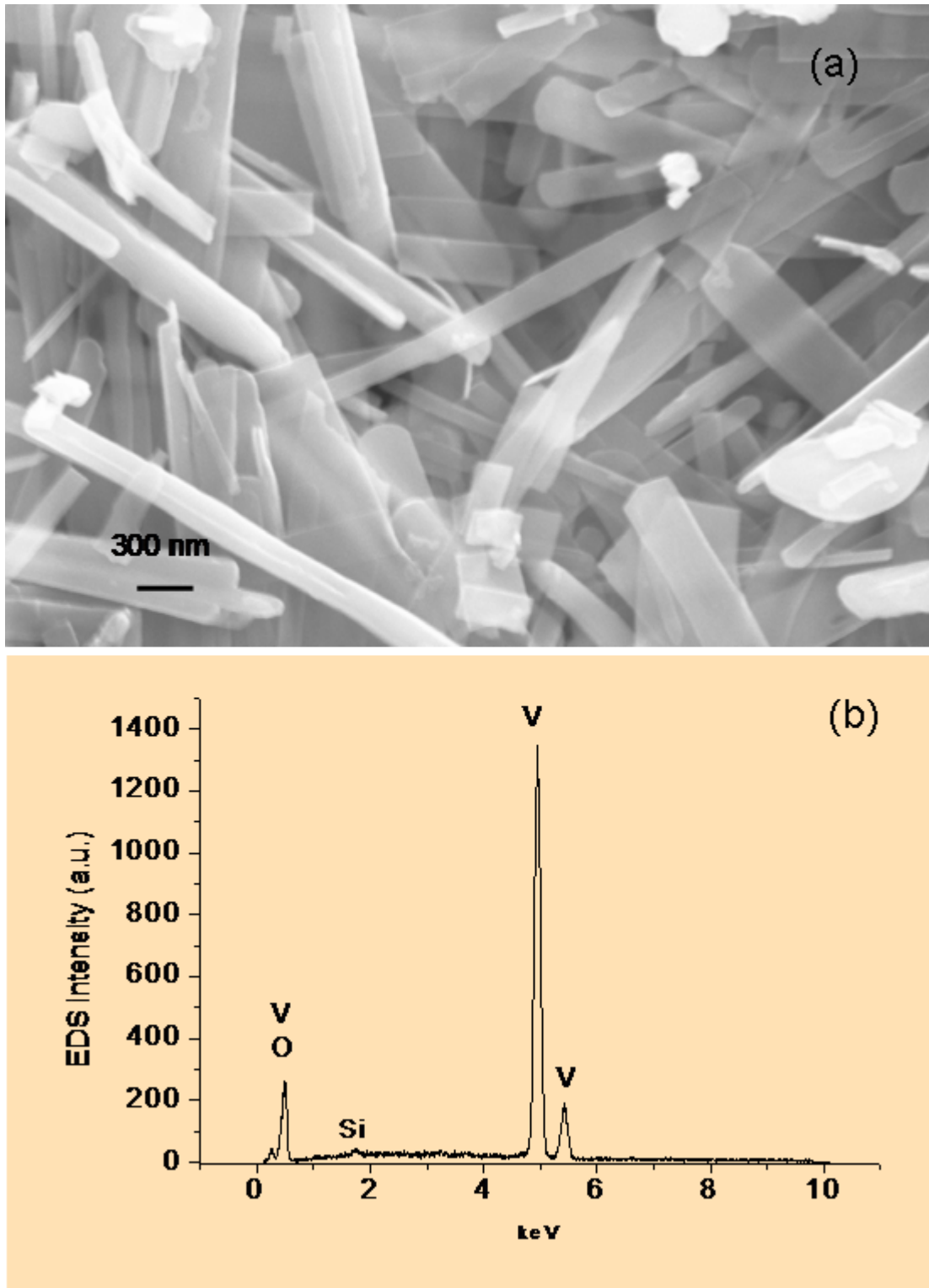


Fig. 5.5 SEM micrographs of VO<sub>2</sub> nano-ribbons (a) a higher resolution with (b) an EDS spectrum showing the V and O peaks. Note how the image reveals how gossamer (transparent) to electron the ribbons are.

Cross-sectional SEM was carried out by tilting the sample so that the electron beam “sees” the sample from the edge. This was done to determine the thickness of the VO<sub>2</sub> layer. The result revealed that the layer is highly inhomogeneous with an undulating profile as one expected from a nano-structured layer such as this one. The cross-section SEM micrographs are given in Fig. 5.6.

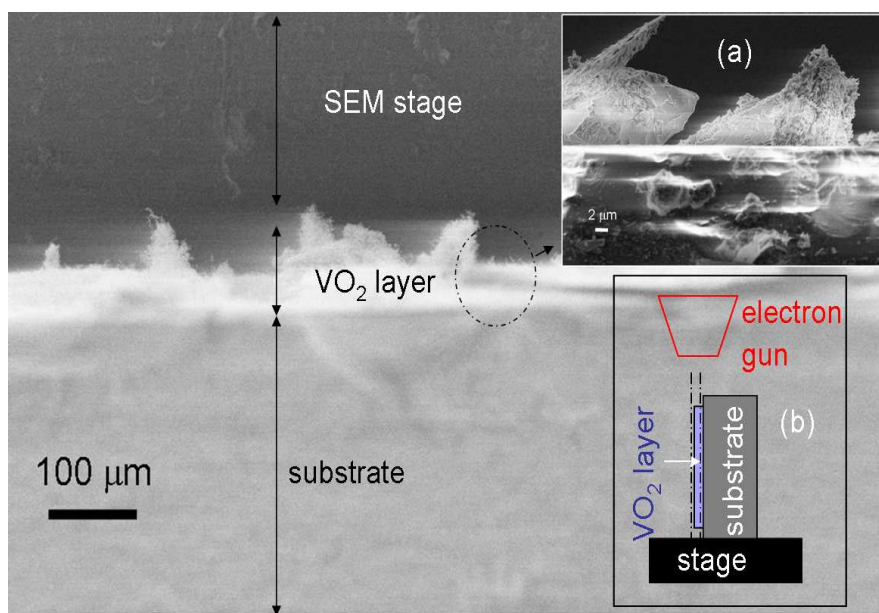


Fig. 5.6 Cross-sectional SEM image of the VO<sub>2</sub> sample prepared by USP Inset (a) is a close-up of the interface between the borosilicate substrate and the VO<sub>2</sub> layer exposing the in-homogeneity of this layer (b) the arrangement of the cross-sectional SEM experiment

### 5.1.3 Atomic force microscopy of the VO<sub>2</sub> nano-ribbons

The procedures for preparing the sample for atomic force microscopy including the AFM setting were described in the previous chapter. The image

shown in Fig. 5.7 shows an isolated ribbon with round corners. When a line profile was performed, the side profile of the ribbon was captured enabling one to measure the third dimension of the ribbon which was not easily measurable with SEM or TEM. The profile clearly shows that the ribbon in the image has a thickness of 10 nm. The other dimensions of width and length are 400 nm and 1000 nm respectively. Other ribbons (not shown here) were as thin as 5 nm. This explains why the ribbons were transparent to electrons as show in the close-up SEM images above.

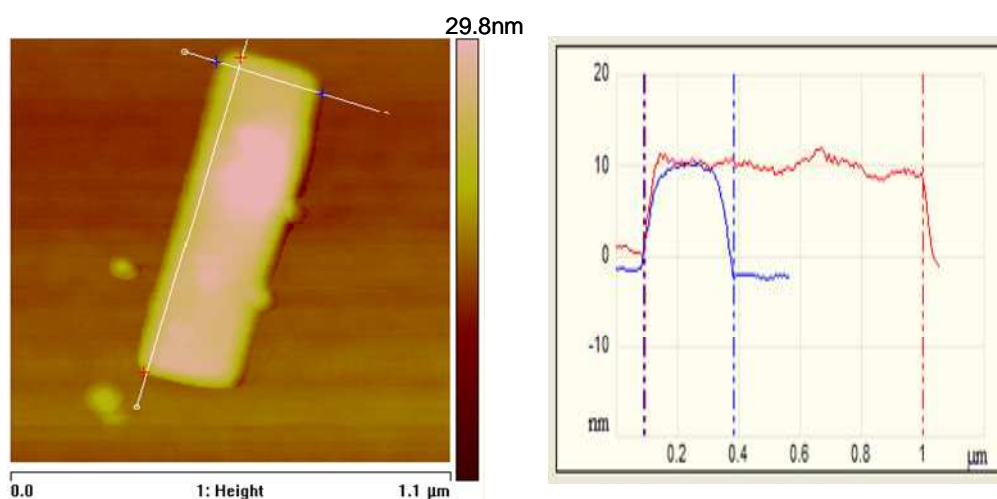


Fig. 5.7 (left) AFM images of a single VO<sub>2</sub> nano-ribbon. The profile (right) shows that the VO<sub>2</sub> ribbon is typically 10 nm thick

#### 5.1.4 Structure of the VO<sub>2</sub> ribbons and the particles from USP

It has been stated in Chapter 3 that there are four polymorphs of VO<sub>2</sub>: VO<sub>2</sub> (M), VO<sub>2</sub> (R), VO<sub>2</sub> (A) and VO<sub>2</sub> (B). It has been reported that VO<sub>2</sub> (M) appears at high temperatures of synthesis. This is the phase that undergoes thermochromic transition to VO<sub>2</sub> (R) when heated to above 340K. VO<sub>2</sub> (B),

which nucleates at lower temperatures than 420°C, is reported by Sahana *et al.* [436] not undergo any thermochromic transition. Sahana noted that the VO<sub>2</sub> (B) structure is formed by the packing of edge-sharing octahedral that are only linked at corners in the (001) planes. In contrast to the VO<sub>2</sub> (R), they also noted that the fourfold axes of the oxygen octahedral are almost aligned along a single crystallographic direction [010]. The (001) planes were made up of a network of corner-sharing octahedral forming close packed planes. Sahana *et al.* from Leroux *et al.* [437] further speculated that these structural features of the VO<sub>2</sub> (B) may be expected to lead to a tendency for its crystallites to grow as platelets.

With better SEM images showing nanoribbons for a sample synthesized at 700°C in hydrogen atmosphere, XRD and TEM experiments were carried on this sample. These XRD results show that the VO<sub>2</sub> is a mixture of two phases - VO<sub>2</sub> (monoclinic) and VO<sub>2</sub>(B). Even those samples that were processed at higher than 420°C show presence of VO<sub>2</sub> (B) phase since the substrate used to collect the VO<sub>2</sub> crystallites was placed at the end of the quartz tube where the temperature was much lower than 420°C (see Fig. 5.70). When the substrate is placed at a zone where the temperature is 700°C, VO<sub>2</sub> (M) nanoparticles were found (Fig. 5.70 (b)). Based on the argument by Sahana *et al.* and Leroux *et al.* above, one can conclude that a substrate temperature of lower than 420°C and a pyrolysis temperature of more than 700°C are the most favourable conditions for obtaining VO<sub>2</sub> (B) belts and

ribbons without further annealing. If further annealing has to be carried out, it has to be done at higher than this temperature.

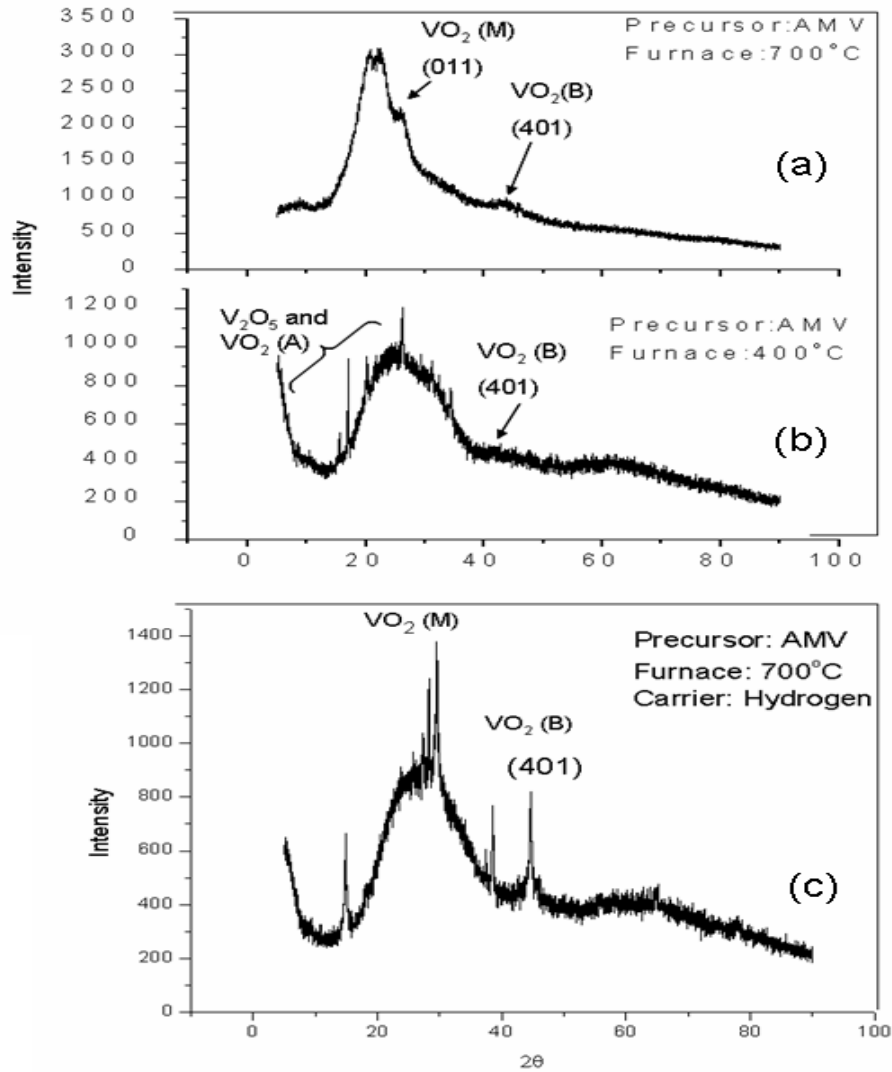


Fig. 5.8 X-ray diffraction of the VO<sub>2</sub> nano-ribbons from USP showing the diminishing presence of VO<sub>2</sub> (A) and V<sub>2</sub>O<sub>5</sub> as the furnace temperature is raised from 400°C in argon (b) to 700 °C in argon (a) and at 700°C in hydrogen (c). A broad hump from  $2\theta = 20 - 40^\circ$  is from the SiO<sub>2</sub> substrate

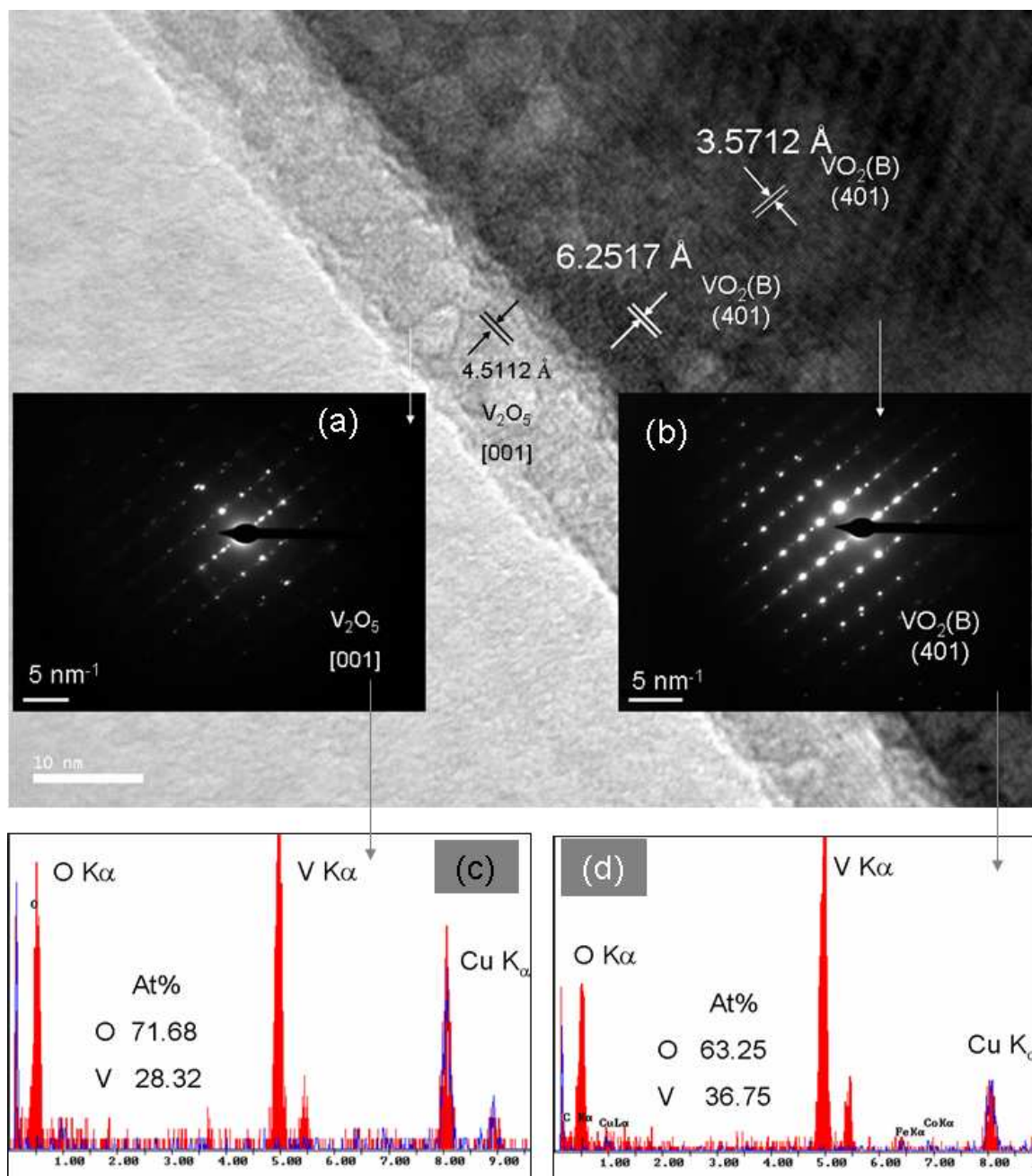


Fig. 5.9 Transmission electron microscopy, SAED pattern and local EDS on a single  $\text{VO}_x$  nano-ribbon revealed bi-layered structure:  $\text{V}_2\text{O}_5$  and  $\text{VO}_2$ . Lattice

parameters for the two regions are as indicated. Inset (a) and (b) are SAED patterns for  $V_2O_5$  and  $VO_2$  regions respectively and inset (c) and (d) are local EDS spectra of outer  $V_2O_5$  and core  $VO_2$  layers respectively. (Detector used was Gatan 1000 camera, accelerating voltage =200 kV and for EDX, the spot size was  $1\mu\text{m}$  and the take off angle of  $15^\circ$ )

TEM results on a single ribbon from a sample synthesized at  $700^\circ\text{C}$  in argon are summarized in Fig. 5.9. Higher magnification in Fig. 5.9 showed that the ribbons has two layers: an outer (shell) layer of oxygen-rich  $VO_x$  with the stoichiometry close to that of  $V_2O_5$  and an inner (core) layer of oxygen-deficient  $VO_x$  with stoichiometry close to that of  $VO_2$ .

The  $d$ -spacings for the monoclinic structure are given by the following well known equation

$$\frac{1}{d^2} = \frac{1}{\sin^2 \beta} \left( \frac{h^2}{a^2} + \frac{k^2 \sin^2 \beta}{b^2} + \frac{l^2}{c^2} - \frac{2hl \cos \beta}{ac} \right) \quad (5.1)$$

where  $d$  is the value of the interplanar spacing,  $a$ ,  $b$ ,  $c$  and  $\beta$  are the lattice parameters of the  $VO_2$  unit cell and  $h$ ,  $k$ ,  $l$  are the Miller indices of the reciprocal lattice giving the co-ordinates of the lattice planes under investigation. Inserting in the above Eq. 5.1 the values of lattice parameter  $a$ ,  $b$ ,  $c$ ,  $\beta$  (respectively as  $12.03\text{\AA}$ ,  $3.70\text{\AA}$ ,  $6.433\text{\AA}$  and  $106^\circ$ ) for the  $VO_2$  (B) as given in Table 3.2 in Chapter 3 and searching for the Miller indices  $h$ ,  $k$ ,  $l$  that would yield the closest experimental  $d$ -spacings gave the following spreadsheet.



Table 5.1 Calculated Miller indices for the system VO<sub>2</sub> (B)

<i>h</i>	<i>k</i>	<i>l</i>	<i>d squared</i>	<i>d (Angstroms)</i>
0	0	1	21.88095	4.677708
0	1	0	13.7048	3.702
0	1	1	8.426803	2.902896
1	0	0	76.51918	8.747524
1	0	1	39.65655	6.297345
1	1	0	11.62308	3.409263
1	1	1	10.185	3.191394

The highlighted row shows that the calculated Miller indices for the plane  $(hkl) = (101)$  have a d-spacing of 6.297Å. The calculated inter-planar spacing is very close to the observed spacing of 6.2517Å as presented by the TEM image of the VO<sub>2</sub>(B) ribbon above. The reflection from plane (401) of the VO<sub>2</sub> (B) is not observed here; only that of plane (101) is seen. This is in conflict with the XRD results above which report the plane (401) instead of the (101) seen by TEM. The conflict should be due to the fact that the ribbons have 5-nm-thick V<sub>2</sub>O<sub>5</sub> layer on top of the VO<sub>2</sub> ribbon. This limits accurate determination of the structure of one of the layers at this local measurement by TEM. The same procedure of analysis was applied to the V<sub>2</sub>O<sub>5</sub> TEM results which gave the growth directions much more easily as indicated in Fig. 5.9 [inset (a)].

### 5.1.5. Raman spectroscopy results from VO<sub>x</sub> ribbons

The reader will recall that Raman spectroscopy of slabs and thin films was introduced in Chapter 3. Phonon confinement in thin films was derived by Faucet and Campbell as re-produced in Eq. 57. Due to the complex nature of the Eq. 57, a simpler phonon confinement model in slab-like structures can be derived as shown below. Kim *et al.*<sup>56</sup> have claimed that the Fourier coefficient must generally be given by

$$|C(0, q)|^2 d^3 q = f(q) \exp\left(\frac{q^2 d^2}{\alpha}\right) dq \quad (5.2)$$

Where  $f(q) = 1$  for slabs and  $f(q) = 4\pi q^2$  for an isolated sphere. No physical explanation was given by Kim *et al.* for setting the above constraints especially the one for slabs.

However, if one follows the simpler approach used by the Piscanec *et al.* and Adu *et al.* of simply changing the dimensionality of the  $d^3q$  momentum volume, one can have an alternative model that would best fit the nano-ribbon data. Consider the following schematic in Fig 5.10 of a ribbon interacting with a laser beam in a typical Raman spectroscopy set up.

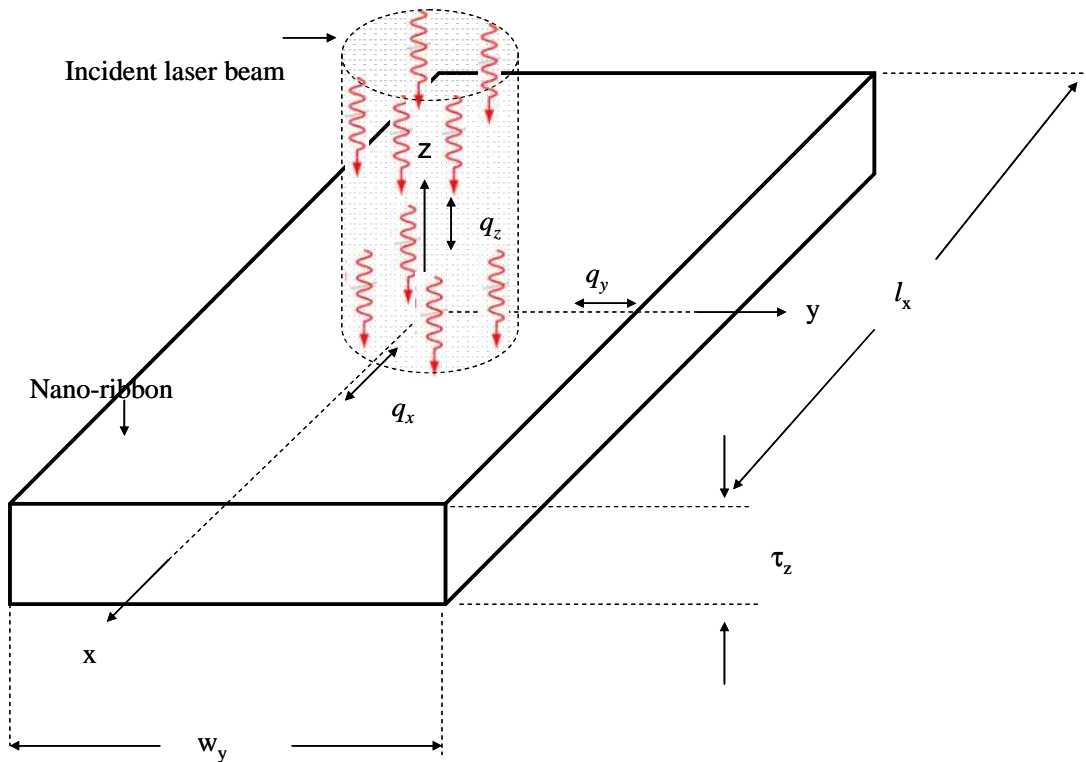


Fig 5.10 Illustration of phonon geometry in a slab as a result of laser excitation

In performing Raman spectroscopy on ribbons whose typical length ( $l_x$ ), width ( $w_y$ ) and thickness ( $\tau_z$ ) are about  $1\mu\text{m} \times 400\text{ nm} \times 10\text{ nm}$  as shown by AFM, one expects that confinement of optical and acoustic phonons ought to be only in one dimension, that is, the  $z$  direction which denotes the thickness of the ribbon as illustrated in Fig. 5.10

Surface phonons in thin films and quantum wells<sup>57</sup> and super-lattices<sup>58</sup> and have been studied. However, these structures have been composed of spherical particles and hence the elaboration of the confinement of optical phonons has been synonymous to that in the Richter-Faucet-Campbell

description. It is possible to re-write Richter-Faucet-Campbell equation which is in polar co-ordinates to an equation that is in Cartesian ones in keeping with the geometry of nano-ribbons illustrated in Fig. 14 as follows

$$I(\omega) = A_0 \int_0^{\frac{\pi}{na}} \int_0^{\theta_y} \int_0^{\theta_x} \frac{\exp\left(-\frac{2(\tau_z^2 + w_y^2 + l_x^2)(q_z^2 + q_y^2 + q_x^2)}{\alpha}\right)}{\left[\omega - A - B(q_z^2 + q_y^2 + q_x^2)\right]^2 + \frac{\Gamma_0^2}{4}} dq_x dq_y dq_z \quad (5.3)$$

Expanding and grouping the like terms, one obtains an equation that is suitable for Raman scattering in thin layers such as ribbons, sheets and belts as follows:

$$I(\omega) = A_0 \int_0^{\theta_y} \int_0^{\theta_x} \exp(-B_1 q_y^2 - B_2 q_x^2) dq_x dq_y \int_0^{\frac{\pi}{na}} \frac{\exp\left(-\frac{2(\tau_z^2 + w_y^2 + l_x^2)(q_z^2)}{\alpha}\right)}{\left[\omega - A - B(Q_{surf}^2 + a q_z^2)\right]^2 + \frac{\Gamma_0^2}{4}} dq_z \quad (5.4)$$

The double integration describes the non-confined vibrational modes in the ribbon's (x-y) surface. Note that, as expected, the profiles of the (x-y) phonon spectra are perfect Gaussians. However, the numerical integration with respect to z is the only component that describes the asymmetrical broadening in the Raman spectrum. The double integration can be a constant and hence the whole equation can be written as

$$I(\omega) = A_0 \int_0^{\frac{\pi}{na}} \frac{\exp\left(-\frac{2(\tau_z^2 + w_y^2 + l_x^2)(q_z^2)}{\alpha}\right)}{\left[\omega - A - B(Q_{surf}^2 + a q_z^2)\right]^2 + \frac{\Gamma_0^2}{4}} dq_z \quad (5.5)$$

These have been fitted to the present Raman spectroscopy data from 10 nm thick ribbons as shown in Fig. 5.11. From this fitting, the phonon dispersion relation for VO<sub>2</sub> for the first time as

$$\omega(q) = 146.70 - 2.54q^2 \quad (5.6)$$

This in agreement with Vikhnin *et al.* (1995) [453a] who found that 145 cm<sup>-1</sup> was the phonon frequency mode in VO<sub>2</sub> that is active during the semiconductor-to-metal transition although the most intense phonon frequency is 600 cm<sup>-1</sup>.

Beyond 5 nm, phonon confinement models have been known to fail to fit the observed data. This is clearly shown in the 5 nm thick ribbon data in Fig. 5.11 where instead of stronger phonon confinement, a 145 cm<sup>-1</sup> phonon splitting was observed. This is attributed to surface phonons which become predominant when then ratio of surface atoms to bulk atoms increases. Eq. 3.9 could not be used because this equation governs the surface phonons modes which come as a result of LO-TO splitting. In the present data there is a single-phonon splitting - TO splitting and/or LO splitting. This begs for another phonon splitting protocol. Similar to the current observations have been Lerman *et al.* (1997) [453b] and Volodin *et al.* (2000) [453c] from their quantum structures by molecular beam epitaxy. Lermann developed a theory of LO wire-width dependent splitting in ZnSe and compared their theory based on strain relaxation to their experiment observations. They found the splitting to have an inverse correlation with the wire-width although the

theoretically calculated data showed departure from experiment when the wire width became smaller than about 50 nm (see inset (a) of Fig. 5.11). Volodin *et al.* compared the TO splitting in two orthogonal direction of the GaAs (311) wires ( $TO_x$  and  $TO_y$ ) and found that the degree of splitting increased with decreasing number of monolayers. A GaAs-free layer labelled (311)B showed no phonon splitting. These results confirm the present study's hypothesis laid out in Chapter 3 that as nanostructures become thinner more atoms become surface atoms and surface and interface phonons manifest and hence the increase in the splitting of individual TO and LO phonons as seen in Fig. 5.10. The same resulted were observed for  $WO_3$  nano-discs (Fig. 5.10 (b)) whose thickness has not yet been determined but whose evident splitting shown in Fig. 5.10 (c) confirms the nano-structuredness of the disc thickness.

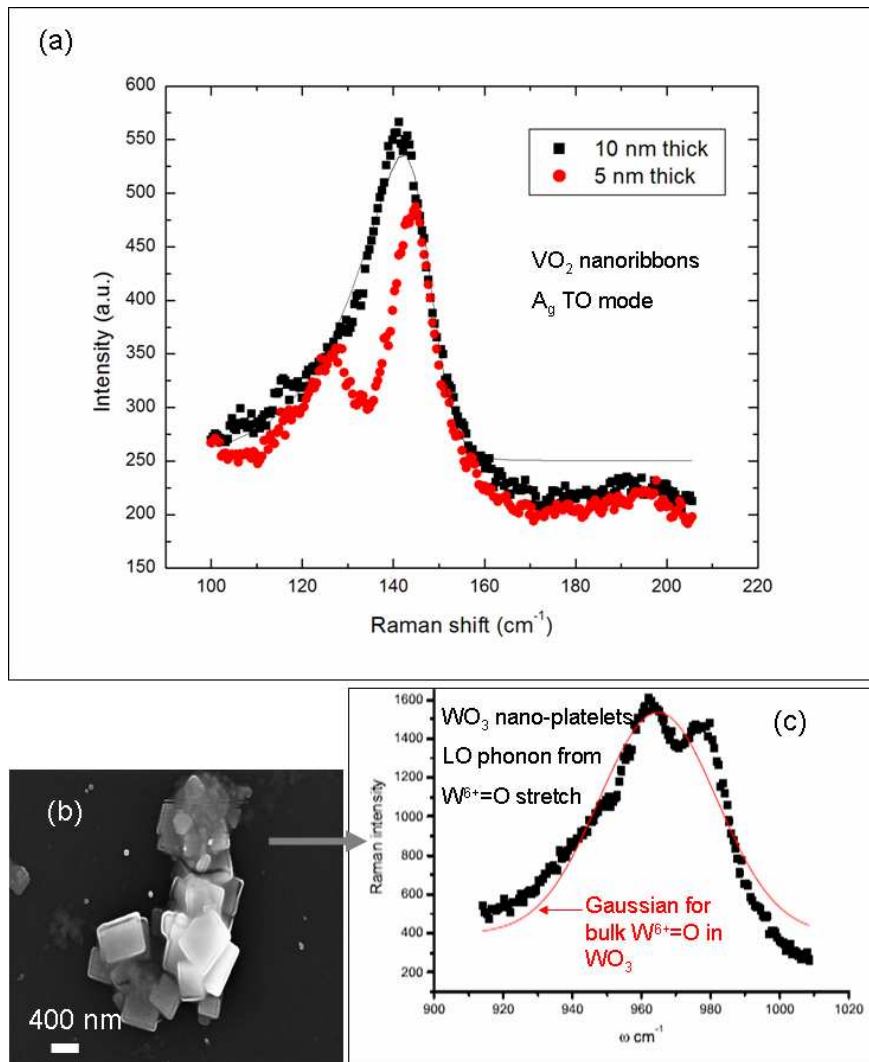


Fig. 5.11 (a) Raman spectroscopy of  $\text{VO}_2$  nanoribbons of different thickness; the new phonon confinement equation 61 has been fitted to the 10 nm thick ribbon data. The 5 nm ribbon data has been described by phonon splitting of equation 64. Compare the TO-splitting in  $\text{VO}_2$  nanoribbons with the LO-splitting (c) in  $\text{WO}_3$  nano-platelets (b) with details in the text.

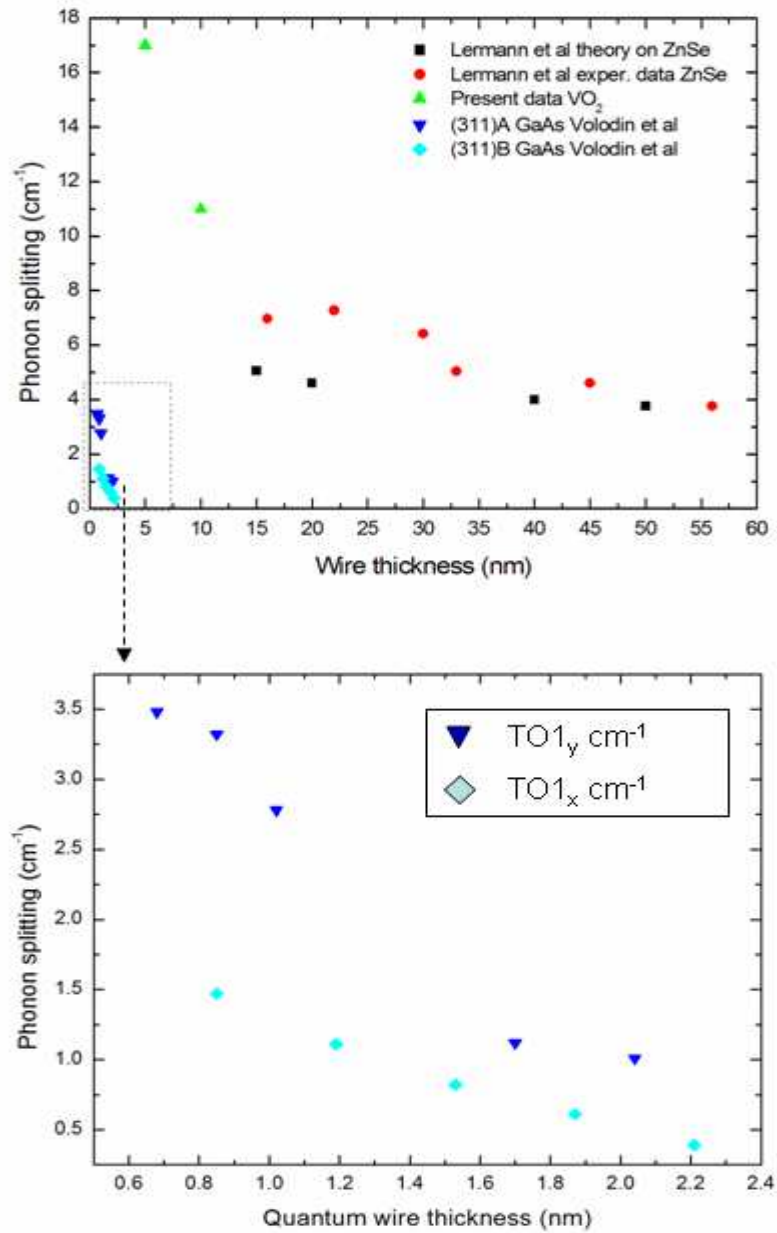


Fig. 5.12 The VO<sub>2</sub> TO phonon (145 cm<sup>-1</sup>) splitting as a function of VO<sub>2</sub> ribbon thickness suggesting that the splitting increases as ribbon thickness decreases. The inverse nature of the present results agrees with the theory and experiment on LO phonons in ZnSe quantum wires from Lerman *et al.* (see text) and the TO splitting in GaAs quantum wires as discussed by Volodin *et al.* (see text for details)



## 5.2 WO<sub>3</sub> nano-sphere produced by USP at varying furnace temperatures

The production of nano-spheres of WO<sub>3</sub> at furnace temperatures 100, 200, 300, 400, 500, and 700°C were reported in Mwakikunga *et al.* [42] attached in the Appendices A2 and also summarized herein [Fig. 5.13].

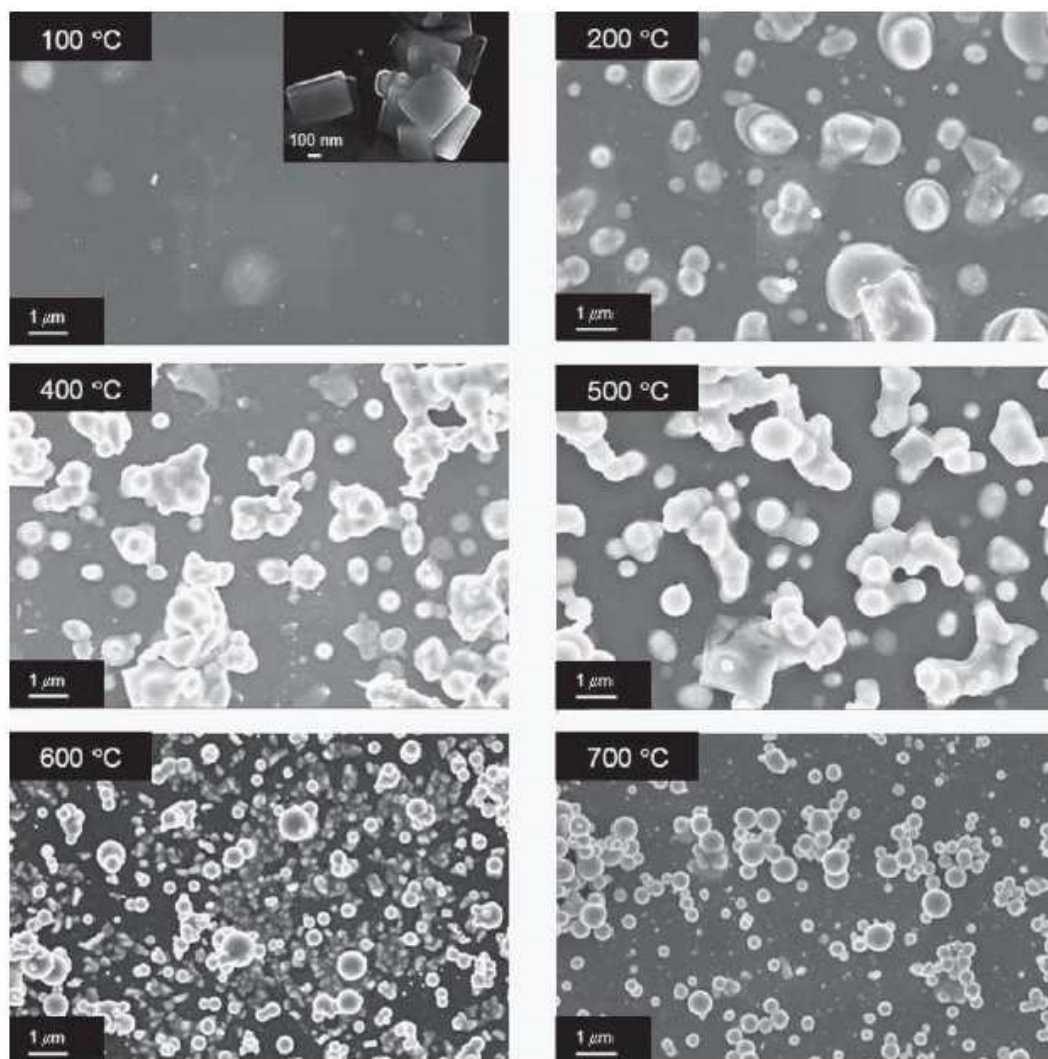


Fig. 5.13 WO<sub>3</sub> nanospheres obtained by ultrasonic spray pyrolysis (Mwakikunga *et al.* [42]) at various temperatures

Briefly, it was observed that the nano-sphere diameter decreased as the furnace temperature was increased in contrast to the so-called Ostwald's ripening. The Tiller equation (Eq. 2.46) was used to explain this shrinking in size. Also nano-crystals of various shapes were observed and the size distribution of the nano-crystals in a sample synthesized at 700°C was characterized. The mean crystal size was 72 nm with a standard deviation of about 24 nm. Rod-like structures were seen in the midst of the as-deposited particles indicative of the onset of one-dimensional growth even before thermal annealing. No such structures were seen at higher temperature than 650°C.

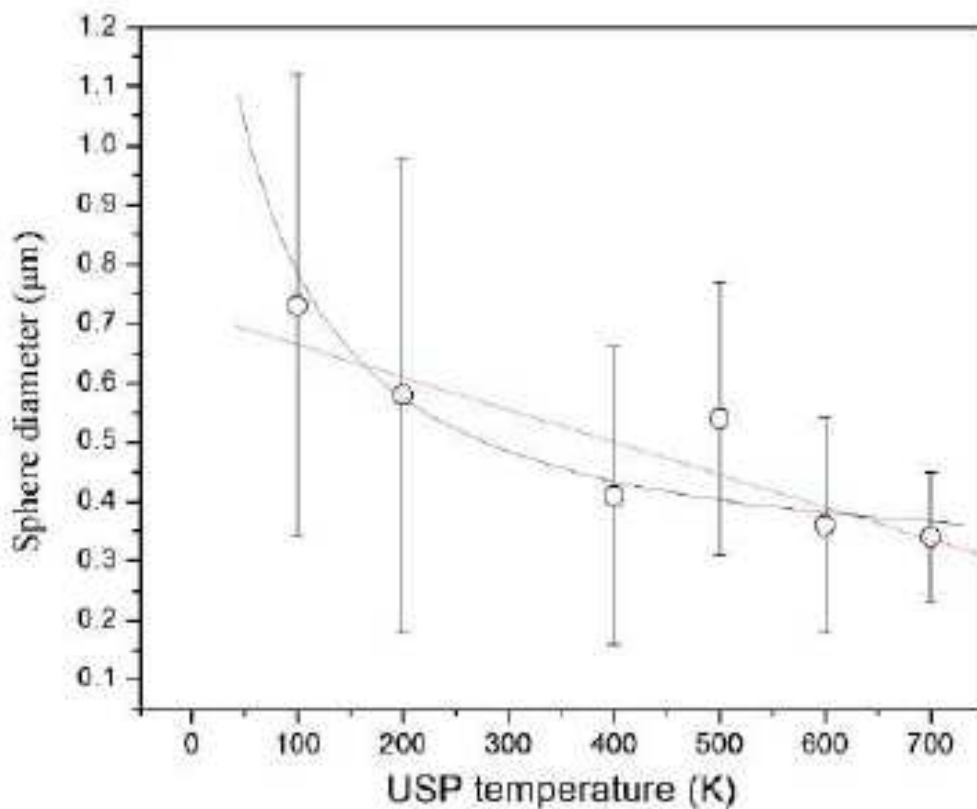


Fig. 5.14 The decrease in diameter of  $\text{WO}_3$  nanospheres as USP furnace temperature is raised (Mwakikunga et al [42])

### 5.2.1 WO<sub>3</sub> spheres into W<sub>18</sub>O<sub>49</sub> nano-tips and nano-belts after thermal annealing

In order to enhance this growth, portions of these samples were further annealed at 500°C for 17 hours as explained in the experimental chapter. Although 1D-structures are seen in all samples annealed under similar conditions, the highest yield of nano-wires and tips was seen in a sample synthesized at 500°C.

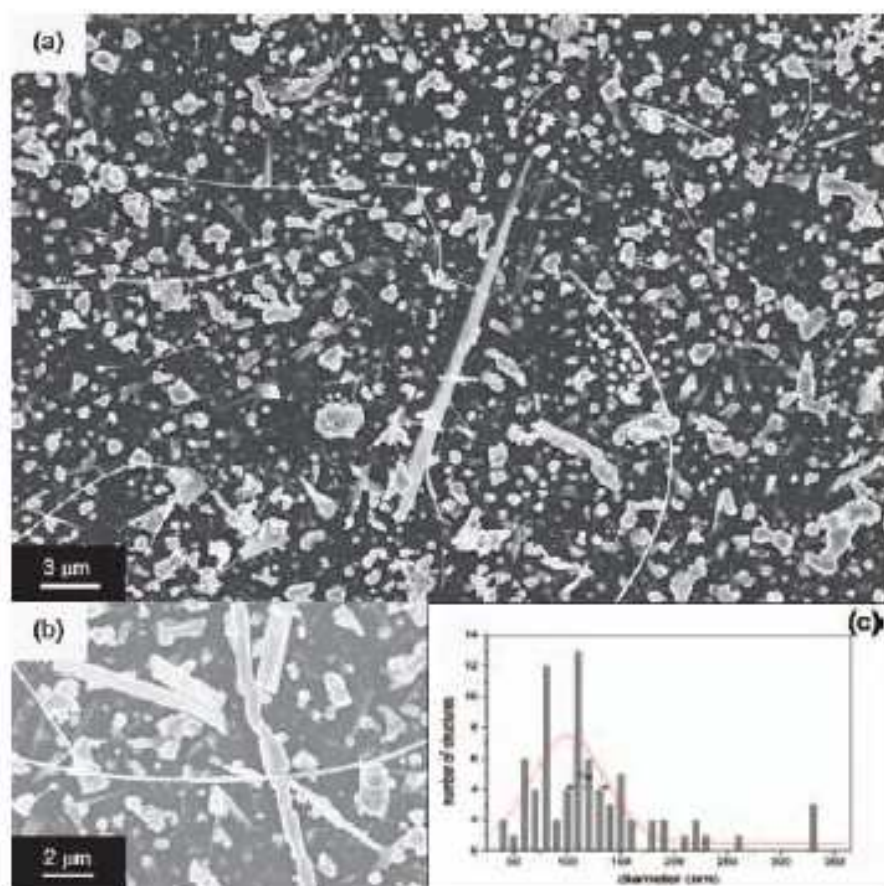


Fig. 5.15 W<sub>18</sub>O<sub>49</sub> nanowires and nanotips after annealing the WO<sub>3</sub> nanospheres produced by USP

At lower and higher temperatures than 500°C the 1D structure are rod-like and the yields are relatively poor. The wires in the sample W5-500 are extremely long with one of the highest aspect ratios. The most probable diameter of the nano-wires was  $(101.1 \pm 6.1)$  nm with a standard deviation of  $(69.6 \pm 14.1)$  nm. This means that some wires can be as small as 31 nm. Another amplified image, is shown, of a remarkably long nano-belt in a sample synthesized at 700°C and annealed at 500°C for 17 hrs (sample W7-500) whose thickness is about 45.95 nm and whose length is 8.67  $\mu\text{m}$ . This can be seen to be growing from either grain boundaries or from spheres themselves.

Transmission microscopy revealed the structure and composition of the  $\text{WO}_x$  nano-wires. The nano-wires are in fact tapered suggesting a needle-like profile.

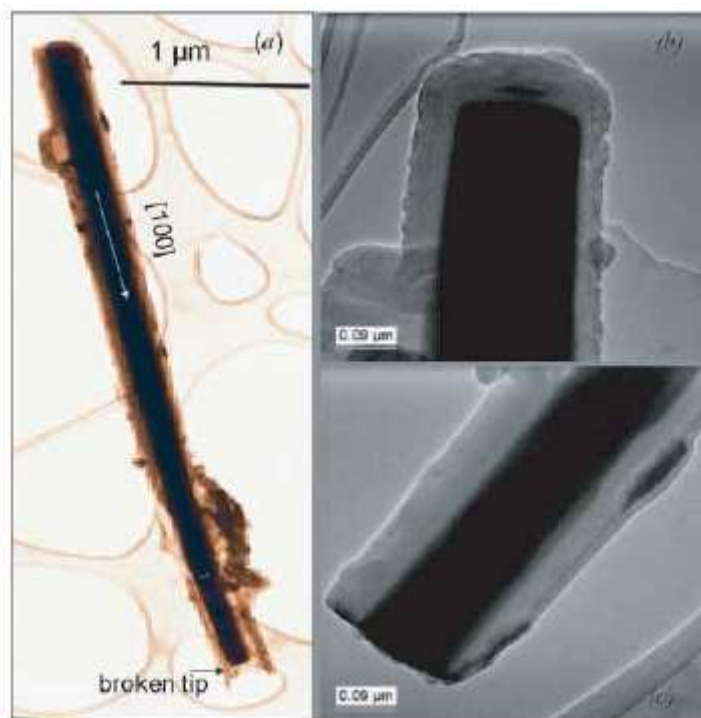


Fig. 5.16. Low resolution TEM of  $\text{W}_{18}\text{O}_{49}$  nanotips (Mwakikunga et al [42])

However, the SAED pattern (not shown here) from the core showed a one-dimensional crystalline arrangement of the atoms in the  $\text{WO}_x$  core as displayed by a spotty pattern. Analysis of spots that were seen to be of similar density, yielded the  $d_{hkl}$  spacing from which the lattice parameters were calculated from possible planes in as many phases of tungsten oxides as could be found in literature. Only the plane (100) belonging to the monoclinic phase of  $\text{W}_{18}\text{O}_{49}$  was found matching the diffraction pattern. Therefore the growth direction of the  $\text{W}_{18}\text{O}_{49}$  nano-tips is [100] and lattice parameters ( $a = 18.28 \text{ \AA}$ ,  $b = 3.775 \text{ \AA}$ ,  $c = 13.98 \text{ \AA}$ ; JCPDS 5-392) were found to match those in literature.

Since the present nanowires were produced in a novel manner, traditional growth models vis-à-vis

- (1) Screw dislocation theory
- (2) Vapor - Liquid - Solid (VLS)
- (3) Solution - Liquid - Solid (SLS)
- 4) Super Critical Fluid Synthesis (SCFS)
- (5) Vapor - Solid (VS)

could not explain the manner of growth.

Although pure tungsten has the highest melting point among known metals (m.pt  $3422^\circ\text{C}$ , b.pt  $5555^\circ\text{C}$ ), Gillet [438] showed that the  $\text{WO}_3$  particles could be sublimated at a relatively low temperature of  $550^\circ\text{C}$ . Also loss of oxygen from tungsten oxide at high temperature and low pressure is well known [439]. Since the annealing temperature of  $500^\circ\text{C}$  is close to the Gillet's

sublimation temperature of  $WO_x$ , it was observed that a new kind of growth mechanism dictates the growth of  $WO_x$  nanowires at  $500^\circ\text{C}$ . A new growth mechanism which was called Solid - Vapor - Solid (SVS) was introduced. One of the unique characteristics of these nano-structures that deserved a new growth model to explain their growth was the fact that thinner wires were longest whereas thicker ones were shortest. This is in contrast to the above listed growth models. More compelling evidence followed when we processed  $WO_x$  nanowires from laser pyrolysis grown spheres and slabs. Further discussion is done in the next section.

### **5.3 Results from Laser Pyrolysis**

#### **5.3.1 $WO_x$ nanowires from laser pyrolysis**

Detailed results from the laser pyrolysis of tungsten-based precursors, for the synthesis of  $WO_3$  are presented in Mwakikunga *et al.* [Ref. 40, 41, 43] also attached in the Appendices A3, A3 and A5. In this article [Ref. 40], it was shown that nanowires appear only after annealing (Fig. 5.17). It was also noted [Ref. 42] that the  $WO_3$  nanowires showed the ability to confine optical phonons the property of which was observed from Raman spectroscopy as shown by the asymmetry of the  $800\text{ cm}^{-1}$  and  $700\text{ cm}^{-1}$  phonon peaks illustrated in Fig. 5.18.

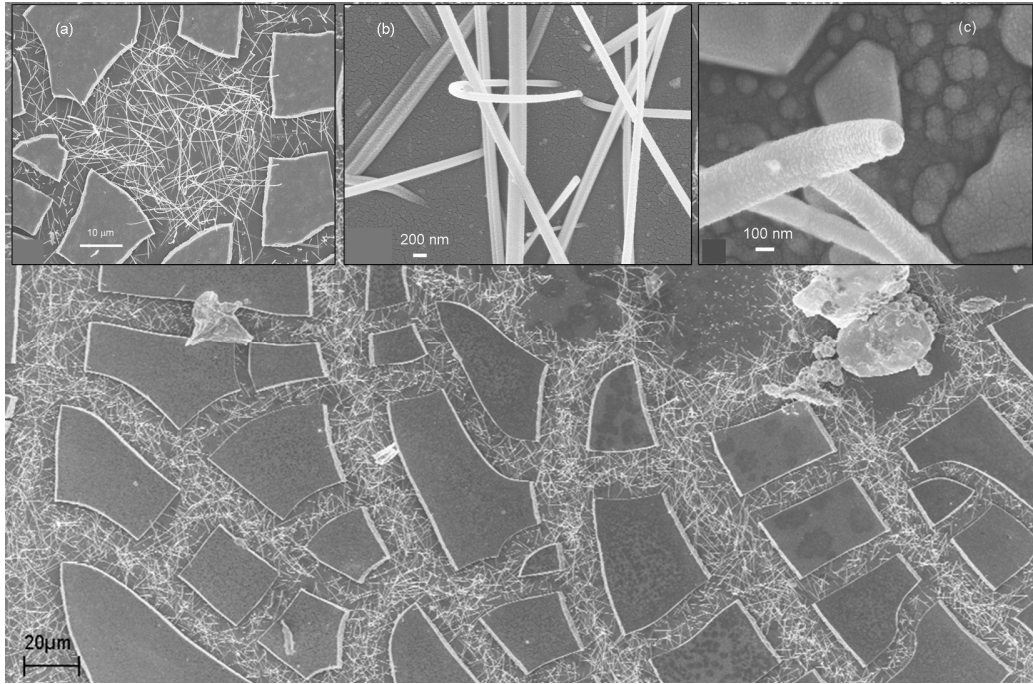


Fig 5.17 FEGSEM micrographs of  $\text{WO}_3$  nano-rods grown under  $\text{O}_2$  as a central carrier gas and  $\text{C}_2\text{H}_2$  as the secondary carrier gas showing a thin film that has flaked up into orderly slabs between which are numerous nano-wires. Inset (a) shows a close look at the nano-wires in between the slabs. Inset (b) zooms in onto the nano-wire area and inset (c) display one nano-wire's end.

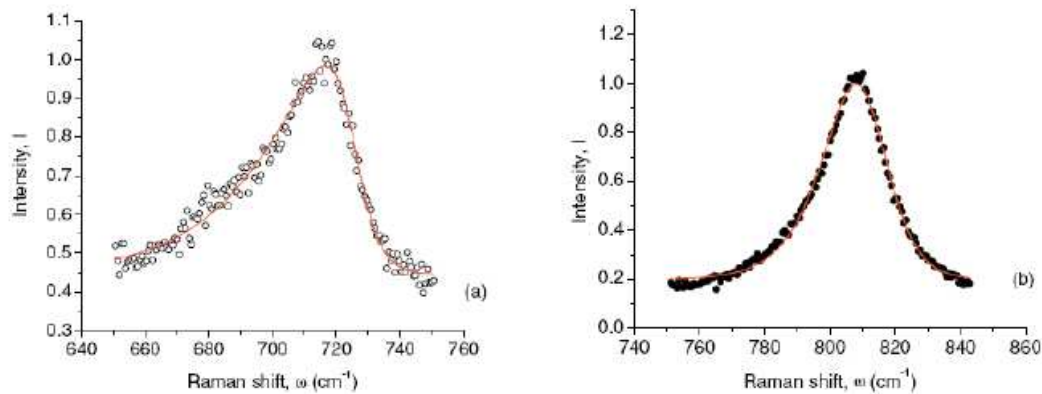


Fig 5.18. Optical phonon confinement observed by the asymmetrical broadening of the  $\text{WO}_3$ 's  $700 \text{ cm}^{-1}$  and  $800 \text{ cm}^{-1}$  phonon peaks (Mwakikunga et al [42]). Eq. 3.6 fitted and shown in red

Also it was reported in Ref. 43 that the yield of nanowires depended on the flow rate of the precursor droplets. The  $\text{C}_2\text{H}_2$ -synthesized sample had a lower yield of  $\text{WO}_3$  nano-wires after annealing (shown in Fig. 5.17) than the  $\text{O}_2$ -synthesize one as seen in Fig. 5.19. These nanowires in  $\text{O}_2$ -ran sample grow in the crevices of the film. The  $\text{C}_2\text{H}_2$ -ran sample has nano-wires with a higher aspect ratio than the  $\text{O}_2$ -ran samples. Also the  $\text{C}_2\text{H}_2$ -ran sample show presence of spherical micro-particle where a complete absence of these spheres is observed in the  $\text{O}_2$ -ran sample. This meant that  $\text{C}_2\text{H}_2$  maintains the spherical shape of the precursor droplets which was clear evidence that  $\text{C}_2\text{H}_2$  was only a sensitizer of the process but does not participate in the decomposition of the precursor. Also, in the presence of tungsten,  $\text{C}_2\text{H}_2$  dissociates and formed carbon structures such as carbon nano-tubes. On the



other hand, O<sub>2</sub> actively participated in the breakdown of the precursor droplets and in the process increased the yield of the WO<sub>3</sub> nano-wires at the expense of aspect ratio of the wires in general. The O<sub>2</sub>-ran sample also had very brittle thin films with cracks in a somewhat ordered manner. This ordered cracking after annealing could be attributed to the growth pressure (thermal stress) from the 1D nano-structures.

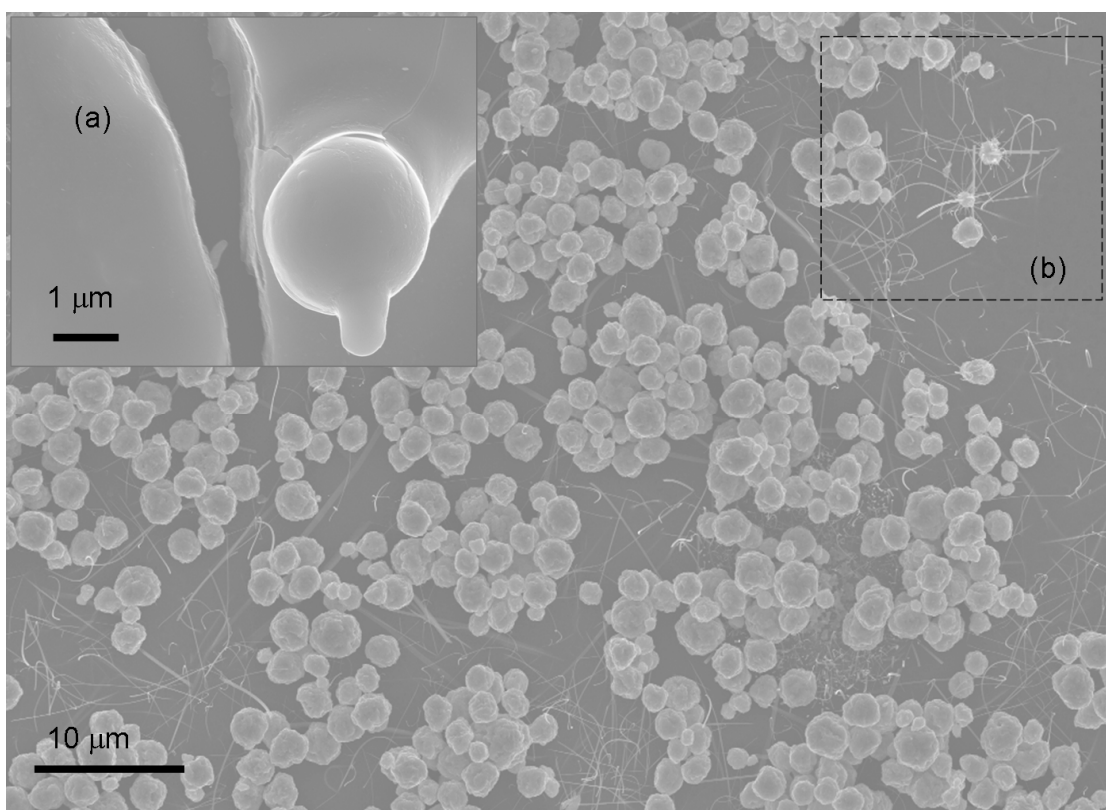


Fig 5.19 Scanning electron micrographs of WO<sub>3</sub> nano-rods grown under C<sub>2</sub>H<sub>2</sub> as a central carrier gas and oxygen as the secondary carrier gas; the spherical droplets from the precursor maintain their shape until their deposition into micro-particles. Inset (a) is a micro-particle before annealing showing the genesis of the growth of a nano-wire. After annealing there are numerous nano-wires growing from and in between the spheres. Dotted box (b) shows a region where a number of nano-wires are seen sprouting from spheres.

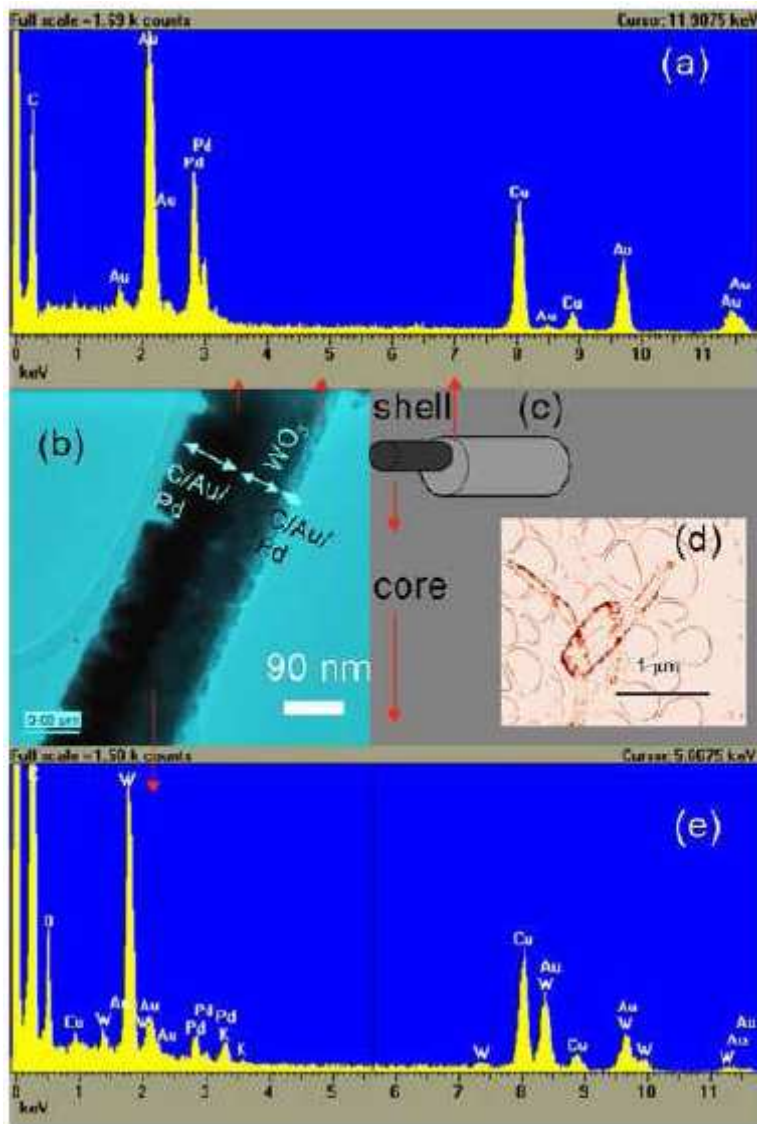


Fig. 5.20 TEM micrograph of a single WO<sub>3</sub> nanowire in (b) reveals that the nanowire is a core with a shell of carbon, Au and Pd from prior-to-SEM coating as confirmed by EDS in (a) and (c). In (d) is the micrograph of carbon nanotube found segregated by the WO<sub>3</sub> nanowires.

The TEM micrograph of a typical wire grown from O<sub>2</sub>-run WO<sub>3</sub> particles revealed a core-shell structure with the WO<sub>x</sub> wire at the core and the carbon-Au-Pd composite around the wire as a shell.

C-Au-Pd is a material used in the prior-to-SEM coating to improve conduction for enhanced imaging. This shell served as a contaminant which obscured the electron diffraction of the wire so that the stoichiometry studies of the  $WO_x$  nanowire could not be accomplished. In line with the previous studies, one could speculate that the wire is  $WO_x$  with  $x$  being less than 3 due to oxygen loss during annealing.

In the  $C_2H_2$ -processed sample it was noted in Mwakikunga *et al.* [Refs. 40 and 43] that the micro-sized  $WO_3$  particles from which the nanowires sprouted were agglomerates of small nano-sized spheres. Recently, a compelling evidence of the speculation in a sample synthesized under  $O_2$  environment was discovered. This is illustrated in Fig. 5.21 (a). In Fig. 5.21(b), the ball of nanospheres is seen propped up by more than three nanowires. Either the nanowires grow from the ball of spheres or from the  $WO_3$  layer on the substrate or both. In Fig. 5.21 (c), the size distribution of the nano-spheres is presented. The most probable diameter of the nano-spheres is 185 nm. Phonon confinement by Raman spectroscopy was observed in these wires and Eq. 58 was used to calculate parameters for the phonon dispersion relations (PDR) for  $WO_3$ . By this technique, it was possible, as reported in Mwakikunga *et al.* [Ref. 41], to obtain, for the first time, the phonon dispersion relations for the two phonon types (where  $a = 0.76$  nm and  $b = 0.38$  nm are lattice parameters) for monoclinic  $WO_3$  given as:

$$\left. \begin{aligned} \omega_{TO}^2(q) &= 713^2 + 101\sin^2(a.q) + 0.0196\sin^4(aq) \\ \omega_{LO}^2(q) &= 808^2 + 8.1\sin^2(b.q) + 0.0001\sin^4(bq) \end{aligned} \right\} \quad (73)$$

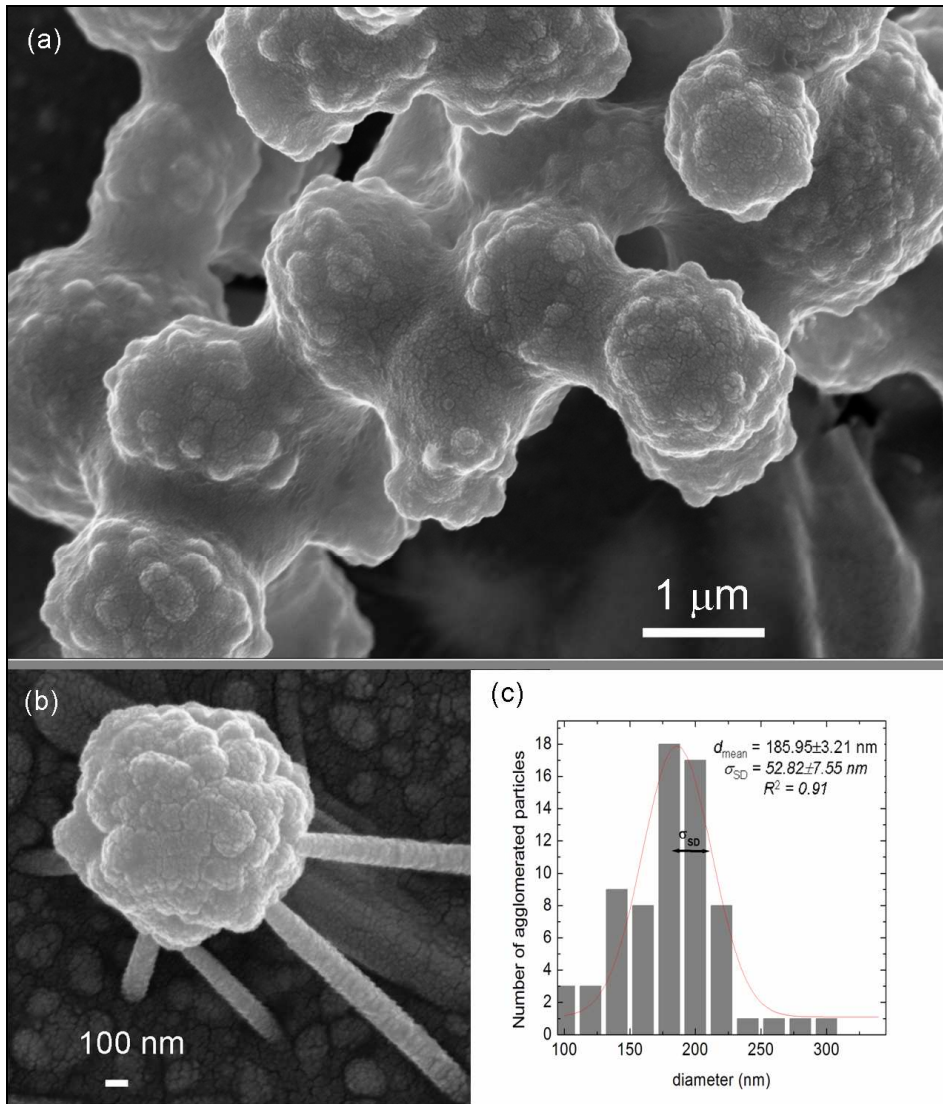


Fig. 5.21 (a) The micro-spheres of  $\text{WO}_3$  are but agglomerates of yet smaller nano-spheres. The nanospheres' size distribution in (c) showing the most probable diameter of 185 nm and nanowires seen propping up a ball of nanospheres in (b)

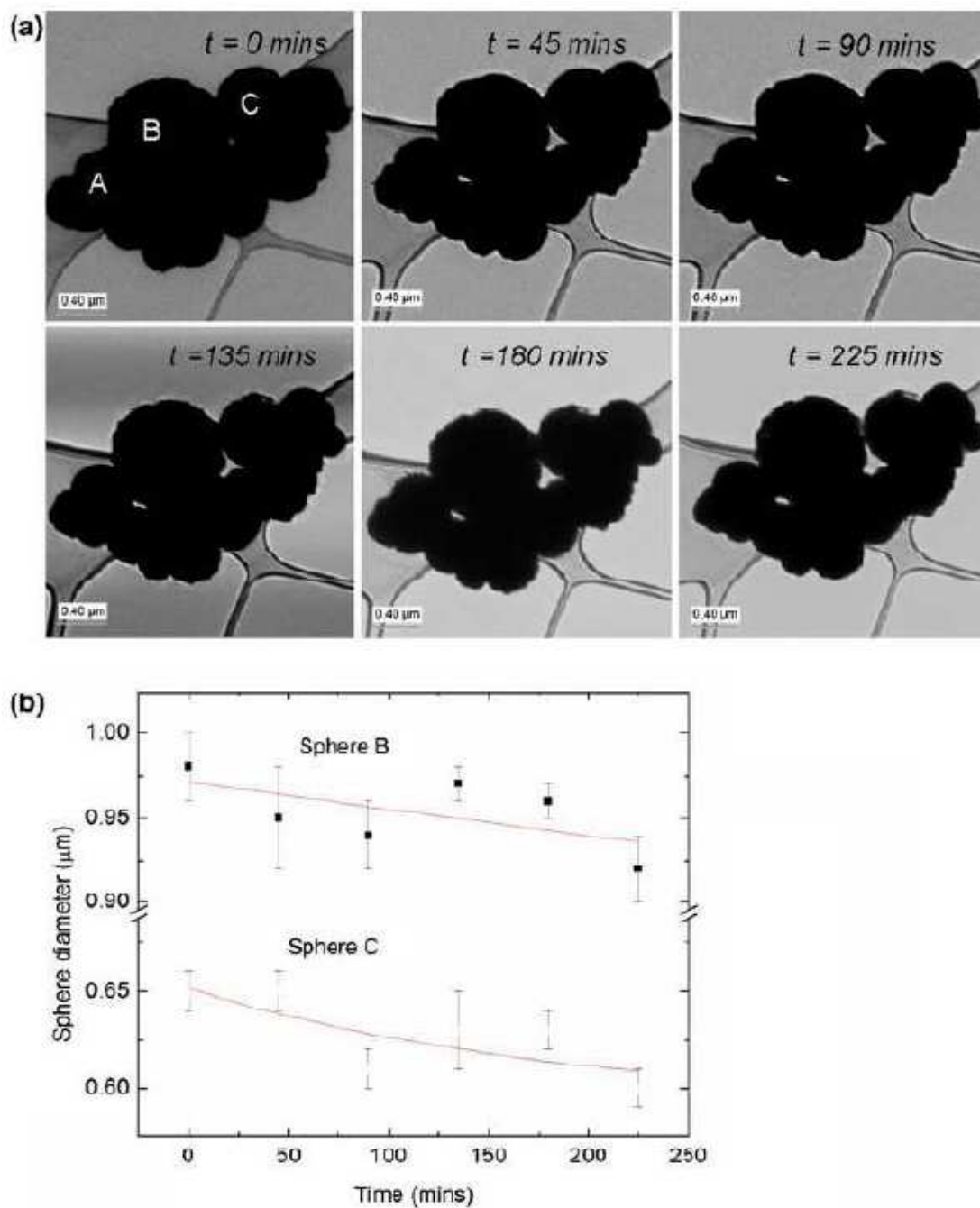


Fig. 5.22 (a) In situ TEM heating of the WO<sub>3</sub> nanospheres with the sphere images taken at different times as indicated (b) sphere diameter as a function of time due to insitu heating.

Some WO<sub>3</sub> nanospheres were placed on a copper grid housed in a specialized heater for TEM for insitu annealing studies while TEM images of

the sphere were taken periodically as shown in Fig. 5.22 (a). This was done in order to find out if growth of nanowires from spheres could be observed in real time. No nanowires were observed. This is simply due to the fact that the environment in TEM is totally different from the environment where the nanowires were obtained- high vacuum in TEM but atmospheric pressure in the annealing environment. However, the most important result in this study was the observation of real time shrinkage of spheres as a function of time in the period that insitu heating occurred [Fig 5.22 (b)].

### 5.3.2 Brief Review of Nanowire Growth Models

In order to understand how these nanowires grow, some of the growth mechanisms proposed by various scientists through the ages have been reviewed briefly. Sir Frederick Frank proposed the 'screw dislocation theory' in 1949. Central to this dislocation theory were Polanyi, Orowan, Taylor, Burger and Mott & Nabarro [440]. Defects and dislocation in the initial crystals initiate one-dimensional growth; "...the crystal face always has exposed molecular terraces on which growth can continue, and the need for fresh 2D nucleation never arises..." [440]. In 1964, detailed studies on the morphology and growth of silicon whiskers by Wagner & Ellis [441] led to a new concept of crystal growth from vapour which was called vapour-liquid-solid (VLS) mechanism. The new growth mechanism was built around three important facts: (a) silicon whiskers did not contain an axial screw dislocation

(b) an impurity was essential for whisker growth and (c) a small globule was always present at the tip of the whisker during growth.

From fact (a), it was clear that growth from vapour did not occur according to Frank's screw dislocation theory and from, facts (b) and (c), it was important that a new growth mechanism be studied.

In 1975, Givartzigov [442] introduced the fundamental aspects of the VLS mechanism. Emphasis was placed on the dependence of the growth rate on the whisker diameter. It was found that the growth rate decreased abruptly for submicron diameters and vanished at some critical diameter  $d_c \leq 0.1 \mu\text{m}$  in accordance with the Gibbs-Thomson effect. Basing on this effect, which states that the solubility limit of a precipitate ( $\beta$ ) in a matrix ( $\alpha$ ) varies with the precipitate's radius, Givartzigov suggested that the effective difference between the chemical potential of the precipitate in the vapour phase and in the terminal precipitate [whisker],  $\Delta\mu$ , is given by

$$\Delta\mu = \Delta\mu_0 - \frac{4\Lambda\sigma}{D} \quad (5.7)$$

$\Delta\mu_0$  is the same difference at a plane boundary (when diameter,  $D$ , of the precipitate tends to  $\infty$ ),  $\Lambda$  is the atomic volume of the precipitate and  $\sigma$  is the surface free energy of the precipitate. The dependence of growth rate,  $G$ , on the super-saturation ( $\Delta\mu/k_B T$ ) given by  $V = b(\Delta\mu/k_B T)^n$ , where  $b$  and  $n$  are coefficients to be evaluated from experimental data, was used to derive an expression



$$V^{1/n} = \frac{\Delta\mu_0}{k_B T} b^{1/n} - \frac{4\Lambda\sigma}{k_B T} b^{1/n} \frac{1}{D} \quad (5.8)$$

The main characteristics of VLS mechanism is (1) the presence of a catalyst and (2) direct proportionality of the diameter of the nanostructure and the growth rate. and hence the larger is the terminal length of the whisker. Thick whiskers grow longer than thinner ones because this growth can be afforded by the continual supply of building blocks in the CVD system. It is shown below that in the absence of constant supply it is only the thin wires that grow long whereas the thick ones grow short. By plotting growth rate,  $V$ , [442] or terminal length  $l_\infty$  [443] of the whisker versus  $D$  gives curves with a positive ascent. A plot of  $V^{1/n}$  versus  $1/D$  gives a straight line graph with a negative slope [442].

Recently, an in situ growth profile in real time for tungsten oxide nano-wires was followed by Kasuya *et al.* (2008) [444] by injecting ultra-small flow rates of  $O_2$  on a heated tungsten surface placed on a scanning electron microscope stage. It was difficult to ascertain if the length-and-diameter data would be in agreement with the VLS mechanism because the images were rather poor. This was due to the poor vacuum caused by the intentional injection of  $O_2$  which was useful for the targeted reaction. The length of the nano-wire as a function time  $l(t)$  was found to take the form of

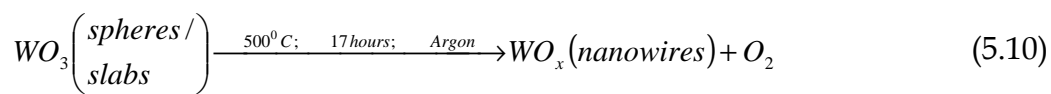
$$l(t) = l_0 [1 - \exp(-\alpha t)] \quad (5.9)$$

where  $l_0$  is the final length and  $\alpha$  is the growth or decay coefficient.

### 5.33 Need for a New Model of Growth Mechanism

What is studied here is the final state of the fully-grown  $\text{WO}_3$  nanostructures. The present data for length and corresponding diameter for each nano-wire show contrary trends to the traditional (VLS) model. Since the production of solid-state nano-wires is after annealing of the solid-state particles, the mechanism of growth can neither be according to liquid-based "Solution-Liquid-Solid" mechanism proposed by Treanter and Buhro [445,446] nor in line with the "Super-Critical Fluid Synthesis" mechanism proposed by J D Holmes [447] and which has been later supported by Korgel and co-workers [448]. These data certainly support the proposed "Solid Vapour Solid (SVS)" mechanism reported in Mwakikunga *et al.* [42] where the solid-state  $\text{W}_{18}\text{O}_{49}$  nano-tips produced by annealing solid-state  $\text{WO}_3$  nano-spheres (prepared by ultrasonic spray pyrolysis) in argon environment was reported. Synthesis of solid materials from solid precursors is not new. Solid-state reactions are very slow and difficult to carry out to completion unless carried out at very high temperatures where reacting atoms can diffuse through solid material to the reaction front more easily. Transformation of one phase to another (with the same chemical composition) can also occur in solid state, either at elevated temperatures or elevated pressures (or both). For the

growth rate of many solid-state reactions (including tarnishing), inter-diffusion of ions through the product layer increases the thickness  $\Delta x$  parabolically with time  $(\Delta x)^2 \propto t$  [449]. This is a sharply different dependence from the Eq. 1 proposed by Kasuya *et al.* [444] above. In some solid-state processes, nucleation can be homogeneous. This is often the case for thermal decomposition, for example, as is the case in the current reactions



In this Letter, Mwakikunga *et al.* introduced for the first time the statistical-mechanical aspects of this proposed SVS model as illustrated in Fig. 2.23. of the nanowires from a spherical layer of atoms

### 5.34 The Solid-Vapour-Solid Nanowire Growth Theory

For the sake of simplicity, consider the source of molecules to be a solid sphere of radius  $R_0$ , containing molecules of mass,  $M$ , and assume the molecules to be spherical of average molecular diameter,  $\Omega$ . Assume further that in changing the morphology from a sphere to a wire, only the surface molecules can migrate from the sphere to the newly-forming wire or rod. For instance it has been demonstrated [450] that the surface diffusive flux,  $J_S$  of atoms on a surface of a slab of length  $L$  given by  $J_S = -(dc/dx)|_0^L D(y) dy$  is different from the more familiar bulk diffusive flux written from the first

Fick's law as  $J_B = -D_B(dc/dx)L$  where  $dc/dx$  is the concentration gradient. In this case, transformation from sphere to rod takes place layer after layer. The sphere shrinks but the as-forming rod lengthens.

If the sphere is amorphous and the wire is crystalline as normally observed experimentally, then the densities of the material in the initial sphere and the final wire are different and can be written respectively as  $\rho_{am}$  and  $\rho_{cryst}$ . The number of atoms in the first layer of the sphere can therefore be written as

$$N_1^{surf} = 4\pi R_0^2 \Omega \frac{\rho_{am}}{M} \quad (5.11)$$

If all these atoms assemble into a rod of diameter  $D$  and length  $l_1$  then the number of molecules in the rod can be written in terms of length  $l_1$  as

$$N_1^{rod} = \frac{\pi}{4} D^2 l_1 \frac{\rho_{cryst}}{M} \quad (5.12)$$

However, not all the atoms in Eq 5 end up making the rod. The actual fraction that self-assembles into the rod is proportional to the Boltzmann's fraction which depends on the temperature  $T$  of the ambient given as

$$\frac{N_1^{rod}}{N_1^{surf}} = \exp\left(-\frac{E_A}{k_B T}\right) \quad (5.13)$$

$E_A$  is the activation energy of the atoms.

After the first layer has assembled into the rod of length  $l_1$ , the next layer in the sphere has a radius of  $R_0 - \Omega$  which forms the next segment of the rod of length  $l_2$ . The subsequent layers have radii of  $R_0 - 2\Omega$ ,  $R_0 - 3\Omega$ ,  $R_0 - 4\Omega$ ,  $R_0 -$

$5\Omega$ , and so forth. The  $i^{\text{th}}$  layer will have a radius of  $R_0-(i-1)\Omega$  such that the number of atoms in  $i^{\text{th}}$  layer is

$$N_i^{surf} = 4\pi\Omega \frac{\rho_{am}}{M} [R_0 - (i-1)\Omega]^2 \quad (5.14)$$

This corresponds to the number of atoms in the  $i^{\text{th}}$  segment of the rod as

$$l_i = 16 \frac{\rho_{am}\Omega}{\rho_{cryst}} \exp\left(-\frac{E_A}{k_B T}\right) [R_0 - (i-1)\Omega]^2 \frac{1}{D^2} \quad (5.15)$$

The total length of the wire is a summation of all the segments of the wire emanating from each corresponding layer in the source sphere.

$$l = l_1 + l_2 + l_3 + l_5 + \dots + l_N = \sum_i^N l_i = \zeta \frac{1}{D^2} \quad (5.16)$$

where

$$\zeta = 16 \frac{\rho_{am}\Omega}{\rho_{cryst}} \exp\left(-\frac{E_A}{k_B T}\right) \sum_i^N [R_0 - (i-1)\Omega]^2 \quad (5.17)$$

Parameter  $\zeta$  is a function of temperature T and also depends on the geometry of the source of the atoms. The higher the annealing temperature, T, the higher the slope,  $\zeta$ . This fact may mean that thinner nanowires can be obtained at higher annealing temperatures. But there must be a lower limit to how thinner nanowires can get in the SVS mechanism since at much higher temperatures all solid state starting material should evaporate away leaving nothing to form the nano-wires with. These limits are yet to be determined. The same question has been asked if there is a thermo-dynamical lower limit to the nano-wires growth by VLS [451]. It can be seen that if the source is equally crystalline then the ratio of the densities in the source to the final structure is unity. By quick inspection, one can see that the geometry

described by the summation in Eq. 84 is proportional to the total surface area of all atomic or molecular layers in the source. A plot of  $l$  versus  $1/D^2$  should be a positive straight line graph with a  $y$ -intercept of zero and a slope of  $\zeta$ . Similarly a plot of aspect ratios  $l/D$  versus  $1/D^3$  is supposed to be a positive straight line going through the origin and having the slope,  $\zeta$ .

In the VLS mechanism, given a constant flux of molecules in the source, a nano-wire that has a large diameter will grow much longer as compared to when it starts out with a small diameter. In the SVS growth, the thinner the wire the longer it is and vice versa [as shown in the plots of Fig. 5.24 (a)]. When aspect ratios, defined here as the ratio of length to diameter, is plotted against diameter, the same profile is obtained [Fig. 5.24 (b)]. When length and aspect ratio are plotted against  $1/D^2$  and  $1/D^3$  respectively, in accordance with Eq. 83, positive slopes are manifest (Fig. 5.24) almost equal to each other as expected from the above theory and of the order of  $\sim 10^{-20} \text{ m}^3$ . This value is related to the order of magnitude of the average volume of the  $\text{WO}_3$  nano-wires. It should be noted that reverse growth from one-dimensional to spherical particles is also possible at suitable annealing conditions. For instance, nano-belts of Zn acetate were converted into aggregates of ZnO nano-particles as reported in this journal [452].

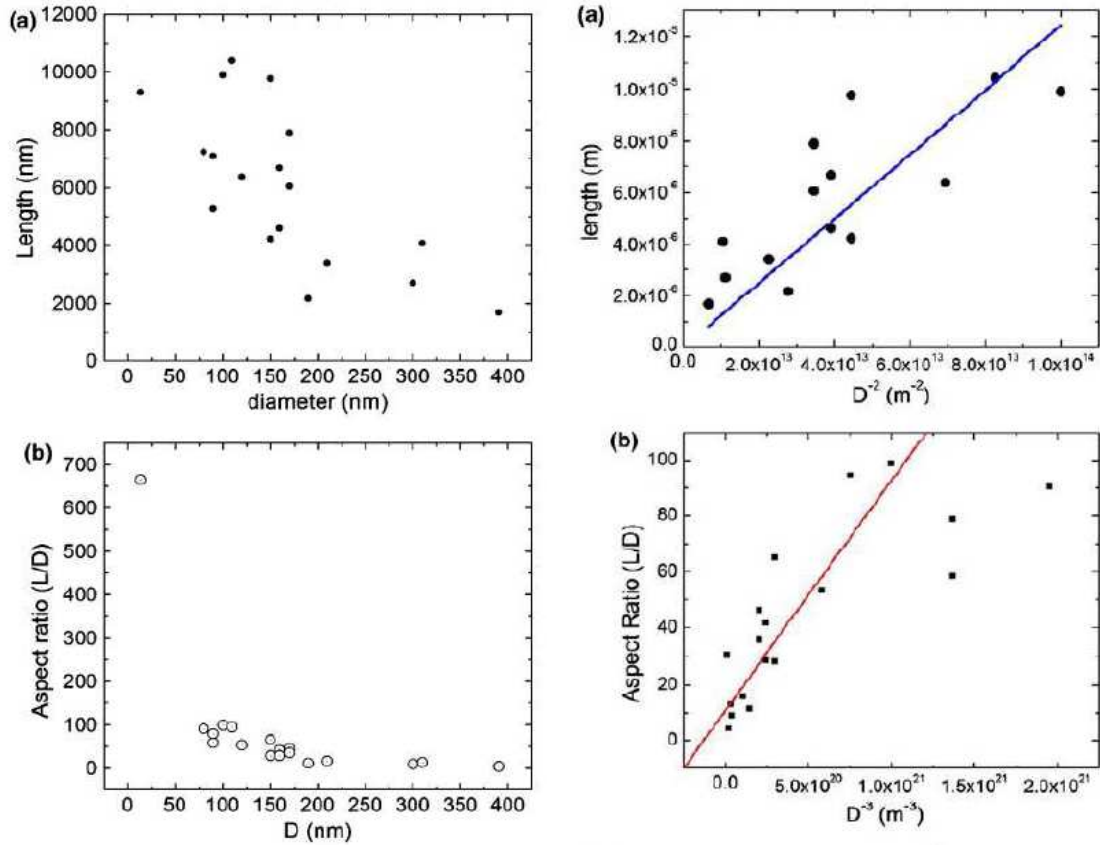


Fig. 5.24 (a) length of nanowire versus its diameter and length versus  $1/d^2$  fitted with Eq. 5.16 and (b) aspect ratio of the nanowire versus  $d$  and  $1/d^3$  fitted with Eq. 5.16 divided by  $d$ .

### 5.36 VO<sub>2</sub> nanobelts from laser pyrolysis

Although production of VO<sub>2</sub> nanobelts by laser pyrolysis of VCl<sub>4</sub> in ethanol and aqueous V<sub>2</sub>O<sub>5</sub> was discussed in Mwakikunga *et al.* [42], the presentation was brief. The procedure here was similar to the one used during the production of WO<sub>x</sub> nanowires. The belts also appeared only after annealing of the as-deposited samples for 17 hours in flowing argon suggesting the same growth model – the SVS theory – is the mechanism of growth. These structures are long drawn-out with some of these extending to

as much 100  $\mu\text{m}$  [Fig. 5.25, 5.26]. The bundling together of nano-belts due to Van der Waal's attractive forces is clearly seen in the VCL1 samples ran under oxygen. The cracks seen in W-based sample above are also seen in this V-based sample ran in the same gas environment. However the yield of nano-belts in the V-based sample is not as high as the W-based one. This could be due to the higher reactivity of vanadium alkoxide in  $\text{O}_2$  than that of tungsten alkoxide. This anomalous reactivity of  $\text{V}(\text{OR})_4$  presents violent decomposition and deposition and hence may impede salient self assembly. No belts or other 1D nanostructures are observed in the VCL<sub>2</sub> sample synthesized under  $\text{C}_2\text{H}_2$  showing that the O atoms in the alkoxide are not enough to sustain self assembly of the decomposed  $\text{V}(\text{OR})_4$ . Also no nano-belts are observed in the V2O5A sample ran under  $\text{O}_2$ . In this case, the vanadium pentoxide already has enough oxygen required to satisfy the stoichiometry of these vanadium oxides. The presence of  $\text{O}_2$  in the carrier gas plays no role in this case and hence no nano-belts could be observed.



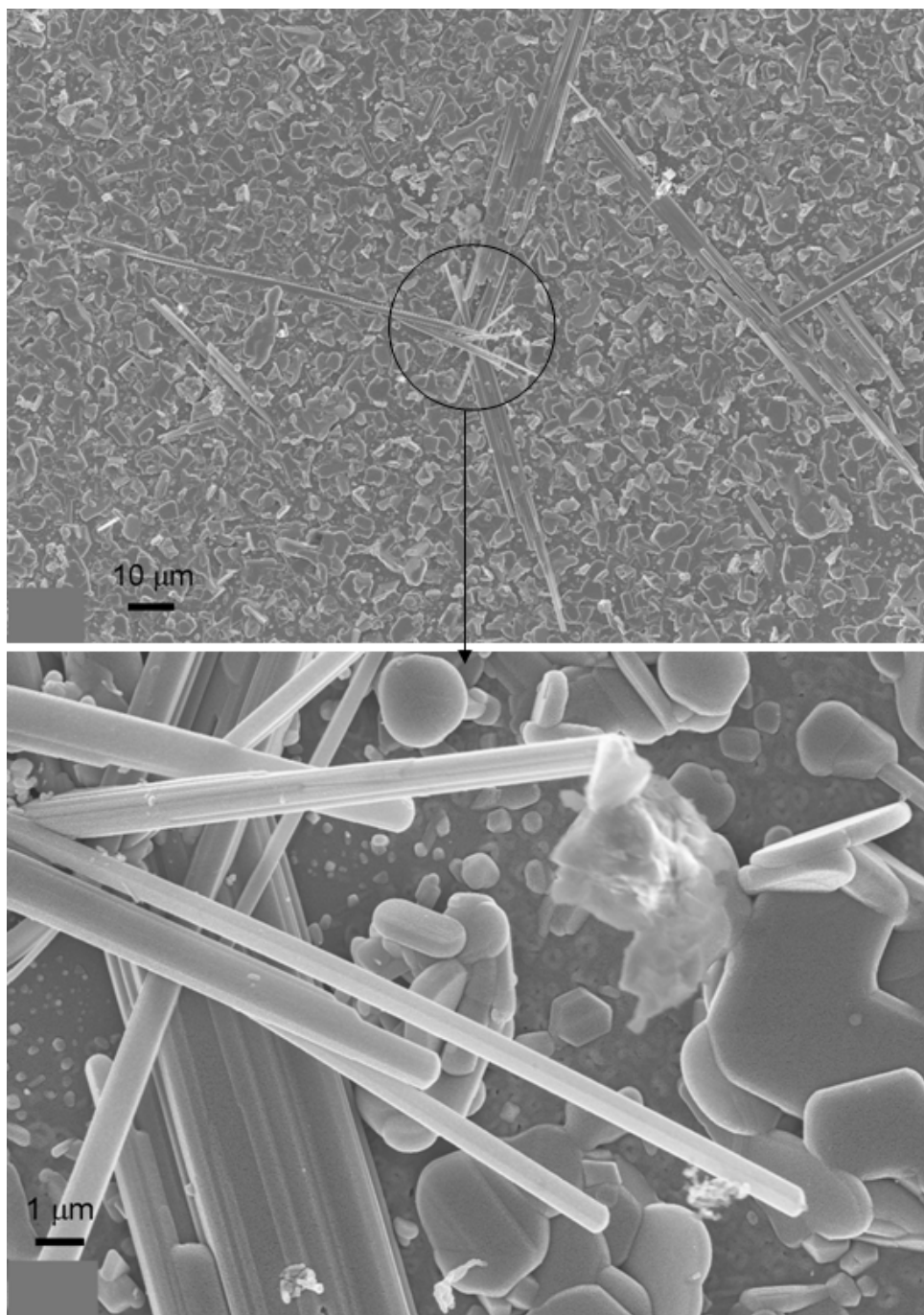


Fig. 5.25 Scanning electron micrographs of VO<sub>2</sub> nano-rods grown from VCl<sub>4</sub> + ethanol under oxygen as a central carrier gas and C<sub>2</sub>H<sub>2</sub> as the secondary carrier gas.

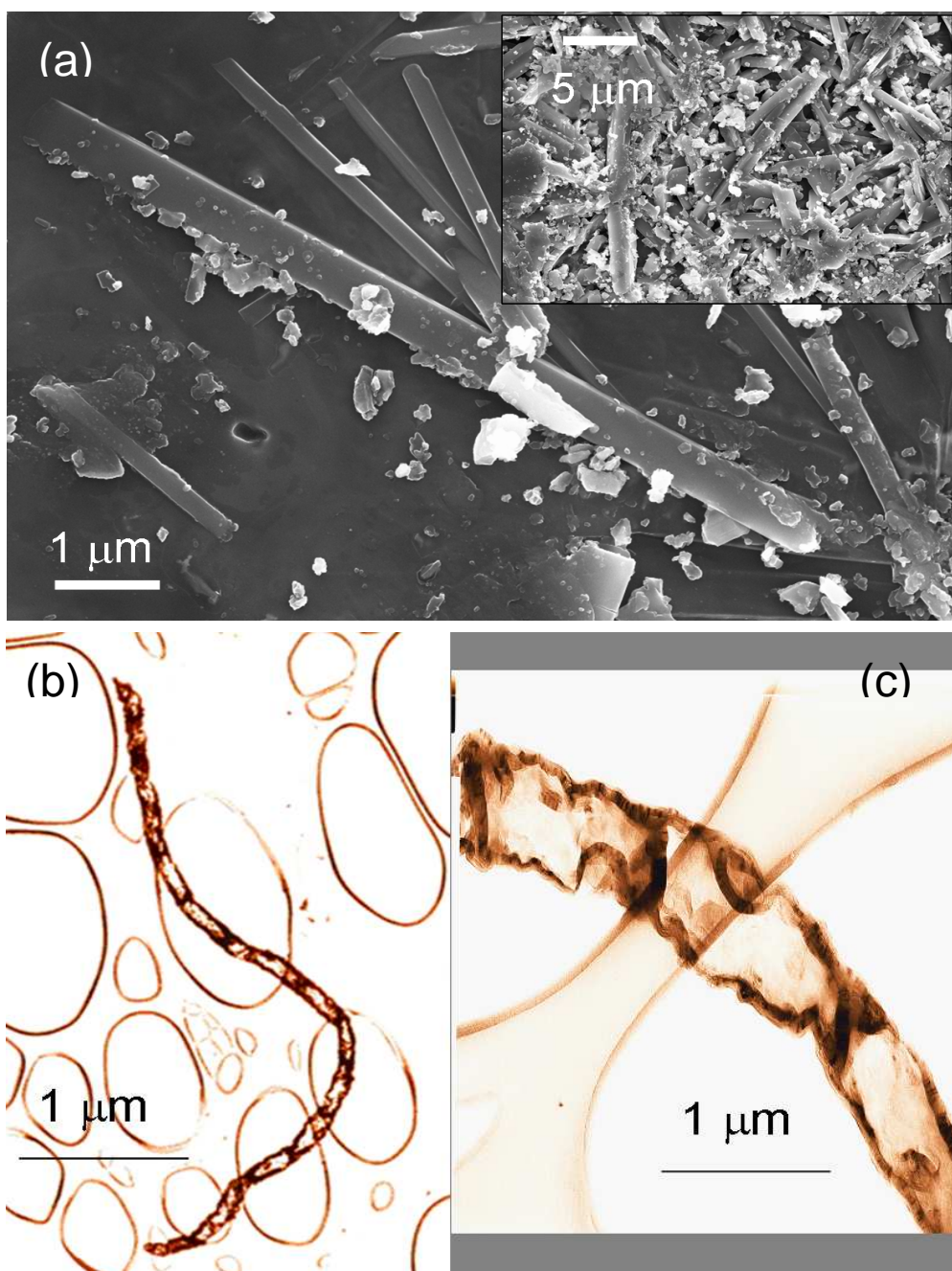


Fig.5.26 (a) Scanning electron micrographs of VO<sub>2</sub> nano-rods grown from aqueous V<sub>2</sub>O<sub>5</sub> under C<sub>2</sub>H<sub>2</sub> as a carrier gas (inset) typical dense distribution of the belts at low resolution (b) low resolution TEM image of bamboo structured carbon nanotube found amidst the VO<sub>2</sub> ribbons and (c) a higher magnification of the CNT showing disorder amidst ordered growth.

### 5.37 Size effects on the thermochromism of VO<sub>2</sub>

The study of thermochromism in the current work was carried out by evaluating the hysteresis width (HW) as shown by a typical resistance versus temperature chart in Fig. 5.27.

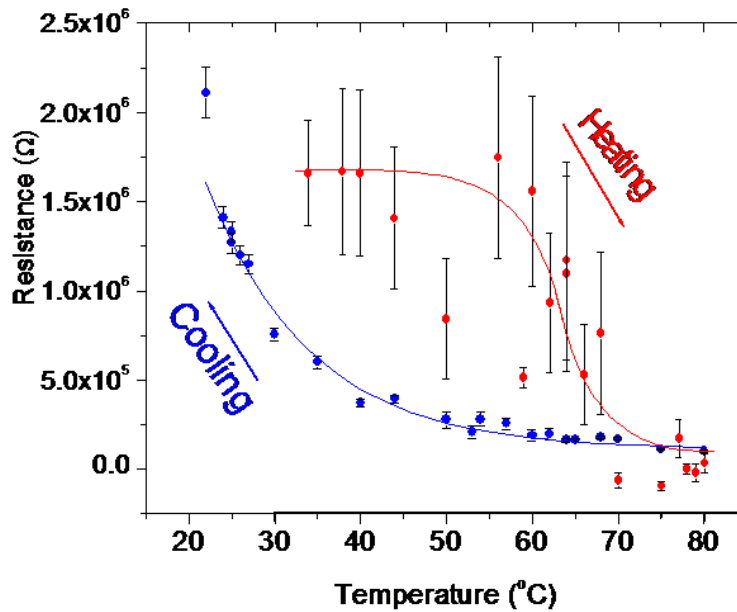


Fig 5.27 Resistance of a VO<sub>2</sub> nanoribbon film versus temperature for heating and cooling phases showing an enhanced hysteresis

The previous models as introduced in Chapter 3 had some shortfalls. Although Lopez *et al.* were initiators in showing the broadening of the hysteresis width (HW) as the grain size decreased, they had no explicit theory that related the two. The Pan *et al.* model based on the Gaussian could fit the hysteresis profiles. In the current study, the Pan *et al.* model was employed in

deriving the relationship between HW and particle size  $d$ . This attempt gave unsatisfactory results.

There was therefore need for another approach. In this study, the Lopez's proposal of a stress-free Gibbs free energy was replaced with the following argument. The energy expended in transforming a crystallite from monoclinic at  $T_{\text{room}}$  to tetragonal structure above the transition temperature  $T_{c+}$  is  $k_B(T_{c+} - T_{\text{room}})$  whereas the energy lost in restoring this crystallite from tetragonal at a temperature  $T > T_{c+}$  back to room temperature via another transition temperature  $T_{c-}$  is  $k_B(T_{c-} - T_{\text{room}})$ . The difference between these energies gives the energy of the hysteresis and this energy difference is  $k_B(T_{c+} - T_{c-})$ . One assumes that this energy is responsible for the amount of stress that is introduced to the structure as the materials transforms from monoclinic phase to that of tetragonal and vice versa. The stress in the structure is proportional to this residual hysteresis energy. In its full form, one would represent stress as rank two tensor written as a 3×3 matrix as first proposed by Einstein. However, for simplicity and relevance to this work, the empirical expression relating yield stress to the grain size was adopted from the so-called Petch relation in metallurgy [431] given as

$$\sigma_s = \sigma_0 + \frac{k_0}{\sqrt{d}} \quad [5.18]$$

Where  $\sigma_0$  is yielding stress for a material in bulk form and  $k_0$  is constant for a particular material. As the particle size  $d$  decreases (to nano-scale) the second term becomes important and yielding stress increases abruptly.

Based on the assumption that the residual energy  $k_B(T_{c+} - T_{c-})$  is proportional to the stress it causes one then can write:

$$k_B(T_{c+} - T_{c-}) = k_B(HW) = \beta_1 \left( \sigma_0 + \frac{k_0}{\sqrt{d}} \right) \quad [5.19]$$

One assumes further from experimental fact that the area under the hysteresis curve remains almost constant, that is, as the HW increases due to size effects the HJ increases due to the same effect. Hence one can write

$$(HW)(HJ) \approx \beta_2 \quad [5.20]$$

where  $\beta_2$  is a constant. Therefore the hysteresis jump (HJ) as a function of particle size can be given as:

$$HJ = \frac{k_B \beta_2 \sqrt{d}}{\beta_1 (\sigma_0 \sqrt{d} + k_0)} \quad [5.21]$$

The charts in Fig. 5.28 illustrate the relationship between HW and particle size  $d$ . In (a) a graph is plotted of HW against  $d$ . This graph compares the present results with those of others as indicated in the caption. The inverse nature of the HW as a function  $d$  is confirmed. In (b) a chart of HW versus  $d^{-0.5}$  is presented and a linear relationship is clearly evident as one expects. However, if the relationship went being linear, then the HW increases to infinity. This means that as  $\text{VO}_2$  particles tend to nano-scale, the HJ tends to zero; meaning that the materials is thermally stable but cannot

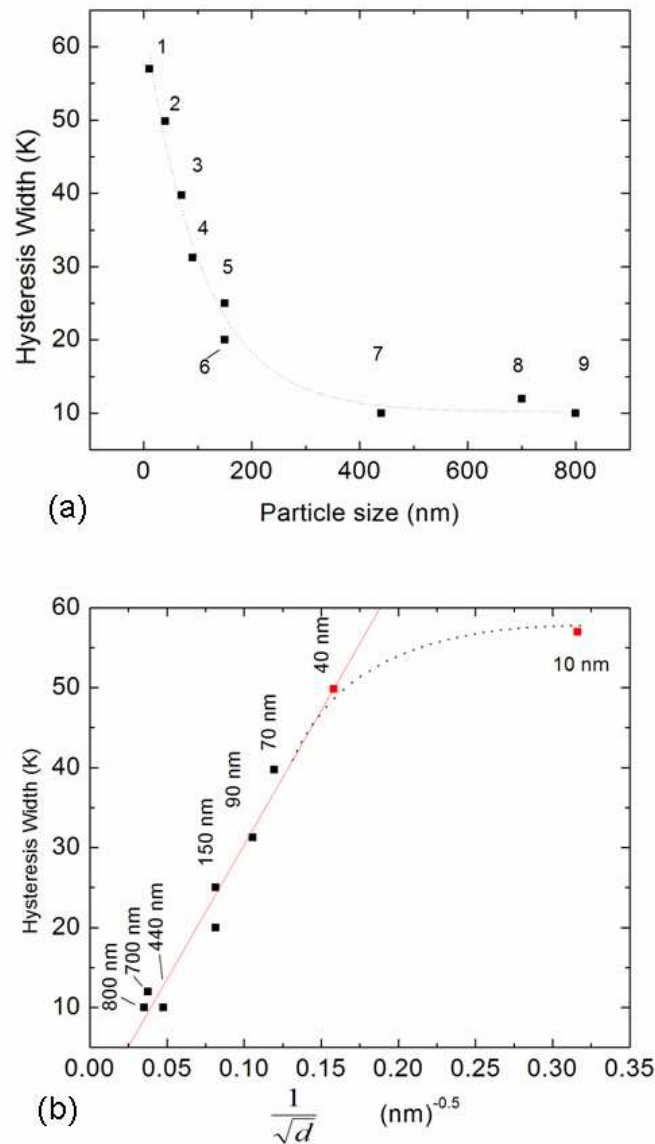


Fig 5.28 (a) HW against  $d$ : The numbers over each point indicate source of data: (1) Current work (unpublished), (2,3,4) Lopez *et al.*, Ref. 429, (5) Miyazaki *et al.*, Ref. 432 (6) Choi *et al.*, Ref 433, (7,9) Current work, Ref. 39, (8) Kivaisi *et al.*, Ref. 434 (b) HW against  $d^{-0.5}$  showing the linearity limited to

switch very well. This is not expected. The reality is that the HJ decreases but is never zero. This places an upper limit to the HW as seen in Fig. 5.28 (b)

where the non-linear curve has been drawn to guide the reader's eye. bulk VO<sub>2</sub>; at nanoscale, linearity is broken as illustrated with a broken line in order to guide the eye.

Further a survey of models on metal- insulator transitions and the VO<sub>2</sub> thermo-chromism can be found in a book chapter by Mwakikunga *et al.* [456] also attached in the Appendices A6 of this thesis. Other relevant publications are not attached to this Thesis but may be found in the public domain.

## **Concluding Remarks and Other Research Spin-offs from the Current Study**

### **6.1 Summary of objectives**

In this study, the pursuit for nano particles of VO<sub>2</sub> and WO<sub>3</sub> was carried out using ultrasonic spray pyrolysis. This was done in order to study the change in the nanoparticles' respective thermochromic and gaso-chromic properties. Nano-crystals of VO<sub>2</sub> were successfully obtained whose average size was determined to be about 800 nm by using a Jeol JSM-5600 scanning electron microscope. After using a better LEO 1525 field emission scanning electron microscope (FESEM) – operated at 3 - 22 kV, the particle size in these samples has been re-determined and shown in this thesis to be about 80 nm instead with smallest particles being about 30 nm. This was arrived at by neglecting the few large agglomerates which were clearly visible under this microscope. Their thermochromic properties showed narrow hysteresis width of 10 K.

### **6.2 From Ultrasonic Spray Pyrolysis to Laser Pyrolysis**

It has been shown how the attention shifted to laser pyrolysis for smaller particles than 30 nm. For VO<sub>2</sub>, nanobelts were discovered rather than the spherical particles that were being sought. The belts had lengths up to 10 microns, widths up to 1 microns and thickness down to 200 nm. On WO<sub>3</sub> from LP, as reported in Mwakikunga *et al.* of Ref. 40 agglomerates of typically



about 1 to 2  $\mu\text{m}$  were obtained, each of them containing particles of diameter of 185 nm.

### **6.3 The Discovery of $\text{WO}_3$ Nanowires by Laser Pyrolysis**

The consolation was the discovery of nanowires sprouting from most of these agglomerates. Naturally, these findings brought in more questions as to how these nano-structures grow from spherical agglomerates and from thin slabs.

Several experiments to solve this puzzle were tried. One major plan was to anneal  $\text{WO}_3$  spheres grown from either LP or USP and image them insitu either with TEM or SEM. TEM was there at hand. From these experiments, no nanowires were seen. This could have been due to high vacuum condition in TEM which are very different conditions used in the normal annealing process in the laboratory- with argon running at almost atmospheric pressure. This important experiment was reported in Ref. 43.

### **6.4 From Laser Pyrolysis Back to Ultrasonic Spray Pyrolysis -Role of Annealing in the Production of the Nanowires and Nanobelts**

The other major and cheaper experiment was to anneal these USP  $\text{WO}_3$  spheres under the same conditions used when annealing the LP samples that led to the discovery of the nanowires and nanobelts. Nanowires again appeared and results of this experiment - the condition for obtaining the

nano-wires of  $W_{18}O_{49}$  – were reported, as it was confirmed from the current TEM studies, in Ref. 42 (attached). A growth mechanism which has been coined solid-vapour-solid (SVS) mechanism was proposed which has recently been followed up and validated with length-diameter data from the nanowires in Ref. 43 (attached).

The search for the small was not over. With the novel results from LP and coupled with a better SEM microscope at the research group's disposal, other nanostructures in old samples synthesized by USP were sought. Ultra thin nano-ribbons of  $VO_2$  were found in two samples grown under argon and hydrogen respectively at a furnace temperature of  $700^\circ\text{C}$ . The TEM, AFM and electronic measurements with a four-point probe technique were reported in the preceding chapter as well as in Mwakikunga *et al.* [454,455]. Of interest were the hysteresis parameters of width (HW) and jump (HJ). A theoretical model has been developed for these parameters in Chapter 4 and these models have been used to explain observed findings in Chapter 5. These findings include results from other authors apart from the present findings and the trend of the present data was in very good agreement with the previous ones and the theoretical model that was developed [455]. Other parameters that would affect the hysteresis width such as the substrate were not considered and this forms part of the present outlook.

## 6.5 Strange Things Happens to Wires at the Nanoscale

Also in this thesis it has been shown that phonon confinement by means of Raman spectroscopy was observed in the  $\text{WO}_3$  nanowires and the phonon confinement models available in literature have been used to obtain, for the first time, the phonon dispersion relations for  $\text{WO}_3$ . This was reported in Ref. 41.

Also Raman spectroscopy of the  $\text{VO}_2$  ribbons has shown optical phonon confinement of the  $145 \text{ cm}^{-1}$  TO-phonon of the 10-cm-thin  $\text{VO}_2$  ribbon. A new phonon confinement model was derived and fitted to the ribbon data. This was accomplished by transforming the polar-coordinate-based Richter *et al.* equation to the Cartesian coordinates and isolating the one-dimension in which optical confinement happens. Also, ribbons with thickness less than 5 nm display both the optical phonon confinement of this phonon and TO phonon splitting. The splitting has been explained by using Lermann *et al.* and Volodin *et al.* previous treatments on ZnSe and GaAs quantum wires respectively. However, Lermann's theory was shown to have a considerable departure from the experimental values of splitting especially when the quantum wire thickness went below 50 nm.

## 6.6 Possible Research Projects From This Study

To end this thesis one can propose by pointing out a few possible areas of this research that would need further pursuit as separate projects.

The first would be improvements on the laser pyrolysis technique to optimise it to further reduce the particle size from the current 185 nm. One way is to prevent agglomeration. There are so many methods in literature which can be used to disperse the nanoparticles so that they end up being mono-disperse including collecting the powder in a dispersing liquid such as iso-propanol. This would mean a major change to the design of the laser pyrolysis. Another way is to replace the pneumatic nozzle system that has been using all along with the ultrasonic spray nozzle system. As seen in Chapter 2, ultrasonic nebulization is very efficient in producing nano-droplets and changing the laser pyrolysis design to harness the USP nozzles would be a way to improving the size of the particles obtained from this setup.

The second aspect is electrochromic properties of the so-obtained  $WO_3$  particles. This would require a fully equipped materials processing clean laboratory with ability to processing different type of materials including transparent conducting oxides such as ZnO, electrolyte materials and ceramics for fabricating devices.

Next are gas-sensing properties of  $WO_3$ . Owing to the fact that sensing of  $WO_3$  particles is a well studied area of research, the new things that can be done would be sensing properties of individual nanowires. With the nanowires of this material at hand, establishing nano-contacts to the individual nanowire and obtaining the current-voltage characteristics of this wire in the presence of various gases at varying ambient temperatures would be another exciting project. One could not perform these intricate experiments

due to lack of facilities that would enable one to build contacts to the nanowires at nano-scale. Gillet *et al.* [435] have previously done i-v curves of a WO<sub>3</sub> nanorod in dry air and humid air with an AFM machine without heating. A number of questions on the so many unknowns were raised in their report. Nanowires that are even thinner than nanorods would certainly bring up so many additional “wonderland-like” unknowns and this would be a route worth considering.

Phonon confinement has been studied widely. The phonon confinement by Richter and the modifications for thin films, nanowires, quantum dots, slabs and the current modification for ribbons have had their achievements. However, in some materials, when the confining dimension(s) become(s) lower than 5 nm, most of the phonon confinement theories fail. Phonon splitting is another phenomenon which is still not conclusive. Lermann’s theory based on strain relaxation between the lattice of the material and the substrate does confirm that as the quantum structure size decreases, the phonon splitting increases. This theory however requires improvement as there is explicit departure from experimental data below 50 nm.

## References

1. E. Chilliest, *Pascal: The Emergence of Genius 2<sup>nd</sup> Ed.*, Harper & Brothers, NY (1961)
2. K. Zeus, *the Computer – My Life*. Springer-Verlag, Berlin/Heidelberg. (1993)  
(translated from the original German edition (1984): *Der Computer – Mein Lebenswerk*. Springer)
3. J. Bardeen and W. H. Brattain, *The transistor, a semi-conductor triode*, Phys. Rev. 74, 230 (1948)
4. G. E. Moore, Proc. Caltech. Conf. on Very Large Scale Integration, California Institute of Technology, Pasadena, California (1979)
5. A. M. Zaitsev, *Optical Properties of Diamond*, Springer, Berlin/Heidelberg/New York (2001)
6. D. D. Awschalom, R. Epstein, R. Hanson, *Coherent manipulation of single spins in semiconductors*, Sci. Am. 297, 84 (2007)
7. A. Persaud, S. J. Park, J. A. Liddle, I. W. Rangelow, J. Bokor, R. Keller, F. I. Allen, D. H. Schneider, T. Schenkel, *Single ion implantation with scanning probe alignment*, J. Vacuum Sci. & Technol. B 22(6), 2992 (2004)
8. A. J Dahma, J. M. Goodkind, I. Karakurti, S. Pillas, *Using Electrons on Liquid Helium for Quantum Computing*, J. Low Temperature Phys. 126, 709 (2002)
9. D. Schneider, *EBIT- The Electron Beam Ion Trap*, Hyperfine Interactions 99, 47 (1996)

10. A. Arnau, F. Aumayr, P. M. Echenique, M. Grether, W. Heiland, J. Limburg, R. Morgenstern, P. Rochin, S. Schipers, R. Schuch, N. Stolterfoht, P. Varga, T. J. M. Zouros, and H. Winter, *Interaction of slow multicharged ions with solid surfaces*, Surf. Sci. Rep. 27, 113 (1997)
11. T. Schenkel, A. V. Hamza, A. V. Barnes, and D. H. Schneider, *Dependence of cluster ion emission from uranium oxide surfaces on the charge state of the incident slow highly charged ion*, Prog. Surf. Sci. 61, 23 (1999)
12. D. L. Weathers, T. A. Tombrello, M. H. Prior, R. G. Stokstad, R. E. Tribblir, *The Angular Distribution of Atoms Sputtered from a Ga-In Eutectic Alloy Target*, Nucl. Instrum. Meth. Phys. Res. B 42, 307 (1989)
13. D. C. Parks, M. P. Stockli, E. W. Bell, L. P. Ratkloff, R. W. Shmieder, F. G. Serpa, and J. P. Gillaspay, *Non-kinetic damage on insulating materials by highly charged ion bombardment*, Nucl. Instrum. Meth. Phys. Res. B 134, 46 (1998)
14. C. Lemell, A. S. El-Said, W. Meissl, I. C. Gebeshuber, C. Trautmann, M. Toulemonde, J. Burgdörfer, F. Aumayr, *On the nano-hillock formation induced by slow highly charged ions on insulator surfaces*, Solid State Electronics 51, 1398 (2007)
15. D. H. Schneider, M. A. Briere, Phys. Scr. 53, 228 (1996)
16. E. Sideras-Haddad, T. Schenkel, D. B. Rebuli, A. Persaud, S. Shrivastava, D. H. Schneider, B. Mwakikunga, *Electron emission and defect formation in the interaction of slow, highly charged ions with diamond surfaces*, Nucl. Instrum. & Methods in Phys. Res. 256 (1), 464-467 (2007)

17. E. Sideras-Haddad, T. Schenkel, S. Shrivastava, T. Makgato, A. Batra, B. Mwakikunga, R. Erasmus, A. Persaud, *Possible diamond-like nanoscale structures induced by slow highly-charged ions on graphite (HOPG)*, Nucl. Instrum. & Methods in Phys. Res. 267 (1), 27774-27777 (2009)
18. (a) F. Jelezko, T. Gaebel, I. Popa, A. Gruber, and J. Wrachtrup, *Observation of Coherent Oscillations in a Single Electron Spin*, Phys. Rev. Lett. 92, 076401 (2004) (b) F. Jelezko, I. Popa, A. Gruber, C. Tietz, J. Wrachtrup, A. Nizovtsev, and S. Kilin, Appl. Phys. Lett. 81, 2160 (2002) (c) F. Jelezko, T. Gaebel, I. Popa, M. Domhan, A. Gruber, and J. Wrachtrup, Phys. Rev. Lett. 93, 130501 (2004)
19. I. Popa, T. Gaebel, M. Domham, C. Wittmann, F. Jelezko, and Wrachtrup, *Energy levels and decoherence properties of single electron and nuclear spins in a defect center in diamond*, Phys. Rev B 70, 201203 (2004)
20. B. E. Kane, *A Silicon-based Nuclear Spin Quantum Computer*, Nature 393, 133 (1998).
21. (a) S. Iijima, *Helical microtubules of graphitic carbon*, Nature 354 (1991) 56-58 (b) A. Oberlin, M. Endo and T. Koyama, J Cryst Growth 32 (1976), pp. 335-349
22. A. Javey, J. Guo, Q. Wang, M. Lundstrom, and H. Dai, Nature 424, 654 (2003)
23. <http://www.mbendi.co.za/indy/ming/vand/af/sa/p0005.htm>
24. J. G. Raith, W. Prochaska, *Tungsten deposits in the Wolfram Schist, Namaqualand, South Africa*, Economic Geology 90 (7), 1934 (1995)



25. (a) B. W. Faughnan, R. S. Crandall, P. M. Heyman, *Electrochromism in tungsten (VI) oxide amorphous films*, R.C.A. Review 36, 177 (1975), (b) B. W. Faughnan, R. S. Crandall, and M A. Lampert, Appl. Phys.Lett 27, 275 (1975)
26. J. Okumu, F. Koerfer, C. Salinga, T. P. Pedersen, M. Wuttig, *In-situ measurements of thickness changes and mechanical stress upon gasochromic switching of thin MoOx films*, J. Appl. Phys. 95, 7632 (2004)
27. A. Besseiere, C. Marcel, M. Morcrette, J. M. Tarascon, V. Lucas, *Flexible electrochromic reflectance device based on tungsten oxide for infrared emissivity control*, J. Appl. Phys. 91, 1589 (2002)
28. D. D. Eden, *Vanadium dioxide storage materials*, Opt. Eng. 20, 337 (1981)
29. S. E. Selkowitz, C. M. Lampert, in: C. M. Lampert, C. G. Granqvist (Eds.), *Large Area Chromogenics: Materials and Devices for Transmittance Control*, SPIE IS4, 22 (1988)
30. W. R. Roach, *Holographic Storage in VO<sub>2</sub>*, Appl. Phys. Lett. 19, 453 (1971)
31. A. W. Smith, *High speed solid state optical display*, Appl. Phys. Lett. 23, 437 (1973)
32. M. Fukuma, S. Zembutsu, S. Miyazawa, *Preparation of VO<sub>2</sub> thin film and its direct optical bit recording characteristics*, Appl. Opt. 22, 265 (1983)
33. M. F. Becker, A. B. Buckman, R. M. Walser, T. Lepine, P. Georges, A. Brun, *Femtosecond laser excitation of the semiconductor-metal phase transition in VO<sub>2</sub>*, Appl. Phys. Lett. 65, 1507 (1994)
34. M. A. Richardson, J. A. Coath, *Infrared optical modulators for missile testing*, Opt. Laser Technol. 30, 137 (1998)

35. G. Katumba, E. Walckegard, B. W. Mwakikunga, A Forbes, J. Phys. D: (2008)
36. G. Katumba, L. Olumekor, A. Forbes, G. Makiwa, B. Mwakikunga, J. Lu, E. Wackelgard, *Optical, thermal and structural characteristics of carbon nanoparticles embedded in ZnO and NiO as selective solar absorbers*, Solar Energy Mater. & Solar Cells 92, 1285 (2008)
37. G. Katumba, B. W. Mwakikunga and T. R. Mothibinyane, *FTIR and Raman spectroscopy of carbon in matrices of ZnO, SiO<sub>2</sub> and NiO*, Nanoscale Res. Lett. 3, 421 (2008)
38. B. W. Mwakikunga, MSc Thesis, University of the Witwatersrand (2006)  
<http://8080-witsetd.wits.ac.za.innopac.wits.ac.za/dspace/handle/123456789/2082>
39. B. W. Mwakikunga, Elias Sideras-Haddad and Malik Maaza, *First synthesis of vanadium dioxide by ultrasonic nebula spray pyrolysis*, Optical Mater. 29(5), 481 (2007)
40. B. W. Mwakikunga, A. Forbes, E. Sideras-Haddad, R M Erasmus, G. Katumba, B. Masina, *Synthesis of tungsten oxide nanostructures by laser pyrolysis* Int. J. Nanoparticles 1, 3 (2008) doi:10.1504/IJNP.2008.020895
41. B. W. Mwakikunga, A. Forbes, E. Sideras-Haddad, C. Arendse, *Raman spectroscopy of WO<sub>3</sub> nanowires and thermochromism study of VO<sub>2</sub> nanobelts produced by laser pyrolysis*, Phys. Stat. Solidi (a) 205, 150 (2008)

42. B. W. Mwakikunga, E. Sideras-Haddad, M. Witcomb, C. Arendse, A. Forbes, *WO<sub>3</sub> nano-spheres into W<sub>18</sub>O<sub>49</sub> one-dimensional nanostructures by thermal annealing*, J. Nanosci. & Nanotechnol 8, 1 (2008)
43. B. W. Mwakikunga, A. Forbes, E. Sideras-Haddad, C. Arendse, *Optimization, yield studies and morphology of WO<sub>3</sub> nanowires synthesized by laser pyrolysis in C<sub>2</sub>H<sub>2</sub> and O<sub>2</sub> ambients – validation of a new growth mechanism*, Nanoscale Res Lett 3, 272 (2008)
44. Greek Lexicon, also from the Hebrew Lexicon, “a pile of fuel, pyre, a pile of wood”
45. E. Mendoza, S.J. Henley, C.H.P. Poa, G.Y. Chen, C.E. Giusca, A.A.D.T Adikaari, J.D. Carey and S.R.P. Silva, *Large area growth of carbon nanotube arrays for sensing platforms*, Sensors and Actuators B: Chemical 109 (1), 75-80 (2005).
46. C.X. Wang and G.W. Yang, *Thermodynamics of metastable phase nucleation at the nanoscale*, Mater. Sci. & Eng.: R: Reports 49 (6) 157 (2005). A. Dollet, Surf. & Coatings Technol. 177-178, 245 (2004)
47. F. Maury and F. Senocq, *Review of CVD technique*, Surf. Coat. Technol. 163-164, 208 (2003)
48. K. L. Choy, *Chemical vapour deposition of coatings*, Prog. Mater. Sci., 48, 57 (2003)
49. S. Stewart and R. Ahmed, *Rolling contact fatigue of surface coatings – a review*, Wear 253 (11-12) 1132 (2002)

50. D. Choudhary and J. Bellare, *Manufacture of gem quality diamonds: a review*, *Ceramics International* 26 (1) 73 (2000)
51. O. I. Buzhinskij and Yu. M. Semenets, *Thick boron carbide coatings for protection of tokamak first wall and divertor*, *Fusion Eng. & Design* 45(4) 343 (1999)
52. K.P de Jong, *Synthesis of supported catalysts*, *Curr. Opinion Solid State & Mater. Sci.* 4(1) 55 (1999)
53. M. Asmann, J. Heberlein and E. Pfender, *A review of diamond CVD utilizing halogenated precursors*, *Diamond and Related Materials* 8(1) 1 (1999)
54. S. Kaplan, *Plasma processes for wide fabric, film and non-wovens*, *Surf. & Coatings Technol.* 186(1-2) 214 (2004)
55. G. M. Ferreira, A. S. Ferlauto, Chi Chen, R. J. Koval, J. M. Pearce, C. Ross, C. R. Wronski and Robert W. Collins, *Kinetics of silicon film growth and the deposition phase diagram*, *J. Non-Cryst. Solids* 338-340, 13 (2004)
56. H. Matsumura, H. Umemoto and A. Masuda, *Cat-CVD (hot-wire CVD): how different from PECVD in preparing amorphous silicon*, *J. Non-Cryst Solids* 338-340, 19 (2004)
57. H. Fujiwara, M. Kondo and A. Matsuda, *Nucleation mechanism of microcrystalline silicon from the amorphous phase*, *J. Non-Cryst Solids* 338-340, 97 (2004)
58. B. Rech, O. Kluth, T. Repmann, T. Roschek, J. Springer, J. Müller, F. Finger, H. Stiebig and H. Wagner, *New materials and deposition techniques for highly*

*efficient silicon thin film solar cells*, Solar Energy Mater. & Solar Cells 74(1-4), 439 (2002)

59. B. R. Rogers and T. S. Cale, *Plasma Processes in Microelectronic Device Manufacturing*, Vacuum 65(3-4), 267 (2002)

60. A. O. Sezer and J. I. Brand, *Chemical vapor deposition of boron carbide*, Mater. Sci. & Eng. B 79(3) 191 (2001)

61. A. G. Aberle, *Overview of SiN surface passivation of crystalline silicon solar cells*, Solar Energy Mater. & Solar Cells 65(1-4) 239 (2001)

63. S. Muhl and J. M. Méndez, *A review of the preparation of carbon nitride films*, Diamond and Related Mater 8(10), 1809 (1999)

64. H. Matsumura, H. Umemoto and A. Masuda, *Cat-CVD (hot-wire CVD): how different from PECVD in preparing amorphous silicon*, J. Non-Cryst Solids 338-340, 19 (2004)

65. R. E. I. Schropp, *Present status of micro- and poly-crystalline silicon solar cells made by hot-wire chemical vapour deposition*, Thin Solid Films 451-452, 455 (2004)

66. B. Schroeder, *Status report: solar cell related research and development using amorphous and microcrystalline silicon deposition by HW (Cat) CVD*, Thin Solid Films 430(1-2), 1 (2003)

67. A. Gallagher, *Some physics and chemistry of hot wire deposition*, Thin Solid Films 395(1-2), 25 (2001)

68. R. S. Crandall and X. Liu, *Elastic properties of amorphous and crystalline silicon*, Thin Solid Films 395(1-2) 78 (2001)

69. B. Schroeder, U. Weber, H. Seitz, A. Ledermann and C. Mukherjee, *Current status of the thermo-catalytic (hot wire) CVD of thin silicon films for photovoltaic applications*, Thin Solid Films 395(1-2) 298 (2001)
70. A.O. Sezer and J. I. Brand, *Chemical vapour deposition of boron carbide*, Mater. Sci. & Eng. B 79 (3), 191 (2001)
71. D. Choudhary and J. Bellare, *Manufacture of gem-quality diamonds: a review*, Ceramics International 26 (1), 73 (2000)
72. P. Patil, *Versatility of chemical spray pyrolysis*, Mater. Chem. & Phys. 59, 185 (1999)
73. A. Sheth, H. Schimdt and V. Lasrado, *Chemical vapour deposition of various silicides*, Appl. Supercond. 6 (10-12), 855 (1998)
74. H. Marsh, M. Martinez-Escandell, F. Rodriguez-Reinoso, *Synthesis of carbon nanostructures*, Carbon 37, 363 (1999)
75. M. Sternitzke, *Production of ceramics by spray pyrolysis*, J. Eur. Ceram. Soc. 17, 1061 (1997)
76. S. Muhl, J. M. Mendez, *Synthesis of diamond by CVD*, Diamond & Related Mater 8, 1809 (1999)
77. P. Tartaj, M. P. Morales, T. Gonzalez-Carreno, S. Veintemillas-Verdaguer, C. J. Serna, *Carbon cokes*, J. Magnetism & Magnetic Mater 290-291, 28 (2005)
78. P. Tartaj, M. P. Morales, S. Veintemillas-Verdaguer, T. Gonzalez-Carreno, C. J. Serna, *CVD for semiconductors*, J. Phys. D: Appl. Phys. 36, R182 (2003)
79. A. J. Yule and Y. Al-Suleimani, *Ultrasonic nebulisation and droplet generation*, Proc. R. Soc. Lond. A 456, 1069 (2000)

80. F. Barreras, H. Amaveda, A. Lozano, *Ultrasonic spray*, Experiments in Fluids 33, 405 (2002)
81. V. G. Nevolin, *Surface phenomena and droplet generation*, Inzhenerno-Fizicheskii Zhurnal 47 (6), 1028 (1984) Translated by Plenum Publishing Corporation UDC 532.59:532.501.34, 1482 (1985)
82. See for example some NASA Tech Briefs “Producing Quantum Dots by Spray Pyrolysis” on <http://www.techbriefs.com/content/view/46/34> or <http://www.techbriefs.com/tsp>
83. R. W. Wood and A. L. Loomis, *Experimental generation of droplets by ultrasonic waves*, Phil. Mag. 7, 417 (1927)
84. M. Faraday, *Capillary waves due to sound*, Phil. Trans. R. Soc. Lond. 121, 319 (1831)
85. J. W. S. Rayleigh, *The Theory of Sound Vol.2*, Dover Publications, N.Y., 344 (1945)
86. H. Lamb, *Hydrodynamics*, Macmillan, London, 708 (1931)
87. T. K McCubbin Jr., *Instability in the Taylor agitation*, J. Acoust. Soc. Am. 25, 1013 (1953)
88. K. Bisa, K Dirnagl and R. Esche, *Taylor waves*, Siemens-Z. 28, 341 (1954)
89. T. B. Benjamin and F Ursell, *Is Taylor instability responsible for droplet generation?* Proc. R Soc London A 225, 505 (1954)
90. V. I. Sorokin, *Taylor instability from sound*, Soviet Phys. Acoust 3, 17 (1957)
91. W. Eisenmenger, *Acoustic phenomenon affects surface stability*, Acoustica 9, 327 (1959)

92. J. N. Antonevich, *Ultrasound waves and water*, TRE Trans. on Ultrasonic Eng. PGUE-7, 6 (1959)
93. R. Lang, *Diameter of droplets from ultrasound waves*, J. Acoust. Soc. Am. 34, 6 (1962)
94. D. Sindayihebura and L. Bolle, *Capillary waves and the diameter of the droplets*, Atomization Sprays 8, 217 (1998)
95. G. I. Taylor, *Instability of capillary waves*, Proc. R. Soc. A CCI 192 (1950)
96. R. L. Peskin and R. J. Raco, *On the modelling of droplet diameter from ultrasonic agitation*, J. Acoust. Soc. Am. 35, 1378 (1963)
97. V. Jokanovic, D. Janackovic, A. M. Spasic, D. Uskokovic, *Design of nanostructures of TiO<sub>2</sub>*, Mater. Trans. JIM 37, 627 (1996)
98. V. Jokanovic, M. D. Dramicanin, Z. Andric, *TiO<sub>2</sub> production by spray pyrolysis*, Acta. Chim. Slov. 53, 23 (2006)
99. J. M. Nedeljkovic, Z. V. Saponjic, Z. Rakocevic, V. Jokanovic, D. P. Uskokovic, *Synthesis of novel oxides by ultrasonic spray pyrolysis*, Nanostructured Mater. 9, 125 (1999)
100. Z. V. Saponjic, Z. Rakocevic, N. M. Dimitrijevic, J. M. Nedeljkovic, V. Jokanovic and D. P. Uskokovic, *Calculated and experimental diameter of deposited TiO<sub>2</sub> particles*, Nanostructured Mater. 10(3), 333 (1998)
101. K. Söllner, *Explanation of the Wood & Loomis demonstration*, Trans. Faraday Soc. 32, 1537 (1936)
102. E. L. Gershenzon, O. K. Eknadiosyants, *Cavitation mechanism re-visited*, Sov. Phys. Acoust. 10, 127 (1964)



103. O. K. Eknadiosyants, *On the cavitation of fluid by turbulent sound waves*, Sov. Phys. Acoust. 14, 80 (1968)
104. H. S. Fogler, K. D. Timmerhaus, *Sound cavitation of liquid medium*, J. Acoust. Soc. Am. 39, 515 (1965)
105. Y. Y. Boguslaskii, O. K. Eknadiosyants, *On the sound agitation from the deep*, Sov. Phys. Acoust. 15, 341 (1969)
106. M. N. Topp, *Generation of droplets from below the liquid surface*, Aerosol. Sci. 4, 17 (1973)
107. C Chiba, *Viscosity of a liquid and the cavitation*, Bull. J. Soc. Mech. Eng. 18, 376 (1975)
108. J. D. Bassett and W. W. Bright, *J. Aerosol Sci.* 7, 47 (1976)
109. R. Bellman, R. H. Pennington, *Effect of viscosity and surface tension on the Taylor instability*, Quant. Appl. Math. 12, 151 (1954)
110. V.M Entov, A. L. Yarin, *On the kinematics of liquids and their viscosity*, J. Fluid Mech. 140, 91 (1984)
111. J. O. Hinze, *Viscosity and surface tension*, A I Ch. E. J. 1, 289 (1955)
112. M. M. Clark, *Effects of surface tension and the relative fluid velocity on the droplet formation*, CES 43, 671 (1988)
113. M. M. Clark, *Effects of viscosity and density on the droplet formation* CES 43, 681 (1988)
114. T. Mochida, *Empirical study of droplet diameter as a function of surface tension, density and the flow rate*, Proc. ICLASS-78, 193 (1978)

115. S. C. Tsai, P. Childs, P. Luu, *Correlation between droplet diameter and viscosity*, AIChE. J. 42 (120, 3340 (1996)
116. R. Rajan, A. B. Pandit, *Correlations to predict the droplet size in ultrasonic atomization*, Ultrasonics 39, 235 (2001)
117. B. Avvaru, M. N. Patil, P. R. Gogate, A. B. Pandit, *Ultrasonic atomization: Effect of liquid phase properties*, Ultrasonics 44, 146 (2006)
118. C. J. Lynde, *The effect of pressure on surface tension*, Phys. Rev. (Series 1) 22, 181 (1906)
119. W. Sachs, V. Meyn, *Pressure and temperature dependence of the surface tension in the system natural gas/water*, Colloids & Surf A: Physicochemical Eng. Aspects 94, 291 (1995)
120. E. W. Hough, M. J. Rzasa and B. B. Wood, Trans. AIME. 192, 57 (1951)
121. H. Y. Jennings and G. H. Newman, Jr., J. Soc. Pet. Eng., 171 (1971)
122. R. Massoudi and A. D. King, Jr., J. Phys. Chem. 78, 2262 (1974)
123. C. Jho, D. Nealon, S. Shogbola and A. D. King, Jr., J. Colloid Interface Sci., 65, 141 (1978)
124. S. J. Palmer, *The effect of temperature on surface tension*, Phys. Ed 11, 119 (1976)
125. R. H. Fowler, *A tentative statistical theory of Macleod's equation for surface tension, and the parachor*, Proc. R. Soc. A159, 229 (1937)
126. H. S. Green, *The Molecular Theory of Fluids*, Dover Publications, NY, 194 (1969)

127. J. R. Henderson, *The surface tension compressibility relation*, Mol. Phys. 39, 709 (1980)
128. H. Park, R. B. Thompson, N. Lanson, C. Tzoganakis, C. B. Park, P. Chen, *Effect of temperature and pressure on surface tension of polystyrene in supercritical carbon dioxide*, J. Phys. Chem. B 111, 3859 (2007)
129. J. Escobedo, G. A. Mansoori, *Surface tension prediction for pure fluids*, AIChE. J. 42, 1425 (1996)
130. M. E. Boudh-Hir, G. A. Mansoori, *Statistical mechanics basis of Macleod's formula*, J. Phys. Chem. 94, 8362 (1990)
131. J. D. Pandey, V. Sanguri, S. B. Tripathi, R. K. Mishra, N. K. Soni, *Theoretical prediction of surface tension of ternary liquid system (nitrogen + oxygen + argon) at elevated temperature and different pressure*, J. Colloid & Interface Sci. 274, 331 (2004)
132. (a) P. L. Wong, R. Wang, S. Lingard, *Pressure and temperature dependence of the density of liquid lubricants*, Wear 201, 58 (1996) (b) O Redlich and J N Kwong, Chem Rev. 44, 1197 (1949)
133. P. G. Wright, *The variation of viscosity with temperature*, Phys. Ed. 12, 323 (1977)
134. P. W. Bridgman, *Viscosities to 30,000 kg/m<sup>3</sup>*, Proc. Am. Acad Arts Sci. 77, 117 (1949)
135. S. Bair, J. Jarzynski, W. O. Winer, *The temperature, pressure and time dependence of lubricant viscosity*, Tribology International 34, 461 (2001)

- 136.** R. S. Fein, *Possible role of compressional viscoelasticity in concentrated contact lubrication*, ASME J Lubr Tech Ser F 89, 127 (1967)
- 137.** G. Harrison, E. G. Trachman, *The role of compressional...*, ASME J Lubr Tech 94, 306 (1972)
- 138.** S. Yasutomi, S. Bair, W. O. Winer, *An application of a free volume model to lubricant rheology*, ASME J Tribology 106, 291 (1984)
- 139.** S. Gürmen, S. Stopić and B. Friedrich, *Synthesis of nanosized spherical cobalt powder by ultrasonic spray pyrolysis*, Mater. Res. Bulletin 41(10), 1882 (2006)
- 140.** J. C. Chen, C. L. Chang, C. S Hsu and B. H. Hwang, *Deposition of Ni-CGO composite anodes by electrostatic assisted ultrasonic spray pyrolysis method*, Mater Res. Bulletin 42(9), 1674 (2007)
- 141.** S. H. Park, S.-W. Oh, S.H. Kang, I. Belharouak, K. Amine and Y.-K. Sun, *Comparative study of different crystallographic structure of  $\text{LiNi}_{0.5}\text{Mn}_{1.5}\text{O}_{4-\delta}$  cathodes with wide operation voltage (2.0-5.0V)*, Electrochimica Acta 52(25), 7226 (2007)
- 142.** X.D. Zhang, H.B. Fan, J. Sun and Y. Zhao, *Effect of substrates on the properties of p-type ZnO films* Physica E: Low-dimensional Systems and Nanostructures 39(2), 267 (2007)
- 143.** P. Singh, A. Kumar, D. Kumar and D. Kaur, *Growth and characterization of ZnO nanocrystalline thin films and nanopowders via a low-cost ultrasonic spray pyrolysis*, J. Cryst. Growth 306(2), 303 (2007)

144. I. Lj. Validžić, V. Jokanović, D. P. Uskoković and J. M. Nedeljković, *Influence of solvent on the structural and morphological properties of AgI particles prepared using ultrasonic spray pyrolysis*, Mater. Chem. & Phys. 107, 28 (2007)
145. V. Jokanović, M.D. Dramićanin, Ž. Andrić, T. Dramićanin, M. Plavšić, S. Pašalić and M. Miljković, *Nanostructure designed powders of optical active materials  $Me_xSiO_y$  obtained by ultrasonic spray pyrolysis*, Optical Mater. 30, 1168 (2007)
146. Y. Luo, J. Bian, J. Sun, H. Liang and W. Liu, *Deposition and tunable photoluminescence of  $Zn_{1-x}(Mg,Cd)_xO$* , J. Mater. Processing Technol. 189 (1-3), 473(2007)
147. U. Alver, T. Kılınc, E. Bacaksız and S. Nezir, *Temperature dependence of ZnO nanorods produced by ultrasonic spray pyrolysis*, Mater. Chem. & Phys. 106, 227 (2007)
148. M. Kul, M. Zor, A. S. Aybek, S. Irmak and E. Turan, *Electrical and optical properties of fluorine-doped CdO films deposited by ultrasonic spray pyrolysis*, Solar Energy Mater. & Solar Cells 91(10), 882 (2007)
149. J. Wienke and A.S. Booij, *ZnO:In deposition by spray pyrolysis – Influence of the growth conditions on the electrical and optical properties*, Thin Solid Films, (2007)
150. K. Ernits, D. Brémaud, S. Buecheler, C.J. Hibberd, M. Kaelin, G. Khrypunov, U. Müller, E. Mellikov and A.N. Tiwari, *Characterization of ultrasonically sprayed  $In_xS_y$  buffer layers for Cu(In,Ga)Se<sub>2</sub> solar cells*, Thin Solid Films 515(15), 6051 (2007)

151. I. Akyuz, S. Kose, F. Atay and V. Bilgin, *Some physical properties of chemically sprayed  $Zn_{1-x}Cd_xS$  semiconductor films*, Mater. Sci. Semicond. Processing 10,103 (2007)
152. L. Castañeda, *Effect of palladium coatings on oxygen sensors of titanium dioxide thin films*, Mater. Sci. & Eng. B 139(2-3), 149 (2007)
153. S. W. Oh, H. J. Bang, Y. C. Bae and Y.-K. Sun, *Effect of calcinations temperature on morphology, crystallinity and electrochemical properties of nano-crystalline metal oxides*, J. Power Sources, 173, 502 (2007)
154. M. Liu, H.L. Suo, Y. Zhao, Y.X. Zhang, D. He, L. Ma and M.L. Zhou, *Improvement of YBCO film properties by two-step deposition using pyrolysis method*, Physica C: Superconductivity 460-462, 1424 (2007)
155. T. H. Teng, M. R. Yang, S. H. Wu and Y. P. Chiang, *Electrochemical properties of  $LiFe_{0.9}Mg_{0.1}PO_4$ /carbon cathode materials prepared by ultrasonic spray pyrolysis*, Solid State Commun. 142(7), 389 (2007)
156. J. Bian, W. Liu, J. Sun and H. Liang, *Synthesis and defect-related emission of ZnO based light emitting device*]. Mater. Processing Technol 184(1-3),451 (2007)
157. X. Zhang, H. Fan, J. Sun and Y. Zhao, *Structural and electrical properties of p-type ZnO films prepared by Ultrasonic Spray Pyrolysis*, Thin Solid Films, , (2007)
158. E. Turan, M. Zor, A. Senol Aybek and M. Kul, *Electrical properties of ZnO/Au/ZnS/Au films deposited by ultrasonic spray pyrolysis*, Thin Solid Films 515, 8017 (2007)
159. M. Kul, M. Zor, A. Senol Aybek, S. Irmak and E. Turan, *Some structural*

*properties of CdO:F films produced by ultrasonic spray pyrolysis method, Thin Solid Films* 515, 8752 (2007)

**160.** A. Senol Aybek, Nihal Baysal, Muhsin Zor, Evren Turan and Metin Kul, *Optical properties of  $CdxZn(1-x)O$  films deposited by ultrasonic spray pyrolysis method, Thin Solid Films* 515, 8590 (2007)

**161.** J.-K. Yang, J.-H Yu, J. Kim and Y.-H Choa, *Synthesis and optimization of nano-porous  $La_{0.6}Sr_{0.4}CoO_{3-\delta}$  on the oxygen separation membrane, Mater. Sci. & Eng. A* 449-451(25), 477 (2007)

**162.** K.-J. Lee, J.-W. Park, J.-K. Yang, K.-S. Lee and Y.-H. Choa, *Synthesis and optimization of nano-porous  $La_{0.6}Sr_{0.4}CoO_{3-\delta}$  on the oxygen separation membrane, Mater. Sci. & Eng. A* 449-451(25), 774 (2007)

**163.** G.-H. An, H.-J. Wang, B.-H. Kim, Y.-G. Jeong and Y.-H. Choa, *Fabrication and characterization of a hydroxyapatite nanopowder by ultrasonic spray pyrolysis with salt-assisted decomposition, Mater. Sci. & Eng. A* 449-451(25), 821 (2007)

**164.** D. Jugović, N. Cvjetičanin, V. Kusigerski, M. Mitrić, M. Miljković, D. Makovec and D. Uskoković, *Structural and magnetic characterization of  $LiMn_{1.825}Cr_{0.175}O_4$  spinel obtained by ultrasonic spray pyrolysis, Mater. Res. Bulletin* 42(3), 515 (2007)

**165.** H. Liu, C. Song, Y. Tang, J. Zhang and J. Zhang, *High-surface-area CoTMPP/C synthesized by ultrasonic spray pyrolysis for PEM fuel cell electrocatalysts, Electrochimica Acta* 52(13), 4532 (2007)

**166.** U. Alver, T. Kılınç, E. Bacaksız and S. Nezir, *Structure and optical properties of  $Zn_{1-x}Fe_xO$  thin films prepared by ultrasonic spray pyrolysis, Mater. Sci. & Eng. B* 138 (1), 74 (2007)

167. L. Castañeda and M. Terrones, *Synthesis and structural characterization of novel flower-like titanium dioxide nanostructures*, *Matter* 390(1-2), 143 (2007)
168. U. Alver, T. Kılınc, E. Bacaksız, T. Küçükömeroğlu, S. Nezir, İ.H. Mutlu and F. Aslan, *Synthesis and characterization of spray pyrolysis Zinc Oxide microrods*, *Thin Solid Films* 515(7-8), 3448 (2007)
169. Zhang Xiaodan, Fan Hongbing, Zhao Ying, Sun Jian, Wei Changchun and Zhang Cunshan, *Fabrication of high hole-carrier density p-type ZnO thin films by N-Al co-doping*, *Appl. Surf. Sci.* 253(8), 3825 (2007)
170. G. Ye and T. Troczynski, *Hydroxyapatite coatings by pulsed ultrasonic spray pyrolysis*, *Ceram. Int.* 34, 511 (2007)
171. M. M. Bučko and J. Oblakowski, *Preparation of BaZrO<sub>3</sub> nanopowders by spray pyrolysis method*, *J. Eur. Ceram. Soc.* 27, 3625 (2007)
172. I. Lj. Validžić, V. Jokanović, D.P. Uskoković and J.M. Nedeljković, *Formation of silver iodide particles from thermodynamically stable clusters using ultrasonic spray pyrolysis*, *J. Eur. Ceram. Soc.* 27(2-3), 927 (2007)
173. C.Y. Chen, T.K. Tseng, S.C. Tsai, C.K. Lin and H.M. Lin, *Effect of precursor characteristics on zirconia and ceria particle morphology in spray pyrolysis*, *Ceram. Int.*, (2006)
174. J. L. Zhao, X. M. Li, J. M. Bian, W. D. Yu and C. Y. Zhang, *Comparison of structural and photoluminescence properties of ZnO thin films grown by pulsed laser deposition and ultrasonic spray pyrolysis*, *Thin Solid Films* 515(4), 1763 (2006)
175. D. Zaouk, Y. Zaatar, R. Asmar and J. Jabbour, *Piezoelectric zinc oxide by electrostatic spray pyrolysis*, *Microelectronics J.* 37 (11), 1276 (2006)



176. J. Bian, W. Liu, H. Liang, L. Hu, J. Sun, Y. Luo and G. Du, *Room temperature electroluminescence from the n-ZnMgO/ZnO/p-ZnMgO heterojunction device grown by ultrasonic spray pyrolysis*, Chem. Phys. Lett. 430(1-3), 183 (2006)
177. A. Kumar, P. Singh and D. Kaur, *Low cost synthesis of high-Tc superconducting films on metallic substrates via ultrasonic spray pyrolysis* Cryogenics 46(10), 749 (2006)
178. H. J. Kim, J. Joo, S. G. Park, S. K. Hong, S. W. Lee, S. W. Lim, G. W. Hong and H. G. Lee, *Effects of deposition conditions on the phase formation of YBCO films prepared by spray pyrolysis method*, Physica C: Superconductivity 445-448, 598 (2006)
179. S. W. Oh, S. H. Park, K. Amine and Y. K. Sun, *Synthesis and characterization of spherical morphology [Ni<sub>0.4</sub>Co<sub>0.2</sub>Mn<sub>0.4</sub>]<sub>3</sub>O<sub>4</sub> materials for lithium secondary batteries*, J. Power Sources 160(1), 558 (2006)
180. M-R Yang, T-H Teng and S-H Wu, *LiFePO<sub>4</sub>/carbon cathode materials prepared by ultrasonic spray pyrolysis*, J. Power Sources 159(1), 307 (2006)
181. S. Y. Lee and B. O. Park, *Structural, electrical and optical characteristics of SnO<sub>2</sub>:Sb thin films by ultrasonic spray pyrolysis*, Thin Solid Films 510(1-2), 154 (2006)
182. S-W Oh, S-H Park, J-H Kim, Y C Bae and Y-K Sun, *Improvement of electrochemical properties of LiNi<sub>0.5</sub>Mn<sub>1.5</sub>O<sub>4</sub> spinel material by fluorine substitution*, J. Power Sources 157(1), 464 (2006)
183. S. H. Park, S. T. Myung, S. W. Oh, C. S. Yoon and Y. K. Sun, *Ultrasonic spray pyrolysis of nano crystalline spinel LiMn<sub>2</sub>O<sub>4</sub> showing good cycling performance in the 3 V range*, Electrochimica Acta 51(19), 4089 (2006)

- 184.** M. Wolborski, M. Bakowski, A. Ortiz, V. Pore, A. Schöner, M. Ritala, M. Leskelä and A. Hallén, *Characterisation of the Al<sub>2</sub>O<sub>3</sub> films deposited by ultrasonic spray pyrolysis and atomic layer deposition methods for passivation of 4H-SiC devices*, *Microelectronics & Reliability* 46(95-6), 743 (2006)
- 185.** S. Suda, S. Takahashi, M. Kawano, H. Yoshida and T. Inagaki, *Effects of atomization conditions on morphology and SOFC anode performance of spray pyrolyzed NiO-Sm<sub>0.2</sub>Ce<sub>0.8</sub>O<sub>1.9</sub> composite particles*, *Solid State Ionics* 177(13-14), 1219 (2006)
- 186.** S. M. Abrarov, Sh. U. Yuldashev, T.W. Kim, Y.H. Kwon and T.W. Kang, *Deep level emission of ZnO nanoparticles deposited inside UV opal*, *Optics Commun.* 259(1), 378 (2006)
- 187.** H. S. Kang, Y. C. Kang, H. Y. Koo, S. H. Ju, D. Y. Kim, S. K. Hong, J. R. Sohn, K. Y. Jung and S. B. Park, *Nano-sized ceria particles prepared by spray pyrolysis using polymeric precursor solution*, *Mater. Sci. & Eng: B* 127(2-3), 99 (2006)
- 188.** J-H Lee, S-Y Lee and B-O Park, *Fabrication and characteristics of transparent conducting In<sub>2</sub>O<sub>3</sub>-ZnO thin films by ultrasonic spray pyrolysis*, *Mater. Sci. & Eng. B* 127(2-3), 267 (2006)
- 189.** K. Y. Choi, K. D. Kim and J. W. Yang, *Optimization of the synthesis conditions of LiCoO<sub>2</sub> for lithium secondary battery by ultrasonic spray pyrolysis process*, *J. Mater. Processing Technol.* 171(1), 118 (2006)
- 190.** C.R. Michel, E.R. López and H.R. Zea, *Synthesis of GdCo<sub>1-x</sub>Cu<sub>x</sub>O<sub>3-δ</sub> (x = 0, 0.15, 0.30) perovskites by ultrasonic spray pyrolysis*, *Mater. Res. Bulletin* 41(1),

209 (2006)

**191.** W. Wang, S. Y. Wang and M. Liu, *Preparation of  $\gamma$ -Gd<sub>2</sub>S<sub>3</sub> films by ultrasonic spray pyrolysis*, Mater. Chem. & Phys. 94(2-3), 182 (2006)

**192.** V. Jokanović, U.B. Mioč and Z.P. Nedić, *Solid State Ionics* 176(39-40), 2955 (2005)

**193.** X. Zhang, X. M. Li, T. L. Chen, J. M. Bian and C. Y. Zhang, *Nanostructured phosphorous tungsten bronzes from ultrasonic spray pyrolysis*, Thin Solid Films 492(1-2), 248 (2005)

**194.** I. Taniguchi and Z. Bakenov, *Spray pyrolysis synthesis of nanostructured LiFe<sub>x</sub>Mn<sub>2-x</sub>O<sub>4</sub> cathode materials for lithium-ion batteries*, Powder Technol. 159(2), 55 (2005)

**195.** V. Bilgin, S. Kose, F. Atay and I. Akyuz, *The effect of substrate temperature on the structural and some physical properties of ultrasonically sprayed CdS films*, Mater. Chem. & Phys. 94(1), 103 (2005)

**196.** W. Wang, S. Y. Wang and M. Liu, *Growth of rod-like crystal BiSI films by ultrasonic spray pyrolysis*, Mater. Res. Bulletin 40(10), 1781 (2005)

**197.** S. H. Park, S. W. Oh and Y. K. Sun, *Molybdenum disulfide made by ultrasonic spray pyrolysis*, J. Power Sources 146(1-2), 622 (2005)

**198.** C. Zhang, X. Li, J. Bian, W. Yu and X. Gao, *Synthesis and structural characterization of layered Li[Ni<sub>1/3+x</sub>Co<sub>1/3</sub>Mn<sub>1/3-2x</sub>Mox]O<sub>2</sub> cathode materials by ultrasonic spray pyrolysis*, Surf. & Coatings Technol. 198(1-3), 253 (2005)

199. I. Taniguchi, *Powder properties of partially substituted  $\text{LiM}_x\text{Mn}_{2-x}\text{O}_4$  ( $M = \text{Al}, \text{Cr}, \text{Fe}$  and  $\text{Co}$ ) synthesized by ultrasonic spray pyrolysis*, Mater. Chem. & Phys. 92(1), 172 (2005)
200. J. L. Zhao, X. M. Li, J. M. Bian, W. D. Yu and C. Y. Zhang, *Growth of nitrogen-doped p-type ZnO films by spray pyrolysis and their electrical and optical properties*, J. Cryst. Growth 280(3-4), 495 (2005)
201. M. Girtan, *Investigations on the optical constants of indium oxide thin films prepared by ultrasonic spray pyrolysis*, Mater. Sci. & Eng. B 118(1-3), 175 (2005)
202. Z. Bakenov and I. Taniguchi, *Electrochemical performance of nanostructured  $\text{LiM}_x\text{Mn}_{2-x}\text{O}_4$  ( $M = \text{Co}$  and  $\text{Al}$ ) powders at high charge-discharge operations*, Solid State Ionics 176(11-12), 1027 (2005)
203. C. H. Lee, Y. C. Kang, K. Y. Jung and J. G. Choi, *Phosphor layer formed from the  $\text{Zn}_2\text{SiO}_4:\text{Mn}$  phosphor particles with spherical shape and fine size*, Mater. Sci. & Eng. B 117(2), 210 (2005)
204. K. D. Kim, K. Y. Choi and J. W. Yang, *Formation of spherical hollow silica particles from sodium silicate solution by ultrasonic spray pyrolysis method*, Colloids & Surf. A: Physicochemical and Engineering Aspects 254(1-3), 193 (2005)
205. S.-H. Park, S. W. Oh, S.T. Myung, Y.C. Kang and Y.K. Sun, *Effects of synthesis condition on  $\text{LiNi}_{1/2}\text{Mn}_{3/2}\text{O}_4$  cathode material for prepared by ultrasonic spray pyrolysis method*, Solid State Ionics 176 (5-6), 481 (2005)

206. V. Jokanović, B. Jokanović, J. Nedeljković and O. Milošević, *Modeling of nanostructured TiO<sub>2</sub> spheres obtained by ultrasonic spray pyrolysis*, *Colloids and Surfaces A: Physicochemical and Engineering Aspects* 249(1-3), 111 (2004)
207. S. -H. Park and Y. K. Sun, *Synthesis and electrochemical properties of 5 V spinel LiNi<sub>0.5</sub>Mn<sub>1.5</sub>O<sub>4</sub> cathode materials prepared by ultrasonic spray pyrolysis method*, *Electrochimica Acta* 50(2-3), 434 (2004)
208. V. Bilgin, S. Kose, F. Atay and I. Akyuz, *The effect of Zn concentration on some physical properties of tin oxide films obtained by ultrasonic spray pyrolysis*, *Mater. Lett* 58(29), 3686 (2004)
209. V. Jokanovic, A. M. Spasi and D. Uskokovi, *Designing of nanostructured hollow TiO<sub>2</sub> spheres obtained by ultrasonic spray pyrolysis*, *J. Colloid and Interface Sci.* 278(2), 342 (2004)
210. C. Zhang, X. Li, J. Bian, W. Yu and X. Gao, *Structural and electrical properties of nitrogen and aluminum codoped p-type ZnO films*, *Solid State Commun.* 132(2), 75 (2004)
211. Y. S. Chung, S. B. Park and D.-W. Kang, *Magnetically separable titania-coated nickel ferrite photocatalyst*, *Mater. Chem. & Phys.* 86(2-3), 375 (2004)
212. S. W. Oh, S. H. Park, C. -W. Park and Y. -K. Sun, *Structural and electrochemical properties of layered Li[Ni<sub>0.5</sub>Mn<sub>0.5</sub>]<sub>1-x</sub>Co<sub>x</sub>O<sub>2</sub> positive materials synthesized by ultrasonic spray pyrolysis method*, *Solid State Ionics* 171(3-4), 167 (2004)

- 213.** J. Bian, X. Li, L. Chen and Q. Yao, *Properties of undoped n-type ZnO film and N-In codoped p-type ZnO film deposited by ultrasonic spray pyrolysis*, Chem. Phys. Lett. 393(1-3), 256 (2004)
- 214.** Z. V. Marinkovic , L. Mancic , J. -F. Cribier, S. Ohara, T. Fukui and O. Milosevic, *Nature of structural changes in LSM-YSZ nanocomposite material during thermal treatments*, Mater. Sci. & Eng. A 375-377, 615 (2004)
- 215.** M. Girtan, *The influence of post-annealing treatment on the electrical properties of In<sub>2</sub>O<sub>3</sub> thin films prepared by an ultrasonic spray CVD process*, Surf. & Coatings Technol. 184(2-3), 219 (2004)
- 216.** J-H Lee and B-O Park, *Transparent conducting In<sub>2</sub>O<sub>3</sub> thin films prepared by ultrasonic spray pyrolysis*, Surf. & Coatings Technol. 184(1), 102 (2004)
- 217.** K. Matsuda and I. Taniguchi, *Relationship between the electrochemical and particle properties of LiMn<sub>2</sub>O<sub>4</sub> prepared by ultrasonic spray pyrolysis*, J. Power Sources 132(1-2), 156 (2004)
- 218.** N. Khare, D. P. Singh, H. K. Singh, A. K. Gupta, P. K. Siwach and O. N. Srivastava, *Preparation and study of silver added La<sub>0.67</sub>Ca<sub>0.33</sub>MnO<sub>3</sub> film*, J. Physics & Chem. Solids 65(5), 867 (2004)
- 219.** J. M. Bian, X. M. Li, T. L. Chen, X. D. Gao and W. D. Yu, *Preparation of high quality MgO thin films by ultrasonic spray pyrolysis*, Appl. Surf. Sci. 228(1-4), 297 (2004)
- 220.** S. H. Park, C. S. Yoon, S. G. Kang, H. -S. Kim, S. -I. Moon and Y. -K. Sun, *Synthesis and structural characterization of layered Li[Ni<sub>1/3</sub>Co<sub>1/3</sub>Mn<sub>1/3</sub>]O<sub>2</sub> cathode*

*materials by ultrasonic spray pyrolysis method*, *Electrochimica Acta* 49(4), 557 (2004)

**221.** J-H Lee and B-O Park, *Characteristics of Al-doped ZnO thin films obtained by ultrasonic spray pyrolysis: effects of Al doping and an annealing treatment*, *Mater. Sci. & Eng. B* 106(3), 242 (2004)

**222.** Z. V. Marinkovic , L. Mancic and O. Milosevic, *The nature of structural changes in nanocrystalline ZnO powders under linear heating conditions*, *J. Eur. Ceram. Soc.* 24(6), 1929 (2004)

**223.** S.-Y. Wang, W. Wang and Z.-H. Lu, *Asynchronous-pulse ultrasonic spray pyrolysis deposition of  $Cu_xS$  ( $x=1, 2$ ) thin films*, *Mater. Sci. & Eng. B* 103(2), 184 (2003)

**224.** Y. -H. Choa, J. -K. Yang, B. -H. Kim, Y. -K. Jeong, J. -S Lee, T. Nakayama, T. Sekino and K. Niihara, *Preparation and characterization of metal/ceramic nanoporous nanocomposite powders*, *J. Magnetism & Magnetic Mater.* 266(1-2), 12 (2003)

**225.** Yong-Ho Choa, Jae-Kyo Yang, Won-Jae Yang and Keun-Ho Auh, *Synthesis and characterization of isolated iron oxide nanoparticle dispersed in MgO matrix*, *J. Magnetism & Magnetic Mater.* 266(1-2), 20 (2003)

**226.** F. Atay, V. Bilgin, I. Akyuz and S. Kose, *The effect of In doping on some physical properties of CdS films*, *Mater Sci. Semicond Processing* 6(4), 197 (2003)

**227.** M. Girtan and G. Folcher, *Structural and optical properties of indium oxide thin films prepared by an ultrasonic spray CVD process*, *Surf. & Coatings Technol.* 172(2-3), 242 (2003)

228. F. Atay, S. Kose, V. Bilgin and I. Akyuz, *CdS:Ni films obtained by ultrasonic spray pyrolysis: effect of the Ni concentration*, Mater Lett 57(22-23), 3461 (2003)
229. M. García-Hipólito, C. D. Hernández-Pérez, O. Alvarez-Fregoso, E. Martínez, J. Guzmán-Mendoza and C. Falcony, *Characterization of europium doped zinc aluminate luminescent coatings synthesized by ultrasonic spray pyrolysis process*, Opt. Mater. 22(4), 345 (2003)
230. M. Liu, M. L. Zhou, L. H. Zhai, D. M. Liu, X. Gao and W. Liu, *A newly designed ultrasonic spray pyrolysis device to fabricate YBCO tapes*, Physica C: Superconductivity 386, 366 (2003)
231. M. Girtan, H. Cachet and G. I. Rusu, *On the physical properties of indium oxide thin films deposited by pyrosol in comparison with films deposited by pneumatic spray pyrolysis*, Thin Solid Films 427(1-2), 406 (2003)
232. S.-Y. Wang and Z.H. Lu, *Preparation of  $Y_2O_3$  thin films deposited by pulse ultrasonic spray pyrolysis*, Mater. Chem. & Phys. 78(2), 542 (2003)
233. K. T. Wojciechowski and J. Ob Kowski, *Preparation and characterisation of nanostructured spherical powders for thermoelectric applications*, Solid State Ionics 157(1-4), 341 (2003)
234. L. Castañeda, J. C. Alonso, A. Ortiz, E. Andrade, J. M. Saniger and J. G. Bañuelos, *Spray pyrolysis deposition and characterization of titanium oxide thin films*, Mater. Chem. & Phys. 77(3), 938 (2003)
235. Y. C. Kang, H. S. Roh, H. D. Park and S. B. Park, *Optimization of VUV characteristics and morphology of  $BaMgAl_{10}O_{17}:Eu^{2+}$  phosphor particles in spray pyrolysis*, Ceram Int. 29(1), 41 (2003)



- 236.** A. Ferreri, A. Berenov, Y. Bugoslavsky, G. Perkins and J. L. MacManus-Driscoll, *Li-ion battery cathode materials by ultrasonic spray pyrolysis method*, Physica C: Superconductivity 372-376 (Part 2), 873 (2002)
- 237.** S. Phok, Ph. Galez, J. L. Jorda, Z. Supardi, D. De Barros, P. Odier, A. Sin and F. Weiss, *Tl- and (Hg,Re)-1223 oxide films by spray pyrolysis for practical applications*, Physica C: Superconductivity 372-376 (Part 2), 876 (2002)
- 238.** I. Taniguchi, D. Song and M. Wakihara, *Electrochemical properties of  $\text{LiM}_{1/6}\text{Mn}_{11/6}\text{O}_4$  ( $M = \text{Mn, Co, Al and Ni}$ ) as cathode materials for Li-ion batteries prepared by ultrasonic spray pyrolysis method*, J. Power Sources 109(2), 333 (2002)
- 239.** M. Dj. Blesic, Z. V. Saponjis, J. M. Nedeljkovic and D. P. Uskokovic, *TiO<sub>2</sub> films prepared by ultrasonic spray pyrolysis of nanosize precursor*, Mater. Lett 54 (4), 298 (2002)
- 240.** T. Y. Ma and D. K. Shim, *Effects of rapid thermal annealing on the morphology and electrical properties of ZnO/In films*, Thin Solid Films 410(1-2), 8 (2002)
- 241.** S.-Y. Wang, W. Wang, W.-Z. Wang and Y.-W. Du, *Mater. Sci. & Eng. B* 90(1-2), 133 (2002)
- 242.** Sheng-Yue Wang and You-Wei Du, *Preparation and characterization of highly oriented NiO(200) films by a pulse ultrasonic spray pyrolysis method*, J. Cryst. Growth 236(4), 627 (2002)
- 243.** I. Taniguchi, C. K. Lim, D. Song and M. Wakihara, *Particle morphology and electrochemical performances of spinel  $\text{LiMn}_2\text{O}_4$  powders synthesized using ultrasonic spray pyrolysis method*, Solid State Ionics 146(3-4), 239 (2002)

- 244.** K. H. Kim, J. K. Park, C. H. Kim, H. D. Park, H. Chang and S. Y. Choi, *Synthesis of SrTiO<sub>3</sub>:Pr,Al by ultrasonic spray pyrolysis*, *Ceram. Int.* 28(1), 29 (2002)
- 245.** A. Huanosta, J. C. Alonso and A. Ortiz, *Spectroscopic impedance studies of Al<sub>2</sub>O<sub>3</sub> films deposited by spray pyrolysis*, *Thin Solid Films* 401(1-2), 284 (2001)
- 246.** A. K. Ivanov-Schitz, A. V. Nistuk, L. N. Demianets and N. G. Chaban, *Li<sub>3</sub>Sc<sub>2-x</sub>Fe<sub>x</sub>(PO<sub>4</sub>)<sub>3</sub> thin films and powders prepared by ultrasonic spray pyrolysis*, *Solid State Ionics* 144(1-2), 133 (2001)
- 247.** A. Ferreri, J. A. G. Nelstrop, A. D. Caplin and J. L. MacManus-Driscoll, *Microstructure and superconducting properties of ultrasonically spray pyrolysed YBa<sub>2</sub>Cu<sub>3</sub>O<sub>7-x</sub> films*, *Physica C: Superconductivity* 351(1), 58 (2001)
- 248.** P. Veluchamy, M. Tsuji, T. Nishio, T. Aramoto, H. Higuchi, S. Kumazawa, S. Shibutani, J. Nakajima, T. Arita, H. Ohyama, *A pyrosol process to deposit large-area SnO<sub>2</sub>:F thin films and its use as a transparent conducting substrate for CdTe solar cells*, *Solar Energy Mater. & Solar Cells* 67(1-4), 179 (2001)
- 249.** A. K. Ivanov-Schitz, A. V. Nistuk and N. G. Chaban, *Li<sub>3</sub>Fe<sub>2</sub>(PO<sub>4</sub>)<sub>3</sub> solid electrolyte prepared by ultrasonic spray pyrolysis*, *Solid State Ionics* 139(1-2), 153 (2001)
- 250.** Z. V. Marinkovic, L. Mancic, R. Maric and O. Milosevic, *Preparation of nanostructured Zn-Cr-O spinel powders by ultrasonic spray pyrolysis*, *J. Eur. Ceram Soc.* 21(10-11), 2051 (2001)

251. S. Wang, W. Wang, W. Wang, Z. Jiao, J. Liu and Y. Qian, *Characterization and gas-sensing properties of nanocrystalline iron(III) oxide films prepared by ultrasonic spray pyrolysis on silicon*, *Sensors & Actuators B: Chemical* 69(1-2), 22 (2000)
252. Y. C. Chang, H. W. Chen, S. S. Yu and K. Y. Cheng, *Optimize the design and operation of ultrasonic nebulizer to maximize production rate in spray pyrolysis*, *J. Aerosol Sci.* 31, 923 (2000)
253. Y. C. Chang, D. H. Huang and K. Y. Cheng, *Morphological control of product powders in spray pyrolysis via chemical engineering approach*, *J. Aerosol Sci.* 31, 925 (2000)
254. S. Wang, W. Wang and Y. Qian, *Preparation and characterization of  $\text{Eu}_2\text{O}_3$  nanometer thin films by pulse ultrasonic spray pyrolysis method*, *Mater. Res. Bulletin* 35(12), 2057 (2000)
255. S. Wang, W. Wang and Y. Qian, *Preparation of  $\text{La}_2\text{O}_3$  thin films by pulse ultrasonic spray pyrolysis method*, *Thin Solid Films* 372(1-2), 50 (2000)
256. P. S. Patil, P. R. Patil and E. A. Ennaoui, *Characterization of ultrasonic spray pyrolyzed tungsten oxide thin films*, *Thin Solid Films* 370(1-2), 38 (2000)
257. L. Manic , O. Miloevic , B. Marinkovic , M. F. de Silva Lopes and F. Rizzo, *The influence of urea on the formation process of  $\text{BiPbSrCaCuO}$  superconducting ceramics synthesized by spray pyrolysis method*, *Mater. Sci. & Eng. B* 76(2), 127 (2000)

258. S. Wang, Z. Qiao, W. Wang and Y. Qian, *XPS studies of nanometer CeO<sub>2</sub> thin films deposited by pulse ultrasonic spray pyrolysis*, *J. Alloys & Compounds* 305(1-2), 121 (2000)
259. M. C. Baykul and A. Balcioglu, *AFM and SEM studies of CdS thin films produced by an ultrasonic spray pyrolysis method*, *Microelectronic Eng.* 51-52, 703 (2000)
260. P. R. Patil and P. S. Patil, *Transient photoconductivity measurements of ultrasonic spray pyrolyzed tungsten oxide thin films*, *Mater. Res. Bulletin* 35(6), 865 (2000)
261. Y. C. Kang, I. W. Lenggoro, S. B. Park and K. Okuyama, *YAG:Ce phosphor particles prepared by ultrasonic spray pyrolysis*, *Mater. Res. Bulletin* 35(5), 789 (2000)
262. Y. C. Kang and S. B. Park, *Preparation of zinc oxide-dispersed silver particles by spray pyrolysis of colloidal solution*, *Mater. Lett* 40(3), 129 (1999)
263. Y. Matsuzaki, M. Hishinuma and I. Yasuda, *Growth of yttria stabilized zirconia thin films by metallo-organic, ultrasonic spray pyrolysis*, *Thin Solid Films* 340(1-2), 72 (1999)
264. A. Ortiz, J. C. Alonso, V. Pankov and D. Albarran, *Violet-blue photoluminescence in aluminium oxide films prepared by ultrasonic spray pyrolysis*, *J. Luminescence* 81(1), 45 (1999)
265. V. Jokanovic, Dj. Janackovic, P. Spasic and D. Uskokovic, *Modeling of nanostructural design of ultrafine mullite powder particles obtained by ultrasonic spray pyrolysis*, *Nanostructured Mater.* 12(4), 349 (1999)

266. S. B. Park, Y. C. Kang, I. W. Lenggoro and K. Okuyama, *Preparation of  $Y_2O_3:Eu$  phosphor without post-treatment by gas phase reaction*, J. Aerosol Sci. 29, S909 (1998)
267. Y. C. Kang, S. B. Park, I. W. Lenggoro and K. Okuyama, *Preparation of non-aggregation YAG-Ce phosphor particles by spray pyrolysis*, J. Aerosol Sci. 29, S911 (1998)
268. F. L. Yuan, C. H. Chen, E. M. Kelder and J. Schoonman, *Preparation of zirconia and yttria-stabilized zirconia (YSZ) fine powders by flame-assisted ultrasonic spray pyrolysis (FAUSP)*, Solid State Ionics 109(1-2), 119 (1998)
269. D. Briand, M. Labeau, J. F. Currie and G. Delabouglise, *Pd-doped  $SnO_2$  thin films deposited by assisted ultrasonic spraying CVD for gas sensing: selectivity and effect of annealing*, Sensors & Actuators B: Chemical 48(1-3), 395 (1998)
270. H. K. Singh and O. N. Srivastava, *Cadmium induced growth of 2223 phase and  $T_c$  enhancement in TBCCO high  $T_c$  thin films*, Phys. Lett. A 240(4-5), 253 (1998)
271. Dj. Janackovic, V. Jokanovic, Lj. Kostic-Gvozdenovic and D. Uskokovic, *Synthesis of mullite nanostructured spherical powder by ultrasonic spray pyrolysis*, Nanostructured Mater. 10(3), 341 (1998)
272. C.H. Chen, F.L. Yuan and J. Schoonman, *Spray pyrolysis routes to electroceramic powders and thin films*, Eur. J. Solid State & Inorganic Chem. 35(2), 189 (1998)
273. R. Abraham, F. Guenard, K. Lebbou, S. Trosset, M. T. Cohen-Adad, J. L. Jorda and M. Couach, *Elaboration of  $Tl_{0.5}Pb_{0.5}Sr_2CaCu_2O_x$  Superconducting*

*Phases By an Ultrasonic Spray-Pyrolysis Process*, Mater. Res. Bulletin 33(2), 253 (1998)

274. Y.J. Lee, H.B. Kim, Y.R. Roh, H.M. Cho and S. Baik, *Development of a saw gas sensor for monitoring SO<sub>2</sub> gas*, Sensors & Actuators A: Physical 64(2), 173 (1998)

275. E. Djurado and M. Labeau, *Second phases in doped lanthanum gallate perovskites*, J. Eur. Ceram. Soc. 18(10), 1397 (1998)

276. P.S. Patil, E.A. Ennaoui, C.D. Lokhande, M. Müller, M. Giersig, K. Diesner and H. Tributsch, *Characterization of ultrasonic spray pyrolysed ruthenium oxide thin films*, Thin Solid Films 310(1-2), 57 (1997)

277. P. Fortunato, A. Reller and H. R. Oswald, *Generation of mixed metal oxides by use of an ultrasonic aerosol thermal decomposition process*, Solid State Ionics 101-103, 85 (1997)

278. Y. Harima, K. Matsumoto, Y. D. Wang and K. Yamashita, *Photoelectrolytic micelle disruption method for preparation of free patterns of pigment images*, Thin Solid Films 301(1-2), 95 (1997)

279. E. Andrade, M. Jergel, J. C. Cheang-Wong, A. Conde-Gallardo and C. Falcony, *Ion beam analysis of HTc superconducting Tl-based films*, Nucl. Instrum. & Meth. Phys. Res. B: Beam Interactions with Materials and Atoms 122(4), 677 (1997)

280. J. M. Nedeljkovi , Z. V. Aponji, Z. Rako evi , V. Jokanovi and D. P. Uskokovi, *Effects of H<sub>2</sub>O<sub>2</sub> on the morphology of ZrO<sub>2</sub> powder prepared by ultrasonic spray pyrolysis*, Nanostructured Mater. 9(1-8), 125 (1997)

281. C. N. R. Rao, *Chemical approaches to the design of oxide materials*, Pure & Appl. Chem. 66, 1765 (1994)
282. M. Langlet and J. C. Joubert in *Chemistry of Advanced Materials* (C. N. R. Rao, Ed.), Blackwell, Oxford, 1992, p23-45
283. Y. T. Tan, N. Li, U. Gösele, *Is there a thermodynamic limit to the size of the nanowire?*, Appl. Phys. Lett. 83, 1199 (2003)
284. M. M. Bućko, J. Obłakowski, J. Eur. Ceram. Soc. 27, 3625 (2007)
285. G. L. Messing, S. C. Zhang, G. V. Jayanthi, *Modeling of particle morphology and size*, J. Am. Ceram. Soc. 76, 2707 (1993)
286. S. C. Zhang, G. L. Messing, *Size of particles after pyrolysis*, J. Am. Ceram. Soc. 73, 61 (1990)
287. M. T. Htay, Y. Hashimoto, K. Ito, *ZnO nanostructures by ultrasonic spray pyrolysis*, Jpn. J. Appl. Phys. 46, 440 (2007)
288. E. F. Nichols, G. F. Hull, *Electromagnetic theory and the calculation of forces on solid bodies*, Phys. Rev. 13, 307 (1901)
289. Crookes radiometer demonstration from the American Association of Physics Teachers
290. D. J. Wineland, W. M. Itano, *Laser cooling*, Phys. Today, June (1987)
291. A. Einstein, *On the interaction of light with atoms*, Phys. Z. 18, 121 (1917)
292. O. Frisch, *Determination of a push from light*, Z. Phys. 86,42 (1933)
293. A. Kastler, *Cooling and heating atoms with light beams*, J. Phys. Radium 11, 255 (1950)

294. H. R. Bachmann, H. Noth, R. Rinck, K. S. Kompa, *BCl<sub>3</sub> by laser synthesis*, Chem. Phys. Lett. 29, 627 (1975)
295. C. M. Bowden, J. D. Stettler and N. M. Witriol, *An excitation model for laser-induced photochemical reactions*, J. Phys. B: At. & Mol. Phys. 34, 1045 (1977)
296. G. S. Hurst, M. G. Payne, *Principles and Applications of Resonance Ionization Spectroscopy*, Adam Hilger & IOP Publishing, Bristol and Philadelphia, (1988)
297. A. Kaldor, R. L. Woodin, *Applications of lasers to chemical processing*, Proceedings of the IEEE 70, 565 (1982)
298. El-Diasty, F. (2004) *Simulation of CO<sub>2</sub> laser pyrolysis during preparation of SiC nanopowders*, Opt. Commun., Vol. 241, p. 121-135.
299. J. S. Haggerty, W. R. Cannon, in J. L. Steinfield (Ed), *Laser Induced Chemical Processes*, Plenum Press, New York, 165 (1981)
300. R. R. Party, G. M. Russwurm, W. A. Mccleny, D. R. Morgan, *Linear absorption of light by atoms* Appl. Opt. 13, 2850 (1982)
301. W. R. Cannon, S. C. Danforth, J. H. Flint, J. S. Haggerty, R. A. Marra, *Laser pyrolysis of silane*, J. Am. Ceram. Soc. 65, 324 (1982)
302. B. A. Lengyel, *Lasers*, Wiley-Interscience, New York, 1971 p24-65.
303. P Gould, *Laser cooling to the Doppler limit*, Am. J. Phys. 65, 1120 (1997)
304. F. Tenegal, S. Petcu, N. Herlin-Boime, X. Armand, M. Mayne, C. Reynaud, *TiO<sub>2</sub> by Laser pyrolysis of TiCl<sub>4</sub>*, Chem. Phys. Lett. 335, 155 (2001)
305. A. Gupta, J. T. Yardley, *Production of light olefins from synthesis gas using catalysts prepared by laser pyrolysis*, Proc. SPIE - The International Society for Optical Engineering 458, 131 (1984)



306. I. F. Kanaev, V. K. Malinovskii, L. A. Ryabova, V. S. Salun, I. A. Serbinov, *Synthesis of graphite microstructures by laser pyrolysis of acetone vapour*, Optoelectronics, Instrumentation and Data Processing (English translation of Avtometriya) (2), 105 (1987)
307. J. A. Kern, H. G. Schwahn, B. Schramm, *Synthesis of fine chromium (III) oxide powders by laser pyrolysis*, Mater. Chem. & Phys. 21, 391 (1989)
308. X. -X. Bi, P. C. Eklund, J. M. Stencel, D. N. Taulbee, H. F. Ni, F. J. Derbyshire, M. Endo, *Carbon coatings on iron carbide particles produced by laser pyrolysis*, Extended Abstracts and Program - Biennial Conference on Carbon 1, 518 (1991)
309. P. R. Buerki, S. Leutwyler, *Substrate-free gas-phase synthesis of diamond powder by CO<sub>2</sub> laser pyrolysis of C<sub>2</sub>H<sub>4</sub>*, Surface and Coatings Technology 47 , 22 (1991)
310. X. Gao, J. Zhang, G. Guo, X. Gao, X. He, F. Yang, *Ultrafine Fe and Fe/C powder preparation via laser-induced chemical vapor pyrolysis*, Zhongguo Jiguang/Chinese J. Lasers 19, 235 (1992)
311. J. M. Stencel, P. C. Eklund, X. X. Bi, F. J. Derbyshire, *Iron ultrafine particle catalysts formed by laser pyrolysis, Synthesis, characterization and coal liquefaction activity*, Catalysis Today 15, 285 (1992)
312. X. X. Bi, P. C. Eklund, *Synthesis of nanocrystalline Fe-based particles by CO<sub>2</sub> laser pyrolysis*, Mater. Res. Soc. Symposium Proc. 286, 161 (1993)

- 313.** X. X. Bi, B. Ganguly, G. P. Huffman, F. E. Huggins, M. Endo, P. C. Eklund, *Nanocrystalline  $\alpha$ -Fe,  $Fe_3C$ , and  $Fe_7C_3$  produced by  $CO_2$  laser pyrolysis*, J. Mater. Res. 8, 1666 (1993)
- 314.** X. Gao, J. Chen, M. Wang, G. Guo, Y. Guangsheng, F. Yang, *Production of ultrafine Si powders by laser pyrolysis*, Beijing huagong xueyuan xuebao Ziran kexue ban 21, 49 (1994)
- 315.** R. Ochoa, G. T. Hager, W. T. Lee, S. Bandow, E. Givens, P.C. Eklund, *Relative activity and selectivity of nanoscale  $Mo_2N$ ,  $Mo_2C$  and  $MoS_2$  catalysts synthesized by laser pyrolysis*, Mater. Res. Soc. Symposium – Proc. 368, 27 (1995)
- 316.** W. E. Rhine, A. S. D. Lightfoot, J. S. Haggerty, Mater. Res. Soc. Symposium – Proc. 365, 101 (1995)
- 317.** X. X. Bi, M. Jagtoyen, M. Endo, K. D. Chowdhury, R. Ochoa, F. J. Derbyshire, M. S. Dresselhaus, P. C. Eklund, J. Mater. Res. 10, 2875 (1995)
- 318.** S. -J. Liaw, A. Raje, X. X. Bi, P. C. Eklund, U. M. Graham, B. H. Davis, *Energy & Fuels* 9 , 921 (1995)
- 319.** S. Bandow, Y. Maruyama, X.-X. Bi, R. Ochoa, J. M. Holden, W.-T. Lee, P. C. Eklund, Mater. Sci. & Eng A A204, 222 (1995)
- 320.** N. Herlin, A. X. Musset, M. Martinengo, H. Luce, M. Cauchetier, *Nanometric Si-based oxide powders: synthesis by laser pyrolysis and characterisation*, J. Eur. Ceram. Soc. 16, 1063 (1996)
- 321.** van Erven, W.J.M., Trzeciak, T.M., Fu, Z., Marijnissen, J.C.M., *Design of a laser assisted aerosol reactor for production of ceramics on a semi-industrial scale*, J. Eur. Ceram. Soc. 17, 1045 (1997)

- 322.** X. Armand, N. Herlin, I. Voicu, M. Cauchetier, *Fullerene synthesis by laser pyrolysis of hydrocarbons*, J. Phys. & Chem. Solids 58 (11), 1853 (1997)
- 323.** E. Borsella, S. Botti, S. Martelli, *Nano-powders from gas-phase laser driven reactions: Characteristics and applications*, Mater. Sci. Forum 235-238 (Part 1), 261 (1997)
- 324.** R. Alexandrescu, F. Huisken, G. Pugna, A. Crunteanu, S. Petcu, S. Cojocaru, R. Cireasa, I. Morjan, *Preparation of carbon nitride fine powder by laser induced gas-phase reactions*, Appl. Phys A: Mater. Sci. & Processing 65, 207 (1997)
- 325.** N. Herlin, I. Bohn, C. Reynaud, M. Cauchetier, A. Galvez, J. N. Rouzaud, *Nanoparticles produced by Laser Pyrolysis of hydrocarbons: Analogy with carbon cosmic dust*, Astronomy & Astrophys 330, 1127 (1998)
- 326.** J. S. Bradley, O. Vollmer, R. Rovai, U. Specht, F. Lefebvre, *High surface area silicon imidonitrides: A new class of microporous solid base*, Adv. Mater. 10, 938 (1998)
- 327.** R. Alexandrescu, I. Morjan, A. Crunteanu, S. Cojocaru, S. Petcu, V. Teodorescu, F. Huisken, M. Ehbrecht, *Iron-oxide-based nanoparticles produced by pulsed infrared laser pyrolysis of Fe(CO)<sub>5</sub>*, Mater. Chem. & Phys. 55, 115 (1998)
- 328.** R. Alexandrescu, X. Armand, M. Cauchetier, N. Herlin, S. Petcu, I. Voicu, *Effect of SF<sub>6</sub> addition in the laser synthesis of fullerene and soot from C<sub>6</sub>H<sub>6</sub>/O<sub>2</sub> or C<sub>6</sub>H<sub>6</sub>/N<sub>2</sub>O sensitized mixtures*, Carbon 36, 1285 (1998)

- 329.** L. E. Depero, L. Sangaletti, B. Allieri, F. Pioselli, C. Casale, M. Notaro, *Microstructural properties of Ta-doped TiO<sub>2</sub> powders obtained by laser pyrolysis*, Mater. Sci. Forum 278-281 (Part 2), 654 (1998)
- 330.** M. Mayne, D. Bahloul-Hourlier, B. Doucey, P. Goursat, M. Cauchetier, N. Herlin, *Thermal behaviour of SiCN nanopowders issued from laser pyrolysis*, J. Eur. Ceram. Soc. 18, 1187 (1998)
- 331.** R. Alexandrescu, R. Cireasa, C. S. Cojocaru, A. Crunteanu, I. Morjan, F. Vasiliu, A. Kumar, *Carbon nitride thin films and nanopowders produced by CO<sub>2</sub> laser pyrolysis*, Surf. Eng. 15, 230 (1999)
- 332.** S. Charpentier, A. Kassiba, A. Bulou, M. Monthieux, M. Cauchetier, *Effects of excess carbon and vibrational properties in ultrafine SiC powders*, EPJ Appl. Phys. 8, 111 (1999)
- 333.** M. Cauchetier, X. Armand, N. Herlin, R. Alexandrescu, I. Morjan, S. Petcu, I. Voicu, *Laser pyrolysis of hydrocarbons in synthesis of soot containing fullerenes*, Fullerene Sci. & Technol. 7, 91 (1999)
- 334.** F. Huisken, B. Kohn, R. Alexandrescu, S. Cojocaru, A. Crunteanu, G. Ledoux, C. Reynaud, *Silicon carbide nanoparticles produced by CO<sub>2</sub> laser pyrolysis of SiH<sub>4</sub>/C<sub>2</sub>H<sub>2</sub> gas mixtures in a flow reactor*, J. Nanoparticle Res. 1, 293 (1999)
- 335.** R. Alexandrescu, *Preparation of iron carbide and iron nanoparticles by laser-induced gas phase pyrolysis*, J. De Physique 9, Pr8-537 (1999)
- 336.** F. Huisken, H. Hofmeister, B. Kohn, M. A. Laguna, V. Pillard, *Laser production and deposition of light-emitting silicon nanoparticles*, Appl. Surf. Sci. 154, 305 (2000)

- 337.** S. Petcu, M. Cauchetier, X. Armand, I. Voicu, R. Alexandrescu, *Formation of fullerenes in laser pyrolysis of benzene*, *Combustion & Flame*, 122, 500 (2000)
- 338.** V. Z. Mordkovich, *The observation of large concentric shell fullerenes and fullerene-like nanoparticles in laser pyrolysis carbon blacks*, *Chem. Mater.* 12, 2813 (2000)
- 339.** S. Martelli, A. Mancini, R. Giorgi, R. Alexandrescu, S. Cojocaru, A. Crunteanu, I. Voicu, I. Morjan, *Production of iron-oxide nano-particles by laser-induced pyrolysis of gaseous precursors*, *Appl. Surf. Sci.* 154, 353 (2000)
- 340.** S. Petcu, M. Cauchetier, X. Armand, I. Voicu, R. Alexandrescu, *Formation of fullerenes in the laser-pyrolysis of benzene*, *Combustion & Flame* 122, 500 (2000)
- 341.** K. E. Gonsalves, H. Li, R. Perez, P. Santiago, M. Jose-Yacaman, *Synthesis of nanostructured metals and metal alloys from organometallics*, *Coordination Chem. Rev.* 206-207, 607 (2000)
- 342.** R. Alexandrescu, A. Crunteanu, I. Morjan, S. Petcu, I. Voicu, L. Diamandescu, X. Armand, C. Reynaud, *Fullerene/iron complexes obtained by laser synthesis from gas/aerosol phases*, *Proc. SPIE - The International Society for Optical Engineering* 4430, 196 (2000)
- 343.** F. Huisken, B. Kohn, R. Alexandrescu, I. Morjan, *Synthesis and characterization of iron clusters coated with hydrocarbons*, *Proc. SPIE - The International Society for Optical Engineering* 4430, 167 (2000)
- 344.** G. Ledoux, O. Guillois, D. Porterat, C. Reynaud, F. Huisken, B. Kohn, V. Paillard, *Photoluminescence properties of silicon nanocrystals as a function of their*

size, *Physical Review B - Condensed Matter and Materials Physics* 62, 15942 (2000)

**345.** B. Doucey, D. Bahloul-Hourlier, J.-L. Besson, P. Goursat, *SiCN nanocomposites: Powder synthesis, materials processing and ductility assessment*, *Key Eng. Mater.* 206-213, 1081 (2001)

**346.** A. Müller, F. Ténégal, X. Armand, F. Berger, R. Dez, R., N. Herlin-Boime, J. Bill, *Amorphous SiCN(B) preceramic powders from laser spray pyrolysis and thermolysis*, *Key Eng. Mater.* 206-213, 167 (2001)

**347.** H. Hofmeister, F. Huisken, B. Kohn, R. Alexandrescu, S. Cojocar, A. Crunteanu, I. Morjan, L. Diamandescu, *Filamentary iron nanostructures from laser-induced pyrolysis of iron pentacarbonyl and ethylene mixtures*, *Appl. Phys. A: Materials Science and Processing* 72, 7 (2001)

**348.** C. Reynaud, O. Guillois, N. Herlin-Boime, J.-N. Rouzaud, A. Galvez, C. Clinard, E. Balanzat, J.-M. Ramillon, *Optical properties of synthetic carbon nanoparticles as model of cosmic dust*, *Spectrochimica Acta - Part A Molecular and Biomolecular Spectroscopy* 57, 797 (2001)

**349.** S. Veintemillas-Verdaguer, M. P. Morales, C. J. Serna, *Effect of the oxidation conditions on the maghemites produced by laser pyrolysis*, *Appl. Organometallic Chem.* 15, 365 (2001)

**350.** S. Botti, M. L. Terranova, V. Sessa, S. Piccirillo, M. Rossi, *Silicon quantum dots in diamond matrix: A new synthesis route*, *Appl. Organometallic Chem.* 15, 388 (2001)

351. S. Martelli, O. Bomati-Miguel, L. De Dominicis, R. Giorgi, F. Rinaldi, S. Veintemillas-Verdaguer, *Synthesis of Fe-Si nanoparticles by cw CO<sub>2</sub> laser assisted pyrolysis from gaseous precursors*, Appl. Surf. Sci. 186, 562 (2002)
352. A. Kassiba, M. Makowska-Janusik, J. Boucle, J. F. Bardeau, A. Bulou, N. Herlin, M. Mayne, X. Armand, *Stoichiometry and interface effects on the electronic and optical properties of SiC nanoparticles*, Diamond & Related Mater. 11, 1243 (2002)
353. O. Bomati Miguel, M. P. Morales, C. J. Serna, S. Veintemillas-Verdaguer, *Magnetic nanoparticles prepared by laser pyrolysis*, IEEE Transactions on Magnetics 38, 2616 (2002)
354. A. Galvez, N. Herlin-Boime, C. Reynaud, C. Clinard, J.-N. Rouzaud, *Carbon nanoparticles from laser pyrolysis*, Carbon 40, 2775 (2002)
355. R. Dez, F. Ténégal, C. Reynaud, M. Mayne, X. Armand, N. Herlin-Boime, *Laser synthesis of silicon carbonitride nanopowders; structure and thermal stability*, J. Euro. Ceram. Soc. 22, 2969 (2002)
356. A. Muller, N. Herlin-Boime, F. Tenegal, A. X. Berger, A. M. Flank, D. Romuald, K. Muller, J. Bill, F. Aldinger, *Comparison of Si/C/N pre-ceramics obtained by laser pyrolysis or furnace thermolysis*, J. Euro. Ceram. Soc., Vol. 23, p. 37-46. (2003)
357. I. Morjan, R. Alexandrescu, I. Soare, F. Dumitrache, I. Sandu, I. Voicu, A. Crunteanu, S. Martelli, *Nanoscale powders of different iron oxide phases prepared by continuous laser irradiation of iron pentacarbonyl-containing gas precursors*, Mater. Sci. & Eng. C 23, 211 (2003)

358. F. Ténégal, I. Voicu, X. Armand, N. Herlin-Boime, C. Reynaud, *Residence time effect on fullerene yield in butadiene-based laser pyrolysis flame*, Chem. Phys. Lett. 379, 40 (2003)
359. F. Dumitrache, I. Morjan, R. Alexandrescu, B. Rand, V. Ciupina, G. Prodan, I. Voicu, E. Vasile, *Iron-carbon nanocomposite obtained by laser induced gas-phase reactions*, Proc. SPIE - The International Society for Optical Engineering 4977, 670 (2003)
360. S. Veintemillas-Verdaguer, M. Del Puerto Morales, O. Bomati-Miguel, C. Bautista, X. Zhao, P. Bonville, R. P. De Alejo, J. Ferreira's, *Colloidal dispersions of maghemite nanoparticles produced by laser pyrolysis with application as NMR contrast agents*, J. Phys. D: Applied Physics 37, 2054 (2004)
361. S. Orlanducci, F. Valentini, S. Piccirillo, M. L. Terranova, S. Botti, R. Ciardi, M. Rossi, G. Palleschi, *Chemical/structural characterization of carbon nanoparticles produced by laser pyrolysis and used for nanotube growth*, Mater. Chem. & Phys. 87, 190 (2004)
362. J. Pola, D. Pokorna, J. Bohacek, Z. Bastl, A. Ouchi, *Nano-structured crystalline Te films by laser gas-phase pyrolysis of dimethyl tellurium*, J. Analytical & Appl. Pyrolysis, 71, 739 (2004)
363. S. Orlanducci, F. Valentini, S. Piccirillo, M. L. Terranova, S. Botti, R. Ciardi, M. Rossi, G. Palleschi, *Chemical/structural characterization of carbon nanoparticles produced by laser pyrolysis and used for nanotube growth*, Mater. Chem. & Phys. 87, 190 (2004)



364. R. Alexandrescu, I. Morjan, F. Dumitrache, I. Voicu, I. Soare, I. Sandu, C. T. Fleaca, *Recent developments in the synthesis of iron-based nanostructures by laser pyrolysis: Integrating structural analysis with the experimental method*, Diffusion & Defect Data Pt.B: Solid State Phenomena 99-100, 181 (2004)
365. R. Dez, D. Porterat, N. H. Boime, *Silicon carbonitride nanopowders by laser pyrolysis for plastic nanocomposites*, Key Eng. Mater. 264-268, 25 (2004)
366. R. Alexandrescu, X. Armand, F. Dumitrache, C. T. Fleaca, N. Herlin-Boime, E. Marino, M. Mayne, I. Voicu, *Relation fullerene-PAH-soot in laser pyrolysis: FTIR investigations*, Proc. SPIE - The International Society for Optical Engineering 5581, 297 (2004)
367. M. Sonu, I. Savu, L. Pastean, I. Voicu, I. Soare, I. Morjan, C. Grigoriu, *Adsorption capacity study of carbon nanopowder produced by laser pyrolysis*, Proc. SPIE - The International Society for Optical Engineering 5581, 428 (2004)
368. X. Q. Zhao, S. Veintemillas-Verdaguer, O. Bomati-Miguel, M. P. Morales, H. B. Xu, *Thermal history dependence of the crystal structure of Co fine particles*, Phys. Rev. B - Condensed Matter and Materials Physics 71, 024106-1 (2005)
369. E. Marino, B. Bouchet-Fabre, D. Porterat, C. Reynaud, *Spectroscopic study of carbon nitride nanoparticles synthesised by laser pyrolysis*, Diamond & Related Mater. 14, 1120 (2005)
370. Y. Leconte, H. Maskrot, N. Herlin-Boime, D. Porterat, C. Reynaud, A. Swiderska-Sroda, E. Grzanka, B. Palosz, *Elaboration of SiC, TiC, and ZrC nanopowders by laser pyrolysis: From nanoparticles to ceramic nanomaterials*, Glass Phys. & Chem 31, 510 (2005)

371. F. Dumitrache, I. Morjan, R. Alexandrescu, V. Ciupina, G. Prodan, I. Voicu, C. Fleaca, I. Soare, *Iron-iron oxide core-shell nanoparticles synthesized by laser pyrolysis followed by superficial oxidation*, Appl. Surf. Sci. 247, 25 (2005)
372. R. Alexandrescu, I. Morjan, I. Voicu, F. Dumitrache, L. Albu, I. Soare, G. Prodan, *Combining resonant/non-resonant processes: Nanometer-scale iron-based material preparation via CO<sub>2</sub> laser pyrolysis*, Appl. Surf. Sci. 248, 138 (2005)
373. C. Reynaud, O. Guillois, N. Herlin-Boime, G. Ledoux, F. Huisken, *Origin of the multi-exponential decay dynamics in light-emitting silicon nanocrystals*, Materials Research Society Symposium Proc. 832, 129 (2005)
374. V. Ciupina, G. Prodan, F. Dumitrache, I. Morjan, R. Alexandrescu, E. Popovici, I. Soare, O. Schneeweiss, *Iron/iron carbides/carbon core-shell nanostructures synthesized by laser pyrolysis*, Proc. SPIE - The International Society for Optical Engineering 5924, 1 (2005)
375. I. Morjan, R. Alexandrescu, F. Dumitrache, I. Sandu, M. Scarisoreanu, L. Albu, I. Soare, V. Ciupina, *Composition influence on the properties of titanium-doped gamma iron oxide nanoparticles prepared by laser pyrolysis method*, Materials Research Society Symposium Proc. 872, 217 (2005)
376. B. David, N. Pizúrová, O. Schneeweiss, P. Bezdička, I. Morjan, R. Alexandrescu, *Iron/graphite core-shell structured nanoparticles prepared by annealing of nanopowder*, Mater. Sci. Forum 480-481, 469 (2005)
377. E. Trave, F. Enrichi, G. Mattei, V. Bello, E. Borsella, F. Fabbri, M. Carpanese, L. Gini, *Investigation and application of size-dependent properties of*

*silicon-based nanoparticles produced by laser pyrolysis*, Proc. SPIE - The International Society for Optical Engineering 5850, 25 (2005)

**378.** Y. Leconte, H. Maskrot, N. Herlin-Boime, D. Porterat, C. Reynaud, S. Gierlotka, A. Swiderska-Sroda, J. Vicens, *TiC nanocrystal formation from carburization of laser-grown Ti/O/C nanopowders for nanostructured ceramics*, J. Phys. Chem. B 110, 158 (2006)

**379.** D. Pokorná, J. Boháček, V. Vorlíček, J. Šubrt, Z. Bastl, E. A. Volnina, J. Pola, *IR laser co-pyrolysis of (CH<sub>3</sub>)<sub>2</sub>Te and (CH<sub>3</sub>)<sub>4</sub>Sn: Gas-phase formation and deposition of nanostructured SnTe*, Analytical & Appl. Pyrolysis 75, 65 (2006)

**380.** B. David, O. Schneeweiss, N. Pizúrová, M. Klementová, P. Bezdička, R. Alexandrescu, F. Dumitrache, I. Morjan, *Fe<sub>3</sub>C nanopowder synthesized by laser pyrolysis and its annealing behaviour*, Surface and Interface Analysis 38, 482 (2006)

**381.** A. Staicu, S. Krasnokutski, G. Rouillé, Th. Henning, F. Huisken, *Electronic spectroscopy of polycyclic aromatic hydrocarbons (PAHs) at low temperature in the gas phase and in helium droplets*, J. Mol. Structure 786, 105 (2006)

**382.** N. Herlin-Boime, M. Mayne-L'Hermite, C. Reynaud, *Advances in the laser pyrolysis synthesis of nanoparticles*, Annales de Chimie: Science des Materiaux 31, 295 (2006)

**383.** M. Bahgat, *Technology of iron carbide synthesis*, J. Mater. Sci. & Technol. 22, 423 (2006)

- 384.** I. Sandu, I. Morjan, I. Voicu, R. Alexandrescu, F. Dumitrache, I. Soare, C. T. Fleaca, E. Popovici, *Self-assembly onto solid surface of some nanopowders synthesized by laser pyrolysis*, Smart Mater. & Structures 15, 816 (2006)
- 385.** M. Amara, M. E. L. Ganaoui, D. Hourlier, *A preliminary study on the nanopowders synthesis: The role of the flow inside the reactor*, Mecanique et Industries 7, 131 (2006)
- 386.** H. Maskrot, Y. Leconte, N. Herlin-Boime, C. Reynaud, E. Guelou, L. Pinard, S. Valange, M. Gervais, *Synthesis of nanostructured catalysts by laser pyrolysis*, Catalysis Today 116, 6 (2006)
- 387.** L. Fa, Z. D. Mei, Z. Hua, Z. Wancheng, *Dielectric and mechanical properties of hot-pressed SiCN/Si<sub>3</sub>N<sub>4</sub>composites*, J. Electroceram. 17, 83 (2006)
- 388.** M. Amara, M. El Ganaoui, *Simulation of heat and mass transfers inside a nanopowders synthesis reactor*, Progress in Computational Fluid Dynamics 6, 371 (2006)
- 389.** H. Du, S. H. Ng, K. T. Neo, M. Ng, I. S. Altman, S. Chiruvolu, N. Kambe, K. Drain, *Inorganic-polymer nanocomposites for optical applications*, Proc. Multifunctional Nanocomposites International Conference(2006)
- 390.** S. V. Verdaguer, B. Bouchet-Fabre, M. P. Morales, Y. Leconte, R. Costo, P. Bonville, N. C. Herlin-Boime, *Continuous synthesis of inorganic magnetic nanocomposites by laser pyrolysis for biomedical applications*, Materials Research Society Symposium Proc. 962, 37 (2006)
- 391.** Y. Leconte, M. Leparoux, X. Portier, N. Herlin-Boime, S. Siegmann, L. Rohr, C. Reynaud, *Structural study of SiC nanoparticles grown by inductively*

- coupled plasma and laser pyrolysis for nanostructured ceramics elaboration*, Materials Research Society Symposium Proc. 981, 47 (2006)
- 392.** O. Bomati-Miguel, P. Tartaj, M. P. Morales, P. Bonville, U. Gollaschindler, X. Q. Zhao, S. Veintemillas-Verdaguer, *Core-shell iron-iron oxide nanoparticles synthesized by laser-induced pyrolysis*, Small 2, 1476 (2006)
- 392.** S. Chiruvolu, W. Li, M. Ng, K. Du, N. K. Ting, W. E. McGovern, N. Kambe, K. Drain, *Laser pyrolysis - A platform technology to produce nanoscale materials for a range of product applications*, NSTI Nanotechnology Conference and Trade Show - NSTI Nanotech 2006 Technical Proc. 1, 325 (2006)
- 392.** A. Tomescu, R. Alexandrescu, I. Morjan, F. Dumitrache, L. Gavrila-Florescu, R. Birjega, I. Soare, J. Pola, *Structural and sensing properties of a novel Fe/ Fe<sub>2</sub>O/ polyoxocarbosilane core shell nanocomposite powder prepared by laser pyrolysis*, J. Mater. Sci. 42, 1838 (2007)
- 393.** F. Lacour, O. Guillois, X. Portier, H. Perez, N. Herlin, C. Reynaud, *Laser pyrolysis synthesis and characterization of luminescent silicon nanocrystals*, Physica E: Low-Dimensional Systems and Nanostructures 38, 11 (2007)
- 394.** Y. Leconte, H. Maskrot, L. Combemale, N. Herlin-Boime, C. Reynaud, *Application of the laser pyrolysis to the synthesis of SiC, TiC and ZrC pre-ceramics nanopowders*, J. Analytical & Appl. Pyrolysis 79, 465 (2007)
- 395.** A. Tavakoli, M. Sohrabi, A. Kargari, *A review of methods for synthesis of nanostructured metals with emphasis on iron compounds*, Chem. Papers 61, 151 (2007)

- 396.** M. Scarisoreanu, I. Morjan, R. Alexandrescu, R. Birjega, I. Voicu, C. Fleaca, E. Popovici, E. Figgemeier, *Effects of some synthesis parameters on the structure of titania nanoparticles obtained by laser pyrolysis*, Appl. Surf. Sci. 253, 7908 (2007)
- 397.** I. Morjan, F. Dumitrache, R. Alexandrescu, R. Birjega, C. Fleaca, I. Voicu, L., Gavrilă, L. Vekas, *Nanoscale maghemite iron oxide powders prepared by laser pyrolysis*, NSTI Nanotechnology Conference and Trade Show - NSTI Nanotech 2007, Technical Proc. 4, 234 (2007)
- 398.** B. David, O. Schneeweiss, M. Mashlan, E. Šantavá, I. Morjan, *Low-temperature magnetic properties of Fe<sub>3</sub>C/iron oxide nanocomposite*, J. Magnetism & Magnetic Mater. 316, 422 (2007)
- 399.** Y. Leconte, S. Veintemillas-Verdaguer, M. P. Morales, R. Costo, L. Rodríguez, P. Bonville, B. Bouchet-Fabre, N. Herlin-Boime, *Continuous production of water dispersible carbon-iron nanocomposites by laser pyrolysis: Application as MRI contrasts*, J. Colloid & Interface Sci. 313, 511 (2007)
- 400.** R. Alexandrescu, F. Dumitrache, L. G. Florescu, I. Morjan, E. Popovici, M. Scarisoreanu, I. Sandu, I. Voicu, *Carbon nanostructures by gas-phase laser pyrolysis*, Proc. SPIE - The International Society for Optical Engineering 6606, art. no. 66060J (2007)
- 401.** R. Alexandrescu, I. Morjan, F. Dumitrache, J. Pola, V. Vorlicek, M. Marysko, L. Gavrilă, G. Prodan, *Structural and magnetic properties of nanosized iron-polyoxocarbosilane core-shell composites prepared by laser pyrolysis*, Proc. SPIE - The International Society for Optical Engineering 6606, art. no. 66060K (2007)

402. A. Reau, B. Guizard, C. Mengeot, L. Boulanger, F. Ténégal, *Large scale production of nanoparticles by laser pyrolysis*, Mater. Sci. Forum 534-536, 85 (2007)
403. E. Figgemeier, W. Kylberg, E. Constable, M. Scarisoreanu, R. Alexandrescu, I. Morjan, I. Soare, G. Prodan, *Titanium dioxide nanoparticles prepared by laser pyrolysis: Synthesis and photocatalytic properties*, Appl. Surf. Sci. 254, 1037 (2007)
404. I. Dinca, A. Stefan, C. Serghie, A. Moga, L. Dumitrache, Z. Vuluga, D. Donescu, I. Sandu, *Hybrid polymer composites reinforced by layered silicate and laser synthesized nanocarbons*, Appl. Surf. Sci. 254, 1032 (2007)
405. N. Herlin-Boime, Y. Leconte, D. Porterat, C. Reynaud, O. Sublemontier, *Laser pyrolysis: A versatile method to produce nanopowder*, Actualite Chimique 317, 14-15 (2008)
406. F. Tuinstra, J. L. Koenig, *Raman spectra of carbon layers*, J. Chem. Phys. 53, 1126 (1970)
407. H. Richter, Z. P. Wang, L. Ley, *The one phonon Raman spectrum in microcrystalline silicon*, Solid State Commun. 39, 625 (1981)
408. I. H. Faucet and P. M. Campbell, *Phonon confinement in small silicon wires*, Solid State Commun. 58 (10), 739 (1986)
409. S. Piscanec, M. Cantoro, A.C. Ferrari, J.A. Zapien, Y. Lifshitz, S.T. Lee, S. Hoffmann, J Robertson, *Raman spectroscopy of silicon nanowires*, Phys. Rev. B 68, (2003) 241312 (R)

- 410.** K.W. Adu, H.R. Gutierrez, U.J. Kim, G.U. Sumanasekera and P.C. Eklund, *Phonons in silicon nanowires*, Nano Lett. 5, 400 (2005)
- 411.** (a) S Bhattacharyya, S Samui, *Phonon confinement in oxide-coated silicon nanowires*, Appl. Phys. Lett. 84, 1564 (2004) (b) K. W. Adu, H. R. Gutierrez, P.C. Eklund, *Surface phonons in silicon layers*, Vibrational Spectroscopy 42 (2006) 165-175
- 412.** Y. K. Kim, H. M. Jang, *Raman spectroscopy of slabs*, Solid State Commun. 127, 433 (2003)
- 413.** (a) F. Comas, C. Trallero-Giner, J. Appl. Phys. 94, 6023 (2003), (b) J. P. Sun, H. B. Teng, G. I. Haddad, M. A. Stroscio, Semicond. Sci. Technol. 13, A147 (1998), (c) N. Mori, T. Ando, Phys. Rev. B 40, 6175 (1989)
- 414.** M. I. Vasilevsky, A. G. Rolo, M. J. M. Gomes, Solid State Commun. 104, 381 (1997)
- 415.** A. K. Arora, T. R. Ravindran, G. L. N. Reddy, A. K. Sikder, D. S. Misra, Diamond Relat. Mater. 10, 1477 (2001)
- 416.** Q. Xiong, J. Wang, O. Reese, L. C. Lew Yan Voon, P. C. Eklund, Nano Lett. 4, 1991 (2004)
- 417.** M. C. Klein, F. Hache, D. Ricard, C. Flytzanis, Phys. Rev. B 42, 11123 (1990)
- 418.** R. Ruppin, J. Phys. C: Solid State Phys. Cond. Matter 17, 1085 (2005)
- 419.** R. Ruppin, R. Englman, Rep. Prog. Phys. 33, 149 (1970)
- 420.** G. Gouadec and Ph. Colomban, Progress in Crystal Growth and Characterization of Materials 53, 1-56 (2007)



- 421.** A. Surca-Vuk, U. Opara-Krasovec, B. Orel, Ph. Colomban, J. Electrochem. Soc. 148 H49 (2002)
- 422.** J. Zi, H. Buscher, C. Falter, W. Ludwig, K. Zhang, X. Xie, Raman shifts in Si nanocrystals, Appl. Phys. Lett. 69 (2), 200 (1996)
- 423.** (a) A. A. Maradudin and Bernstein, Phys. Rev. 164, 1081 (1981) (b) S. Go, H. Bilz, and M. Cardona, Phys. Rev. Lett. 34, 580 (1975)
- 424.** F.J. Morin, Phys. Rev. Lett. 3, 34 (1959)
- 425.** S. Mathur, T. Ruegamer, I Grobelsek, Chem. Vapor. Deposition 13, 42 (2007)
- 426.** M. Occhiuzzi, D Cordischi, R Dragone, J. Solid State Chem. 178, 1551 (2005)
- 427.** A. Haras, M. Witko, D. R. Salahub, K. Hermann, R. Tokarz, Surf. Sci. 491, 77 (2001)
- 428.** (a) M. Borek, F. Quian, V. Nagabushnam, R. K. Singh, Appl. Phys. Lett. 63, 3288 (1993), (b) F. C. Case, J. Vac. Sci. Technol A 2, 1509 (1984), (c) J. F. DeNatale, P. Hood, A. B. Harker, J. Appl. Phys. 66, 5844 (1989), F. Guinneton, L. Sauques, J. C. Valmalette, F. Cros, J. R. Gavarri, J. Phys. Chem. Solids 62, 1229 (2001), (d) F. Guinneton, J.C. Valmalette, J. R Gavarri, Opt. Mater. 15, 111 (2000)
- 429.** R. Lopez, T. E. Haynes, L. A. Boatner, L. C. Feldman, R. F. Haglund, Jr., Phys. Rev. B 65, 224113 (2001)
- 430.** M. Pan, J. Liu, H. Zhong, S. Wang, Z. Li, X. Chen, W. Lu, J. Cryst. Growth 268, 178 (2004)

- 431.** (a) W. J. M. Tegart, *Elements of Mechanical Metallurgy*, Macmillan, NY, 175 (1966), (b) R. A. Flinn, P. K. Trojan, *Engineering Materials and Their Applications 2<sup>nd</sup> Ed.*, Houghton Mifflin, Boston, 93 (1981)
- 432.** H Miyazaki, I. Yasui, *VO<sub>2</sub> powders and the transition*, *Appl. Surf. Sci.* 252, 8367 (2006)
- 433.** H. S. Choi, J. S. Ahn, J. H. Jung, T. W. Noh, D. H. Kim, *Phys. Rev. B* 54, 4621 (1996)
- 434.** R. T. Kivaisi, M. Samiji, *Characterization of VO<sub>2</sub> thin films produced by r.f. sputtering*, *Solar Energy Materials & Solar Cells* 57, 141 (1999)
- 435.** R. Delamare, M. Gillet, E. Gillet, P. Guaino, *Surface roughness at VO<sub>2</sub>'s transition temperature*, *Surf. Sci.* (2007) doi:10.1016/j.susc.2006.12.081
- 436.** M. B. Sahana, G. N. Subbanna, S. A. Shivashankar, *Nanoribbons of VO<sub>2</sub>(B) and the substrate temperature*, *J. Appl. Phys.* 92, 6495 (2002)
- 437.** Ch. Leroux, G. Nihoul, G. van Tendeloo, *Phys. Rev. B* 57, 5111 (1998)
- 438.** M. Gillet, R. Delamare, E. Gillet, *Eur. Phys. J. D* 34, 291 (2005)
- 439.** S. Santucc, L. Lozzi, E. Maccallin, M. Passacantando, L. Ottariano, *J. Vac. Sci. Technol. A* 19, 1467 (2001)
- 440.** F. C. Frank, *Screw dislocations*, *Discussions Farady Soc.* 5, 48 (1949)
- 441.** R. S. Wagner, W. S. Ellis, *Vapor-Liquid-Solid growth of silicon columns*, *Appl. Phys. Lett.* 4, 89 (1964)
- 442.** E. I. Givargizov, *Understanding the VLS mechanism*, *J. Cryst. Growth* 31, 20 (1975)

443. J. Kikkawa, Y. Ohno, and S. Takeda, *Is there a thermodynamic limit to the diameter of the nanowires?*, Appl. Phys. Lett. 86, 123109-1 (2005)
444. K. Kasuya, T. Ooi, Y. Kojima, and M. Nakao, *Observation of the growth rate of WO<sub>3</sub> nanorods in SEM*, Appl. Phys. Express 1, 034005 (2008)
445. T.J. Trenter, *Solid - liquid- solid synthesis of nanowires*, Science 270, 1791(1995)
446. W. Buhro, *SLS of GaS nanowires*, Advanced Materials for Optics and Electronics 6, 175 (1996)
447. J D Holmes, *TiN wires by supercritical fluid synthesis*, Chem. Eur. J. 9, 2144 (2003)
448. T. Hanrath, B. Korgel, *Synthesis of SiC nanowires by SCFS mechanism*, Adv. Mater. 5, 15 (2003)
449. S. Elliot, *The Physics of Chemistry of Solids*, Wiley, (Chichester, England 2000) pp449-451
450. J. B. Hudson, *Surface Science - An Introduction*, (Butterworth-Heinemann, Boston 1992) pp 51-67
451. T. Y. Tan, N. Li, U. Gosele, *VLS growth mechanism via wire diameter and lengths*, Appl. Phys. Lett. 83, 1199 (2003)
452. Y. Zhang, F. Zhu, J. Zhang, L. Xia, *Nanoscale Res. Lett.* 3, 201 (2008)
453. (a) V. S. Vikhnin, S. Lysenko, A. Rua, F. Fernandez, H. Liu, *Phys. Lett.* 343, 446 (2005), (b) G. Lermann, T. A. Bishop, T. A. Materny, W. Keifer, *Phys. Rev. B* 56, 7469 (1997), (c) V. A. Volodin, M. D. Efremov, V. V. Preobrazhenskii, B. R. Semyagin, V. V. Bolotov, V. Sachkov, *Semiconductors*

34, 61 (2000) [Translated from Fizika I Tekhnika Poluprovodnikov 34, 62 (2000)]

**454.** B. W. Mwakikunga, E. Sideras-Haddad, C. Arendse and A. Forbes, OAtube Nanotechnol. 2, 109 (2009) <http://www.oatube.org/2009/01/bwmwakikunga.html>

**455.** B. W. Mwakikunga, E. Sideras-Haddad, C. Arendse, A. Forbes, P. C. Eklund, T. Malwela, T. K. Hillie, S. Sinha-Ray *VO<sub>2</sub>(B) nanoribbons by ultrasonic spray pyrolysis*, (2009) (unpublished)

**456.** B. W. Mwakikunga, E. Sideras-Haddad, A. Forbes, S. S. Ray, C. Arendse, G. Katumba, *Thermochromism of VO<sub>2</sub> at Nanoscale* To appear in *Chromic Materials, Phenomena and Their Applications* (Ed. P. Somani), Applied Science Innovations Private Limited (ASIPL), Maharashtra, India (2009)

Appendix\_T1 Table showing research in materials synthesized by ultrasonic spray pyrolysis from 1999 to 2008

Final material	Starting Materials	Synthesis parameters ( <i>f</i> , <i>G</i> , <i>t<sub>A</sub></i> , <i>t<sub>R</sub></i> , <i>t<sub>D</sub></i> , <i>T<sub>F</sub></i> , <i>T<sub>A</sub></i> , <i>T<sub>S</sub></i> )*	Refs.
NiO-Ce <sub>0.9</sub> Gd <sub>0.1</sub> O <sub>1.95</sub>	Ce(NO <sub>3</sub> ) <sub>2</sub> ·6H <sub>2</sub> O, Ni(NO <sub>3</sub> ) <sub>2</sub> ·6H <sub>2</sub> O, Gd(NO <sub>3</sub> ) <sub>2</sub> ·6H <sub>2</sub> O	1.65 MHz, N <sub>2</sub> , 1Lmin <sup>-1</sup> , 2 min (t <sub>D</sub> )	[98,145,1588,160]
LiM <sub>0.5</sub> Mn <sub>1.5</sub> O <sub>4-δ</sub>	Li(NO <sub>3</sub> ), Ni(NO <sub>3</sub> ) <sub>2</sub> ·6H <sub>2</sub> O, Mn(NO <sub>3</sub> ) <sub>2</sub> ·4H <sub>2</sub> O	1.7 MHz, air, 10 L min <sup>-1</sup> , 500°C(T <sub>F</sub> )	[99,142,143,200,201,198,236]
LiFe <sub>1-x</sub> M <sub>x</sub> PO <sub>4</sub>	LiNO <sub>3</sub> , FeNO <sub>3</sub> , H <sub>3</sub> PO <sub>4</sub> , Mg(NO <sub>3</sub> ) <sub>2</sub> , C <sub>6</sub> H <sub>8</sub> O <sub>6</sub>	T <sub>F</sub> =450°C, T <sub>A</sub> =700°C	[113,140,154,211]
La <sub>0.6</sub> Sr <sub>0.4</sub> CoO <sub>3-δ</sub>	La, Sr, Co nitrates in dist. H <sub>2</sub> O	1.6MHz, oxygen, T <sub>F</sub> =1000°C	[120]
[Ni <sub>0.4</sub> Co <sub>0.2</sub> Mn <sub>0.4</sub> ]O <sub>4</sub>	Ni, Co, Mn nitrates in dist. H <sub>2</sub> O	1.7MHz, air 10L/mn, t <sub>R</sub> =2s, 500-900°C	[139]
LiMn <sub>1.825</sub> Cr <sub>0.175</sub> O <sub>4</sub>	Li, Mn, Cr nitrates,	1.7MHz, air, 0.5dm <sup>3</sup> /mn, t <sub>R</sub> =5s, 1073K	[122]
LiM <sub>x</sub> MnO <sub>4</sub>	Li, Co, Mn, Al nitrates	1.67MHz, 0.38 m <sup>3</sup> /mn t <sub>R</sub> =1.5s, 900°C	[149,163,166,169]
CoTMPP/C	CO(NO <sub>3</sub> ), tetramethoxyphenylporphyrin-H <sub>2</sub> TMPP	2.4MHz, N <sub>2</sub> , 5dm <sup>3</sup> /mn, 800°C	[123]
In <sub>x</sub> S <sub>y</sub>	InCl <sub>3</sub> + SC(NH <sub>2</sub> ) <sub>2</sub> in ethanol	N <sub>2</sub> , 15Lmin <sup>-1</sup> t <sub>D</sub> =20min, T <sub>S</sub> =380°C	[109]
ZnO:(Al,N)	Zn(CH <sub>3</sub> COO) <sub>2</sub> ·2H <sub>2</sub> O, CH <sub>3</sub> COONH <sub>4</sub> , Al(NO <sub>3</sub> ) <sub>3</sub>	N <sub>2</sub> , Corning 7059, 450°C (T <sub>A</sub> )	[100,127,133,161,159]
ZnO	Zn(NO <sub>3</sub> ) <sub>2</sub> +H <sub>2</sub> O, σ=7.2×10 <sup>-3</sup> Nm <sup>-1</sup> , ρ=1030.3kgm <sup>-3</sup>	1.7 MHz, (2.8 μm droplet)	[101,134,146]
ZnO μ-rods	ZnCl <sub>2</sub> + distilled H <sub>2</sub> O	1.63 MHz, air, 2mLmn <sup>-1</sup> , 100min (t <sub>D</sub> )	[105,126]
Zn(Mg, Cd) <sub>x</sub> O	Zn(CH <sub>3</sub> COO) <sub>2</sub> , Mg(CH <sub>3</sub> COO) <sub>2</sub> , Cd(CH <sub>3</sub> COO) <sub>2</sub>	N <sub>2</sub> , Si(100)	[104,115,135, 153]
ZnO:In	Zn(CH <sub>3</sub> COO) <sub>2</sub> ·2H <sub>2</sub> O, Doping In/Zn=1/5	120 kHz, air, 200 mbar, 370°C (T <sub>S</sub> )	[107,114,115,203]
Zn <sub>1-x</sub> Cd <sub>x</sub> S	ZnCl <sub>2</sub> + dist H <sub>2</sub> O, CdCl <sub>2</sub> ·H <sub>2</sub> O, CS(NH <sub>2</sub> ) <sub>2</sub>	Air, 5 mL min <sup>-1</sup> , 20min (t <sub>D</sub> ), 250°C (T <sub>S</sub> )	[109,118]
ZnO LEDs	Zn(CH <sub>3</sub> COO) <sub>2</sub> , Mg(CH <sub>3</sub> COO) <sub>2</sub> , CH <sub>3</sub> COONH <sub>4</sub> :In	GaAs(100), T <sub>S</sub> =450°C	[114,243]
p:ZnO	Zn(CH <sub>3</sub> COO) <sub>2</sub> , CH <sub>3</sub> COONH <sub>4</sub> , Al(NO <sub>3</sub> ) <sub>3</sub> ·9H <sub>2</sub> O	1.7MHz, T <sub>S</sub> =450°C	[115]
ZnO/Au/Zn/Au	ZnCl <sub>2</sub> , CS(NH <sub>2</sub> ) <sub>2</sub> thiourea	T <sub>S</sub> =490°C	[116]
Zn <sub>1-x</sub> M <sub>x</sub> O	ZnCl <sub>2</sub> +HCl, FeCl <sub>3</sub> , AgNO <sub>3</sub>	1.63MHz, air, 2mLmn <sup>-1</sup> , T <sub>S</sub> =500°C	[124,224]
Zn(Si,Cr) <sub>4</sub> :Mn	TEOS+ Zn, Mn nitrates	1.7MHz, air, 2dm <sup>3</sup> mn <sup>-1</sup> , t <sub>R</sub> =4.8mn, 800°C	[164,212]
TiO <sub>2</sub>	TiO[CH <sub>3</sub> COH=COCH <sub>3</sub> ] <sub>2</sub> , CH <sub>3</sub> OH	1.2MHz, air, 3.5L/m, t <sub>D</sub> =7mn, 450°C	[110,125,167,173,201]
SrTiO <sub>3</sub> :Pr,Al	Sr,Al,Pr,TiO nitrates, acac	1.67MHz, air 0.5dm <sup>3</sup> /mn, 1300°C	[206]
Co <sub>3</sub> O <sub>4</sub> ,CuO,NiO	Co, Cu, Ni nitrates, C <sub>6</sub> H <sub>8</sub> O <sub>7</sub> ·H <sub>2</sub> O	1.7MHz, air, 500°C	[111]
ZrO <sub>2</sub> :Ba,Y	Zr, Ba,Y nitrates, chlorides in dist. H <sub>2</sub> O	2.6MHz, O <sub>2</sub> , 150dm <sup>3</sup> /h, 800-1200°C	[129,215,226]
ZrO <sub>2</sub> ,CeO <sub>2</sub> ,YSZ	Zr, Y, Ce acetate hydrates	1.65MHz, air 20L/mn, t <sub>R</sub> =3.2s, 650°C	[231,236,244,236]
AgI	AgNO <sub>3</sub> , KI	1.7 MHz	[103,131]
F:CdO	Cd-acetate, NH <sub>4</sub> F	58 kHz, N <sub>2</sub> , 1mLmin <sup>-1</sup> , 15min (t <sub>D</sub> )	[106,117]
γ-Fe <sub>2</sub> O <sub>3</sub> /MgO	Mg(NO <sub>3</sub> ) <sub>2</sub> ·6H <sub>2</sub> O, Fe(NO <sub>3</sub> ) <sub>2</sub> ·7H <sub>2</sub> O	3L/mn, T <sub>F</sub> =500-800°C	[119]
Ca(PO <sub>4</sub> ) <sub>4</sub> (OH)2-Hδap	Ca(NO <sub>3</sub> ) <sub>2</sub> ·4H <sub>2</sub> O, H <sub>3</sub> PO <sub>4</sub> , H <sub>2</sub> O, NaNO <sub>3</sub>	1.6MHz, Ar, 3L/m, 500-700°C	[121,129]
VO <sub>2</sub>	NH <sub>4</sub> VO <sub>3</sub> +VCL <sub>3</sub> in dist. H <sub>2</sub> O	1.7MHz, 11L/mn, t <sub>D</sub> =30mn, 500-700°C	[131]
Co nanoparticles	Cemented W carbide scrap	800kHz, H <sub>2</sub> 12mL/mn, 700-900°C	[136]
SnO <sub>2</sub> :Sb,F (TCO)	Sn, Sb chlorides in alcohol, NH <sub>4</sub> F	O <sub>2</sub> & N <sub>2</sub> 200cm <sup>3</sup> /mn, t <sub>D</sub> =60mn 500°C	[141,169,210,232]
Al <sub>2</sub> O <sub>3</sub>	Al acetylacetonate in methanol + H <sub>2</sub> O	1.5L/mn, t <sub>D</sub> =14mn, 375°C	[144]
CeO <sub>2</sub>	Ce nitrate	1.7MHz, air 40L/mn, 600-1000°C	[147,220]
In <sub>2</sub> O <sub>3</sub> -ZnO	In acetate + Zn acetate in alcohol	O <sub>2</sub> 600cm <sup>3</sup> /mn, t <sub>D</sub> =90mn, 550°C	[148,162]
GdCo <sub>1-x</sub> Cu <sub>x</sub> O <sub>3-δ</sub>	Gd,Cu,Co nitrate hydrates	1.7Mhz, t <sub>R</sub> =3s, T <sub>F</sub> =900°C	[150]
γ-Gd <sub>2</sub> S <sub>3</sub>	GdCl <sub>3</sub> , CS(NH <sub>2</sub> ) <sub>2</sub> thiourea	N <sub>2</sub> 2-3L.mn <sup>-1</sup> , as-USP, 280-350°C	[151]

\* *f* = frequency of nebulizer, *G* = type of carrier gas, *t<sub>A</sub>* = annealing period of time, *t<sub>R</sub>* = residence time, *t<sub>D</sub>* = period of deposition, *T<sub>F</sub>* = furnace temperature, *T<sub>A</sub>* = annealing temperature, *T<sub>S</sub>* = substrate temperature

Final material	Starting Materials	Synthesis parameters ( $f, G, t_A, t_R, t_D, T_F, T_A, T_S$ ) <sup>*</sup>	Refs.
WPA	29-tungstophosphoric acid	1.7MHz, N <sub>2</sub> 0.022L/mn, 800°C	[152]
CdS	CdCl <sub>2</sub> , (NH <sub>2</sub> ) <sub>2</sub> CS thiourea	N <sub>2</sub> 5mL/mn, T <sub>S</sub> =473-623K	[155,221,239]
BiSI rods	BiCl <sub>3</sub> , CS(NH <sub>2</sub> ) <sub>2</sub> , I in ethanol	N <sub>2</sub> 2.5L/mn, as-USP, 320°C	[156]
Bi <sub>2</sub> S <sub>3</sub>	Bi(NO <sub>3</sub> ) <sub>3</sub> ·5H <sub>2</sub> O, CS(NH <sub>2</sub> ) <sub>2</sub> , H <sub>2</sub> O	N <sub>2</sub> 200L/hr, asy-USP, 450°C	[204]
Silica	Na <sub>2</sub> O·3SiO <sub>2</sub> ·5H <sub>2</sub> O, H <sub>3</sub> BO <sub>3</sub> , (NH <sub>2</sub> ) <sub>2</sub> CO	1.67MHz, air 5-25L/mn 1000°C	[265]
NiO	NiNO <sub>3</sub> ·6H <sub>2</sub> O, ethanol	Air 5L/mn, t <sub>R</sub> =5s as-USP, 400°C	[203]
Al <sub>2</sub> O <sub>3</sub>	Al acetylacetonate, MeOH, acetic acid	t <sub>D</sub> =120mn,240-440°C	[207,227]
Fe(III) oxide	Fe acetylacetonate, ethanol, H <sub>2</sub> O	air, 4-9L/mn,asy-USP	[213]
Eu <sub>2</sub> O <sub>3</sub>	Eu Acac [Eu(CH <sub>3</sub> COCHCOCH <sub>3</sub> ) <sub>3</sub> ]	Air 7L/mn asy-USP, 550°C	[213]
Y <sub>2</sub> O <sub>3</sub> :Eu	Y,Eu,Ce nitrates	2L/mn,500-600°C, T <sub>A</sub> =900°C	[229]
La <sub>2</sub> O <sub>3</sub>	La(CH <sub>3</sub> COCHCOCH <sub>3</sub> ) <sub>3</sub>	Air, 6-7Lmn, asy-USP, 550°C	[217]
WO <sub>3</sub>	H <sub>26</sub> N <sub>6</sub> O <sub>41</sub> W <sub>12</sub> in dist. H <sub>2</sub> O	40kHz, Argon 1L/mn with urea	[219,222]
Y <sub>0.9</sub> Ba <sub>2</sub> Cu <sub>0.4</sub> O	Y(NO <sub>3</sub> ) <sub>3</sub> , Ba(NO <sub>3</sub> ) <sub>2</sub> , Cu(NO <sub>3</sub> ) <sub>2</sub> , dist. H <sub>2</sub> O	700-900-500°C, 90 mins	[213,137,139,198,199,209]
Bi <sub>2</sub> Sr <sub>2</sub> CaCu <sub>2</sub> O <sub>x</sub>	Bi <sub>2</sub> O <sub>3</sub> +2SrCO <sub>3</sub> +CaCO <sub>3</sub> +2CuO	1.5MHz, 500-900°C	[139,219]
Cd:Tl-2223	Ba,Ca,Cd,Cu nitrates, H <sub>2</sub> O	T <sub>S</sub> =150°C, T <sub>A</sub> =890°C	[233,237]
La <sub>1-x</sub> Sr <sub>x</sub> Ga <sub>1-y</sub> Mg <sub>y</sub> O	La,Sr,Ga oxides, carbonates or nitrates	T <sub>F</sub> =1173K, T <sub>A</sub> =1400°C	[239]
Ba-Ca-Cu-O	Ba,Ca,Cu nitrates	t <sub>D</sub> =5min, T <sub>S</sub> =150°C, T <sub>A</sub> =450°C	[243]
YAG(Y <sub>3</sub> Al <sub>5</sub> O <sub>12</sub> ):Ce	Y, Al, Ce nitrates	1.75MHz, N <sub>2</sub> 2L/mn, 900°C	[223,230]
Mullite (AlTiO <sub>x</sub> )	TEOS in ethanol, aq. Al nitrates in HNO <sub>3</sub>	30-40dm <sup>3</sup> /h, 900°C	[229,234,235,245]
TiO <sub>2</sub>	Ti(i-C <sub>3</sub> H <sub>7</sub> O <sub>4</sub> ) <sub>4</sub> , C <sub>4</sub> H <sub>9</sub> OC <sub>2</sub> H <sub>4</sub> OH	ESD-USP, T <sub>F</sub> =250°C	[236]
Cu <sub>1.1</sub> Mn <sub>1.9</sub> O <sub>4</sub> spinel	Cu, Mn nitrates	2MHz, N <sub>2</sub> 5-10L/mn, 725-1200K	[241]
RuO <sub>2</sub>	RuCl <sub>3</sub> , ethanol, H <sub>2</sub> O	40kHz, 1mL/mn, T <sub>S</sub> =190°C	[240]

\*  $f$  = frequency of nebulizer,  $G$  = type of carrier gas,  $t_A$  = annealing period of time,  $t_R$  = residence time,  $t_D$  = period of deposition,  $T_F$  = furnace temperature,  $T_A$  = annealing temperature,  $T_S$  = substrate temperature

Appendix T2: List by year of materials synthesized by laser pyrolysis from 1974

Year	Articles/year	Materials	References
1974	1		294
1975	1		295
1977	1		
1978	2		
1983	3		
1984	1	Light olefins	305
1987	1	Graphite rods	306
1989	1	Cr <sub>2</sub> O <sub>3</sub>	307
1990			
1991	2	C: Fe <sub>x</sub> C <sub>y</sub> particles Diamond	309,310
1992	2	Fe and Fe/C Fe	311,312
1993	2	Fe α-Fe, Fe <sub>3</sub> C, Fe <sub>7</sub> C <sub>3</sub>	313
1994	1	Si	314,315
1995	5	Si-nitride C blacks Naphtha & MoN <sub>2</sub> Rb:MoS <sub>2</sub>	316-320
1996	1	Si oxides	321
1997	5	fullerenes nanopowders carbon nitride	322-325
1998	6	Hydrocarbons, Si, Fe <sub>x</sub> O <sub>y</sub> , Fullerene /soot Ta:TiO <sub>2</sub> , SiCN	325-330

Year	Articles/year	Materials	References
1999	5	Carbon nitride Fullerenes Fe <sub>x</sub> C <sub>y</sub> & Fe	SiC 331,333,335 332,334
2000	9	Si NPs Fe <sub>x</sub> O <sub>y</sub> Fullerene	Fullerenes Fullerene Metal NPs Si & Fe NP 336 337 338 339 340 341 342 343 344
2001	6	SiC SiC(B)	Fe NCs C NPS Maghemites SiQDs:Diamond 345 346 347 349 349 350 351
2002	5	Fe-Si NP NPs	SiC Maghemites 351 352 353 354 355
2003	4	Si/C/N Fe <sub>x</sub> O <sub>y</sub>	Fullerenes Fe:C 356 357 358 359
2004	8	Fe:C C	Te films Fe Fullerenes Maghemite 360 361 362 363 364 365 366 367
2005	10	Co CN SiC,TiC Fe:Fe <sub>x</sub> O <sub>y</sub> coreshell	Ti:γFe <sub>x</sub> O <sub>y</sub> Fe Fe:Graphite coreshells Si NCs Fe/FeC/C coreshells Si 368 369 370 371 372 373 374 375 376
2006	16	TiC PAHs NPs SiCN Mag.	SnTe general simulation simulation SiC General Fe <sub>3</sub> C Fe <sub>x</sub> C <sub>y</sub> Ncatalysts M:polymer Fe:Fe <sub>x</sub> O <sub>y</sub> coreshells 377 378 379 380 381 382 383 384 385 386 387 388 389 390 391
2007	13	Si NCs Fe Fe <sub>3</sub> C Fe:py CS Nano C	Fe/Fe <sub>2</sub> O <sub>3</sub> /p TiO <sub>2</sub> C:Fe NPs SiC,TiC,ZrC Maghemite C TiO <sub>2</sub> 392 393 394 395 396 397 398 399 400 401 402 403 404
2008	3	General	WO <sub>3</sub> NWs WO <sub>3</sub> NWs 405 40 43





## First synthesis of vanadium dioxide by ultrasonic nebula-spray pyrolysis

Bonex Wakufwa Mwakikunga<sup>a,\*</sup>, Elias Sideras-Haddad<sup>a</sup>, Malik Maaza<sup>b</sup>

<sup>a</sup> School of Physics, University of the Witwatersrand, Private Bag X3, P.O. Wits, Johannesburg, Gauteng 2050, South Africa

<sup>b</sup> iThemba Labs, P.O. Box 722, Somerset West 7129, Cape Town, South Africa

Received 3 June 2005; accepted 12 October 2005

Available online 19 January 2006

### Abstract

Vanadium dioxide synthesis is a special problem from any precursor material due to the multi-valence nature of vanadium oxides and the fact that, among these oxides, VO<sub>2</sub> is one of the most unstable of them. Its synthesis therefore must be done under properly controlled conditions. This paper reports on the results of the production of the sub-micrometer structured VO<sub>2</sub> thin films for the first time by the ultrasonic nebula-spray pyrolysis from the precursor vanadium tri-chloride in an aqueous solution of 0.085 M ammonium meta-vanadate. The optimized flow rate of the argon carrier gas was 11 ml min<sup>-1</sup> and VO<sub>2</sub> was obtained at deposition temperature well above 600 °C. Infrared switching confirms the VO<sub>2</sub> transition temperature in the neighborhood of 60 °C for samples prepared under argon whereas, those prepared under oxygen show a drastic shift in transition temperature to the neighborhood of room temperature (23 °C). © 2005 Elsevier B.V. All rights reserved.

PACS: 81.05.Z

Keywords: Vanadium dioxide; Ultrasonic spray pyrolysis; Raman; Transition; Thermo-chromism

### 1. Introduction

Thermo-chromic materials are characterized by a semiconductor-to-metal transition occurring from a reversible change in their crystalline structure as a function of the temperature. Along with a change in optical properties are also electronic transitions evidenced by a change in electrical resistivity. This change has been observed in transition-metal oxides [1,2] such as Ti<sub>2</sub>O<sub>3</sub>, Fe<sub>3</sub>O<sub>4</sub>, and Mo<sub>9</sub>O<sub>26</sub> and in several magneli phases of vanadium oxide, V<sub>n</sub>O<sub>2n-1</sub>. Among them, VO<sub>2</sub> has received the most attention because of the large reversible change of electric, magnetic and optical properties at temperatures around 70 °C [3].

During the semiconductor-to-metal transition, the optical properties of vanadium dioxide are characterized by a sharp decrease in optical transmission in the infrared spectrum. This is coupled with an increase in its reflectivity.

Because of this anomalous behaviour, vanadium dioxide has been presented as an attractive thin film material for electrical or optical switches, optical storage, laser protection, and solar energy control for windows in space satellites.

The transition temperature of vanadium dioxide of 70 °C may be decreased by the addition of high-valent transition metals such as niobium, molybdenum or tungsten. Trivalent cations (chromium and aluminium) increase the transition temperature. The hysteresis profile associated with the transition depends on the microstructure and crystallinity of the sample.

Since the discovery of the VO<sub>2</sub> semiconductor to metal transition by Morin in 1959 [3] VO<sub>2</sub> has been a subject of numerous experimental and theoretical studies. In the first-order [3] phase transition of VO<sub>2</sub>, the material undergoes a reversible change from a tetragonal rutile structure phase, space group *P4<sub>2</sub>/mnm* with typical lattice constants  $a = 4.5546 \text{ \AA}$  and  $c = 2.8514 \text{ \AA}$ , at higher temperature to a monoclinic structure, space group *C2/m* with lattice constants  $a = 12.09 \text{ \AA}$ ,  $b = 3.702 \text{ \AA}$ ,  $6.433 \text{ \AA}$  and  $\beta = 106.6^\circ$ ,

\* Corresponding author.

E-mail address: bonex\_mwakikunga@yahoo.com (B.W. Mwakikunga).

below the phase transition temperature [4]. These structural characteristics led Goodenough [5] to propose a model of the electronic structure based on the molecular field theory that has accounted for some properties of VO<sub>2</sub> metallic and semiconducting phases [6]. This model has subsequently undergone further improvements by incorporating electron–electron correlations [7] and electron–phonon interactions.

Because of the ability to change the transition temperature by doping, Lee et al. [8] and more recently Jin et al. [9], suggested that tungsten doped vanadium dioxide can be used in energy efficient windows. These smart windows or electro-chromic displays find special applications in the architectural, automotive and aerospace sectors [11]. Roach [11] pointed out that, due to the changes in reflectivity during the phase transition, VO<sub>2</sub> films can be used as a kind of optical disc medium and demonstrate holographic storage. Bit recording on VO<sub>2</sub> films using a near-infrared laser was demonstrated [12]; stability during long-term storage and over 10<sup>8</sup> time cycles of write and erase were achieved without degradation. Switching time of about 30 ns and writing energy of the order of a few mJ/cm<sup>2</sup> were reported [13]. Bit density has been estimated to be 350 bits/mm. Such low threshold recording energy and erase-re-write abilities encourage the use of VO<sub>2</sub> films as a recording medium [14]. More recently, the use of VO<sub>2</sub> thin films was suggested in ultra-fast optical switching devices. The high-temperature metallic state attained in 5 ps by using femto-second laser excitation at 780 nm was reported [15]. In summary, vanadium dioxide is an interesting candidate for modern applications of active thin films in optical or electric [16] switches.

VO<sub>2</sub> has been prepared by vapour transport method [17], ion implantation [18], hydrothermal technique [19] for nano-wires and nano-belts; r.f. sputtering [20,21], sol gel technique [22] and pulsed laser deposition [23] for thin films. In this article, synthesis for the first time of micro-structured thin films of VO<sub>2</sub> by ultrasonic spray pyrolysis process is reported. The only work that precedes this work was on V<sub>2</sub>O<sub>5</sub> by spray pyrolysis by Bouzidi et al. [24]. V<sub>2</sub>O<sub>5</sub> is the most stable of vanadium oxides and this is the initial candidate that is present in most synthesis processing. To obtain VO<sub>2</sub>, one of the most unstable oxides, controlled conditions are required. The present article reports on the work geared to obtaining VO<sub>2</sub> with optimized conditions in ultrasonic spray pyrolysis process.

## 2. Experimental

A precursor solution of ammonium meta-vanadate mixed with vanadium tri-chloride, NH<sub>4</sub>VO<sub>3</sub> + VCl<sub>3</sub> (coded AMVC) was prepared. The AMV was a whitish yellowish powder with molecular weight of 116.98, density of 2.326 g cm<sup>-3</sup> and a melting temperature of 200 °C. Surface tension of the precursor solution was measured using the capillary rise method. A scoop weighing 6.1 g of AMV and was dissolved in 600 ml of distilled water and mixed

well using a magnetic stirrer on a hot plate at around 70 °C for about 3 h. The so-made solution was then decanted into the container that was housing the ultrasonic nebulizer operating at a frequency of 1.7 MHz as illustrated in the schematic diagram of Fig. 1. Substrate mate-

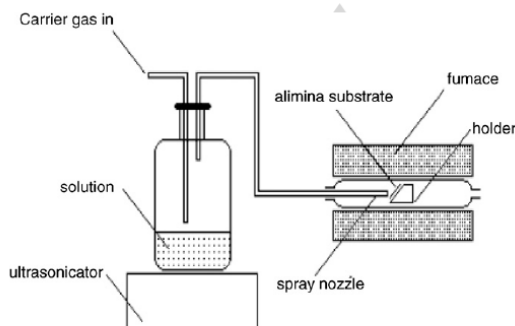


Fig. 1. A diagrammatic layout of a typical set-up of the ultrasonic nebulizer spray pyrolysis technique.

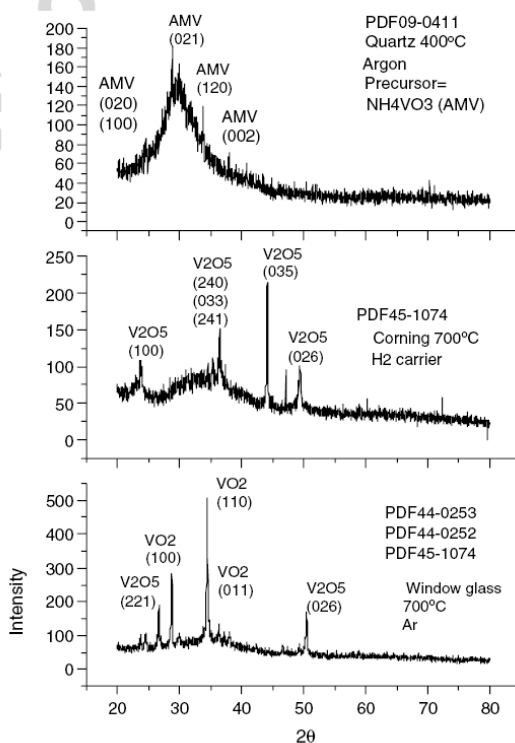


Fig. 2. Typical X-ray spectra of VO<sub>2</sub> under different synthesis conditions—carrier gas type, carrier gas flow rate, substrate type, substrate temperature.

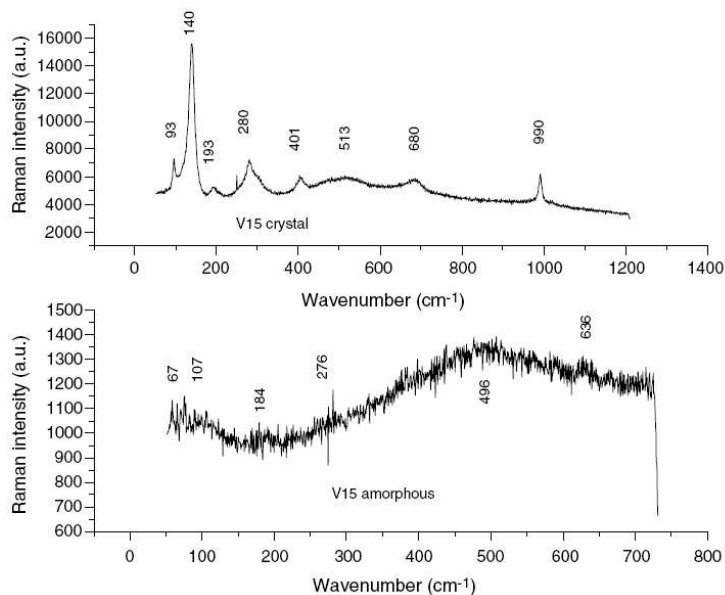


Fig. 3. Typical Raman spectra for crystalline islands (above) and the rest of the amorphous film of powder (below) of  $\text{VO}_2$ .

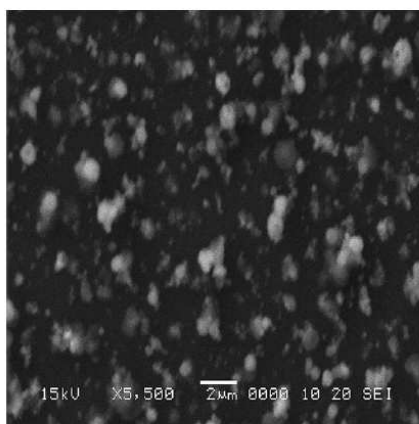


Fig. 4. A typical scanning electron micrograph of the  $\text{VO}_2$  on a Corning glass substrate shows the morphology of the surface of these samples.

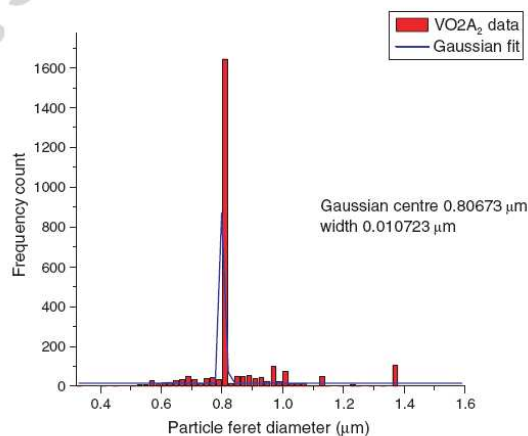


Fig. 5. Size distribution of the  $\text{VO}_2$  image in Fig. 4 using Image Tool™ reveals the grains are preferentially spherical with a modal diameter of 800 nm.

rials underwent the usual rigorous cleaning procedure of detergent–ultrasonic bath–alcohol–ultrasonic bath until the substrates qualified for deposition. Depositions were done on quartz, borosilicate and Corning glass substrates, at furnace temperatures varied from 100 to 700 °C, at various substrate positions in the furnace and using oxygen, argon and hydrogen for carrier gases at flow rates varied from 18 to 8 ml min<sup>-1</sup>. The optimum conditions for obtaining  $\text{VO}_2$  by ultrasonic spray pyrolysis were found

to be as follows: substrate temperature of 500–700 °C, carrier gas type of argon, carrier gas flow rate of 11 ml min<sup>-1</sup> and system pressure of 4–10 N cm<sup>-2</sup> and substrates of either borosilicate window glass or Corning glass.

Structural studies of the as-deposited nano-particles were done using a Powder X-ray Diffractometer with a  $\text{Cu K}_\alpha$  wavelength of 0.154184 nm; optical properties of transmittance or absorbance were conducted using a Var-

ian Cary UV–Vis–IR spectrophotometer in the wavelength range from 200 nm to 3000 nm. Morphology studies by scanning electron microscopy (SEM) were carried out using a Jeol JSM-5600 SEM microscope. Because the SEM illuminates them with electrons, the samples also have to be made to conduct electricity. To improve the conductivity of the VO<sub>2</sub>, the samples were coated with a thin film of carbon. In order to unveil the phonon behaviour and the grain size distribution in the so-synthesized VO<sub>2</sub>, Raman spectroscopy was carried out using a Jobin-Yvon T64000 Raman spectrograph with a 514.5 nm line from an argon ion laser.

### 3. Results and discussion

X-ray diffraction revealed very prominent peaks belonging to VO<sub>2</sub> crystal faces such as (100), (110) and (011) in a sample prepared on window glass at 700 °C as illustrated in Fig. 2. This suggests that VO<sub>2</sub> crystallites are randomly ordered rather than preferring some direction. Hydrogen carrier gas tends to bring other phases of VO<sub>2</sub>. In all cases in this group of samples, the presence of other phases inhibits the manifestation of the VO<sub>2</sub> properties hence the switching factor so observed. In order to characterize the morphology of the particulates and crystallites on the so-obtained samples, the Scherrer equation was used to estimate the particulate sizes. –5.2186 nm as mean crystallite diameter was obtained.

A number of authors have published their Raman study findings in various forms of VO<sub>2</sub> whether crystalline, amorphous or single crystals. Raman intensities are much higher from single crystals. However, not much has been done on micro- and nano-sized powders due to the weakness of the Raman signal from these samples. In the present work, a considerable amount of intensity of the incident laser beam had to be set to get some Raman signal from the samples. At about 200× magnification, one could see that these VO<sub>2</sub> samples were amorphous mixed with islands of single crystals. Fig. 3 illustrates the typical Raman spectra (top) from the islands of single crystals and (bottom) from the amorphous nano-sized powder background. A scanning electron micrograph of 5500× magnification of the same sample is presented in Fig. 4. Image Tool™ image analysis software was used to analyze the surface morphology of the SEM images for a size distribution pattern of the grains and islands of single crystals on the thin films. The size distribution chart given in Fig. 5 shows that the grains are uniformly structured with almost all of them having a spherical ferret diameter of around 800 nm. Table 1 presents the previous alongside the present findings on Raman shifts and phonon frequencies in VO<sub>2</sub>. In this table it can be seen that, apart from the fact that the present results account for a wider range of Raman shift, the phonon frequencies agree very well with previous findings.

UV–Vis–IR transmittance spectroscopy is supposedly useful in revealing the switching properties of VO<sub>2</sub> from

Table 1  
An outline of previous and present findings of Raman phonon modes in VO<sub>2</sub>

Petrov et al.	Shilbe	Aronov et al. (100 K)	Srivastava and Chase (300 K)	Vikhnin et al. (300 K)	Pan et al. (300 K)	Present work V8 (300 K)	Present work V9 (300 K)	Present work V10 (300 K)
							58 67	93
						119	104	
142 –	149 –	149 –		144 –		141	153	140
191 Ag	199 Ag	200 Ag	208 B1g	194 Ag	192 Ag	204		193
221 Ag	225 Ag	226 Ag	236	226 Ag	225 Ag			
258 Ag	259 Bg	259 Ag		260 Ag	258 Bg			
	265 Bg				265 Bg	264		
308 Ag	313 Ag	313 Ag		311 Ag	308 Ag	304	307	280
335 Ag	339 Bg	340 Ag		337 Ag	339 Bg			
392 Ag	392 Ag	392 Ag		389 Ag	392 Ag			
	395 Bg				395 Bg			
	444 Bg	436 Ag	450 E1g	438 Ag	444 Bg	424	413	401
	453 Bg				453 Bg		444	
	489 Bg			493 Ag	489 Bg	484		
497 Ag	503 Ag	501 Ag			503 Ag	504	501	513
						564		
594 Bg	595 Ag	594 Bg		595 Ag	585 Ag			583
612 Ag	618 Ag	620 Ag		615 Ag	618 Ag		612	613
	670 Bg		655 A1g	627 Ag		627		684
					650 Bg	676		691
	830 Bg				825 Bg		693	
			850 B2g					995

the room temperature monoclinic structure to a tetragonal rutile-type structure at a temperature above 68 °C. Very small amount of switching was observed in samples prepared from a precursor of  $\text{NH}_4\text{VO}_3$  with carrier gases of argon or hydrogen or oxygen. The samples prepared using  $\text{NH}_4\text{VO}_3$  enriched with  $\text{VCl}_3$  had a remarkable switching improvement when transmittance was measured at different ambient temperatures. Typical switching under varying ambient temperature was observed by measuring transmittance at wavelengths in the range 200 nm to 3000 nm when the sample was being cooled (Fig. 6) and when it was being heated (Fig. 7). The sample synthesized at 600 °C under argon shows a transition temperature around 65 °C and a switching temperature resolution or a hysteresis width (HW) equal to 20 °C (as shown in the hysteresis plot in Fig. 8) not only reveals the crystal quality but also signifies the broadening possibly due to particulate size. The switching contrast is significantly reduced in the sample synthe-

sized at 700 °C, shown in Fig. 9, as expected, where the particulate size is supposedly larger than on the preceding sample. This sample shows an average resolution of about 7 °C. One can also easily see the relationship between switching factor of a sample and the temperature at which it was synthesized. The sample prepared at 700 °C under the carrier gas of oxygen showed a remarkable shift in transition temperature to about 23 °C as presented in Fig. 10. This confirms the observation that changing the oxygen to vanadium ratio sensitively affects the transition temperature of vanadium dioxide as shown in the plot given in Fig. 11. This shows that impregnating  $\text{VO}_2$  with dopants

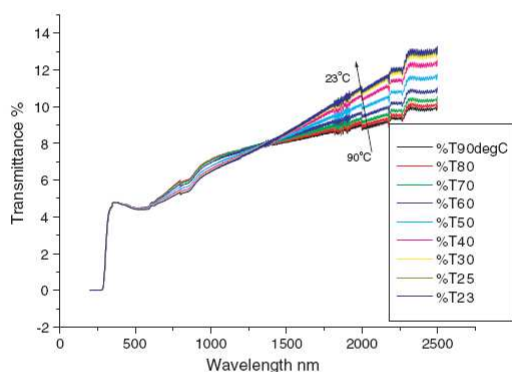


Fig. 6. Typical wavelength-related transmittance with varying ambient temperature on the  $\text{VO}_2$  sample. This was a cooling cycle.

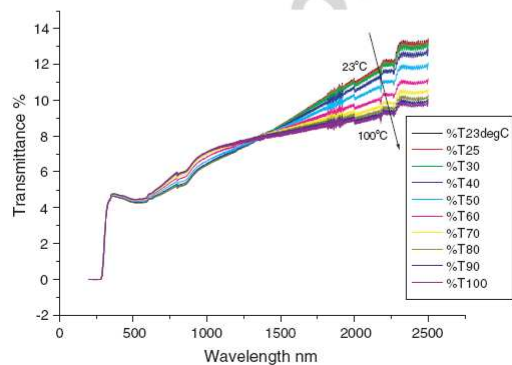


Fig. 7. Typical wavelength-related transmittance with varying ambient temperature on the  $\text{VO}_2$  sample. This was a heating cycle.

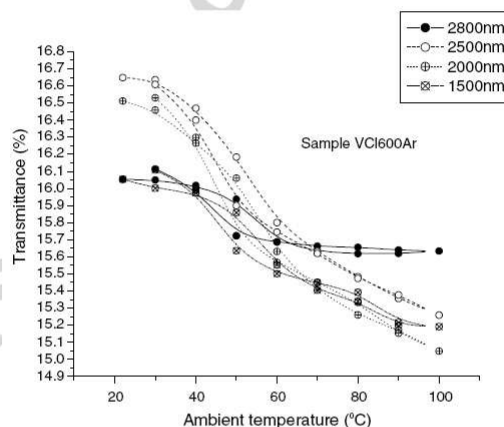


Fig. 8. Transmittance versus ambient temperature at different optical wavelengths for a  $\text{VO}_2$  sample prepared at 600 °C in an argon environment.

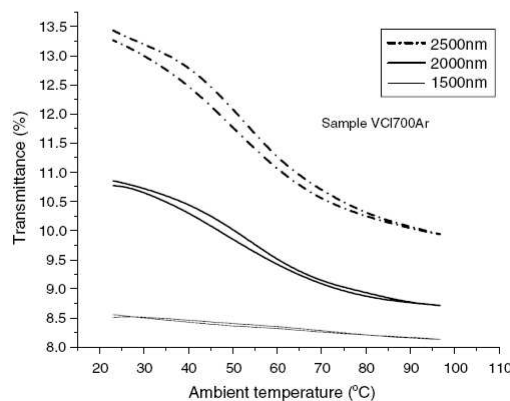


Fig. 9. Transmittance versus ambient temperature at different optical wavelengths for a  $\text{VO}_2$  sample prepared at 700 °C in an argon environment.

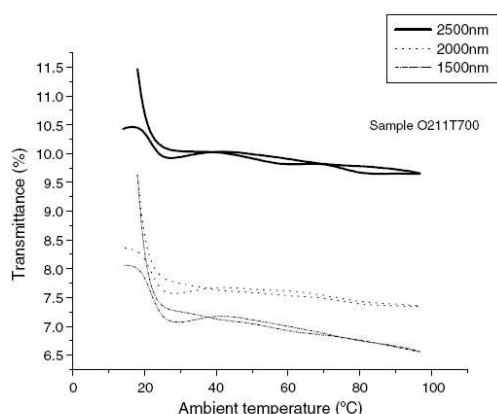


Fig. 10. Transmittance versus ambient temperature at different optical wavelengths for a  $\text{VO}_2$  sample prepared at 700 °C in an oxygen environment.

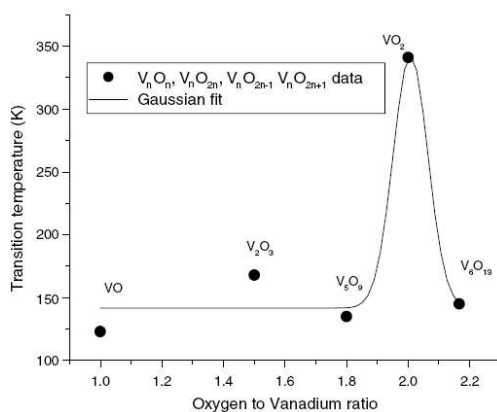


Fig. 11. Transition temperatures of a selected number of vanadium oxide phases as function of the oxygen to vanadium ratio. A Gaussian fit shows the exclusivity of  $\text{VO}_2$  in comparison with the other phases.

is not the only route to reducing the transition temperature of  $\text{VO}_2$ . In this case, the findings suggest that keeping the oxygen to vanadium ratio in the vicinity of 1.93 or 2.05 should bring the transition temperature to room temperature. In both routes, this reduction of the transition temperature apparently comes at the expense of the switching quality and transmittance or reflectance contrast.

#### 4. Conclusion

Vanadium dioxide is difficult to obtain because of its instability among the many phases of vanadium oxides.

This article has presented the synthesis of  $\text{VO}_2$  by ultrasonic spray pyrolysis for the first time. A precursor solution of ammonium meta-vanadate enriched with vanadium tri-chloride was found to be one of the most suitable starting solutions from which droplets were generated by an ultra-sonicator operated at 1.7 MHz. The optimum conditions for obtaining  $\text{VO}_2$  have been presented. X-ray characterization shows  $\text{VO}_2$  crystals with randomized rather than preferential ordering of the crystal faces. Raman spectra of the  $\text{VO}_2$  materials confirm the  $\text{VO}_2$  signatures obtained from previous studies. The size distribution by scanning electron microscopy shows preferentially spherical grains with modal ferret diameters of around 800 nm. Infrared switching confirms the  $\text{VO}_2$  transition temperature in the neighborhood of 65 °C for samples prepared under argon whereas those prepared under oxygen show a drastic shift in transition temperature to the neighborhood of room temperature. In the latter case, transmittance contrast and, hence, switching quality is heavily hampered.

#### Acknowledgements

Sponsorship from the Japanese Government through the Joint Japan/World Bank Graduate Scholarship Programme (JJWBGSP), Washington, DC, USA is highly appreciated. The support of the Schools of Physics at the University of the Witwatersrand and the University of Johannesburg in South Africa is also acknowledged.

#### References

- [1] N.F. Mott, Rev. Modern Phys. 40 (4) (1968) 677.
- [2] D. Adler, Rev. Modern Phys. 40 (4) (1968) 714.
- [3] F.J. Morin, Phys. Rev. Lett. 3 (1959) 34.
- [4] Z. Iqbal, F.J. Owens (Eds.), Vibrational Spectroscopy of Phase Transitions, Academic, Orlando, FL, 1984.
- [5] J.B. Goodenough, J. Solid State Chem. 3 (1971) 490.
- [6] S. Shin, S. Suga, M. Taniguchi, M. Fujisawa, H. Kansaki, A. Fujimori, H. Damon, Y. Ueda, K. Kosuge, S. Kachi, Phys. Rev. B41 (1990) 4993.
- [7] D. Paquet, P. Leroux-Hugon, Phys. Rev. B22 (1980) 5284.
- [8] J.C. Lee, G.V. Jorgenson, R.J. Lin, Proc. SPIE 692 (1986) 2.
- [9] P. Jin, M. Tazawa, T. Miki, S. Tanemura, The 3rd IUMRS-ICAM, Int. Conf. On Advanced Materials, 31 August–4 September 1993, Tokyo, Paper No. KP 57 in Ecomaterial session.
- [10] S.M. Babulanam, T.S. Eriksson, G.A. Niklasson, C.G. Granqvist, Solar Energy Mater. 16 (5) (1987) 347; K. Kuwabara, S. Ichikawa, K. Sugiyama, J. Electrochem. Soc. 135 (1988) 2432.
- [11] W.R. Roach, Appl. Phys. Lett. 19 (1971) 453.
- [12] A.W. Smith, Appl. Phys. Lett. 23 (1973) 437.
- [13] D.D. Eden, Opt. Eng. 20 (1981) 337.
- [14] M. Fukuma, S. Zembutsu, S. Miyazawa, Appl. Opt. 22 (2) (1983) 265.
- [15] M.F. Becker, A.B. Buckman, R.M. Walsler, T. Lépine, P. Georges, A. Brun, Appl. Phys. Lett. 65 (12) (1994) 1507.
- [16] G. Guzman, F. Beteille, R. Morineau, J. Livage, J. Mater. Chem. 6 (1996) 505.
- [17] Beth S. Guiton, Qian Gu, Amy L. Prieto, Mark S. Gudiksen, Hongkun Park, J. Am. Chem. Soc. 127 (2005) 498.

- [18] R. Lopez, L.A. Boatner, T.E. Haynes, L.C. Feldman, R. Hugland, *J. Appl. Phys.* 92 (2002) 4031.
- [19] J. Liu, Y. Li, T. Wang, D. Yu, *Angew. Chem.* 116 (2004) 5158.
- [20] R.T. Kivaisi, M. Samiji, *Solar Energy Mater. Solar Cells* 57 (1999) 141.
- [21] E.E. Chain, *J. Vac. Sci. Technol. A* 4 (1986) 432.
- [22] An excellent article on VO<sub>2</sub> as an infrared active coating by G. Guzman can be accessed from: <<http://www.solgel.com/articles/August00/thermo/Guzman.htm>>.
- [23] D.H. Kim, H.S. Kwok, *Appl. Phys. Lett.* 65 (1994) 3188.
- [24] A. Bouizidi, N. Benramdane, A. Nakrela, C. Mathieu, B. Khelifa, R. Desfeux, A. Da Costa, *Mater. Sci. Eng. B* 95 (2002) 141.



## WO<sub>3</sub> Nano-Spheres into W<sub>18</sub>O<sub>49</sub> One-Dimensional Nano-Structures Through Thermal Annealing

B. W. Mwakikunga<sup>1,2,3,\*</sup>, E. Sideras-Haddad<sup>2</sup>, C. Arendse<sup>1,\*</sup>,  
M. J. Witcomb<sup>4</sup>, and A. Forbes<sup>5,6</sup>

<sup>1</sup>CSIR National Centre for Nano-Structured Materials, P.O. Box 395, Pretoria 0001, South Africa

<sup>2</sup>School of Physics, University of the Witwatersrand, Private Bag 3, WITS 2050, South Africa

<sup>3</sup>Department of Physics and Biochemical Sciences, University of Malawi, The Polytechnic,  
Private Bag 303, Chichiri, Blantyre 3, Malawi

<sup>4</sup>DST/NRF Centre of Excellence in Strong Materials and Electron Microscope Unit,  
University of the Witwatersrand, Private Bag 3, WITS 2050, South Africa

<sup>5</sup>CSIR National Laser Centre, P.O. Box 395, Pretoria 0001, South Africa

<sup>6</sup>School of Physics, University of Kwazulu-Natal, Private Bag X54001, Durban 4000, South Africa

We elaborate the size controlled synthesis of nano-spheres and nano-crystals of WO<sub>3</sub> by ultrasonic spray pyrolysis. The as-deposited particles are predominantly spherical in shape and tend to exhibit less agglomeration and a decrease in diameter as the process temperature is increased. Characterization was carried out using transmission (TEM) and scanning (SEM) electron microscopy, energy dispersive X-ray spectroscopy (EDS) and X-ray diffraction (XRD). One-dimensional nano-structures with the highest yield of WO<sub>x</sub> nano-wires were observed in a sample synthesized at 500 °C but only after thermal annealing of this sample at 500 °C for 17 hour in flowing argon. XRD revealed a high deficiency in oxygen in all samples suggesting that the nano-structures are transformed to sub-oxides of tungsten. Micro-diffraction patterns of a typical nano-wire reveal the monoclinic phase of W<sub>18</sub>O<sub>49</sub>.

**Keywords:**

### 1. INTRODUCTION

Among several materials which can be used as active layers, tungsten oxides are highly promising. For instance, WO<sub>3</sub> is used in flat panel displays<sup>1–5</sup> and for the detection of nitrogen oxides (NO, NO<sub>2</sub> and NO<sub>x</sub>), carbon monoxide, H<sub>2</sub>S, NH<sub>3</sub> and hydrocarbons such as ethanol, benzene and methane.<sup>2–7</sup> WO<sub>x</sub> electro-chromism has been found to be enhanced when mixed with Au and Al,<sup>8</sup> Ti,<sup>9</sup> Au, Pd and Pt<sup>10–13</sup> and a composite with MoO<sub>3</sub>.<sup>14</sup> Influence of substrate temperature,<sup>15</sup> annealing,<sup>16</sup> and proton insertion<sup>17</sup> on the properties of WO<sub>x</sub> has been reported. Performance of WO<sub>x</sub> has been compared with NiO<sub>x</sub> on electro-chromism<sup>18</sup> and with V<sub>2</sub>O<sub>5</sub> as sensitive elements for NO detection,<sup>19</sup> as well as with nano-powders of tin and indium oxides as CO and O<sub>2</sub> detectors.<sup>20</sup> In most of these species sensing studies WO<sub>3</sub> selectivity and sensitivity optimisation has been central, with the maximum sensitivity typically around 350 °C. This requirement of a high operating temperature

can be a major setback with regard to operational costs of the sensor, hence the desire to find similar performance at lower temperatures. It has been shown<sup>6</sup> that reducing the WO<sub>3</sub> particulate sizes to sub-micrometer and nanometer levels decreases this optimum temperature to 200 °C. Room temperature sensitivity has been reported<sup>17</sup> although more work is required in order to ensure scalability and repeatability of such findings.

The aim of the present study was to consider means to decrease the particle size of WO<sub>3</sub> in order to enhance the above properties at suitably low temperatures. Various methods were employed, including ultrasonic spray pyrolysis (USP), reported here, and laser pyrolysis (LP), reported elsewhere.<sup>22</sup> Successful synthesis of stoichiometric VO<sub>2</sub> (one of the most difficult transition metal oxides to synthesize) by ultrasonic spray pyrolysis was reported in a previous paper<sup>21</sup> while nano-wires of WO<sub>3</sub> by LP were reported by some of the authors previously.<sup>22</sup> Based on these successes, we attempted to synthesize WO<sub>3</sub> by USP. It must be mentioned that WO<sub>3</sub> particles have been synthesized by Patil's group before by USP;<sup>16</sup> however

\*Authors to whom correspondence should be addressed.



their processing temperatures and post-synthesis annealing conditions were different from those reported here. Morphology and structure of our post-annealed samples yielded very unique findings.

## 2. ULTRASONIC SPRAY PYROLYSIS EXPERIMENTS

A precursor solution of 4.1 g of ammonium meta-tungstate hydrate, [(NH<sub>4</sub>)<sub>6</sub>W<sub>7</sub>O<sub>24</sub>·6H<sub>2</sub>O (AMTH), a white powder of molecular weight of 2972.0 a.m.u., solubility of 0.1 g ml<sup>-1</sup> and melting temperature of 700 °C] was prepared by dissolving the powder form in 600 ml of distilled water and mixing well using a magnetic stirrer on a hot plate at around 70 °C. Substrate materials (Corning's microscope cover glass) underwent the usual cleaning procedure until the substrates qualified for deposition. The surface tension of the precursor solution was determined by a capillary rise method to be 5.4 × 10<sup>-3</sup> kg·m<sup>-1</sup> and its density was measured to be 1.033 × 10<sup>-3</sup> kg m<sup>-3</sup>. The so-made solution was then decanted into a container which housed the ultrasonic nebula generator, operating at a frequency of 1.67 MHz. A more complete description of the experimental set-up can be found in Refs. [21] and [22].

Depositions were done on Corning glass positioned at the exit of the furnace for 30 minutes with an argon carrier gas flow rate optimized to 11 ℓ min<sup>-1</sup>. Samples were collected without any annealing at furnace temperatures of 100, 200, 400, 500, 600 and 700 °C, labeled W1 through W7 respectively. Some were subsequently annealed at 500 °C for 17 hours and labeled correspondingly: W1-500, W2-500, W4-500, W5-500, W6-500 and W7-500. In each session of annealing, the annealing furnace was programmed to increase the temperature to 500 °C, at a heating rate of 10 °C/minute, and then remained constant at this temperature for 17 hours before being cooled down to room temperature.

We used a Powder X-ray Diffractometer (Philips Xpert) with a Cu K<sub>α</sub> wavelength of 0.154184 nm for structural studies of the as-deposited micro- and nano-particles. Morphology studies were carried out using a LEO 1525 field emission scanning electron microscope (FESEM) operated at 3–15 kV equipped with EDS system.

## 3. CHARACTERIZATION RESULTS AND DISCUSSION

Scanning electron micrographs are presented in Figures 1, 4 and 5. At low furnace temperature most particles are formless with islands of thin crystalline platelets in the shape of rhombuses (see inset (a) of Fig. 1), with internal corresponding angles of approximately 87° and 99°. From Figure 1 it is evident that the particles become more spherical as the furnace temperature is increased, appearing as almost perfect spheres at around 500 °C and higher. There

is however crystals of various shapes in the midst of the spheres, indicating a distribution in both size and shape. The as-deposited WO<sub>3</sub> spherical particles were analyzed for their size distribution as a function of furnace temperature (using Image Tool™ software), with the results shown in Figure 2. From regression analysis, we speculate that the relationship between the sphere diameters (*d*) and the furnace temperature (*T*) is:  $d = \alpha + \beta T$ , with  $0.680 < \alpha < 0.937$  and  $-6.8 \times 10^{-4} < \beta < -3.2 \times 10^{-4}$  within a 95% confidence interval. The expected values of  $\alpha$  and  $\beta$  are 0.808 and  $(-5.1 \times 10^{-4})$  respectively. The null hypothesis of  $\beta = 0$  was rejected in favor of the linear relationship quoted above, again within a 95% confidence interval. Thus it seems that as the furnace temperature increases, so the mean grain diameter decreases; in addition, the decrease in variance of the distributions as temperature increases confirms that there is less randomness in size at higher temperatures, pointing to a more controlled deposition process. A similar general trend is noted for the nano-platelets and nano-crystals of various shapes (not shown here) suggesting that "Oswald's ripening," a phenomenon of agglomeration of nano-structures due to high temperatures, is minimal in the present samples. The regression analysis above, however, only helps us to see the trend of the (*T*, *d*) data; we cannot use this trend to extrapolate diameters to lower or higher temperatures. A more realistic theory of condensation and crystallization based on laws of thermodynamics, after Tiller,<sup>24,25</sup> was thus used to explain the data. This theory states that for condensation of the vapor species, critical nuclei diameter, *d<sub>c</sub>*, depends on the super-saturation of the condensing material. The relation<sup>24,25</sup> for *d<sub>c</sub>* as a function of temperature and partial pressure is reproduced here as

$$d_c = \frac{4 \cdot \sigma \cdot \Omega}{RT \ln(p/p^*)} \quad (1)$$

$\sigma$  is the interfacial energy between the substrate (SiO<sub>2</sub>) and the condensing species (WO<sub>3</sub>),  $\Omega$  is the molar volume of the WO<sub>3</sub> condensing material, *T* is the temperature, *p* is the partial pressure of the growth species which in turn depends on temperature and *p*<sup>\*</sup> is the partial pressure at equilibrium. The assumption of the ideal gas law,  $pV = nRT$ , becomes more valid at higher temperatures and the we can re-write Eq. (1) as

$$d_c = \frac{4 \cdot \sigma \cdot \Omega}{RT \ln(RT/\Omega \cdot p^*)} \quad (2)$$

Equation (2) has been fitted to our experimental data in Figure 2(a) with the assumption that *d<sub>c</sub>* is the final diameter of the particles and the values of interfacial energy  $\sigma$  ( $0.6 \pm 0.2$  mJ m<sup>-2</sup>) at a partial pressure at equilibrium, *p*<sup>\*</sup> (2% atm.), for WO<sub>3</sub> were determined. Note that in both Eqs. (1) and (2), the possibilities of *T* = 0 and *T* < 0 are completely disallowed in keeping with the laws of thermodynamics. The linear regression equation has also been plotted in Figure 2 for illustration and to guide the eye.

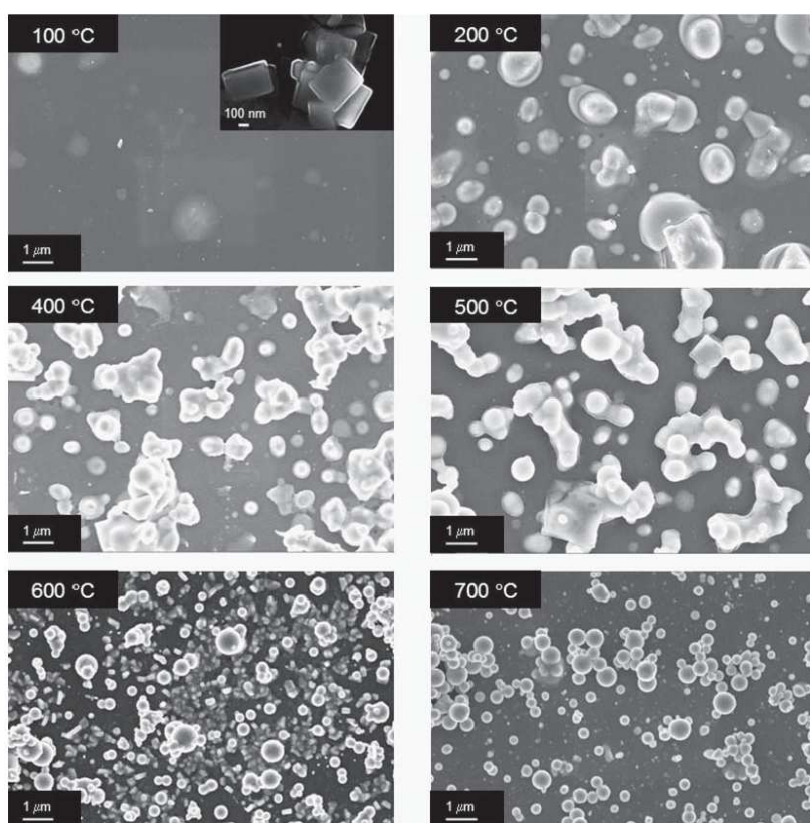


Fig. 1. Scanning electron micrographs of as-deposited samples synthesized at different temperatures (W1 = 100 °C, W2 = 200 °C, W4 = 400 °C, W5 = 500 °C, W6 = 600 °C and W7 = 700 °C). Note the improvement in the roundness of the spheres and the presence of platelet and sheets (inset of 100 °C sample) amongst the spheres.

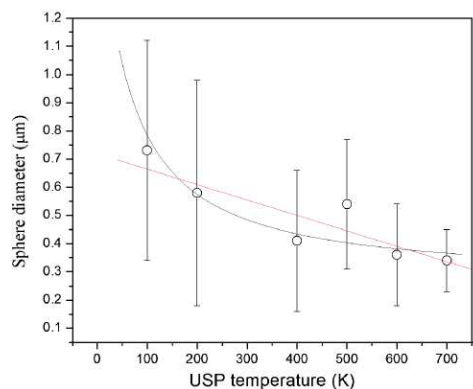
Spheres were easier to characterize since only the radius was measured. In comparison to crystals of other shapes, dimensions such as length, width and depth have to be measured with difficulty in SEM and TEM images. Figure 3 presents size distribution of the nano-crystals in a sample synthesized at 700 °C. The mean crystal size is  $73 \pm 2$  nm with a standard deviation of  $12 \pm 3$  nm.

At temperatures below 650 °C rod-like (nano-wire) structures were observed in the midst of the as-deposited particles, indicative of the onset of one-dimensional (1D) growth even before thermal annealing. In order to enhance this growth, portions of these samples were further annealed at 500 °C for 17 hours as explained in the experimental section above. Although nano-wire structures were observed in all samples annealed under similar conditions, the highest yield was found in a sample synthesized at 500 °C. The wires in the sample W5-500 are extremely long and with a high aspect ratio. An amplified image and

size distribution chart for this optimum sample are shown in Figure 4. The most probable diameter of the nano-wires was calculated to be  $101 \pm 6$  nm, with a standard deviation of  $35 \pm 7$  nm.

Figure 5(a) illustrates a magnified image of a remarkably long nano-belt in a sample synthesized at 700 °C and annealed at 500 °C for 17 hrs (sample W7-500) whose thickness is about 50 nm and whose length is roughly 10 μm. Figure 5(b) suggests that these nano-belts are growing out of the spheres themselves, which is in agreement with previous observations of similar structures.<sup>22</sup>

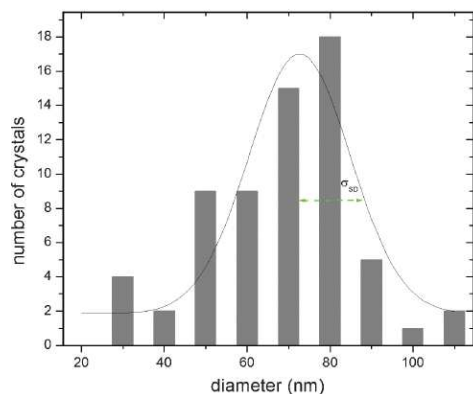
A fast XRD scan (not shown here) of all samples of the WO<sub>x</sub> nano-spheres showed that at low furnace temperature the as-deposited particles are molecular ammonium metatungstate. The transition to WO<sub>3</sub> was observed to take place when the furnace temperature reached 500 °C. Beyond this temperature the as-deposited particles assumed the WO<sub>3</sub> monoclinic structure. The fact that the transition from



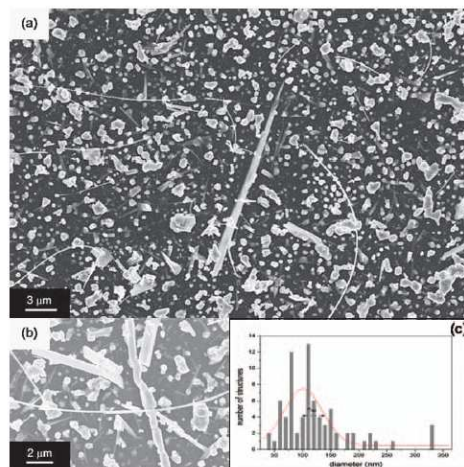
**Fig. 2.** Sphere size as a function of the USP process furnace temperature. Each datum point is the most probable diameter value from a size distribution histogram with the error bars on each datum point taken from the standard deviation of each distribution. This shows that as the process temperature is increased the powder particle distribution becomes narrow. Equation (2) (black curve) and the regression analysis equation (red line) have been fitted to the experimental data.

precursor to WO<sub>3</sub> happened at 500 °C might explain the high yield of the 1D structures in the sample synthesized at this temperature after annealing at 500 °C.

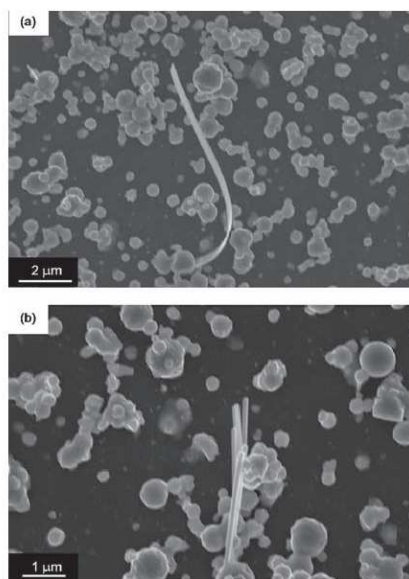
In the temperature range -70 °C to 1000 °C, tungsten trioxide is reported to undergo no less than eight phase transformations in the solid state.<sup>25</sup> Crystallographic information has become available<sup>26</sup> on the WO<sub>3</sub> phases which occur between 900 °C and -70 °C. Below 900 °C, WO<sub>3</sub> is tetragonal with space group P4/nmm (D<sub>4h</sub>)<sup>27</sup> and transforms at about 740 °C into an orthorhombic modification with space group Pmnb (D<sub>2h</sub>)<sup>28</sup>. Between 17 °C and



**Fig. 3.** Size distribution of nano-crystals in a typical sample (W7) in the as-prepared USP particles. The most probable crystal size is 72.6 ± 2.4 nm and a standard deviation of 24.4 ± 6.0 nm.



**Fig. 4.** Scanning electron micrographs of samples annealed at 500 °C for 17 hours in argon (a) 1D growth region of nanostructures comprising nanotips, nanobelts and nanowires (b) a magnified image showing nanowires, belts and tips, (c) the size distribution of the diameter of the nanowire. The histogram reveals that the most probable nanowire diameter is 101 ± 6.1 nm with the smallest nanowires having diameters less than 30 nm.



**Fig. 5.** Belts or ribbon-like structure growing from among the spheres (a) A belt growing from within the WO<sub>3</sub> spherical particles with a length of 8.67 µm and a thickness of 45.95 nm and (b) three to four nano-rods growing from amongst spheres.

RESEARCH ARTICLE

**Table I.** Structural transformations of stoichiometric WO<sub>3</sub> at different temperatures and crystallographic information of know pure tungsten phases.

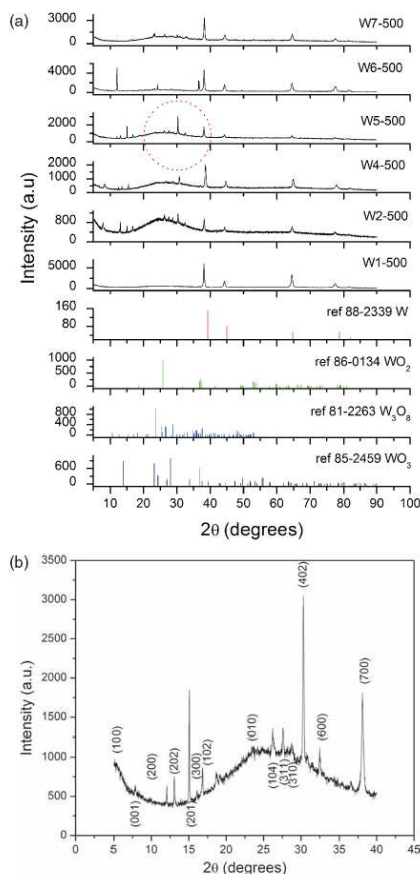
Temperature (°C)	Space group	a (Å)	b (Å)	c (Å)	α (°)	β (°)	γ (°)	Refs.
900–740	D <sub>2h</sub> <sup>7</sup> -P4/nmm (tetragonal)	5.3358	5.3358	3.7882	90.00	90.00	90.00	[27]
740–330	D <sub>2h</sub> <sup>16</sup> -Pmnb (orthorhombic)	7.35	12.51	7.70	90.00	90.00	90.00	[28, 39]
330–17	D <sub>2h</sub> <sup>7</sup> -P2 <sub>1</sub> /n (monoclinic)	7.297	7.539	7.688	90.00	90.91	90.00	[29–31, 40]
17 to –40	C <sub>2</sub> <sup>1</sup> -P1 (triclinic)	7.2944	7.4855	3.7958	89.38	90.42	90.80	[32, 33]
–40 to –70	C <sub>2</sub> <sup>2</sup> -Pc (monoclinic)	7.297	7.539	7.70	90.00	90.91	90.00	[34, 35]
α-W	O <sub>h</sub> <sup>9</sup> -Im3m (bcc A2 type)	3.16524	3.16524	3.16524	90.00	90.00	90.00	[43, 44]
β-W <sup>a</sup>	O <sub>h</sub> <sup>9</sup> -Im3m (fcc A15 type)	5.0512	5.0512	5.0512	90.00	90.00	90.00	[43, 44]
γ-W	O <sub>h</sub> <sup>9</sup> -Im3m (bcc A1 type)	4.13	4.13	4.13	90.00	90.00	90.00	[43, 44]
W <sub>18</sub> O <sub>49</sub>	P2/m(10)	18.31	3.782	14.028	90.00	115.21	90.00	PDF841516

<sup>a</sup>β-W was first discovered structurally as a sub-oxide (W<sub>3</sub>O<sub>8</sub>). As such it is still listed in the International Diffraction File (41-1230). β-W forms at least partially during low-temperature hydrogen reduction of tungsten oxides besides α-W. Several foreign elements such as P, As, Al, K etc. promote its formation (see Ref. [43]).

330 °C, WO<sub>3</sub> exhibits monoclinic symmetry with space group P2<sub>1</sub>/n (C<sub>2h</sub><sup>5</sup>).<sup>29–31</sup> Below 17 °C WO<sub>3</sub> is triclinic with space group P1 (C<sub>1</sub><sup>1</sup>)<sup>32,33</sup> and transforms at –40 °C into another monoclinic phase with space group Pc (C<sub>2</sub><sup>2</sup>).<sup>34,35</sup> These WO<sub>3</sub> phases have more or less distorted ReO<sub>3</sub>-type crystal structures. The lattice parameters of these structures are tabulated in Table I.

There are however numerous other phases of WO<sub>x</sub>, such as WO<sub>x</sub> (x = 3 to 5),<sup>36</sup> W<sub>2</sub>O<sub>x</sub> (x = 1 to 6)<sup>37</sup> and W<sub>3</sub>O<sub>x</sub> (x = 7 to 10).<sup>38</sup> Among these phases, W<sub>18</sub>O<sub>49</sub> is becoming a material of research interest. The oxygen rich oxides tend to show ionic properties<sup>36</sup> while on the other hand the oxygen deficient compounds, such as W<sub>18</sub>O<sub>49</sub>, show similar structural properties as pure tungsten. Table I compares the structural information for some WO<sub>3</sub> phases to that of pure tungsten, whose technological importance cannot be over emphasized. Besides amorphous tungsten, three other phases of the metal exist, labeled α-W, β-W and γ-W. α-W is the most stable of the three and has a body centred cubic structure<sup>39</sup> with space group O<sub>h</sub><sup>9</sup>-Im3m of type A2, whereas the other two are meta-stable, have face centered structures (space groups O<sub>h</sub><sup>3</sup>-Pm3m of type A15 and O<sub>h</sub><sup>3</sup>-Pm3m of type A1 respectively)<sup>39</sup> and assume the α-W structure when heated to beyond 600 °C.

The higher resolution X-ray diffraction scan of the optimum sample (W5) before annealing showed oxygen deficient monoclinic WO<sub>3-x</sub> with peaks belonging to the WO<sub>3</sub> monoclinic<sup>40</sup> (see Fig. 6(a)). The peaks in the range of 2θ = 22–40 belong to W<sub>18</sub>O<sub>49</sub> and other WO<sub>3-x</sub> phases<sup>40,41</sup> (see Fig. 6(b)). The intense peak at around 2θ = 38.12° is closer to the (700) plane of W<sub>18</sub>O<sub>49</sub> than the (110) of α-W or the (012) plane of β-W. There are no peaks for pure tungsten below 2θ = 37°; many peaks indexed from the W<sub>18</sub>O<sub>49</sub> ICDD file PDF 84–1516 showed that the W<sub>18</sub>O<sub>49</sub> wires are layered structures growing preferentially in the (n00) direction with peaks for (100), (200), (300), (600) and (700) present in the X-ray diffraction pattern. There is also the presence of a layered growth along the (n02) direction, although this direction is not as highly preferred, with peaks for (102), (202) and (402); this is consistent with the previous findings.<sup>44</sup> Pure tungsten undeniably shows up after annealing; it is interesting that the tungsten peaks at



**Fig. 6.** X-ray diffraction spectra (a) for all samples compared to the spectra of standard tungsten and tungsten oxides. Note the broken circle in the XRD spectrum for the nanowire optimum W5-500 sample which has been re-plotted for clarity in (b). In (b), the spectrum matches that of W<sub>18</sub>O<sub>49</sub> (see text for full detail).

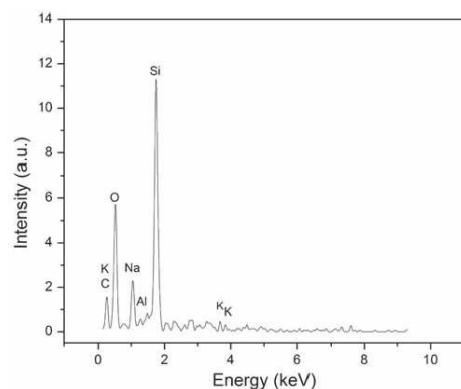


Fig. 7. EDS of microscope cover glass from Corning Glass showing the stoichiometry of SiO<sub>2</sub> with some impurities such as Na and K which are believed to be catalysts of one-dimensional growth. Reprinted with permission from [22], B. W. Mwakikunga et al. *Int. J. Laser Nanomanuf.* (2007), accepted. © 2007. Note also the strong O peak from the substrate.

$2\theta > 40^\circ$  point more to  $\beta$ -W rather than the more stable  $\alpha$ -W, contrary to what is suggested in the literature.<sup>39</sup>

In order to ascertain the level of oxygen in the substrate, a clean substrate was prepared for EDS in the SEM described above. The EDS spectrum for a blank substrate is shown in Figure 7, indicating that the Corning glass (microscope cover glass) contains high amounts of O and Si atoms, with trace amounts of Al, K and Na. Potassium has previously been suggested to be a catalyst for WO<sub>3</sub> nano-rods<sup>42,43</sup> and nano-wires.<sup>22</sup> The EDS spectrum for the optimum nano-wire sample (W5-500) is shown in Figure 8 and the qualitative elemental composition data is summarized in Table II. The presence of the O peak relative to

Table II. Elemental analysis and quantification for a sample W5-500 with the highest yield of one-dimensional nanostructures.

Element	Weight %	Atomic%
W	36.1 ± 1.8	4.6
O	26.4 ± 1.3	38.9
C	22.3 ± 2.1	43.8
Si	9.6 ± 0.8	8.0
Na	3.0 ± 0.4	3.1
K	2.7 ± 0.7	1.6

the W (Si) suggests that some of O is from the substrate rather than from tungsten oxides. This confirms the fact that these 1D nanostructures are by and large either oxygen-deficient WO<sub>x</sub> or pure tungsten of  $\beta$ -W phase as shown by X-ray diffraction. The deconvoluted spectrum for the near-overlapping Si and W peaks (inset (a) of Fig. 8) show that the intense WM (1.774 keV) peak is about 92% higher than that from the close Si K <sub>$\alpha$</sub>  (1.739 keV)<sup>44,45</sup> peak suggesting that contribution is predominantly W, with Si (from the substrate) contributing very little to the observed main peak in the EDS spectrum. Also, the Al (from the substrate) and W peaks, sitting on another broad tungsten peak (inset (b) of Fig. 8), are distinct sharp peaks when resolved with Al assigned to the Al K <sub>$\alpha$</sub>  (1.47588 keV) line, and the W to the W N <sub>$\alpha$</sub>  (1.4357 keV) line.<sup>44,45</sup> The latter are inter-shell transitions of electrons from the incomplete W-O shell coming to fill the vacant positions in the N shell. The X-ray energy obtained for the W N <sub>$\alpha$</sub>  line agrees well with the preceding higher energy transitions (1.774 keV) in the M shell of tungsten. The W L <sub>$\alpha$</sub>  (8.396 keV) peak is also clearly seen in Figure 8; confirmation of the presence of pure tungsten.

Transmission microscopy revealed the structure and composition of the WO<sub>x</sub> nano-wires. It can be seen in Figure 9 that the nano-wires are in fact tapered suggesting a needle-like profile. The nano-needle identified had a broken tip as illustrated in Figure 9(a) which probably results from sonication in ethanol during TEM sample preparation. These structures have a sheath around them as shown in a higher magnification image in Figures 9(b) and (c). EDS analysis of both the sheath and the core showed that these were amorphous carbon and WO<sub>x</sub> respectively. The carbon was due to coating of the sample prior to SEM for improvement of conductivity. Thus it is likely that the nano-structures are smaller than presented by SEM above by a factor of about 0.4 as determined from the TEM images. Micro-diffraction patterns from the core provided a match for the W<sub>18</sub>O<sub>49</sub> structure with lattice parameters  $a = 18.28 \text{ \AA}$ ,  $b = 3.775 \text{ \AA}$ ,  $c = 13.98 \text{ \AA}$ ; JCPDS 5-392. The growth direction of the nano-wire was [100]. This would be in agreement with the X-ray diffractogram in Figure 6(b) which indicated a layered structure with peaks 100, 200, 300, 600, 700.

Localized EDS on the core of the nano-wire is presented in Figure 10 and confirms the tungsten oxide identification. Whether Na is taking part in the nano-wire growth or that

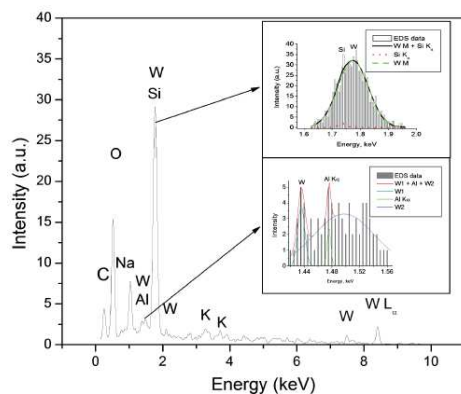
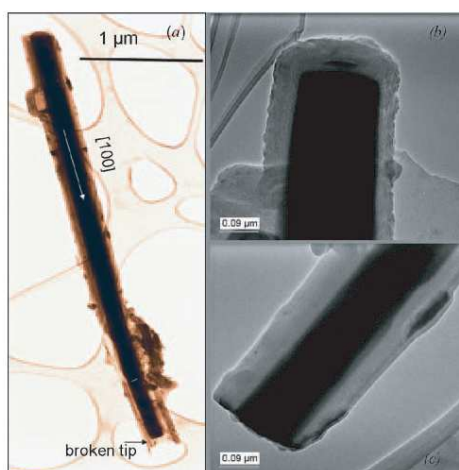


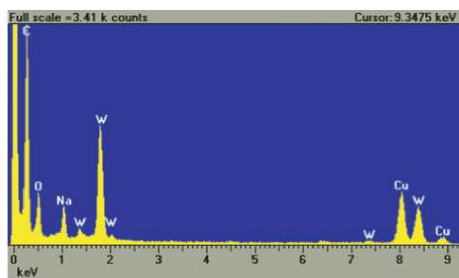
Fig. 8. EDS of the sample W5-500 after annealing at 500 °C for 17 hrs in flowing argon (see text for detail).



**Fig. 9.** TEM images of the W<sub>18</sub>O<sub>49</sub> nano-wire (a) low magnification of the nano-wire revealing a tip-like structure; this corroborates the SEM images (Figs. 4(a) and (b)), (b) and (c) are base and broken tip higher magnification images revealing the amorphous carbon layer around the W<sub>18</sub>O<sub>49</sub> nano-wire.

it is simply a catalyst is not yet obvious. Sodium could be contamination from the glass substrate as the nano-wires were scrapped off the substrate for transfer to the lacey-carbon coated copper TEM support grid.

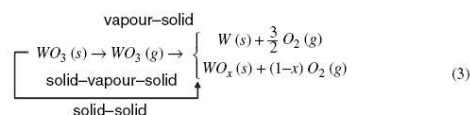
In order to discuss briefly the growth of 1D structures from 3D structures, reference is made to some of well known growth mechanisms proposed in the history of crystal growth: (1) the screw dislocation theory,<sup>46</sup> (2) the vapor-liquid-solid (VLS)<sup>47</sup> mechanism, (3) solution-liquid-solid (SLS)<sup>48</sup> growth and (4) the vapor-solid mechanism.<sup>49</sup> The first two mechanisms explain 1D growth in vapour deposition methods with catalysts for the case of VLS and promoted by dislocations and indentations in the case of the



**Fig. 10.** Localized EDS in TEM on the core of the W<sub>18</sub>O<sub>49</sub> nano-wire, the copper peaks resulting from electron scattering onto the sample support grid.

screw dislocation theory. The latter can explain growth of helical structures.<sup>49,50</sup> The third mechanism is based on wet and soft chemistry techniques. The vapor-solid mechanism contrasts the VLS in that this can proceed without the need for a catalyst with vapours undergoing sublimation into solid state bypassing the liquid state. Typical experimental arrangement in this mechanism involves evaporating the starting material and carrying the vapour onto a substrate placed at a lower temperature than that of its evaporating region. A number of publications including conversion of ZnO nano-belts into nano-helices have been reported<sup>49,50</sup> by this mechanism. In the present study, to the contrary, the 3D to 1D growth takes place on the same substrate. Recently direct synthesis of W<sub>18</sub>O<sub>49</sub> nano-rods was achieved by thermal annealing of CVD grown W<sub>2</sub>N films.<sup>51</sup> If one assumes that the starting materials (in present study, nano-spheres and nano-crystals) are vaporized, then the vapour sublimates into a solid state 1D structure on the same substrate. The present observation calls for a new mechanism whose experimental aspects are currently being explored.

Although pure tungsten has the highest melting point among known metals (m. pt. 3422 °C, b. pt. 5555 °C), Gillet<sup>52</sup> showed that the WO<sub>3</sub> particles could be sublimated at a relatively low temperature of 550 °C. Also oxygen loss of tungsten oxide at high temperature and low pressure is well known.<sup>53</sup> Based on these facts, the reaction routes toward either pure tungsten or mixed phases of WO<sub>x</sub> of low oxygen content can be visualized as illustrated



A new possible growth model comparable to the vapor-solid (VS) growth model was identified in this case to be either a solid-vapor-solid (SVS) or a solid-solid (SS) mechanism. The SVS proposal is quite interesting since the throughput of the 1D nano-structures should be heavily dependent on temperature, pressure and, most importantly, the flow rate of the ambient gas. For instance, if the flow rate is too high most of the starting material's vapor can be swept away leaving very little to assemble back onto the substrate. In this mechanism therefore optimization of the flow rate, heating rates and the ambient pressure are important. Nano-rods, nano-wires and nano-sheets could be evidence of the proposed SVS mechanism. On the other hand, the SS route should demand a good amount of mechanical energy derived from thermal annealing in causing the 3D structure to expand and elongate into 1D configuration with O loss in the process. Electromagnetic forces which become more important than gravitational force at nano-scale should be very crucial in aligning and condensing atoms and atomic clusters that are in constant

motion due to thermal energy supply. Nano-tips and nano-belts with tapered ends seen in Figures 4 and 5 growing from other solid 3D structure are possibly all good examples of the proposed SS route. Since oxygen loss at some temperature and pressure is time dependent, production of pure tungsten has to proceed for a good amount of time. In this study, the annealing time of 17 hrs was good enough.

#### 4. CONCLUSION

Size controlled WO<sub>3</sub> nano- and micro-sized grains were successfully synthesized by varying substrate temperatures from 100 °C to 700 °C, and it has been shown how the size and shape of the particles change as a function of furnace temperature. Spherical particles, after annealing at 500 °C, transformed into 1D structures such as rods, wires and belts, with the highest yield observed for a sample synthesized at 500 °C and annealed at 500 °C for 17 hrs. The stoichiometry of the 1D nano-structures in the former sample was found to be consistent with W<sub>18</sub>O<sub>49</sub> and pure tungsten of the β-W phase.

**Acknowledgments:** We acknowledge fruitful contributions from Professor Karin Pruessner of the School of Physics of the University of the Witwatersrand. We would like also to acknowledge the technical assistance of Retha Rossouw and Loukie Adlem of the National Metrology Institute of South Africa (NMISA), and financial support to the first author from the World Bank through the Joint Japan/World Bank Graduate Scholarship Programme (JJWBGSP). Part of this work was accomplished with funds from the CSIR Project No HGERA2S and Department of Science and Technology/National Research Foundation Centre of Excellence in Strong Material at the University of the Witwatersrand (AKF# 001.403.4311104 Project# CEJL000).

#### References and Notes

- C. Bittencourt, R. Landers, E. Llobet, X. Correig, and J. Calderer, *Semicond. Sci. and Technol.* 17, 522 (2002).
- S. H. Wang, T. C. Chou, and C. C. Liu, *Sens. Actuators, B* 94, 343 (2003).
- V. Guidi, M. Blo, M. A. Butturri, M. C. Carotta, S. Galliera, A. Giberti, C. Malagu, G. Martinelli, M. Piga, M. Sacerdoti, and B. Vendemiati, *Sens. Actuators, B* 100, 277 (2004).
- P. Ivanov, J. Hubalek, K. Malysz, J. Prasek, X. Vilanova, E. Llobet, and X. Correig, *Sens. Actuators, B* 100, 221 (2004).
- M. Bendahan, R. Boulmani, J. L. Seguin, and K. Aguir, *Sens. Actuators, B* 100, 320 (2004).
- A. Hoel, L. F. Reyes, P. Heszler, V. Lantto, and C. G. Granqvist, *Curr. Appl. Phys.* 4, 547 (2004).
- H. Kawasaki, J. Namba, K. Iwatsuji, Y. Suda, K. Wada, K. Ebihara, and T. Ohshima, *App. Surf. Sci.* 197–198, 547 (2002).
- Q. Sun, B. K. Rao, P. Jena, D. Stoljic, G. Gantefor, and Y. Kawazoe, *Chem. Phys. Lett.* 387, 29 (2004).
- G. Leftheriotis, S. Papaefthimiou, P. Tianoilis, A. Siokou, and D. Kefalas, *Appl. Surf. Sci.* 218, 275 (2003).
- J. Shieh, H. M. Feng, M. H. Hon, and H. Y. Juang, *Sens. Actuators, B* 86, 75 (2002).
- A. H. Jayatissa, S. Cheng, and T. Gupta, *Mater. Sci. and Eng. B* 109, 192 (2004).
- M. Ando, R. Chabircovsky, and M. Haruta, *Sens. Actuators, B* 76, 13 (2001).
- P. R. Patil and P. S. Patil, *Thin Solid Films* 382, 13 (2001).
- S. Djerad, L. Tifouti, M. Crocoll, and W. Wesweiler, *J. Mol. Catalysis A: Chemical* 208, 257 (2004).
- H. Kamal, A. A. Akl, and K. Abdel-Hady, *Physica B* 349, 192 (2005).
- R. Agarwal and C. M. Lieber, *Appl. Phys. A* 85, 209 (2006).
- J. Arakaki, R. Reyes, M. Horn, and W. Estrada, *Solar Energy Mater. and Solar Cells* 37, 33 (1995).
- S. Capanoe, R. Rella, P. Siciliano, and L. Vasanelli, *Thin Solid Films* 350, 264 (1999).
- M. I. Baraton, L. Merhari, H. Ferkel, and J. F. Castagnet, *Mater. Sci. Eng. C* 19, 315 (2002).
- B. W. Mwakikunga, E. Sideras-Haddad, and M. Maaza, *Opt. Mater.* 29, 481 (2007).
- B. W. Mwakikunga, A. Forbes, E. Sideras-Haddad, R. M. Erasmus, G. Katumba, and B. Masina, *Int. J. Laser Nanomanuf.* (2007), accepted.
- W. A. Tiller, *The science of crystallization: Microscopic interfacial phenomenon*, Cambridge University Press, New York (1991).
- S. Vaddiraju, H. Chandrasekaran, and M. K. Sunkara, *J. Am. Chem. Soc.* 125, 10792 (2003).
- I. Levkowitz, M. Dowell, and M. A. Shields, *J. Solid State Chem.* 15, 21 (1975).
- K. L. Kehl, R. G. Hay, and D. Wahl, *J. Appl. Phys.* 23, 212 (1952).
- X. G. Wang, Y. S. Jang, N. H. Yang, Y. M. Wang, L. Yuan, and S. J. Pang, *Solar Energy and Solar Cells* 63, 197 (2000).
- E. Salje, *Acta Cryst. B* 33, 574 (1977).
- S. Tanisaki, *J. Phys. Soc. Jpn.* 15, 573 (1960).
- B. O. Loopstra and P. Boldrini, *Acta Cryst. B* 25, 158 (1966).
- B. O. Loopstra and H. M. Rietveld, *Acta Cryst. B* 25, 1420 (1969).
- H. Braekken, *Z. Kristallogr.* 78, 484 (1931).
- S. Tanisaki, *J. Phys. Soc. Jpn.* 15, 573 (1960).
- E. Salje, *Ferroelectrics* 12, 215 (1976).
- S. Tanisaki, *J. Phys. Soc. Jpn.* 16, 566 (1960).
- H. Zhai, X. Huang, L. Cui, X. Li, and L. Wang, *J. Phys. Chem.* 109, 6019 (2005).
- X. Huang, H. Zhai, L. Cui, X. Li, and S. Wang, *J. Phys. Chem.* 110, 85 (2006).
- H. Zhai, B. Kiran, X. Huang, L. Cui, D. A. Dixon, and X. Li, *J. Am. Chem. Soc.* 126, 16135 (2004).
- E. Lassner and W. D. Schubert, *Tungsten: Properties, Chemistry, Technology of the Element, Alloys and Chemical Compounds*, Springer, Berlin (1999), p. 416.
- C. H. Chen, S. J. Wang, R. M. Ko, Y. C. Kuo, K. M. Uang, and T. M. Chen, *Nanotechnology* 17, 217 (2006).
- S. Wang, Y. He, B. Huang, J. Zou, C. T. Liu, and P. K. Liaw, *Chem. Phys. Lett.* 427, 350 (2006).
- A. Al Muhammad and M. Gillet, *Thin Solid Films* 408, 302 (2002).
- M. Gillet, A. Al Muhammad, and C. Lemire, *Thin Solid Films* 410, 194 (2002).
- G. A. Swift and R. Koc, *J. Mater. Sci.* 36, 803 (2001).
- J. Goldstein, D. Newbury, D. Joy, C. Lyman, P. Echlin, E. Lifshin, L. Sawyer, and J. Michael, *Scanning Electron Microscopy and X-ray Analysis*, 3rd edn., Springer, Berlin (2003).

46. F. C. Frank, *Discussions Faraday Society* 5, 48 (1949).
47. R. S. Wagner and W. S. Ellis, *Appl. Phys. Lett.* 4, 89 (1964).
48. T. J. Trenter et al. *Science* 270, 1791 (1995).
49. W. Buhro, *Adv. Mater. Opt. Electron.* 6, 175 (1996).
50. Z. W. Pan, Z. R. Dai, and Z. L. Wang, *Science* 291, 1947 (2001).
51. S. Jeon and K. Yong, *Nanotechnology* 18, 245602 (2007).
52. M. Gillet, R. Delamare, and E. Gillet, *Eur. Phys. J. D* 34, 291 (2005).
53. S. Santucci, L. Lozzi, E. Maccallin, M. Passacantando, and L. Ottariano, *J. Vac. Sci. Technol. A* 19, 1467 (2001).
54. Y. Li, Y. Bando, and D. Goldberg, *Adv. Mater.* 15, 194 (2003).

Received: 21 October 2007. Revised/Accepted: 19 March 2008.



---

## **Synthesis of tungsten oxide nanostructures by laser pyrolysis**

---

### **Bonex Wakufwa Mwakikunga\***

School of Physics,  
University of the Witwatersrand,  
Private Bag 3, PO Wits 2050,  
Johannesburg, South Africa

CSIR National Centre for Nano-Structured Materials,  
P.O. Box 395,  
Pretoria 0001,  
South Africa

Department of Physics and Biochemical Sciences,  
University of Malawi,  
Private Bag 303,  
Chichiri, Blantyre 3, Malawi  
E-mail: bmwakikunga@csir.co.za  
\*Corresponding author

### **Andrew Forbes**

Council for Scientific and Industrial Research,  
National Laser Centre,  
P.O. Box 395,  
Pretoria 0001, South Africa

School of Physics,  
University of Kwazulu-Natal,  
Private Bag X54001,  
Durban 4000, South Africa  
E-mail: aforbes1@csir.co.za

### **Elias Sideras-Haddad and Rudolph Marthinus Erasmus**

School of Physics,  
University of the Witwatersrand,  
Private Bag 3, PO Wits 2050,  
Johannesburg, South Africa  
E-mail: Elias.Sideras-Haddad@wits.ac.za  
E-mail: Rudolph.Erasmus@wits.ac.za

## Gift Katumba

Department of Physics,  
University of Zimbabwe,  
P.O. Box MP 167,  
Mt Pleasant, Harare, Zimbabwe

CSIR National Laser Centre,  
P.O. Box 395,  
Pretoria,  
South Africa  
E-mail: gkatumba@csir.co.za

## Bathusile Masina

Council for Scientific and Industrial Research,  
National Laser Centre,  
P.O. Box 395,  
Pretoria 0001, South Africa

Department of Physics,  
University of Zululand,  
Private Bag X1001,  
Kwadlangezwa 3886, South Africa  
E-mail: bmasina@csir.co.za

**Abstract:** Since the proposal to synthesise materials by laser assisted pyrolysis in the 1970s, and its practical realisation in 1982, a number of researchers have used this method in obtaining nano-powders from liquid droplets. This study revisits this technique by introducing a new aspect in that it considers obtaining thin films rather than powders. A full experimental arrangement, including laser optimisation, optical layout and materials processing procedures is described. Synthesis of  $\text{WO}_3$  nanostructures by this method is reported for the first time, with the mean diameter and length determined to be 51 nm and 6.8  $\mu\text{m}$ , respectively. A possible mechanism for production of such nanostructures is proposed owing to the selective dissociation of the O–C bonds in the tungsten ethoxide precursor liquid which resonate with the 10.6  $\mu\text{m}$  emission wavelength of the  $\text{CO}_2$  laser employed.

**Keywords:**  $\text{WO}_3$ ; nano-rods; laser pyrolysis; multiphoton dissociation; laser beam propagation.

**Reference** to this paper should be made as follows: Mwakikunga, B.W., Forbes, A., Sideras-Haddad, E., Erasmus, R.M., Katumba, G. and Masina, B. (2008) 'Synthesis of tungsten oxide nanostructures by laser pyrolysis', *Int. J. Nanoparticles*, Vol. 1, No. 3, pp.185–202.

**Biographical notes:** Bonex Wakufwa Mwakikunga is a Senior Lecturer in Physics in the Department of Physics and Biochemical Sciences, University of Malawi at the Polytechnic in Blantyre, Malawi. He received an MSc in Experimental Solid State Physics at the NanoScale in the University of the Witwatersrand in Johannesburg, South Africa in 2005 and presently, he is

pursuing his PhD in the same university. He is now serving as a candidate researcher at the CSIR National Centre for Nano-Structured Materials in Pretoria, South Africa.

Andrew Forbes is a Principal Researcher at the Council for Scientific and Industrial Research, National Laser Centre in Pretoria, South Africa. He also holds an Honorary Senior Lecturer position in the School of Physics, University of KwaZulu-Natal, Durban, South Africa. He received his MSc and PhD at the University of Natal (South Africa). His current research interest is in both theoretical and experimental aspects of laser beam propagation and digital holography.

Elias Sideras-Haddad is a Professor of Physics in the School of Physics at the University of the Witwatersrand in Johannesburg, South Africa. He received an MSc and a PhD in Accelerator Physics at the same University and had taken a number of Postdoctoral positions including one at Lawrence Livermore National Laboratory. His current interests are in nuclear physics, diamond physics, solid state quantum computing and cryptography and transition metal oxide nanostructures for quantum computational and information systems applications.

Rudolph Marthinus Erasmus is a Senior Research Officer in the School of Physics at the University of the Witwatersrand and is responsible for the Raman and Luminescence Laboratory. His research interests include characterisation of stress and defects in ultra-hard materials. He received an MSc in Semiconductor Physics at the University of Pretoria and is currently finalising his PhD at the University of the Witwatersrand.

Gift Katumba is a Lecturer in the Department of Physics in the University of Zimbabwe, in Harare, Zimbabwe. He received a PhD in Solid State Physics in the University of Zimbabwe in 2006 in collaboration with Uppsala University in Sweden. His work focused on selective solar absorption properties of carbon in different dielectric matrices such as ZnO, NiO and SiO<sub>2</sub>. He is now a post-doctoral at the CSIR National Laser Centre in Pretoria, South Africa.

Bathusile Masina has completed a BSc Hons at the University of Zululand and is presently completing her MSc (University of Zululand) while working on the application of lasers to material studies of diamond at CSIR-National Laser Centre.

---

## 1 Introduction

Laser pyrolysis is based on a resonant interaction between a laser beam and a gaseous or liquid precursor (Cannon et al., 1982; Dez et al., 2004; Herlin et al., 1996; Muller et al., 2003), where energy is transferred by a multiphoton process between the emission line of the laser and at least one absorption band of the precursor. An aerosol generator produces droplets of the precursor which are carried by an inert gas (usually argon or nitrogen) into the laser beam. Multiphoton absorption by the precursor leads to dissociation; radicals are formed and the subsequent reactions result in nanoparticles by homogeneous nucleation (Haggerty and Cannon, 1981), exhibiting a narrow size distribution and high purity because the reaction takes place in an interaction zone without walls. There has been many attempts at modelling the mechanisms involved in laser pyrolysis. Bowden

et al. (1977) proposed a model for laser-induced photo-chemical reactions in which selective low-level excitation of a molecular species by the laser beam was assumed to incorporate coherent resonant energy transfer with collision damping. Other models have been specific to certain materials, for example, the simulation of CO<sub>2</sub> laser pyrolysis during preparation of SiC nano-powders (Amara et al., 2003; Bowden et al., 1977; El-Diasty, 2004).

In the early 1980s Haggerty and Cannon (1981) developed a laser synthesis process to produce silicon containing nanoparticles (e.g. SiC, Si<sub>3</sub>N<sub>4</sub>). First experiments in laser pyrolysis were reported in 1982 by Cannon et al. (1982), and since then the technique has been expanded to cover many new materials such as ceramics (van Erven et al., 1997), light-emitting Si nanoparticles (Huisken et al., 2000), fullerenes (Petcu et al., 2000; Tenegal et al., 2001), silicon-germanium alloys (Watanabe et al., 2003), Te films (Pola et al., 2004) and recently VO<sub>2</sub> (Mwakikunga et al., 2007).

Among several materials that can be used as active layers, tungsten oxide is highly promising. Several studies have shown that WO<sub>3</sub> can be used for the detection of green-house gases such as nitrogen oxides (NO and NO<sub>2</sub> and NO<sub>x</sub>) (Kawasaki et al., 2002), carbon monoxides, H<sub>2</sub>S, NH<sub>3</sub> and hydrocarbons such as ethanol, benzene and methane (Wang et al., 2003). WO<sub>x</sub> electrochromism has been investigated (Leftheriotis et al., 2003) and found to be enhanced when mixed with Au and Al (Hoel et al., 2004), Ti (Sun et al., 2004; Shieh et al., 2002), Au, Pd and Pt (Ando et al., 2001) and with MoO<sub>3</sub> (Patil and Patil, 2001). Influence of substrate temperature (Patil et al., 2001), annealing (Jayatissa et al., 2004) and proton irradiation on the properties of WO<sub>x</sub> have been reported (Kamal et al., 2005). Performance of WO<sub>x</sub> has been compared with NiO<sub>x</sub> on electrochromism (Arakaki et al., 1995), with V<sub>2</sub>O<sub>5</sub> as sensitive elements for NO detection (Capanoe et al., 1999; Djerad et al., 2004) and with nano-powders of tin and indium oxides as CO and O<sub>2</sub> detectors (Baraton et al., 2002). However, despite the wide range of applications for WO<sub>3</sub>, it has to date, not been synthesised using the laser pyrolysis technique.

In this paper we report on the synthesis of WO<sub>3</sub> nano-rods by laser pyrolysis in the far infra-red without the introduction of a flame (induced by the presence of acetylene and oxygen in other studies). In Section 2 we introduce the basic theory of laser propagation and derive expressions for the dissociation zone inside the reactor. In Section 3 the general methodology and experimental setup is presented, followed by experimental results and discussion in Section 4. The results include the production of thin films by laser pyrolysis whereas most of the few previous publications on this technique concentrated on powders. The findings are summarised in Section 5.

## 2 Laser dissociation zone

In this section the laser beam propagation parameters are defined and applied to determine the interaction volume of the laser beam and the precursor. A comprehensive review of laser beam definitions and laser beam propagation can be found in literature (Belanger, 1991; Siegman, 1991; Siegman and Townsend, 1993; Wright et al., 1992). We present a brief summary here to aid the reader in understanding the experimental parameters to follow.

The multimode laser beam radius  $w(z)$  of the output from a stable-cavity laser is defined using the second moments of the intensity distribution  $I(r,z)$ . Using this

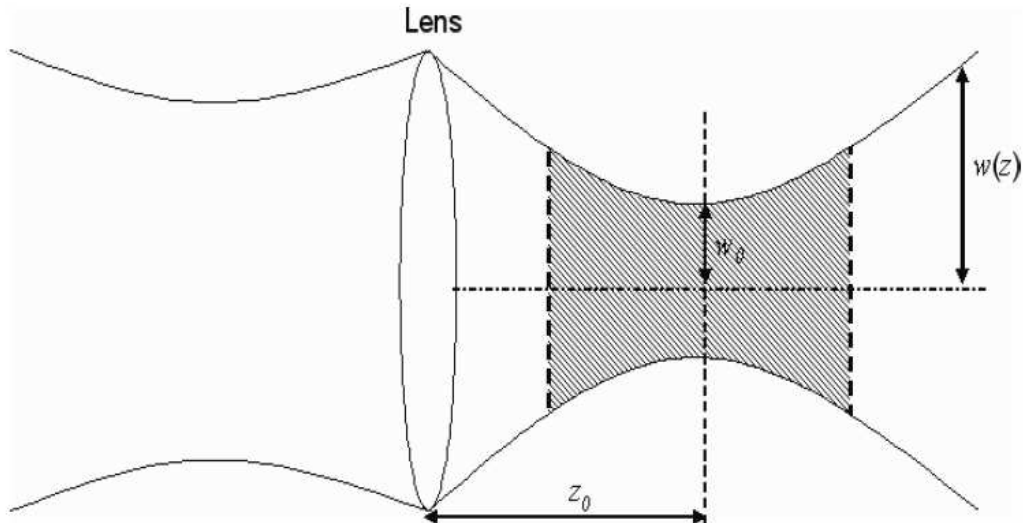
formalism, the laser beam propagation in the  $z$  direction can be described by the modified Gaussian propagation law (see Figure 1):

$$w(z) = w_0 \sqrt{1 + \left( \frac{z - z_0}{z_R} \right)^2} \quad (1)$$

where  $w_0$  is the minimum laser beam width at position  $z_0$ , and  $z_R$  is the so-called Rayleigh range that is related to the beam quality factor  $M^2$  and the wavelength ( $\lambda$ ) of the laser light through the relation:

$$z_R = \frac{\pi w_0^2}{M^2 \lambda} \quad (2)$$

**Figure 1** A schematic laser beam propagation after a focusing element, showing the waist and waist position



*Note:* The interaction volume of the laser beam with the aerosol is depicted here by the shaded area.

The Rayleigh range equals the distance at which the cross-sectional area of the laser beam doubles from the waist value and is often interpreted as a measure of how far the laser beam propagates without significant divergence. For applications where the laser beam interacts over a length rather than at a fixed plane, such as in laser pyrolysis, long Rayleigh ranges are desirable. The beam quality factor is a measure of how many modes are oscillating in the laser and impacts on the space-beam-width product:

$$w_0 \theta_0 = \frac{M^2 \lambda}{\pi} \quad (3)$$

where  $\theta_0$  is the half-angle divergence of the laser beam. Ideal Gaussian laser beams have  $M^2 = 1$ , while all other laser beams have  $M^2 > 1$ . We note that Gaussian beams will have the longest Rayleigh range of all beam types, and the smallest divergence for a given

waist size. In processes such as laser pyrolysis, where long propagation distances are desirable but with high power densities, good laser beam quality is essential.

With these parameters known, the power density  $P(r,z)$  of a near Gaussian laser beam everywhere inside the reactor may be described as follows:

$$P(r,z) = \frac{2P_0}{\pi w^2(z)} \exp\left(-2\left(\frac{r}{w(z)}\right)^2\right) \quad (4)$$

where  $z$  is the propagation distance from the final focusing element,  $r$  is the radial coordinate, and  $P_0$  is the total power contained in the output beam. The peak power density of the laser beam is given by:

$$P_{\text{peak}}(z) = \frac{2P_0}{\pi w^2(z)} \quad (5)$$

and clearly decreases with increasing spot size, reaching a maximum at  $z = z_0$ . If the reactor is placed at a distance  $d$  from the final focusing element and is of length  $L$ , then the laser beam will fill a volume given by:

$$V = \int_d^{d+L} \pi w^2(z) dz = \frac{\pi w_0^2 L (3d^2 + L^2 + 3d(L - 2z_0) - 3Lz_0 + 3(z_0^2 + z_R^2))}{3z_R^2} \quad (6)$$

A special case of the aforementioned is when the interaction volume is chosen to be exactly two Rayleigh ranges; in this case the volume is given by:

$$\int_{z_0 - z_R}^{z_0 + z_R} \pi w^2(z) dz = \frac{8\pi^2 w_0^4}{3M^2 \lambda} \quad (7)$$

This analytical result is useful in getting an intuitive feel for the optimal optical delivery system: large focal spots (large  $w_0$ ) will give a larger interaction volume, but the peak power density of the laser beam decreases with increasing size. If threshold power densities are required for the process, then a compromise must be made. In addition, if the process has a threshold power of  $P_t$ , then only that part of the laser beam above this threshold will be effective for dissociation, resulting in a reduced dissociation volume of:

$$V = \int_d^{d+L} \pi r_0^2(z) dz \quad (8)$$

where  $r_0$  is the radius of the 'effective' beam:

$$r_0(z) = \frac{w^2(z)}{2} \text{Ln}\left(\frac{2P_0}{\pi w^2(z) P_t}\right) \quad (9)$$

The impact of laser beam parameters on such multiphoton dissociation processes has been discussed elsewhere in detail (Forbes and Botha, 2005; Forbes et al., 2002), and is beyond the scope of this paper to review. However we end this section with a brief summary of the salient points to be used in later sections: high power densities are

achieved through focusing the laser beam to reduce the beam size, but this in turn reduces the laser beam volume and Rayleigh range, thereby reducing the volume in which the precursor interacts with the laser beam. In such problems a compromise is always necessary, the extent of which is largely determined by what can be extracted from the laser in terms of laser power and beam quality.

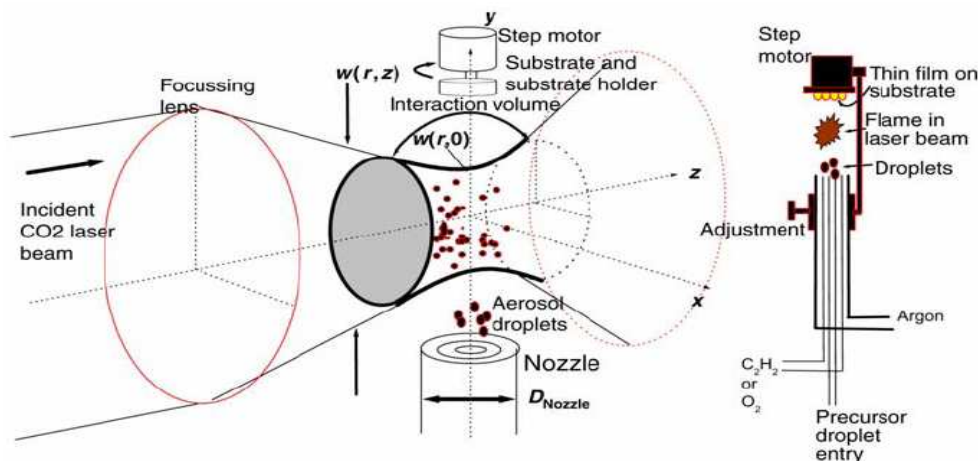
### 3 Experimental methodology and setup

A six arm chamber was designed and built with adjacent arms orthogonal to one another. Two opposite arms were mounted with 2 inch ZnSe windows tilted slightly from normal incidence to avoid back reflections into the laser cavity; these formed the input and output windows for the laser beam, which propagated in the horizontal plane, parallel to the optical table, through the two-arm length. The entrance window was 145 mm from the focusing element and the total length from entrance to exit window was 590 mm. Orthogonal to the laser beam axis, in the vertically upwards direction, the precursor droplets were released into the chamber and travelled into the laser beam volume. The subsequent products were collected in one of two configurations:

- 1 onto a substrate for production of thin films
- 2 onto a filter, connected to a pump, for the production of powders.

In the thin film configuration, the substrate was mounted on a rotating stage driven by a controllable step-motor, which in turn was powered and controlled from outside the chamber via vacuum-to-atmosphere adaptors. The last pair of arms, not used in this experiment, allows for viewing the pyrolysis process through either visual or spectroscopic means. A schematic representation of the laser pyrolysis concept is shown in Figure 2.

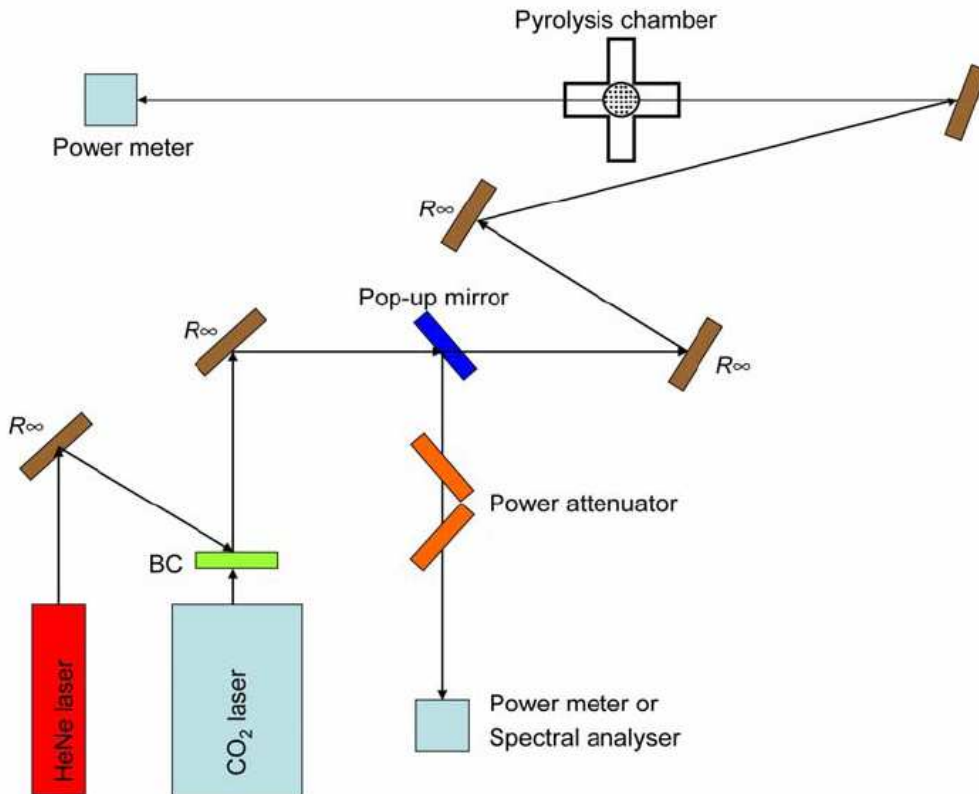
**Figure 2** An illustration of the laser pyrolysis setup (see online version for colours)



*Note:* The laser beam introduces a certain interaction volume into which the aerosol droplets of the precursor are released. The insert on the right illustrated the multiflow nozzle used, which allowed the separate entry of the precursor and carrier gases.

The experimental system for delivery of the laser beam is shown in Figure 3. A wavelength tuneable Continuous Wave (CW) CO<sub>2</sub> laser was used in the experiments (Edinburgh Instruments, model PL6). Wavelength tuneability of the laser was possible with an intra-cavity mounted grating, allowing line tuneable output in the 9.2–10.8 μm range. A pop-up mirror in the optical setup allowed the laser beam to be directed to a diagnostics table for power measurements (Coherent power meter, model 201) and for determining the lasing wavelength using a spectrum analyser (Optical Engineering Inc., model 16A). A polarisation based attenuator was used to allow power variability (this could also be achieved through adjustment of the laser discharge current). A Helium Neon laser was aligned colinear with the CO<sub>2</sub> beam for ease of alignment through the optical system. The laser beam was focused using a 2 m radius of curvature concave mirror (gold coated from II – VI Inc.) and the profile of the laser beam was measured at various distances from the mirror with a scanning slit to determine the complete propagation characteristics inside the reactor. Careful choice of the slit width was made for each measurement in order to ensure accurate results following the approach of Chapple (1994). Since it was clear that the intensity profile was very Gaussian-like, the beam radius at each position was calculated by using a Gaussian fit to the data. A non-linear least squares fit was used to extract the necessary laser beam parameters, such as waist, waist position and laser beam quality.

**Figure 3** A schematic representation of the laser beam delivery for the synthesis of tungsten trioxide by laser pyrolysis, with the six arm pyrolysis chamber shown (two arms are in and out of the page) (see online version for colours)



*Note:* The HeNe laser was used only for visible alignment of the CO<sub>2</sub> laser beam. The final focusing element was a 2 m curvature gold coated mirror.



The synthesis of  $\text{WO}_3$  commenced with 5.4 mg of dark blue powder of  $\text{WCl}_6$  (Aldrich 99.99%) dissolved in 500 ml of ethanol. Since  $\text{WCl}_6$  is highly reactive with air and moisture, its dissolution was conducted in argon atmosphere. Optical absorption properties of the precursor were determined using a Bomem DA8 FTIR spectrometer in the wavelength range  $200\text{--}4500\text{ cm}^{-1}$ . The precursor was decanted into a nebuliser (Microlife, model NEB 50) which was attached to the laser pyrolysis system via a multichannel nozzle (see Figure 2), allowing acetylene ( $\text{C}_2\text{H}_2$ ) and/or oxygen to be included in the mix. The precursor droplets were injected into the  $\text{CO}_2$  laser beam with an argon carrier gas. Often in such experiments a combustible combination of gases are used. In this experiment only the multiphoton dissociation route was explored, without the introduction of a flame. Particles from this process were collected on Corning glass substrates, placed on a rotating stage, at room temperature. The so-obtained samples were further annealed in argon atmosphere at  $500^\circ\text{C}$  for 17 hr. Morphology studies were carried out using a Jeol JSM-5600 Scanning Electron Microscopy (SEM) microscope, which was also equipped for Energy Dispersive X-ray (EDX) spectroscopy. In order to avoid charging effects during SEM analysis, the samples were made conductive by carbon coating. In order to unveil molecular composition, phonon behaviour and grain size distribution, Raman spectroscopy was carried out using a Jobin-Yvon T64000 Raman spectrograph with a  $514.5\text{ nm}$  line from an argon ion laser. The power of the laser at the sample for Raman spectroscopy of the postannealed samples was  $0.384\text{ mW}$  in order to minimise localised heating of the sample. The T64000 was operated in single spectrograph mode, with a  $1800\text{ lines/mm}$  grating and a  $20\times$  objective on the microscope. The experimental procedure showed good reproducibility of results.

#### 4 Results and discussion

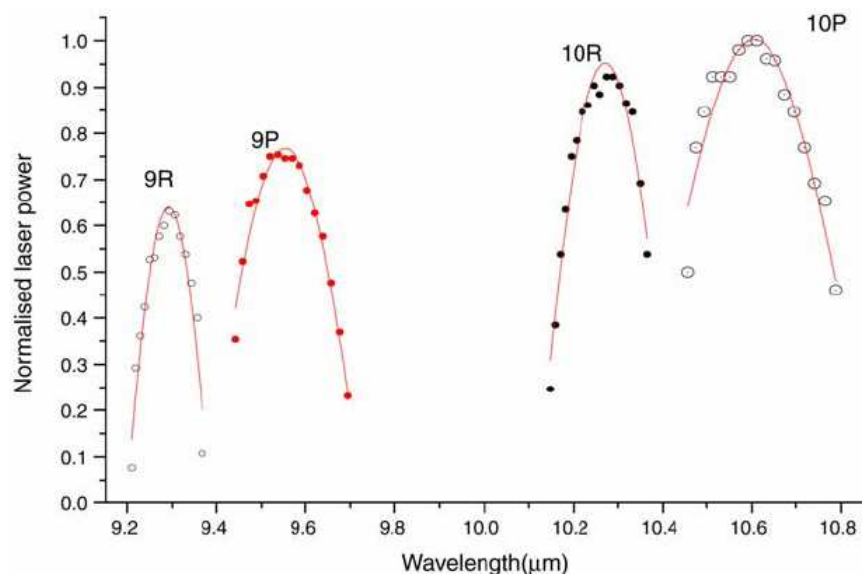
Experiments were performed in order to maximise both the power density of the laser beam inside the reactor and the interaction of the laser beam with the precursor. The latter requires understanding of the absorption bands of the precursor, resulting in an optimal operating wavelength, while the former requires optimising the laser output power and propagation parameters in the reactor near this desired wavelength, guided by the theoretical model described in the previous section.

The precursor's absorption characteristics were studied by infrared spectroscopy in order to determine the absorption bands that overlapped with emission lines of the  $\text{CO}_2$  laser. The absorption spectrum of the precursor showed an absorption band around  $1000\text{ cm}^{-1}$ , which is close to the 10P(20) ( $\lambda = 10.591\text{ }\mu\text{m}$ ) laser emission line at  $944\text{ cm}^{-1}$ , leading to the necessary dissociation. The power spectrum of the  $\text{CO}_2$  laser was obtained in the wavelength range  $9.2\text{--}10.8\text{ }\mu\text{m}$ , and is shown in Figure 4. The major bands correspond to the rotational and vibrational modes of the  $\text{CO}_2$  molecule. In all the results that follow the laser was set to the 10P(20) line, at roughly  $10.6\text{ }\mu\text{m}$ , since this had the largest power of approximately  $50\text{ W}$  and was close to a measured absorption band of the precursor.

The laser beam was focused inside the reactor and the resulting propagation was measured. The measured data was fitted to Equation (1) and the unknown parameters  $w_0$ ,  $z_0$  and  $M^2$  were determined. This allowed calculation of the peak power density as a function of position (from Equation (5)) and the interaction volume (from Equation (6)). The beam radius and power density as a function of position is shown in Figure 5,

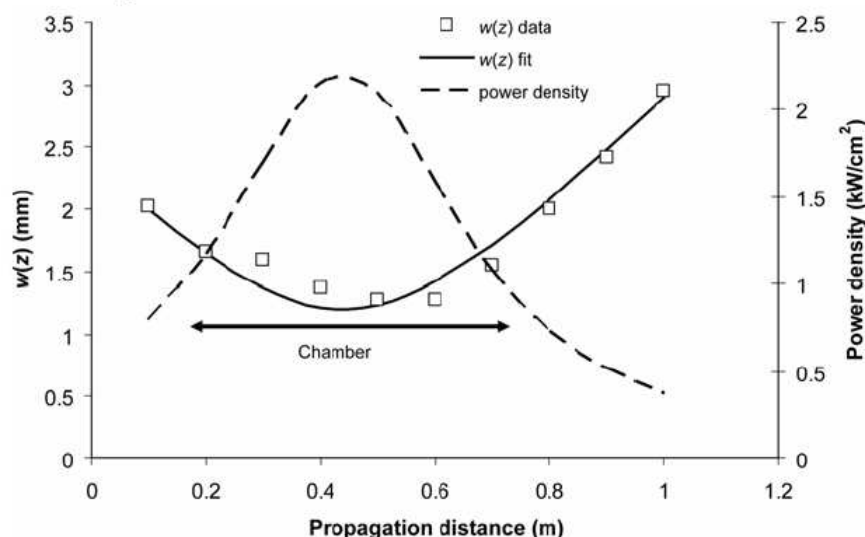
with the extracted laser characteristics listed in Table 1. The laser beam was found to be near Gaussian in intensity profile, and focused to a waist diameter of roughly 2.4 mm with a maximum power density at the waist position of approximately 2.2 kW/cm<sup>2</sup>. This ensured a volume large enough for the aerosol from the nozzle to completely interact with the laser (i.e. the entire aerosol passed through the laser beam), at roughly 4 cm<sup>3</sup>.

**Figure 4** Experimental data on the power spectrum of the laser, showing the well-known four distinct emission bands from the CO<sub>2</sub> laser (see online version for colours)



*Note:* The 10P(20) line showed the highest output power of roughly 50 W.

**Figure 5** Change in laser beam radius and power density as the laser propagates after the focusing element



*Note:* The pyrolysis chamber was placed centred with the laser beam waist position, and is depicted in length on the plot. The power density reaches in excess of 2 kW/cm<sup>2</sup> at its most intense position.

**Table 1** Important laser parameters for the pyrolysis experiment; some are measured directly while others are calculated from experimental data using the relations in Section 2

Propagation parameters			Wavelength	Interaction volume	Power/power density		
$w_0$	$z_0$	$M^2$	$\lambda$	$V$	$P_0$	Max $P_{peak}$	Min $P_{peak}$
1.2 mm	440 mm	1.68	10.6 $\mu\text{m}$	4 $\text{cm}^3$	50 W	2.2 $\text{kW}/\text{cm}^2$	0.9 $\text{kW}/\text{cm}^2$

We have noted a general lack of detail in the literature on full laser propagation parameters used in such experiments, with most authors concentrating only on the total power delivered. We point out here that since laser pyrolysis processes follow non-linear like responses to laser intensity (El-Diasty, 2004), it is imperative that all parameters relevant to calculating these intensities inside the reactor should be reported (such as those reported in Table 1). By not doing so, direct comparison of results becomes difficult to impossible, as is reproducibility. In addition, the laser beam's intensity distribution will also play an important role in the process (Forbes and Botha, 2005) and should where possible be reported. For example, multimode laser output will result in an ever changing intensity distribution due to propagation alone, whereas a Gaussian-like beam will remain Gaussian during free-space propagation. On the contrary, it has been shown (Forbes, 2006) that multimode like beams may in fact maintain their intensity distribution if the medium is suitably non-linear, as it most likely is in laser pyrolysis experiments (El-Diasty, 2004). Thus the laser beam parameters, such as spatial intensity distribution, beam quality and beam waist need to be reported, as they have been here.

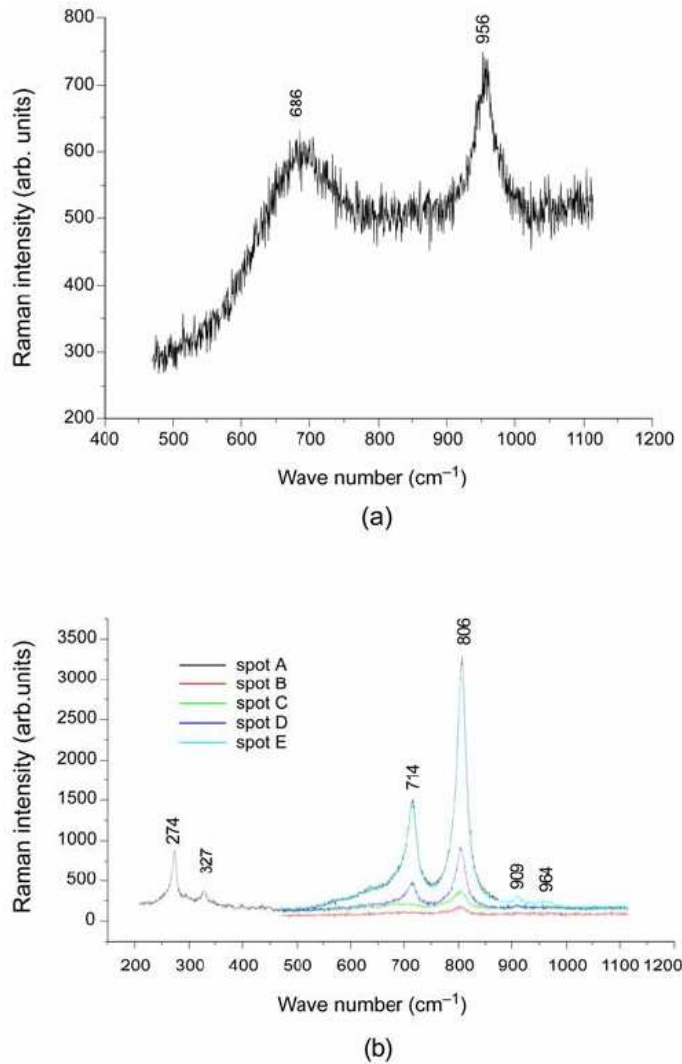
Raman studies on the synthesised samples showed (see Figure 6(a)) two peaks near  $700 \text{ cm}^{-1}$  and  $960 \text{ cm}^{-1}$ , assigned to the O–W–O bending mode and W=O stretching mode, respectively (Grabrusenoks et al., 2001), but an absence of the characteristic peak at  $804 \text{ cm}^{-1}$  assigned to the O–W–O stretching mode of  $\text{WO}_3$  (Lee et al., 1999). This signature is not consistent with that expected from the stoichiometry of  $\text{WO}_3$ , but rather is similar to that of  $\text{W}_3\text{O}_7$  (Salje, 1977). After annealing an intense characteristic peak at  $800 \text{ cm}^{-1}$  appears as can be seen in Figure 6(b), indicating that  $\text{WO}_3$  is formed. The Raman spectra do not change with the addition of  $\text{O}_2$  or  $\text{C}_2\text{H}_2$ , indicating that these gases do not contribute to the dissociation process, as suspected. A SEM micrograph of the annealed samples at  $5000 \times$  magnification is shown in Figure 7(a), with the preannealed sample micrograph shown as an insert in the top left corner. The spherical particles before annealing are not clearly visible but after annealing almost perfectly spherical microsized particles of  $\text{WO}_3$  are accompanied with very interesting additional nanosized features in the form of extended rods. Close examination of the microsized spheres suggests that they are actually composed of smaller spheres in the nanosize scale; this might play an important role regarding the thermochromic and electrochromic properties of the material. A SEM micrograph of the annealed samples at  $20,000 \times$  magnification is shown in Figure 7(b), showing that rod-like nano structures are emanating from the sphere-like  $\text{WO}_3$  structures. These rod-like nano structures are distinct entities with very little to no agglomeration. Image Tool™ image analysis software was used to analyse the surface morphology of the SEM images for size distribution of the rod-like nano structures formed. The size distribution charts, shown in Figure 8, indicated that the mean diameter of the rod-like structures was 51 nm, with a

mean length of 6.8  $\mu\text{m}$ . We propose here that most (if not all) of these nano structures are in fact  $\text{WO}_3$  nano-rods, which we base on the following argument:

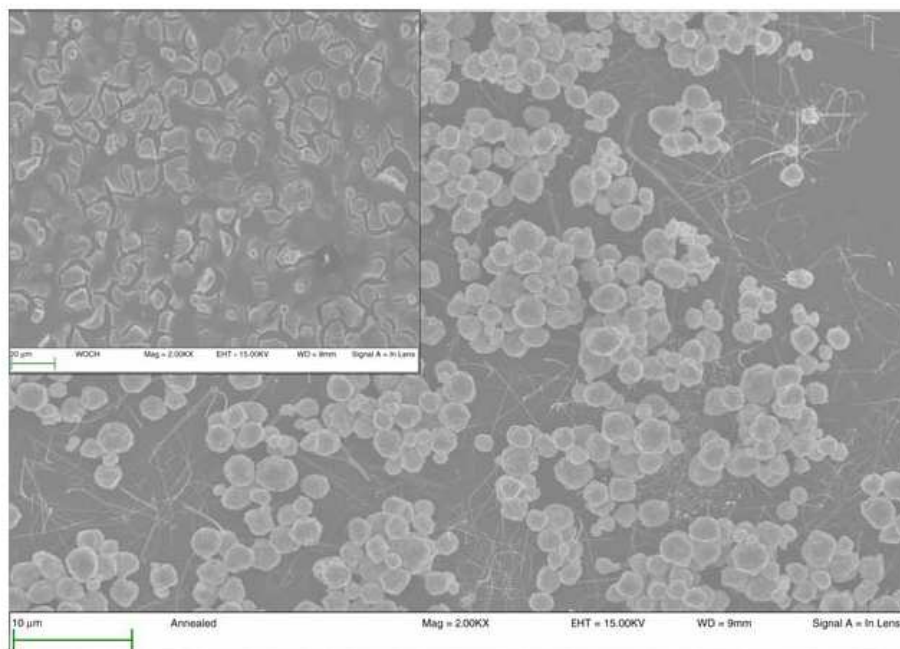
- 1 Gillet et al. (2005) have observed that  $\text{WO}_3$  nano-rods can be formed when potassium is present during the annealing process to act as a catalyst. We observe the presence of potassium through EDX analysis of the samples both before and after annealing (see Figure 9), and it is known that this is an impurity in the glass substrate.
- 2 Our SEM images (Figure 7(b)) show clearly that the nanosized structures are emanating from microsized spheres (actually growing out of the structures), which we know to be  $\text{WO}_3$  from Raman analysis.

These two facts lead us to conclude that the nano structures are in fact  $\text{WO}_3$  nano-rods, formed for the first time during a laser pyrolysis process.

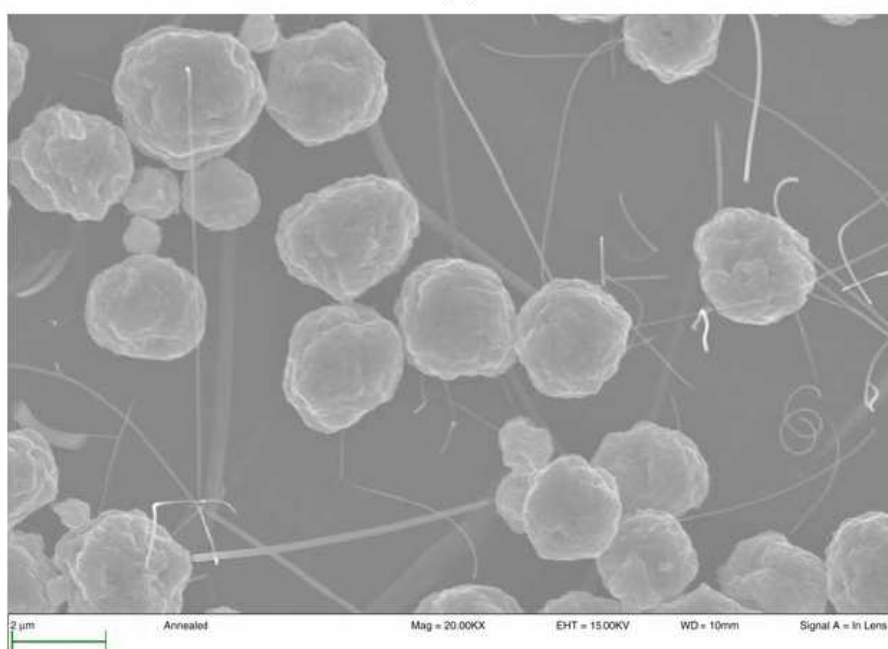
**Figure 6** Raman spectra of tungsten oxides synthesised under oxygen and  $\text{C}_2\text{H}_2$  conditions with: (a) as deposited and (b) after annealing at 500°C for 17 hr in argon (see online version for colours)



**Figure 7** (a) SEM micrographs of a  $\text{WO}_3$  sample prepared with the laser pyrolysis method, and (b) a close up on some of the nano-rods showing the emergence of the rod from the large spheres (see online version for colours)



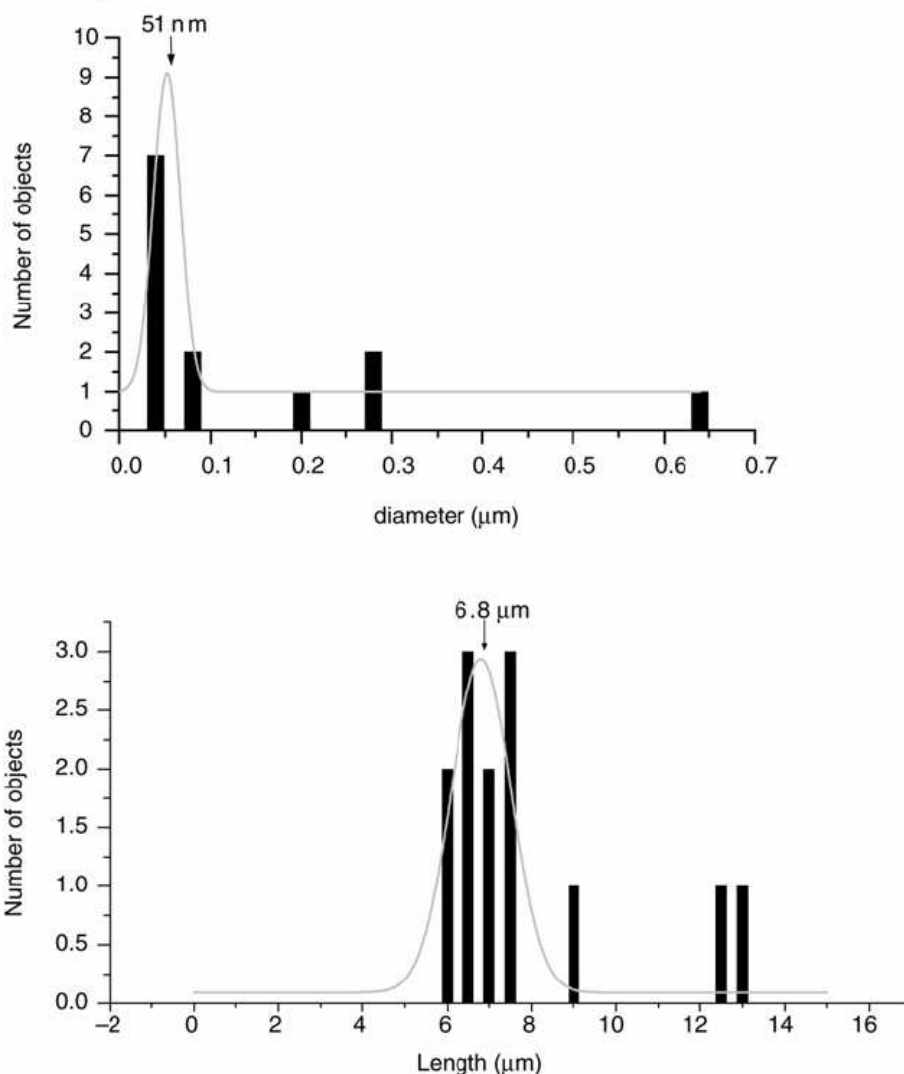
(a)



(b)

*Note:* The insert shows the sample prior to annealing while the larger image shows the same sample after annealing. The morphology change is clearly apparent, with tungsten oxide nano-wires in the background of the almost uniformly spherical particles of  $\text{WO}_3$ .

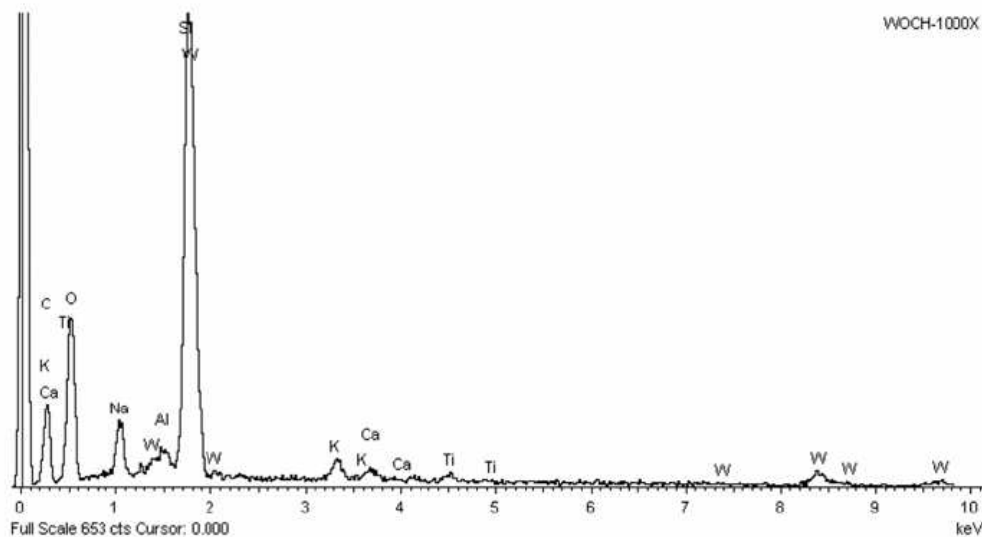
It also appears that some of these nano structures might be tubular in nature; this has yet to be confirmed by transmission electron microscopy.

**Figure 8** Histograms of the diameter and length of a selection of the nanostructures shown in Figure 7

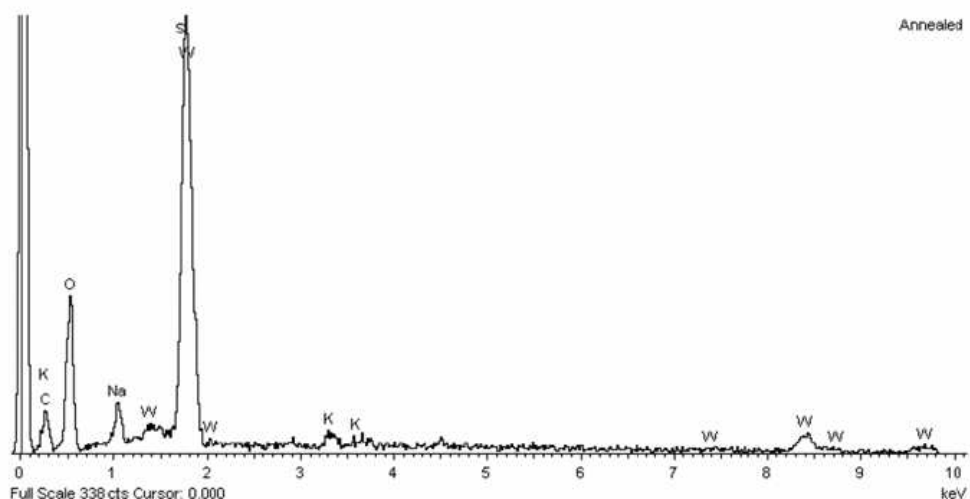
*Note:* The mean diameter and length of the  $\text{WO}_3$  nano-rods (as determined from the fits) are 51 nm and 6.8  $\mu\text{m}$ , respectively.

Finally we point out that the nanograins, although not having the desirable size necessary for affecting positively the thermo/electrochromic properties of  $\text{WO}_3$ , were produced without the flame contributing component (mixture of  $\text{O}_2$  and  $\text{C}_2\text{H}_2$ ) common in such experiments. This was a deliberate attempt at providing an environment for multiphoton dissociation only, with resulting reactions. Despite this nanosize spheres (around 200 nm diameter) formed an agglomeration leading to microsize particles. Since the results with only  $\text{O}_2$  or  $\text{C}_2\text{H}_2$  are identical and given that with only one of these gases present one does not produce a flame, we also propose that in this case the production of such nanostructures is owing to the selective dissociation of the O–C bonds in the tungsten ethoxide precursor liquid, which is close to resonance with the 10.6  $\mu\text{m}$  emission wavelength of the  $\text{CO}_2$  laser employed. This ‘first observation’ report will in due course be followed with a more detailed study on the formation and properties of these structures.

**Figure 9** EDX spectra for  $\text{WO}_3$  samples (a) before annealing and (b) after annealing, showing the presence of the catalytic potassium (K) in both cases



(a)



(b)

## 5 Summary

The synthesis of nanograin tungsten trioxide thin films for the first time by laser pyrolysis has been reported. A detailed description of the experimental set up has been outlined, and the need to present detailed information on the laser beam characteristics for comparison and repeatability of results has been highlighted. Investigation of the so-produced  $\text{WO}_3$  thin films by Raman, EDX and by SEM was conducted and the results have been presented and discussed. The well-known Raman band at  $800\text{ cm}^{-1}$  observed in all samples confirms the presence of  $\text{WO}_3$  as agglomeration of nanosize particles. The present study also reports for the first time the presence of  $\text{WO}_3$  nano-rods from laser pyrolysis. The fact that these structures appear in the presence of potassium seems to add weight to a previous proposal (Gillet et al., 2005) that potassium acts as a catalyst for the

formation of  $\text{WO}_3$  nano-rods. The preliminary results from this study have shown that laser pyrolysis has great potential as a tool for fabricating nano-rods of high quality, given the straightness and lengthy nature of most of these nano-rods.

## Acknowledgements

Sponsorship from the South African National Research Foundation (NRF) through project numbers: LREG 0001 and User Facility of the CSIR National Laser Centre of South Africa are greatly appreciated. We also acknowledge partial support of the Japanese Government through the Joint Japan/World Bank Graduate Scholarship Programme.

## References

- Amara, M., Hourlier, D. and El Ganaoui, M. (2003) 'A CFX-based model for Si/C/N ceramic nanopowder synthesis by laser pyrolysis', *3rd International Conference on CFD in the Minerals and Process Industries CSIRO*, Melbourne, Australia, pp.241–245.
- Ando, M., Chabicoovsky, R. and Haruta, M. (2001) 'Optical hydrogen sensitivity of noble metal-tungsten oxide composite films prepared by sputtering deposition', *Sensors and Actuators B*, Vol. 76, pp.13–17.
- Arakaki, J., Reyes, R., Horn, M. and Estrada, W. (1995) 'Electrochromism in  $\text{NiO}_x$  and  $\text{WO}_x$  obtained by spray pyrolysis', *Solar Energy Materials and Solar Cells*, Vol. 37, pp.33–41.
- Baraton, M.I., Merhari, L., Ferkel, H. and Castagnet, J.F. (2002) 'Comparison of the gas sensing properties of tin, indium and tungsten oxides nanopowders: carbon monoxide and oxygen detection', *Materials Science and Engineering C*, Vol. 19, pp.315–321.
- Belanger, P.A. (1991) 'Beam propagation and the ABCD ray matrices', *Optics Letters*, Vol. 16, No. 4, p.196–198.
- Bowden, C.M., Stettler, J.D. and Witriol, N.M. (1977) 'An excitation model for laser-induced photochemical reactions', *Journal of Physics B: Atomic and Molecular Physics*, Vol. 34, pp.1045–1050.
- Cannon, W.R., Danforth, S.C., Flint, J.H., Haggerty, J.S. and Marra, R.A. (1982) 'Sinterable ceramic powders from laser-driven reactions', *Journal of the American Ceramic Society*, Vol. 65, pp.324–330.
- Capano, S., Rella, R., Siciliano, P. and Vasanelli, L. (1999) 'A comparison between  $\text{V}_2\text{O}_5$  and  $\text{WO}_3$  thin films as sensitive elements for NO detection', *Thin Solid Films*, Vol. 350, pp.264–268.
- Chapple, P.B. (1994) 'Beam waist and  $M^2$  measurement using a finite slit', *Optical Engineering*, Vol. 33, No. 7, pp.2461–2466.
- Dez, R., Porterat, D. and Boime, H. (2004) 'Silicon carbonitride nanopowders by laser pyrolysis for plastic nanocomposites', *Engineering Materials*, Vols. 264–268, pp.25–28.
- Djerad, S., Tifouti, L., Crocoll, M. and Wesweiler, W. (2004) 'Effect of vanadia and tungsten loadings on the physical and chemical characteristics of  $\text{V}_2\text{O}_5$ - $\text{WO}_3/\text{TiO}_2$  catalysts', *Journal of Molecular Catalysis A: Chemical*, Vol. 208, pp.257–265.
- El-Diasty, F. (2004) 'Simulation of  $\text{CO}_2$  laser pyrolysis during preparation of SiC nanopowders', *Optics Communication*, Vol. 241, pp.121–135.
- Forbes, A. (2006) 'Laser beam propagation in non-linearly absorbing media', *Proceedings of SPIE*, Vol. 6290, pp.31–37.



- Forbes, A. and Botha, L.R. (2005) 'Isotope separation with infrared laser beams', in F.M. Dickey, S.C. Holswade and D.L. Shealy (Eds). *Laser Beam Shaping Applications*, Chapter 5, New York: CRC Taylor & Francis, pp.183–209.
- Forbes, A., Strydom, H.J., Botha, L.R. and Ronander, E. (2002) 'Beam delivery for stable isotope separation', *Proceedings of SPIE*, Vol. 4770, pp.13–27.
- Gillet, M., Delamare, R. and Gillet, E. (2005) 'Growth of epitaxial tungsten oxide nanorods', *Journal of Crystal Growth*, Vol. 279, pp.93–99.
- Grabrusenoks, J., Veispals, A., von Czarnowski, P. and Meiwes-Broer, K.H. (2001) 'Raman and infrared characterization of tungsten trioxide', *Electrochimica Acta*, Vol. 46, p.2229–2231.
- Haggerty, J.S. and Cannon, W.R. (1981) 'Sinterable powders from laser-driven reactions in laser-induced chemical processes', in J.I. Steinfeld (Ed). *Laser Induced Chemical Processes*, New York: Plenum Press, pp.105–121.
- Herlin, N., Musset, A.X., Martinengo, M., Luce, H. and Cauchetier, M. (1996) 'Nanometric Si-based oxide powders: synthesis by laser pyrolysis and characterisation', *Journal of the European Ceramic Society*, Vol. 16, pp.1063–1073.
- Hoel, A., Reyes, L.F., Heszler, P., Lantto, V. and Granqvist, C.G. (2004) 'Nanomaterials for environmental applications: novel WO<sub>3</sub>-based gas sensors made by advanced gas deposition', *Current Applied Physics*, Vol. 105, pp.283–289.
- Huisken, F., Hofmeister, H., Kohn, B., Laguna, M.A. and Pillard, V. (2000) 'Laser production and deposition of light-emitting silicon nanoparticles', *Applied Surface Science*, Vols. 154–155, pp.305–313.
- Jayatissa, A.H., Cheng, S.H. and Gupta, T. (2004) 'Annealing effect on the formation of nanocrystals in thermally evaporated tungsten oxide thin films', *Materials Science and Engineering B*, Vol. 109, pp.283–289.
- Kamal, H., Akl, A.A. and Abdel-Hady, K. (2005) 'Influence of proton insertion on the conductivity, structural and optical properties of amorphous and crystalline electrochromic WO<sub>3</sub> films', *Physica B: Condensed Matter*, Vol. 349, pp.192–205.
- Kawasaki, H., Namba, J., Iwatsuji, K., Suda, Y., Wada, K., Ebihara, K. and Ohshima, T. (2002) 'NO<sub>x</sub> gas sensing properties of tungsten oxide thin films synthesised by pulsed laser deposition method', *Applied Surface Science*, Vols. 197–198, pp.547–551.
- Lee, S.H., Cheong, H.M., Tracy, C.E., Mascarenhas, A., Benson, D.K. and Deb, S.K. (1999) 'Effects of W valency on Raman', *Electrochimica Acta*, Vol. 44, pp.3111–3115.
- Leftheriotis, G., Papaefthimiou, S., Tianoulis, P., Siokou, A. and Kefalas, D. (2003) 'Structural and electrochemical properties of opaque sol-gel deposited WO<sub>3</sub> layers', *Applied Surface Science*, Vol. 218, pp.275–280.
- Muller, A., Herlin-Boime, N., Tenegal, F., Berger, A.X., Flank, A.M., Romuald, D., Muller, K., Bill, J. and Aldinger, F. (2003) 'Comparison of Si/C/N pre-ceramics obtained by laser pyrolysis or furnace thermolysis', *Journal of the European Ceramic Society*, Vol. 23, pp.37–46.
- Mwakikunga, B.W., Sideras-Haddad, E. and Maaza, M. (2007) 'First synthesis of vanadium dioxide by ultrasonic nebula-spray pyrolysis', *Optical Materials*, Vol. 29, pp.481–487.
- Patil, P.R. and Patil, P.S. (2001) 'Preparation of mixed oxide MoO<sub>3</sub>-WO<sub>3</sub> thin films by spray pyrolysis technique and their characterisation', *Thin Solid Films*, Vol. 382, pp.13–22.
- Patil, P.S., Nikam, S.B. and Kadam, L.D. (2001) 'Influence of substrate temperature on the properties of sprayed WO<sub>3</sub> thin films', *Materials Chemistry and Physics*, Vol. 69, pp.77–83.
- Petcu, S., Cauchetier, M., Armand, X., Voicu, I. and Alexandrescu, R. (2000) 'Formation of fullerenes in laser pyrolysis of benzene', *Combustion and Flame*, Vol. 122, pp.500–507.
- Pola, J., Pokorna, D., Bohacek, J., Bastl, Z. and Ouchi, A. (2004) 'Nano-structured crystalline Te films by laser gas-phase pyrolysis of dimethyl tellurium', *Journal of Analytical and Applied Pyrolysis*, Vol. 71, pp.739–746.
- Salje, E. (1977) 'Normal WO<sub>3</sub> crystal vibration modes', *Acta Crystallographica B*, Vol. 33, pp.574–577.

- Shieh, J., Feng, H.M., Hon, M.H. and Juang, H.Y. (2002) 'WO<sub>3</sub> and W-Ti-O thin film gas sensors prepared by sol-gel dip-coating', *Sensors and Actuators B*, Vol. 86, pp.75–80.
- Siegman, A.E. (1991) 'Defining the effective radius of curvature for a nonideal optical beam', *IEEE Journal of Quantum Electronics*, Vol. 27, No. 5, pp.1146–1148.
- Siegman, A.E. and Townsend, S.W. (1993) 'Output beam propagation and beam quality from a multimode stable-cavity laser', *IEEE Journal of Quantum Electronics*, Vol. 29, No. 4, pp.1212–1217.
- Sun, Q., Rao, B.K., Jena, P., Stolcic, D., Gantefor, G. and Kawazoe, Y. (2004) 'Effect of sequential oxidation on the electronic structure of tungsten clusters', *Chemical Physics Letters*, Vol. 387, pp.29–34.
- Tenegal, F., Petcu, S., Herlin-Boime, N., Armand, X., Mayne, M. and Reynaud, C. (2001) 'Effect of the C/O ratio on the C<sub>60</sub> and C<sub>70</sub> formation rates in soot synthesised by laser pyrolysis of benzene-based mixtures', *Chemical Physics Letters*, Vol. 335, pp.155–162.
- van Erven, W.J.M., Trzeciak, T.M., Fu, Z. and Marijnissen, J.C.M. (1997) 'Design of a laser assisted aerosol reactor for production of ceramics on a semi-industrial scale', *Journal of the European Ceramic Society*, Vol. 17, pp.1045–1052.
- Wang, S.H., Chou, T.C. and Liu, C.C. (2003) 'Nano-crystalline tungsten oxide NO<sub>2</sub> sensor', *Sensors and Actuators B*, Vol. 94, pp.343–351.
- Watanabe, A., Unno, M., Hojo, F. and Miwa, T. (2003) 'Silicon-germanium alloy prepared by laser-induced pyrolysis of organo-germanium nanocluster spin-coated on Si substrates', *Materials Letters*, Vol. 57, pp.3043–3047.
- Wright, D., Greve, P., Fleischer, L. and Austin, L. (1992) 'Laser beam width, divergence and beam propagation factor: an international standardization approach', *Optical and Quantum Electronics*, Vol. 24, pp.S993–S1000.

## Raman spectroscopy of WO<sub>3</sub> nano-wires and thermo-chromism study of VO<sub>2</sub> belts produced by ultrasonic spray and laser pyrolysis techniques

B. W. Mwakikunga<sup>1,2,3</sup>, E. Sideras-Haddad<sup>\*,2</sup>, A. Forbes<sup>4,5</sup>, and C. Arendse<sup>1</sup>

<sup>1</sup> CSIR National Centre for Nano-Structured Materials, P.O. Box 395, Pretoria 0001, South Africa

<sup>2</sup> School of Physics, University of the Witwatersrand, Private Bag X3, P.O. Wits, Johannesburg 2050, South Africa

<sup>3</sup> Department of Physics and Biochemical Sciences, University of Malawi, The Polytechnic, Private Bag 303, Chichiri, Blantyre 3, Malawi

<sup>4</sup> CSIR National Laser Centre, P.O. Box 395, Pretoria 0001, South Africa

<sup>5</sup> School of Physics, University of Kwazulu-Natal, Private Bag X54001, Durban 4000, South Africa

Received 2 May 2007, accepted 25 October 2007

Published online 15 January 2008

PACS 63.22.+m, 73.63.Bd, 78.30.Hv, 81.07.Bc, 81.15.Rs, 81.16.Mk

\* Corresponding author: e-mail [elias.sideras-haddad@wits.ac.za](mailto:elias.sideras-haddad@wits.ac.za), Fax: 0027 11 717 6879

Novel optical and electrical properties of newly synthesized nano-wires of monoclinic WO<sub>3</sub> and nano-belts of rutile VO<sub>2</sub> have been investigated by Raman spectroscopy and thermo-chromism studies respectively. Phonon confinement is observed in the WO<sub>3</sub> nano-wires and the previously modified Richter equation is fitted to the experimental Raman spectroscopy data to obtain the optical phonon dispersion rela-

tions for the 713 cm<sup>-1</sup> branch and the 808 cm<sup>-1</sup> branch of WO<sub>3</sub> phonon spectra for the first time. Electrical measurements on the VO<sub>2</sub> nano-belts at varying temperature reveal an enhanced hysteresis width of about 83 °C surpassing previously reported values on the thermo-chromism studies on VO<sub>2</sub>.

© 2008 WILEY-VCH Verlag GmbH & Co. KGaA, Weinheim

**1 Introduction** Single crystalline semiconductor nano-wires are being extensively investigated due to their unique electronic and optical properties and their novel use in electronic and photonic devices. These unique properties arise from their anisotropic geometry, large surface-to-volume ratio, and carrier and photon/phonon confinement in two dimensions (1D system). More focus, in terms of electronic and photonic applications, is currently directed towards controlled synthesis and characterization of nano-wires (NWs) rather than nano-tubes (NTs) due to inability to control the electronic properties of NTs during synthesis. By contrast, the ability to rationally fabricate NWs with precisely controlled and tuneable chemical composition, size, structure and morphology and to accurately dope them with both p- and n-type dopants has opened up opportunities for assembling almost any kind of functional nano-system ranging from integrated solid-state photonics

and electronics to biological sensors [1]. For example, NWs have been organized into field effect transistors, bipolar junction transistors, integrated logic calculators, high frequency ring oscillators and biological and chemical sensors, with some having detection limits down to a single virus [2]. Nano-photonic devices such as light-emitting diodes (LEDs), waveguides, electrically-driven single NW-based lasers, photo-detectors and avalanche photodiodes have all been successfully demonstrated [3].

WO<sub>3</sub> and VO<sub>2</sub> rutile (VO<sub>2</sub> (R)) are transition metal oxides (TMOs) whose properties are superior in their respective families of WO<sub>x</sub> and VO<sub>x</sub> (*x* is the O/metal ratio). At room temperature they both adopt distorted structures of some more symmetrical TMOs respectively ReO<sub>3</sub> and TiO<sub>2</sub> [4]. WO<sub>3</sub> has been used as an active layer with outstanding electro-chromic [5], gaso-chromic [6] and photo-chromic [7] properties. For this reason, WO<sub>3</sub> has been used to con-

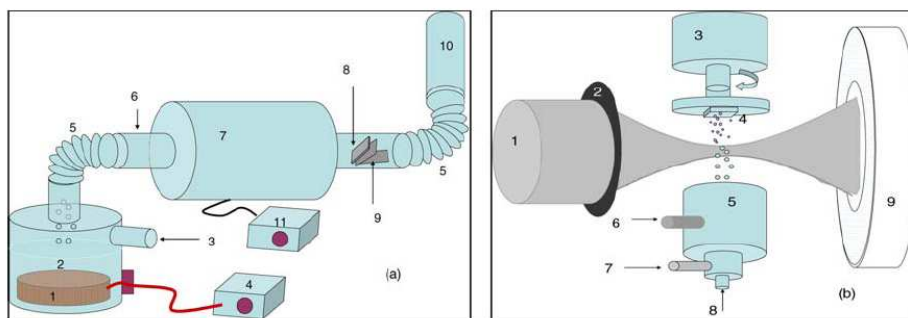
struct flat panel displays, photo-electro-chromic ‘smart’ windows [8], writing-reading-erasing optical devices [9], optical modulation devices [10], gas sensors and humidity and temperature sensors [11]. On the other hand,  $\text{VO}_2$  is thermo-chromic [12] and due to this structural change, depending on ambient temperature,  $\text{VO}_2$  has a myriad of quite similar application to  $\text{WO}_3$ : energy efficient windows, optic disc media and holographic storage, bit recording, write-erase stable devices ultra fast switches and I.R. and radar camouflage and laser protection in the military [12].

For a perfect crystal of diameter  $d$  having vibrational modes of momentum  $q$ , the Heisenberg’s uncertainty principle ( $\delta d \delta q \sim h$ ) means that as  $\delta d \rightarrow \infty$  (bulk) then  $\delta q \rightarrow 0$  (the  $q = 0$  selection rule applies). As the diameter,  $\delta d \rightarrow 0$  (nano-metric) then the vibrational momentum,  $\delta q \rightarrow \infty$ . In this case, a contribution from the  $q \neq 0$  phonons determined by the dispersion relation  $\omega(q)$  is allowed. This accounts for the asymmetric broadening of the peaks in a Raman spectrum. The Richter equation for confined phonons in spherical nano-particles [15], modified to include Gaussian distribution of the phonon momenta and particle size by Faucet and Campbell [16], and further modified to account for the geometry of nano-wires by Adu et al. [11, 17] has been used herein to obtain phonon dispersion spectra for  $\text{WO}_3$ .

Thermo-chromism – the ability to change  $\text{VO}_2$  (R)’s colour at different ambient temperatures – is one of this material’s many important optical properties. This colour change displays a hysteresis around 68 °C. The hysteresis width (HW) determines the materials stability especially when used in optical data storage and optical/electrical switching applications. HW values in the range 1–10 °C have been reported by DeNatale et al. (1989) (in Ref. [14]). We have reported an HW of 5 °C in  $\text{VO}_2$  (R) produced by ultrasonic spray pyrolysis [12]. A remarkably enhanced hysteresis was reported by Lopez et al. [14] to the value of 34 °C on which we have made an improvement in the current study as discussed in the results section.

**2 Experimental** Two techniques were used in the synthesis of  $\text{WO}_3$  and  $\text{VO}_2$  (R) nanostructures: ultrasonic spray pyrolysis (USP) and laser pyrolysis (LP) [20, 21]. Synthesis of  $\text{WO}_3$  and  $\text{VO}_2$  by USP has been reported previously [12]. In brief, and as illustrated in Fig. 1(a), these processes involve decomposition of the relevant precursor droplets at atmospheric pressure in temperature regions of 100–700 °C and depositing the solid state particles that form on Corning glass substrates. The precursor droplets for USP were generated by focussing ultrasound waves of frequency,  $f$ , to the surface of the precursor liquid of surface tension,  $\sigma$  and density,  $\rho$  thereby producing droplets of typical diameter  $D = k(\pi\sigma/\rho)^{1/3}$ . The solid state particles so-obtained have typical diameters  $d = D(c_{pr} \cdot M_p/\rho_p \cdot M_{pr})^{1/3}$  where  $c_{pr}$  is concentration of precursor,  $M_p$  and  $M_{pr}$  are molar masses of precursor and deposited particles respectively; and  $\rho_p$  being the density of the as-deposited particles. Synthesis by LP has also been reported elsewhere [12, 20, 21]. This is schematically illustrated in Fig. 1(b). Droplets from precursors of  $\text{WCl}_6$  (Aldrich 99.99%) in ethanol,  $\text{VCl}_4$  (Aldrich 99.99%) in ethanol and aqueous  $\text{V}_2\text{O}_5$  pre-molten at 800 °C were injected in a 50 W  $\text{CO}_2$  laser beam by a nebuliser (Microlife, model NEB50). The beam, tuned at a wavelength of 10.59  $\mu\text{m}$ , was focussed to 2.4 mm to completely engulf the injected droplets. Particles from these processes were deposited onto Corning glass ( $\text{SiO}_2$ ) substrates and these were further annealed in argon atmosphere at 500 °C for 17 hours.

Morphology studies were carried out using a LEO 1525 field emission scanning electron microscope (FESEM) operated at 3–20 kV. Raman spectroscopy was carried out using a Jobin–Yvon T64000 Raman spectrograph with a 514.5 nm line from an argon ion laser. The power of the laser at the sample for Raman spectroscopy of the post-annealed samples was small enough (0.384 mW) in order to minimise localised heating of the sample. The T64000 was operated in single spectrograph mode, with



**Figure 1** (online colour at: [www.pss-a.com](http://www.pss-a.com)) (a) Schematic set up of ultrasonic spray pyrolysis: (1) ultrasonic nebuliser transducer, (2) precursor liquid, (3) carrier gas inlet, (4) nebuliser power supplier, (5) connecting bellow, (6) quartz tube, (7) tube furnace, (8) substrate, (9) substrate holder, (10) exhaust pipe, (11) furnace temperature controller. Figure 1(b) is the outline of the laser pyrolysis set up: (1) laser beam, (2) focussing lens, (3) stepper-motor, (4) droplet stream, (5) three-way nozzle, (6) argon gas inlet, (7) carrier gas inlet, (8) precursor liquid droplets and carrier gas inlet, (9) substrate.

the 1800 lines/mm grating and a 20× objective on the microscope. The Richter equation given in Refs. [17, 18] and herein reproduced as Eq. (1) was fitted to experimental data and the pertinent parameters were extracted:

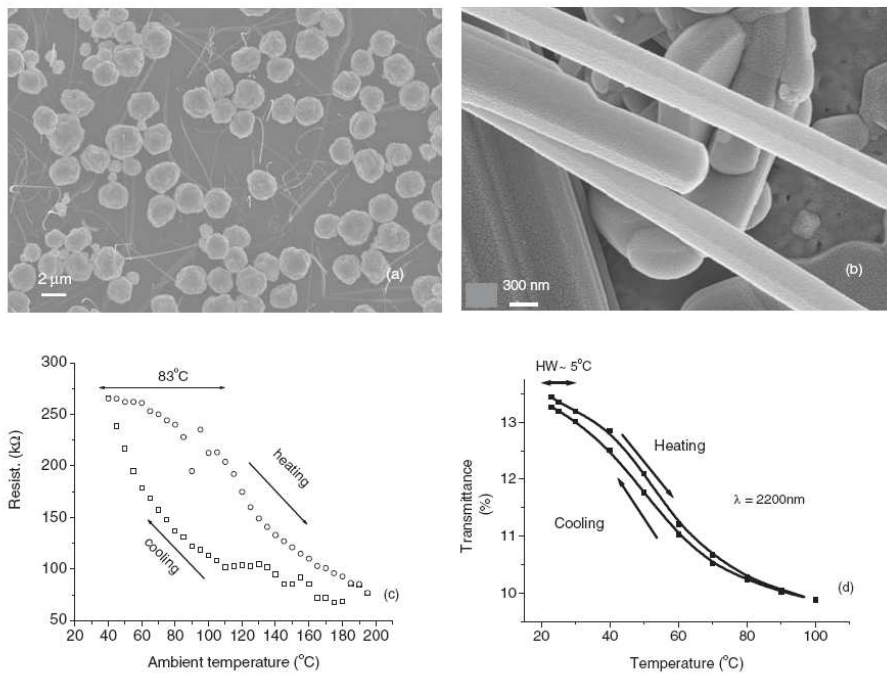
$$I(\omega) = A_0 \int_{-\infty}^{\infty} \left[ 2\pi q_{\perp} \frac{\exp\left(-\frac{q_{\perp}^2 d^2}{2\alpha}\right)}{(\omega - \omega(\mathbf{q}))^2 + \Gamma_0^2/4} \right] dq_{\perp} \quad (1)$$

In the equation,  $d$  is the nano-wire diameter,  $\alpha$  is the scaling factor,  $\Gamma_0$  is the full-width-at-half-maximum (FWHM) for bulk material Raman peak ( $\Gamma_0 = 6.5 \text{ cm}^{-1}$  for WO<sub>3</sub>) [18],  $q_{\perp}$  signifies the momentum vectors perpendicular to the wire length,  $\omega(\mathbf{q})$  is the phonon dispersion curve relation (PDR) for the material,  $A = 713 \text{ cm}^{-1}$ ,  $a = 0.76 \text{ nm}$  for the  $713 \text{ cm}^{-1}$  phonon branch whereas  $A = 808 \text{ cm}^{-1}$  and  $b = 0.38 \text{ nm}$  [22–25] for the  $808 \text{ cm}^{-1}$  phonon branch. For the purposes of the fitting session, the phonon dispersion relation,  $\omega^2(\mathbf{q}) = A^2 + AB \sin^2(a\mathbf{q}) + B^2 \sin^4(a\mathbf{q})$ , was derived from the simple relation of the form  $\omega(\mathbf{q}) = A + Ba^2q^2$ . The latter assumes isotropic dispersion curves [26]; however the former provided a much smoother fit than the latter for the present WO<sub>3</sub> Raman spectroscopy

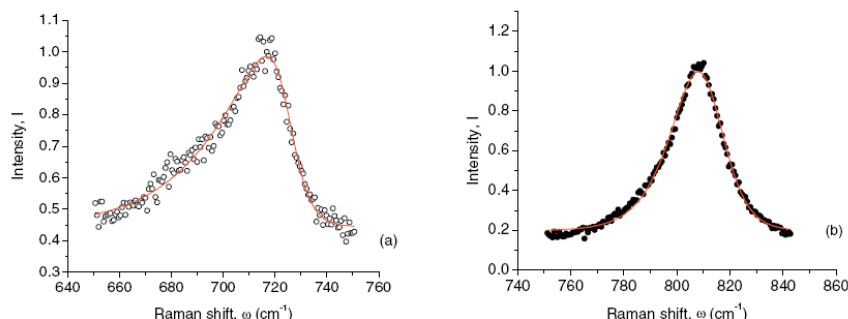
data.  $B$  was determined after non-linear fitting of Eq. (1) to experimental Raman spectral data. This was carried out using Mathematica™.

Electrical resistances of the VO<sub>2</sub> (R) nanobelts (NBs) were measured at different points on the sample using a digital multi-meter and heated base coupled with a temperature controller. The Varian Cary 500 spectrophotometer was used to obtain transmittance of the material in the UV–Vis and near IR ranges for optical transition studies in VO<sub>2</sub> nano-structure. All experimental procedures showed good reproducibility of results.

**3 Results and discussion** Typical SEM results of WO<sub>3</sub> and VO<sub>2</sub> (R) by USP and LP are shown in Fig. 2. LP WO<sub>3</sub> NWs have the most probable diameter of 51 nm (14–300 nm) and the LP the VO<sub>2</sub> (R) NBs have the most probable (width × length) of (3 μm × 15 μm). The thickness of these belts is observed to be in tens of nano-meters as unveiled by X-ray diffraction (not shown). Raman spectra for LP WO<sub>3</sub> NWs display remarkable asymmetrical broadening. The phonon frequencies affected are 260 cm<sup>-1</sup> and 700 cm<sup>-1</sup> respectively assigned to W<sup>4+</sup> states and the O–W–O bending modes [19, 22–25]. Minor phonon confinement effects are observed on the major phonon of



**Figure 2** Characterization methods and results for WO<sub>3</sub> NWs and VO<sub>2</sub> NBs, (a) a typical SEM micrograph for WO<sub>3</sub> NWs and (b) SEM for VO<sub>2</sub> NBs; (c) VO<sub>2</sub> NBs enhanced electronic hysteresis plot compared to (d) the USP VO<sub>2</sub> optical transmittance hysteresis.



**Figure 3** (online colour at: [www.pss-a.com](http://www.pss-a.com)) Raman spectroscopy data plots for  $\text{WO}_3$  NWs pertaining to the  $713\text{ cm}^{-1}$  TO phonon (a) and the  $808\text{ cm}^{-1}$  LO phonon (b) fitted with Eq. (1). The nano-wire diameter considered was 14 nm.

$800\text{ cm}^{-1}$  assigned to O–W–O stretching mode and the  $960\text{ cm}^{-1}$  assigned to  $\text{W}^{6+}=\text{O}$  surface dangling bonds [18, 22–25]. Fitting of the Richter equation to the O–W–O bending mode Raman peak at  $713\text{ cm}^{-1}$  (TO) yields a confinement scale factor of  $\alpha = 7.0 \pm 3.0$ , a pre-factor  $A_0 = 9.9 \times 10^{-9}$  and a phonon dispersion parameter of  $B = 0.14 \pm 0.05\text{ cm}^{-2}$ . Similarly, for the LO phonon at  $808\text{ cm}^{-1}$ , the scaling factor,  $\alpha = 14 \pm 2$  and,  $A_0 = 8.7 \times 10^{-13}$  and  $B = 0.011 \pm 0.005$ . The fitting sessions are summarised by an illustration in Fig. 2. By this technique, we have been able to obtain the phonon dispersion relations for the two phonon types (where  $a = 0.76\text{ nm}$  and  $b = 0.38\text{ nm}$  are lattice parameters [22]) for monoclinic  $\text{WO}_3$  given as:

$$\begin{aligned}\omega_{\text{TO}}^2(\mathbf{q}) &= 713^2 + 101 \sin^2(a \cdot \mathbf{q}) + 0.0196 \sin^4(a \cdot \mathbf{q}) \\ \omega_{\text{LO}}^2(\mathbf{q}) &= 808^2 + 8.1 \sin^2(b \cdot \mathbf{q}) + 0.0001 \sin^4(b \cdot \mathbf{q})\end{aligned}\quad (2)$$

Neutron scattering measurements on single crystals of  $\text{M}_{0.33}\text{WO}_3$ , a traditional experimental method for the determination of phonon dispersion curves, revealed low frequency, relatively dispersion-less phonon branches [26] but in the present study photon scattering shows considerable dispersion in stoichiometric  $\text{WO}_3$ . Different materials and different phonon types show differing values of the scale factor,  $\alpha$ : For example,  $\alpha = 6.3$  for Si NWs [18],  $\alpha = 4$  for Si nano-particles [15], a contradictory  $\alpha = 16\pi^2$  for Si NWs [31],  $\alpha = 8\pi^2$  for (CdSe nano-crystals [28], c-BN nano-crystals [16],  $\text{ZnO}_2$  nano-crystals [29]) where phonons are considered to be heavily confined and  $\alpha = 30$  for anatase  $\text{TiO}_2$  [30].

X-ray diffraction results (not shown here) show that the USP materials are a mixture of amorphous and polycrystalline particles whereas for LP high quality single crystals [(100) for LP  $\text{WO}_3$  NWs] and bi-crystalline [(110) and (210) peaks in LP  $\text{VO}_2$  NBs] are obtained. The broadening in a strong  $\text{WO}_3$  NW X-ray diffraction peak centred at  $2\theta = 26.81 \pm 0.02$  with an FWHM of  $0.88 \pm 0.10$  was used to calculate the crystallite size. By employing the De-

bye–Scherrer equation assuming a standard width of  $0.33^\circ$  for bulk  $\text{WO}_3$ , the calculation yielded a crystallite size of 4.6 nm. The metal-to-semiconductor and optical and electronic transitions in  $\text{VO}_2$  (R) are given in Fig. 1(c) and (d) and these display enhanced hysteresis especially in  $\text{VO}_2$  (R) NBs synthesized by LP with a hysteresis width of  $>83^\circ\text{C}$  which is much higher than the highest previously reported value according to Lopez et al. [14] of only about  $34^\circ\text{C}$ . Our HW value by USP was equally low ( $\sim 5^\circ\text{C}$ ) [see Fig. 1(d)]. This anomalous behaviour could be due to resilience to structural-transformation in ultra-thin  $\text{VO}_2$  belts (as confirmed by the broadened X-ray diffraction peaks (not shown)). However, the shift to higher temperature is attributed to carbon impregnation when running the synthesis under acetylene gas. It has been found in numerous previous studies that doping  $\text{VO}_2$  with ions of lower valence than  $4+$  increases its transition temperature whereas doping with ions of greater valence than  $4+$  does the reverse. Since the valences for carbon and vanadium are comparable in this case, we can conclude that comparable valence increases the  $\text{VO}_2$  transition temperature; this fact has to be investigated further using other types of elements of valence of  $4+$ .

**4 Conclusion** We have synthesized  $\text{WO}_3$  and  $\text{VO}_2$  (R) nanostructures by two related methods: USP and LP. Micro-sized and nano-sized particles were obtained by USP; however,  $\text{WO}_3$  NWs and  $\text{VO}_2$  (R) NBs were obtained by LP. Phonon confinement is observed especially in those materials synthesized by LP and phonon dispersion relations for  $\text{WO}_3$  (given in Eq. (2)) were obtained for the first time by fitting the Richter equation for confined phonons to experimental data. Thermo-chromic characterization of  $\text{VO}_2$  (R) NBs revealed an enhanced hysteresis width (HW  $\sim 83^\circ\text{C}$ ) surpassing the highest reported value so far. This study shows the highly promising potential of LP as a materials processing technique in terms of improving the optical, photonic and electrical/electronic properties of materials.

**Acknowledgements** Financial and/or infrastructural sponsorship from C.S.I.R., National Research Foundation of South Africa and the African Laser Centre are acknowledged. The assistance of Retha Rossouw of NMISA and Henk van Wyk of CSIR-National Laser Centre is also acknowledged.

### References

- [1] R. Agarwal and C. M. Lieber, *Appl. Phys. A* **85**, 209 (2006).
- [2] A. M. Morales and C. M. Lieber, *Science* **279**, 208 (1998).
- [3] X. Duan, Y. Huang, R. Agarwal, and C. M. Lieber, *Nature* **421**, 241 (2003).
- [4] P. A. Cox, *Transition Metal Oxides: An Introduction To Their Electronic Structure and Properties* (Oxford University Press, 1992), p. 20.
- [5] C. G. Granqvist et al., *Solar Energy* **63**, 199 (1998).
- [6] A. Hoel, L. F. Reyes, P. Hesler, V. Lantto, and C. G. Granqvist, *Curr. Appl. Phys.* **4**, 547 (2004).
- [7] M. Bendahan, R. Boulmani, J. L. Seguin, and K. Aguir, *Sens. Actuators* **100**, 320 (2004).
- [8] C. Bittencourt, R. Landers, E. Lobet, G. Molas, X. Correig, M. A. P. Silva, J. E. Sueiras, and J. Calderer, *Electrochem. Soc.* **149**, H81 (2002).
- [9] M. Gillet, K. Aguir, M. Bendahan, and P. Mennini, *Thin Solid Films* **484**, 358 (2005).
- [10] S. W. Wang, T. C. Chou, and C. C. Liu, *Sens. Actuators B* **94**, 343 (2003).
- [11] V. Guidi et al., *Sens. Actuators B* **100**, 277 (2004).
- [12] B. W. Mwakikunga, E. Sideras-Haddad, and M. Maaza, *Opt. Mater.* **29**, 481 (2007).
- [13] B. W. Mwakikunga, A. Forbes, E. Sideras-Haddad, R. Erasmus, G. Katumba, and B. Masina, *Int. J. Laser Nanomanuf.* (2007) (accepted).
- [14] R. Lopez, L. A. Boatner, T. E. Haynes, L. C. Feldman, and R. Hugland, *J. Appl. Phys.* **92**, 4031 (2002).
- [15] H. Richter, Z. P. Wang, and L. Ley, *Solid State Commun.* **39**, 625 (1981).
- [16] P. M. Fauchet and I. H. Campbell, *Solid State Commun.* **58**, 739 (1986); *Crit. Rev. Solid State Mater. Sci.* **14**, 79 (1988).
- [17] K. W. Adu, H. R. Gutierrez, U. J. Kim, G. U. Sumanasekera, and P. C. Eklund, *Nano Lett.* **5**, 400 (2005).
- [18] K. W. Adu, H. R. Gutierrez, and P. C. Eklund, *Vib. Spectrosc.* **42**, 165 (2006).
- [19] M. Boulova, N. Rosman, P. Bouvier, and G. Lucazeau, *J. Phys.: Condens. Matter* **14**, 5849 (2002).
- [20] J. S. Hagerty, in: *Laser-Induced Chemical Process*, edited by J. I. Steinfield (Plenum, New York, 1981).
- [21] P. C. Eklund, X. X. Bi, and F. J. Derbyshire, *Am. Chem. Soc., Fuel Chemistry Division* **37**, 1781 (1992).
- [22] E. Salje, *Acta Cryst. B* **33**, 574 (1977).
- [23] S. H. Lee, H. M. Cheong, C. E. Tracy, A. Mascarenhas, D. K. Benson, and S. K. Deb, *Electrochim. Acta* **44**, 3111 (1999).
- [24] Y. S. Huang, Y. Z. Zhang, X. T. Zeng, and X. F. Hu, *Appl. Surf. Sci.* **202**, 104 (2002).
- [25] J. Grabrusenoks et al., *J. Electrochim. Acta* **46**, 2229 (2001).
- [26] W. A. Kamitakahara, K. Scharnberg, and M. Shanks, *Phys. Rev. Lett.* **43**, 1607 (1979).
- [27] A. K. Arora, M. Rajalakshmi, T. R. Ravindran, and V. Sivasubramanian, *J. Raman Spectrosc.* **38**, 604 (2007).
- [28] A. Tanaka, S. Onari, and T. Arai, *Phys. Rev. B* **45**, 6587 (1992).
- [29] T. Werninghaus, J. Hahn, F. Richter, and D. R. T. Zahn, *Appl. Phys. Lett.* **70**, 958 (1997).
- [30] K. R. Zhu, M. S. Zhan, Q. Chen, and Z. Yin, *Phys. Lett. A* **340**, 220 (2005).
- [31] S. Piscanec, M. Cantoro, A. C. Ferrari, J. A. Zapien, Y. Lifshitz, S. T. Lee, S. Hoffmann, and J. Robertson, *Phys. Rev. B* **68**, 241312 (R) (2003).

## Optimization, Yield Studies and Morphology of WO<sub>3</sub> Nano-Wires Synthesized by Laser Pyrolysis in C<sub>2</sub>H<sub>2</sub> and O<sub>2</sub> Ambients—Validation of a New Growth Mechanism

B. W. Mwakikunga · A. Forbes · E. Sideras-Haddad · C. Arendse

Received: 28 July 2008 / Accepted: 3 September 2008 / Published online: 25 September 2008  
© to the authors 2008

**Abstract** Laser pyrolysis has been used to synthesize WO<sub>3</sub> nanostructures. Spherical nano-particles were obtained when acetylene was used to carry the precursor droplet, whereas thin films were obtained at high flow-rates of oxygen carrier gas. In both environments WO<sub>3</sub> nano-wires appear only after thermal annealing of the as-deposited powders and films. Samples produced under oxygen carrier gas in the laser pyrolysis system gave a higher yield of WO<sub>3</sub> nano-wires after annealing than the samples which were run under acetylene carrier gas. Alongside the targeted nano-wires, the acetylene-ran samples showed trace amounts of multi-walled carbon nano-tubes; such carbon nano-tubes are not seen in the oxygen-processed WO<sub>3</sub> nano-wires. The solid–vapour–solid (SVS) mechanism [B. Mwakikunga et al., *J. Nanosci.*

*Nanotechnol.*, 2008] was found to be the possible mechanism that explains the manner of growth of the nano-wires. This model, based on the theory from basic statistical mechanics has herein been validated by length-diameter data for the produced WO<sub>3</sub> nano-wires.

**Keywords** Laser pyrolysis · Tungsten trioxide · Nano-wires · Growth mechanism

### Introduction

Amongst many transition metal oxides, WO<sub>3</sub> has excellent electro-chromic, gaso-chromatic and photo-chromatic properties. At room temperature it adopts the distorted monoclinic structure of ReO<sub>3</sub> [1]. For this reason, WO<sub>3</sub> has been used to construct flat panel displays, photo–electro–chromic ‘smart’ windows [2–4], writing–reading–erasing optical devices [5, 6], optical modulation devices [7, 8], gas sensors and humidity and temperature sensors [9–11]. Self assembly of these materials has been achieved by hydro-thermal techniques, additive-free hydrothermal means, templating either with a polymer or pre-assembled carbon nano-tubes, epitaxial growth, sol-gel, electro-chemical means and hot-wire CVD methods. Recently, WO<sub>3</sub> nano-rods produced by a facile chemical route and CVD have been reported [12, 13] in this journal. In laser pyrolysis, authors have reported synthesis of, for instance, ceramics, silicon and silicon compounds, carbon compounds, olefins, chromium oxides, diamond, fullerenes and many other classes of materials. These experiments have largely been performed at high laser powers and hence at high temperatures. At such high levels, where anharmonicity cannot be ruled out, laser pyrolysis is equivalent to traditional pyrolysis with the photo-thermal process overwhelming the

B. W. Mwakikunga (✉) · C. Arendse  
CSIR, National Centre for Nano-Structured Materials,  
P.O. Box 395, Pretoria 0001, South Africa  
e-mail: bmwakikunga@csir.co.za

B. W. Mwakikunga · E. Sideras-Haddad  
School of Physics, University of the Witwatersrand,  
Private Bag 3, P.O. Wits 2050 Johannesburg, South Africa

B. W. Mwakikunga  
Department of Physics and Biochemical Sciences,  
University of Malawi, The Polytechnic, Chichiri,  
Private Bag 303, Blantyre 0003, Malawi

A. Forbes (✉)  
CSIR National Laser Centre, P.O. Box 395, Pretoria 0001,  
South Africa  
e-mail: aforbes1@csir.co.za

A. Forbes  
School of Physics, University of Kwazulu-Natal,  
Private Bag X54001, Durban 4000, South Africa



photo-chemical one. However, it has long been realized that even at low intensity, the CO<sub>2</sub> laser has successfully been used in the synthesis of boron compounds from BCl<sub>3</sub> [14, 15]. At these low power values, the laser is used to selectively excite the reactant to a relatively low vibrational level from which a chemical reaction with other reactants present is initiated. One expects to achieve product formation distinctly different from that achieved by traditional pyrolysis for the same chemical reaction provided that the laser energy absorbed is channelled mainly into the chemical process rather than into heating.

In this Letter, we report optimization of parameters that led to the synthesis of WO<sub>3</sub> nano-spheres and thin films at relatively low laser power (50 W in a 2.4-mm focal region). We demonstrate the role of thermal annealing in the conversion of the spheres and slabs into nano-wires. We also show the morphological differences and yields when carrier gases—C<sub>2</sub>H<sub>2</sub> or O<sub>2</sub>—are used during the synthesis.

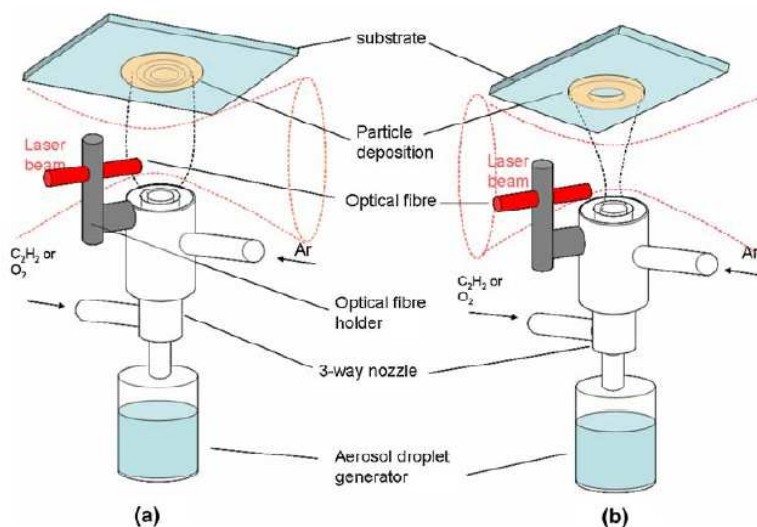
### Experimental

Our laser pyrolysis experimental set up was fully described in our previous publication [16]. Briefly, the method involves injecting a stream of very fine droplets of a precursor solution into an infrared laser beam and depositing the resulting aerosol onto a Corning glass substrate. A wavelength tuneable continuous wave (cw) CO<sub>2</sub> laser was used in the experiments (Edinburgh Instruments, model PL6). By selecting a wavelength of 10.6 μm, the laser was

within, but not exactly on, the absorption region of the pre-made precursor (WCl<sub>6</sub> in ethanol or tungsten ethoxide) for the production of WO<sub>3</sub>. From the fact that (1) the excitation wavelength of 10.6 μm is not exactly at the main resonance peak of the W-ethoxide precursor of 9.44 μm and (2) the laser power of 50 W (focussed into 2.4-mm beam diameter at the waist) is not low enough to rule out anharmonic effects in the excitation, the decomposition of this precursor could be due to both photochemical (resonance) and photo-thermal (anharmonic) processes. The as-produced materials showed decomposition of W-ethoxide into WO<sub>3</sub> nano-particles suggesting that the photo-chemical process indeed occurred. Also worth describing here is the carrier gas system which is accomplished by a three-way nozzle having three concentric cylinders. The outer cylinder is connected to an argon supply. The argon guides the aerosol droplets which are carried by either C<sub>2</sub>H<sub>2</sub> (supposedly non-reactive) or O<sub>2</sub> (highly reactive) gases interchangeably in the middle and second cylinder. This is illustrated in Fig. 1.

An aliquot of 5.4 mg of dark blue powder of WCl<sub>6</sub> (Aldrich 99.99%) was dissolved in 500 mL of ethanol. Since WCl<sub>6</sub> is highly reactive with air and moisture, its dissolution was conducted in an argon atmosphere. Particles from this process were collected on Corning glass substrates, placed on a rotating stage, at room temperature and at atmospheric pressure. The particle deposition showed a void at the centre (Fig. 1b) when the encapsulating carrier gas flow-rate was higher than the carrier gas driving the precursor droplets. When the flow-rates were reversed, the deposition showed the profile of a hump (Fig. 1a) showing there was more deposition at the centre

**Fig. 1** Laser pyrolysis illustration and the role of carrier gas and precursor relative flow-rates (a) when the precursor flow-rate is larger than the encapsulating carrier gas (Ar) and (b) when the precursor flow-rate is smaller than the flow-rate of Ar. The precursor is driven either by C<sub>2</sub>H<sub>2</sub> or O<sub>2</sub>. The particle deposition in (a) has profile of a hump, whereas the deposition in (b) has a vacancy at the centre as indicated on the substrates



**Table 1** The experiment parameter used to obtain the WO<sub>3</sub> samples by laser pyrolysis

Sample	Precursor	Gas 1 (8 cm <sup>3</sup> /min)	Gas 2 (8 cm <sup>3</sup> /min)	Gas 3 variable	Nano-wire yield	Morphology
W1	WCl <sub>6</sub> + Ethanol	O <sub>2</sub>	Ar	Ar	High	Slabs + Rods
W2	WCl <sub>6</sub> + Ethanol	C <sub>2</sub> H <sub>2</sub>	Ar	Ar	Low	Sphere + Rod

of the substrate than in periphery. This was found to be in agreement with Bernoulli's theorem, which requires that there should be reduced pressure in fast flowing fluids. When the flow rate of the central gas is larger, the pressure is lower in this region and hence the droplets and the particles (after laser pyrolysis) are trapped in this low pressure region. Therefore there is high deposition at the centre of the substrate and vice versa. Table 1 lists the experimental procedures employed. The so-obtained samples were further annealed in argon atmosphere at 500 °C for 17 h. Morphology studies were carried out using a Jeol JSM-5600 scanning electron microscopy (SEM) microscope, which was also equipped for energy dispersive X-ray spectroscopy (EDX). In order to avoid charging effects during SEM analysis, the samples were made conductive by carbon/Au/Pd coating. Infrared and Raman spectroscopy experiments on the as-obtained WO<sub>3</sub> are reported elsewhere [17]. Structural studies were done using a Philips Xpert powder diffractometer equipped with a CuK $\alpha$  wavelength of 0.154184 nm. The experimental procedure showed good reproducibility of results.

Lengths and corresponding diameters of the nano-wires were measured by means of a software package Image-Tool. As is the required procedure, calibration is initially made against the marker of known length in both the image scale and the real space scale. Then the distance between two points is measured for each point with accuracy that heavily depends on (1) the pixel density of the projecting screen, (2) the random errors from operator's hand and (3) the magnification of the image.

## Results

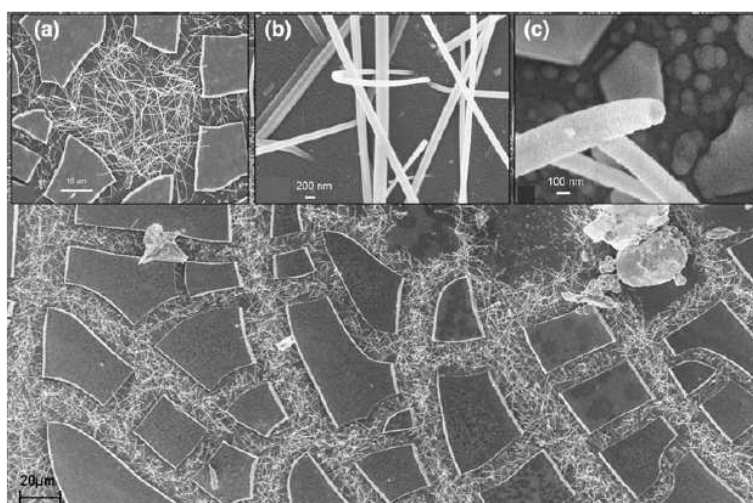
Laser pyrolysis of tungsten-based precursors, with C<sub>2</sub>H<sub>2</sub> as carrier gas, shows remarkable differences in morphology from when O<sub>2</sub> is the carrier gas as shown in Figs. 2 and 3. The C<sub>2</sub>H<sub>2</sub>-synthesized sample has a lower yield of WO<sub>3</sub> nano-wires after annealing than the O<sub>2</sub>-synthesized one. These nano-wires in O<sub>2</sub>-ran sample grow in the crevices of the film. The C<sub>2</sub>H<sub>2</sub>-ran sample has nano-wires with a higher aspect ratio than the O<sub>2</sub>-ran samples. Also the C<sub>2</sub>H<sub>2</sub>-ran sample shows the presence of spherical micro-particles where as complete absence of these spheres is observed in the O<sub>2</sub>-ran sample. This means that C<sub>2</sub>H<sub>2</sub> maintains the spherical shape of the precursor droplets, which is clear

evidence that C<sub>2</sub>H<sub>2</sub> is only a sensitizer of the process but does not participate in the decomposition of the precursor. Also, in the presence of tungsten, C<sub>2</sub>H<sub>2</sub> dissociates and forms carbon structures such as carbon nano-tubes. It was shown that vanadium surfaces can be used as catalysts for the growth of carbon nano-tubes [18] from C<sub>2</sub>H<sub>2</sub>. On the other hand, O<sub>2</sub> actively participates in the breakdown of the precursor droplets and in the process increases the yield of the WO<sub>3</sub> nano-wires at the expense of aspect ratio of the wires in general. The O<sub>2</sub>-ran sample also has very brittle thin films with cracks in a somewhat ordered manner. This ordered cracking after annealing could be attributed to the growth pressure (thermal stress) from the 1D nano-structures.

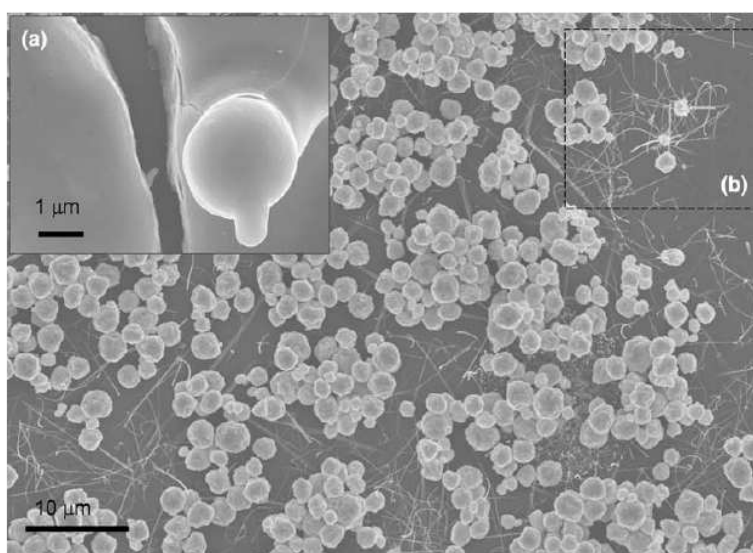
The TEM micrograph of a typical wire grown from O<sub>2</sub>-run WO<sub>3</sub> particles shown in Fig. 4b revealed a core-shell structure (redrawn in Fig. 4c) with the WO<sub>x</sub> wire at the core (EDS in Fig. 4a) and the carbon–Au–Pd composite around the wire as a shell (EDS in Fig. 4e). C–Au–Pd is a material used in the prior-to-SEM coating to improve conduction for enhanced imaging. The shell is thicker on one side than on the other; that is, the wire is not centred through the C–Au–Pd wrapping. This shell served as a contamination, which obscured the electron diffraction of the wire so that the stoichiometry studies of the WO<sub>x</sub> nano-wire could not be accomplished. In line with our previous studies, we can speculate that the wire is WO<sub>x</sub> with  $x$  being less than three due to oxygen loss during annealing even as elaborated in chemical reactions of the type in Eq. 4.

In order to observe the growth of nano-wires, we sonicated a few spheres of WO<sub>3</sub> into iso-propanol and placed them on carbon-hole Cu grid for in-situ annealing and imaging in a Jeol CM200 transmission electron microscope. A series of images, shown in Fig. 5, were taken periodically of intervals of 45 min whilst heating at temperatures ranging from 700 °C to 900 °C using a heating device specially tailored for this microscope. The images showed no indication of growth of one-dimensional structures. This is attributed to the vacuum typical of TEM. Any atoms that are sublimated from the spheres are immediately removed by the high vacuum giving a very small probability of condensing and growing into 1D nano-structured geometry. However, the shrinking of the spheres is an indication that the atoms are indeed evaporating from the surface. However, not all sublimated atoms are removed from their parent spheres; some return to make

**Fig. 2** Scanning electron micrographs of  $\text{WO}_3$  nano-rods grown under oxygen as a central carrier gas and  $\text{C}_2\text{H}_2$  as the secondary carrier gas showing a thin film that has flaked up into orderly slabs between which are numerous nano-wires. Inset (a) shows a close look at the nano-wires in between the slabs. Inset (b) zooms in onto the nano-wire area and inset (c) display one nano-wire's end



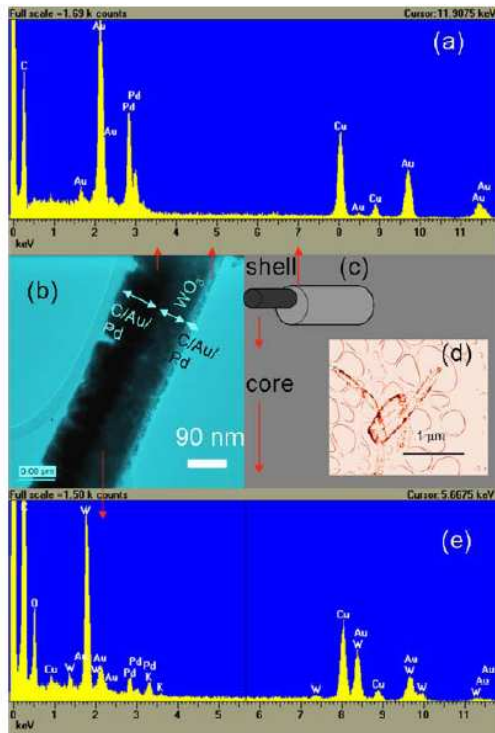
**Fig. 3** Scanning electron micrographs of  $\text{WO}_3$  nano-rods grown under  $\text{C}_2\text{H}_2$  as a central carrier gas and oxygen as the secondary carrier gas. The spherical droplets from the precursor maintain their shape until their deposition into micro-particles. Inset (a) is a micro-particle before annealing showing the genesis of the growth of a nano-wire. After annealing there are numerous nano-wires growing from and in between the spheres. Dotted box (b) shows a region where a number of nano-wires are seen sprouting from spheres



small mounds on the sphere surface making the sphere rougher. The rate of sphere size reduction due to loss of atoms is depicted in Fig. 5b. It is interesting to note that the smaller sphere C shrank faster than the larger sphere B. This means that wires grown from small spheres grow faster than those that grow from large spheres.

For us to understand the novel growth of these nano-wires, it is important to briefly review some related growth mechanisms available in literature. Sir Frederick Frank

proposed the 'screw dislocation theory' in 1949. Central to this dislocation theory were Polanyi, Orowan, Taylor, Burger and Mott & Nabarro [19]. Defects and dislocation in the initial crystals initiate one-dimensional growth; "...the crystal face always has exposed molecular terraces on which growth can continue, and the need for fresh 2D nucleation never arises..." [19]. In 1964, detailed studies on the morphology and growth of silicon whiskers by Wagner & Ellis [20] led to a new concept of crystal growth



**Fig. 4** TEM image of a  $\text{WO}_3$  nano-wires in (b) reveals that the wire is a core with a shell of carbon, Au and Pd from prior-to-SEM coating as confirmed by EDS in (a) and (e). Inset (c) is an illustration of the core-shell structure of the  $\text{WO}_3$  nano-wire and C/Au/Pd layer and (d) is TEM image of carbon nanotubes found alongside the  $\text{WO}_3$  nano-wires

from vapour, which was called the vapour–liquid–solid (VLS) mechanism. The new growth mechanism was built around three important facts: (a) silicon whiskers did not contain an axial screw dislocation (b) an impurity was essential for whisker growth and (c) a small globule was always present at the tip of the whisker during growth. From fact (a), it was clear that growth from vapour did not occur according to Frank’s screw dislocation theory and from, facts (b) and (c), it was important that a new growth mechanism be studied.

In 1975, Givargizov [21] introduced the fundamental aspects of the VLS mechanism. Emphasis was placed on the dependence of the growth rate on the whisker diameter. It was found that the growth rate decreased abruptly for submicron diameters and vanished at some critical diameter  $d_c \leq 0.1 \mu\text{m}$  in accordance with the Gibbs–Thomson effect. Basing on this effect, which states that the solubility limit of a precipitate ( $\beta$ ) in a matrix ( $\alpha$ ) varies with the precipitate’s radius, Givargizov suggested that the

effective difference between the chemical potential of the precipitate in the vapour phase and in the terminal precipitate [whisker],  $\Delta\mu$ , is given by

$$\Delta\mu = \Delta\mu_0 - \frac{4\Lambda\sigma}{D} \quad (1)$$

$\Delta\mu_0$  is the difference at a plane boundary (when diameter,  $D$ , of the precipitate tends to  $\infty$ ),  $\Lambda$  is the atomic volume of the precipitate and  $\sigma$  is the surface free energy of the precipitate. The dependence of growth rate,  $G$ , on the super-saturation ( $\Delta\mu/k_B T$ ) given by  $V = b(\Delta\mu/k_B T)^n$ , where  $b$  and  $n$  are coefficients to be evaluated from experimental data, was used to derive an expression

$$V^{1/n} = \frac{\Delta\mu_0}{k_B T} b^{1/n} - \frac{4\Lambda\sigma}{k_B T} b^{1/n} \frac{1}{D} \quad (2)$$

The main characteristics of VLS mechanism are (1) the presence of a catalyst and (2) direct proportionality of the diameter of the nanostructure to the growth rate. Thick whiskers grow longer than thinner ones because this growth can be afforded by the continual supply of building blocks in the CVD system. Plotting the growth rate,  $V$ , [21] or terminal length  $l_\infty$  [22] of the whisker versus  $D$  gives curves with a positive ascent. A plot of  $V^{1/n}$  versus  $1/D$  gives a straight line graph with a negative slope [21].

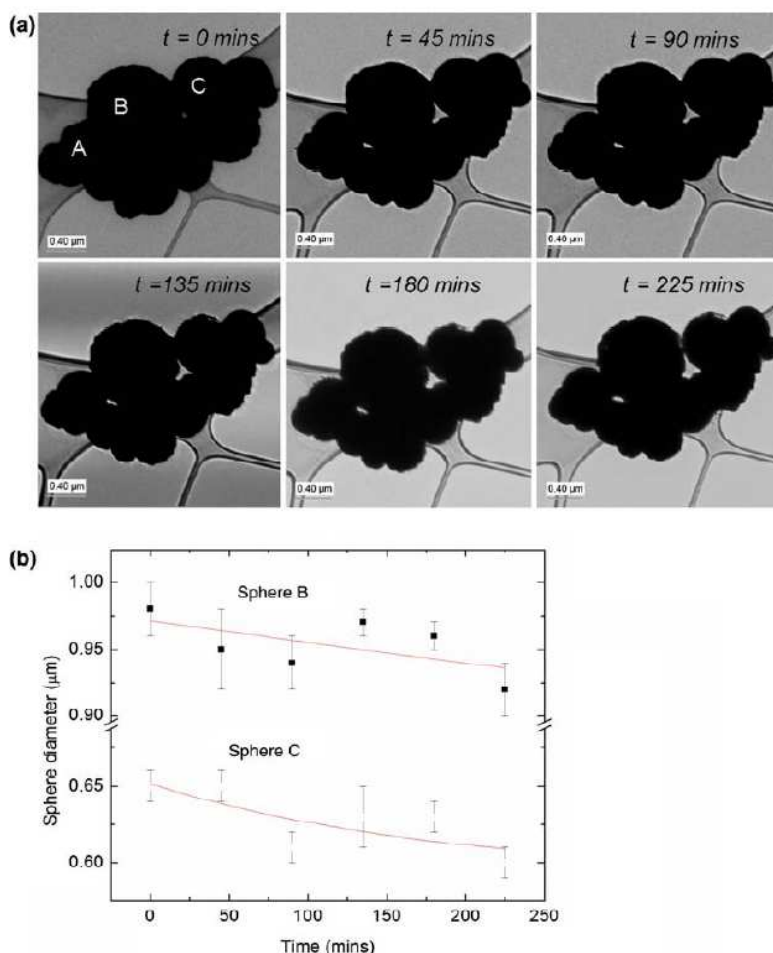
Recently, an in situ growth profile in real time for tungsten oxide nano-wires was followed by Kasuya et al. (2008) [23] by injecting ultra-small flow-rates of  $\text{O}_2$  on a heated tungsten surface placed on a scanning electron microscope stage. It was difficult to ascertain if the length-and-diameter data would be in agreement with the VLS mechanism because the images were rather poor. This was due to the poor vacuum caused by the intentional injection of  $\text{O}_2$ , which was useful for the targeted reaction. The length of the nano-wire as a function time  $l(t)$  was found to take the form of

$$l(t) = l_0[1 - \exp(-\alpha t)] \quad (3)$$

where  $l_0$  is the final length and  $\alpha$  is the growth or decay coefficient.

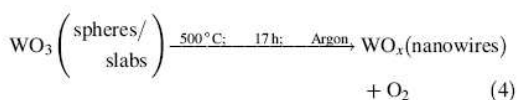
We however study the final state of the fully grown  $\text{WO}_3$  nanostructures. Our present length-diameter data for the nano-wires could not agree with the above VLS theory for two conflicting reasons: (1) no particular catalyst could be identified with certainty (2) we found an inverse proportionality between length and diameter of the nano-wires. It was therefore important to study a new model to attempt to explain the new findings. Since the production of solid-state nano-wires is after annealing of the solid-state particles, the mechanism of growth can neither be according to liquid-based “Solution-Liquid-Solid” mechanism proposed by Treter and Buhro [24, 25] nor in line with the “Super-Critical Fluid Synthesis” mechanism proposed by Holmes

**Fig. 5** In situ TEM annealing of WO<sub>3</sub> micro-spheres in vacuum at 700–900 °C. Micrographs were taken periodically as shown in (a). Note the variation of spheres A, B and C and the enlargement of space around these spheres as time of annealing increases. The variation of sphere diameter with time for sphere B and C are plotted in (b). Exponential decay curves are fitted and show that the smaller sphere C shrinks faster than B



[26] and which has been later supported by Korgel and co-workers [27]. These data certainly support our newly proposed “Solid–Vapour–Solid (SVS)” mechanism reported in our previous publication [28] where we reported solid-state W<sub>18</sub>O<sub>49</sub> nano-tips produced by annealing solid-state WO<sub>3</sub> nano-spheres (prepared by ultrasonic spray pyrolysis) in argon environment. Synthesis of solid materials from solid precursors is not new. Solid-state reactions are very slow and difficult to carry out to completion unless carried out at very high temperatures where reacting atoms can diffuse through solid material to the reaction front more easily. Transformation of one phase to another (with the same chemical composition) can also occur in solid state, either at elevated temperatures or elevated pressures (or both). For the growth rate of many solid-state reactions (including tarnishing), inter-diffusion of ions through the product layer increases the

thickness Δx parabolically with time (Δx)<sup>2</sup> ∝ t [29]. This is a sharply different dependence from the Eq. 1 proposed by Kasuya et al. [23] above. In some solid-state processes, nucleation can be homogeneous. This is often the case for thermal decomposition, for example, as is the case in the current reactions



In this Letter, we introduce for the first time the statistical-mechanical aspects of this proposed SVS model and fit the ensuing mathematical expressions to the data.

For the sake of simplicity, we consider the source of molecules to be a solid sphere of radius R<sub>0</sub>, containing

molecules of mass,  $M$  and assume the molecules to be spherical of average molecular diameter,  $\Omega$ . We assume further that in changing the morphology from a sphere to a wire, only the surface molecules can migrate from the sphere to the newly forming wire or rod. For instance it has been demonstrated [30] that the surface diffusive flux,  $J_S$  of atoms on a surface of a slab of length  $L$  given by  $J_S = -(dc/dx)|_0^L D(y)dy$  is different from the more familiar bulk diffusive flux written from the first Fick's law as  $J_B = -D_b(dc/dx)L$  where  $dc/dx$  is the concentration gradient. In this case, transformation from sphere to rod takes place layer after layer. The sphere shrinks but the as-forming rod lengthens as illustrated in Fig. 6.

If the sphere is amorphous and the wire is crystalline as normally observed experimentally, then the densities of the material in the initial sphere and the final wire are different and can be written, respectively, as  $\rho_{am}$  and  $\rho_{cryst}$ . The number of atoms in the first layer of the sphere can therefore be written as

$$N_1^{surf} = 4\pi R_0^2 \Omega \frac{\rho_{am}}{M} \tag{5}$$

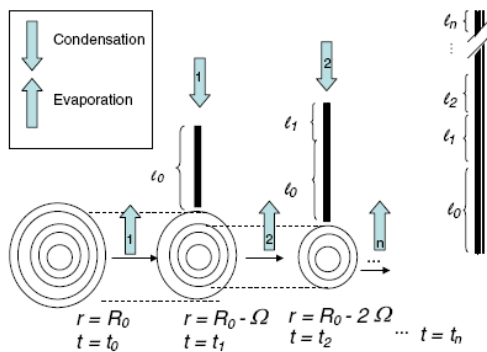
If all these atoms assemble into a rod of diameter  $D$  and length  $l_1$  then the number of molecules in the rod can be written in terms of length  $l_1$  as

$$N_1^{rod} = \frac{\pi}{4} D^2 l_1 \frac{\rho_{cryst}}{M} \tag{6}$$

However, not all the atoms in Eq. 5 end up making the rod. The actual fraction that self-assembles into the rod is proportional to the Boltzmann's fraction, which depends on the temperature  $T$  of the ambient given as

$$\frac{N_1^{rod}}{N_1^{surf}} = \exp\left(-\frac{E_A}{k_B T}\right) \tag{7}$$

$E_A$  is the activation energy of the atoms.



**Fig. 6** Proposed schematic of the solid–vapour–solid mechanism of growth of 1D nano-structure from a spherical layer of atoms in a tip growth

After the first layer has assembled into the rod of length  $l_1$ , the next layer in the sphere has a radius of  $R_0 - \Omega$  which forms the next segment of the rod of length  $l_2$ . The subsequent layers have radii of  $R_0 - 2\Omega$ ,  $R_0 - 3\Omega$ ,  $R_0 - 4\Omega$ ,  $R_0 - 5\Omega$  and so forth. The  $i$ th layer will have a radius of  $R_0 - (i-1)\Omega$  such that the number of atoms in the  $i$ th layer is

$$N_i^{surf} = 4\pi \Omega \frac{\rho_{am}}{M} [R_0 - (i-1)\Omega]^2 \tag{8}$$

This corresponds to the number of atoms in the  $i$ th segment of the rod of length  $l_i$  given as

$$l_i = 16 \frac{\rho_{am} \Omega}{\rho_{cryst}} \exp\left(-\frac{E_A}{k_B T}\right) [R_0 - (i-1)\Omega]^2 \frac{1}{D^2} \tag{9}$$

The total length of the wire is a summation of all the segments of the wire emanating from each corresponding layer in the source sphere.

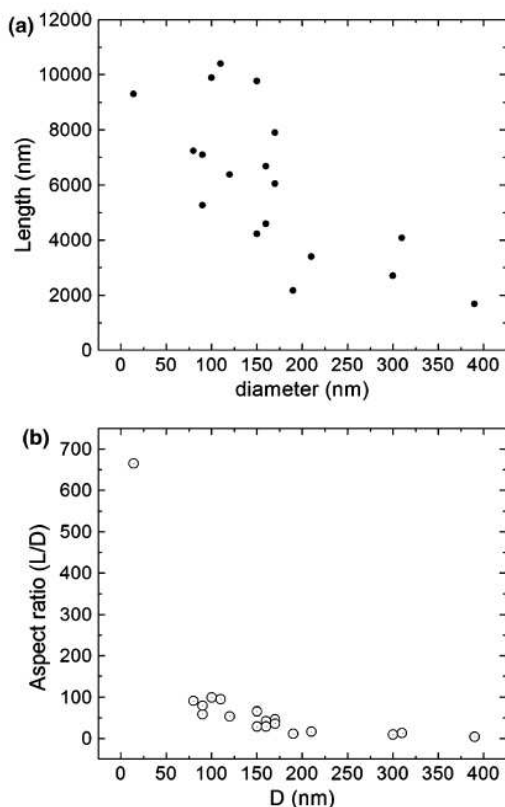
$$l = l_1 + l_2 + l_3 + \dots + l_N = \sum_i^N l_i = \zeta \frac{1}{D^2} \tag{10}$$

where

$$\zeta = 16 \frac{\rho_{am} \Omega}{\rho_{cryst}} \exp\left(-\frac{E_A}{k_B T}\right) \sum_i^N [R_0 - (i-1)\Omega]^2 \tag{11}$$

Parameter  $\zeta$  is a function of temperature  $T$  and also depends on the geometry of the source of the atoms. The higher the annealing temperature,  $T$ , the higher the slope,  $\zeta$ . This fact may mean that thinner nano-wires can be obtained at higher annealing temperatures. But there must be a lower limit to how thinner the nano-wires can get in the SVS mechanism since at much higher temperatures all solid-state starting material should evaporate away leaving nothing to form the nano-wires with. These limits are yet to be determined. The same question has been asked if there is a thermo-dynamical lower limit to the nano-wires growth by VLS [31]. It can be seen that if the source is equally crystalline then the ratio of the densities in the source to the final structure is unity. By quick inspection, one can see that the geometry described by the summation in Eq. 11 is proportional to the total surface area of all atomic or molecular layers in the source. A plot of  $l$  versus  $1/D^2$  should be a positive straight line graph with a y-intercept of zero and a slope of  $\zeta$ . Similarly a plot of aspect ratios  $l/D$  versus  $1/D^3$  is supposed to be a positive straight line going through the origin and having the slope,  $\zeta$ .

In the VLS mechanism, given a constant flux of molecules in the source, a nano-wire that has a large diameter will grow much longer compared to when it starts out with a small diameter. In the SVS growth, the thinner the wire the longer it is and vice versa as shown in the plots of Fig. 7a. When aspect ratios, defined here as the ratio of length to diameter, is plotted against diameter, the same

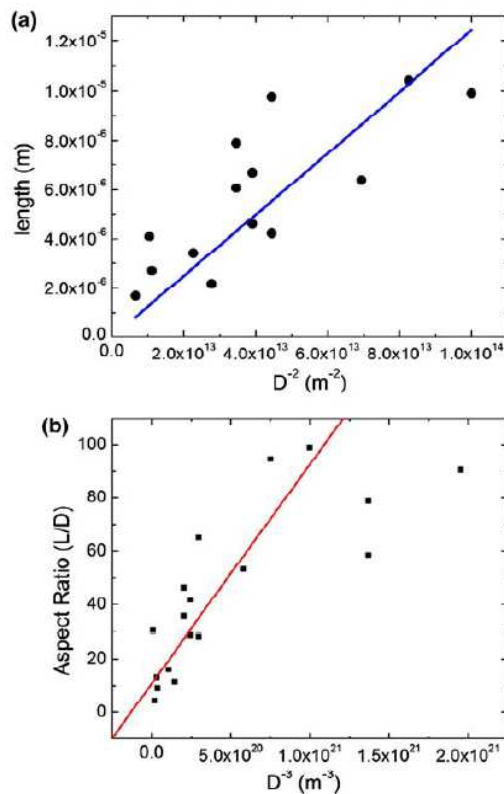


**Fig. 7** Scatter plots of (a) length of the nano-wire versus the corresponding diameter (b) aspect ratio versus diameter

profile is obtained (Fig. 7b). When length and aspect ratio are plotted against  $1/D^2$  and  $1/D^3$ , respectively, in accordance with Eq. 10, positive slopes are manifested (Fig. 8) almost equal to each other as expected from the above theory and of the order of  $\sim 10^{-20} m^3$ . This value is related to the order of magnitude of the average volume of the  $WO_3$  nano-wires. It should be noted that reverse growth from one-dimensional to spherical particles is also possible at suitable annealing conditions. For instance, nano-belts of Zn acetate were converted into aggregates of ZnO nanoparticles as reported in this journal [32].

**Conclusion**

In summary, liquid atomization and subsequent laser pyrolysis were carried out using a  $CO_2$  laser tuned at its  $10P_{20}$  line of wavelength 10.6  $\mu m$ . SEM characterization of the as-produced  $WO_3$  samples showed that selective



**Fig. 8** Scatter plots of (a) length versus  $1/D^2$  and (b) aspect ratio ( $L/D$ ) versus  $1/D^3$ . The linearized plots (a) and (b) have similar slopes within experimental error as predicted by the current theory [ $(6.22 \pm 2.77) \times 10^{-20} m^3$  and  $(6.25 \pm 0.831) \times 10^{-20} m^3$ , respectively]

photochemical reactions by the laser have a part to play in initiating self assembly growth centres even without the need for a catalyst. Self assembly is only continued by further annealing. We have shown that oxygen carrier gas gives a higher yield of  $WO_3$  nano-wires by laser pyrolysis than acetylene. The latter also shows trace amounts of multi-walled carbon nano-tubes. The transmission electron microscopy reveals that the nano-wires are core-shell structures of a mixture of Au, Pd and C in the shell and  $WO_3$  at the core. The shell is due to the prior-to-SEM coating to improve imaging. The absence of catalysts in addition to the analysis of the nano-wire length-and-diameter data has validated a new growth mechanism, which we have called SVS growth as proposed earlier [28].

**Acknowledgements** Authors would like to thank Prof. Michael Witcomb, Mr. Mthokozisi Masuku, Mr. Henk van Wyk and Ms. Retha Rossouw. The South African Department of Science and

Technology (DST) project for the African Laser Centre, the National Research Foundation (NRF), the DST/NRF Centre for Excellence in Strong Materials and the CSIR National Centre for Nano-Structured Materials are acknowledged.

## References

1. P.A. Cox, *Transition Metal Oxides: An Introduction to Their Electronic Structure and Properties* (Oxford University Press, Oxford, 1992)
2. C.G. Granqvist, A. Azens, A. Hjelm, L. Kullman, G.A. Niklasson, D. Rönnow et al., *Sol. Energy* **63**, 199 (1998). doi:10.1016/S0038-092X(98)00074-7
3. C.G. Granqvist, E. Avendano, A. Azens, *Thin Solid Films* **442**, 201 (2003). doi:10.1016/S0040-6090(03)00983-0
4. A. Hoel, L.F. Reyes, P. Heszler, V. Lantto, C.G. Granqvist, *Curr. Appl. Phys.* **4**, 547 (2004). doi:10.1016/j.cap.2004.01.016
5. M. Bendahan, R. Boulmani, J.L. Seguin, K. Aguir, *Sens. Actuators* **100**, 320 (2004). doi:10.1016/j.snb.2004.01.023
6. R.F. Mo, G.Q. Jin, X.Y. Guo, *Mater. Lett.* doi:10.1016/j.matlet.2006.12.061
7. Y. Shigaya, T. Nakayama, M. Aono, *Sci. Technol. Adv. Mater.* **5**, 647 (2004). doi:10.1016/j.stam.2004.02.021
8. M. Gillet, K. Aguir, M. Bendahan, P. Mennini, *Thin Solid Films* **484**, 358 (2005). doi:10.1016/j.tsf.2005.02.035
9. C. Bittencourt, R. Landes, E. Llobert, G. Molas, X. Correig, M.A.P. Silva et al., *J. Electrochem. Soc.* **149**, H81 (2002). doi:10.1149/1.1448821
10. P. Ivanov, J. Hubalek, K. Malysz, J. Prasek, X. Vilanova, E. Llobert et al., *Sens. Actuators B* **100**, 293 (2004). doi:10.1016/j.snb.2003.12.065
11. C.L. Dai, M.C. Liu, F.S. Chen, C.C. Wu, M.W. Chang, *Sens. Actuators B Chem.* (2006). doi:10.1016/j.snb.2006.10.055
12. J. Rajeswari, P.S. Kishore, B. Viswanathan, T.K. Varadarajan, *Nanoscale Res. Lett.* **2**, 496 (2007). doi:10.1007/s11671-007-9088-y
13. X.P. Wang, B.Q. Yang, H.X. Zhang, P.X. Feng, *Nanoscale Res. Lett.* **2**, 405 (2007)
14. H.R. Bachmann, H. Noth, R. Rinck, K.S. Kompa, *Chem. Phys. Lett.* **29**, 627 (1974). doi:10.1016/0009-2614(74)85107-9
15. C.M. Bowden, J.D. Stettler, N.M. Witriol, *J. Phys. B Atom. Mol. Phys.* **10**, 1789 (1977). doi:10.1088/0022-3700/10/9/028
16. B.W. Mwakikunga, A. Forbes, E. Sideras-Haddad, R.M. Erasmus, G. Katumba, B. Masina, *Int. J. Laser Nanoparticles* (2008) (in press)
17. B.W. Mwakikunga, E. Sideras-Haddad, A. Forbes, C. Arendse, *Phys. Status Solidi* **205**, 150 (2008). doi:10.1002/pssa.200776829
18. J.W. Seo, K. Hernadi, C. Miko, L. Forro, *Appl. Catal. Gen.* **260**, 87 (2004). doi:10.1016/j.apcata.2003.10.003
19. F.C. Frank, *Discuss Faraday Soc.* **5**, 48 (1949). doi:10.1039/d9490500048
20. R.S. Wagner, W.S. Ellis, *Appl. Phys. Lett.* **4**, 89 (1964). doi:10.1063/1.1753975
21. E.I. Givargizov, *J. Cryst. Growth* **31**, 20 (1975). doi:10.1016/0022-0248(75)90105-0
22. J. Kikkawa, Y. Ohno, S. Takeda, *Appl. Phys. Lett.* **86**, 123109-1 (2005). doi:10.1063/1.1888034
23. K. Kasuya, T. Ooi, Y. Kojima, M. Nakao, *Appl. Phys. Express* **1**, 034005 (2008). doi:10.1143/APEX.1.034005
24. T.J. Trenter et al., *Science* **270**, 1791 (1995). doi:10.1126/science.270.5243.1791
25. W. Buhro, *Adv. Mater. Opt. Electron.* **6**, 175 (1996). doi:10.1002/(SICI)1099-0712(199607)6:4<175::AID-AMO236>3.0.CO;2-C
26. J.D. Holmes et al., *Chem. Eur. J.* **9**, 2144 (2003). doi:10.1002/chem.200204521
27. T. Hanrath, B. Korgel, *Adv. Mater.* **5**, 15 (2003)
28. B.W. Mwakikunga, E. Sideras-Haddad, C. Arendse, M.J. Witcomb, A. Forbes, *J. Nanosci. Nanotechnol.* (2008) (in press)
29. S. Elliot, *The Physics of Chemistry of Solids* (Wiley, Chichester, 2000)
30. J.B. Hudson, *Surface Science—An Introduction* (Butterworth-Heinemann, Boston, 1992)
31. T.Y. Tan, N. Li, U. Gosele, *Appl. Phys. Lett.* **83**, 1199 (2003). doi:10.1063/1.1599984
32. Y. Zhang, F. Zhu, J. Zhang, L. Xia, *Nanoscale Res. Lett.* **3**, 201 (2008). doi:10.1007/s11671-008-9136-2



## OAtube Nanotechnology

Peer-Reviewed Video Access to Science

Tuesday, January 27, 2009

**B.W.Mwakikunga**

Can universal conductance fluctuations (UCFs) be observed at temperatures above room temperature at nanoscale?

B. W. Mwakikunga<sup>1,2,3</sup>, E. Sideras-Haddad<sup>1,4</sup>, C. Arendse<sup>2</sup> and A. Forbes<sup>5</sup>

<sup>1</sup>School of Physics , University of the Witwatersrand, PO Box Wits, Johannesburg , 2050 South Africa

<sup>2</sup>CSIR National Centre for Nano-Structured Materials, PO Box 395, Pretoria

<sup>3</sup>Department of Physics and Biochemical Sciences, University of Malawi, The Polytechnic, P. B. 303, Chichiri, Blantyre 0003, Malawi

<sup>4</sup>Themba Labs Gauteng, Johannesburg, South Africa

<sup>5</sup>CSIR National Laser Centre, PO Box 395, Pretoria, South Africa

We report conductance fluctuation in VO<sub>2</sub> nano-ribbons of 10 nm thickness at moderate temperatures. Synthesis of these nano-ribbons was reported elsewhere [1-4]. The fluctuations are periodic at room temperature up to the VO<sub>2</sub> transition temperature of 70 °C. These are surprising results since dc currents are producing a.c. potential difference values in i-v characteristics of the nano-ribbons of VO<sub>2</sub> contrary to those of normal bulk materials. Three main theories were considered in order to explain these findings (1) The LRC equivalent circuit theory (2) the Gunn effect [5] and (3) the Universal Conductance Fluctuations theories [6-15]. The first two theories failed to explain our experimental data. We have explained this anomalous behaviour by the third theory which is a manifestation of the wave nature of electrons. The wave nature of electrons has been demonstrated in many instances including the Nobel-prize-winning Davisson & Germer experiment on electron diffraction. In electronic circuits, quantum interference in metallic wires [6-8], the so-called 'weak localization' [9,10] and universal conductance fluctuations (UCF) [11-13] are all manifestations of this wave nature. Fluctuations originate from coherence effects for electronic wave-functions and thus the phase-coherence length,  $l_{\phi}$  needs to be smaller than the momentum relaxation length  $l_m$ . UCF is more profound when electrical transport is in the weak localization

## Can universal conductance fluctuations (UCFs) be observed at temperatures above room temperature at nanoscale?

B. W. Mwakikunga<sup>1,2,3</sup>, E. Sideras-Haddad<sup>1</sup>, C. Arendse<sup>2</sup>, A. Forbes<sup>7</sup>

<sup>1</sup>School of Physics, University of the Witwatersrand, PO Box Wits, Johannesburg, 2050 South Africa

<sup>2</sup>CSIR National Centre for Nano-Structured Materials, PO Box 395, Pretoria

<sup>3</sup>Department of Physics and Biochemical Sciences, University of Malawi, The Polytechnic, P. B. 303, Chichiri, Blantyre 0003

<sup>4</sup>Themba Labs Gauteng

<sup>5</sup>E. O. Lawrence Berkeley

<sup>6</sup>Lawrence Livermore National Laboratory, University of California, Livermore, California 94551

<sup>7</sup>CSIR National Laser Centre, PO Box 395, Pretoria, South Africa

▶ View Presentation



B. W. Mwakikunga

**CSIR**  
our future through science



[Video Content](#) Length 15:08 Copyright ©2009 Mwakikunga et al

**Chapter X\*****Thermo-chromism at Nanoscale**

**Bonex Wakufwa Mwakikunga<sup>1,2,3,†</sup>, Elias Sideras-Haddad<sup>1</sup>, Andrew Forbes<sup>4</sup>, Gift Katumba<sup>4</sup>, Suprakas Sinha Ray<sup>2</sup>, Chris Arendse<sup>5</sup>**

<sup>1</sup>School of Physics, University of the Witwatersrand, Private Bag 3, P. O. Wits 2050, Johannesburg, South Africa

<sup>2</sup>Council for Scientific and Industrial Research, National Centre for Nano-Structured Materials, P. O. Box 395, Pretoria, South Africa

<sup>3</sup>Department of Physics and Biochemical Sciences, University of Malawi, The Polytechnic, PB 303, Blantyre 0003, Malawi

<sup>4</sup>Council for Scientific and Industrial Research, National Laser Centre, P. O. Box 395, Pretoria 0001, South Africa

<sup>5</sup>Department of Physics, University of Western Cape, Cape Town, South Africa

**Content :**

1. Introduction:
2. Known thermo-chromic materials and VO<sub>2</sub> thermo-chromism
3. Hysteresis thermal profile of the VO<sub>2</sub> MIT
  - 3.1 Khakhaev et al's hysteresis profile
  - 3.2 Hysteresis profile based on magnetic hysteresis
  - 3.3 Pan et al's hysteresis profile
4. Band Models for the System VO<sub>2</sub>
  - 4.1 Goodenough's model
  - 4.2 Paquet et al model
  - 4.3 Vikhnin et al's models
5. Thermo-chromism at nano-scale
  - 5.1 Lopez's hysteresis width broadening at nanoscale
  - 5.2 Hysteresis width and stress
6. Brief review of VO<sub>2</sub> production efforts
  - 6.1 VO<sub>2</sub> nano-ribbons by ultrasonic spray pyrolysis
  - 6.2 VO<sub>2</sub> nanobelts from laser pyrolysis
7. VO<sub>2</sub> thermo-chromism and applications
  - 7.1 Coatings on windows for energy regulation and temperature control
  - 7.2 VO<sub>2</sub> for ultrafast switching applications
8. Open questions on thermo-chromism
9. Conclusions
- References

**1. Introduction:**

The colour of an object depends on the temperature of the object. This phenomenon is known as thermo-chromic effect. It may be noticed even at room temperature if the temperature varies by a few centi-

\* To appear in "Chromic Materials and their Applications" (Ed. Prakash R. Somani), Applied Science Innovations Pvt. Ltd, India (2009)

† Author to whom all correspondence must be addressed: [bmwakikunga@csir.co.za](mailto:bmwakikunga@csir.co.za), Fax: 00 27 12 841 229

grades. Red and orange objects are especially sensitive to temperature variation and colour measurements are known to be difficult to perform from objects with such colours. In this section we define thermo-chromism from basic materials optics. Simple formulas for the temperature-dependent optical characteristics of the materials are outlined.

When light falls on a non-fluorescent material, it is well known that the sum of the incident reflected, absorbed and transmitted energy is equal to the incident energy such that the following law holds

$$R(\lambda) + A(\lambda) + T(\lambda) = 1 \quad (1.1)$$

Where  $R(\lambda)$  is spectral reflectance,  $A(\lambda)$  is spectral absorbance and  $T(\lambda)$  is spectral transmittance. For transmitting materials with finite absorption, we have the usual expression for the spectral intensity  $I(\lambda)$  of the transmitted signal given as

$$I(\lambda) = I_0(\lambda) \exp[-\mu(\lambda)\tau] \quad (1.2)$$

where  $I_0(\lambda)$  is the intensity of the incoming light at the front surface,  $\tau$  is the thickness of the sample and  $\mu(\lambda)$  is the spectral absorption coefficient at a wavelength  $\lambda$ . Definitely,  $\mu(\lambda)$  is the main quantity responsible for the thermal effect.

We also have the optical density,  $D$ , for a transmitting sample given as

$$D = -\log(T(\lambda)) = -\log\left(\frac{I(\lambda)}{I_0(\lambda)}\right) = \mu(\lambda)\tau \log e = \frac{\mu(\lambda)\tau}{\ln 10} \quad (1.3)$$

Here, the changes in the absorption co-efficient change the optical density, the absorbance and thus the transmittance of the sample. In the case of a glossy opaque sample,  $T(\lambda)$  is zero and the changes in the absorbance directly change the reflectance. The reflected part is comparable to the transmitted part in transmitting samples and the optical density can be calculated from

$$D = -\log\left(\frac{I_R(\lambda)}{I_0(\lambda)}\right) \quad (1.4)$$

Where  $I_R(\lambda)$  is the reflected intensity. On the other hand, the intensity falling upon some material attenuates exponentially and, in the case of opaque materials, the light reflected from the material experiences similar attenuation. Thus, Eq. 3 holds for the reflected light if  $\tau$  is the distance the reflected light has passed in the material.

It can be seen therefore that all observed thermo-chromism as perceived by the transmitted and reflected light that strikes the observer's eye is really as a result of the absorption coefficient's dependency on wavelength.

## 2. Known thermo-chromic materials and VO<sub>2</sub> thermo-chromism :

Thermochromism is a macroscopic phenomenon that is based on microscopic electronic properties as a material undergoes a transition between an insulator and a metal. Metal-insulator transitions (MIT) or semiconductor-metal transitions (SMT) are accompanied by huge resistivity changes, even tens of orders of magnitudes. Since electronic properties give rise to the observed optical properties, the MIT has also been quantified by optical properties such as transmittance, absorbance and reflectivity introduced in the

previous section. There are a number of materials that undergo MIT transitions and these are listed in Table 1 adapted from Ref.1 In order to understand this table, this section briefly introduces the underlying physics of MIT and the terminologies used in this area of research.

The transition from metal to insulator has been an illusive subject. The first successful theoretical description of metals, insulators and the transition between them is based on non-interacting or weakly interacting electron system. Electrons are classified in terms of levels where in insulators the valence band is fully filled whereas the conduction band is empty. In metals the two band of energies overlap. The Fermi level lies in the band gap insulators while the level is inside a band for metals.

In the past seventy years progress has been made from both theoretical and experimental sides in understanding correlated electrons and the MITs. In the theoretical approaches, N. F. Mott took the first important step towards understanding how electron-electron correlations could explain the insulator state and this is called the Mott insulator. For details of Mott's work see Mott (1949, 1956, 1961, 1990) [2]. A more difficult and challenging subject has been to describe and understand metallic phases near the Mott insulator. In this regime fluctuations of spin, charge and orbital correlations are strong and sometimes critically enhanced toward the MIT, if the transition is continuous or weakly first order. This has been observed in vanadium oxide phases such as  $V_2O_3$ . To understand this mass enhancement, the earlier pioneering work by J. Hubbard (Hubbard 1963, 1964a, 1964b) [3] known as the Hubbard approximation, employing lattice fermion models, has been hailed. A class of materials that show these characteristics are called Mott-Hubbard (MH) insulators. In the Hubbard model, interactions between electrons between elements and between sites that are hosting these elements are characterized by spins and orbits. In  $d$ -electron systems orbital degeneracy is an important and unavoidable source of complicated behaviour. In transition metal oxides, another aspect of orbital degeneracy is the overlap or closeness of the  $d$  band and  $p$  band of ligand atoms which bridge these elements. When the closeness gets to some critical value, the interaction changes from one of MH insulator to one called the charge transfer (CT) insulator. This kind of insulator was clarified by Zaanen, Sawatzky and Allen in 1985 [4]. In the Hubbard model, there are two important variables: the electron correlation strength  $U/t$  and the band filling  $n$ . When plotted one against the other a very interesting phase diagram is obtained. At low integer band filling numbers ( $n = 1$ ), one gets predominantly Mott insulator phases and in this regime, when the electron correlation strength is low, the transition to metallic phase is governed by what is called bandwidth control (BC) process or BC-MIT. Otherwise, when  $n$  is non-integer and the electron correlation strength is large, one gets a metallic phase near the  $n = 1$  insulating anti-ferromagnetic (AF) phase derived by a process called filling control (FC). The structure of the electron spins in metals close to the MIT can either be paramagnetic (P), ferri-magnetic (Ferri), fluctuating and displaying what is called a spin density wave (SDW) and/or superconducting (SC). Each material also shows a unique Neel temperature: the temperature at which an anti-ferromagnetic material becomes paramagnetic synonymous to the Curie temperature at which a ferromagnetic material becomes paramagnetic.

It is a fact that the understanding of the MIT is still an experimental and theoretical point of contention with new experimental findings proving and disproving some previous theoretical approaches. For a fuller review on the MIT transition, the reader is referred to Imada et al [1]. Table 1, adapted from Imada et al, lists some of the materials that have shown MIT behaviours of different types as indicated in the above discussion and in the Table's legend.

Table 1. List of some of the materials that show MIT behaviours

Compound	Mott insulator		Néel temperature (K)	MIT Transition temperature(K)	Metal near MIT Spin order
	Type	Spin order			
VO <sub>2</sub>	$d^1$ (MH)	gap	-	T, 340	P
V <sub>2</sub> O <sub>3-y</sub>	$d^2$ (MH)	(AF)	180	(FC) (BC)	SDW for FC, P for BC
NiS <sub>2-x</sub> Se <sub>x</sub>	$d^8$ (CT), S=1	(AF)	40-80	T, BC	AF
RNiO <sub>3</sub>	$d^7$ (CT),S=1/2	(AF)	130-240	T, BC	P
NiS <sub>1-x</sub> Se <sub>x</sub>	$d^8$ (CT)	(AF)	260, x=0	260 at x=0	P
Ca <sub>1-x</sub> Sr <sub>x</sub> VO <sub>3</sub>	S=1	-	-	-	P
La <sub>1-x</sub> Sr <sub>x</sub> TiO <sub>3</sub>	$d^1$ MH S=1/2	(AF)	140	FC, $x_c=0.05$	P
La <sub>2-x</sub> Sr <sub>x</sub> VO <sub>3</sub>	$d^2$ MH S=1	(AF)	~150	FC, $x_c=0.2$	P
La <sub>2-x</sub> Ce <sub>x</sub> CuO <sub>4</sub>	$d^9$ (CT),S=1/2	(AF)	300	FC, $x_c\sim 0.05-0.06$	P
Nd <sub>2-x</sub> Ce <sub>x</sub> CuO <sub>4</sub>	$d^9$ (CT),S=1/2	(AF)	~240	FC, $x_c\sim 0.14$	SC,P
YBa <sub>2</sub> Cu <sub>3</sub> O <sub>7-y</sub>	$d^9$ (CT),S=1/2	(AF)	~400	FC, $y_c\sim 0.6$	P, SC
Bi <sub>2</sub> Sr <sub>2</sub> Ca <sub>1-x</sub> R <sub>x</sub> Cu <sub>2</sub> O <sub>8+δ</sub>	$d^9$ (CT),S=1/2	*	*		P,SC
La <sub>1-x</sub> Sr <sub>x</sub> CuO <sub>2.5</sub>	$d^9$ (CT),S=1/2	(AF)	110	FC, $x_c=0.15$	P
Sr <sub>14-x</sub> Ca <sub>x</sub> Cu <sub>24</sub> O <sub>41</sub> BaVS <sub>3</sub>	$d^9$ (CT),S=1/2	gap	-	FC, $x_c=13.5$	SC
BaVS <sub>3</sub>	$d^9$ (CT),S=1/2	(AF)	~35	T, 74	P
Fe <sub>3</sub> O <sub>4</sub>	$d^1$ (MH)S=1/2	Ferri	-	T, 121	P, Ferri
La <sub>1-x</sub> Sr <sub>x</sub> FeO <sub>3</sub>	$d^6, d^5$ S=2.5/2	(AF)	740 $x=0$	FC, T at $T_{CO}$	P ( $x<0.7$ )
	$d^5$ (CT),S=5/2		134 $x=1$		FC( $x=1$ )
La <sub>2-x</sub> Sr <sub>x</sub> NiO <sub>4+y</sub>		(AF)	~500	FC, $x_c\sim 0.7-0.8$	P
	$d^8$ (CT)		$x=y=0$		
La <sub>1-x</sub> Sr <sub>1+x</sub> MnO <sub>4</sub>		(AF)	120	-	
La <sub>1-x</sub> Sr <sub>x</sub> MnO <sub>3</sub>	$d^4$ (CT),S=2	(AF)	140	FC, $x_c\sim 0.17$	F
La <sub>2-2x</sub> Sr <sub>1+2x</sub> Mn <sub>2</sub> O <sub>7</sub>	$d^4$ (CT),S=2	*	*	FC, $x_c\sim 0.3$	
FeSi	$d^4$ (CT),S=2	gap	-	T, 300	
Ti <sub>2</sub> O <sub>3</sub>	-	gap	-	FC,T,400-600	
LaCoO <sub>3</sub>	$d^1$ (MH),S=2	gap	-	T, 500	
La <sub>1.17-x</sub> A <sub>x</sub> VS <sub>3.17</sub>	$d^6$ CT,S=0,1,2	gap	-	FC, $x_c\sim 0.35$ ,T,28	
	$d^2$ (MH)			0	

Anti-ferromagnetic order (AF), Filling control (FC) & Bandwidth control (BC), charge-transfer type (CT), accompanied by a change of structural symmetry (ACSM), Spin (S), critical concentration for MIT ( $x_c$ ), Paramagnetic (P), Spin density wave (SDW), superconducting (SC).

One notes that there are two materials whose MIT temperatures are in the neighbourhood of room temperature: FeSi (300 K) and VO<sub>2</sub> (340 K). Both of these systems display transition between metal and non-magnetic insulators. FeSi is semiconducting below 300K and weakly metallic above it. This means that the switching efficiency is not very high. Due to the switching efficiency, tuneability of its transition temperature, production feasibility and aesthetic beauty, this chapter concentrates on VO<sub>2</sub>.

**Table 2 Lattice parameters for the polymorphs of VO<sub>2</sub>**

VO <sub>2</sub> phase + space group + spontaneous values of the order parameters, $\eta$ .	$a$ (Å)	$b$ (Å)	$c$ (Å)	$\alpha$	$\beta$	$\gamma$	$T_t$ (K)	Ref
VO <sub>2</sub> (R) rutile, P4 <sub>2</sub> /mmm	4.554	4.554	2.854	90	90	90	> 340	[8]
VO <sub>2</sub> (M1) monoclinic1, P2 <sub>1</sub> /c $\eta_1 = \pm\eta_2 \neq 0$	12.09	3.702	6.433	90	122	90	300	[8,107]
VO <sub>2</sub> (M2) monoclinic2, B2/m $\eta_1 = 0 \eta_2 \neq 0$ or $\eta_1 \neq 0 \eta_2 = 0$	12.09	3.702	6.433	90	122	90	300	[8,109]
VO <sub>2</sub> (A)	8.4403	8.4403	7.666	90	90	90	435	[107-109]
VO <sub>2</sub> (B)	12.03	3.693	6.42	90	106	90	300	[107-109]
VO <sub>2</sub> (T) triclinic $\eta_1 \neq 0 \eta_2 \neq 0 \eta_1 \neq \eta_2$	-	-	-	-	-	-	-	[20]

A number of transition-metal oxides exhibit insulator - (or semiconductor-) to-metal transition [5, 6]. The three main groups among the vanadium oxides are V<sub>n</sub>O<sub>2n-1</sub> (e.g. V<sub>2</sub>O<sub>3</sub>, V<sub>7</sub>O<sub>13</sub> [424]), V<sub>n</sub>O<sub>2n+1</sub> (e.g. V<sub>2</sub>O<sub>5</sub>, V<sub>6</sub>O<sub>13</sub> [7] and V<sub>3</sub>O<sub>7</sub> [7,8]), V<sub>n</sub>O<sub>n</sub> (e.g. VO) and V<sub>n</sub>O<sub>2n</sub>. Among these, VO<sub>2</sub> is the most interesting because its transition temperature is close to room temperature ( $T_c \sim 340$  K), and it displays a  $\sim 10^5$  decrease in resistivity as well as a large change in transparency in the infrared region. VO<sub>2</sub> belongs to the V<sub>n</sub>O<sub>2n</sub> class and it is known to exist in four polymorphs – VO<sub>2</sub>(R), VO<sub>2</sub> (M), VO<sub>2</sub> (A), VO<sub>2</sub> (B) – given in Table 2 (a) the most stable VO<sub>2</sub> rutile VO<sub>2</sub>(R) (b) the meta-stable VO<sub>2</sub>(M) with a slightly distorted rutile structure (c) a tetragonal VO<sub>2</sub> (A) and (d) the meta-stable VO<sub>2</sub>(B) with a monoclinic structure.

Thermo-chromism of VO<sub>2</sub> is attributed largely to structural change [9]. Characteristics of this change include the formation of cation – cation pairs and the displacement of vanadium from the centre of its interstice in the monoclinic phase- a feature characteristic of an anti-ferroelectric-type distortion. The actual values of the transition temperature and its sharpness [10] and the lack thereof, have previously been related to variations in stoichiometry [11], mis-orientation between grains [12], and other morphological faults [13] only in a qualitative fashion.

### 3. Hysteresis thermal profile of the VO<sub>2</sub> MIT :

When a particular VO<sub>2</sub> material property– electronic, morphological, structural and optical e.t.c. – is measured at varying temperature during the heating-up and cooling-down cycles a hysteresis step is observed. The hysteresis profiles may show an inverse relationship with temperature such as one for resistance ( $\Omega$ ) and optical transmittance (%T); it may also show the opposite effect such as for conductance, reflectance. The mirror effect between resistance and conductance is as a result of their basic definition- that is conductance  $S$  is equal to the inverse of resistance. Similarly, for the mirror effect of the transmittance and reflectance hystereses, Eq. 1.1 explains the fact that, for same optical absorption, reflectance is inversely related to transmittance. It is interesting to note that roughness increases as temperature is increased and also displays a sharp jump at the transition temperature [23]. Recently, Lopez et al [39] used another property, scattering intensity, to study the VO<sub>2</sub> MIT. The hysteresis profile of scattering intensity shows very unique changes revealing non-linear absorption characteristics in VO<sub>2</sub>. Some of the properties with varying temperature are illustrated in Fig. 3.1

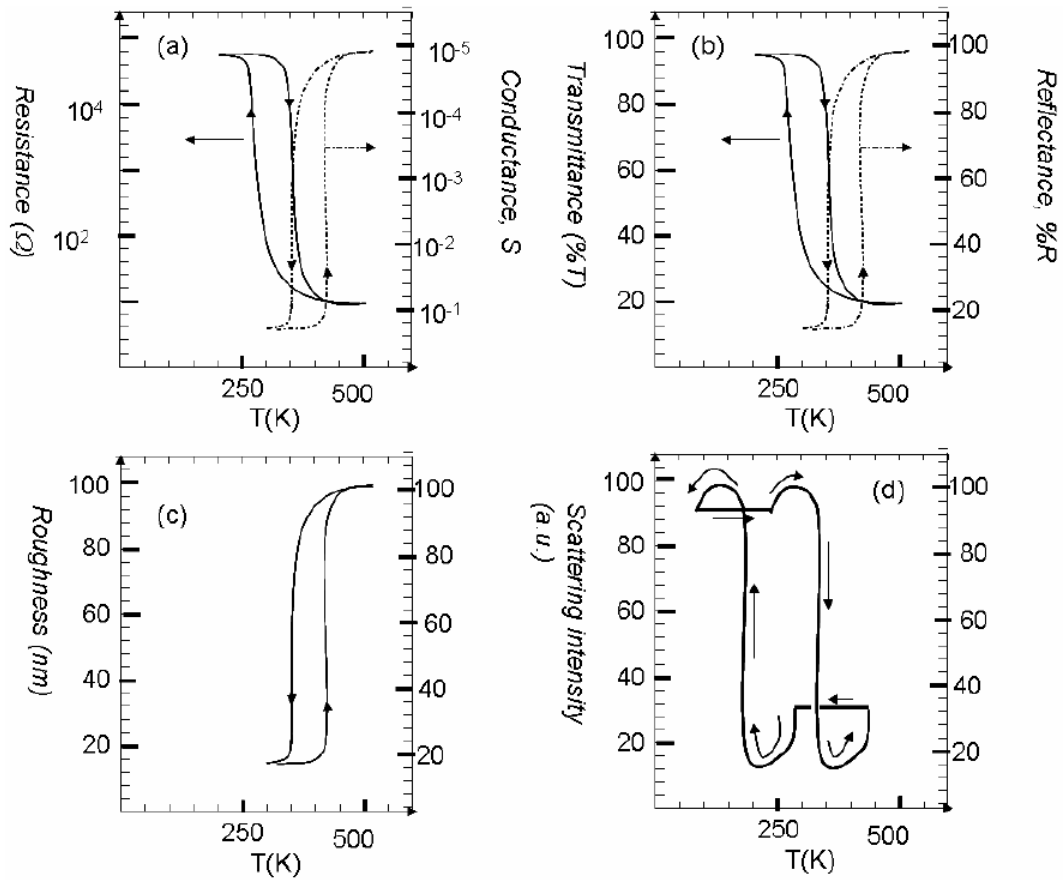


Fig 3.1 Variation of VO<sub>2</sub> properties with temperature close to its MIT: Resistance and conductance (a), Transmittance and Reflectance (b), Roughness (c) and Scattering intensity (d)

### 3.1 Khakhaev et al's hysteresis profile :

In order to construct the distribution function of the coercive temperatures, Khakhaev et al [13] considered the hysteresis loops of the reflectivity (R) and introduced some definitions: (1) the lowering of the temperature was taken as the forward direction of temperature variation so that the corresponding transition takes place from a more symmetrical phase to a less symmetrical one; (2) the branch of the hysteresis corresponding to the cooling (heating) of the sample was called the forward (reverse) branch; (3) the forward and reverse branches of the principal hysteresis loop are bound by the hysteresis existence region in the R×T plane; (4) there are partial hysteresis loops and these lie with the hysteresis region in one way or another; (5) the maximum temperature at which the hysteresis exists is was the starting temperature,  $T_{sm}$ , of the principal loop (6) the final temperature,  $T_{fm}$ , of the principal loop is the minimum temperature of the existence of the hysteresis and (7) large partial loops were partial loops for which the starting temperature  $T_s$  was one of the branches of the principal loop and the final temperature,  $T_f$ , was equal to  $T_{sm}$  or  $T_{fm}$ . Thus their reflectivity-temperature hysteresis loop showed the principal hysteresis loop and a family of large partial loops whose starting temperatures lie on the direct branch of the princi-



pal loop. Their distribution function was constructed in accordance with T. Lanskaya et al (1978) [14] as the second derivative of the reflectivity  $R(T_s, T)$ :

$$F(T_0, T_{c0}) = \frac{2}{\Delta R_f} \frac{\partial^2 R(T_s, T)}{\partial T_s \partial T} \tag{3.1.1}$$

where

$$T_0 = \frac{T_s + T}{2} \text{ and } T_{c0} = \frac{T_s - T}{2} \tag{3.1.2}$$

$T$  is the current temperature and  $T_s$  is the starting temperature of the partial loop. In order to obtain a smooth second derivative, it was necessary to have a sufficiently large number of partial hysteresis loops so that an interpolation algorithm was required for their construction. Using least squares, Khakhaev et al found a class of functions that described the branches of the main hysteresis loop and the branches of the large partial loops in the same manner. The functions had the form:

$$R(T, T_s) = A(T_s) + \frac{B(T_s)}{T} + \frac{D(T_s)}{1 + \exp\left(-\frac{T - T_m(T_s)}{\Delta T(T_s)}\right)} \tag{3.1.3}$$

where

$$A(T_s) = a_1 + \frac{b_1}{T_s} + \frac{d_1}{1 + \exp\left(-\frac{T_s - t_{m1}}{\Delta t_1}\right)}; \quad B(T_s) = a_2 + \frac{b_2}{T_s} + \frac{d_2}{1 + \exp\left(-\frac{T_s - t_{m2}}{\Delta t_2}\right)} \tag{3.1.4}$$

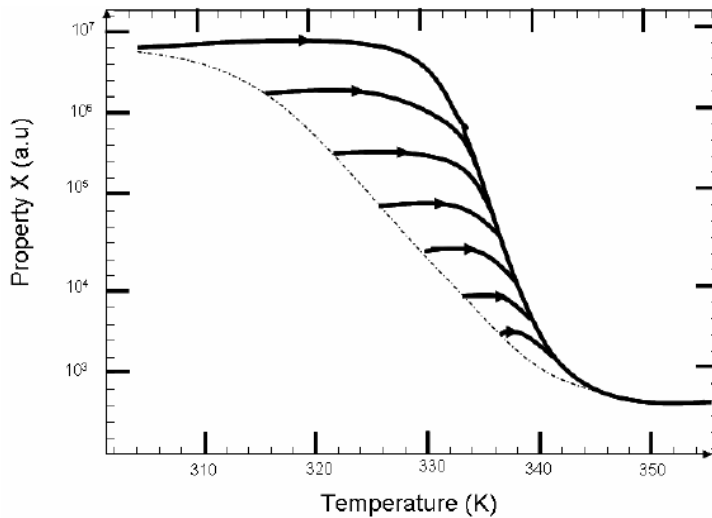


Fig 3.2 Major and minor loops in the resistance hysteresis of VO<sub>2</sub>

$$A(T_s) = a_3 + \frac{b_3}{T_s} + \frac{d_3}{1 + \exp\left(-\frac{T_s - t_{m1}}{\Delta t_3}\right)}; T_m(T_s) = a_4 + \frac{b_4}{T_s} + \frac{d_4}{1 + \exp\left(-\frac{T_s - t_{m4}}{\Delta t_4}\right)} \quad (3.1.5)$$

$$\Delta T(T_s) = \frac{a_5 + c_5 T_s + e_5 T_s^2}{1 + b_5 T_s + d_5 T_s^2} \quad (3.1.6)$$

Here  $A$ ,  $B$ ,  $D$ ,  $T_m$  and  $\Delta T$  depend only on  $T_s$  and all the quantities whose designations begin with lower-case letters are constant coefficients.

A typical plot of Eq. 3.1.3 is illustrated in Fig. 3.2

### 3.2 Hysteresis profile based on magnetic hysteresis :

There exist various physical and mathematical models to describe hysteretic phenomena. Some of these models are derived from magnetic hysteresis like the Preisach model [15] and the Jiles model [16]. These explain the magnetization in terms of the movement of magnetic domain walls. de Almeida et al [17] have noted that due to its mathematical generality, the Preisach model is very widely accepted as a suitable tool to formally describe hysteresis phenomena. In this section, in agreement with de Almeida et al , we show how the Preisach model can be adapted to describe thermal (rather than magnetic) hysteresis in VO<sub>2</sub> thin films.

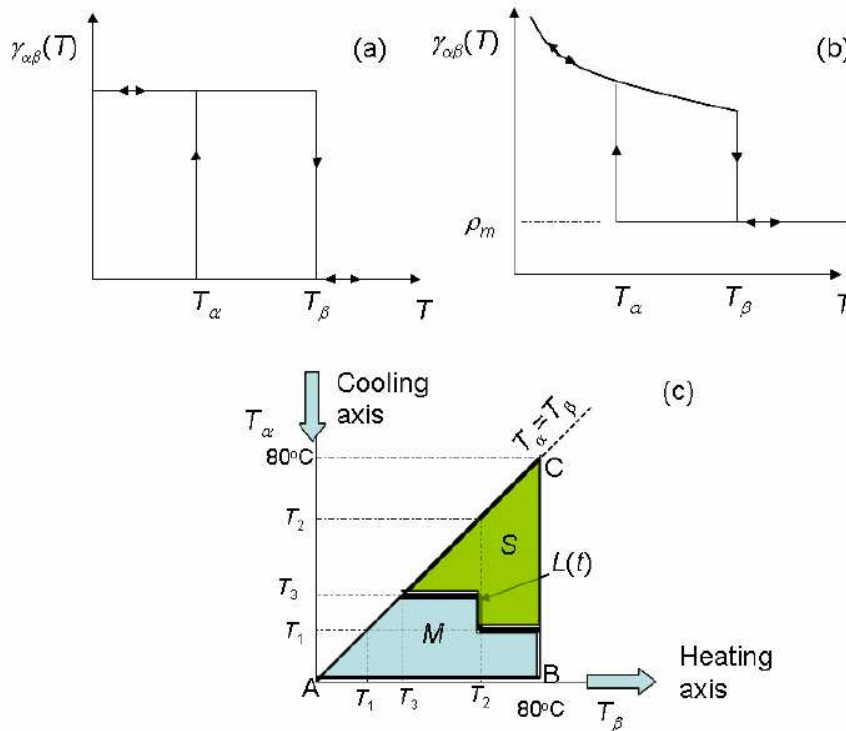


Fig 3.3 Graphical representation of the relay operator for VO<sub>2</sub> (a) in the simple bistable operator (b) the operator which exhibits reversible and irreversible components and (c) the Preisach triangle

The original classic Preisach model was proposed in 1935. The model was conceived on an intuitive basis and is based on some plausible hypothesis about the magnetization mechanism. During the 1970's M. Kransnoselskii [17] showed that the Preisach model was quite general and it is possible to adapt it to hysteresis phenomena other than magnetic. Khakhaev et al in previous section have presented experimental evidence that the VO<sub>2</sub> film is composed of microcrystals that exhibit individually very sharp hysteresis transitions. The overall film characteristics are therefore associated with the existence of an ensemble of either metallic or semi-conducting microcrystals of VO<sub>2</sub>.

The classical Preisach model for VO<sub>2</sub> starts by describing the film properties (electronic, optical etc) as a sum of a simple relay operator  $\gamma_{T_\alpha T_\beta}$  representing microcrystal states weighted by a statistical distribution  $\mu(T_\alpha, T_\beta)$  and resistance of the film as a function of time is given by

$$R(t) = \iint_{ABC} \hat{\gamma}_{T_\alpha T_\beta} T(t) \mu(T_\alpha, T_\beta) dT_\alpha dT_\beta \tag{3.2.1}$$

The simple bistable operator, as illustrated in Fig. 3.3 (a), is given as

$$\hat{\gamma}_{T_\alpha T_\beta} = \begin{cases} 1 & T \leq T_\alpha \\ \text{unchanged} & T_\alpha \leq T \leq T_\beta \\ 0 & T \geq T_\beta \end{cases} \tag{3.2.2}$$

In a more realistic case, each microcrystal behaves as an intrinsic semiconductor when T is lower than T<sub>α</sub> and hence, as illustrated in Fig. 3.3(b), the relay operator changed to

$$\hat{\gamma}_{T_\alpha T_\beta} = \begin{cases} \rho_0 \exp\left(\frac{E_a}{k_B T}\right) & T \leq T_\beta \\ \text{unchanged} & T_\alpha \leq T \leq T_\beta \\ \rho_m & T \geq T_\beta \end{cases} \tag{3.2.3}$$

When cooling axis values are plotted against the heating axis ones an interesting graphical feature called the Preisach triangle ABC is obtained. This is illustrated in Fig. 3.11.1 (c). This essentially is a simplified graphical representation of Eq. 3.11.1. This right triangle is associated only with the hysteretic portion of the R×T characteristics lying between 20°C and 80°C. In other words the distribution  $\mu(T_\alpha, T_\beta)$  is assumed to be zero outside the triangle ABC. This triangle can be divided into two parts: S and M representing the region where the operators are in state 1 and 0 respectively. The surface areas of these regions depend on the history of the thermal cycling.

Since the simple bistable operator has been shown to lead to an R(T) profile which does not very well at low temperatures of the hysteresis, this chapter will concentrate on using only Eq. 3.2.3 to transform Eq. 3.2.1 into a more tractable form. First it assumed that the operator  $\gamma_{T_\alpha T_\beta}$  can take on two distinct forms of temperature dependence, and these functional dependencies have neither statistical relation with the distribution  $\mu(T_\alpha, T_\beta)$  nor with the variables T<sub>α</sub> and T<sub>β</sub>. Thus the integral in Eq. 3.2.1 can be written as

$$\rho = \rho_0 \exp\left(\frac{E_a}{k_B T}\right) \iint_S \mu(T_\alpha, T_\beta) dT_\alpha dT_\beta + \rho_m \iint_M \mu(T_\alpha, T_\beta) dT_\alpha dT_\beta \quad (3.2.4)$$

The other assumption is that the distribution function  $\mu(T_\alpha, T_\beta)$  over the whole Preisach triangle is unity, that is

$$\iint_{S+M} \mu(T_\alpha, T_\beta) dT_\alpha dT_\beta = 1 \quad (3.2.5)$$

Thus the integral of the distribution function  $\mu(T_\alpha, T_\beta)$  over the surface area  $S$  is defined as the volume fraction  $v$  of the microcrystals that are in the semiconducting state, thus:

$$\iint_S \mu(T_\alpha, T_\beta) dT_\alpha dT_\beta = 1 - \iint_M \mu(T_\alpha, T_\beta) dT_\alpha dT_\beta \quad (3.2.6)$$

or

$$v = 1 - (1 - v) \quad (3.2.7)$$

Consequently, the integral of the distribution function  $\mu(T_\alpha, T_\beta)$  over the area  $M$  is the fraction  $(1-v)$  of the micro-crystals that are in the metallic state.

From the above considerations and the geometrical interpretations of the Preisach triangle, the integral in Eq. 3.2.1 simplifies to

$$\rho = \rho_0 \exp\left(\frac{E_a}{k_B T}\right) v + \rho_m (1 - v) \quad (3.2.8)$$

For a thin slab of length  $l$ , width  $w$  and thickness  $\tau$ ,  $R_0 = \rho_0 l/w \tau$  and  $R_m = \rho_m l/w \tau$ , then the slab resistance can be represented as

$$R = v R_0 \exp\left(\frac{E_a}{k_B T}\right) + (1 - v) R_m = v R_s + (1 - v) R_m \quad (3.2.9)$$

In the case of bulk  $\text{VO}_2$ , the resistance of the semiconducting phase is much higher than that of the metallic phase  $R_s \gg R_m$  and hence the Eq. 3.11.9 reduces to

$$R(T) = R_0 \exp\left(\frac{E_a}{k_B T}\right) \iint_S \mu(T_\alpha, T_\beta) dT_\alpha dT_\beta + R_m = v R_s + R_m \quad (3.2.10)$$

The task is to determine the  $\mu(T_\alpha, T_\beta)$ . A procedure by Mayergoyz [15] employs the experimental first order descending transition (FODT) curves. The reader can find details of an illustration of how this is accomplished in de Almeida's work [17]. It must be mentioned that, as much as the hysteresis nature is dictated by the particle size and size distribution in the sample, then  $\mu(T_\alpha, T_\beta)$  also has to be particle size dependent. The profile of the  $R(T)$  can easily be seen to follow that of the observed experimental results as illustrated in Fig 3.4

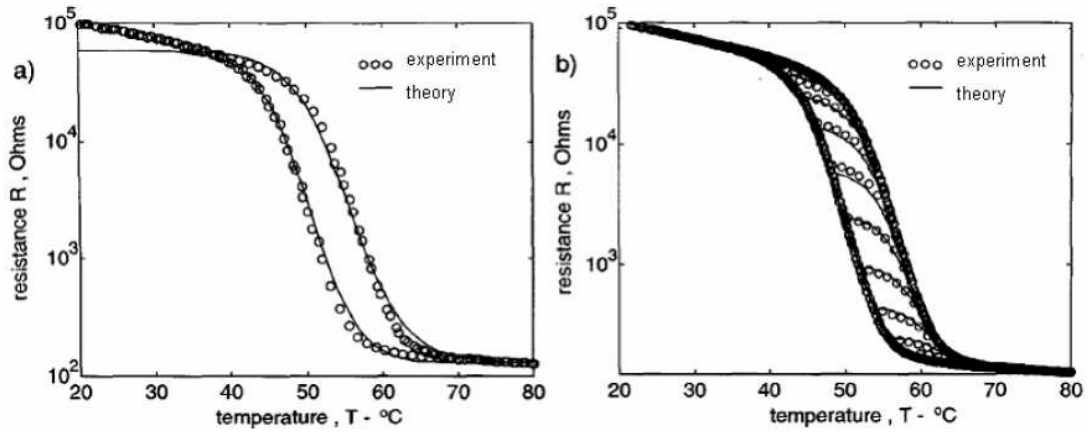


Fig 3.4 Comparison between de Almeida model simulation and the experimental results for (a) the bistable operator and (b) two-phase operator

### 3.3 Pan et al's hysteresis profile :

Pan et al [18], using Raman spectroscopy of VO<sub>2</sub> noted that some phonons that are present in the low-temperature monoclinic structure of VO<sub>2</sub> are not present in the high-temperature tetragonal structure. Since the existence of a phonon is either yes or no before and after the phase transition, Pan et al gave the following delta function:

$$\theta(T - T_c) = \begin{cases} 1 & (T < T_c) \\ 0 & (T > T_c) \end{cases} \tag{3.3.1}$$

Where  $\theta$  indicates the existence or not of a certain phonon mode in a crystal grain with either semiconductor or metallic phase,  $T_c$  is the equilibrium phase transition temperature.

Pan et al also considered the effect of the spread in the grain size on the hysteresis loop during the transition process. It was assumed that each grain had its own hysteresis loop and that each elementary loop was located normally to the temperature axis. Pan et al were able to develop expressions for the intensity of the Raman mode as a function of the temperature by using the delta function above and performing integration of all the loops of grains whose size distribution was assumed to be Gaussian distribution. However, no direct dependency of the HW and HJ on the particle size was shown. We observe that, while it is true that grain size has a distribution which is assumed to be Gaussian, it is the temperature which leads to a force of change. The Gaussian is expressed to take into account the independent variable  $T$  (expressed as thermal energy  $k_B T$ ) and strain energy (expressed as  $\sigma_E V$ - where  $\sigma_E$  is the strain energy per unit area at transition and  $V$  is the volume of the grain where the thermal energy is expended). So during the heating up cycle, the number  $N_+$  of grains that transform from monoclinic phase to tetragonal phase is given as

$$N_+ = \begin{cases} 0 & \infty > T > T_{c1} \\ A_+ \exp \left[ -\alpha \left( \frac{(T - T_{c1})}{\sigma_{sd}} \right)^2 \right] & T_{c1} > T > 0 \end{cases} \tag{3.3.2}$$

Similarly, during the cooling down cycle, the number of crystallites  $N_-$  that transform from tetragonal back to monoclinic is

$$N_- = \begin{cases} 0 & T_{c2} > T > 0 \\ A_- \exp\left[-\alpha\left(\frac{(T-T_{c2})}{\sigma_{sd}}\right)^2\right] & \infty > T > T_{c2} \end{cases} \quad (3.3.3)$$

The dependent variable value (transmittance, intensity of the Raman phonon mode or the resistivity) can be found by using the delta function in Eq. 3.3.1 and the number of crystallites that give rise to the observed property, thus:

$$I_+ \approx 1 - C_+ \int_{-\infty}^T N_+ dT \quad (3.3.4)$$

$$I_- \approx C_- \int_{-\infty}^T N_- dT \quad (3.3.5)$$

We have been able to calculate the HW as a difference between  $T_{c1}$  and  $T_{c2}$  in Eqs. 3.3.2 and 3.3.3. We find that HW increases as the particle size increases- a fact that opposes experimental observations by ourselves and several others. Also, the limits of integration are not physical. For instance, there is no such thing as negative temperature on the Kelvin scale and lowest on the Celsius is  $-273^\circ\text{C}$  and not  $-\infty$ . The current improvement of this model and its application to the derivation of hysteresis widths are presented in Section 5

## 4. Band Models for the System $\text{VO}_2$ :

### 4.1 Goodenough's model :

Between 1971 and 1973 J. B. Goodenough [19] proposed an electronic band structure for  $\text{VO}_2$  as a merger of the separate electronic band configurations of  $\text{V}^{4+}$  anion and the  $\text{O}^{2-}$  cation. These band structures were analyzed in both the room-temperature monoclinic phase and the high temperature tetragonal phase of  $\text{VO}_2$ . In vanadium oxides, the Fermi energy  $E_F$  falls above the top of the  $\text{O}^{2-}$  2p band and below the vanadium 4s band. In the monoclinic phase, the V-V pairing splits the narrow  $d_{||}$  band in two possibly due to electron correlations. The semiconducting character of the monoclinic phase requires that the  $\pi^*$  bands be raised above the  $E_F$  and that the formation of V-V pairs stabilize V-V homo-polar orbitals below the  $E_F$  level as shown in Fig. 4.1 (a). As a result, an energy band gap  $E_g$  of  $\sim 0.7 \text{ eV}$  can be seen at room temperature.

At higher than  $70^\circ\text{C}$ , bulk  $\text{VO}_2$  shows contrary electronic ordering. Orthorhombic crystalline field splits the  $d^1$  energies at the  $\text{V}^{4+}$  ions into two unstable  $\sigma$ -bonding orbitals, two quasi-degenerate  $\pi$ -bonding orbitals and a stable orbital oriented along the  $c_{\text{rutile}}$  of the tetragonal cell. A critical  $\text{V}^{4+}$ - $\text{V}^{4+}$  separation of  $R_c = 2.94 \text{ \AA}$  has been estimated for the transition from mobile to localized behaviour of the  $3d^1$  band in oxides containing a  $\text{V}^{4+}$  - ion sub-array. Therefore, the  $3d$  orbitals parallel to the  $c_{\text{rutile}}$  axis should form a narrow  $d_{||}$  band in tetragonal  $\text{VO}_2$  as in Fig 4.1 (b). Transition metal oxides with perovskite structure are known to possess covalent mixing between oxygen  $2p$ , both  $p_\pi$  and  $p_\sigma$ , and the  $\text{V}^{4+}$ -ion  $3d$  orbital a phe-

nomenon which is strong enough to create itinerant-electron  $d$ -like orbitals. Therefore, the two  $\sigma$ -bonding  $d$ -orbitals per  $V^{4+}$ -ion form unstable  $\sigma^*$  bands and the two  $\pi$ -bonding  $d$  orbitals form quasi-degenerate  $\pi^*$  bands via  $V^{4+} - O^{2-} - V^{4+}$  interactions. Observations of a nearly isotropic conductivity in single crystal  $VO_2$  was interpreted to indicate that the  $\pi^*$  bands overlap the Fermi energy  $E_F$  as shown in Fig. 4.1 (b). In nano- $VO_2$ , however, this picture is expected to be different since the ratio of surface atoms to those of bulk  $VO_2$  is much higher at this scale. These nano-scale phenomena are discussed in the forthcoming sections of this chapter

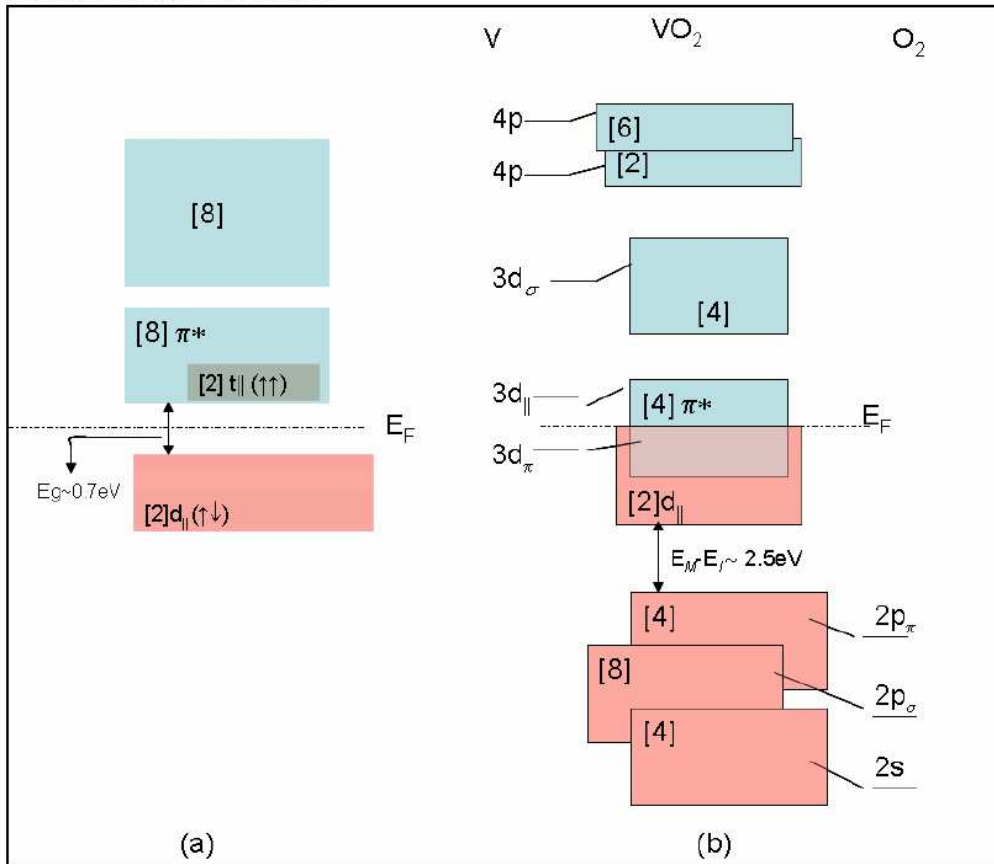


Fig 4.1 Changes in electronic configurations of  $VO_2$  on passing from (a) the monoclinic to (b) the tetragonal phases. Note the changes in the  $d$  bands where and energy gap of  $0.7\text{eV}$  disappears as the  $\pi^*$  and the  $d_{||}$  overlap at high temperature.

#### 4.2 Paquet et al model :

Paquet and Leroux-Hugon [20] presented a model of the  $VO_2$  phase transition which incorporated both the electron-electron and electron-lattice interactions and this accounted for the presence of two  $d$  bands ( $\pi^*$  and  $d_{||}$ ) overlapping at the Fermi level of the metallic phase. Attention was paid to the crystallographic symmetry change at the transition and to the properties of the associated order parameter. The  $e-e$  interactions were explained by using the functional-integral treatment of the Hubbard Hamiltonian

whereas the  $e$ -phonon interactions were treated by choosing the centre-of-gravity and the shape of the  $d$ -bands so that they depended on the lattice distortion. Spin-spin interactions were described in terms of the Ising-like model. These treatments lead to a free energy expression which when minimized with respect to the order parameter ( $\eta$ ) and the local magnetic moment ( $\mu$ ) gave the temperature dependency of these parameters.

The following discussion is a brief outline of this treatment. The Hubbard Hamiltonian for the  $e$ - $e$  interaction is given by

$$H = H_{0\parallel} + H_{0*} + H_{e-e} + H_{latt} \quad (4.2.1)$$

where

$$H_{0\parallel} = \sum_{i,\sigma} \epsilon_{\parallel} (\eta) a_{i,\sigma}^{+(\parallel)} a_{i,\sigma}^{(\parallel)} + \sum_{i,j,\sigma} t_{ij}^{(\parallel)} (\eta) a_{i,\sigma}^{+(\parallel)} a_{j,\sigma}^{(\parallel)} \quad (4.2.2)$$

$$H_{0*} = \sum_{\substack{i,\sigma \\ l=1,2}} \epsilon_* (\eta) a_{i,\sigma}^{+(*l)} a_{i,\sigma}^{(*l)} + \sum_{\substack{i,j,\sigma \\ l=1,2}} t_{ij}^{(*)} (\eta) a_{i,\sigma}^{+(*l)} a_{j,\sigma}^{(*l)} \quad (4.2.3)$$

$$H_{e-e} = \sum_{\substack{i,j,k,l \\ \alpha,\beta,\gamma,\delta}} U_{ijkl}^{\alpha\beta\gamma\delta} a_{i,\alpha}^+ a_{j,\beta}^+ a_{k,\gamma}^+ a_{l,\delta}^+ \quad (4.2.4)$$

where  $i, j, k, l$  are site indices and  $\alpha, \beta, \gamma, \delta$  label both orbital and spin states of the  $d$ - wave functions and  $\epsilon_{\parallel}, \epsilon_*$  and  $t_{ij}$  are distortion dependent energies in the  $d_{\parallel}, d_*$  and  $t$  bands respectively. When  $i = j = k = l$  the case for one site and if  $n_i(\alpha) = a_i^{-\langle\alpha\rangle} a_i(\alpha)$  which is a case where spin and charge fluctuations are assumed non-existent, one then get for the electron-electron interaction Hamiltonian as

$$H_{e-e} = \sum_i \left[ U_{\parallel} n_{i\uparrow}^{(\parallel)} n_{i\downarrow}^{(\parallel)} + U_* (n_{i\uparrow}^{(*1)} n_{i\downarrow}^{(*1)} + n_{i\uparrow}^{(*2)} n_{i\downarrow}^{(*2)}) + W_{**} (n_{i\uparrow}^{(*1)} + n_{i\downarrow}^{(*1)}) (n_{i\uparrow}^{(*2)} + n_{i\downarrow}^{(*2)}) \right. \\ \left. + W_{*\parallel} (n_{i\uparrow}^{(\parallel)} + n_{i\downarrow}^{(\parallel)}) (n_{i\uparrow}^{(*1)} + n_{i\downarrow}^{(*1)} + n_{i\uparrow}^{(*2)} + n_{i\downarrow}^{(*2)}) \right] \quad (4.2.5)$$

where  $U_{\parallel}$  and  $U_*$  are the specific Hubbard terms describing the Coulomb interaction of two electrons of like orbits and opposite spins and  $W_*$  and  $W_{*\parallel}$  account for the electrons of unlike orbitals and finally

$$H_{lattice} = C\eta^2 + D\eta^4 \quad (4.2.6)$$

The  $H_{latt}$  describes the bare potential energy associated with the normal phonon mode which is the order parameter of the transition, but does not encompass the changes in the other phonon modes which accompany the change of the electronic spectrum.

Several decoupling procedures and approximations are necessary for one to surmount the VO<sub>2</sub> MIT problem with the above four components of the total Hamiltonian. These include neglecting spin and charge fluctuations. However, the free energy of the VO<sub>2</sub> MIT can be estimated from this treatment and which comes into three components as

$$F = F_{orb} + F_{spm} + F_{latt} \quad (4.2.7)$$



where

$$F_{orb}(T, \eta, \mu) = E_F - k_B T \int_{-\infty}^{+\infty} [\rho^{\parallel}(E, \eta, \mu) + \rho^*(E, \eta, \mu)] \times \ln(1 + e^{\beta(E_F - E)}) dE + \Delta E_{int}(T, \eta, \mu) \tag{4.2.8}$$

with  $\rho$  being the density of states dependent on energy  $E$ , distortion  $\eta$  and local magnetic moment  $\mu$ .  $\Delta E_{int}$  is further given by

$$\Delta E_{int} = \sum_i \left[ \frac{1}{4} U_{\parallel} \mu^2 - \left( \frac{1}{4} U_{\parallel} + \frac{1}{8} U_* - W_{* \parallel} \right) \left( \langle n_{i \uparrow}^{(0)} - n_{i \downarrow}^{(0)} \rangle^2 - N_0^2 \right) + \left( W_{* \parallel} - \frac{1}{4} U_* - \frac{1}{2} W_{**} \right) \left( \langle n_{i \uparrow}^{(0)} - n_{i \downarrow}^{(0)} \rangle - N_0 \right) \right] \tag{4.2.9}$$

$$F_{spin}(T, \eta, \mu) = -\frac{1}{2} k_B T \ln \left( 4 \cosh \frac{\left[ \frac{1}{16} U_{\parallel}^2 + 4t_s^2(\eta) \right]^{1/2} - \frac{1}{4} U_{\parallel} \mu^2}{k_B T} \cosh \frac{\left[ \frac{1}{16} U_{\parallel}^2 + 4t_i^2(\eta) - \frac{1}{4} U_{\parallel} \right]^{1/2} - \frac{1}{4} U_{\parallel} \mu^2}{k_B T} \right) \tag{4.2.10}$$

$F_{latt}$  is reduced to the potential energy of the  $H_{exch}$  – the anti-ferromagnetic exchange interaction given as

$$H_{exch} = \sum_{i,j} J_{ij} \mu^2 \in_i \in_j \tag{4.2.11}$$

where  $J_{ij}$  is the magnetic coupling between spins. That is

$$F_{latt} = H_{exch} \psi_{ij} \tag{4.2.12}$$

where  $\psi_{ij}$  is the wave-function system of spins

In order to visualize the free energy,  $F(T, \eta, \mu)$ , surface the following parameters are first determined or sought from prevailing literature:  $\Delta_{\parallel}(\eta = 0) = 0.55 \text{ eV}$ ,  $\Delta_{*0} = 0.89 \text{ eV}$ ,  $\Omega_{*0} = 0.56 \text{ eV}$ ,  $U_{\parallel} = 1.1 \text{ eV}$ ,  $U_* = 0.55 \text{ eV}$ ,  $E_F + \Delta_{\parallel} = 0.44 \text{ eV}$ ,  $\Delta_{\parallel}(\eta = 0) + \Delta_* + \Omega_{*0} = 2 \text{ eV}$ ,  $W_{* \parallel} = 0.61 \text{ eV}$ ,  $W_{**} = 0.49 \text{ eV}$ ,  $C = 17.3 \text{ eV} \text{ \AA}^{-2}$ ,  $D = 260 \text{ eV} \text{ \AA}^{-4}$ .

The most important feature of this model for the purposes of this discussion is the prediction of the  $\text{VO}_2$  transition temperatures (1) at  $T_c = 340 \text{ K}$  when the calculated order parameter,  $\eta$  is plotted against the temperature  $T$  and (2) at  $T_{\mu} \sim 800 \text{ K}$  when the magnetic moment  $\mu$  is plotted against temperature as shown in Fig. 4.2

It must be noted that this model agrees very well with the usual Landau expansion of the free energy in terms of the variational parameters  $\mu$  and  $\eta$ . The simplest expansion is given as

$$F = \frac{1}{2} a (T - T_{\mu}) \mu^2 + \frac{1}{4} b \mu^4 + \frac{1}{2} \alpha \eta^2 - \frac{1}{4} \beta \eta^4 + \frac{1}{6} \gamma \eta^6 - \frac{1}{2} g \eta^2 \mu^2 \tag{4.2.13}$$

Where the co-efficients  $a, b, \alpha, \beta, \gamma$  and  $g$  are positive and temperature independent and where  $T_{\mu}$  is the temperature at which local moments appear ( $T_{\mu} \sim 800 \text{ K}$ ). At this temperature the transition is second order and corresponds to the building up of the local magnetic moment amplitude  $\mu$  in an undistorted phase ( $\eta = 0$ ). The other one, occurring at a lower temperature,

$$T_c = T_\mu - \frac{3}{16} \frac{b}{ag\gamma} \left\{ \left[ 4 \left( \frac{1}{3} \alpha \gamma \right)^{1/2} \right]^2 - \left( \beta + \frac{g^2}{b} \right)^2 \right\} \quad (4.2.14)$$

is a first-order one and describes the onset of a finite distortion  $\eta$  together with a jump of  $\mu$

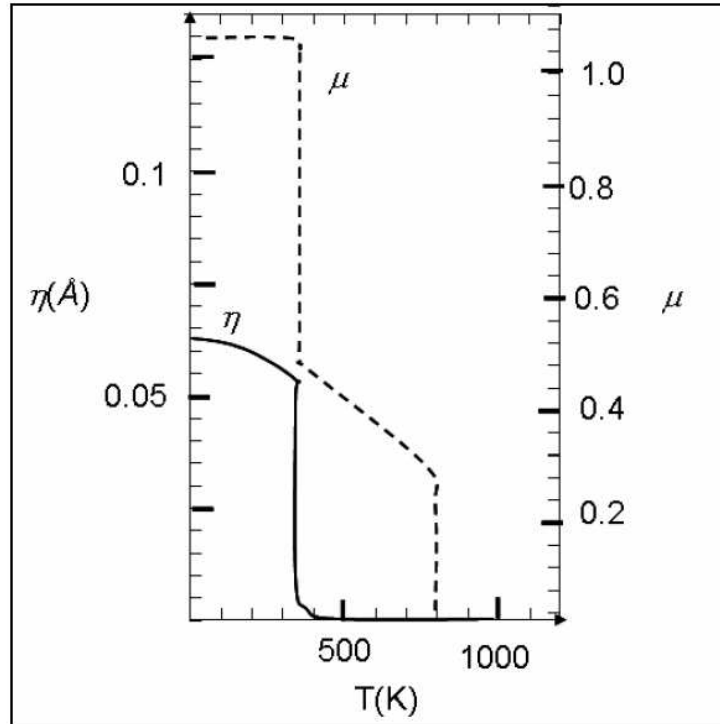


Fig. 4.2 Temperature variation of the amplitudes of the distortion  $\eta$  and of the local magnetic moment  $\mu$  plotted from Eq. 4.2.7 in comparison with 4.2.13

#### 4.3 Vikhnin et al's models :

Although in the previous sections we have shown that, according to Imada and Fujimori's review paper [1],  $\text{VO}_2$  is a Mott-Hubbard insulator, Vikhnin et al (2005) [21] developed a phenomenological model for the  $\text{VO}_2$  SMT by assuming that the SMT is governed by charge transfer (CT) mechanism instead. Vikhnin et al motivated the importance of their theory after noting that, from experimental Raman spectroscopy data around the  $\text{VO}_2$  SMT, the SMT has a smooth temperature dependency which is an indication that vibrational instability as the driving force of the SMT cannot be satisfactory. The charge transfer mechanism has two competing phenomena- (1) the negative dielectric parameter  $\epsilon$  due to Coulomb repulsion between electron density (at the oxygen sites) and hole density (at the vanadium site) leading to electron-hole pair instability and (2) the electron-hole pair (exciton) "negative U" effect due to the exciton's interactions with the lattice leading to attraction and electron-hole stability charge transfer. This Coulombic repulsion is derived from a dielectric constant function which takes into account the interac-

tion between the carriers and their subsequent interactions with the ionic lattice given by the following expression

$$\epsilon(\omega) = \epsilon_{\infty} + \delta\epsilon_{carrier}(\omega) + \delta\epsilon_{ionic}(T, \omega) \tag{4.3.1}$$

Where

$$\delta\epsilon_{carrier}(\omega) = -\frac{\omega_n^2}{\omega^2 - \omega_c^2} \tag{4.3.2}$$

Where  $\omega_h$  is the plasma frequency, and  $\omega_c$  is the collision frequency and

$$\delta\epsilon_{ionic}(\omega, T) = \sum_i \epsilon_i(\omega) + \delta\epsilon_{soft}(\omega, T) \tag{4.3.3}$$

The  $\delta\epsilon_{soft}(\omega, T)$  term is characterized by the temperature dependent frequency of possible soft phonon mode within the SMT region given by

$$\omega_{soft}^2 = \omega_{0,soft}^2 + W_{anh} T \tag{4.3.4}$$

Where  $\omega_{0,soft} = 145 \text{ cm}^{-1}$  for VO<sub>2</sub> and  $W_{anh}$  is constant in the temperature – Raman shift linear part of the SMT as also given in the phenomenological equation for the dielectric constant

$$\epsilon = -C_{carrier} n_e + B_0 - \frac{W_{anh}}{\omega_{0,soft}^2} T \tag{4.3.5}$$

The reader can verify that this first process leads to a temperature–dependent free energy given by

$$\alpha_{Coulomb}(T) = \frac{e^2}{r_{V-O}} \frac{1}{C_{carrier} n_e - B_0 + B_1 T} \tag{4.3.6}$$

Where  $e$  is the electronic charge,  $r_{V-O}$  is the O-V nearest neighbour distance,  $C_{carrier}$  is the  $n_e$  is the carrier density

The second process which is seen to compete with the Coulomb repulsion above is the excitonic attraction between the electron – hole pairs existing between the V4+ and O2- ions. The interaction between the electron-hole pairs is pseudo – Jahn –Teller type of interaction whose Hamiltonian for the splitting  $\Delta_h$  at the hole site and  $\Delta_e$  at the electron site is given as

$$H_{pair,PJT} = \tilde{T} + V_h [\hat{\sigma}_x^{xz} Q_{xz} + \hat{\sigma}_x^{yz} Q_{yz}] + V_e [\hat{\sigma}_x^{xz} Q_{xz} + \hat{\sigma}_x^{yz} Q_{yz}] + \frac{K}{2} (Q_{xz}^2 + Q_{yz}^2) + \frac{\Delta_h}{2} \hat{\sigma}_z + \frac{\Delta_e}{2} \hat{\sigma}_z \tag{4.3.7}$$

Where  $\tilde{T}$  is the kinetic energy operator,  $V_e, V_h$ , are vibronic parameters,  $\sigma_x^{ij}, \sigma_z$  are non-diagonal and diagonal Pauli matrices for holes,  $\sigma_x^{ij}, \sigma_z$  are non-diagonal and diagonal matrices for electrons and  $Q_{xz}$  and  $Q_{yz}$  are lattice variables. By operating this Hamiltonian on the wave function of the exci-

tonic system one get, in the limit of strong vibronic interaction, the potential of the problem given by

$$U_{ad}^{PJTpair} = -|V_h| \sqrt{\left(\frac{A_h}{2V_h}\right)^2 + (Q_{xz}^2 + Q_{yx}^2)} - |V_e| \sqrt{\left(\frac{A_e}{2V_e}\right)^2 + (Q_{xz}^2 + Q_{yx}^2)} + \frac{K}{2}(Q_{xz}^2 + Q_{yx}^2) \tag{4.3.8}$$

This solution of such a problem leads to an equation

$$\frac{|V_h|/K}{\sqrt{\left(\frac{A_h}{2V_h}\right)^2 + (Q_{xz}^2 + Q_{yx}^2)}} + \frac{|V_e|/K}{\sqrt{\left(\frac{A_e}{2V_e}\right)^2 + (Q_{xz}^2 + Q_{yx}^2)}} = 1 \tag{4.3.9}$$

One of the approximations of this problem is that

$$\left(\frac{A_h}{2V_h}\right)^2 \approx \left(\frac{A_e}{2V_e}\right)^2 \tag{4.3.10}$$

Therefore from the PJT pair potential equation one finds that

$$\sqrt{(Q_{xz}^2 + Q_{yx}^2)} \approx \sqrt{\left(\frac{|V_e| + |V_h|}{2K}\right)^2 - \frac{1}{2} \left\{ \left(\frac{A_h}{2V_h}\right)^2 - \left(\frac{A_e}{2V_e}\right)^2 \right\}} \tag{4.3.11}$$

Note that there is an additional requirement as a criterion of the electron-hole pair in the PJT effect whose form is

$$\left(\frac{|V_e| + |V_h|}{2K}\right)^2 > \frac{1}{2} \left\{ \left(\frac{A_h}{2V_h}\right)^2 - \left(\frac{A_e}{2V_e}\right)^2 \right\} \tag{4.3.12}$$

Substitution of Eq. 4.3.11 into Eq. 4.3.8 and also taking into account the approximation in Eq. 4.3.10 leads to the following:

$$U_{ad}^{PJT-pair} \approx (-q^2) \tag{4.3.13}$$

This means that we can write the total free energy of Eq. 4.3.6 as

$$\alpha(T) = \alpha_{neg-U} + \alpha_{Coulomb}(T) = -A_{neg-U} + \frac{e^2}{r_{V-O}} \frac{1}{C_{carrier} n_e - B_0 + B_1 T} \tag{4.3.14}$$

At a critical temperature for the soft mode condensation  $T = T_{CT}$  one has the free energy for electron-hole pair interaction equal to zero or  $\alpha(T_{CT}) = 0$ ; therefore this critical temperature is derived from Eq. 4.3.14 as

$$T_{CT} = \frac{C_{carrier} n_e - B_0 - A_{neg-U} \frac{e^2}{r_{V-O}}}{B_1} \quad (4.3.15)$$

The other characteristic temperatures of the VO<sub>2</sub> MIT are obtained by the usual Landau expansion of the free energy as introduced in the previous section. Some changes are introduced in this treatment, however, in that the local magnetic moment variable,  $\mu$  is replaced with the so-called charge transfer order parameter  $q$  and the distortion  $\eta$  is re-defined as the ion displacement. Hence the Eq. 4.2.13 transforms to

$$F = \frac{1}{2} a (T - T_{cr}) q^2 + \frac{1}{4} b q^4 + \frac{1}{2} \alpha \eta^2 + \frac{1}{4} \beta \eta^4 + \frac{1}{6} \gamma \eta^6 + \frac{1}{2} g \eta^2 q^2 + \dots \quad (4.3.16)$$

Minimising Eq. 4.3.16 with respect to both  $q$  and  $\eta$  leads to  $F_{min}$  at

$$\eta_{min}^2 = -\frac{\alpha + gq^2}{\beta} \quad (4.3.17)$$

And

$$q_{min}^2 = \frac{\left( \frac{g^2}{\beta} - b \right) + \sqrt{\left( \frac{g^2}{\beta} - b \right)^2 - 4\gamma \left[ a(T - T_{cr}) - \frac{\alpha g}{\beta} \right]}}{2\gamma} \quad (4.3.18)$$

Substituting Eq. 4.3.17 and Eq. 4.3.18 into Eq. 4.3.16 to obtain  $F_{min}$  and taking  $F_{min}$  to equal to zero at a second critical temperature  $T_I$  (which is the temperature of the energy coincidence of the absolute minimum (for metallic phase  $T_M$ ) and of the relative minimum (insulating phase)) one obtains for  $T_I$  and  $T_M$  the following expressions:

$$T_I = T_{cr} + \frac{\alpha g}{a\beta} + \left\{ \frac{1}{4} \frac{\left( b - \frac{g^2}{\beta} \right)^2}{a\gamma} \right\} \quad (4.3.19)$$

$$T_M = T_{cr} + \frac{\alpha g}{a\beta} + \left\{ \frac{3}{16} \frac{\left( b - \frac{g^2}{\beta} \right)^2}{a\gamma} \right\} \quad (4.3.20)$$

Hence one can calculate the hysteresis width (HW) as follows

$$HW = \Delta T_{\text{hysteresis}} = T_i - T_{cT} = \frac{\alpha g}{a\beta} + \left\{ \frac{1}{4} \frac{\left( b - \frac{g^2}{\beta} \right)^2}{a\gamma} \right\} \quad (4.3.21)$$

It must be noted that HW increases as  $a$ ,  $\beta$  and  $\gamma$  decrease. The parameter  $a$  is obtained from Eq. 4.3.14 and is written as

$$a = B_1 A_{\text{neg}}^2 \frac{r_{V-O}}{e^2} \quad (4.3.22)$$

A type of this behaviour has been attributed to oxygen vacancies and grain interfaces due to their elastic fields. The most sensitive part of the Eq. 4.3.22 is the  $A_{\text{neg-U}}^2$  which decreases with increase in electron and hole splitting,  $\Delta_e$ ,  $\Delta_h$ . Similarly the parameter  $\beta$  is decreased due to oxygen vacancies and grain interfaces as a result of elastic tension appearing in the vicinity of these defects. VO<sub>2</sub> deposited on highly crystalline substrates should therefore reduce these defects and hence the HW should be sharper than when deposited on amorphous substrates. Also, when deposited on the same kind of substrates, crystalline VO<sub>2</sub> should have fewer defects than amorphous VO<sub>2</sub> and hence a narrower and sharper HW.

## 5. Thermo-chromism at nano-scale :

### 5.1 Lopez's hysteresis width broadening at nanoscale :

Lopez et al [22] have shown that as the grain size is reduced the hysteresis width increases with an accompanied loss in what we call the hysteresis jump (HJ). We reproduce the Lopez et al illustration of their experimental observation of this fact in Fig. 5.1 with our additional labels of HW, HJ for the sake of illustration.

In order to understand the dependence of the transition on the VO<sub>2</sub> particle size, Lopez proposed that the semiconductor-to-metal transition is related to the nucleation mechanism of the VO<sub>2</sub> crystals. They assumed that (1) the VO<sub>2</sub> particles were spherical (2) the classical nucleation theory applied in which the stress-free Gibbs free energy expression

$$\Delta G = -\frac{4\pi}{3} d^3 \Delta g_{\text{ex}} + 4\pi d^2 \gamma_{\text{surf}} \quad (5.1.1)$$

(with  $d$  being the particle size,  $\Delta g_{\text{ex}}$  being the bulk free energy decrease per unit volume which was assumed to be proportional to  $|T-T_c|$  determined by the entropy energy difference between the parent and the product phase as 0.657 MJ/(m<sup>3</sup>K) and  $\gamma_{\text{surf}}$  being the surface energy per unit area which was estimated to lie in the range 10-20 mJ/m<sup>2</sup>). From this equation, a barrier of 10<sup>-16</sup> J ( $-6 \times 10^2$  eV) was estimated which translated to 10<sup>4</sup> k<sub>B</sub>T at the temperature where the VO<sub>2</sub> transition occurs spontaneously.

Since the thermal energy was too small for homogenous nucleation, Lopez et al suggested that nucleation took place at special sites like those observed in the martensitic transformations. Lopez's assumption of spherical shape of the VO<sub>2</sub> particles is the first weakness in the whole of their attempt to attribute particle size to the STM transition since, according to their SEM micrographs, their VO<sub>2</sub> particles are far from spherical. In fact they are belt-like as we have clearly observed in our results.

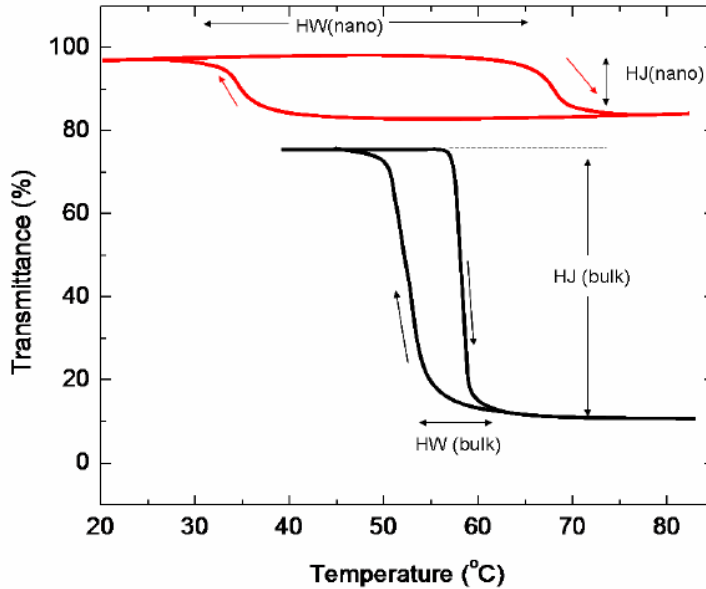


Fig. 5.1 Hysteresis loops for heating-up and cooling-down cycles in  $\text{VO}_2$  thin films and  $\text{VO}_2$  nanocrystals. Note the variations in the hysteresis width and hysteresis jump as the size of the  $\text{VO}_2$  crystals tends to nano-scale

Also their nucleation theory as it is assumed to affect the SMT transition cannot be stress-free as it is well known that there is tremendous amount of stress as the  $\text{VO}_2$  crystal changes from a monoclinic structure with volume of  $12.05 \sin(122) \times 3.702 \times 6.433 \text{ \AA}^3$  to the smaller volume of tetragonal symmetry of  $4.554^2 \times 2.854 \text{ \AA}^3$ . This stress cannot be negligible and has to be accounted for. Also, Lopez et al's important work shows that as annealing time of the samples is increased that equivalent radius increases. Hysteresis loops at different annealing times (and hence particle sizes) are compared only qualitatively. We extend Lopez et al's important pioneering observation of the dependency of the SMT transition on particle size,  $d$ . From their qualitative comparison of the SMT- $d$ , one can draw a conclusion: the smaller the particles the larger the hysteresis width (HW) and the smaller the hysteresis jump (HJ) as shown in the illustration in Fig. 5.1. We introduced the first quantity, HW, in Ref. 23 also only qualitatively. In the section that follows, we introduce the relations that are employed in the study of thermochromism at nanoscale.

## 5.2 Hysteresis width and stress :

The energy expended in transforming a crystallite from monoclinic at  $T_{\text{room}}$  to tetragonal structure above the transition temperature  $T_{c+}$  is  $k_B(T_{c+} - T_{\text{room}})$  whereas the energy lost in restoring this crystallite from tetragonal at a temperature  $T > T_{c+}$  back to room temperature via another transition temperature  $T_c$  is  $k_B(T_c - T_{\text{room}})$ . The difference between these energies gives the energy of the hysteresis and this energy difference is  $k_B(T_{c+} - T_c)$ . We assume that this energy is responsible for the amount of stress that is intro-

duced to the structure as the materials transforms from monoclinic phase to that of tetragonal and vice versa. The stress in the structure is proportional to this residual hysteresis energy. In its full form, we would represent stress as rank two tensor written as a 3×3 matrix as first proposed by Einstein. However, for simplicity and relevance to this work, we will adopt the empirical expression relating yield stress to the grain size from the so-called Petch relation in metallurgy [24] given as

$$\sigma_s = \sigma_0 + \frac{k_0}{\sqrt{d}} \tag{5.2.1}$$

Where  $\sigma_0$  is yielding stress for a material in bulk form and  $k_0$  is constant for a particular material. As the particle size  $d$  decreases (to nano-scale) the second term becomes important and yielding stress increases abruptly.

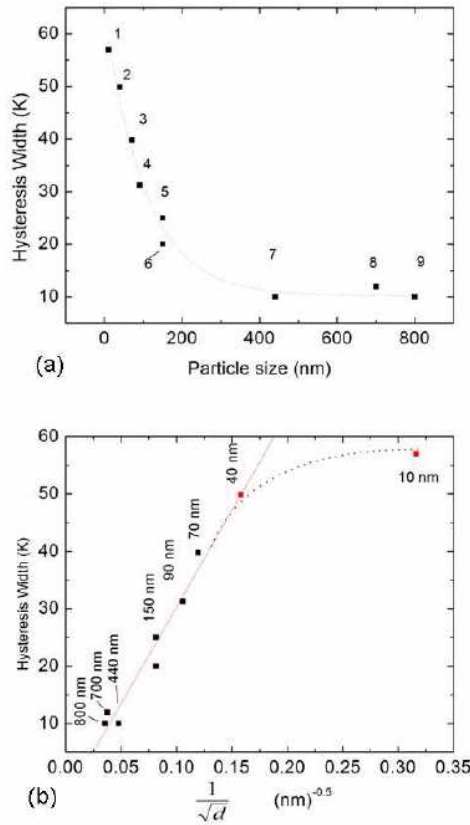


Fig 5.2 (a) HW against  $d$ : The numbers over each point indicate source of data: (1) Current work (unpublished), (2,3,4) Lopez et al, (5) Miyazaki et al (6) Choi et al, (7,9) Current work, (8) Kivaisi et al, (b) HW against  $d^{-0.5}$  showing the linearity limited to bulk  $\text{VO}_2$ ; at nanoscale, linearity is broken as illustrated with a broken line in order to guide the eye.



Based on the assumption that the residual energy  $k_B(T_{c+} - T_{c-})$  is proportional to the stress it causes we then can write:

$$k_B(T_{c+} - T_{c-}) = k_B(HW) = \beta_1 \left( \sigma_0 + \frac{k_0}{\sqrt{d}} \right) \quad (5.2.2)$$

We assume further from experimental fact that the area under the hysteresis curve remains almost constant, that is, as the HW increases due to size effects the HJ increases due to the same effect. Hence we can write

$$(HW)(HJ) \approx \beta_2 \quad (5.2.3)$$

where  $\beta_2$  is a constant. Therefore the hysteresis jump (HJ) as a function of particle size can be given as:

$$HJ = \frac{k_B \beta_2 \sqrt{d}}{\beta_1 (\sigma_0 \sqrt{d} + k_0)} \quad (5.2.4)$$

The charts in Fig. 5.2 illustrate the relationship between HW and particle size  $d$ . In (a), a graph of HW is plotted against  $d$ . This graph compares the present results with those of others as indicated in the caption. The inverse nature of the HW as a function  $d$  is confirmed. In (b) a chart of HW versus  $d^{-0.5}$  is presented and a linear relationship is clearly evident as one expects. However, if the relationship went being linear, then the HW increases to infinity. This means that as  $\text{VO}_2$  particles tend to nano-scale, the HJ tends to zero; meaning that the materials is thermally stable but cannot switch. This is not expected. The reality is that the HJ decreases but is never zero. This places an upper limit to the HW as seen in Fig. 5.2 (b) where the non-linear curve has been drawn to guide the reader's eye.

## 6. Brief review of $\text{VO}_2$ production efforts :

Stoichiometric  $\text{VO}_2$  has been regarded as a difficult material to obtain. The reason is that there are more than four phases of stoichiometric  $\text{VO}_2$  known as shown in Table 2. Besides, of all vanadium oxides,  $\text{V}_2\text{O}_5$  rather than  $\text{VO}_2$  is the most stable of them. The phase diagram gives an indication that  $\text{VO}_2$  can be obtained at low oxygen partial pressures at high temperatures above  $550^\circ\text{C}$ . At high  $\text{O}_2$  partial pressure and low temperatures, the stable  $\text{V}_2\text{O}_5$  is prevalent. In reality, trace  $\text{V}_2\text{O}_5$  is still found in the  $\text{VO}_2$  even at high temperature since it is very difficult to avoid environmental  $\text{O}_2$  to creep into the reaction zone.

Since the discovery of  $\text{VO}_2$ 's MIT transition at 340K in 1959 by Morin [6], many techniques have been employed in obtaining stoichiometric  $\text{VO}_2$ . Among them pulsed laser deposition [25-58], ion implantation [59-63], laser pyrolysis [65,66], ultrasonic spray pyrolysis [5,67,208], chemical vapor deposition[68-90], hydrothermal synthesis [91-109] sputtering techniques[110-186] ball milling [187], soft chemistry [188], firing [189-190] and solgel [191-207] have been the most prevalent. In this chapter, we discuss the  $\text{VO}_2$  results obtained by two related methods: ultrasonic spray pyrolysis and laser pyrolysis. The schematic illustrations of these methods are given in Fig. 6.1 (a) and (b) respectively. In both methods, the precursor material comes in form of fine droplets produced either by a tradition pneumatic sprayer or an ultrasonic nebulizer sprayer. These are carried into a heated zone whose heat source is a furnace or a laser and the pyrolyzed particles are either deposited on a planar substrate or on a filter.

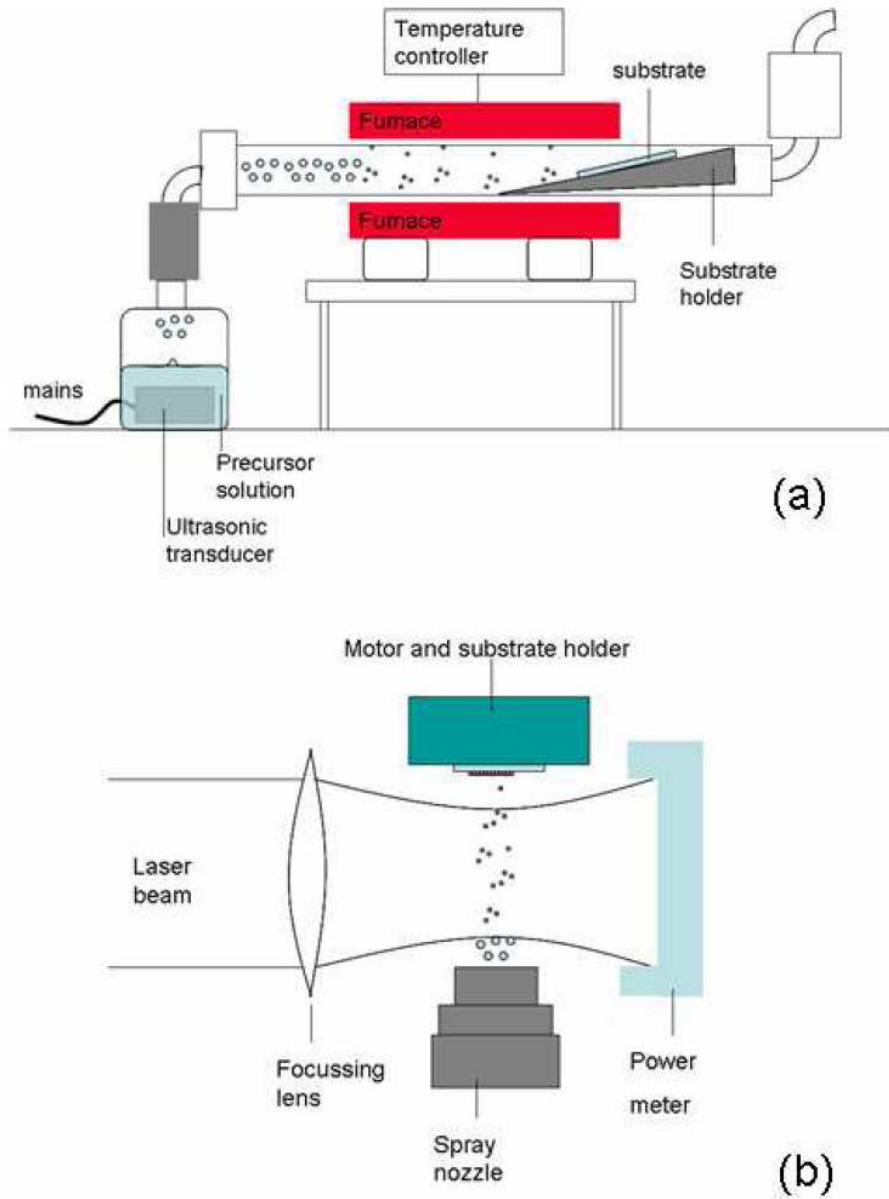


Fig. 6.1 Two VO<sub>2</sub> synthesis methods employed in Refs. [5], [65],[66], [67] and [208]- (a) ultrasonic spray pyrolysis and (b) laser pyrolysis

### 6.1 VO<sub>2</sub> nano-ribbons by ultrasonic spray pyrolysis :

The first synthesis of VO<sub>2</sub> by ultrasonic spray pyrolysis was reported in [5]. New images of nano-particles of VO<sub>2</sub> synthesized by ultrasonic spray pyrolysis presented in Fig. 6.2 with a size distribution in Fig. 6.3. However nano-ribbons of VO<sub>2</sub> [208] by the same method as shown in Fig. 6.4 are seen at the following synthesis parameters: (1) at higher flow rate of 18 cm<sup>3</sup>/min of argon of the NH<sub>4</sub>VO<sub>3</sub> precursor (2) the substrate of borosilicate glass (3) positioned at a region in the furnace where the substrate temperature was ~300°C and (4) the furnace temperature of 700°C in the central zone which is regarded to be the pyrolysis temperature. No post-synthesis annealing was done on this sample. Scanning electron microscopy was done on the LEO microscope and samples were prepared by scrapping a small portion of the powder on to a carbon tape tailored for the SEM.

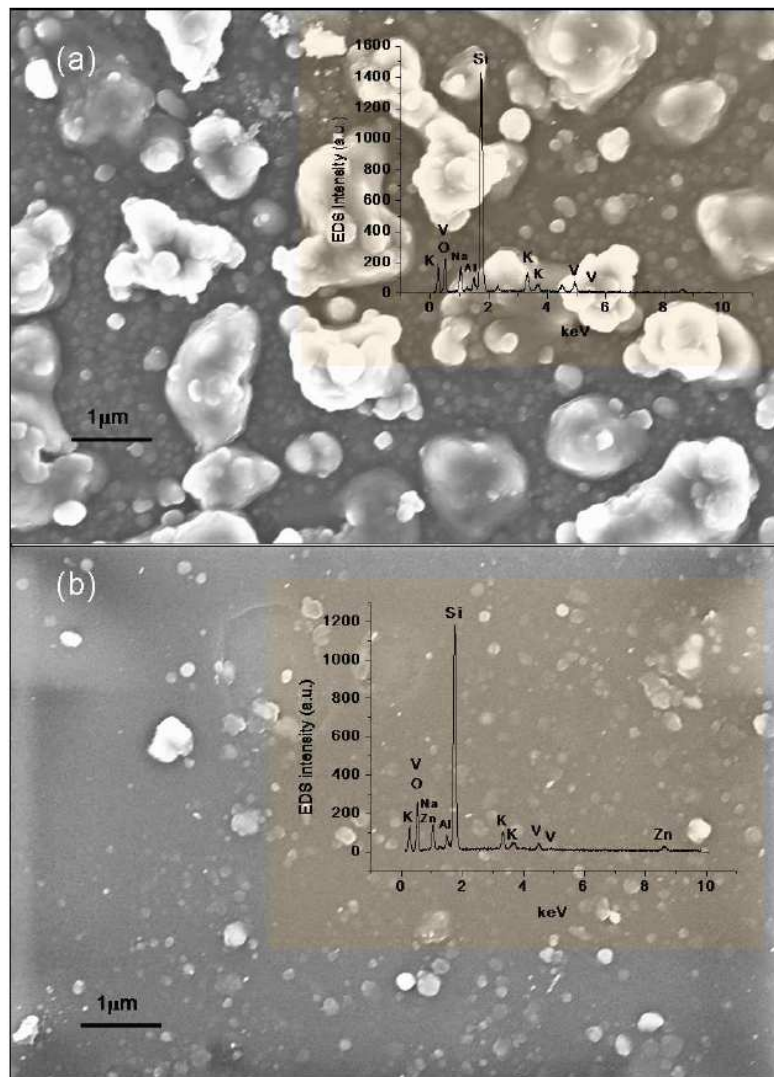


Fig. 6.2 Scanning micrographs of VO<sub>2</sub> nano-particles synthesized on Corning glass in 11 L/min of argon with a deposition time of 25 min at (a) 600°C (inset is EDS) (b) 700°C (EDS in inset)

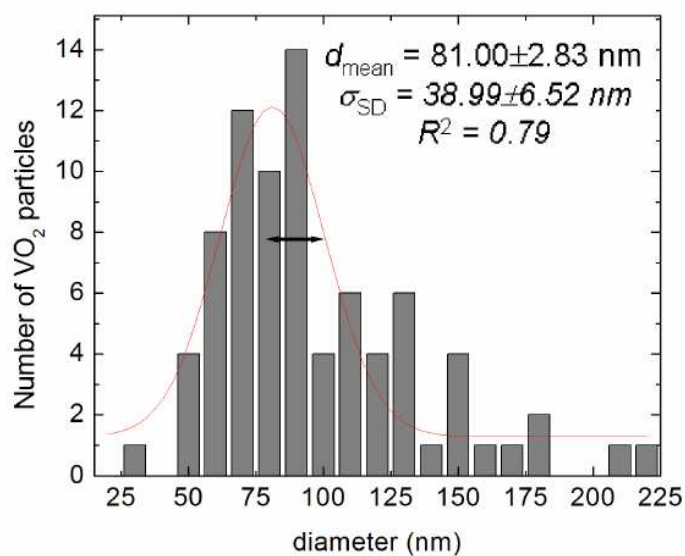


Fig. 6.3 Size distribution of the particles of VO<sub>2</sub> on the samples grown by USP at 600°C

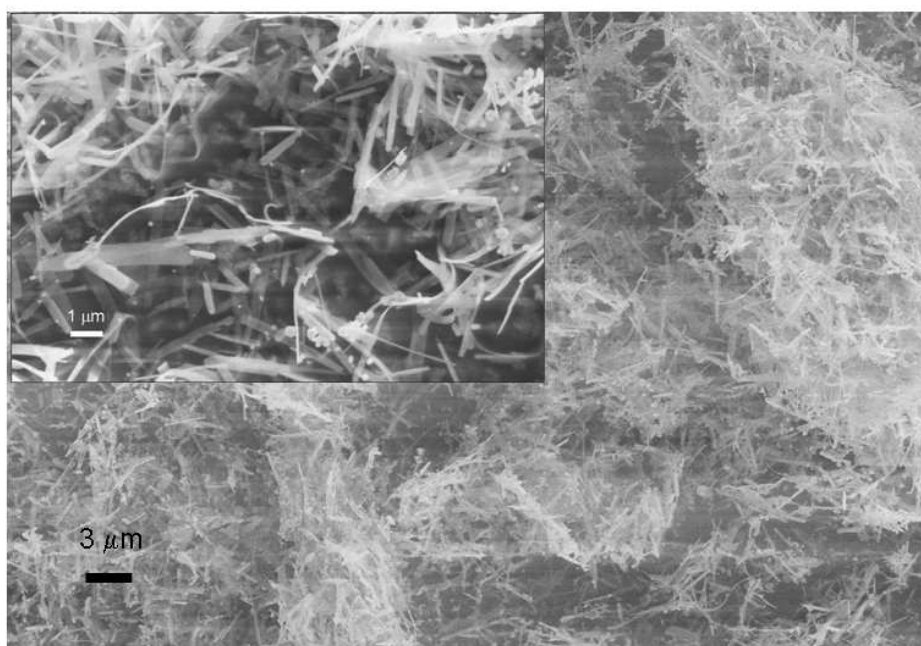


Fig. 6.4 SEM micrographs of VO<sub>2</sub> nano-ribbons a low resolution image showing the overall density of the nanostructures with an inset the same on a different spot of the sample

## 6.2 VO<sub>2</sub> nanobelts from laser pyrolysis :

The production of VO<sub>2</sub> nanobelts by laser pyrolysis of VCl<sub>4</sub> in ethanol and aqueous V<sub>2</sub>O<sub>5</sub> was discussed briefly in Mwakikunga et al [65]. These structures are long drawn-out with some of these extending to as much as 100 μm. The bundling together of nano-belts due to Van der Waal's attractive forces is clearly seen in the VCL1 samples ran under oxygen. The cracks are seen in this V-based sample ran in the same gas environment. However the yield of nano-belts in the V-based sample is relatively low compared to those WO<sub>3</sub> nanowires obtained by the same method [65]. This could be due to the higher reactivity of vanadium alkoxide in O<sub>2</sub> than that of tungsten alkoxide. This anomalous reactivity of V-(OR)<sub>4</sub> presents violent decomposition and deposition and hence may impede salient self assembly. It is interesting to note that among these belts are bamboo-shaped carbon nanotubes. These tubes could be coming from the carbon in ethanol from the precursors are prepared and/or from some of the C<sub>2</sub>H<sub>2</sub> carrier gas molecules that are able to dissociate in the laser beam.

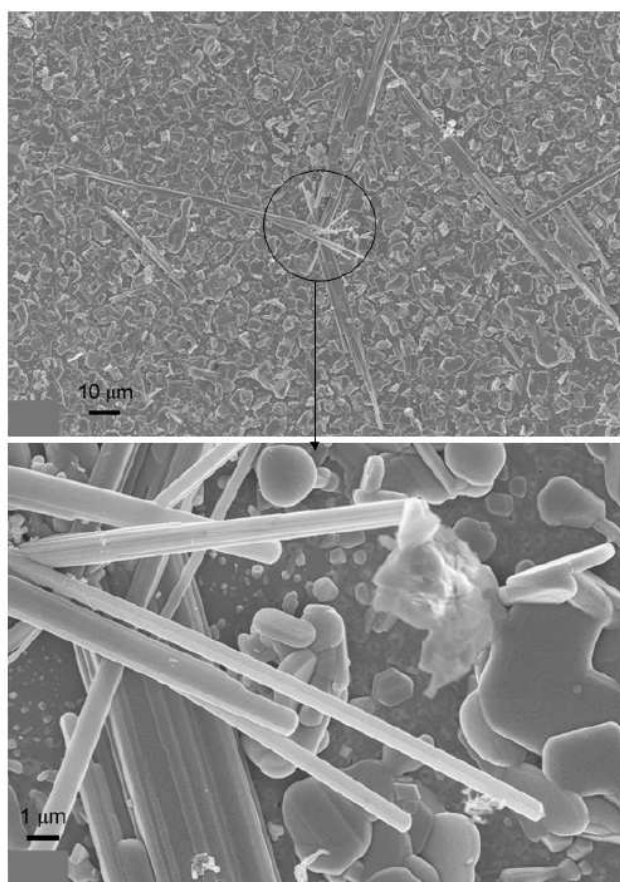


Fig. 5.15 Scanning electron micrographs of VO<sub>2</sub> nano-rods grown from VCl<sub>4</sub> + ethanol under oxygen as a central carrier gas and C<sub>2</sub>H<sub>2</sub> as the secondary carrier gas.

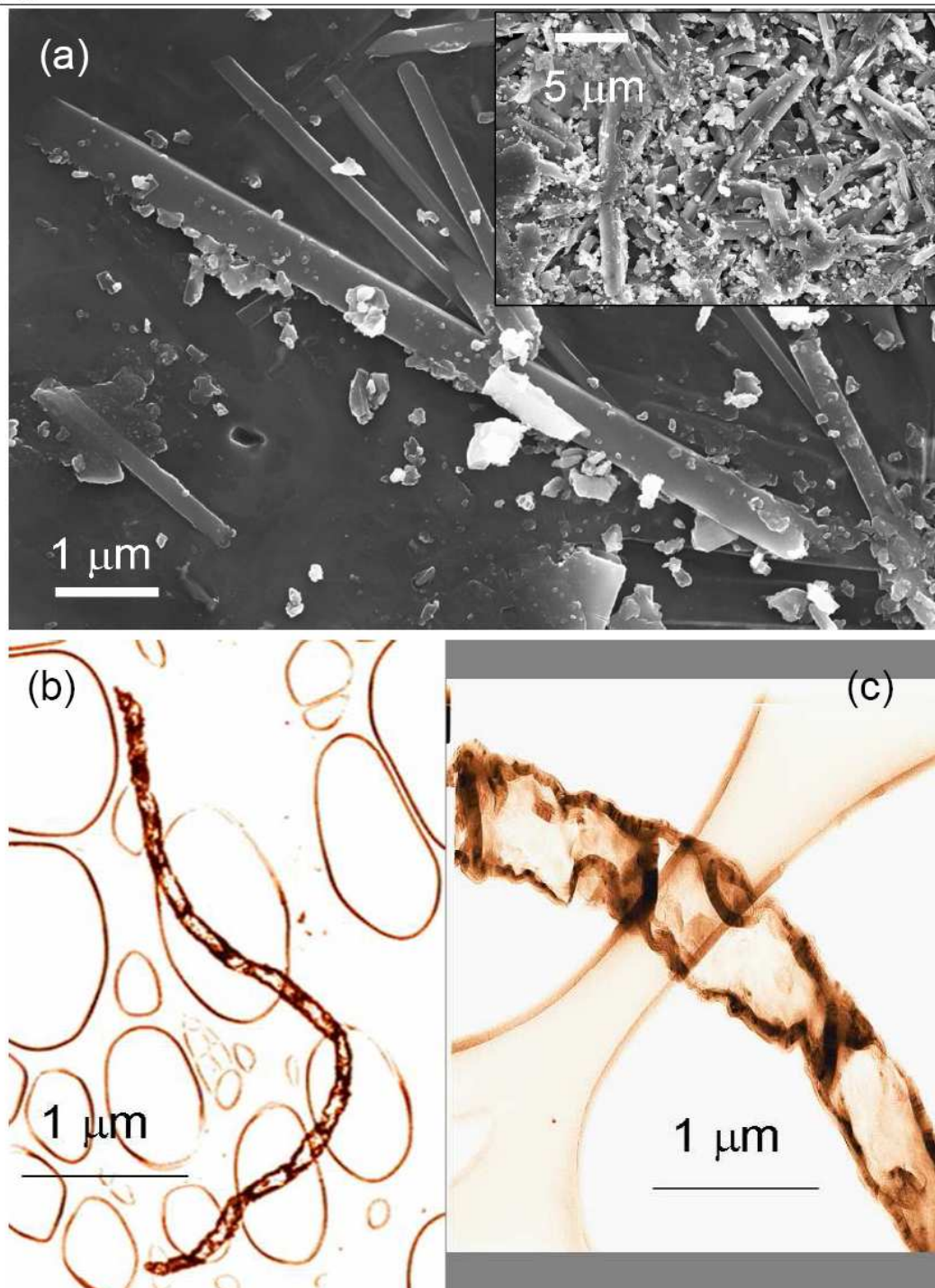


Fig.5.16 (a) Scanning electron micrographs of VO<sub>2</sub> nano-rods grown from aqueous V<sub>2</sub>O<sub>5</sub> under C<sub>2</sub>H<sub>2</sub> as a carrier gas (inset) typical dense distribution of the belts at low resolution (b) low resolution TEM image of bamboo structured carbon nanotube found amidst the VO<sub>2</sub> ribbons and (c) a higher magnification of CNT showing disorder amidst ordered growth.

## 7. VO<sub>2</sub> thermochromism and applications :

Many researchers engaged in the lowering of the intrinsic transition temperature of 68°C to room temperature of about 25°C so that VO<sub>2</sub> films could be exploited for autonomous control of solar radiation entry into a room by ambient temperature. The transition temperature has been tuned by doping the VO<sub>2</sub> with tungsten [210, 211], molybdenum [212], titanium dioxide [213, 214], silicon dioxide nanoparticles [215] or cerium dioxide [216].

### 7.1 Coatings on windows for energy regulation and temperature control :

The role of advanced glazing in the reduction of energy consumption in buildings and the consequent reduction in the greenhouse gas (GHG) emissions is growing, especially in Europe where 40% of houses are now double glazed in an attempt to save energy [216]. Considering the climatic conditions and dwelling needs, suitably selected energy efficient windows can be implemented to minimise heating, cooling and lighting loads in buildings. Presently there is a growing demand for architectural designers and building constructors to consider the visual and thermal comfort of the building occupants [217-219]. Coupled to these recent efforts by researchers to formulate policy and co-ordinate the activities related to optical coated glasses, China has suddenly become a world supplier of such optical glazing [220]. In 2006 China already had 150 production lines for two types of architectural glass: *viz.* solar control glass which has high reflection and absorption of sunlight radiation, and the low emission glass which reflects MIR to FIR. Both these types of glasses are popular and suitable for cold and hot climates, respectively.

### 7.2 VO<sub>2</sub> for ultra-fast switching applications :

It is well understood by now that the VO<sub>2</sub> MIT happens so fast – to the order of about 100 fs. A number of studies have been dedicated to understand the origin of this rapid transformation [21, 37-39, 43-45, 47]. Roach [221] pointed out that, due to the changes in reflectivity during the phase transition, VO<sub>2</sub> films can be used as a kind of optical disc medium and demonstrate holographic storage. Bit recording on VO<sub>2</sub> films using a near-infrared laser was demonstrated [222]; stability during long-term storage and over 108 time cycles of write-and-erase were achieved without degradation. Switching time of about 30 ns and writing energy of the order of a few mJ/cm<sup>2</sup> were reported [223]. Bit density has been estimated to be 350 bits/mm. Such low threshold recording energy and write-erase abilities encourage the use of VO<sub>2</sub> films as a recording medium [224]. More recently, the use of VO<sub>2</sub> thin films was suggested in ultra-fast switching devices. The high temperature metallic state attained in 5 ps by using the femtosecond laser excitation at 780 nm was reported [225].

### 7.3 Thermo-chromism and colorimetry :

Room temperature VO<sub>2</sub> looks transparent in thin film form but takes deep bluish color when in thicker film form. Its color continuously changes as the temperature is increased. After transition to metallic state, that is, above 340 K, the color adopted is brown or completely opaque. The color of the VO<sub>2</sub> can be controlled by accurately controlling the temperature of the material's surroundings. This is the basic principle of thermo-chromism-based colorimeter. For more details on the science of thermochromism with specific application to colorimetry, the reader is referred to the work of Hiltunen [226]. In the introduction section, it was found that the color of an object depends on the spectral absorption coefficient. Properties of the absorption band are usually given in electron volts. The Gaussian shape of the absorption coefficient and hence the absorption band is given by [227]

$$\mu(\epsilon) = \mu_{max} \exp\left[-4 \ln 2 \left(\frac{\epsilon - \epsilon_0}{\Delta\epsilon}\right)^2\right] \quad (7.1)$$

where  $\epsilon_0$  is the energy of the absorption maximum and  $\Delta\epsilon$  is the full width at half maximum. By taking the usual conversion procedure between the electron volts to the wavelength in (nm) given by

$$\epsilon(eV) = \frac{1239.5}{\lambda(nm)} \quad (7.2)$$

And substituting it in Eq. 7.2 transform the photon energy- dependent absorption coefficient into a wavelength-dependent absorption coefficient derived herein as

$$\mu(\lambda) = \mu_{max} \exp\left[-4 \ln 2 (\Delta\lambda)^2 (\lambda_0 - \lambda)^2\right] \quad (7.3)$$

where  $\Delta\lambda$  is the new full width at half maximum and  $\lambda_0$  is the wavelength at the peak absorption. It must be noted that when the absorption is plotted against wavelength,  $\lambda$ , the profile is asymmetrical as opposed to the perfect Gaussian for the case when the same is plotted against photon energy  $\epsilon$ . These plots are sketched in Fig. 7.1

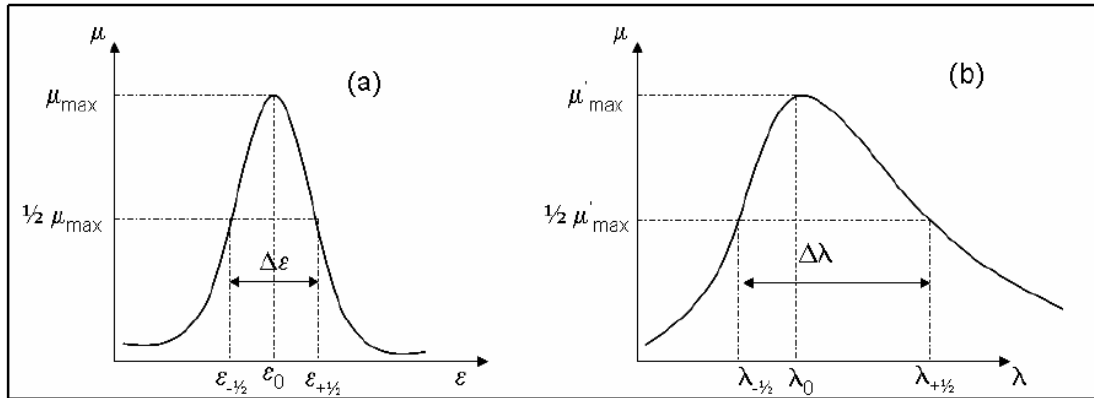


Fig.7.1 (a) Absorption band of a typical material plotted in energy scale showing a perfect Gaussian profile (b) when the same band is plotted in wavelength scales the profile is asymmetrical

For the Gaussian profile one can integrate the absorption peak within the visible range (1.59 - 3.3 eV) and the result is area A given by

$$A = \mu_{max} \sqrt{\frac{\pi}{4 \ln 2}} \Delta\epsilon \quad (7.4)$$

The area remains constant regardless of the temperature changes. The width of the Gaussian curve  $\Delta\epsilon$  increases as the temperature increases and the value of  $\mu_{max}$  decreases proportionally. That is

$$\Delta\epsilon = \xi \cdot \sqrt{T} \quad (7.5)$$



where  $\xi$  is a constant. Note that the opposite effect applies when it is emitted energy instead of absorbed energy. This can be illustrated by a sketch in Fig. 7.2

Therefore the energy at half maximum absorption as a function of temperature is given as

$$\varepsilon_{\pm\frac{1}{2}}(T) = \varepsilon_0 \pm \Delta\varepsilon_0 \sqrt{\frac{T}{T_0}} \tag{7.6}$$

It can be shown that the shifts in the half width energy  $\delta\varepsilon_{\pm\frac{1}{2}}$  are given by

$$\delta\varepsilon_{\pm\frac{1}{2}} = \varepsilon_{\pm\frac{1}{2}}(T) - \varepsilon_{\pm\frac{1}{2}}(T_0) = \pm \frac{1}{2} \Delta\varepsilon_0 \left( \sqrt{\frac{T}{T_0}} - 1 \right) \approx \pm \frac{1}{4} \Delta\varepsilon_0 \frac{\Delta T}{T_0} \tag{7.7}$$

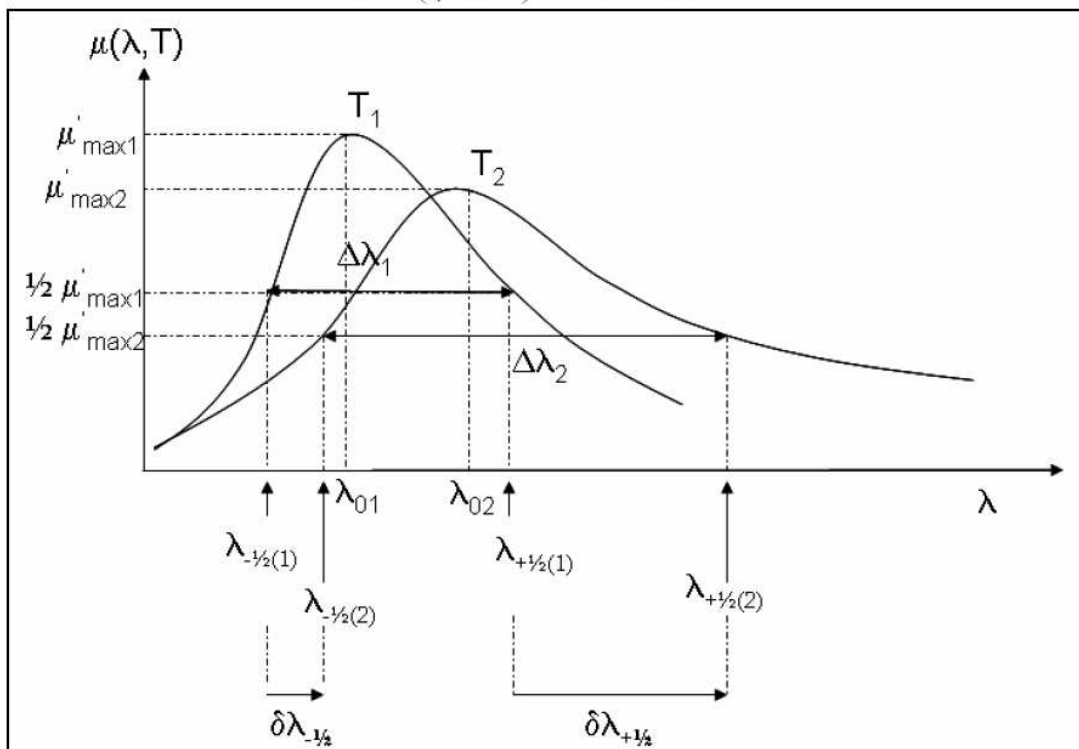


Fig.7.2 Absorption as a function of wavelength and temperature where  $T_2 > T_1$ . Note the shift in half width wavelength before the peak maximum is less than the shift in half width wavelength after the peak maximum.

For the case when absorption is plotted against the wavelength scale where the absorption curves are not symmetric, the shift in wavelength,  $\lambda_{\pm\frac{1}{2}}$  corresponding to the points  $\varepsilon_{\pm\frac{1}{2}}$  can be written thus

$$\frac{1}{\lambda_{\pm\frac{1}{2}}(T)} = \frac{1}{\lambda_0} \pm \frac{1}{2} \frac{\Delta\epsilon_0}{hc} \sqrt{\frac{T}{T_0}} \quad (7.8)$$

where  $\lambda_0$  is the wavelength corresponding to the peak maximum. The shift of the half width points are therefore given by

$$\delta\lambda_{\pm\frac{1}{2}}(T) = \lambda_{\pm\frac{1}{2}}(T) \pm \lambda_{\pm\frac{1}{2}}(T_0) = \pm \frac{1}{2} \frac{\Delta\epsilon_0}{hc} \left(1 - \sqrt{\frac{T}{T_0}}\right) \frac{(\lambda_{\pm\frac{1}{2}}(T_0))^2}{1 \mp \frac{1}{2} \frac{\Delta\epsilon_0}{hc} \left(1 - \sqrt{\frac{T}{T_0}}\right) \lambda_{\pm\frac{1}{2}}(T_0)} \quad (7.9)$$

This equation is clear demonstration of the change of the apparent color of a thermo-chromic material as temperature is raised. It should be noted that while absorption decreases and shifts to longer wavelengths as the temperature is raised, emission increases and shifts to shorter wavelength in accordance with the blackbody radiation theory.

## 8. Open questions on thermo-chromism :

Significant progress has been achieved in understanding the metal-to-insulator transition which the fundamental phenomenon resulting in the observed thermo-chromism. Most of this achievement comes from the study of bulk materials. Several challenges have confronted scientists recently with the emergence of nano-materials and nano-structured materials of different geometries.

(1) For the band models from Mott to Hubbard, through Goodenough to Paquet and Vikhnin, it still remains a puzzle as to how to adapt these models to nanomaterials. One of the problems is the many-level spin and energy splitting in nanomaterials which never existed in bulk material experimental data. This would require more terms in the Hamiltonian of Eq. 4.2.1. This should affect the free energy expression and hence transition temperature calculations need to be re-done. Reyes et al [228] have discussed a model based on the free energy expression in Eq. 4.2.13 after finding the following interesting results of Cr-doping on  $\text{VO}_2$  – that the transition temperature on heating  $T_{c+}$  increases with increase in Cr-doping level whereas the transition temperature on cooling  $T_{c-}$  remains constant regardless of the Cr-doping level. It was argued that the dopant introduces distortion  $\eta$  which either stabilizes or destabilizes the  $\text{VO}_2$  high-temperature tetragonal structure. If the tetragonal is stabilized the transition temperature decreases otherwise it increases. This was explained in terms of the ionic radii (that is valency) of the dopant ion in comparison to that of the metal ion of the host  $\text{VO}_2$ . If the dopant ion radius is larger than that for the  $\text{V}^{4+}$  ion, which is the case for  $\text{W}^{6+}$ , the overall structure becomes less stable and hence transition happens at a lower temperature than 340K. The opposite is true for  $\text{Cr}^{3+}$ , for instance. Reyes et al however could not explain why the cooling transition temperature  $T_{c-}$  remain constant regardless of the Cr-doping level; only the heating up transition temperature  $T_{c+}$  increased as Cr-doping level increased. This is still a puzzle to many researchers.

(2) Fitting the  $\text{VO}_2$  hysteresis with equation adapted from magnetic hysteresis such those based on Preisach as presented by de Almeida in section is another next interesting area which may require pursuit. The equation fit very well for bulk  $\text{VO}_2$ . In the light of the hysteresis profile changing significantly in nano- $\text{VO}_2$  as presented by Lopez et al and ourselves, it would be interesting to see how one can adapt the distribution function  $\mu(T\alpha, T\beta)$  to the particle distribution function of the sample. The fact is the resistivity of the metallic phase of nano- $\text{VO}_2$  does not come to real metals. In other words the  $\text{VO}_2$  high temperature tetragonal phase is never a perfect metal and its resistivity is much higher than bulk  $\text{VO}_2$  at the same temperature.

Otherwise, for the case of nano-structured VO<sub>2</sub>, where  $R_s^{\text{nano}}$  is comparable to  $R_m^{\text{nano}}$  and both are dependent on the particle size and particle size distribution of the VO<sub>2</sub> sample, one can say that

$$R(T, d) = \left[ R_0^{\text{nano}}(d) \exp\left(\frac{E_a}{k_B T}\right) - R_m^{\text{nano}}(d) \right] \iint_S \mu(T_\alpha, T_\beta) dT_\alpha dT_\beta + R_m^{\text{nano}}(d) \quad (8.0)$$

with all other parameters as defined previously in section 3. This is still open for further research.

(3) Vikhniin et al's argument that the hysteresis width depends on defect and also interfacial effects at the junction between the VO<sub>2</sub> thin film and the substrate material is also an interesting and controversial subject. In their presentation, crystalline interfaces should produce sharper transitions than the amorphous ones. The Landau expansion of the free energy was partly employed in this explanation. However what would hysteresis width in non-thin film VO<sub>2</sub> such as in composite powders, suspension and single nanostructures confirm Vikhniin's model? Nano-VO<sub>2</sub> has shown wider hysteresis width than thin films. This experimental fact is not accounted for in Vikhniin's expression for hysteresis width and therefore this is another open question.

(4) Our present proposed model based on stress at transition as VO<sub>2</sub> changes from monoclinic structure to the tetragonal one and vice versa also some short falls when the particle size is less than about 20 nm. This is another area that would require more in-depth study

## 8. Conclusions :

This work has shown the several fundamental models of the metal-to-insulator transition, first, in several materials, and, then specific to VO<sub>2</sub>. The initial steps were made by N. F. Mott followed by Hubbard. It was only until Goodenough saw the effect of doping on the tuneability of the transition temperature of VO<sub>2</sub>, that the band model was realized for the VO<sub>2</sub> system and the chapter shows some of the studies that have spawned after that, for instance, Reyes, Paquet's model and Vikhniin. The chapter also has discussed the adaptation of the magnetic hysteresis theories based on Preisach to the VO<sub>2</sub> thermal hysteresis. Later in the chapter, our own proposed model based on stress studies due to structural change has been outlined and has been found to be in good agreement with present and previous experimental results only up to a particle size of about 20 nm. The chapter also presents the many production efforts of this important material and a case for ultrasonic spray pyrolysis and laser pyrolysis has been briefly discussed. The applications – industrial and scientific - of VO<sub>2</sub> thermo-chromism have been briefly reviewed. The chapter wraps up with some suggested areas of research on this material that need further pursuit.

## 9. Acknowledgement :

The first author wishes to thank the CSIR's National Centre for Nano-Structured Materials for the sponsorship

## References :

- [1] M. Imada, A. Fujimori, Y. Tokura, Reviews of Modern Physics 70 (1998) 1039-1263
- [2] (a) N. F. Mott, Proc. Phys. Soc. London, Ser. A 49 (1937) 72 (b) Proc. Phys. Soc. London, Ser. A62 (1949) 416 (c) Can. J. Phys. 34 (1956) 1356 (d) Philos. Mag. 6 (1961) 287 (e) *Metal-Insulator Transitions* (Taylor and Francis, London/Philadelphia)
- [3] (a) J. Hubbard, Proc. Phys. Soc. London, Ser. 276 (1963) 238 (b) Proc. Phys. Soc. London, Ser. A 277 (1964) 237 (c) Proc. Phys. Soc. London, Ser. A 281 (1964) 401

- [4] Zaanen, Sawatzky and Allen in 1985
- [5] B. W. Mwakikunga, E. Sideras-Haddad and M. Maaza, *Optical Mater.* 29(5) (2007) 481
- [6] F. J. Morin, *Physical Review Letters* 3 (1959) 34-36
- [7] (a) S. Mathur, T. Ruegamer, I Grobelsek, *Chem. Vapor. Deposition* 13 (2007) 42 (b) M. Occhiuzzi, D. Cordischi, R Dragone, *J. Solid State Chem.* 178 (2005) 1551
- [8] A. Haras, M. Witko, D. R. Salahub, K. Hermann, R. Tokarz, *Surf. Sci.* 491 (2001) 77
- [9] D. Addler, *Rev. Modern Phys.* 40 (4) (1968)714-736
- [10] M. Borek, F. Quian, V. Nagabushnam, and R.K. Singh, *Appl. Phys. Lett.* 63 (1993) 3288
- [11] F. C. Case, *J. Vac. Sci. Technol. A* 2 (1984) 1509
- [12] (a) J. F. DeNatale, P. Hood, and A.B. Harker, *J. Appl. Phys.* 66, (1989) 5844
- [13] I. A. Khakhaev, F. A. Ghudnovskii, E. B. Shadrin, Martensitic effects in the metal-insulator phase transition in a vanadium dioxide film, *Phys. Solid State* 36 (1994) 898
- [14] T. Lanskaya, I. A. Merkulov, F. A. Chudnovskii, *Sov. Phys. Solid State* 20 (1978) 193
- [15] I. D. Mayergoyz, *Mathematical Models of Hysteresis*, Springer-Verlag, 1991
- [16] D. C. Jiles, D. L. Atherton, *Ferromagnetic hysteresis*, *IEEE Transactions on Magnetics* 19 (5) (1983) 2183-2185
- [17] (a) L. A. L. de Almeida, G. S. Deep, A. M. N. Lima, Anchorage, Alaska, USA, 21-23 May (2002) 281-286 (b) M. Krasnoselskii, A. Pokrovskii, *Systems with Hysteresis*, Nauka, Moscow (1983)
- [18] (a) M. Pan, H. Zhong, S. Wang, J. Liu, Z. Li, X. Chen, W. Lu, *Journal of Crystal Growth* 265 (1-2) (2004) 121-126, (b) M. Pan, J. Liu, H. Zhong, S. Wang, Z. F. Li, X. Chen, W. Liu, *J. Cryst. Growth* 268 (2004) 178-183
- [19] (a) J. B. Goodenough, *J. Solid State Chem.* 3 (1971) 490-500 (b) J. B. Goodenough, H. Y.-P. Hong, *Phys. Rev. B* 8 (4) (1973) 1323-1331
- [20] D. Paquet, P. Leroux-Hugon, *Phys. Rev. B* 22 (11) (1980) 5284-5301
- [21] (a) V. S. Vikhnin. S. Lysenko, A. Rua, F. Fernandez, H. Liu, *Phys. Lett. A* 343 (2005) 446-453 (b) V. S. Vikhnin. S. Lysenko, A. Rua, F. Fernandez, H. Liu, *Opt. Mater.* 29 (2007) 1385-1389
- [22] (a) R. Lopez, J. Y. Suh, L. C. Feldman, R. F. Haglund Jr., *Mater. Res. Soc. Symposium Proc.* 820 art no R1.5 (2004) 319-324 (b) R. F. Haglund Jr., R. Lopez, J. Y. Suh, L. C. Feldman, T. E. Haynes, L. A. Boatner, *Proc. SPIE - The Int. Soc. Opt. Eng.* 5339 (2004) 601-610 (c) R. Lopez, L. C. Feldman, R. F. Haglund Jr., *Physical Review Letters* 93 (17), (2004) 177403-1-177403-4 (d) R. Lopez, R. F. Haglund Jr., L. C. Feldman, L. A. Boatner, T. E. Haynes, *Appl. Phys. Lett.* 85 (22) (2004) 5191-5193 (e) R. Lopez, T. E. Haynes, L. A. Boatner, L. C. Feldman, R. F. Haglund Jr., *Phys. Rev. B* 65 (2002) 224113-1 - 224113-5 (f) J. Y. Suh, R. Lopez, L. C. Feldman, R. F. Haglund Jr., *Journal of Applied Physics* 96 (2) (2004) 1209-1213
- [23] B. W. Mwakikunga, A. Forbes, E. Sideras-Haddad, C. Arendse, *Phys. Stat. Solidi (a)* 205, 150 (2008)
- [24] (a) W. J. M. Tegart, *Elements of Mechanical Metallurgy*, Macmillan, NY, 175 (1966), (b) R. A. Flinn, P. K. Trojan, *Engineering Materials and Their Applications 2<sup>nd</sup> Ed.*, Houghton Mifflin, Boston, 93 (1981) (c) B W Mwakikunga, PhD Thesis, University of the Witwatersrand (2009)
- [25] J. Lappalainen, S. Heinilehto, H. Jantunen, V. Lantto, *J. Electroceramics* 22 (1-3) (2009) 73-77
- [26] A. Sharoni, J.G. Ramirez, I.K. Schuller, *Phys. Rev. Lett.* 101 (2) (2008) art. no. 026404
- [27] J. Nag, R. F. Haglund Jr., *J. Physics Condensed Matter* 20 (26), (2008) art. no. 264016
- [28] J. Y. Suh, E. U. Donev, D. W. Ferrara, K. A. Tetz, L. C. Feldman, R. F. Haglund Jr., *J. Opt. A: Pure and Applied Optics* 10 (5) (2008) art. no. 055202
- [29] Y. L. Wang, M. C. Li, X. K. Chen, G. Wu, J. P. Yang, R. Wang, L. C. Zhao, *J. Nanosci. & Nanotechnol.* 8 (5) (2008) 2604-2608
- [30] S. J. Yun, J. W. Lim, J.-S. Noh, B.-G. Chae, H.-T. Kim, *Japanese J. Appl. Phys.* 47 (4 PART 2) (2008) 3067-3069
- [31] J. Lappalainen, S. Heinilehto, S. Saukko, V. Lantto, H. Jantunen, *Sensors and Actuators, A: Physical* 142 (1) (2008) 250-255
- [32] M. E. Pemble, I. M. Povey, F. Chalvet, *ECS Transactions* 11 (7) (2007) 155-166

- [33] S. A. Pauli, R. Herger, P. R. Willmott, E. U. Donev, J. Y. Suh, R. F. Haglund Jr., *J. Appl. Phys.* 102 (7) (2007) art. no. 073527
- [34] B.-J. Kim, Y. W. Lee, S. Choi, B.-G. Chae, H.-T. Kim, *J. Korean Phys. Soc.* 50 (3), (2007) 653-656
- [35] Y. L. Wang, X. K. Chen, M. C. Li, R. Wang, G. Wu, J. P. Yang, W. H. Han, L.C. Zhao, *Surf. & Coatings Technol.* 201 (9-11 SPEC. ISS.), (2007) 5344-5347
- [36] K. Nagashima, T. Yanagida, H. Tanaka, T. Kawai, *J. Appl. Phys.* 100 (6), (2006) art. no. 063714
- [37] H. Liu, S. Lysenko, A. Rua, V. Vikhnin, O. Vasquez, F. E. Fernandez, *J. Luminescence* 119-120 (SPEC. ISS.), (2006) 388-394
- [38] H. Liu, S. Lysenko, A. Rua, V. Vikhnin, G. Zhang, O. Vasquez, F. E. Fernandez, *J. Luminescence* 119-120 (SPEC. ISS.) (2006) 404-411
- [39] S. Lysenko, A. J. Rua, V. Vikhnin, J. Jimenez, F. Fernandez, H. Liu, *Appl. Surf. Sci.* 252 (15), (2006) 5512-5515
- [40] M. Soltani, M. Chaker, E. Haddad, R. V. Kruzelesky, *J. Vacuum Sci. & Technol. A: Vacuum, Surfaces and Films* 24 (3), (2006) 612-617
- [41] M. Soltani, M. Chaker, E. Haddad, R. Kruzelesky, *Measurement Sci. & Technol.* 17 (5), (2006) 1052-1056
- [42] Y. J. Chang, C. H. Koo, J. S. Yang, Y. S. Kim, D. H. Kim, J. S. Lee, T. W. Noh, B. G. Chae, *Thin Solid Films* 486 (1-2) (2005) 46-49
- [43] H. Liu, O. Vasquez, V. R. Santiago, L. Diaz, R. Rua, F. E. Fernandez, *J. Electronic Mater.* 34 (5), (2005) 491-496
- [44] H. Liu, A. Rua, O. Vasquez, V. S. Vikhnin, F. E. Fernandez, L. F. Fonseca, O. Resto, S. Z. Weisz, *Sensors* 5 (4-5) (2005) 185-198
- [45] H. Liu, O. Vasquez, R. Santiago, L. Diaz, F. E. Fernandez, *J. Electronic Mater.* 33 (10) (2004) 1171-1175
- [46] M. Soltani, M. Chaker, E. Haddad, R. V. Kruzelesky, J. Margot, *Appl. Phys. Lett.* 85 (11) (2004) 1958-1960
- [47] H. Liu, O. Vasquez, V. R. Santiago, L. Díaz, F. E. Fernandez, *J. Luminescence* 108 (1-4), (2004) 233-238
- [48] M. Soltani, M. Chaker, E. Haddad, R. V. Kruzelesky, D. Nikanpour, *J. Vac. Sci. & Technol. A: Vacuum, Surfaces and Films* 22 (3) (2004) 859-864
- [49] D.-H. Youn, H.-T. Kim, B.-G. Chae, Y.-J. Hwang, J.-W. Lee, S.-L. Maeng, K.-Y. Kang, *J. Vac. Sci. & Technol. A: Vacuum, Surfaces and Films* 22 (3) (2004) 719-724
- [50] R. T. R. Kumar, B. Karunakaran, D. Mangalaraj, Sa. K. Narayandass, P. Manoravi, M. Joseph, *J. Mater. Sci.* 39 (8) (2004) 2869-2871
- [51] G. Garry, O. Durand, A. Lordereau, *Thin Solid Films* 453-454 (2004) 427-430
- [52] D.-H. Youn, J.-W. Lee, B.-G. Chae, H.-T. Kim, S.-L. Maeng, K.-Y. Kang, *J. Appl. Phys.* 95 (3) (2004) 1407-1411
- [53] R. M. Bowman, J. M. Gregg, *J. Mater. Sci.: Materials in Electronics* 9 (3) (1998) 187-191
- [54] P.-R. Zhu, S. Yamamoto, A. Miyashita, H. Naramoto, *Chinese Physics Letters* 15 (12), (1998) 904-906
- [55] J. M. McGraw, J. D. Perkins, J.-G. Zhang, P. Liu, P. A. Parilla, J. Turner, D. L. Schulz, D. S. Ginley, *Solid State Ionics* 113-115, (1998) 407-413
- [56] J. M. Gregg, R. M. Bowman, *Appl. Phys. Lett.* 71 (25), (1997) 3649-3651
- [57] H. S. Choi, J. S. Ahn, J. H. Jung, T. W. Noh, D. H. Kim, *Phys. Rev. B - Condensed Matter and Materials Physics* 54 (7), (1996) 4621-4628
- [58] D. H. Kim, H. S. Kwok, *Appl. Phys. Lett.* 65 (25) (1994) 3188-3190
- [59] J.-H. Li, N.-Y. Yuan, H.L.W. Chan, C.-L. Lin, *Acta Physica Sinica* 51 (8) (2002) 1792
- [60] L.A. Gea, J. D. Budai, L. A. Boatner, *J. Mater. Research* 14 (6) (1999) 2602-2610
- [61] P. Jin, S. Nakao, S. Tanemura, *Thin Solid Films* 324 (1-2) (1998) 151-158
- [62] P. Jin, S. Nakao, S. Tanemura, *Nuc. Instrum. & Methods Phys. Res., Section B: Beam Interactions with Materials and Atoms* 141 (1-4), (1998) 419-424

- [63] L. A. Gea, L. A. Boatner, H. M. Evans, R. Zuhr, *Nuc. Instrum & Methods Phys. Res., Section B: Beam Interactions with Materials and Atoms* 127-128 (1997) 553-556
- [64] L. A. Gea, L.A. Boatner, *Appl. Phys. Lett.* 68 (22) (1996) 3081-3083
- [65] B. W. Mwakikunga, E. Sideras-Haddad, A. Forbes, C. Arendse, *Physica Status Solidi (A) Applications and Materials* 205 (1) (2008) 150-154
- [66] B. W. Mwakikunga, A. Forbes, E. Sideras-Haddad, R M Erasmus, G. Katumba, B. Masina, *Int. J. Nanoparticles* 1 (2008) 3
- [67] B. W. Mwakikunga, E. Sideras-Haddad, C. Arendse and A. Forbes, *Can universal conductance fluctuations (UCFs) be observed at temperatures above room temperature at nanoscale?*, *OAtube Nanotechnol.* 2, 109 (2009) <http://www.oatube.org/2009/01/bwmwakikunga.html>
- [68] C. S. Blackman, C. Piccirillo, R. Binions, I. P. Parkin, *Thin Solid Films* Article in Press (2009)
- [69] R. Binions, C. Piccirillo, R. G. Palgrave, I. P. Parkin, *Chem. Vapor Deposition* 14 (1-2) (2008) 33-39
- [70] M. B. Sahana, M. S. Dharmapakash, S. A.. Shivashankar, *J. Mater. Chem.* 12 (2) (2002) 333-338
- [71] J. Nag, R. F. Haglund Jr., *J. Phys. Condensed Matter* 20 (26) 2008 art. no. 264016
- [72] Y. Nihei, Y. Sasakawa, K. Okimura, *Thin Solid Films* 516 (11) (2008) 3572-3576
- [73] C. Piccirillo, R. Binions, I. P. Parkin, *Thin Solid Films* 516 (8) (2008) 1992-1997
- [74] D. Vernardou, M. E. Pemble, D. W. Sheel, *Thin Solid Films* 515 (2007) 8768-8770
- [75] J.-M. Chen, Z.-L. Huang, Y. Liu, S.-G. Wang, *J. Functional Materials* 38 (5) (2007) 743-745+749
- [76] I. P. Parkin, T. D. Manning, *J. Chem. Ed.* 83 (3) (2006) 393-400
- [77] T. D. Manning, I. P. Parkin, C. Blackman, U. Qureshi, *J. Mater Chem* 15 (42) (2005) 4560-4566
- [78] D. Vernardou, M. E. Pemble, D. W. Sheel, *Surf. & Coatings Technol.* 188-189 (2004) 250-254
- [79] T. D. Manning, I. P. Parkin, M. E. Pemble, D. Sheel, D. Vernardou, *Chem. Mater.* 16 (4) (2004) 744-749
- [80] K. Kato, P. K. Song, H. Odaka, Y. Shigesato, *Japanese J. Appl. Phys., Part 1: Regular Papers and Short Notes and Review Papers* 42 (10) (2003) 6523-6531
- [81] M. B. Sahana, G. N. Subbanna, S.A. Shivashankar, *J. Appl. Phys.* 92 (11) (2002) 6495-6504
- [82] F. Béteille, J. Livage, *J. Sol-Gel Sci. & Technol.* 13 (1-3) (1999) 915-921
- [83] C. M. Foster, R. P. Chiarello, H. L. M. Chang, H. You, T. J. Zhang, H. Frase, J. C. Parker, D. J. Lam, *J. Appl. Phys.* 73 (6) (1993) 2841-2847
- [84] T. Maruyama, Y. Ikuta, *J. Mater. Sci.* 28 (18) (1993) 5073-5078
- [85] H. M. Pinto, J. Correia, R. Binions, C. Piccirillo, I. P. Parkin, V. Teixeira, *Mater. Sci. Forum* 587-588 (2008) 640-644
- [86] C. Piccirillo, R. Binions, I. P. Parkin, *Synthesis and characterisation of W-doped VO<sub>2</sub> by Aerosol Assisted Chemical Vapour Deposition* *Thin Solid Films* 516 (8) (2008) 1992-1997
- [87] C. Piccirillo, R. Binions, I. P. Parkin, *Eur. J. Inorganic Chem.* (25) (2007) 4050-4055
- [88] P. Evans, M. E. Pemble, D. W. Sheel, H. M. Yates, *J. Photochem. & Photobiol. A: Chemistry* 189 (2-3) (2007) 387-397
- [89] T. D. Manning, I. P. Parkin, C. Blackman, U. Qureshi, *J. Mater. Chem.* 15 (42), (2005) 4560-4566
- [90] T. D. Manning, I. P. Parkin, *Polyhedron* 23 (18), (2004) 3087-3095
- [91] Ch. V. Subba Reddy, E. H. Walker Jr., S. A. Wicker Sr., Q. L. Williams, R. R. Kalluru, *Current Appl. Phys.* Article in Press (2009)
- [92] C. Cao, Y. Gao, H. Luo, *J. Phys. Chem. C* 112 (48) (2008) 18810-18814
- [93] X. Li, X. Chen, X. Chen, C. Han, C. Shi, *J. Cryst. Growth* 309 (1) (2007) 43-47
- [94] J. Park, I. H. Oh, E. Lee, K. W. Lee, C. E. Lee, K. Song, Y.-J Kim, *Applied Physics Letters* 91 (15) (2007) art no 153112
- [95] K.-F. Zhang, X. Liu, Z.-X Su, H.-L. Li, *Materials Letters* 61 (13) (2007) 2644-2647
- [96] F. Sediri, N. Gharbi, *Mater. Sci. & Eng. B: Solid-State Materials for Advanced Technology* 139 (1) (2007) 114-117
- [97] M. Luo, J. Gao, X. Zhang, D. Ouyang, J. Yang, J. Zhu, *Key Eng. Mater.* 336-338 III (2007) 2021-2023

- [98] M. Wei, Z.-M. Qi, M. Ichihara, M. Hirabayashi, I. Honma, H. Zhou, *J. Cryst. Growth* 296 (1) (2006) 1-5
- [99] F. Sediri, F. Touati, N. Gharbi, *Mater. Sci. & Eng. B: Solid-State Materials for Advanced Technology* 129 (1-3) (2006) 251-255
- [100] W. Chen, J. Peng, L. Mai, H. Yu, Y. Qi, *Solid State Commun.* 132 (8) (2004) 513-516
- [101] W. Chen, J. Peng, L. Mai, H. Yu, Y. Qi, *Chem. Lett.* 33 (10) art. no. CL-040820 (2004) 1366-1367
- [102] J. Liu, Q. Li, T. Wang, D. Yu, Y. Li, *Angewandte Chemie - International Edition* 43 (38) (2004) 5048-5052
- [103] L. Mai, W. Chen, Q. Xu, J. Peng, Q. Zhu, *International J. Nanoscience* 3 (3), (2004) 225-231
- [103] W. Chen, J.-F. Peng, L.-Q. Mai, Q. Xu, Q.-Y. Zhu, *Chinese J. Inorganic Chem.* 20 (2) (2004) 147-151
- [105] M. S. Whittingham, R. Chen, T. Chirayil, P. Zavalij, *Solid State Ionics* 94 (1-4) (1997) 227-238
- [106] T. A. Chirayil, P. Y. Zavalij, M. S. Whittingham, *J. Electrochem. Soc.* 143 (9) (1996) L193-L195
- [107] Y. Oka, T. Yao, N. Yamamoto, *J. Mater Chem* 1 (5) (1991) 815-818
- [108] Y. Oka, T. Yao, N. Yamamoto, *J. Solid State Chem* 86 (1) (1990) 116-124 24
- [109] Y. Oka, T. Ohtani, N. Yamamoto, T. Takada, *J. Ceram. Soc. Japan* 97 (10) (1989) 1134-1137
- [110] H. Kakiuchida, P. Jin, M. Tazawa, *International J. Thermophysics*, (2009) 1-8 Article in Press
- [111] T. Ben-Messaoud, G. Landry, J. P. Gariépy, B. Ramamoorthy, P. V. Ashrit, A. Haché, *Opt. Commun.* 281 (24) (2008) 6024-6027
- [112] C. Ko, S. Ramanathan, *J. Appl. Phys.* 104 (8) (2008) art. no. 086105
- [113] H. Kakiuchida, P. Jin, M. Tazawa, *Solar Energy Mater. & Solar Cells* 92 (10) (2008) 1279-1284
- [114] J. Dai, X.-Z. Wang, S.-W. He, Y. Huang, X.-J. Yi, *J. Infrared & Millimeter Waves* 27 (5) (2008) 374-377
- [115] X.-J. Wang, C.-J. Liang, K.-P. Guan, D.-H. Li, Y.-X. Nie, S.-O. Zhu, F. Huang, Z.-W. Cheng, *Chinese Phys. B* 17 (9) (2008) 3512-3515
- [116] Y. Shin, J. Moon, H. Ju, C. Park, *J. Korean Phys Soc* 52 (6) (2008) 1828-1831
- [117] J. Liang, M. Hu, Z. Liu, L. Han, T. Chen, *Transactions Tianjin Univer.* 14 (3) (2008) 173-177
- [118] J. B. K. Kana, J. M. Ndjaka, P. O. Ateba, B. D. Ngom, N. Manyala, O. Nemraoui, A. C. Beye, M. Maaza, *Appl. Surf. Sci.* 254 (13) (2008) 3959-3963
- [119] C. Chen, J. Wang, Q. Chen, Y. Fang, X. Wang, *J. Vac. Sci. & Technol.* 28 (2) (2008) 153-158
- [120] Y. Nihei, Y. Sasakawa, K. Okimura, *Thin Solid Films* 516 (11), (2008) 3572-3576
- [121] S. J. Yun, J. W. Lim, B.-G. Chae, B. J. Kim, H.-T. Kim, *Physica B: Condensed Matter* 403 (5-9) (2008) 1381-1383
- [122] X.-B. Wei, Z.-M. Wu, X.-D. Xu, J.-J. Tao-Wang, J.-J. Tang, W.-Z. Li, Y.-D. Jiang, *J. Phys. D: Applied Physics* 41 (5) (2008) art. no. 055303
- [123] X. Tian, J. Liu, L. Li, J. Liu, Q. Wang, *Chinese Journal of Lasers* 35 (2008) 161-163
- [124] Z.-F. Tang, J. Zhao, H. Wei, Z.-F. Zhang, *J. Synthetic Cryst.* 37 (1) (2008) 88-92
- [125] R. Balu, P. V. Ashrit, *Appl. Phys. Lett.* 92 (2) (2008) art. no. 021904
- [126] D. Ruzmetov, K. T. Zawilski, V. Narayanamurti, S. Ramanathan, *J. Appl. Phys.* 102 (11) (2007) art. no. 113715
- [127] K. Okimura, Y. Nihei, Y. Sasakawa, *Diffusion and Defect Data Pt. B: Solid State Phenomena* 124-126 (PART 1) (2007) 703-706
- [128] S. He, Y. Huang, J. Dai, J. Lai, X. Wang, X. Yi, *Chinese Journal of Materials Research* 21 (6) (2007) 609-612
- [129] S. Saitzek, F. Guinneton, L. Sauques, K. Aguir, J.-R. Gavarrí, *Thermochromic Opt. Mater.* 30 (3) (2007) 407-415
- [130] K. Okimura, N. Kubo, *Thin Solid Films* 515 (12) (2007) 4992-4995
- [131] Y. L. Wang, M. C. Li, L. C. Zhao, *Surf. & Coatings Technol.* 201 (15) (2007) 6772-6776
- [132] S. Chen, H. Ma, J. Dai, X. Yi, *Applied Physics Letters* 90 (10), art. no. 101117 (2007)
- [133] H. Kakiuchida, P. Jin, S. Nakao, M. Tazawa, *Japanese J. Applied Physics, Part 2: Letters* 46 (4-7) (2007) L113-L116

- [134] H. Kakiuchida, P. Jin, M. Okada, M. Tazawa, Japanese J. Appl. Phys., Part 1: Regular Papers and Short Notes and Review Papers 46 (2) (2007) 621-626
- [135] K. Okimura, Y. Sasakawa, Y. Nihei, Japanese J. Appl. Phys., Part 1: Regular Papers and Short Notes and Review Papers 45 (12) (2006) 9200-9202
- [136] L. Wang, J. Li, X. Gao, X. He, Prog. Natural Sci. 16 (11) (2006) 1193-1197
- [137] H. Miyazaki, I. Yasui, Applied Surface Science 252 (23) (2006) 8367-8370
- [138] N. R. Mlyuka, R. T. Kivaisi, J. Mater. Sci. 41 (17) (2006) 5619-5624
- [139] L.-X. Wang, J.-P. Li, X.-L. He, X.-G. Gao, Acta Physica Sinica 55 (6), (2006) 2846-2851
- [140] N. Shen, Y. Li, X.-J. Yi, J. Infrared & Millimeter Waves 25 (3) (2006) 199-202
- [141] Y.-Q. Luo, W.-P. Wang, F. Luo, High Power Laser & Particle Beams 18 (5) (2006) 713-716
- [142] X.-S. Tian, J.-C. Liu, L.-J. Li, Q. Wang, Chinese J. Lasers 33 (2006) 327-329
- [143] H.-T. Yuan, K.-C. Feng, X.-H. Zhang, J. Functional Mater. 37 (2) (2006) 241-242+246
- [144] H. Wang, X. Yi, S. Chen, Infrared Phys. & Technol. 47 (3) (2006) 273-277
- [145] H. Wang, X. Yi, Y. Li, Fabrication of VO<sub>2</sub> films with low transition temperature for optical switching applications, Optics Communications 256 (4-6) (2005) 305-309
- [146] Y. Li, X. Yi, T. Zhang, Chinese Optics Letters 3 (12) (2005) 719-721
- [147] D. Brassard, S. Fourmaux, M. Jean-Jacques, J. C. Kieffer, M. A. El Khakani, Appl. Phys. Lett. 87 (5) (2005) art. no. 051910
- [148] H. Wang, X. Yi, S. Chen, X. Fu, Sensors and Actuators, A: Physical 122 (2005) 108-112
- [149] N. Y. Shishkin, A. A. Komarov, D. V. Kosov, V. A. Cherkasov, L. A. Bashkirov, U. Bardi, Y. K. Gunko, Sensors and Actuators, B: Chemical 108 (2005) 113-118
- [150] G. Xu, P. Jin, M. Tazawa, K. Yoshimura, Appl. Surf. Sci. 244 (1-4) (2005) 449-452
- [151] S.-B. Zhou, S.-B. Wang, S.-H. Chen, X.-J. Yi, Infrared & Laser Eng. 34 (1) art. no. 1007-2276(2005)01-0027-04 (2005) 27-30
- [152] F. Guinneton, L. Sauques, J.-C. Valmalette, F. Cros, J.-R. Gavarrı, J. Phys. Chem. Solids 66 (1) (2005) 63-73
- [153] S. Chen, H. Ma, X. Yi, T. Xiong, H. Wang, C. Ke, Sensors and Actuators, A: Physical 115 (1), (2004) 28-31
- [154] S. Chen, H. Ma, X. Yi, H. Wang, X. Tao, M. Chen, X. Li, C. Ke, Infrared Phys. & Technol. 45 (4), (2004) 239-242
- [155] G. Xu, P. Jin, M. Tazawa, K. Yoshimura, Solar Energy Mater. & Solar Cells 83 (1) (2004) 29-37
- [156] S. Saitzek, G. Guirleo, F. Guinneton, L. Sauques, S. Villain, K. Aguir, C. Leroux, J.-R. Gavarrı, Thin Solid Films 449 (1-2) (2004) 166-172
- [157] F. Guinneton, L. Sauques, J.-C. Valmalette, F. Cros, J.-R. Gavarrı, Thin Solid Films 446 (2) (2004) 287-295
- [158] S. Chen, X. Yi, H. Ma, T. Xiong, H. Wang, C. Ke, Int. J. Infrared & Millimeter Waves 25 (1) (2004) 157-163
- [159] H.-T. Yuan, K.-C. Feng, X.-J. Wang, C. Li, C.-J. He, Y.-X. Nie, Chinese Phys. 13 (1) (2004) 82-84
- [160] S. Chen, X. Yi, H. Ma, H. Wang, X. Tao, M. Chen, C. Ke, Opt. Quant. Electronics 35 (15) (2003) 1351-1355
- [161] K. Kato, P. K. Song, H. Odaka, Y. Shigesato, Japanese J. Applied Physics, Part 1: Regular Papers and Short Notes and Review Papers 42 (10) (2003) 6523-6531
- [162] P. Jin, G. Xu, M. Tazawa, K. Yoshimura, Appl. Phys. A: Materials Science and Processing 77 (3-4) (2003) 455-459
- [163] K.-Y. Tsai, T.-S. Chin, H.-P.D. Shieh, Japanese J. Appl. Phys., Part 1: Regular Papers and Short Notes and Review Papers 42 (7 A) (2003) 4480-4483
- [164] X. Yi, C. Chen, L. Liu, Y. Wang, B. Xiong, H. Wang, S. Chen, Infrared Phys. Technol. 44 (2) (2003) 137-141
- [165] X. Yi, S. Chen, Y. Wang, B. Xiong, H. Wang, Int. J. Infrared & Millimeter Waves 23 (12) (2002) 1699-1704
- [166] J.-H. Li, N.-Y. Yuan, H. L. W. Chan, C.-L. Lin, Acta Physica Sinica 51 (8) (2002) 1792



- [167] D. Zintu, G. Tosone, A. Mercuri, *Infrared Phys. Technol.* 43 (3-5) (2002) 245-250
- [168] M.-H. Lee, *Solar Energy Mater. & Solar Cells* 71 (4), (2002) 537-540
- [169] T. J. Hanlon, R. E. Walker, J. A. Coath, M. A. Richardson, *Thin Solid Films* 405 (2002) 234-237
- [170] F. Guinneton, L. Sauques, J. C. Valmalette, F. Cros, J. R. Gavarrí, *J. Phys. Chem. Solids* 62 (7) (2001) 1229-1238
- [171] C. H. Chen, X. J. Yi, J. Zhang, B. F. Xiong, *J. Infrared & Millimeter Waves* 20 (2) (2001) 136-138
- [172] M.-H. Lee, J.-S. Cho, *Thin Solid Films* 365 (1) (2000) 5-6
- [173] R. T. Kivaisi, M. Samiji, *Solar Energy Mater. & Solar Cells* 57 (2) (1999) 141-152
- [174] H. Miyazaki, M. Kamei, Y. Shigesato, I. Yasui, *Japanese J. Appl. Phys., Part 1: Regular Papers and Short Notes and Review Papers* 38 (1) (1999) 186-191
- [175] W. Burkhardt, T. Christmann, B. K. Meyer, W. Niessner, D. Schalch, A. Scharmann, *Thin Solid Films* 345 (2) (1999) 229-235
- [176] C. Petit, J.-M. Frigerio, M. Goldmann, *J. Phys. Condensed Matter* 11 (16) (1999) 3259-3264
- [177] M.A. Richardson, J. A. Coath, *Optics and Laser Technology* 30 (2) (1998) 137-140
- [178] J. Cui, D. Da, W. Jiang, *Appl. Surf. Sci.* 133 (3) (1998) 225-229
- [179] A. P. Gruzdeva, V. Y. Zerov, O. P. Konovalova, Y. V. Kulikov, V. G. Malyarov, I. A. Khrebtov, I. I. Shaganov, *J. Opt. Technol. (A Translation of Opticheskii Zhurnal)* 64 (12), (1997) 1110-1113
- [180] T. Christmann, B. Felde, W. Niessner, D. Schalch, A. Scharmann, *Thin Solid Films* 287 (1-2) (1996) 134-138
- [181] P. Jin, S. Tanemura, *Japanese J. Appl. Phys., Part 1: Regular Papers and Short Notes and Review Papers* 33 (3 A), (1994) pp. 1478-1483 44
- [182] K. A. Khan, M. S. Rahman Khan, *Pramana* 38 (4) (1992) 389-396
- [183] T. E. Phillips, R. A. Murphy, T. O. Poehler, *Mater. Res. Bulletin* 22 (8), (1987) 1113-1123
- [184] G. V. Jorgenson, J. C. Lee, *Solar Energy Mater.* 14 (3-5) (1986) 205-214
- [185] R. G. Cope, A. W. Penn, *J. Physics D: Applied Physics* 1 (2), art. no. 304 (1968) 161-168
- [186] E. N. Fuls, D. H. Hensler, A. R. Ross, *Appl. Phys. Lett.* 10 (7) (1967) 199-201
- [187] D. L. Zhang, G. Adam, *Mater. Sci. Forum* 386-388, (2002) 293-298
- [188] J. L. G. Fierro, L. A. Gambaro, A. R. González-Elípe, J. Soria, *Colloids and Surfaces* 11 (1-2) (1984) 31-38
- [189] N. J. Ali, P. A. Gillespie, W. R. Mcwhinnie, *Polyhedron* 9 (7) (1990) 999-1007
- [190] K. L. Kavanagh, H. M. Maguib, *Thin Solid Films* 91 (3) (1982) 231-240
- [191] J. Yan, W. Huang, Y. Zhang, X. Liu, M. Tu, *Physica Status Solidi (A) Applications and Materials* 205 (10) (2008) 2409-2412
- [192] Y. Jiazhen, Z. Yue, H. Wanxia, T. Mingjin, *Thin Solid Films* 516 (23) (2008) 8554-8558
- [193] J. Nag, R. F. Haglund Jr., *J. Phys. Condensed Matter* 20 (26) (2008) art. no. 264016
- [194] J. Yan, W. Huang, Y. Zhang, X. Liu, M. Tu, *Rare Metal Mater. & Eng.* 37 (5) (2008) 819-822
- [195] O. Y. Berezina, A. A. Velichko, L. A. Lugovskaya, A. L. Pergament, G. B. Stefanovich, D. V. Artyukhin, A. N. Strelkov, *Technical Phys. Lett.* 33 (7) (2007) 552-555
- [196] O. Y. Berezina, A. A. Velichko, L. A. Lugovskaya, A. L. Pergament, G. B. Stefanovich, *Inorganic Mater.* 43 (5), (2007) 505-511
- [197] Z. Li, D. Cao, K. Zhou, *Rare Metal Materials and Engineering* 35 (2006) 316-320
- [198] I. P. Parkin, T. D. Manning, *J. Chem. Ed.* 83 (3) (2006) 393-400
- [199] L. Mai, W. Chen, W., Xu, Q., Peng, J., Zhu, Q. *Int. J. Nanosci.* 3 (3) (2004) 225-231
- [200] S. Xu, H. Ma, S. Dai, Z. Jiang, *J. Mater. Sci.* 39 (2), (2004) 489-493
- [201] T. J. Hanlon, J. A. Coath, M. A. Richardson, *Thin Solid Films* 436 (2) (2003) 269-272
- [202] S. -Q. Xu, H. -P. Ma, S. -X. Dai, Z. -H. Jiang, *Chinese Phys. Letts.* 20 (1) (2003) 148-150
- [203] T. J. Hanlon, R. E. Walker, J. A. Coath, M. A. Richardson, *Thin Solid Films* 405 (2002) 234-237
- [204] I. Takahashi, M. Hibino, T. Kudo, *Japanese J. Appl. Phys., Part 1: Regular Papers and Short Notes and Review Papers* 40 (3 A) (2001) 1391-1395
- [205] T. Mori, K. Kawano, N. Oda, *Key Eng. Mater.* (181-182) (2000) 117-120
- [206] F. Bêteille, J. Livage, *J. Sol-Gel Sci. & Technol.* 13 (1999) 915-921
- [207] S. Lu, L. Hou, F. Gan, *Thin Solid Films* 353 (1999) 40-44

- [208] B. W. Mwakikunga, E. Sideras-Haddad, C. Arendse, A. Forbes, P. C. Eklund, T. Malwela, T. K. Hillie, S. Sinha-Ray, *Nano Lett* (2009) (unpublished)
- [209] J. B. MacChesney, J.F. Potter and H.J. Guggenheim, *J. Electrochem. Soc.* **115** (1968) 52-55.
- [210] Jianqiu Shi, Shuxue Zhou, Bo You and Limin Wu, *Sol. Energy Mater. Sol. Cells* **91** (2007) 1856-1862.
- [211] A. Romanyuk, R. Steiner, L. Marot and P. Oelhafen, *Sol. Energy Mater. Sol. Cells* **91** (2007) 1831-1835.
- [212] Y. Jiazhen, Z. Yue, H. Wanxia, T. Mingjin, *Thin Solid Films* **516** (2008), 8554-8558.
- [213] H. Kakiuchida, P. Jin, M. Tazawa, *Thin Solid Films* **516** (2008) 4563-4567.
- [214] I. Tsuyumoto, K. Nawa, *Solid State Ionics* **179** (2008) 1227-1229.
- [215] H. Suzuki, K. Yamaguchi, H. Miyazaki, *Composites Sci. & Technol.* **67** (2007) 3487-3490.
- [216] S. Papaefthimiou, E. Syrakou and P. Yianoulis, *Energy and Buildings* **41** (2009) 17-26.
- [217] L. Peeters, R. de Dear, J. Hensen and W. D'haeseleer, *Applied Energy* **86** (2009) 772-780.
- [218] A. M. Nilsson and A. Roos, *Thin Solid Films* **517** (2009) 3173-3177.
- [219] A. Picollo and F. Simone, *Building & Environment* **44** (2009) 1171-1180.
- [220] F. X. Gan, *Thin Solid Films* **502** (2006) 4-8.
- [221] W. R. Roach, *Appl. Phys. Lett.* **19** (1971) 453
- [222] A. W. Smith, *Appl. Phys. Lett.* **23** (1973) 437
- [223] D. D. Eden, *Opt. Eng.* **20** (1981) 337
- [224] M. Fukuma, S. Zembutsu, S. Miyazam, *Appl. Opt.* **22** (2) (1983) 265
- [225] M. F. Becker, A. B. Buckman, R. M. Walser, T. Lepine, P. Georges, A. Brun, *Appl. Phys. Lett.* **65** (1994) 1507
- [226] J. Hiltunen, PhD Thesis, University of Joensuu, ISSN 1458-5332, ISBN 952-458-077-2 (2002)
- [227] W. Hayes, A. M. Stoneham, *Defects and Defect Processes in Non-Metallic Solids* (Wiley & Sons, NY) (1991)
- [228] J. M. Reyes, J. R. Marko, M. Sayer, *Solid State Commun.* **13** (1973) 1953-1957